C 55.612:175/v.2

U.S. DEPARTMENT OF COMMERCE

National Oceanic and Atmospheric Administration

COLLECTED REPRINTS-1975

Volume II

PENNSYLVANIA STATE UNIVERSITY
MAY 5 1977
DOCUMENTS COLLECTION

ATLANTIC OCEANOGRAPHIC AND METEOROLOGICAL LABORATORIES

Digitized by the Internet Archive
in 2012 with funding from
LYRASIS Members and Sloan Foundation

http://archive.org/details/collectedreprint1975atla

U.S. DEPARTMENT OF COMMERCE
Juanita M. Kreps, Secretary

NATIONAL OCEANIC AND ATMOSPHERIC ADMINISTRATION
Robert M. White, Administrator
ENVIRONMENTAL RESEARCH LABORATORIES
Wilmot N. Hess, Director

Collected Reprints-1975
Volume II

ATLANTIC OCEANOGRAPHIC AND METEOROLOGICAL LABORATORIES

ISSUED FEBRUARY 1977
Boulder, Colorado

Atlantic Oceanographic and Meteorological Laboratories
Miami, Florida 33149

For sale by the Superintendent of Documents, U. S. Government Printing Office, Washington, D. C. 20402

U. S. Depository Copy

FOREWORD

This is the tenth annual publication of the collected reprints of NOAA's Atlantic Oceanographic and Meteorological Laboratories. It brings together our research results published during 1975 in a wide range of scientific and technical journals as well as in some internal NOAA publications. Although the generation of new knowledge is of itself satisfying to the researcher who does it, the usefulness to others is largely a function of how well the knowledge is disseminated. For this reason, our collected reprints receive a wide distribution to the libraries of universities, research institutions, and government agencies in this country and abroad.

The Atlantic Oceanographic and Meteorological Laboratories conduct research on the physical, chemical, and geological characteristics and processes of the ocean waters, the seafloor, and the overlying atmosphere. During 1975, these research efforts were carried out by four major groups:

Physical Oceanography Laboratory
Marine Geology and Geophysics Laboratory
Sea-Air Interaction Laboratory
Ocean Remote Sensing Laboratory

The reprints in this volume are arranged alphabetically by the last name of the first author within each of these groups.

Harris B. Stewart, Jr.
Director, AOML

Atlantic Oceanographic and
Meteorological Laboratories
15 Rickenbacker Causeway
Virginia Key
Miami, Florida 33149, U.S.A.

CONTENTS

VOLUME I

Page No.

GENERAL

1. Stewart, H. B., Jr.

   Bologna Workshop on Marine Science-Concluding Observations. Report of the Marine Science Workshop held by the Johns Hopkins University, Bologna, Italy, October 15-19, 1973, Annex D, 73-78. 1

2. Stewart, H. B., Jr.

   Book Review: Handbook of Marine Science, Volume I and II. *Sea Frontiers 21*, No. 1, 58. 7

3. Stewart, H. B. Jr.

   The National Oceanic and Atmospheric Administration and the Outer Continental Shelf. Proc. of the Estuarine Research Federation, OCS Conference and Workshop, Marine Environmental Implications of Offshore Oil and Gas Development in the Baltimore Canyon Region of the Mid-Atlantic Coast, VIMS, Wachapreague, Virginia, 27-38. 8

PHYSICAL OCEANOGRAPHY LABORATORY

4. Beardsley, R. C., W. C. Boicourt, and D. V. Hansen.

   Physical Oceanography of the Middle Atlantic Bight. Proc. of Special Symposium, "The Middle Atlantic Continental Shelf and the New York Bight," American Museum of Natural History, New York City, 3-4-5 November 1975, 1 p. 20

5. Brown, W., W. Munk, F. Snodgrass, H. Mofjeld, and B. Zetler.

   MODE Bottom Experiment. *Journal of Physical Oceanography 5*, No. 1, 75-85. 21

6. Charnell, R. L. (Editor), D. A. Mayer, D. V. Hansen, D. Swift, A. Cok, D. Drake, G. Freeland, W. Lavelle, T. McKinney, T. Nelson, R. Permenter, W. Stubblefield, D. Segar, P. Hatcher, G. Berberian, L. Kiester, M. Weiselberg.

   Assessment of Offshore Dumping in the New York Bight, Technical Background: Physical Oceanography, Geological Oceanography, Chemical Oceanography. NOAA Technical Report ERL 332-MESA 3, 83 p. 32

7. Charnell, R. L., and D. A. Mayer.

Water Movement Within the Apex of the New York Bight During Summer and Fall of 1973. NOAA Technical Memorandum ERL MESA-3, 32 p. 122

8. Chew, F.

The Interaction Between Curvature and Lateral Shear Vorticities in a Mean and an Instantaneous Florida Current, A Comparison. *Tellus XXVII*, No. 6, 606-618. 154

9. Gordon, H. R. and W. R. McCluney.

Estimation of the Depth of Sunlight Penetration in the Sea for Remote Sensing. *Applied Optics 14*, 413-416. 167

10. Hansen, D. V.

Review of: Progress in Oceanography, Volume 6. Edited by B. A. Warren, Pergamon Press, New York. *Bulletin of the American Meteorological Society 56*, No. 9, 997-998. 171

11. Hazelworth, J. B., B. L. Kolitz, R. B. Starr, R. L. Charnell, G. A. Berberian, and M. A. Weiselberg.

New York Bight Project, Water Column Sampling Cruises #6-8 of the NOAA Ship FERREL, April-June 1974. NOAA Data Report MESA-1, 177 pages. * 172

12. Hazelworth, J. B., and R. B. Starr.

Oceanographic Conditions in the Caribbean Sea During the Summer of 1971. NOAA Technical Report ERL 344-AOML 20, 144 p. 200

13. Hazelworth, J. B., B. L. Kolitz, R. B. Starr, R. L. Charnell, G. A. Berberian, and M. A. Weiselberg.

New York Bight Project, Water Column Sampling Cruises 9-12, of the NOAA Ship FERREL, July-November 1974. NOAA Data Report ERL MESA-3, 234 p.** 347

14. Kirwan, A. D., Jr., G. McNally, M. S. Chang, and R. Molinari.

The Effect of Wind and Surface Currents on Drifters. *Journal of Physical Oceanography 5*, No. 2, 361-368. 348

*Text only; pp. 26-177 are station data.
**Abstract only; complete text on microfiche.

15. Maul, G. A.

Circulation of the Eastern Gulf of Mexico and Its Possible Relation to Red Tides. Proc. of the Florida Red Tide Conference, Florida Marine Research Publication, Florida Department of Natural Resources, Marine Research Laboratory, Sarasota, Florida, October 10-12, No. 8, 9-10. 356

16. Maul, G. A.

An Evaluation of the Use of the Earth Resources Technology Satellite for Observing Ocean Current Boundaries in the Gulf Stream System. NOAA Technical Report ERL 335-AOML 18, 125 p. 357

17. Maul, G. A. and S. R. Baig.

A New Technique for Observing Mid-Latitude Ocean Currents from Space. Proc. of the American Society of Photogrammetry, 41st Annual Meeting, Washington, D. C., March 9-14 1975, 713-716. 485

18. Maul, G. A. and H. R. Gordon.

On the Use of the Earth Resources Technology Satellite (LANDSAT-1) in Optical Oceanography. *Remote Sensing of Environment 4*, No. 2, 95-128. 489

19. Mayer, D. A.

Examination of Water Movement in Massachusetts Bay. NOAA Technical Report ERL 328-AOML 17, 46 p. 523

20. Mayer, D. A. and D. V. Hansen

Observations of Currents and Temperatures in the Southeast Florida Coastal Zone During 1971-1972. NOAA Technical Report ERL 346-AOML 21, 36 p. 572

21. Mofjeld, H. O. and M. Rattray, Jr.

Barotropic Rossby Waves in a Zonal Current: Effects of Lateral Viscosity. *Journal of Physical Oceanography 5*, No. 3, 421-429. 611

22. Mofjeld, H. O.

Empirical Model for Tides in the Western North Atlantic Ocean. NOAA Technical Report ERL 340-AOML 19, 24 p. 620

23. Molinari, R. L.

A Comparison of Observed and Numerically Simulated Circulation in the Cayman Sea. *Journal of Physical Oceanography 5*, No. 1, 51-62. 647

24. Molinari, R. L. and A. D. Kirwan, Jr.

Calculations of Differential Kinematic Properties from Lagrangian Observations in the Western Caribbean Sea. *Journal of Physical Oceanography 5*, No. 3, 483-491. 659

25. Segar, D. A. and A. Y. Cantillo.

Direct Determination of Trace Metals in Seawater by Flameless Atomic Absorption Spectrophotometry. *Advances in Chemistry Series, Number 147, Analytical Methods in Oceanography*, 56-81. 668

26. Segar, D. A. and G. A. Berberian.

Trace Metal Contamination by Oceanographic Samplers. A Comparison of Various Niskin Samplers and a Pumping System. *Advances in Chemistry Series, Number 147, Analytical Methods in Oceanography*, 9-15. 694

27. Zetler, B., W. Munk, H. Mofjeld, W. Brown, and F. Dormer.

MODE Tides. *Journal Physical Oceanography 5*, No. 3, 430-441. 701

VOLUME II

MARINE GEOLOGY AND GEOPHYSICS LABORATORY

28. Ballard, R. D., W. B. Bryan, J. R. Heirtzler, G. Keller, J. G. Moore, and T. van Andel.

Manned Submersible Observations in the FAMOUS Area: Mid-Atlantic Ridge. *Science 190*, 103-108. 713

29. Dietz, R. S., J. F. McHone, and N. M. Short.

Oman Ring: Suspected Astrobleme. *Meteoritics 10*, No. 4, 393. 719

30. Freeland, G. L. and D. J. P. Swift.

New York Alternative Dumpsite Assessment-Reconnaissance Study of Surficial Sediments. IX International Congress of Sedimentology; Nice, France, Theme 10, 13-18. Also appeared in Offshore Technology Conference, Paper #OTC 2385, 505-511. 720

31. Freeland, G. L., D. J. P. Swift, W. L. Stubblefield, and A. E. Cok.

Surficial Sediments of NOAA-MESA Study Areas in the New York Bight. Mid-Atlantic Shelf/New York Bight ASLO Symposium, 24-25. 727

32. Gadd, P. E., J. W. Lavelle, and D. J. P. Swift.

Calculations of Sand Transport on the New York Shelf Using Near-Bottom Current Meter Observations. *American Geophysical Union, Fall Annual Meeting 56,* No. 12, 1003. 729

33. Hatcher, P. G. and L. E. Keister.

Carbohydrates and Organic Carbon in the New York Bight Sediments as Possible Indicators of Sewage Contamination. Mid-Atlantic Shelf/New York Bight ASLO Symposium, 31-33. 730

34. Hatcher, P. G., B. R. Simoneit, and S. M. Gerchakov.

Mangrove Lake, Bermuda; Its Sapropelic Sedimentary Environment. Seventh International Meeting on Organic Geochemistry, Madrid, Spain, 61. 733

35. Hulbert, M. H. and R. H. Bennett.

Electrostatic Cleaning Technique for Fabric SEM Samples. *Clays and Clay Minerals 23,* 331-335. 734

36. Kearey, P., G. Peter, and G. K. Westbrook.

Geophysical Maps of the Eastern Caribbean. *Journal of the Geological Society 131*, 311-321. 739

37. Keller, G. H.

Sedimentary Processes in Submarine Canyons off Northeastern United States. IX International Congress of Sedimentology, Nice, France, Theme 6, 77-80. 750

38. Keller, G. H.

Book Review: The Ocean Basins and Margins - Volume 2: The North Atlantic. Edited by A.E.M. Nairn and F.G. Stehli, Plenum Publ., New York. *Marine Geotechnology 1,* No. 1, 159-161. 757

39. Keller, G. H. and L. L. Minter.

Cariaco Trench - Sediment Geotechnical Properties. *Journal of Sedimentary Petrology 45,* No. 1, 292-294. 760

40. Keller, G. H., S. H. Anderson, and J. W. Lavelle.

Near-Bottom Currents in the Mid-Atlantic Ridge Rift Valley. *Canadian Journal of Earth Science 12,* No. 4, 703-710. 763

41. Lavelle, J. W., G. H. Keller, and T. L. Clarke.

Possible Bottom Current Response to Surface Winds in the Hudson Shelf Channel. *Journal of Geophysical Research 80,* No. 15, 1953-1956. 771

42. Lavelle, J. W., D. J. P. Swift, H. R. Brashear, and F. N. Case.

Tracer Observations of Sand Transport on the Long Island Inner Shelf. *American Geophysical Union, Fall Annual Meeting 56,* No. 12, 1003. 775

43. McGregor, B. A. and P. A. Rona.

Crest of the Mid-Atlantic Ridge at 26° N. *Journal of Geophysical Research 80,* No. 23, 3307-3314. 776

44. McGregor, B. A., G. H. Keller, and R. H. Bennett.

Seismic Profiles Along the U.S. Northeast Coast Continental Margin. *EOS 56,* No. 6, 382. 784

45. McHone, J. F., Jr. and R. S. Dietz.

Impact Structures on LANDSAT Imagery (Abstract). *Geological Society of America Annual Meetings, Abstracts with Programs 7,* No. 7, 1196. 785

46. Maupome, L., R. Alvarez, S. W. Kieffer, and R. S. Dietz.

On the Terrestrial Origin of the Tepexitl Crater, Mexico. *Meteoritics 10*, No. 3, 209-214. 786

47. Maupome, L., R. Alvarez, S. W. Kieffer, and R. S. Dietz.

Tepexitl Crater, Mexico: Not Meteoritic (Abstract). *Meteoritics 10*, No. 4. 454-455 792

48. Minter, L. L., G. H. Keller, and T. E. Pyle.

Morphology and Sedimentary Processes in and Around Tortugas and Agassiz Sea Valleys, Southern Straits of Florida. *Marine Geology 18,* 47-69. 793

49. Permenter, R. W., W. L. Stubblefield, and D. J. P. Swift.

Substrate Mapping by Sidescan Sonar. *Florida Scientist 38,* Supplement 1, 13-14. 816

50. Richards, A. F., K. Oien, G. H. Keller, and J. V. Lai.

Differential Piezometer Probe for an In Situ Measurement of Sea-Floor Pore-Pressure. *Geotechnique 25*, No. 2, 229-238. 817

51. Rona, P. A.

Book Review: Sonographs of the Sea Floor. *Journal of Geology 83*, No. 4, 536. 827

52. Rona, P. A.

Letters to the Editors: Minerals and Plate Tectonics. *Science 190*, No. 4213, 422. 828

53. Rona, P. A.

Relation of Offshore and Onshore Mineral Resources to Plate Tectonics. Proc. Offshore Technology Conference, Paper No. OTC 2317, 713-715. 829

54. Rona, P. A.

Salt Deposits of the Eastern and Western Atlantic (Abstract). Proc. International Symposium on Continental Margins of Atlantic Type, Brazil, 1-15. 833

55. Rona, P. A.

Viewpoint. *Encounter with the Earth*, edited by L. F. Laporte, Canfield Press, San Francisco, CA, 83-86. 834

56. Rona, P. A., B. A. McGregor, P. R. Betzer, G. W. Bolger, and D. C. Krause.

Anomalous Water Temperatures Over Mid-Atlantic Ridge Crest at 26° North Latitude. *Deep-Sea Research 22*, 611-618. 838

57. Scott, R. B., J. Malpas, G. Udintsev, and P. A. Rona.

Submarine Hydrothermal Activity and Seafloor Spreading at 26° N, MAR. *Geological Society of America, Abstracts with Programs 7*, No. 7, 1263. 846

58. Stubblefield, W. L. and R. W. Permenter.

Temporal and Spatial Substrate Variation in the New York Bight Apex. *Geological Society of America, Abstracts with Programs 7*, No. 7, 1285-1286. 847

59. Stubblefield, W. L., J. W. Lavelle, D. J. P. Swift, and T. F. McKinney.

Sediment Response to the Present Hydraulic Regime on the Central New Jersey Shelf. *Journal of Sedimentary Petrology 45*, No. 1, 337-358. 848

60. Swift, D. J. P.

Barrier-Island Genesis: Evidence From the Central Atlantic Shelf, Eastern U.S.A. *Sedimentary Geology 14*, 1-43 870

61. Swift, D. J. P.

Response of the Shelf Floor to Geostrophic Storm Currents, Middle Atlantic Bight of North America. Sedimentary Mechanics, IX International Congress of Sedimentology, Nice, France, Theme VI, 193-198. 913

62. Swift, D. J. P.

Tidal Sand Ridges and Shoal-Retreat Massifs. *Marine Geology 18*, 105-134. 921

63. Swift, D. J. P., G. L. Freeland, P. E. Gadd, J. W. Lavelle, and W. L. Stubblefield.

Morphologic Evolution and Sand Transport in the New York Bight. Mid-Atlantic Shelf/New York Bight ASLO Symposium, 65-66. 950

SEA-AIR INTERACTION LABORATORY

64. McLeish, W. L. and G. E. Putland.

The Initial Water Circulation and Waves Induced by an Airflow. NOAA Technical Report ERL 316-AOML 16, 45 p. 952

65. McLeish, W. and G. E. Putland.

Measurements of Wind-Driven Flow Profiles in the Top Millimeter of Water. *Journal of Physical Oceanography 5*, No. 3, 516-518. 999

66. Ostapoff, F., J. Proni and R. Sellers.

Preliminary Analysis of Ocean Internal Wave Observations by Acoustic Soundings. Preliminary Scientific Results of the GARP Atlantic Tropical Experiment, prepared by the International Scientific and Management Group (ISMG) of the World Meteorological Organization, Volume II, GATE Report No. 14, 392-397. 1002

67. Ross, D.

A Comparison of SKYLAB S-193 and Aircraft Views of Surface Roughness and a Look Toward SEASAT. Proceedings of the NASA Earth Resources Survey Symposium, Houston, Texas, June 1975, Vol. 1-C, 1911-1936. 1008

68. Stegen, G. R., K. Bryan, J. L. Held, and F. Ostapoff.

Dropped Horizontal Coherence Based on Temperature Profiles in the Upper Thermocline. *Journal of Geophysical Research 80*, No. 27, 3841-3847. 1034

OCEAN REMOTE SENSING LABORATORY

69. Apel, J. R.

Seasat: A Spacecraft Views the Marine Environment with Microwave Sensors. *Remote Sensing: Energy-Related Problems*, edited by Dr. T. Veziroglu, J. Wiley & Sons, 47-60. 1041

70. Apel, J. R., H. M. Byrne, J. R. Proni, and R. L. Charnell.

Observations of Oceanic Internal and Surface Waves from the Earth Resources Technology Satellite. *Journal of Geophysical Research 80*, No. 6, 865-881. 1055

71. Apel, J. R., J. R. Proni, H. M. Byrne, and R. L. Sellers.

Near-Simultaneous Observations of Intermittent Internal Waves on the Continental Shelf from Ship and Spacecraft. *Geophysical Research Letters 2*, No. 4, 128-131. 1072

72. Proni, J. R., and J. R. Apel.

On the Use of High-frequency Acoustics for the Study of Internal Waves and Microstructure. *Journal of Geophysical Research 80*, No. 9, 1147-1151. 1076

73. Proni, J. R., D. C. Rona, C. A. Lauter, Jr., and R. L. Sellers.

Acoustic Observations of Suspended Particulate Matter in the Ocean. *Nature 254*, No. 5499, 413-415. 1081

Reprinted from: *Science 190*, 103-108.

Manned Submersible Observations in the FAMOUS Area: Mid-Atlantic Ridge

Volcanic and tectonic processes associated with an active spreading center have been directly observed.

R. D. Ballard, W. B. Bryan, J. R. Heirtzler, G. Keller, J. G. Moore, Tj. van Andel

Project FAMOUS (French-American Mid-Ocean Undersea Study) was conceived three years ago, its objectives being to define the tectonic and volcanic processes associated with genesis of new oceanic crust. A small area on the Mid-Atlantic Ridge centered at about 36°50′N was selected for detailed study on the basis of scientific and logistic criteria (Fig. 1). More than 25 cruises were made to the area by surface ships from the United States, France, Canada, and England, culminating in the first manned submersible studies of a mid-ocean ridge by the French submersible *Archimède* in 1973, and by *Archimède*, *Cyana*, and the American submersible *Alvin* during the summer of 1974. The regional setting of the dive site was established by narrow-beam echo sounding, dredging, side-scan sonar and deep-tow surveys, photography, aeromagnetic surveys, and magnetic and gravity surveys from shipboard. The *Glomar Challenger*, on leg 37 of the Deep Sea Drilling Project (DSDP), drilled four holes starting about 18 nautical miles west of the dive site. The final phase of the surface ship surveys, carried out by R.V. *Knorr* concurrently with the submersible program, consisted of dredging, coring, detailed photographic and thermal surveys, and deployment of ocean bottom seismographs. In this article we present a preliminary summary and interpretation of some of the unique observations made by the manned submersible *Alvin* during the summer of 1974. Data from the surface ship surveys, most of which are yet unpublished, have contributed significantly to the success of the project and to some of the interpretations presented here. The accompanying article describes the related French program.

The submersible *Alvin* carries two scientists and a pilot; normal bottom time was 4 to 5 hours, during which time the submersible traversed from 1 to nearly 4 kilometers across the bottom. The submersible was continuously navigated in real time relative to three acoustic beacons. Precision varied with bottom conditions but was generally better than ± 5 meters. Headings were obtained by gyrocompass, with a backup magnetic system. Precise measurements of depth, height off bottom, and heading were automatically logged as a function of time; these combined with the navigation data were plotted as *X*, *Y*, *Z* coordinates of the track at 20- or 40-second intervals. Rock, water, and sediment samples were collected routinely and stored in a compartmented "lazy susan" basket. Nearly continuous visual records by the scientists were augmented by photographs recorded by semiautomatic external still cameras, internal still and movie cameras, and a television camera with video tape recording. The *Alvin* completed 15 dives in the median valley and two dives in Fracture Zone B (Fig. 1). Overall, *Alvin* collected about 400 kilograms of rock samples, 50 water samples, and 42 sediment samples, all precisely located relative to a 5-fathom contour map of the inner rift valley floor. Some 15,000 color and black-and-white photographs were taken, and about 140 scientific manhours of visual observation and notes documented the 27 km of sea floor traversed.

Geologic Setting

The area selected for the prime dive site (Fig. 1) consists of a median valley segment about 20 km long, bounded on the north and south by transform faults, which are called Fracture Zone A and Fracture Zone B, respectively. The median valley floor is about 1 km wide at its center, with depths averaging about 1400 fathoms; at either end it widens to more than 8 km with depths reaching 1700 fathoms. The west wall rises abruptly within a distance of 1 to 2 km to a broad, undulating terrace with an average depth of about 1000 fathoms. To the east, the slopes rise more gradually in a series of steps to the base of the main east wall 2 to 3 km from the center of the valley. This bathymetric asymmetry is matched by a corresponding asymmetry in magnetic anomalies, with an inferred spreading rate of about 0.8 cm/year to the west and about 1.3 cm/year to the east (*1*). Within 10 to 12 km from the center of the valley, rift mountain peaks rise to depths typically about 800 fathoms. Each of the transform faults is marked by a narrow trough and by a linear zone of microearthquakes (*2*).

The center of the median valley floor is marked by a series of rugged linear hills which have been considered to be recent volcanic extrusions (*3*). Much of the submarine operation was centered around two of these hills, the French working on the flanks and to the north of Mt. Venus, and the American group working south of Mt. Venus and around Mt. Pluto (Fig. 1).

R. D. Ballard, W. B. Bryan, and J. R. Heirtzler are at the Department of Geology and Geophysics, Woods Hole Oceanographic Institution, Woods Hole, Massachusetts 02543. G. Keller is at the Atlantic Oceanographic and Meteorological Laboratories of the National Aeronautics and Space Administration, Miami, Florida 33149. J. G. Moore is at the U.S. Geological Survey, Menlo Park, California 94025. Tj. van Andel is at Oregon State University, Corvallis 97331.

Real-Time Events

For reasons of both scientific interest and personal safety, much attention was devoted to the detection of volcanic, seismic, and thermal activity in the process of occurrence. Sonobuoy arrays were deployed on the sea surface and seismometers on the sea floor by the R.V. *Knorr* during some of the dives. Although microearthquakes were noted in the general area of the submersible, no movement of the sea floor or unusual disturbance of the sediment was observed. In fact, no evidence of ambient acoustic energy of any sort was observed in the submersible for the frequency range of about 100 hertz to 100 kilohertz for which she was instrumented. No volcanic features were seen being extruded and, as suggested elsewhere in this article, visual observation of the degree of sediment cover and attached faunal population suggested that the youngest lava forms were at least hundreds, if not thousands, of years old.

Thermal measurements of the water mass were made by *Alvin* and by probes on a camera frame used extensively from the *Knorr*. The *Alvin* probe had a resolution of about 0.01°C and observed no sea floor anomalies, either over recent volcanic forms or inside fissures. The *Knorr* probe, also with a resolution of about 0.01°C, did observe several anomalies due to entrapment of water in major enclosed basins and to small-scale water movement. It did not observe any anomalies that could be attributed to hydrothermal circulation.

Volcanic Processes

Observations confirmed that Mt. Venus and Mt. Pluto are the sites of most recent volcanic activity. The flanks of these hills consist of broad, steep-fronted flow lobes with relatively little sediment cover or attached organisms. The flow fronts consist of tubular lava extrusions elongated downslope, resembling in some respects terrestrial pahoehoe lava. On the near-horizontal upper surfaces of these flows, a variety of bulbous, pillow-like lava forms are developed (Fig. 2). Often the surfaces of these pillows are partly covered by abundant lumpy or tubular lava extrusions, which may be variously described as lava "fingers" or "toes." Some bulbous pillows are hollow, blister-like forms and are found in various stages of collapse. Many of these hollow pillows, and hollow lava tubes as well, show multiple internal, nearly horizontal "high lava marks," which indicate successive falls in lava level before final quenching (Fig. 3). These frozen-in lava levels provide a reliable guide to sample orientation for paleomagnetic studies. Other pillows display a variety of intriguing "trapdoor" extrusions, in which a broken piece of crust sits like a hat on a projecting neck of lava. The pillows and tubes are typically 30 to 100 cm in diamter, and the fingers and toes are several centimeters in diameter.

The summit of Mt. Pluto consists of a series of conical peaks 20 to 30 m high aligned parallel to the trend of the median valley. Tubular pahoehoe lava descends in all directions on the flanks of the peaks and forms a radiating pattern in the surrounding region; collapsed blister pillows are common on summits of the peaks. Similar conical peaks on a smaller scale were occasionally observed elsewhere in the median valley. They may mark the main vents that fed the principal lava flows. The summits of peaks on Mt. Pluto are remarkably con-

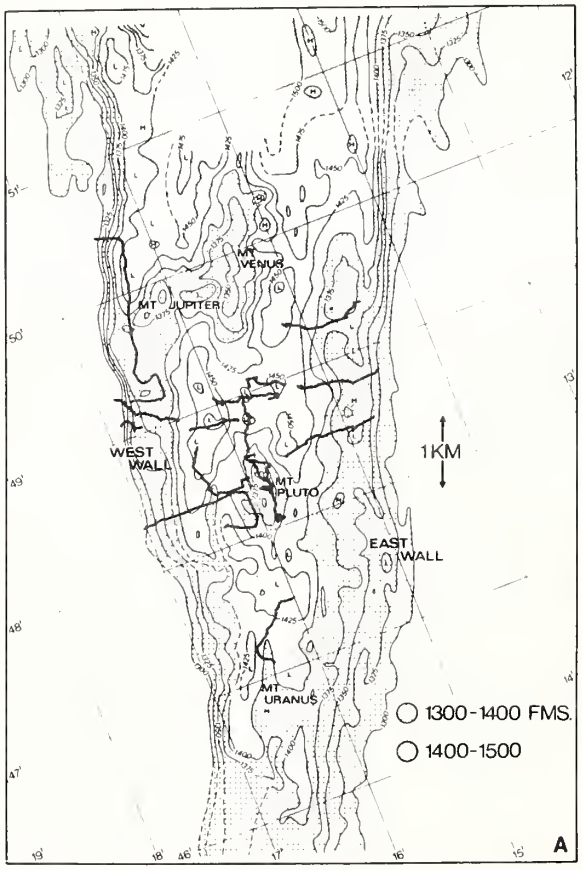

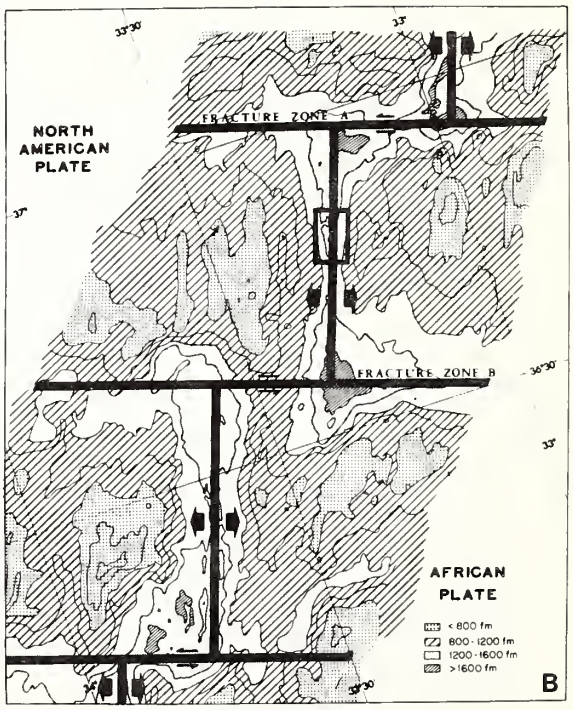

Fig. 1. (A) Location of dive area and tracks of *Alvin* in the median valley. (B) Regional reference map; small rectangle in area covered by (A).

cordant at about 1300 fathoms, suggesting that they have grown in response to a common hydraulic head of lava in a shallow magma chamber.

Large tumuli, 4 m or more in diameter, were occasionally observed on flow surfaces. Some resemble small-scale driblet cones, while others are better described as giant pillows. As on terrestrial lava flows, they appear to represent short-lived secondary centers of tumescence and extrusion.

Growth of the central volcanic hills and advancement of the lava flows appears to take place almost entirely by tumescence, fracturing of crust, budding, tumescence of the new extrusions, fracturing, budding, and so on. In fact, the large volcanic hills probably could be regarded as very large compound tumuli which have repeatedly fractured and budded to give rise to the major lava flows. The flows themselves fracture and bud down to the scale of the individual lava fingers and toes, at which point the available lava presumably becomes exhausted. Detached, subspherical pillows were rarely seen; the few examples appeared to have pulled loose from the ends of lava tubes on steep slopes, but this is not common.

Most of the recent extrusive activity appears to be restricted to vents in the median valley associated with Mt. Pluto or Mt. Venus. However, limited flank volcanism was observed on the lower walls of the valley immediately to the east and west of the valley floor. This zone of flank volcanism seems wider and better developed to the east than to the west, in harmony with the faster spreading rate to the east. However, in all traverses from the center of the valley outward to the flanks we were impressed by the rapid increase in sediment cover and bottom life and by the intense tectonic degradation to which the extrusive lava forms were subjected. Generally, within 300 m of the valley center to the west and within 500 m to the east, most of the delicate extrusive forms had been destroyed, the flows were sliced and offset by numerous faults, and the surfaces were reduced to broken, jumbled lava blocks and extensive talus fans at the base of fault scarps.

Preliminary petrographic study and analysis of rock glasses by electron microprobe have shown considerable variation in composition of the lavas, which can be related to their apparent age and position within the median valley. Table 1 shows examples of the more extreme compositions. The analysis shown in column A is typical of recent lavas from Mt. Pluto on the central volcanic axis and closely resembles that of the unusual low-TiO_2, high-MgO glass reported from DSDP sites 3-14 and 3-18 (*4*). The analysis in column B is typical of lavas on the east and west flanks of the valley, as well as of older flows near the central axis that have not been covered by the younger extrusions. This composition is more typical of basalts reported from other parts of the ocean ridge system. The regional variation in percentage by weight of SiO_2 is shown in Fig. 4; a similar variation can be demonstrated for most of the other oxides of major elements, as implied by the data in Table 1. Especially notable are the increases in FeO/MgO, TiO_2, and K_2O from the center to the margins of the median valley.

The slight asymmetry in the compositional distribution is consistent with the bathymetric asymmetry and differences in spreading rates and suggests that all of these features reflect operation of common processes at depth. The chemical variations, although subtle, are matched by distinct differences in liquidus mineral phases (microphenocrysts). As SiO_2 increases, olivine becomes less abundant, chrome spinel disappears, plagioclase becomes more abundant, and pyroxene appears. The chemical and petrographic variations are similar to those observed previously only over distances of hundreds of kilometers along the length of the Mid-Atlantic Ridge (*5*). It seems unlikely that these variations, which we observe over a distance of a few kilometers, can be related to separate mantle sources or to deep mantle processes, although transition element geochemis-

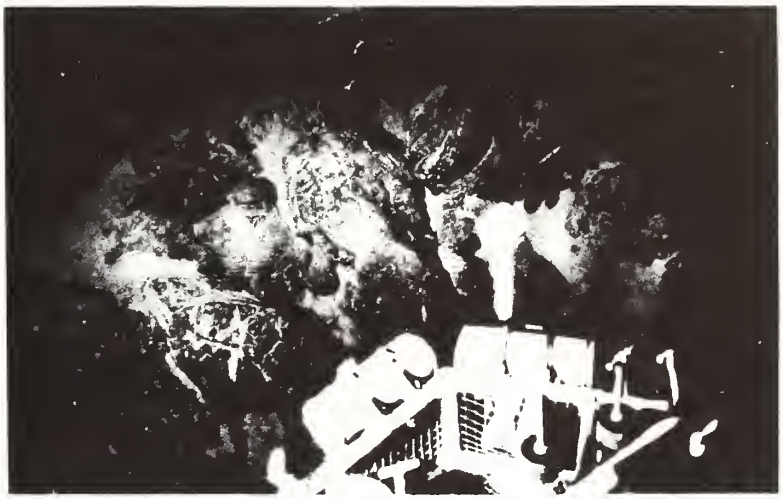

Fig. 2. Elongated bulbous and bun-shaped lava pillows. Note multiple fracturing of crust due to expansion combined with surface quenching.

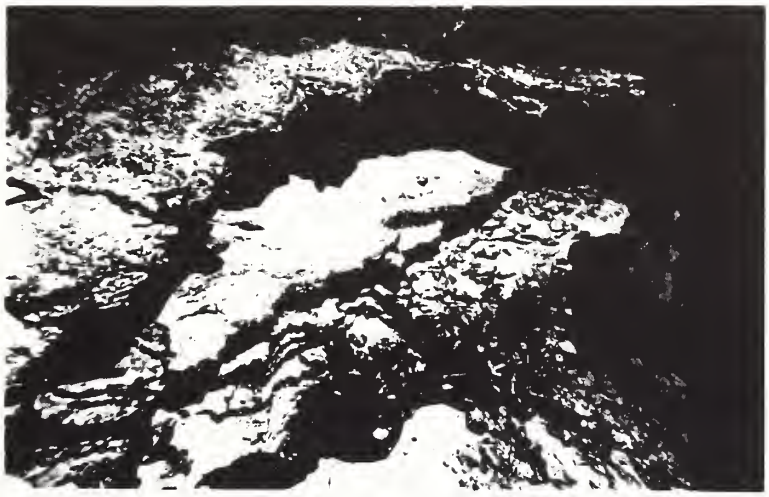

Fig. 3. Layered interior of lava tube exposed at the top of the wall of a tensional fracture.

try implies separate magma types in the R.V. *Charcot* dredge samples from the FAMOUS area (*6*).

Preliminary dating of lavas based on measurements of manganese and palagonite crusts, along with our impressions of outcrop freshness based on direct observation of sediment cover and faunal abundances, indicates that at least some of the apparently differentiated flank lavas are of about the same age as lava from the central valley, although the flank eruptions are much less voluminous. This differentiation between central magma and contemporaneous flank magma is well known at Kilauea volcano (*7*) and implies the existence of a shallow, compositionally zoned magma chamber beneath the median valley (*8*). Calculations indicate that simple fractional crystallization of olivine and plagioclase, as suggested by the petrographic data, can account for most of the major element variation, although serious discrepancies remain for TiO_2 and alkalies. Frey *et al.* (*4*) showed that TiO_2 and FeO/MgO are apparently the most critical major element parameters in sea floor lavas, and any process proposed to account for compositional differences in lavas across the median valley will have to account for the simultaneous variation in these parameters.

Tectonics

In contrast to recent volcanic activity, which appears to be concentrated in a narrow central zone, recent tectonic movement is evident throughout the entire width of the inner rift valley floor. Faults and fissures are numerous, striking 020° parallel to the rift axis (Fig. 5). Locally, faults trend perpendicular to the axis, but these are few in number and are truncated by the more dominant 020° structures.

The dominance of tectonic activity is reflected in the fine-scale geomorphology of the central valley. From the west wall across the central depression between Mt. Venus and Mt. Pluto to the first major step fault of the east wall is a predominantly block-faulted terrain. Normal faulting is common, and when combined with tensional extension it yields open fissures with differential movement between the two walls. Dips range from 45° to nearly vertical, with 70° to 80° common on smaller faults. Displacements vary from less than 1 to more than 100 m, 10 to 20 m being the most common. The faulted blocks are back-tilted 5° to 7° and in some instances have rotated away from one another, producing a rubble-filled V-shaped notch.

Observations in the region of Mt. Pluto agree with those of the French on Mt. Venus to the north, that the morphology of the central topographic highs results from constructional volcanic processes, but the remainder of the inner floor to the east and west is in part shaped by tectonic forces. Even in the central region of Mt. Pluto, small postvolcanic tensional fissures occur. South of Mt. Pluto, one scissors fault was traced with displacement down to the west at its northern end and down to the east at its southern end.

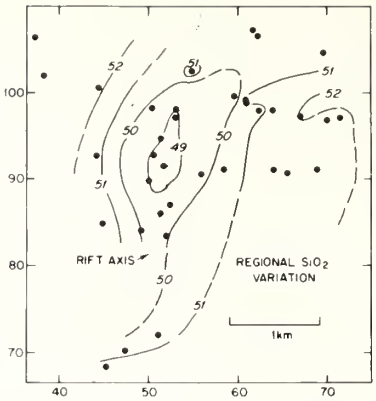

Fig. 4. Regional variation in SiO_2 content of rock samples recovered by *Alvin*. Dots are station locations for which data are available. These stations are located along the dive tracks shown in Fig. 1. Numbers are percentages of SiO_2 by weight.

The nature of fissure development was varied. The most typical feature in the central volcanic zone was a small crack 2 to 4 cm wide with no vertical displacement, striking 020° across otherwise undisturbed volcanic terrain. Small cracks traced over the young sediment-free central region may extend 50 to 100 m before being offset in an en echelon pattern. To the east and west the fissure widths vary, show vertical displacement, and may show considerable variation along strike. Beginning as 1-m openings 10 m deep, they may then be completely filled with rubble or divide to form two fissures isolating a down-dropped block. Farther to the east and west vertical fault scarps predominate over open fissures.

Table 1. Electron microprobe analyses of basalt glasses. The analysis in column A is from the west flank of Mt. Pluto, dive 525, station 5, sample 2. That in column B is from the east flank of the median valley, dive 527, station 6, sample 3.

Constituent	Percentage	
	A	B
SiO_2	48.9	51.1
TiO_2	0.84	1.42
Al_2O_3	16.1	14.9
FeO	8.74	10.1
MnO	0.15	0.18
MgO	10.5	7.89
CaO	11.8	11.8
Na_2O	2.41	2.46
K_2O	0.09	0.21
Cr_2O_3	0.09	0.08
Totals	99.62	100.14

Proceeding from the central valley toward the walls, the submarine typically passed over a series of outward-dipping faults with displacement down toward the valley walls. This outward and downward displacement is maintained even though the general bottom gradient is upward. The structure of the central valley is thus a horst with a central sag. Beyond the marginal graben, the normal faults increase in throw and become inward-dipping, as exemplified by the scarps forming the main east and west walls.

One of these inward-dipping faults was investigated during four dives on the west wall. Here, the displacement observed on two of the dives was at least 300 m, from the top of the scarp to the top of the talus. The upper 130 m of the scarp consisted of truncated lava tubes and pillows lacking any intercalated sedimentary material. These grade through an interval of 30 to 50 m into a more massive outcrop characterized by a blocky, angular surface without the elliptical outlines and radial joint patterns typical of truncated pillows. Lenticular intrusions 20 to 30 cm wide and more than 2 m long strike obliquely across the exposed surface; they are most common 15 to 50 m below the top of the massive outcrop. The total number of dike-like or sill-like intrusions observed on three dives, however, was surprisingly small on the order of a dozen or so.

The nature of the fault zone on the west wall was strikingly different from that of the faults in the inner valley. The latter were generally clean, fresh, and free of fault breccia and fault gouge. On the lower west wall, on the other hand, the fault zone was 100 to 150 m wide, and exposed alternating, subvertical shells of fault breccia and massive basalt, dipping parallel to the face inward toward the inner rift valley floor at about 80° (Fig. 6). Elsewhere the west wall appears to have been uplifted along a series of parallel normal faults, with individual displacements of less than 100 m showing exposures only of truncated lava. The upper surfaces of these fault slices form structural terraces capped by primary volcanic material which are back-tilted 5° to 7°. Major talus fans develop at the base of these scarps and, in many cases, on the back-tilted surfaces of the fault blocks.

The faulting appears to be a continuing process with repeated episodes of displacement. Narrow fissures cut across individual pillow forms with no disruption oth-

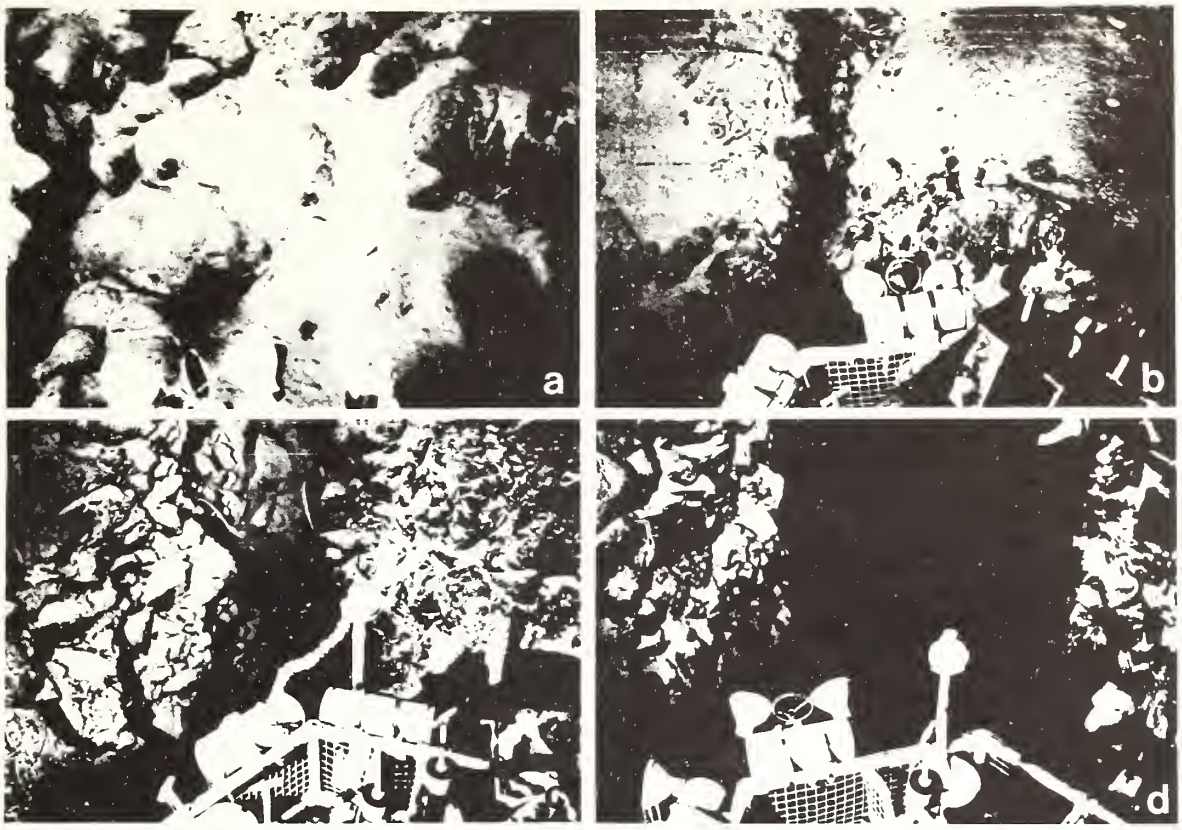

Fig. 5. Varieties of minor and major tensional fractures, increasing in size from (a) to (d). In (d), the submarine is about 8 m into the fracture.

er than a single plane of failure. Broken pillows on opposite sides of fissures up to 1 to 2 m wide can usually be visually matched, and indicate mainly dilation with minor vertical displacement. Coherent pillow forms preserved in the fault scarps sometimes made it difficult to determine whether the slope was a fault scarp or a primary flow front. Renewed tectonic activity along older fault planes is indicated by faulted lithified calcareous sediments, a few centimeters to a meter in thickness, overlying the older pillow surfaces.

During the diving operations, more than 50 fault scarps were inspected. In no instance were sediments found interbedded with the igneous rocks. It was common, however, to see sediments accumulated in open fissures. Since tectonic activity dominates in the older flanking region, where sediments have had a greater time to accumulate, open fissures may represent the primary avenue by which sediments enter the geologic section.

Two dives on the north and south sides of the active transform section in Fracture Zone B encountered heavy sediment cover in the topographic trough and on its walls. This cover consisted of a semiconsolidated blanket of calcareous sediment draped over the terrain, with only local exposures of weathered basalt talus or greenstone. On the north side of the transform, there was minor shearing and tilting of sediment and igneous rocks. No mafic or ultramafic rocks were recovered, although dredging on the topographic saddle to the south has recovered serpentinite, pyroxenite, and veined greenstone. No thermal anomalies were observed from the submarine, although many of the dredged greenstones are strongly fractured and brecciated, and are traversed by vuggy veins containing both calcite and aragonite which may be due to hydrothermal circulation.

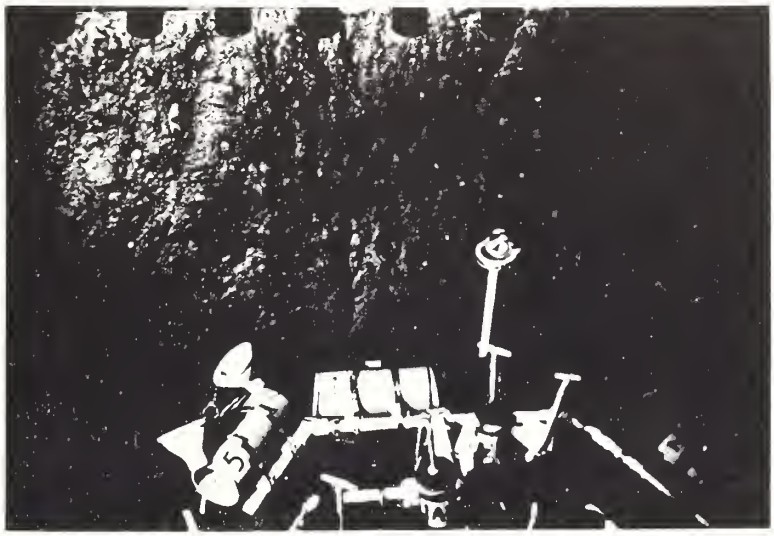

Fig. 6. Brecciated and vertically striated basalt on the west wall of the median valley.

Summary

Lava forms resemble those observed on terrestrial pahoehoe lava flows; the features that appear in truncated fault scarps as circular or elliptical pillows are elongated, tubular forms in three dimensions. Detached, subspherical pillows are very rare. The lavas show systematic chemical and mineralogical variation, with the olivine basalts associated with the central volcanic highs and plagioclase-pyroxene basalts being typical of the west and east walls. Active volcanism is mainly restricted to a narrow (0.5 to 1 km wide) central zone in the median valley.

The central valley has a horst-like structure which is bounded by graben at the base of the east and west walls. Intrusive sills and dikes are exposed only at the base of one 300-m scarp on the west wall. Most fault displacements are less than 100 m and expose only breccia, truncated lava pillows, and tubes.

In general, faulting appears to be a continuing process, while volcanic activity is episodic. Structural deformation rapidly degrades the primary volcanic morphology typical of the central highs, although volcanic features are locally preserved on the wider structural terraces on the west and east flanks of the median valley. Dives in Fracture Zone B revealed minor deformation of recent sediment cover, but there was no evidence of recent volcanic or hydrothermal activity.

References and Notes

1. H. D. Needham and J. Francheteau, *Earth Planet. Sci. Lett.* **22**, 29 (1974).
2. R. C. Spindel *et al.*, *Nature (Lond.)* **246**, 88 (1974).
3. J. G. Moore, H. S. Fleming, J. D. Phillips, *Geology* **2**, 437 (1974).
4. F. A. Frey, W. B. Bryan, G. Thompson, *J. Geophys. Res.* **79**, 5507 (1974).
5. J. G. Schilling, *Nature (Lond.)* **242**, 565 (1973).
6. H. Bougault and R. Hékinian, *Earth Planet. Sci. Lett.* **24**, 249 (1974).
7. T. L. Wright and R. S. Fiske, *J. Petrol.* **2**, 1 (1971).
8. J. R. Cann, *Geophys. J. R. Astron. Soc.* **39**, 169 (1974); D. Greenbaum, *Nat. Phys. Sci.* **238**, 18 (1972).
9. Supported by the Submarine Geology Branch, National Science Foundation, through grants GA-35976 and GA-41694; by the Seabed Assessment Program, International Decade of Ocean Exploration, through grant GX-36024; and by the Manned Undersea Science and Technology Office, National Oceanic and Atmospheric Administration, through grant 04-3-158-17. We wish to acknowledge the development of submersible instrumentation and operation procedures under contract N00014-71-C-0284; NR293-008 of the Advanced Research Projects Agency, and the substantial contribution of the U.S. Navy and the Naval Research Laboratories in providing narrow-beam bathymetry and detailed sea floor photography. We are especially grateful to pilots J. Donnelly, D. Foster, L. Shumaker, and V. Wilson for their skillful handling of the *Alvin*, and to Captain R. Flegenheimer and the personnel of the R.V. *Lulu*, and Captain E. Hiller and the crew of the R. V. *Knorr* for outstanding support. This article is Woods Hole Oceanographic Institution Contribution No. 3508.

Reprinted from: *Meteoritics 10*, No. 4, 393.

OMAN RING: SUSPECTED ASTROBLEME

Robert S. Dietz*, John F. McHone, Nicolas M. Short***,**
**NOAA, Atlantic Ocean. and Met. Lab., Miami, FL 33149*
***Dept. Geology, University Illinois, Urbana, IL*
****NASA, Goddard Space Flight Center, Greenbelt, MD*

A LANDSAT image (ERTS-1, 1217-06090, 25 Feb., 73) of Oman reveals a circular double ring structure (19°55′N, 56°58′E) in the desert region of Oman, on the Arabian Peninsula, which is a suspected astrobleme, ancient impact scar. Little is known about the surface geology except that the Oman Ring deforms a terrane of flat-lying Cretaceous rocks of marine shallow-water shelf facies. Although the exact geologic structure remains uncertain, it seems likely that the inner ring, 2.0 km across, marks a central domal uplift, while the outer ring, 6.0 km across, marks the outer ring fault, so that this suspected impact site is of moderate dimensions. The 1:3 ratio between the dome and the outer ring is typical of impact scars. The central dome suggests that the impacting body was a comet head (Milton and Roddy, 1972). I.M. ElBoushi of Oman has offered to make a field investigation of this structure. Geologic maps show a NE-SW trending zone of Hormuz (Cambrian) piercement salt domes lying about 100 km to the NW of the Oman Ring. But we have been unable to detect any of these on LANDSAT imagery, so it is doubtful that the Oman Ring is an outlying member of this field.

30 Reprinted from: IX International Congress of Sedimentology; Nice, France, Theme 10, 13-18. Also appeared in Offshore Technology Conference, Pater #OTC 2385, 505-511.

THIS PRESENTATION IS SUBJECT TO CORRECTION

New York Alternative Dumpsite Assessment - Reconnaissance Study of Surficial Sediments

By

George L. Freeland and Donald J. P. Swift, NOAA

©Copyright 1975

Offshore Technology Conference on behalf of the American Institute of Mining, Metallurgical, and Petroleum Engineers, Inc. (Society of Mining Engineers, The Metallurgical Society and Society of Petroleum Engineers), American Association of Petroleum Geologists, American Institute of Chemical Engineers, American Society of Civil Engineers, American Society of Mechanical Engineers, Institute of Electrical and Electronics Engineers, Marine Technology Society, Society of Exploration Geophysicists, and Society of Naval Architects and Marine Engineers.

This paper was prepared for presentation at the Seventh Annual Offshore Technology Conference to be held in Houston, Tex., May 5-8, 1975. Permission to copy is restricted to an abstract of not more than 300 words. Illustrations may not be copied. Such use of an abstract should contain conspicuous acknowledgment of where and by whom the paper is presented.

ABSTRACT

Evaluation of offshore areas as potential dumpsites requires assessment of bottom sediment character and transport. Preliminary evaluation of the potential for deposition of dumped materials, primarily sewage sludge, were made at two sites 60 nm from New York Harbor in 20 to 30 fm water depths. Since sludge particle density is barely over 1.0, geological data were analysed for potential deposition and transport of fines in particular in addition to the sand-sized fraction. Results suggest a net southwestward bottom sediment transport, intensifying during winter storms.

I. INTRODUCTION

Purpose of the Study

Waste disposal at the present New York Bight apex sewage sludge dumpsite is currently 5.9 million yd^3/yr. The dumpsite and its surroundings are presently undergoing intensive study by NOAA's Marine Ecosystems Analysis Program (MESA) in order to determine the environmental impact of this dumping. MESA oceanographers are also examining two interim alternative dumpsites in the central part of the Bight shelf (Fig. 1). Preliminary results from these studies are presented in this paper.

Areas of Investigation

Location criteria of the northern site requires that it be a minimum of 25 nm from the Long Island shoreline, 10 nm from the axis of the Hudson Shelf Valley, and no more than 65 nm from the New York Harbor entrance. The southern dumpsite is proposed to be located seaward of lines connecting the most shoreward 20 fm isobath, 10 nm from the Hudson Shelf Valley axis, and 65 nm from the New York Harbor entrance.

Geological Setting of the Dumpsite Area

The New York Bight is a pentagonal sector of the middle Atlantic shelf, approximately 100 nm wide at its maximum extent from the New York harbor mouth to the shelf edge (Fig. 1). Depths range between 20 and 30 fm over much of this area. The most prominent topographic feature of the shelf surface is the Hudson Shelf Valley, a broad, shallow channel extending from the Bight apex seaward as far as the outer shelf in the vicinity of Hudson Canyon.

The shelf sediment surface has been profoundly modified by events associated with the Pleistocene ice age. During the last major ice advance, the Laurentide ice sheet extended to south-central Long Island and westward across New Jersey. Ancient shorelines near the head of Hudson Canyon indicate a sea-level lowering of about 450 ft. During this and preceeding periods of lowered sea level, stream erosion, amplified by meltwater discharge, dissected the uppermost shelf strata. The ancestral Northern

References and illustrations at end of paper.

New Jersey, Long Island, and Hudson Rivers scoured out their shelf valleys and incised the margins of the low divides that separated these drainage systems.

As post-glacial sea level rose, shoreline advance across the shelf resulted in erosion and beveling of the divides by the action of surf and coastal currents, and winnowing of fines from much of the shelf surficial sediment. Material released was transported by littoral drift southwestward along the slowly advancing shoreline into the shelf valley floors. The area of the Long Island Shelf Valley was a broad bay during much of this time, shielded from storm waves by a peninsula formed by the submerging Block Divide (Fig. 1)(Swift, et al., 1972). Thus, the pattern of trunk and tributary streams of the ancestral Long Island River are still clearly seen. The Hudson Shelf Valley, however, is so deeply incised that sedimentation by the transgressing shoreline and by subsequent storm-driven flows across the shelf have not sufficed to fill it in. To the south, the North New Jersey Shelf Valley has been partly buried beneath sand ridges which stream southwestward from the crest of the Hudson Divide. Scour in the trough floors between the ridges has resulted in erosion of up to 20 ft. into early Holocene/late Pleistocene lagoonal clays and deposition of 20 ft. of sand on older strata to form ridges.

Field Work

Each of the two sites studied covered a 10 x 10 nm square and contained 36 sample stations, plus geophysical tracklines spaced 2 nm apart. In the northern area the grid was placed slightly seaward of the center of the proposed dumpsite to investigate, in part, a tributary valley system which could be an area of deposition of dumped fines. The grid was oriented north-south so that sample lines would cross the valley. In the southern area, the broad, flat high area of the Hudson Divide and the strong ridge and swale topography to the west were of interest, therefore tracklines were oriented northwestward.

At sample stations a Smith-MacIntyre bottom grab sample and bottom photos were taken; at every fourth station bottom water samples 2 m from the bottom were collected. In the southern area, additional bottom grab samples (Shipek) were collected at 1/4 nm intervals along a centrally located line. On geophysical tracklines 3.5 kHz shallow-penetration seismic reflection profiling and side-scan sonar records were taken. In addition, the submersible NEKTON was used for two geological and three biological dives in the southern area.

Field aliquots and two 15 cm Phleger cores were taken from the Smith-MacIntyre samples for geological processing, and two vials of sample from the top centimeter were taken for chemical and fine-sediment analysis. From the 10-liter bottom water samples, two 2-liter samples were filtered onboard through a Wattman glass fiber GF/C filter for organic analysis, and a one 1-liter sample was filtered through a 0.45 micron Nucleopore filter for suspended sediment analysis. Filters were immediately frozen.

Data Processing

Size analysis consisted of splitting and dry screening freeze-dried samples on a 2-mm screen; passed material was washed of fines on a 230 mesh (62.5 micron) screen, and run through an automated rapid sediment analyzer for grain size distribution. Geophysical records were examined for areas of interest which were photographed.

II. PHYSICAL NATURE OF THE PROPOSED DUMPSITES

Northern Site

Bathymetry: The area contains flat to gently sloping topography with depths from 25 fm in the northwest corner to nearly 32 fm in the east (Fig. 2). The most prominent feature is the remnant of an early Holocene/late Pleistocene northwest-trending stream tributary in the northern halfof the area, while to the southwest a flat shoulder gently slopes eastward. There probably has been only a slight smoothing of the basic topography formed before sea level rise.

Stratigraphy: 3.5 kHz seismic data reveal the presence of a thin (5-6 ft.) surface layer, presumed to be Holocene, overlying a reflector similar to the early Holocene/late Pleistocene "basement" reflector which outcrops in the southern area. This upper layer is the sand sheet which was deposited over the Pleistocene erosional surface as sea level rose. The lack of additional, more modern sediment over the basal sand sheet is due to a limited sediment supply since transgression. In many places the "basement", a lagoonal clay, is exposed or eroded.

Surficial Sediments: Sand, with some areas of over 5% gravel, comprise the surficial sediment (Figs. 2 & 3). Fine sands lie in the northeastern part of the area near the axis of the ancient stream valley, while coarser medium sands lie in the western and southern parts of the area. Mud deposits are restricted to only two stations with over 5% mud (5.7% and 8.2%). A pronounced gravel deposit (39% gravel) associated with coarser medium sand, is mapped in the southeastern part of the area.

Assessment of sediment transport from grain-size distribution data is not very obvious as medium sand occurs in both topographic lows

and highs. The coarser sediment in the southern and western parts of the area could result from these areas being on northeast-facing slopes. Since the strongest storm-generated currents are throught to come from the northeast, these "upcurrent-facing" slopes may have been winnowed of finer sand, leaving a coarser lag deposit. The lack of large areas of mud deposition indicates a) a nearly complete lack of mud as a source material, and/or b) what little, if any, mud being transported into the area is not remaining.

Bedforms: Bottom photographs indicate that the northern area is characterized by smooth, slightly undulatory, mounded or rippled bottom. These patterns reflect the competing activities of bottom wave surge, which tends to ripple the bottom, and the plowing activities of benthic fauna (mainly sand dollars) which smooth the bottom. Ripples form during storms and are slowly erased with intervening fair weather. Their spacing and height increase with increasing grain size: as ripples become larger, coarser sand appears on the crests, and finer sand in the troughs. If there is a wide range of grain sizes, or if sand or shell fragments are too coarse to be moved at all, the coarse particles accumulate in the troughs along with medium sand, finer sand then collecting on crests. Under such conditions, sand dollars preferentially collect on ripple crests and flanks where they preserve ripple structure through armoring rather than degrading them.

Mesoscale bedforms appear on the sonographs as highly reflective, low relief, east-west trending zones 30 to 45 ft apart which are linear erosional windows exposing the basal Holocene pebbly sand. These zones appear to be aligned parallel to the main current flow direction, while degraded sand waves, which appear as poorly-defined patterns of repeating diamond shapes, are transverse to current flow.

Southern Site

Bathymetry: The southern area is considerably more complex than the northern area (Fig. 4). The crest of the Hudson Divide is aligned northwest-southeast through the center of the area separating irregular bottom sloping northeastward into the Hudson Shelf Valley and Tiger Scarp from a strong-developed area of northeast-trending ridge and swale topography on the west side of the area. The ridge and swale topography probably formed from the pre-existing New Jersey Shelf Valley through the action of strong southwestward currents which have apparently transported sand from the crest and east flank of the Hudson Divide westward to build ridges obliquely across the Valley and to scour the areas in between the ridges.

Stratigraphy: Seismic reflection profiles reveal the early Holocene/late Pleistocene reflector outcropping in the area of ridge and swale topography, and a lower event probably within the Pleistocene.

Surficial Sediments: Grain-size patterns in the southern area are more clearly related to bottom topography than in the northern area and thus are more easily related to sediment transport. The crest and east flank of the Hudson Divide are floored by coarse sand, the coarser fractions of medium sand (Fig. 5), and by up to over 20% gravel (Fig. 6). In the ridge and swale topography to the west of the Divide crest lie finer medium sand and fine sand. Submersible observations in the bottom of Veach and Smith Trough revealed the presence of a veneer of shelly, pebbly sand with large, angular clay pebbles in the troughs of ripples which were eroded from the underlying early Hollcene/late Pleistocene substrate.

The coarser sand and gravel deposits on the crest and east flank of the Hudson Divide point to southwest currents winnowing finer material from this "upcurrent" side of the Divide and depositing it as longitudinal ridges in deeper water to the west. Currents must have scoured the intervening troughs at the same time. Bottom photos taken on the Hudson Divide show flat topography which has been rippled by bottom currents, then reworked by benthic organisms (surf clams, sand dollars and worms). In the troughs of the ridge and swale topography, considerable coarse shell debris lies in the ripple troughs along with coarser sand grains. The many small mounds of gray subsurface sediment brought up by the worms contrasts with the tan to reddish-brown color and more even appearance of undistrubed oxidized surface sediment. On ridge crests and upper flanks vast concentrations of small sand dollars occur, sometimes covering 100% of the bottom, amoothing ripples to the point where they are no longer distinguishable.

Bedforms: Micro-relief in the southern area is quite similar to that in the northern area on the bottom away from the ridge and swale topography. Moderately rippled bottom, bioturbated ripples, and bioturbated mounded topography are present on the Hudson Divide and its flanks. In the troughs between ridges west of the Divide, strongly developed ripples and sand ribbon patterns appear in the thin veneer of coarse pebbly sand overlying the clay substrate. Most of the strong rippling probably forms during winter storms and then is modified during the summer.

III. PROBABLE NATURE OF SEDIMENT TRANSPORT

General

The nature and pattern of sediment transport on the continental shelf is still poorly understood (Swift, et al., 1972). Measurements of sediment transport rates have been largely confined to shallow laboratory flumes, while wave-driven transport and unidirectional transport have rarely been studied together at full scale. Empirical equations for sediment transport resulting from these laboratory studies must be applied with great caution to the shelf floor.

Nevertheless, these laboratory studies, and field studies from other areas (usually nearer to the coast) permit the drawing of the following inferences concerning sediment transport in the study area.

Sand Transport

Cohesionless sediment (mainly sand) is entrained by bottom flow only during major storms, primarily in the winter. If the trajectory of a mid-latitude low pressure cell across the New York Bight is such that a day or more of intense northeast winds occurs, then a southward quasi-geostrophic flow may develop across the entire shelf with velocities in excess of 40 cm/sec, sufficient to entrain bottom sand (Beardsley & Butman, 1974). Sand flow may be more intense than indicated by laboratory studies of unidirectional currents since the storm flow field has a marked wave surge component which "lubricates" the entrainment of sand. Storm trajectories with winds from other directions do not result in such close coupling between wind and water flow (ibid.). Between storms the shelf flow field is rarely sufficiently intense to entrain sand.

The response of the shelf floor to intermittent southwest-trending shelf flows may be seen in the gross pattern of distribution of surficial sediment and in the mesoscale morphologic pattern of ridges and swales. Shelf highs such as the Block, Long Island, and Hudson Divides are floored by coarser sand than are the lows, suggesting that the storm flow field tends to accelerate slightly over the highs due to the decreased water cross-sectional area, and expand and decelerate over lows, with the result that finer sand is swept off the highs into the lows. Apparently, local interaction between substrate and flow has resulted in ridge and swale topography with relief of up to 40 ft, and ridge crests 2.5 nm apart and several miles long. Side slopes are usually less than a degree. These drifts may possibly be the result of helical flow cells in the storm flow field coupling with the substrate. If so, zones of downwelling and flow acceleration occur over troughs causing scour, while upwelling and flow deceleration occurs over crests causing deposition. These velocity perturbations probably need be only a few percent of the ambient value to induce the observed topography. Smaller scale flow cells with spacing of tens to hundreds of feet are probably responsible for the streaky patterns (linear erosional windows) seen by side-scan sonar.

In areas where regional flow fields characteristically decelerate, sand willtend to settle from the flow more rapidly than it is entrained, creating constructional ridge topography. Subdued contours trending nearly east-west in the northern area (Fig. 2) may be a consequence of the overprinting of such a pattern on the old Long Island drainage system.

The pronounced ridge topography in the western part of the southern area (Fig. 4) seems to be the result of the acceleration of storm flow over the Hudson Divide. The deeply incised troughs are a clear response to this flow. Cohesive clays are locally exposed in trough axes and appear on seismic records as subsurface reflections that are truncated along ridge flanks. If these troughs are not being actively flushed, they should have been largely filled in by fine sand from adjacent ridges. In fact, the opposite may be occurring. Along the western side of the southern area, ridges tend to peak near the deepest portions of the adjacent troughs, suggesting build-up of crests at the expense of troughs.

The ridge and swale topography, where developed, modifies the regional pattern of grain size distribution (Stubblefield, et al., 1975). Trough axes contain discontinuous zones of coarse, rippled, pebbly sand, cohesive clay locally exposed in ripple troughs, and clay pebbles. Ridge crests tend to consist of medium-grained sand, while ridge flanks contain finer sand which may bridge across trough axes. The down-flank fining of grain size may reflect transport towards the end of storm periods, or milder events when flow is weaker and no longer couples with topography, when the finer sand fraction is mobilized on ridge crests and disperses down flank.

Mud Transport

General: Finer particulate material consists of agglomerates of silt and clay-sized quartz and clay mineral particles bound together with organic matter. This material is cohesive, and settles out as mud patches on the sea floor after periods of peak flow when such muds are reentrained into the water column. Unlike sands, muds may continue to remain suspended for days or weeks after the storm event, particularly

in the near-bottom turbid layer. Wave surge tends to resuspend particles that settle out, creating a continuous exchange between the turbid layer and the bottom. Strong waves favor suspension in the turbid layer; wave decay favors deposition on the bottom. The behavior of suspended fine sediment is particularly relevant to the issue of ocean dumping of sewage sludge, as sludge mixes with natural suspended materials during dispersal.

Suspended Sediment Concentrations: Over 90% of the fluvial sediment discharge from the northeast United States is effectively trapped near the coast in estuaries and coastal wetlands. Consequently, the terrigenous fraction of the suspended matter decreases rapidly seaward (Manheim, et al., 1970; Meade, et al., 1975; Schubel & Okubo, 1972). Solids in suspension at levels of the water column over the alternative dumpsites are predominately combustible plankton and their non-combustible remains (Drake, D., pers. comm.). Total suspended matter concentration in surface water is from 100 to 500 ug/liter, comprised of 5% or less terrigenous matter, 80% combustible planktonic matter, and 15% siliceous and calcareous non-combustible planktonic remains. Subsurface water concentration is similar or somewhat less, except in the nepheloid layer 15 to 30 ft above the bottom. Concentration in this layer is 500 to 2000 ug/liter, consisting of 10 to 20% terrigenous matter, 30 to 60% combustible matter, and 50 to 80% non-combustible matter (ibid.). Textural properties of bottom sediments in the alternative dumpsites show that very little sediment finer than 62 ug is deposited.

Fairweather currents in these areas are generally to the southwest at net velocities of a few cm/sec. Because of greater average depths in the northern dumpsite, fines dumped there are more likely to be transported further prior to deposition than at the southern dumpsite. However, after deposition, fine sediments would be less likely to be resuspended, except during major storms.

CONCLUSIONS

Both dumpsites are floored by sand, predominately medium-grained (0.25 to 0.5 mm). At the northern dumpsite, moderate sediment transport is indicated to the south and west over a gently sloping bottom incised by broad, low-gradient, pre-existing valleys. Evidence of more active sediment transport to the southwest is indicated at the southern dumpsite.

This work is funded by NOAA's Marine Ecosystems Analysis (MESA) Program in the New York Bight.

References Cited

Beardsley, R.C., and Butman, B., 1974. Circulation on the New England Continental Shelf: Response to Strong Winter Storms, Geophysical Research Letters, v. 1, pp. 181-184.

Manheim, F.T., Meade, R.H., and Bond, G.C. 1970. Suspended Matter in Surface Waters of the Atlantic Continental Margin from Cape Cod to the Florida Keys. Science, v. 167, pp. 371-376.

Meade, R.H., Sachs, P.L., Manheim, F.T., Hathaway, J.C., and Spencer, D.W., 1975. Sources of Suspended Matter in Waters of the Middle Atlantic Bight, Journal of Sedimentary Petrology, in press.

Schubel, J.R., and Okubo, A., 1972. Comments on the Dispersal of Suspended Sediment Across the Continental Shelves, pp. 333-346 in, Swift, D.J.P., Duane, D.B., and Pilkey, O.H. (eds.), Shelf Sediment Transport: Process and Pattern, Dowden, Hutchinson and Ross, Inc., Stroudsburg, Pa.

Stubblefield, W.L., Lavelle, W.J., McKinney, T.F., and Swift, D.J.P., 1975. Sediment Response to the Hydraulic Regime on the Central New Jersey Shelf. Journal of Sedimentary Petrology, in press.

Swift, D.J.P., Kofoed, J., Sears, P., and Saulsbury, F., 1972. Holocene Evolution of the Shelf Surface, Central and Southern Shelf of North America, pp. 499-574, in Swift, D.J.P., Duane, D.B., and Pilkey, O.H. (eds.), Shelf Sediment Transport: Process and Pattern, Dowden, Hutchinson and Ross, Stroudsburg, Pa.

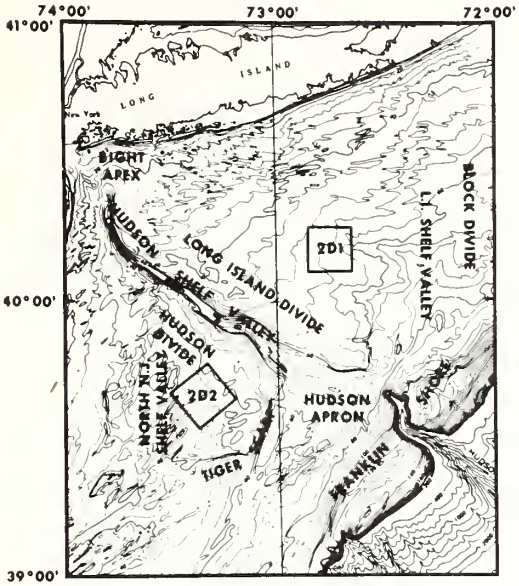

Fig. 1 - Index map of the New York Bight. Contour interval 4 meters. Blocked out areas 2D1 and 2D2 are the proposed interim alternative dumpsites.

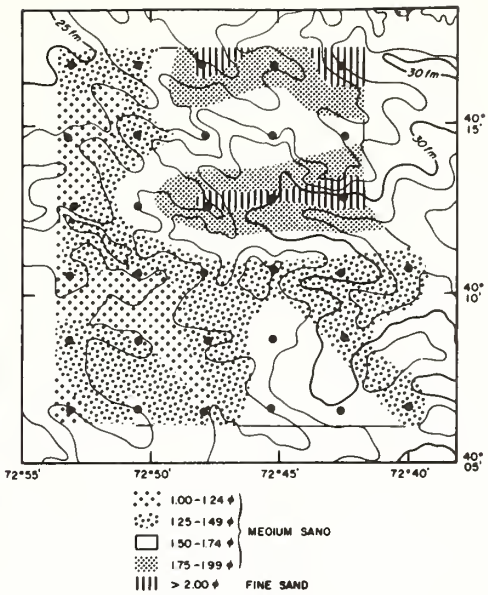

Fig. 2 - Northern alternative dumpsite, area 2D1. Contour interval 1 fathom. Grain size distribution of the sand-sized fraction (1/16 mm [4ϕ] to 2 mm [-1ϕ]). Dots are Smith-MacIntyre bottom grab sample and photo stations.

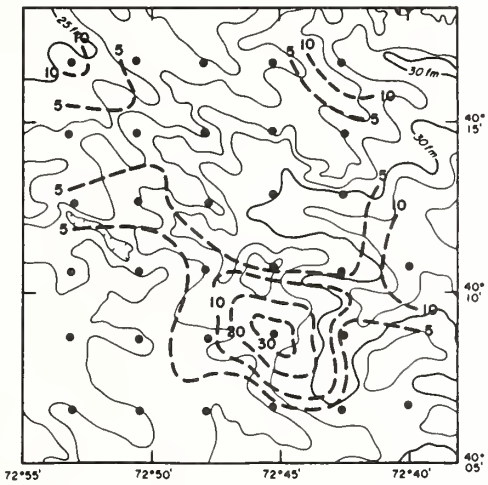

Fig. 3 - Northern alternative dumpsite, area 2D1. Percent gravel over 5 percent. Bathymetric contour interval 1 fathom. Gravel contour interval 5 percent.

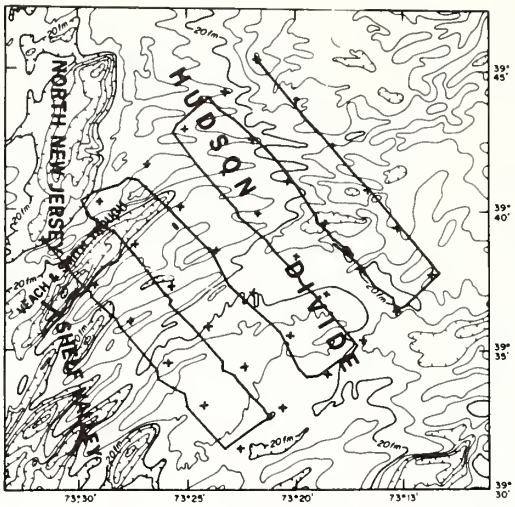

Fig. 4 - Southern alternative dump-site, area 2D2. Bathymetric contour interval 1 fathom.
+ Smith MacIntyre bottom grab sample and photo station.
- Geophysical trackline.
━Submersible dives.

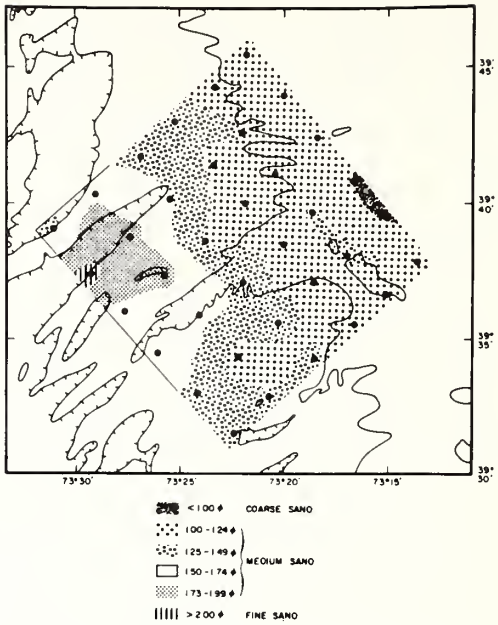

Fig. 5 - Southern alternative dump-site, area 2D2. Grain size distribution of the sand-sized fractions. Dots are Smith-MacIntyre grab and photo stations. Contours are the 20 fathoms isobath.

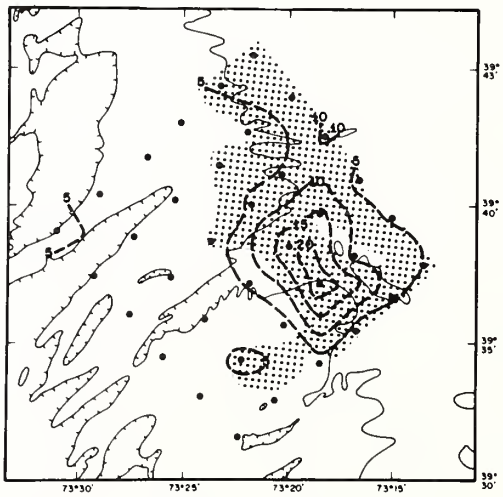

Fig. 6 - Southern alternative dump-site, area 2D2. Percent gravel (heavy contours) over 5%, contour interval 5%. Dot pattern is area of 1.00 to 1.24φ sized medium sand from Fig. 5. Large dots are sample stations. Light contours are the 20 fathom isobath.

Reprinted from: Mid-Atlantic Shelf/New York Bight ASLO Symposium, 24-25.

George L. Freeland, Donald J.P. Swift and William L. Stubblefield, NOAA/AOML, 15 Rickenbacker Cswy., Miami, Florida 33149; Anthony E. Cok, Adelphi University, Garden City, New York 11530.

SURFICIAL SEDIMENTS OF NOAA-MESA STUDY AREAS IN THE NEW YORK BIGHT

The nature of bottom sediments and sediment particles suspended in the water column becomes of interest to environmental managers when man's activities in the ocean cause perturbations on the bottom and in the near-bottom water column. In addition to the immediate results of anthropogenic (man's) activities, one must also consider the effect of long term natural phenomena.

Sediments on the ocean floor in the New York Bight are important as there is extensive ocean usage by man. Users of sedimentological data are fisheries biologists, sanitary and ocean engineers, public health experts, vessel captains, and a myriad of government planners. The more important categories of human usage of the shelf surface are for food resources, waste disposal, foundations, mineral resources and recreation.

The distribution of surficial sediments across the surface of the Bight may be explained in terms of sea level fluctuation caused by continental glaciation during the past several million years. During the last such episode, when the North American ice sheet extended from Canada down as far as Long Island and northern New Jersey, sea level was lowered to about 155 meters below present sea level in the vicinity of Hudson Canyon. From the time of the maximum ice advance about 15,000 years ago (Milliman and Emery, 1968), to about 5,000 years B.P. the ice has been melting and the shoreline has advanced over the shelf to its present position. The surficial sediments and features seen on the shelf today are the result of this fall and rise of sea level. As transgression progressed, fluvial and older sediments of the land surface now occupied by the shelf were first covered by estuarine and lagoonal sediments behind barrier islands or directly reworked by the advancing shoreline. Sand eroded at the shoreface was swept partly back onto the barrier islands by storms and buried there, only to be re-exposed as the shoreface advanced. Most of the material, however, has been washed downcoast and seaward to accumulate as a discontinuous sand blanket 0 to 10 m thick (Stahl et al., 1974). Thus the dominant material present on the shelf floor is sand-sized sediment, unconsolidated fine-grained sediment having been resuspended and transported back into the estuaries or off the shelf edge. Locally, the underlying stratum of transgressed lagoonal and estuarine semi-consolidated mud deposits are exposed on the sea floor (Swift et al., 1972; Stahl et al., 1974; Sheridan et al., 1974), recognizable by angular clay fragments and oyster shells.

Studies off the New Jersey coast have been made of nearshore and central shelf areas of ridge and swale topography (McKinney et al., 1974; Stubblefield et al., 1974; Stubblefield et al., 1975; Stubblefield and Swift, 1975). Results suggest that fine sands are scoured from depressions during winter northeast storms, and are deposited on crests which appear to build up concurrently. The underlying early Holocene lagoonal clay is exposed in particularly deep troughs. Trough axes are locally floored with coarse sand, shell debris, occasional to common lagoonal clay fragments, or may have a mud covering in deep holes. Sandy bottoms are usually strongly rippled. Flanks are covered with fine to very fine sand; the crests consist of medium to fine sand.

In the Bight apex, extensive sedimentological studies and a 1973 bathymetric survey reveal that the only significant change in bottom topography since 1936 is at the dredge spoil dumpsite, where the dumping of 88 million cubic meters of dredged material has caused up to 10 meters of shoaling. The center of the Christiaensen Basin, a natural collecting area for fine-grained sediment, is no doubt contaminated with sludge, but shows no apparent sediment build-up during the intervening 37 years.

Preliminary sediment distribution maps show the apex outside of the Christiaensen Basin to be floored primarily by sand ranging from silty fine sand to coarse sand, with small areas of sandy gravel, artifact (anthropogenic) gravel, and mud. The nearshore mud patches which have caused environmental concern appear to be periodic, at times being covered with sand, and occasionally scoured out. Side-scan sonar records show linear bedforms indicative of sand movement over most of the apex area.

To the east of the apex along the south shore of Long Island, sediment samples and geophysical data have been collected and are currently being processed. Closely-spaced data were collected in an area of ridge and swale topography near the terminus of the Suffolk County sewer outfall.

Two mid-shelf areas, located 120 km from the entrance to Lower Bay and 18 km north and south, respectively, of the axis of the Hudson Shelf Valley have been designated by the MESA Project Office as proposed interim alternative dumping areas for sewage sludge and possibly dredge spoil. Each of the areas studied is an 18 by 18 km square within which bottom samples, photographs, and side-scan sonar and seismic reflection profiles were taken.

The northern area is located in a tributary valley of the ancestral Long Island River System where the surficial sediments consist of fine sands to the northeast, coarser medium sands to the west and south, and 39% gravel at one station in the south. Only two stations contained over 5% mud (5.7% and 8.2%). Bottom photographs indicate that the area is characterized by smooth, slightly undulatory, mounded or rippled bottom.

In the southern area coarser sand and gravel deposits lie on the crest and east flank of the Hudson Divide, while medium and fine sand occur in the ridge and swale topography to the west. These distributions point to the winnowing of fine sediment from the crest and east flank of the Divide and deposition to the west. Submersible observations in Veatch and Smith Trough reveal a veneer of shelly, pebbly sand with large, angular clay pebbles and occasional oyster shells derived from the underlying early Holocene lagoonal clay.

Based on these studies, if sewage sludge were dumped, widespread dispersion, mostly to the southwest, could be expected, with winter-time resuspension and transport out of the areas of fine material on the bottom. Higher volumes of dumped particles would find their way into the Hudson Shelf Valley if the northern area were used. Considerably more rapid build-up and possibly permanent build-up of dumped particles on the bottom could be expected if dredged material were dumped.

REFERENCES

McKinney, T.F., W.L. Stubblefield and D.J.P. Swift. 1974. Large-scale current lineations on the central New Jersey shelf: investigations by side-scan sonar. Mar. Geol. 17:79-102.

Milliman, J.D. and K.O. Emery. 1968. Sea levels during the past 35,000 years. Science 162:1121-1123.

Sheridan, R.E., C.E. Dill, Jr. and J.C. Kraft. 1974. Holocene sedimentary environment of the Atlantic inner shelf off Delaware. Bull. Geol. Soc. Amer. 85:1319-1328.

Stahl, L., J. Koczan and D. Swift. 1974. Anatomy of a shoreface-connected sand ridge on the New Jersey shelf: implications for the genesis of the surficial sand sheet. Geology 2:117-120.

Stubblefield, W.L., M. Dicken and D.J.P. Swift. 1974. Reconnaissance of bottom sediments on the inner and central New Jersey shelf. NOAA-MESA Report No. 1. 39 pp.

Stubblefield, W.L., J.W. Lavelle, T.F. McKinney and D.J.P. Swift. 1975. Sediment response to the present hydraulic regime on the central New Jersey shelf. Jour. Sed. Petrol. 45:337-358.

Swift, D.J.P., J.W. Kofoed, F.P. Saulsbury and P. Sears. 1972. Holocene evolution of the shelf surface, central and southern Atlantic shelf of North America, p. 499-574. *In* D.J.P. Swift, D.B. Duane and O.H. Pilkey (eds.), Shelf Sediment Transport: Process and Pattern. Dowden, Hutchinson and Ross.

Stubblefield, W.L. and D.J.P. Swift. 1975. Ridge development as revealed by sub-bottom profiles on the central New Jersey shelf. In press in Mar. Geol.

Reprinted from: *American Geophysical Union, Fall Annual Meeting 56*, No. 12, 1003.

CALCULATIONS OF SAND TRANSPORT ON THE NEW YORK SHELF USING NEAR-BOTTOM CURRENT METER OBSERVATIONS

P. E. Gadd
J. W. Lavelle
D. J. P. Swift (all at: ATLANTIC OCEANOGRAPHIC & METEOROLOGICAL LABORATORIES, 15 Rickenbacker Causeway, Miami, Florida 33149)

Using near-bottom current meter and surficial sediment size observations in conjunction with empirical transport formulae, calculations of cohesionless bedload sediment movement within the New York Bight have been made. The study employed data collected from 23 long-term current meter records which span a 2 1/2 year period. Measured bottom current speeds suggest that shelf sand transport occurs in intense pulses, associated with storms, separated by relatively long periods of quiescence. The percentage of time that the threshold velocity is exceeded during an entire current meter record serves as a measure of the transport activity existing in that particular area. It has been determined that these percentages vary from less than 1% in offshore areas during fair weather flow regimes to 90% in the shoal regions adjacent to the New York Harbor Entrance which are regularly subjected to intense tidal currents. On the gentle slope of the continental shelf south of Long Beach, Long Island, transport quantities tend to increase logarithmically as the water depth decreases. The Hudson Shelf Valley exhibits anomalously high sediment transporting capabilities coincident with periods of strong westerly winds.

33

Reprinted from: Mid-Atlantic Shelf/New York Bight ASLO Symposium, 31-33.

Patrick G. Hatcher and Larry E. Keister
NOAA/AOML, 15 Rickenbacker Causeway, Miami, Florida 33149

CARBOHYDRATES AND ORGANIC CARBON IN NEW YORK BIGHT SEDIMENTS AS POSSIBLE INDICATORS OF SEWAGE CONTAMINATION

As part of NOAA's Marine Ecosystem Analysis Program in the New York Bight, sediment samples have been collected over a wide area of the Bight, including the Hudson Shelf Valley, and analyzed for total organic carbon (TOC) and total carbohydrates (TCH). These parameters were primarily examined to provide a gross qualitative analysis of the bulk organic matter in the sediments.

The TOC distribution indicates that organic matter is primarily associated with silty sands which accumulate in topographic lows such as the Christiaensen Basin and the Hudson Shelf Valley. The high concentrations of TOC (usually 3-5%) have previously been attributed to sewage sludge which is being released in large quantities to the area by ocean dumping (Gross, 1972; Pearce, 1972). However, the TOC distribution may largely be attributed to the fact that its occurrence in sediments is usually inversely related to particle size distribution (Hunt, 1961) and that fine particles tend to accumulate in topographic lows. The TOC distribution would thereby be closely related to the isobaths.

TCH distribution in sediments of the New York Bight is very similar to that of TOC. In fact, a correlation coefficient of .99 between TOC and TCH at the head of the Shelf Valley typifies their relationship in the Apex. However, progressing seaward this relationship deteriorates and the correlation coefficient drops to .82. From this observation we can deduce that the organic matter in the Apex is fairly uniform in carbohydrate content (as if from a singular source) whereas seaward the organic matter is less uniform in carbohydrate, suggesting that it may be derived from more than one source. This could possibly be resulting from the fact that carbohydrates, introduced in large amounts in the Apex, are transported seaward and diluted with oceanic sedimentary organic matter which is generally depleted of carbohydrates (Degens, 1967).

From the previous discussion we can see that both TOC and TCH are dependent on the particle size or the total amount of organic matter present. By reporting TCH as a percentage of TOC the new parameter (TCH/TOC) becomes independent of particle size or total organic content. TCH/TOC is, thereby, a qualitative parameter for organic matter. Figure 1 shows the distribution of TCH/TOC in sediments of the New York Bight. Values generally range from 20 to 60 with the high values located near the Long Island shore, the head of the Hudson Shelf Valley, and in the Shelf Valley itself. The high values are at least a factor of 2 greater than expected for shelf sediments (Shabarova, 1955; Degens, 1967). Since TCH/TOC is qualitative, the contours are suggestive of the fact that a source of organic matter exists at the head of the Shelf Valley and it is being diluted seaward within the Valley. We propose that the major source of this high carbohydrate organic matter is sewage-derived, based on known concepts about the carbohydrate content of various organic matter sources entering the Bight.

Organic matter derived from terrestrial soils and transported to the Bight by the Hudson River is expected to have a TCH/TOC of approximately 20. However, little of this material reaches the Bight but, rather, is trapped in the estuary (Meade, 1969). Its contribution to the TCH/TOC in sediments of the Bight is, therefore, expected to be minimal.

A major fraction of the particulate material in near-shore areas is composed of living planktonic organisms. These contain substantial amounts of carbohydrates and the TCH/TOC is often around 30 to 80 (Strickland, 1965). Easily hydrolyzable sugars such as glucose and galactose compose the major fraction with structural carbohydrates such as cellulose and hemicellulose composing only a minute fraction (Parsons et al., 1961). By the time these organisms die and settle to the sea floor as detritus, most of the carbohydrates (and also up to 90% of the organic matter) are decomposed with only the resistant ones surviving bacterial decomposition. The TCH/TOC thereby decreases to a value of less than 10 in the upper layers of sediment (Degens, 1967).

In the New York Bight, phytoplankton production may well surpass all other inputs of organic matter in the water column with an average annual production of 800×10^6 kg carbon (Malone, 1975). However, if the sedimentary organic matter were to be exclusively derived from phytoplankton, we would observe a TCH/TOC of less than 10. The sediments in the Apex have a TCH/TOC ranging from 40 to 50, suggesting the presence of a high-carbohydrate source other than phytoplankton.

Sewage sludge is presently being released to the New York Bight at a rate of 5×10^6 m^3/yr (U.S. EPA, 1975) which represents roughly 160×10^6 kg C/yr. Sewage outfalls located along the Long Island and New Jersey shores discharge an undetermined amount of sewage to the Bight. Outfalls located in the Hudson River estuary, the Hudson River, the East River, and various other locations in Metropolitan New York also discharge an undetermined amount of sewage. This material most likely settles out within the estuary but eventually may be dredged and dumped in the New York Bight. As we can see, the New York Bight receives a substantial amount of sewage-derived organic materials, possibly half that supplied by phytoplankton.

Sewage contains a substantial amount of carbohydrates, mostly in the form of cellulose and hemicellulose (Hunter and Heukelekian, 1965). The TCH/TOC is roughly 30 for sewage sludge. Once sewage is released to the environment it undergoes relatively rapid decomposition and a certain amount of TOC is lost. However, more resistant components such as cellulose and hemicellulose may not undergo an equivalent amount of decay. The TCH/TOC may therefore increase to values of 40 to 60 or more as the TOC is being preferentially lost. Therefore, as sewage-derived components settle to the sediment the TCH/TOC increases and it may continue to increase as more decomposition takes place.

For the New York Bight the value of TCH/TOC will be influenced by the relative contribution of organic matter from each of the sources and also the degree of decomposition which has occurred. The largest source of organic matter to the Bight is phytoplankton; however, up to 90% of this may be lost before being incorporated in the sediment. Sewage is the other major source and a much larger fraction is expected to reach the sediments due to the fact that most of its organic matter is relatively resistant to microbial decomposition. We therefore are confident in stating that the major source of organic matter to the sediments is derived from sewage and the high TCH/TOC ratios (30-50) observed in

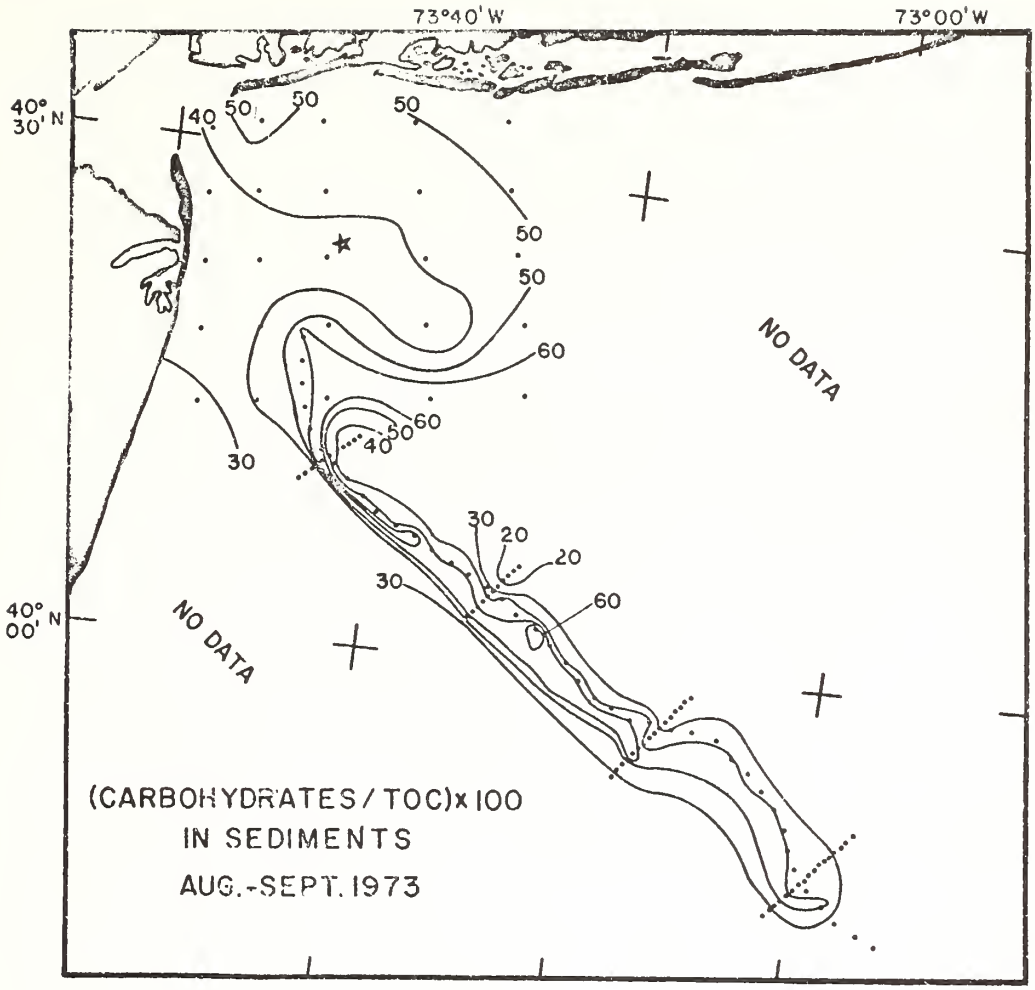

Fig. 1. The distribution of TCH/TOC in sediments of the New York Bight. The ★ denotes the sewage sludge dumpsites.

the Bight are in turn due to the large percentage of sewage-derived organic matter.

A TCH/TOC of 40 or 50 in the sediment indicates that the organic matter contains a substantial amount of sewage which has undergone some decomposition. A TCH/TOC of 20 or less suggests that sewage-derived organic matter is a small fraction of the sediment organic matter which is dominated by phytoplankton organic matter.

REFERENCES

Degens, E.T. 1967. Diagenesis of organic matter. *In* G. Larsen and G.V. Chilingar (eds.), Diagenesis in Sediments. Elsevier.

Gross, M.G. 1972. Geologic aspects of waste solids and marine waste deposits, New York metropolitan region. Geol. Soc. Am. Bull. 83:3163-3176.

Hunt, J.M. 1961. Distribution of hydrocarbons in sedimentary rocks. Geochim. Cosmochim. Acta 22:37-49.

Hunter, J.V., and H. Heukelekian. 1965. The composition of domestic sewage fractions. J. Water Pollut. Control Fed. 37:1142-1163.

Malone, T. 1975. Phytoplankton productivity: nutrient recycling and energy flow in the inner New York Bight. Unpublished report to NOAA, Contract #03-4-043-310.

Meade, R.H. 1969. Landward transport of bottom sediments in estuaries of the Atlantic Coastal Plain. J. Sed. Petrol. 39:222-234.

Parsons, T.R., K. Stephens, and J.D.H. Strickland. 1961. On the chemical composition of eleven species of marine phytoplankters. J. Fish. Res. Bd. Canada 18:1011-1016.

Pearce, J.B. 1972. The effects of solid waste disposal on benthic communities in the New York Bight. *In* M. Ruivo (ed.), Marine pollution and sea life. Fishing News, Surrey, England.

Shabarova, N.T. 1955. The biochemical composition of deep-water marine mud deposits (ocean bottoms). Biokhimiya 20:146-151.

Strickland, J.D.H. 1965. Production of organic matter in primary stages of the marine food chain. *In* J.P. Riley and G. Skirrow (eds.), Chemical oceanography. Academic.

U.S. Environmental Protection Agency. 1975. Ocean disposal in the New York Bight. Technical Brief Report #2. U.S. Govt. Printing Office.

Reprinted from: Seventh International Meeting on Organic Geochemistry, Madrid, Spain, 61.

MANGROVE LAKE, BERMUDA; ITS SAPROPELIC SEDIMENTARY ENVIRONMENT

PATRIC G. HATCHER (1), - BERND R. SIMONEIT (2), - SOL M. GERCHAKOV (3)

Over 9000 years since its origin, Mangrove Lake, Bermuda has accumulated 18 m of sediment representing three different lithologies: a peat overlain by a fresh–water sapropel, and a brackish–wate sapropel. The organic geochemistry of this anoxic, organic –rich, and multi–banded gel was examined to identify various organic constituents (TOC, H, N, carbohydrates, proteins, alkanes, fatty acids, and other bitumens) and their early diagenetic changes.

Major diagenetic changes are observed for carbohydrates and proteins which constitute a large fraction of the organic matter and may be undergoing condensation to humates. Total extracts of the sediment reveal the presence of hydrocarbons, fatty acids, polycyclic hydrocarbons, aromatic hydrocarbons, phenols, esters, and nitrogenous compounds. The n–alkanes and n–fatty acids are of algal, bacterial, and terrigenous source. No correlations between n–alkanes and n–fatty acids are observed to indicate any significant chemical maturation. In addition to diagenetic changes, distinct changes are observed in the depth distributions of all organic geochemical parameters relating to the abrupt changes in depositional environments within each of the lithologies.

Mangrove Lake is presented as an interesting site for studies in early diagenesis in that it is an enclosed marine ecosystem where large amounts of organic matter are rapidly accumulating.

(1) NOAA, Atlantic Oceanographic and Meteorological Laboratories, 15 Rickenbacker Causeway, Miami, Florida 33149.

(2) Space Sciences Laboratory, University of California, Berkeley, California 94720.

(3) Department of Microbiology, University of Miami, Miami, Florida 33152.

Reprinted from: *Clays And Clay Minerals 23*, 331-335.

NOTES

ELECTROSTATIC CLEANING TECHNIQUE FOR FABRIC SEM SAMPLES

(*Received* 19 *March* 1975)

During clay fabric investigations of slightly consolidated submarine sediments, a technique was developed for electrostatically cleaning surfaces of scanning electron microscope (SEM) samples. One of the two surfaces resulting from a single fracture of an oven-dried sample was cleaned using the conventional peeling technique (100 applications of cellophane tape; Barden and Sides, 1971) (Fig. 1a). The opposite surface was cleaned using the electrostatic technique now routinely employed in this laboratory (Fig. 1b). Both surfaces were cleaned satisfactorily. In sharp contrast, uncleaned fracture surfaces of this sample (not shown) were noted to be debris-cluttered*. Both micrographs of Fig. 1 show predominately stepped face-to-face arrangement of the particles in regions which appear more dense whereas numerous oblique edge-to-face contacts occur in areas which appear less dense. The relatively greater proportion of the clay particles lying approximately perpendicular to the surface of the peeled sample may be an artifact produced by the cleaning technique. The process of pressing tape against the sample and pulling it away not only removes debris but also may preferentially remove flat-lying particles of the sample or pull them up on edge. Although we have not shown definitively that peeling does produce such an artifact, numerous peeled surfaces have a similar 'lifted' appearance and these features are highly suspect.

Slightly consolidated clay sediments which are prepared using air or oven-drying techniques have been shown to undergo severe stresses and deformation with large reductions in pore space (Yong, 1972; Naymik, 1974). For this reason, in recent investigations of sediment fabric, samples have been prepared by freeze drying or by critical point drying. These less disruptive drying methods result in relatively fragile material when applied to uncemented, high-porosity clay sediments. Consequently, these dried samples may lack sufficient structural integrity for peeling techniques to be applied. Fracture surfaces of such fragile samples can be cleaned using the electrostatic technique (Fig. 2). The micrograph in Fig. 2(a) shows bands running roughly diagonally which have relatively more edge-to-edge (EE) and edge-to-face (EF) particle contacts alternating with bands which have the predominant face-to-face (FF) structure. The EE and EF contacts lead to a structure far more open in appearance than the FF contacts (Fig. 2b).

In electrostatic surface cleaning, loose particles are lifted from the sample in an electrostatic field without any physical contact with the surface. A field of approximately 20 kV/cm at the sample surface is satisfactory. The field is produced in this laboratory by briskly rubbing a piece of cellulose acetate butyrate tubing with a piece of polyester cloth. The charged tubing is then moved slowly over the fracture surface at a distance of about 1 cm. In order to reduce charge build up, the specimen is fractured and attached to the microscope stub before cleaning, and the stub is grounded at least intermittently during cleaning. A sample can be cleaned in less than 1 min. No features have been observed that indicate any disturbance of the clay fabric due to electrostatic cleaning. The electrostatic cleaning technique is rapid and very economical and has performed satisfactorily in routine SEM sample preparation.

Acknowledgements—We wish to thank Dr. D. Latham of the University of Miami for his assistance in measuring the electrical field. Dr. W. R. Bryant supplied the Mississippi Delta sample. Mr. W. B. Charm assisted with microscopy and Drs. G. H. Keller and W. D. Keller reviewed this manuscript. M. Hulbert acknowledges the support of a National Research Council Associateship.

National Oceanic and Atmospheric Administration, MATTHEW H. HULBERT
RICHARD H. BENNETT
Atlantic Oceanographic and Meteorological Laboratories,
Marine Geology and Geophysics Laboratory,
15 Rickenbacker Causeway,
Miami, Florida 33149, U.S.A.

REFERENCES

Barden, L. and Sides, G. (1971) Sample disturbance in the determination of clay structure: *Geotech.* **21**, 211–222.

Naymik, T. G. (1974) The effects of drying techniques on clay-rich soil texture. In: *Proc. 32nd Ann. Meeting Electron Microscopy Soc. Am.* (Edited by Arceneaux, C. J.) pp. 466–467. Saint Louis, MO.

Tovey, N. K. and Yan, W. K. (1973) The preparation of soils and other materials for the SEM: *Proc. Int. Symp. Soil Structure*, Gothenberg, Sweden, pp. 59–67.

Yong, R. N. (1972) Soil technology and stabilization. In: *Proc. 4th Asian Regional Conf. Soil Mechanics*, (Edited by Moh, Z. C.) Vol. 2, pp. 111–124. Bangkok, Thailand.

* See also photomicrographs of uncleaned and peeled fractured surface in Tovey and Yan (1973).

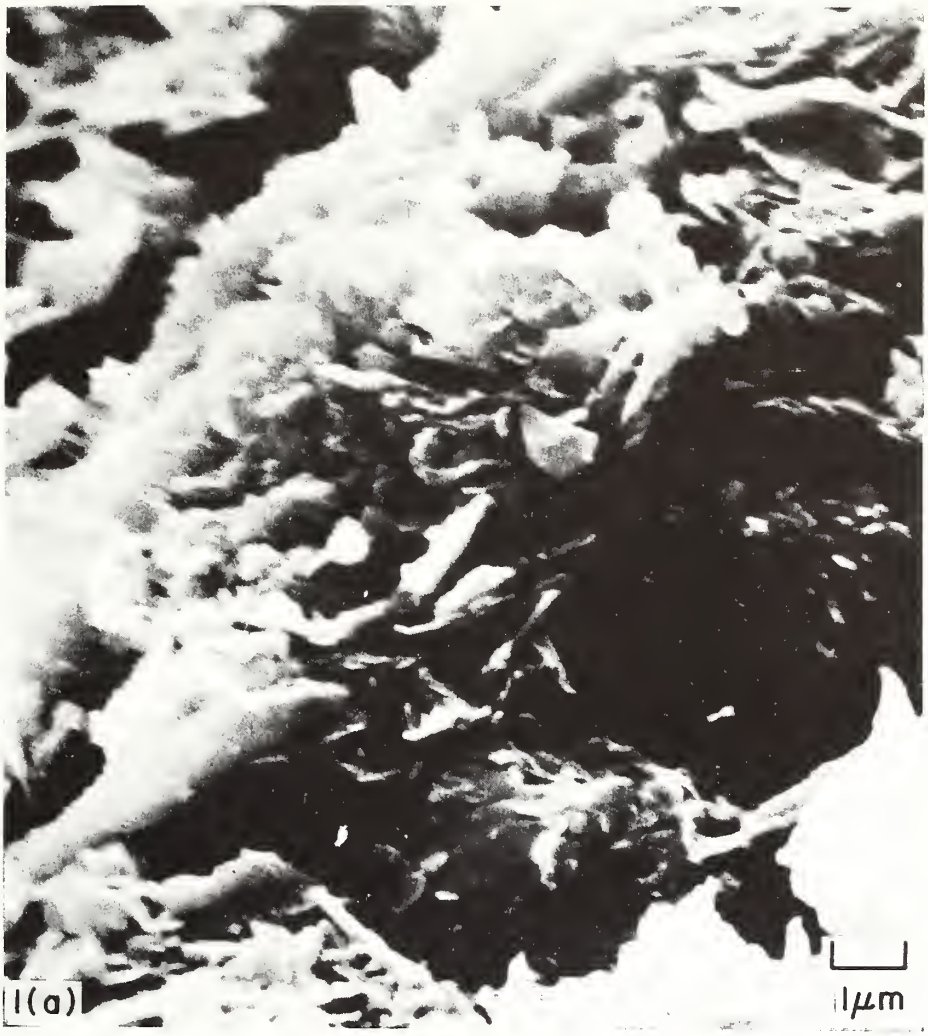

Fig. 1. Opposite surfaces from a fracture of oven-dried continental slope sediment (Wilmington Canyon; (a) peeled, (b) electrostatically cleaned.

1(b)

Fig. 2. Critical-point dried, electrostatically cleaned submarine sediment (Mississippi Delta); (a) general view, (b) detail of EE, EF structure (rosette).

2(b)
1 μm

Reprinted from: *Journal of the Geological Society 131*, 311-321.

Geophysical maps of the eastern Caribbean

PHILIP KEAREY, GEORGE PETER
& GRAHAM K. WESTBROOK

SUMMARY

The results of marine geophysical surveys by NOAA, Miami and the University of Durham with the Royal Navy in the eastern Caribbean region are presented as maps of the bathymetry, free-air gravity anomaly, Bouguer gravity anomaly and total field magnetic anomaly. These maps show in greater detail features which were already known, such as the negative gravity anomaly belt east of the Lesser Antilles, and reveal new features not previously mapped, such as easterly trending anomalies east of the Lesser Antilles and the complicated anomaly pattern of the Aves Ridge. They provide a detailed coverage of the area bounded by latitudes 10°N. and 17°N., and longitudes 57°W. and 65°W.

THE EASTERN MARGIN of the Caribbean Sea is formed by several arcuate structures (Fig. 1). The westernmost is the Aves Ridge, which is a submarine feature with many of the characteristics of an old, submerged island arc. The most prominent is the Lesser Antilles Island Arc, which is a pronounced ridge with a series of volcanic islands situated along it, the oldest of which are of Eocene age. It is separated from the Aves Ridge by a sediment-filled depression, the Grenada Trough. The easternmost element is the Barbados Ridge Complex which is essentially a thick, complexly deformed sediment pile filling a crustal depression that once held the former trench of the Lesser Antilles Arc.

In the late 1960s and early 1970s, Durham University with the Royal Navy, and the Atlantic Oceanographic and Meteorological Laboratories of NOAA, Miami, conducted an extensive marine geophysical survey programme over this area as part of the Cooperative Investigation of the Caribbean and Adjacent Regions (CICAR). The results of these surveys, supplemented by earlier work where available, are presented here in the form of maps of the bathymetry, free-air and Bouguer gravity anomalies, and total field magnetic anomaly (larger scale dyeline copies of the maps are deposited in the Geological Society's Library).

The maps are based on a system of closely-spaced track-lines, (Fig. 1). Navigation in the Durham–Royal Navy survey areas was by Decca Lambda electronic fixing system, which provided an accuracy of approximately ±200 m, with positions fixed every ten minutes. Satellite and radar fixes near land were used for checks. Navigation for most of the NOAA survey lines was by satellites and Loran C, with positions fixed about every two hours. On some of the earlier NOAA lines and on those of other institutions, navigation was mainly by celestial fixes and Loran C. The method of positioning and data collected by the various ships concerned are given in Supplementary Publication No. 18008 (1 page), deposited at The British Library, Boston Spa, Yorkshire, U.K. and at The Geological Society Library.

Bathymetry was monitored mostly by conventional sonic transducers (with the exception of the 1971–1972 NOAA lines, most of which were done with a narrow-beam transducer), the total magnetic field by proton precession

Jl geol. Soc. Lond. vol. **131**, 1975, pp. 311–321, 5 figs. Printed in Northern Ireland.

magnetometers, and the gravity by Graf-Askania or La Coste-Romberg sea gravity meters. Gravity was tied into several established reference stations on the islands (Masson Smith & Andrew 1965; Dorman *et al.* 1973).

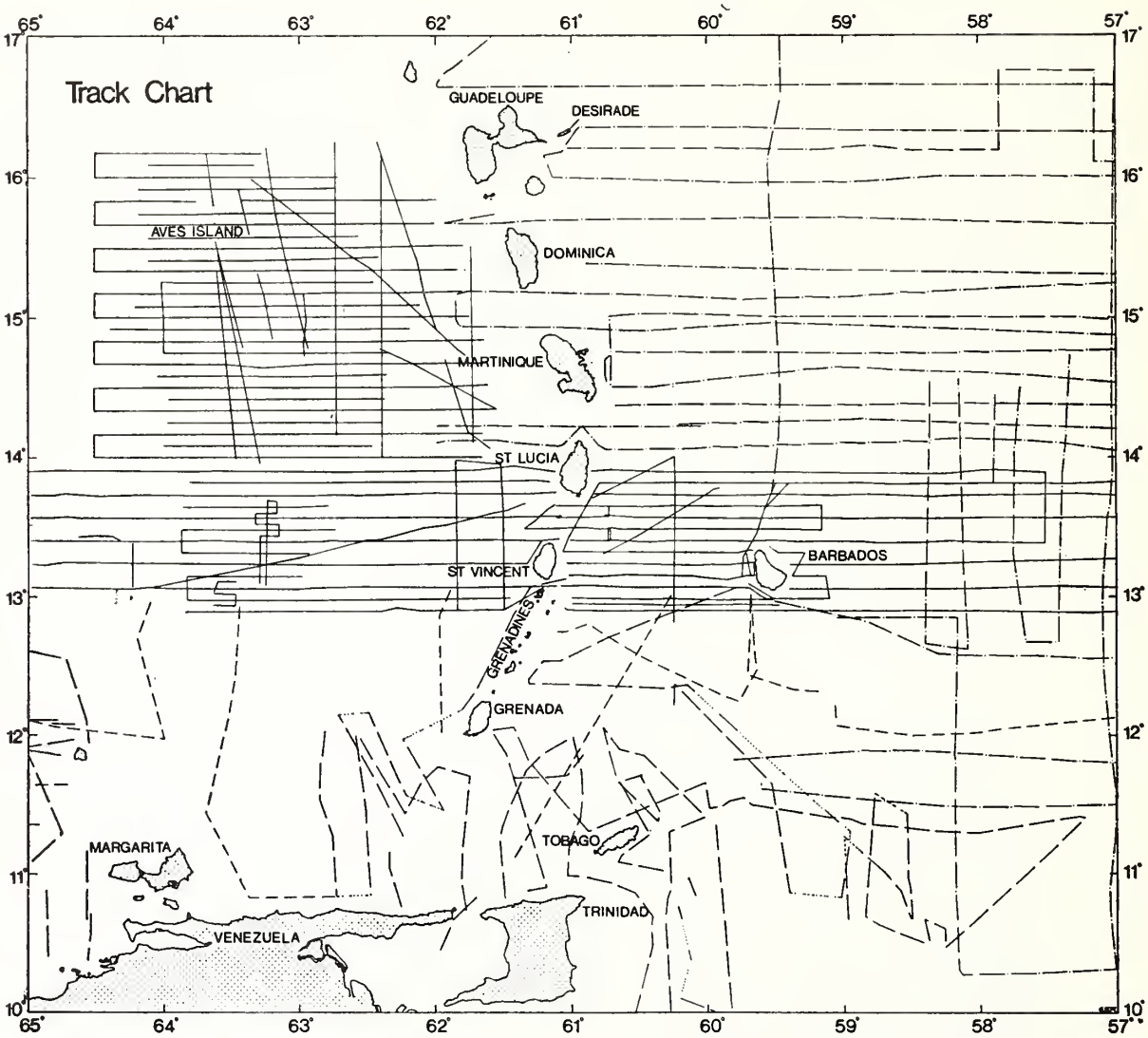

Key

- Durham University & Royal Navy 1971, 1972
- N.O.A.A. 1971, 1972
- N.O.A.A. 1968, 1969
- Other institutions

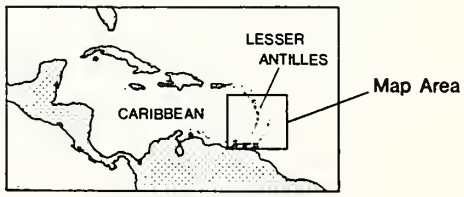

FIG. 1. Chart showing the ships' tracks on which data used in the map compilation were collected.

1. Bathymetry—Map 1

The bathymetry of the eastern margin of the Caribbean is presented at 200 m contour intervals. The depth values are given in corrected metres using Matthews tables (Matthews 1939), except in the area surveyed by H.M.S. HECLA, where depths were obtained for a seawater sound velocity of 1·5 km s^{-1}. Uncorrected depths with this velocity assumption yield an error up to 40 m in depths over 4 km, but over most of the area the error is less than 10 m. Data reduction methods for the NOAA data are contained in Peter *et al.* (1973a). Bathymetric data were supplemented by existing charts to improve interpolation between survey lines south of latitude 13°N. and around the islands.

The major bathymetric features from W. to E. are the Aves Ridge, the Grenada Trough, the Lesser Antilles Island Arc, the Tobago Trough–Lesser Antilles Trench, and the Barbados Ridge Complex.

The Aves Ridge is a broad, linear feature characterized by a series of prominent, N.–S. trending ridges on its western flank and less well-developed ridges on its eastern flank. Its western edge is a fairly straight, N.–S. trending slope, but its eastern edge exhibits a radius of curvature (c. 400 km) which is similar to that of the Lesser Antilles Island Arc. The Grenada Trough exhibits subdued topography south of 15°N, while in the north it becomes increasingly rugged. The ridge upon which the Lesser Antilles Islands are situated is a major feature steeper on its western side than its eastern side, S. of Marie Galante. East of Guadeloupe, La Désirade lies on a prominent high which is the southernmost of a series of highs forming a shelf outside the northern islands of the arc. Between the Barbados ridge, on which the island of Barbados is located, and the Lesser Antilles Arc lies a smooth bottomed depression, the Tobago Trough. The so-called Lesser Antilles Trench is located east of Martinique. The two are separated by a saddle east of St. Lucia. East of these two depressions lies a broad region, approximately 300 km across, of irregular bathymetry, referred to as the Barbados Ridge Complex. There are certainly many more minor peaks and troughs in this region than those that could be resolved with the trackline spacing of the surveys.

The Barbados Ridge Complex is about 1000 m higher south of 14°N, than to the north. In the southern half there is a well-developed series of N.–S. trending ridges and troughs, a large trough being well developed on the eastern flank of the Barbados Ridge. These features are more subdued north of 14°N., and are cut by E.–W. trending troughs and ridges. To the N. the Barbados Ridge Complex terminates along a NW.–SE. trend south of 16°N. (parallel with the trend of the Barracuda Ridge to the NE.), and to the south it merges with the S. American continental shelf. Its eastern margin is well defined by a relatively steep slope down to the Atlantic Ocean floor.

2. Free-air gravity anomaly—Map 2

In the regions surveyed in 1971 and 1972 the anomalies shown are accurate to within ±5 mgal, elsewhere they may be in error by up to ±10 mgal.

The most conspicuous feature of the map is the large, linear negative anomaly,

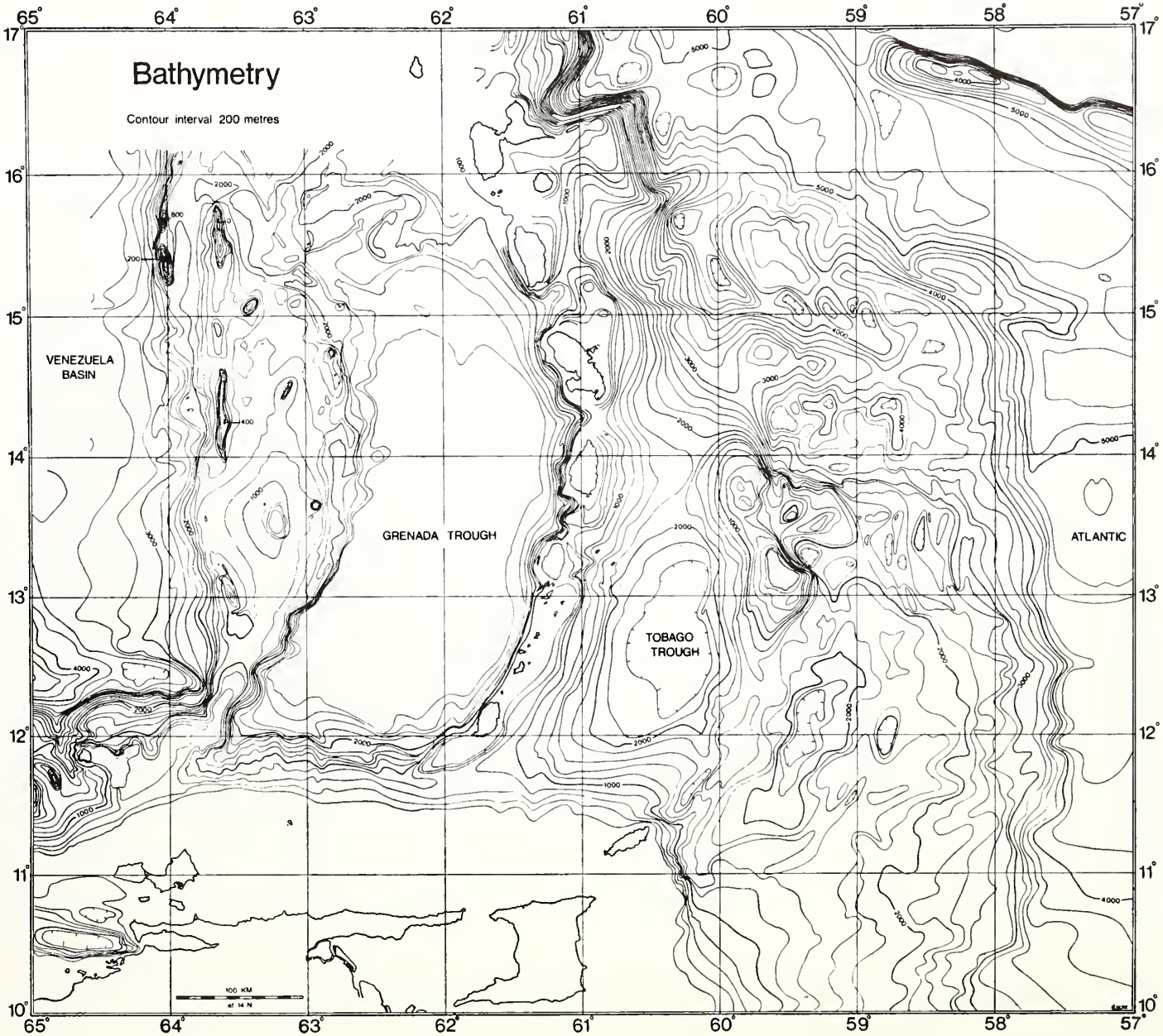

FIG. 2

Map 1—Eastern Caribbean. Bathymetry.

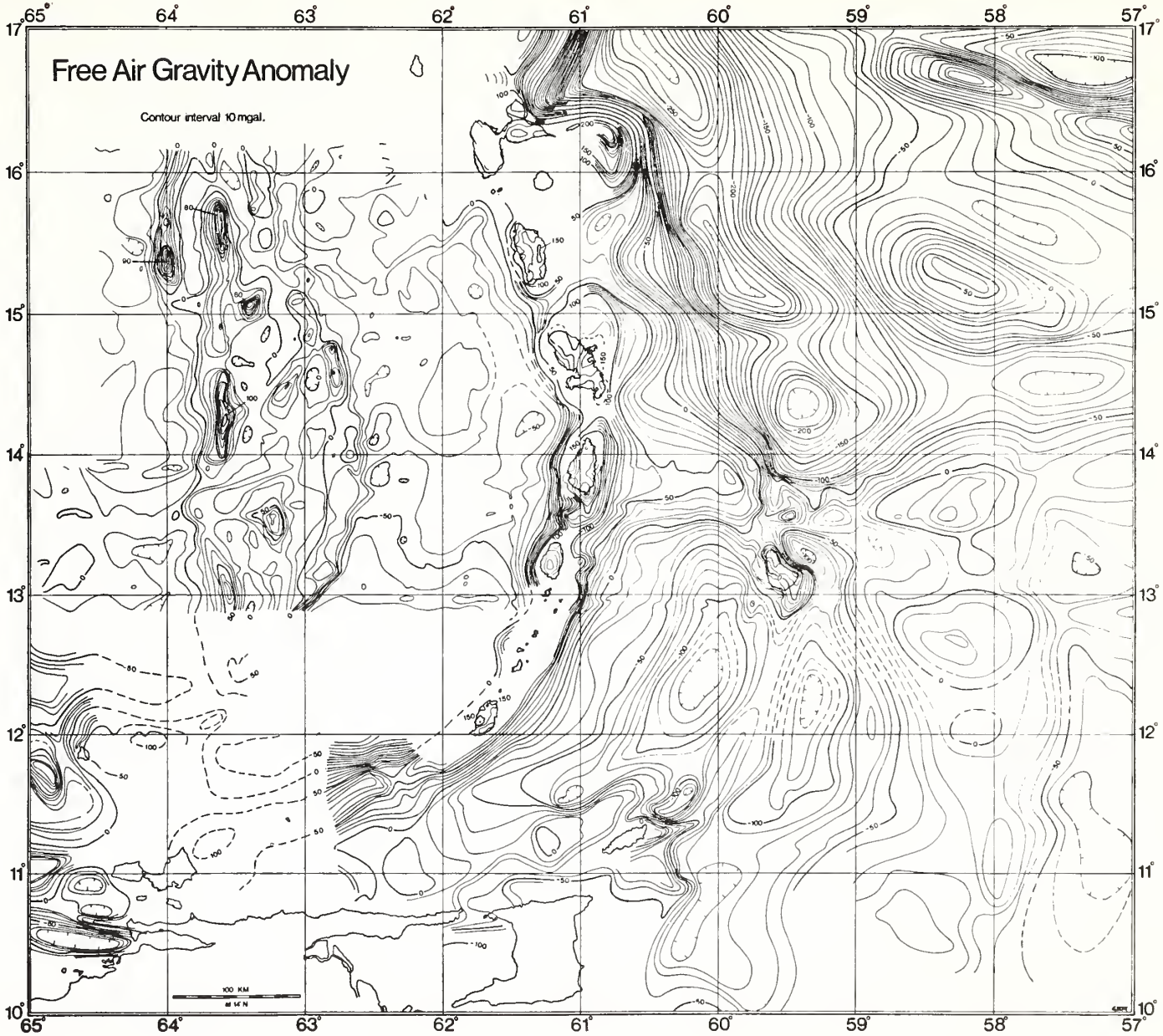

FIG. 3

Map 2—Eastern Caribbean. Free air gravity anomaly.

reaching −270 mgal, E. of the Lesser Antilles Island Arc. The presence of this anomaly was first noted by Hess (1933, 1938) and later workers have delineated it further (Andrew *et al.* 1970; Bunce *et al.* 1971; Bowin 1972). Our surveys show that the axis of this negative anomaly, instead of being a smooth arcuate curve as was once supposed is offset in a sinistral sense along the major E.–W. topographic trends that are present north of 14°N. South of 14°N, where the Barbados Ridge is best developed, the anomaly is split by the ridge into two distinct parts; one follows the eastern side of the Tobago Trough (−120 mgal), the other runs over the eastern flank of the Barbados Ridge. Over the eastern part of the Barbados Ridge Complex and the directly adjacent Atlantic Basin there are E.–W. trending anomalies.

A linear belt of positive free-air anomalies (100–180 mgal) defines the Lesser Antilles Island Arc. The Aves Ridge is also characterized by positive free-air anomalies, which may reach maxima in excess of 100 mgal over topographic prominences. Over the Grenada Trough the free-air anomalies are negative in the south, reaching a minimum of at least −70 mgal; free-air anomalies increase northwards to small positive values.

3. Bouguer gravity anomaly—Map 3

Bouguer gravity anomalies were computed for an average crustal density of 2·67 g cm^{-3}. Around the volcanic islands a value of 2·8 g cm^{-3} would have been more suitable, but in the region of sedimentary relief a density of 2·2 g cm^{-3} would have given a more realistic result. In view of these differences a compromise value of 2·67 g cm^{-3} was adopted, which is the commonly used average. It is also the value most suitable for the region of the continental shelf and slope. In computing the anomalies a correction for the two-dimensional effect of seabed relief was applied along most of the tracklines. The exception is in the NE. corner of the map where a simple Bouguer correction was applied over the region where the deep-sea topography is not of a two-dimensional nature. Bouguer anomalies along the 1968 and 1969 NOAA lines south of 13°N were adapted from Laving (1971); those on the islands are from Masson Smith & Andrew (1965).

The dominant feature of the Bouguer anomaly map is the large linear minimum that follows the crest of the Barbados Ridge in the south and the Lesser Antilles Trench in the north. The amplitude of the anomaly decreases northward from about −300 mgal at Barbados (with respect to the value over the Atlantic) to −220 mgal NE. of Guadeloupe. In the south the axis of the anomaly passes east of Tobago and Trinidad and apparently turns southwest towards the southern part of Trinidad. The Bouguer anomalies vary between 150 and 180 mgal over the islands of the Lesser Antilles. Between Guadelope and St. Lucia there are three higher maxima east of the islands. Over the Aves Ridge there is a relative Bouguer anomaly low with respect to both the Venezuela Basin and the Atlantic Ocean. Superimposed on this low are local maxima which are probably caused by structures in the sediment/basement interface. Both the Aves Ridge minimum and the higher values over the Grenada Trough probably reflect the relative position of the Moho under these features.

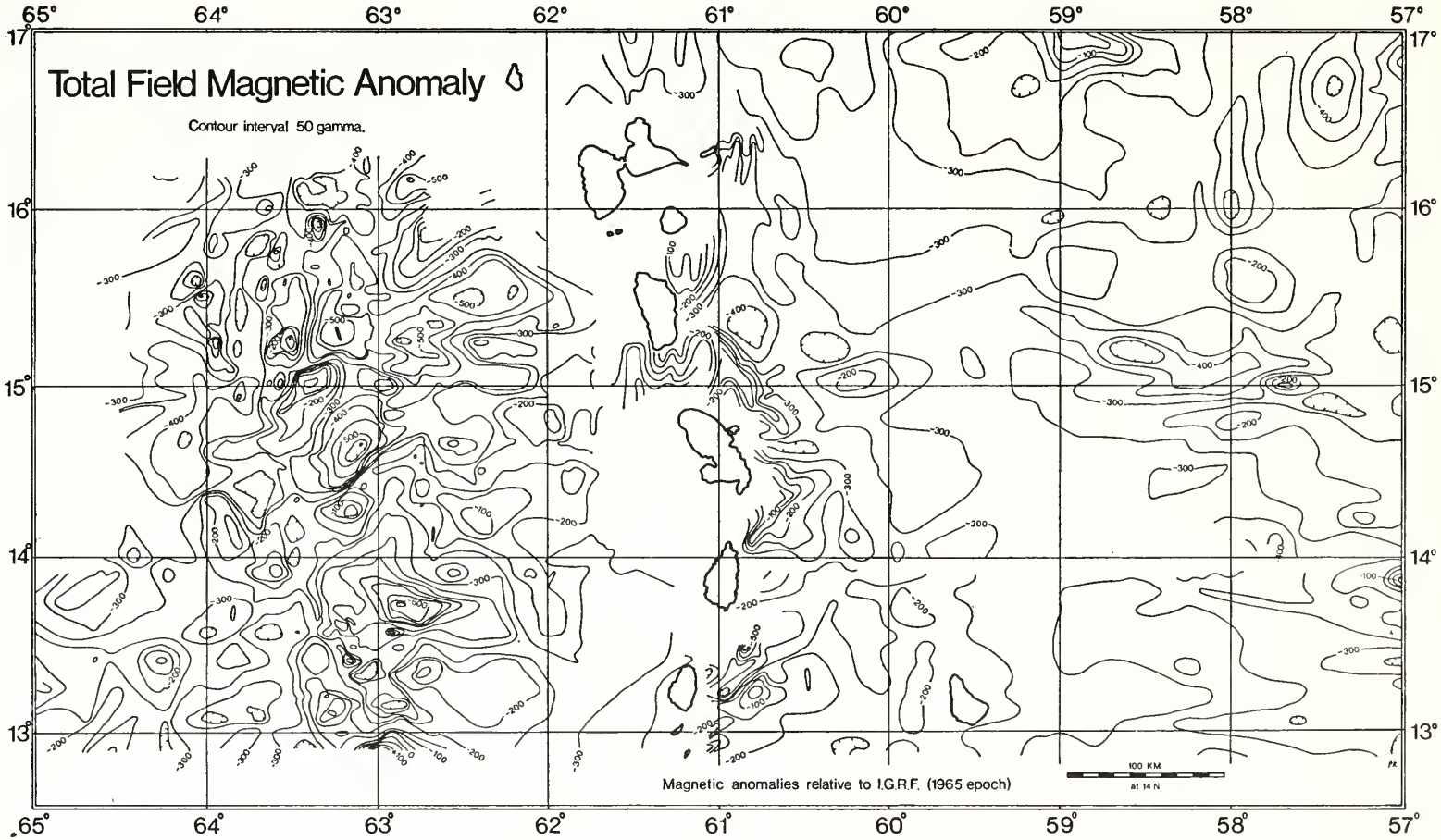

FIG. 5. Map 4—Eastern Caribbean. Total field magnetic anomaly; relative to I.G.R.F. (1965 epoch).

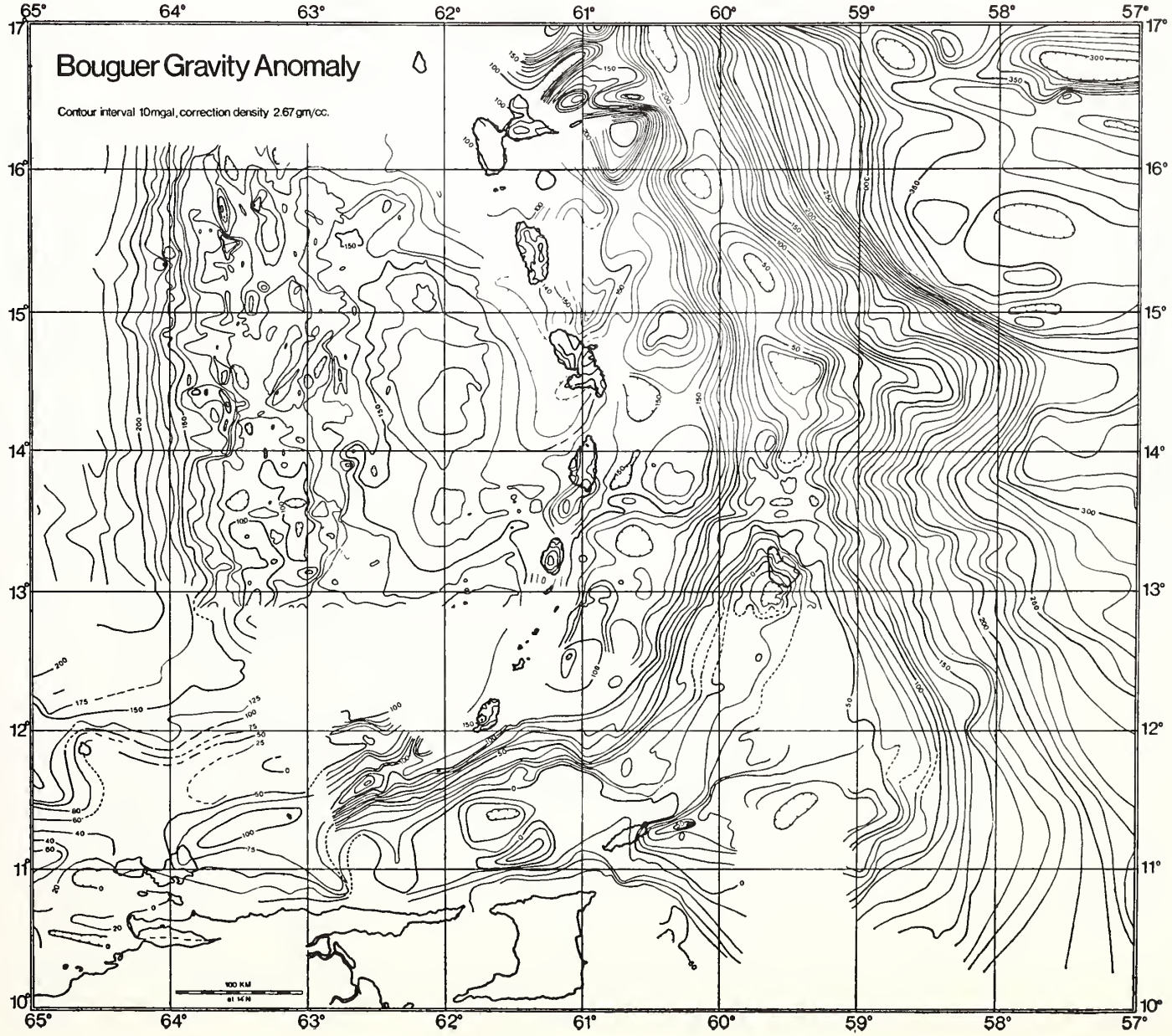

FIG. 4

Map 3—Eastern Caribbean. Bouguer anomaly; 2·67 g cm^{-3}. Two-dimensional correction for bathymetric relief along ships' tracks applied.

4. Total field magnetic anomaly—Map 4

The total field magnetic anomalies of this map represent values with respect to the I.G.R.F. (I.A.G.A. 1969). For this reason the values are generally negative with an average background of −230 gamma. Only the area north of 12°54′N. is shown because the line spacing south of this latitude is not sufficiently dense for contouring. In the area between latitudes 12°54′ and 13°54′N. the data were corrected for ionospheric effects using magnetogram data from geomagnetic observatories at Paramaribo, Surinam and San Juan, Puerto Rico.

The region of the Lesser Antilles Island Arc near the islands is characterized by numerous short-wavelength magnetic anomalies, some reaching an amplitude in excess of 600 gamma. These in most instances could not be contoured due to the line spacing of the surveys which much exceeds the wavelength of these anomalies. A series of somewhat smaller amplitude anomalies characterizes the platform E. of the islands, roughly following the same trend as the Bouguer anomalies.

The western half of the Barbados Ridge Complex exhibits magnetic anomalies of low amplitude. Over the eastern half, however, and over the adjacent Atlantic Basin, there are prominent E.–W. trending anomalies at 15°N., and similar anomalies of somewhat reduced amplitude at 14°N. and 13°N. These are related to the E.–W. ridges and troughs in the igneous basement of the Atlantic (Peter *et al.* 1973a, 1973b; Peter & Westbrook 1974).

Over the Grenada Trough the magnetic field is relatively smooth, but over the Aves Ridge there are numerous anomalies of a few hundred gamma amplitude. These anomalies, as well as those over the Lesser Antilles Island Arc, indicate the presence of mafic igneous rocks near the sea floor.

5. Discussion

The most westerly unit of the map area, the Aves Ridge, is probably an ancient island arc which may have been active during Cretaceous time. The magnetic anomaly map of the Aves Ridge exhibits numerous short wavelength anomalies which may be expected over the lava flows and volcanic plugs characteristic of an island arc. Rock dredged from the ridge have calc-alkaline affinities and ages of 80 to 57 m.y. (Fox *et al.* 1971, Nagle 1971). Bouguer anomalies indicate the presence of an underlying mass deficiency probably caused by depression of the Moho beneath the Ridge.

The calc–alkaline volcanism of the Lesser Antilles has existed since the upper Eocene. A general summary of the geology of the islands of the Lesser Antilles has been presented by Martin-Kaye (1969) and there has been much work performed on the petrology and source of magmas feeding the volcanoes (e.g. Lewis 1971; Robson & Tomblin 1966; Sigurdsson *et al.* 1973). The positive Bouguer anomalies and the short wavelength, high amplitude magnetic anomalies near the islands indicate the presence of near surface, high density igneous rocks. The Jurassic spilites and keratophyres on La Désirade (Fink *et al.* 1972) on the eastern edge of the island platform are in striking contrast to the

Eocene and younger calc–alkaline volcanic rocks of the rest of the Lesser Antilles. Bouguer anomalies suggest that buried structures containing rocks similar to those on La Désirade may continue south from La Désirade as far as St. Lucia.

The negative Bouguer anomaly zone east of the Lesser Antilles over this area is caused by depression of the igneous basement which is filled with sediments reaching a maximum depth of 20 km below Barbados (Westbrook *et al.* 1973). The eastern limit of the seismicity associated with the Benioff zone which dips westward beneath the Lesser Antilles (Molnar & Sykes 1969, Tomblin 1972) coincides approximately with the axis of the negative Bouguer anomaly. Consequently one may suggest that subduction of the igneous crust of the Atlantic Plate beneath the Caribbean Plate, as required by plate tectonics theory, begins at the axis of the anomaly.

Much of the rough topography of the eastern part of the Barbados Ridge Complex seems to be a direct result of deformation. Seismic reflection profiles provide ample evidence of the deformation of the underlying sediments (e.g. Chase & Bunce 1969, Peter *et al.* 1974). Both the topography and gravity anomalies indicate a major discontinuity across the Barbados Ridge Complex at around 14°N. The E.–W. ridges and trough in the sediment pile which cause local offsets of the negative free air anomaly seem to be directly related to E.–W. trending features in the Atlantic ocean floor that are probably ancient transform faults (Peter & Westbrook 1974).

The purpose of this paper has been to present new data in a region which is geologically complex and the object of much interest. Detailed interpretations of some of the data have been published or are in preparation (Kearey 1973, Westbrook 1973, Westbrook *et al.* 1973, Peter & Westbrook 1974, Kearey 1974).

ACKNOWLEDGEMENTS. We gratefully acknowledge the assistance of the captains and crews of H.M.S. HECLA and the NOAA ships DISCOVERER and RESEARCHER in the data collection. We thank M. H. P. Bott for his advice and encouragement. This work was supported in part by N.E.R.C. research grant GR/3/937 awarded to M. H. P. Bott and NSF-IDOE grant AG-253 awarded to G. Peter.

6. References

ANDREW, E. M., MASSON SMITH, D. & ROBSON, G. R. 1970. Gravity anomalies in the Lesser Antilles. *Inst. Geol. Sci. Geophys. Paper* **5**, 21 pp.

BOWIN, C. O. 1972. Puerto Rico Trench gravity anomaly belt. *Mem. geol. Soc. Amer.* **132**, 339–50.

BUNCE, E. T., PHILLIPS, J. D., CHASE, R. C. & BOWIN, C. O. 1971. The Lesser Antilles Arc and the eastern margin of the Caribbean Sea. *In* A. E. Maxwell (ed.), *The Sea* **4** (2), 359–85.

CHASE, R. L. & BUNCE, E. T. 1969. Underthrusting of the eastern margin of the Antilles by the floor of the western North Atlantic Ocean, and the origin of the Barbados Ridge. *J. geophys. Res.* **74**, 1413–20.

DORMAN, C. M., BASSINGER, B. G., BERNARD, E., BUSH, S. A., DEWALD, O. E., CAPINE, L. A., LATTIMORE, R. K. & PETER, G. 1973. Caribbean Atlantic Geotraverse, IDOE 1971, Report No. 3, Gravity. *NOAA Tech. Rept* EP-L 277-AOML11, 35 pp.

FINK, L. K. JR., HARPER, C. T., STIPP, J. J. & NAGLE, F. 1972. The tectonic significance of La Désirade. Possible relict sea-floor crust. *In* C. Petzall (ed.) *Trans. VIth Caribbean geol. Conf. Margarita, Venezuela* 1971, 302.

FOX, P. J., SCHREIBER, E. & HEEZEN, B. C. 1971. The geology of the Caribbean crust: Tertiary sediments, granites and basic rocks from the Aves Ridge. *Tectonophysics* **12**, 89–109.

HESS, H. H. 1933. Interpretation of geological and geophysical observations in the Navy–Princeton Gravity Expedition to the West Indies in 1932. *Bull. geol. Soc. Amer.* **49**,

—— 1938. Gravity anomalies and island arc structures with particular reference to the West Indies. *Proc. Amer. phil. Soc.* **79**, 71–96.

KEAREY, P. 1973. *Crustal structure of the eastern Caribbean in the region of the Lesser Antilles and Aves Ridge*. Ph.D. thesis, Univ. Durham (unpubl.).

—— 1974. Gravity and seismic reflection investigations into the crustal structure of the Aves Ridge, eastern Caribbean. *Geophys. J. Roy. astr. Soc.* **38**, 435–48.

LAVING, G. J. 1971. *Automatic methods for interpretation of gravity and magnetic field anomalies and their application to marine geophysical surveys*. Ph.D. thesis, Univ. Durham (unpubl.).

LEWIS, J. F. 1971. Composition, origin and differentiation of basaltic magmas in the Lesser Antilles. *Mem. geol. Soc. Amer.* **130**, 159–79.

MARTIN-KAYE, P. H. A. 1969. A summary of the geology of the Lesser Antilles. *Overseas Geology and Mineral Resources Inst. Geol. Sci.* **10**, 172–206.

MASSON SMITH, D. J. & ANDREW, E. M. 1965. Gravity and magnetic measurements in the Lesser Antilles. *Overseas Geological Surveys (Geophysical Division) Preliminary Report and illustrations* 16 pp.

MATTHEWS, D. J. 1939. *Tables of the velocity of sound in pure water and sea water for use in echo sounding and sound ranging*. Admiralty Office, London. 52 pp.

MOLNAR, P. & SYKES, L. R. 1969. Tectonics of the Caribbean and the Middle America regions from focal mechanisms and seismicity. *Bull. geol. Soc. Amer.* **80**, 1639–84.

PETER, G., MERRILL, G. & BUSH, S. A. 1973. Caribbean Atlantic Geotraverse, NOAA-IDOE 1971, Report No. 1, Project Introduction—Bathymetry. *NOAA Tech. Rept.* ERL 293-AOML 13, 29 pp.

——, DEWALD, O. E. & BASSINGER, B. G. 1973. Caribbean Atlantic Geotraverse, NOAA-IDOE 1971, Report No. 2, Magnetic Data. *NOAA Tech. Rept.* ERL 288-AOML 12, 19 pp.

——, SCHUBERT, C. & WESTBROOK, G. K. 1974. NOAA-IDOE Caribbean Atlantic Geotraverse. *Geotimes* **19**, (8), 12–5.

—— & WESTBROOK, G. K. 1974. Tectonics of the Barbados Ridge and the adjacent Atlantic Basin. *Trans. Am. Geophys. Union* **55**, 284.

ROBSON, G. R. & TOMBLIN, J. F. 1966. *Catalogue of the active volcanoes of the world including solfatara fields. Part XX West Indies*. International Association of Volcanology, Rome.

SIGURDSSON, H., TOMBLIN, J. F., BROWN, G. M., HOLLAND, J. G. & ARCULUS, R. J. 1973. Strongly undersaturated magmas in the Lesser Antilles. *Earth planet. Sci. Letters* **18**, 285–95.

TOMBLIN, J. F. 1972. Seismicity and plate tectonics of the eastern Caribbean. *In* C. Petzall (ed.) *Trans. VIth Caribbean Geol. Conf. Margarita, Venezuela* 1971, 277–82.

WESTBROOK, G. K. 1973. *Crust and upper mantle structure in the region of Barbados and the Lesser Antilles*. Ph.D. thesis, Univ. Durham (unpubl.).

——, BOTT, M. H. P. & PEACOCK, J. H. 1973. The Lesser Antilles subduction zone in the region of Barbados. *Nature Phys. Sci.* **244**, 18–20.

Received 13 August 1974; revised typescript received 23 October 1974.

PHILIP KEAREY, Department of Geological Sciences, The University, South Road, Durham DH1 3LE.

GEORGE PETER, N.O.A.A. Marine Geology and Geophysics Laboratory, Atlantic Oceanographic and Meteorological Laboratories, 15 Rickenbacker Causeway, Virginia Key, Miami, Florida 33149.

GRAHAM KAREL WESTBROOK, Department of Geology, The University, Keele, Staffordshire ST5 5BG.

37

Reprinted from: IX International Congress of Sedimentology, Nice, France, Theme 6, 77-80.

Sedimentary Processes in Submarine Canyons off Northeastern United States

by George H. Keller
Geological Oceanographer, National Oceanic and Atmospheric Administration, Atlantic Oceanographic and Meteorological Laboratories, Miami, Florida, USA.

Submarine canyons off the northeast United States are characteristically found to head at the shelf break, extending down to the upper rise and the abyssal plain in a few cases. Only in the case of the Hudson canyon is there visible surface expression of the drowned channel extending to the present Hudson river channel. The Hudson shelf valley and canyon system appears to tell the story for the origin of a number of the canyons bordering the northeast United States. Seismic reflection profiling has revealed in most cases buried channels extending from the vicinity of present canyon heads shoreward. Most of the canyons cannot be identified with earlier or present rivers as can the Hudson, but it is apparent from the reflection profiles that they were part of drainage systems extending across various parts of the continental shelf. During the Pleistocene and possibly earlier as well, the canyons and their drainage systems served as distinct channels for the transport of coarse-grained sediments from the shelf to the rise and abyssal plain. Horn and others (1971)[1], in their study of sediment cores from the western margin of the Atlantic basin, clearly showed the effectiveness of the canyons in channeling coarse sediments onto the abyssal plain (Fig. 1).

Today, with the higher sea level, the canyons have lost their shelf valleys due to infilling and appear topographically only as canyons in the continental slope, heading on the order of 160 km off the coast. The rise in sea level has also served to eliminate the fluvial transport of coarse material across the shelf to the canyons.

---

[1]Horn, D. R., Ewing, M., Horn, B. M., and Delach, M. N., 1971. Turbidites of the Hatteras and Sohm abyssal plains, western North Atlantic. Marine Geology, 11: 287-323.

Recent studies in canyons off northeastern United States reveal that currents within the canyons are far from unidirectional, but possess a strong up- and down-canyon component as well as distinct across-canyon flow in some cases. This reversal in flow direction is a distinctive characteristic of both shelf and canyon dynamics. It is readily apparent that the tidal component is the most influencial factor on this flow regime (Fig. 2). Internal waves appear to play some role in canyon dynamics (Keller and others, 1973[2]; Shepard and others, 1974[3]), but an understanding of their influence has not yet been developed.

For the most part, net transport within the canyons appears to be downcanyon based on both current measurements and the observation of such bottom features as ripples and leeside tailings. In Hudson and Hydrographer canyons bottom transport downcanyon is quite distinct (Fig. 3). It is also apparent from current observations that current shears are present at different levels in canyons and flow within a canyon is far from uniform from its lip to the floor. In the Wilmington canyon area, it appears that the westerly set of shelf currents and, at greater depths, the Western Boundary Undercurrent strongly influence the current dynamics within the canyon. Current observations from depths of 700 and 900 m show the typical up- and down-canyon flow, but calculation of net transport over a 19-day period revealed a flow across (to the west) and up the canyon. Conflicting evidence, such as the orientation of ripple marks and leeside tailings, point to downcanyon transport of bedload material in the canyon head, but further downcanyon these same features indicate across-canyon flow (Fenner and others, 1971[4]).

---

[2]Keller, G. H., Lambert, D., Rowe, G., and Staresinic, N., 1973. Bottom currents in the Hudson canyon. Science, 180: 181-183.

[3]Shepard, F. P., Marshall, N. F., and McLoughlin, P. A., 1974. "Internal waves" advancing along submarine canyons. Science, 183: 195-198.

[4]Fenner, P., Kelling, G., and Stanley, D. J., 1971. Bottom currents in Wilmington submarine canyon. Nature Phys. Science, 229: 52-54.

In this case where bottom feature orientations contradict the measured flow regime, the long-term transport regime is undoubtedly that reflected in the bottom features and not that of the 19-day observations.

North of the Hudson canyon there is a distinct difference in the sediment being carried through the canyons. To the north, off Georges Bank the canyons in general appear to be quite active. For the most part, these canyons are areas of active coarse-grained sediment erosion and transport downslope. Relatively little fine-grained material is present in the upper parts of the canyons, with rock outcrops the rule rather than the exception. Hydrographer canyon appears to be extremely active with bottom currents of 55 cm/sec having been measured and the migration of sand ripples down-canyon recorded photographically. In Hudson canyon and those to the south (Wilmington, Baltimore, and Norfolk) the overall sedimentary regime is primarily one of fine-grained sediment (silt, clayey silt, and silty clay) with the sands and gravels being confined to the "head" portion of the canyons. These "southern" canyons take on the appearance of being relatively inactive, although bottom velocities of 25 to 35 cm/sec are common. Current velocities in the Georges Bank canyons do appear to be higher than those recorded in the "southern" canyons, but velocities in themselves do not seem to explain the differences in the sedimentary regimes found associated with these various canyons. Sediment source material undoubtedly plays a major role in regard to sediment transport through the canyons. In the case of Georges Bank canyons, the source material is primarily coarse-grained, reworked glacial deposits, whereas to the south, less and less of this coarse material is available. Although current velocities of 35 cm/sec have been recorded in Hudson canyon, there is no indication of coarse-grained material being transported downcanyon. Based on geochemical studies of the carbohydrate and total organic carbon content of the sediments, however, there is evidence that the Hudson canyon does serve as a

conduit for the movement of fine silt and clay size material out onto the abyssal plain.

Today the submarine canyons off the northeast United States appear to transport little, if any, coarse-grain sediment from the shelf to the abyssal plain. Exceptions to this may be some of the canyons off Georges Bank, where strong currents (55 cm/sec) and sand migration downcanyon have been observed. Canyons are, however, zones of considerable current flow with common velocities of 15 to 25 cm/sec and frequently as high as 30 to 35 cm/sec. The northeast canyons are certainly active, but appear now to be primarily the conduits for the transport of fine-grained, rather than coarse-grained sediment to the deep sea.

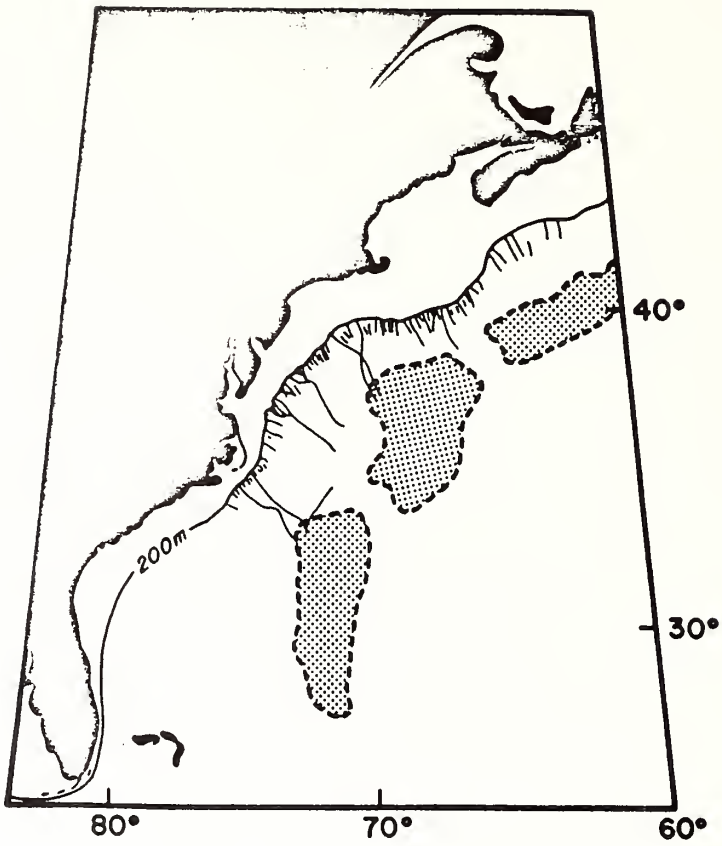

Fig. 1. Areas of coarse-grained turbidite concentrations; attributed to transport through nearby canyons. After Horn and others (1971).

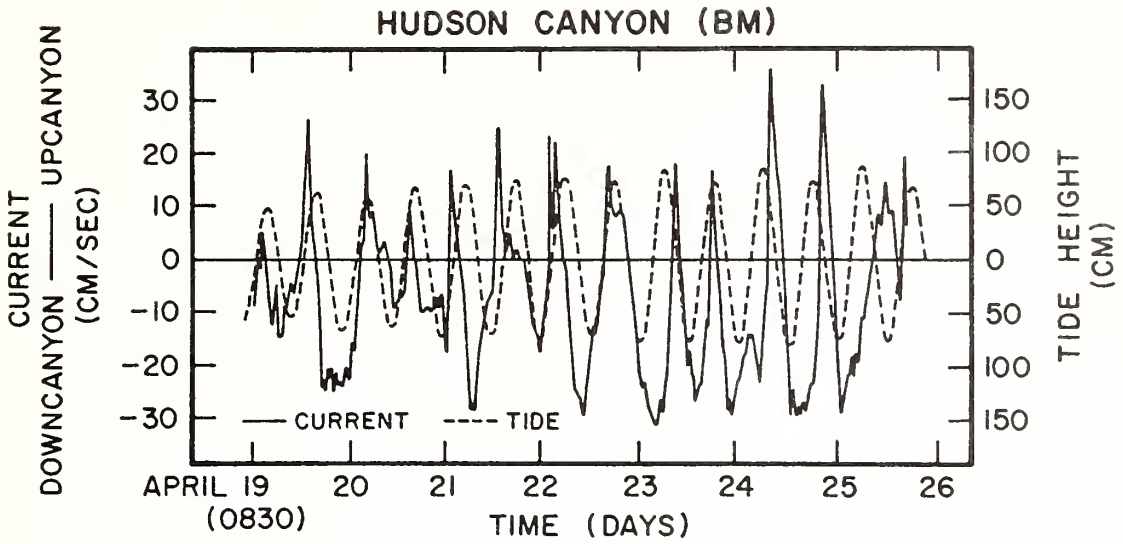

Fig. 2. Characteristic up- and down-canyon flow with the tide superimposed on the current data. (BM) bottom meter.

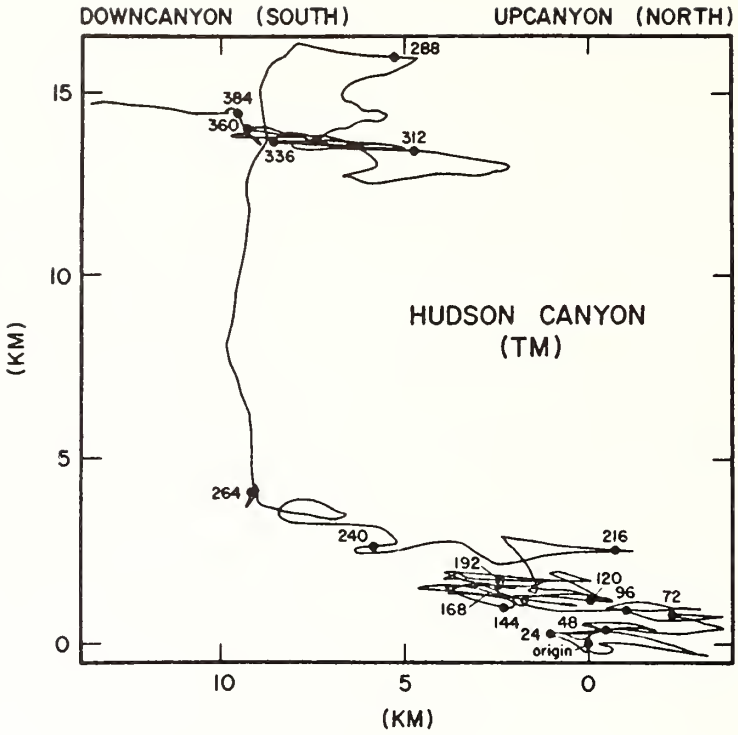

Fig. 3. Vector analysis plot showing the net transport over 390 hours through Hudson canyon (depth 230 m) (TM) top meter.

Reprinted from: *Marine Geotechnology 1*, No. 1, 159-161.

Book Review

The Ocean Basins and Margins—Volume 2: The North Atlantic by A. E. M. Nairn and F. G. Stehli (Editors). Plenum Publishing, New York, 1974. 598 pp. $38.00.

Reviewed by George H. Keller*

This volume consists of fourteen chapters or papers by various authors who have compiled an up-to-date summary of the geological framework of the North Atlantic basin and its margin. It is organized so that the reader is led through a series of geological discussions starting with the Bahamas and moving north along the east coast of North America, east to the margins of Greenland and Norway, then south through the British Isles to Brittany. Although Spain and Portugal are not discussed, a substantial chapter is devoted to West Africa. The reader is thus given a fish-eye view of the geology ringing the North Atlantic. The geology and tectonism of the major oceanic islands are discussed in light of their relationship to the basin's development. Tectonic events influencing the margin along with their ages are adeptly summarized in one of the later chapters. A regional scan of the geophysical data available from the basin itself is presented in the final chapter in an effect to define the history of the North Atlantic.

The editors, A. E. M. Nairn and F. G. Stehli, set the stage in the first chapter by briefly summarizing the model for tectonic evolution of the North Atlantic basin. Stehli in the following chapter draws heavily from the literature to discuss the geology of the continental shelf from North Carolina to Florida, the geology of Florida, the northern Antilles, and the Bahamas. Much of the discussion centers on the Bahamas and the hypotheses as to the origin of this platform. Mention is made of the age and distribution of surficial sedimentary sequences as well as outlining the geological section underlying the Blake Plateau. A good synthesis of the stratigraphy, sediments, physiography, and structure of the continental margin from Florida to Newfoundland, including a brief discussion of the magnetic quiet zone and the overall continent-to-ocean transition zone of

*Atlantic Oceanographic & Meteorological Laboratories, Miami, Florida.

Marine Geotechnology, Volume 1, Number 2
Copyright © 1975 Crane, Russak & Company, Inc.

the western Atlantic is provided by M. J. Keen. The northeastern terminus of the Appalachian orogeny is discussed by H. Williams, M. J. Kennedy, and E. R. W. Neal, and is basically a synthesis and interpretation of Newfoundland geology and tectonism which pretty well defines the significant elements of the Appalachian system.

T. Birkelund, D. Bridgewater, A. K. Higgins, and K. Perch-Nielsen present a summary of the geological and structural history of the Greenland margin. Particular attention is given to the hypothesis that Greenland represents a fragment of an earlier North Atlantic continental mass as well as pointing out the pronounced matching of stratigraphic units, both in type and age with those of Europe. A thorough summary of the geology of the Caledonides sequence of Scandinavia is given by R. Nicholson, with a discussion of the respective units and their tectonic setting. Some mention is made of the comparison of the Caledonides with those of the British Isles as well as commenting on the paleogeographic reconstruction of the Caledonides. Further, J. F. Dewey continues the discussion of the Caledonides by summarizing the detailed geological data from the British Isles and then goes on to discuss the entire orogenic belt, its extent and geological variations in light of various global tectonic models. The geological and tectonic histories of the western approaches (Southern Ireland, Great Britain, and Brittany) are summarized by T. R. Owen. Not only is the terrestrial geology and structure discussed but the adjacent continental shelf geology as well. A good synthesis of the paleogeographic tectonism from the Precambrian to Quaternary is also presented.

M. Vigneaux reviews the geological framework of the Bay of Biscay, discusses the available geophysical data, and addresses certain aspects of the geomorphology and sedimentation pattern of littoral, continental shelf, and bathyal regions. It is a fine discussion of the sedimentary history as well as touching upon the origin and age for the opening of the Bay. Skipping to the south, an excellent survey of the geological history and stratigraphic sequences of West Africa from the Precambrian to the Holocene is presented by W. Dillon and J. M. A. Sougy. Discussion centers on specific geological aspects and their interrelationships in light of the formation of the North Atlantic. The authors also briefly mention the geology and volcanic history of the Canary and Cape Verde Islands. A good summary of Cenozoic to Recent volcanism in and along the northern margins of the Atlantic has been compiled by A. Noe-Nygaard. The discussion is primarily concerned with the terrestrial geology rather than that of the seafloor. A brief summary of volcanism in relation to the theory of seafloor spreading is given. A fine discussion of the geological and tectonic framework of the seafloor in and around the Azores Islands is presented by W. L. Ridley, N. D. Watkins, and D. J. MacFarlane. They discuss the volcanism of the Islands as well

as giving considerable attention to the geophysical observations made in the vicinity of these mid-ocean islands. Speculation on the cause of changes in spreading direction and the overall tectonic model for this juncture of the seafloor are set forth.

A well-organized overview for North America, Greenland, Eurasia, and Iberia of tectonic patterns and events that have influenced the margin of the North Atlantic basin as well as the later events involved in the breakup and formation of the basin is presented by F. J. Fitch and others. Also included is a discussion on the verification of events by means of radiometric-age dates. The final chapter by H. C. Noltimier is a summary of the geological and tectonic framework of the North Atlantic basin itself. Various geophysical data such as seismic refraction and reflection, magnetics, gravity, and heatflow are reviewed in light of plate tectonics and formation of the North Atlantic. Overall, this volume serves as an excellent reference to the student of plate tectonics and seafloor spreading. The authors have drawn heavily on the literature thus providing an excellent source book of previous studies.

Reprinted from: *Journal of Sedimentary Petrology 45*, No. 1, 292-294.

CARIACO TRENCH-SEDIMENT GEOTECHNICAL PROPERTIES[1]

G. H. KELLER AND L. L. MINTER[2]
NOAA, Atlantic Oceanographic & Meteorological Labs
15 Rickenbacker Causeway, Miami, Florida 33149

ABSTRACT: A study of the mass physical properties of a sediment core from the anaerobic Cariaco Trench shows there to be a noticeable difference in these properties relative to those of the eastern Caribbean and Atlantic basins, and an even greater difference from those of the anoxic Black Sea. The variations in physical properties appear to reflect the respective concentrations of organic carbon in the four areas compared.

The Cariaco Trench, which lies parallel to and just off the northern coast of Venezuela, is one of the few deep-sea areas exhibiting anaerobic conditions. Circulation below 150 m (sill depth) is limited, and from about 375 m to the bottom at 1,400 m an anoxic environment exists (Richards and Vaccaro, 1956).

Earlier investigators have discussed various oceanographic conditions (Richards, 1960; Richards and Vaccaro, 1956; Curl, 1960; and Fanning and Pilson, 1972) in the trench as well as its geological setting (Ball, *et al.*, 1971; and Peter, 1972). Sediment cores have been collected from different parts of the trench and discussed to varying degrees by Heezen, *et al.*, (1959), Athearn (1965), and Lidz, *et al.*, (1969). These studies have dealt mainly with the discussion of sedimentary features, limited micropaleontological and chemical analyses, and geochronology as related to the occurrence of stagnant conditions in the trench.

The trench, in addition to its physical configuration and anaerobic environment, is characterized by a very high rate of productivity (2.30 $gC/m^2/day$) in the overlying waters (Curl, 1960) and a rather high sedimentation rate (50 cm/1000 yr) (Heezen, *et al.*, 1959).

During a cruise of the NOAA Ship DISCOVERER in 1972 a large diameter (8.9 cm) gravity core, 106 cm long, was taken from a depth of 1302 m in the eastern part of the trench (10°29.8′N, 64°29.2′W). This relatively undisturbed sample was collected in order to examine in detail the geotechnical properties of the anaerobic trench deposits.

The cored interval consists primarily of a silty clay with a considerable amount of fine layering. Some laminae are made up of distinctly coarser material such as angular quartz grains, Foraminifera, ostracods, and pteropods. Others, however, are not texturally different but are distinguished by color changes in the silty clay. Radiographs of the silty-clay intervals do not distinguish the laminae indicating a uniform density. These coloration laminae may result from varying concentrations of organic carbon which in turn probably reflect the high productivity levels of the overlying waters.

Athearn (1965) suggested that these laminated sediments be attributed to the alternation of wet and dry seasons. He also speculated that some of the coarser layers containing Foraminifera and pteropods may have been due to "mass kills" on a local basis. In our examination of these layers we found both benthic and pelagic Foraminifera as well as angular quartz grains. The presence of shallow water benthic forms and a high concentration of quartz suggest transport of these coarser materials into the trench from the adjacent shelf. Turbidites appear to be relatively rare (Athearn, 1965; Lidz, *et al.*, 1969) and large turbidity currents in themselves do not seem to be a major means of transport into the trench. It would appear that runoff, transport of shelf sediments, and local slumping play the major role in the overall infilling process.

The one-meter interval sampled consists primarily of clay (54%) with lesser amounts of silt (24%) and sand (22%) (Fig. 1). Disregarding the three major sandy layers, the overall texture is more that of a silty clay (clay 63%, silt 24%, and sand 13%). Water content is given in percent dry weight as normally de-

[1] Manuscript received June 28, 1974; revised August 29, 1974.
[2] Present address: Dept. of Oceanography, Texas A&M Univ., College Station, Texas.

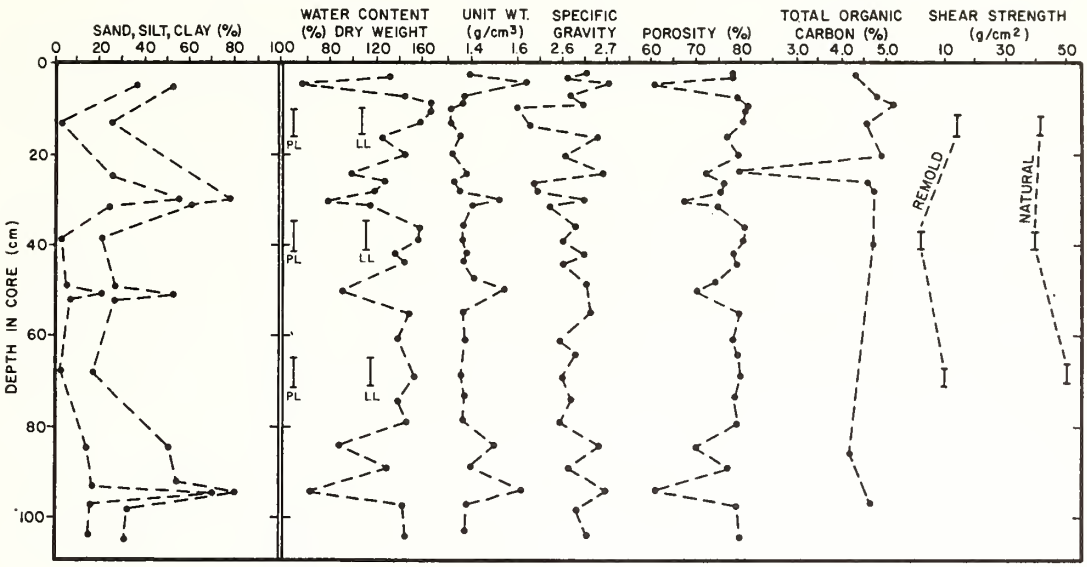

FIG. 1.—Physical and chemical properties for Cariaco Trench core.

termined in engineering practice. Other properties such as unit weight, porosity, shear strength, and the plastic and liquid limits to be discussed later, are adequately explained in any soil mechanics text and will not be defined here. Water content varies from about 145–170% in the silty clay to 60–80% in the coarser sandy layers (Fig. 1).

Liquid and plastic limits define the water content at the stages where a sediment flows when shocked under laboratory testing and when it loses its plasticity respectively. These limits for the silty clay intervals are remarkably similar within the one meter sampled, with a plastic limit of 47 and liquid limits of 114–117. Using Casagrande's (1948) classification, which is based on the liquid and plastic limits, these sediments are classed as "organic clays of medium to high plasticity." Few deep-sea sediments fall into this class, but more commonly are classified as "inorganic clays of high plasticity," (Richards, 1962). Being classed as organic clays is, however, not surprising owing to the high concentrations of organic material common to the trench deposits.

Unit weight or wet bulk density varies relatively little throughout the sampled interval except where layers of coarser material occur. The higher unit weights (1.51–1.65 g/cm^3) of the sandy sequences are quite distinct from the 1.30–1.37 g/cm^3 values found for the silty clay. Such low densities are attributed to the mineralogy of the fines and the high organic content found associated with these finer sediments.

Grain specific gravity varies considerably even within the silty clay sequences indicating that these intervals are not as uniform in composition as some of the other data imply. Values range from 2.50–2.72, tending to average about 2.63.

Porosity is strongly influenced by grain size as shown in Figure 1. Porosities of 60–70% characterize the coarser sediments whereas much higher values of 77–82% are identified with the silty clays.

Shear strengths as determined by the laboratory vane-shear test, using a 2.50 cm × 1.25 cm vane at a rotation speed of 70 degrees per minute, range from 39–50 g/cm^2 for the silty clay intervals. In comparing natural versus remolded shear strength, sensitivities of 3–4.5 are found, indicating a 50–75% loss of strength due to remolding (Richards, 1962). Sensitivities such as these, in the case of the Cariaco Trench, are probably the result of the high organic content. A similar relationship has been reported for the organic-rich deposits of the Black Sea (Keller, 1974).

Organic carbon, as might be expected, is abnormally high in the sediments of the Cariaco Trench. Total organic carbon was determined by the combustion method (Gustin and Tefft, 1966) and showed values ranging from 4.17 to 5.12% except in a layer of coarse material where a value of 1.63% was recorded (Fig. 1). These values are slightly higher than those reported by Athearn (1965) for the same general area of the trench, but are well within the limits

of 1–6% reported by Lidz and others (1969) for the trench as a whole.

Assuming grain size to be similar, it might be expected that sediments from anoxic and aerobic environments would exhibit physical properties quite distinct from one another. Such a distinction has been pointed out between open-ocean deposits and those of the Black Sea (Keller, 1974). Although the Cariaco Trench sediments are in an anoxic environment, they differ considerably from the Black Sea deposits yet contrast relatively less with the aerobic deposits of the Caribbean and Atlantic basins.

Water contents and porosities in the trench sediments are only slightly higher than those reported for the Atlantic (Keller and Bennett, 1970), quite similar to those in the Tobago Trough in the eastern Caribbean (Keller, *et al.*, 1972), but much lower than the Black Sea deposits. Unit weight and grain specific gravity values on the other hand are lower in the trench than is commonly found in the Atlantic or Caribbean sediments, but considerably higher than those reported from the Black Sea.

In regard to mass physical properties, Cariaco Trench sediments, although from an anoxic environment, are more closely related to the aerobic Atlantic and Caribbean deposits than to those of the Black Sea.

These relationships seem to best correlate with organic carbon content. Cariaco Trench deposits are much richer in organic carbon (4–5%) than Atlantic and Caribbean sediments (0.25–2%) (Trask, 1939; Froelich *et al.*, 1971); yet are considerably below the very high concentrations (5–20%) reported for the Black Sea (Ross *et al.*, 1970). The difference in organic carbon content between the Cariaco Trench and the Atlantic and Caribbean deposits is much less than between the Trench and the Black Sea sediments. The Black Sea is basically an enclosed sea with unique circulation characteristics both in its upper and lower levels whereas, the Cariaco Trench has relatively good circulation in its upper waters with little or no influx of fresh water. The different circulation characteristics are undoubtedly a major cause for the contrasting concentrations of organic carbon in the two anoxic basins and in turn the differing sediment physical properties.

REFERENCES

Athearn, W. D., 1965, Sediment cores from the Cariaco Trench, Venezuela: Woods Hole Ocean. Inst. Tech. Rep. 65–37, 31 p.

Ball, M. M., G. C. A. Harrison, P. R. Supko, W. Bock, and N. J. Maloney, 1971, Marine geophysical measurements on the southern boundary of the Caribbean Sea: *in* Donnelly, T. W. (*ed.*), Caribbean Geophysical, Tectonic, and Petrologic Studies, Geol. Soc. America Mem. 130, p. 1–33.

Casagrande, A., 1948, Classification and identification of soils: Am. Soc. Civil Engineers Trans., v. 113, p. 901–931.

Curl, H., Jr., 1960, Primary production measurements in the north coastal waters of South America: Deep-Sea Res., v. 7, p. 183–189.

Fanning, K. A., and M. E. Q. Pilson, 1972, A model for the anoxic zone of the Cariaco Trench: Deep-Sea Res., v. 19, p. 847–863.

Froelich, P., B. Golden, and O. H. Pilkey, 1971, Organic carbon in sediments of the North Carolina continental rise: Southeastern Geology, v. 13, p. 91–97.

Gustin, G. M., and M. L. Tefft, 1966, Improved accuracy of rapid micro carbon and hydrogen method by modified combustion absorption technique: Microchemical Jour., v. 10, p. 236–243.

Heezen, B. C., R. J. Menzies, W. S. Broecher, and M. Ewing, 1959, Date of stagnation of the Cariaco Trench, southeast Caribbean (Abs.): Geol. Soc. America Bull., v. 69, p. 1579.

Keller, G. H., and R. H. Bennett, 1970, Variations in the mass physical properties of selected submarine sediments: Marine Geology, v. 9, p. 215–223.

———, D. N. Lambert, R. H. Bennett, and J. B. Rucker, 1972, Mass physical properties of Tobago Trough sediments: VI Conf. Geologica del Caribe, Margarita, Venezuela, Mem., p. 405–408.

———, 1974, Mass physical properties of some western Black Sea sediments: p. 332–337; *in* Degens, E. T., and D. Ross (*eds.*), Black Sea—Geology, Chemistry, Biology: Am. Assoc. Petroleum Geologists, Mem. 20, 633 p.

Lidz, L., W. B. Charm, M. M. Ball, and S. Valdes, 1969, Marine basins of the coast of Venezuela: Bull. Marine Science, v. 19, no. 1, p. 1–17.

Peter, G., 1972, Geology and geophysics of the Venezuelan continental margin between Blanquilla and Orchilla Islands: N.O.A.A. Tech. Rept. ERL 226-AOML 6, 82 p.

Richards, A. F., 1962, Investigations of deep-sea sediment cores, II. Mass physical properties: U. S. Hydrographic Office Tech. Rept. 106, 146 p.

Richards, F. A., and R. F. Vaccaro, 1956, The Cariaco Trench, an anaerobic basin in the Caribbean Sea: Deep-Sea Res., v. 3, p. 214–228.

———, 1960, Some chemical and hydrographic observations along the north coast of South American I. Cabo Tres Puntas to Curacao, including the Cariaco Trench and the Gulf of Cariaco: Deep-Sea Res., v. 7, p. 163–182.

Ross, D. A., E. T. Degens, and J. MacIlvaine, 1970, Black Sea: recent sedimentary history: Science, v. 170, p. 163–165.

Trask, P. D., 1939, Organic content of recent marine sediments: p. 428–453, *in* Trask, P. D. (*ed.*), Recent Marine Sediments, a symposium: Soc. Econ. Paleontologists and Mineralogists, Spec. Pub. 4, 736 p.

Reprinted from: *Canadian Journal of Earth Science 12*, No. 4, 703-710.

Near-bottom Currents in the Mid-Atlantic Ridge Rift Valley[1]

GEORGE H. KELLER
Atlantic Oceanographic and Meteorological Laboratories, 15 Rickenbacker Causeway, Miami, Florida 33149
SUSAN H. ANDERSON
Woods Hole Oceanographic Institution, Woods Hole, Massachusetts 02543
AND
J. WILLIAM LAVELLE
Atlantic Oceanographic and Meteorological Laboratories, 15 Rickenbacker Causeway, Miami, Florida 33149

Received September 18, 1974
Revision accepted for publication December 11, 1974

Near-bottom current measurements during a 46 day period (October to December 1973) in the rift valley of the Mid-Atlantic Ridge just south of the Azores reveal a mean flow at two stations of 2.6 and 8.2 cm/s, predominantly trending parallel to the northeast orientation of the valley. Maximum velocities recorded at the sites were 14.4 and 24.2 cm/s. Semi-diurnal tidal currents appear to strongly influence the flow within the valley causing current reversals, except in areas where local topography and constrictions in the valley apparently result in a unidirectional flow to the northeast.

Les mesures de courant de fond durant une période de 46 jours (octobre à décembre 1973) dans la vallée du rift de la crête Mid-Atlantique au sud des Açores révèlent une coulée moyenne aux deux stations de 2.6 et 8.2 cm/s avec prédominance d'une tendance parallèle à l'orientation nord-est de la vallée. Les vitesses maximums enregistrées à ces endroits atteignaient 14.4 et 24.2 cm/s. Les courants de marée semi-diurne semblent influencer grandement la coulée dans la vallée causant ainsi des renversements de courant, excepté dans les régions où la topographie locale et les ressercements dans la vallée résultent apparemment en une coulée unidirectionnelle vers le nord-est. [Traduit par le journal]

Can. J. Earth Sci., 12, 703–710 (1975)

Introduction

The Mid-Atlantic Ridge is a major topographic feature extending the length of the Atlantic Basin which, in many places, serves as a barrier to the circulation of bottom water from the eastern to the western Atlantic (Wüst 1933). Offsetting fracture zones running perpendicular to the ridge often provide controlling sills for bottom-water movement across the ridge system (Garner 1972). Independent of these large-scale water movements, considerable local variability of current dynamics may be expected due to extreme local variations in relief that characterize the ridge and axial rift valley.

Through the French American Mid-Ocean Undersea Study (FAMOUS), a series of submersible dives were planned in the rift valley and fracture zones of the Mid-Atlantic Ridge between 36°30′N and 37°N. During preliminary dives made by the ARCHIMEDE in 1973, the French believed that they had encountered currents averaging 39 cm/s (0.75 knots) on four out of seven dives (J. Francheteau, personal communication 1973). These relatively high velocities occurred in several places within the dive area but were not consistently encountered in areas where the submersible dived more than once. Furthermore, the estimates were not consistent with five short-period measurements made in the same area by J. D. Phillips in 1972 (personal communication). To obtain better data on the currents in the prime dive area prior to the major operations scheduled for July and August 1974, three current meters were deployed in the rift valley from the USNS MIZAR and retrieved 46 days later (19 October to 5 December 1973) by the USNS LYNCH.

Steep rift walls define the floor of the rift valley in the area chosen for the FAMOUS study. The valley floor is up to 5.8 km wide at its intersections with the north and south bounding fracture zones, narrowing to 2.2 km midway between these fracture zones (Fig. 1). A series of ridges rising as much as 250 m above the surrounding floor and flanked by lateral troughs characterize the center of the valley floor (Needham and Francheteau 1974). The trend of the rift valley is to the north northeast, approximately 022°.

To monitor the currents within this highly variable topography, two current meters were to be placed in lateral troughs and one on a central high in the narrower portion of the rift valley (Fig. 1). Although positioning was determined by satellite navigation and a bottom-mounted transponder beacon in the rift valley, it appears that the final positions of the moorings were slightly offset from the intended features by drift during descent to the sea floor, but were well within the rift valley. The moorings were at varying depths as desired, with the northern meter (A) being set at 36°49.2′N, 33°16.5′W at a depth of 2509 m (1394 fathoms), meter (B) at 36°48.43′N, 33°15.75′W at 2412 m (1340 fathoms), and meter (C) at a depth of 2351 m (1306 fathoms) at 36°46.78′N, 33°16.46′W.

Each current meter mooring had the same configuration: a model 102 Geodyne current meter (film recording) suspended 35 m above the sea floor on a dacron line and held in place by a 204 kg anchor and a number of glass floats located a few metres above the current meter. The mooring was retrieved on demand by means of triggering an AMF model 324 acoustic transponding release positioned on the line mid-way between the meter and the anchor.

Current Observations

The current meters recorded velocity and direction every 10 min averaging over a period of about 50 s. An electronics failure resulted in unreliable velocity data from current meter (B), although good directional measurements were recorded. The records from current meters (A) and (C) along with the tidal height expected at Ponta Delgada, using the high and low water prediction tables (National Ocean Survey 1972), are plotted as a time series in Fig. 2. Current flow at all three stations was predominantly to the north and northeast, paralleling the general trend of the rift valley. At Station A, flow reversals of a semidiurnal nature occurred, presumably tidal, whereas at stations B and C a more or less constant northward and northeastward flow was recorded during the 46 day period. At station C velocity varied considerably during that time, but at both stations B and C the flow direction was always to the north of northeast. This would indicate that, at these particular sites, a north or northeasterly current is superimposed on the oscillatory flow regime so as to mask out the south and southwest flow recorded at station A. Flow direction can be more clearly visualized from progressive vector diagrams. The diagram for station A (Fig. 3) reveals the current fluctuations and reversals that are more typical of deep ocean currents. The more or less unidirectional

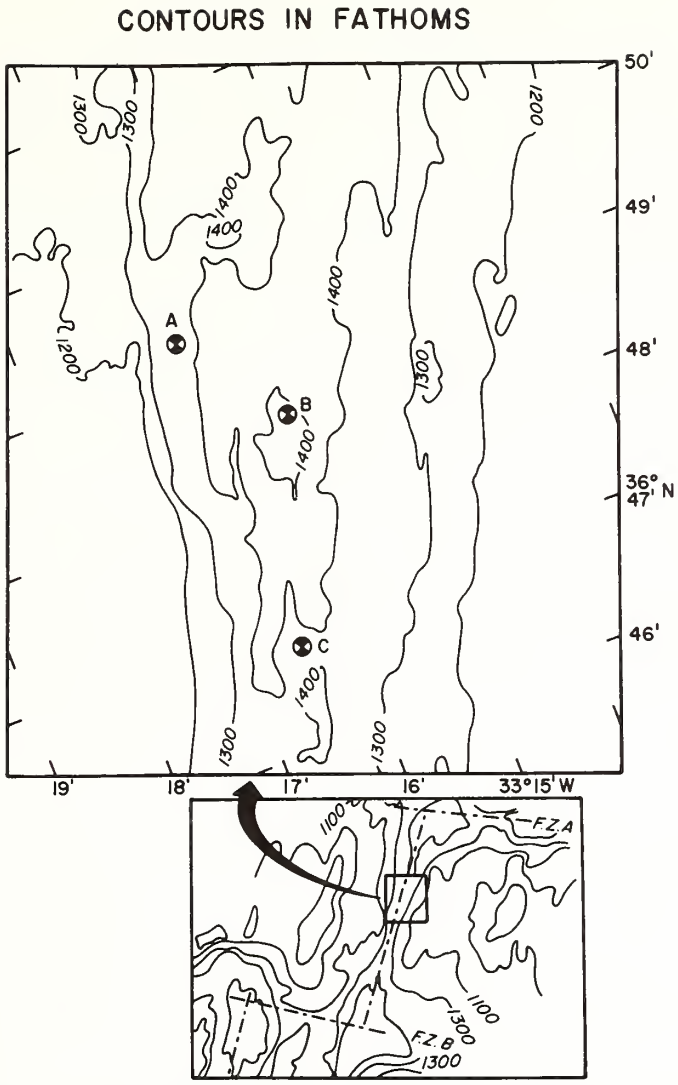

FIG. 1. Current meter stations and bathymetry of the rift valley of the Mid-Atlantic Ridge. Fracture zones A and B (F.Z. A; F.Z. B) delimit the northern and southern boundaries of the FAMOUS study area. Contours are in fathoms.

flow observed at stations B and C (Fig. 4) is anomalous and would be suspect if recorded on the abyssal plain. Although an assumption, it seems reasonable that this unique flow pattern is the result of local topographic control on the flow regime. A similar unidirectional flow, but in a slightly different deep-ocean setting was reported from the Gibbs fracture zone by Garner (1972). In that case the unique topography of the fracture zone appeared to serve to funnel the flow from the east to the west side of the ridge.

Current speeds at station A reached a maximum of 14.4 cm/s (0.28 knots), but were commonly much lower as shown by a mean speed of 2.6 cm/s (0.05 knots) for the 46 day period. At station C, current speeds were considerably greater, reaching a maximum of 24.2 cm/s (0.47 knots) and a mean for the recording period of 8.2 cm/s (0.16 knots). The stalling speeds of meters A and C were near 1 cm/s and 1.5 cm/s respectively, and the speeds reported above are biased low for that reason. However, only the average speed at station A where stalling occurred 35% of the time would be noticeably affected,

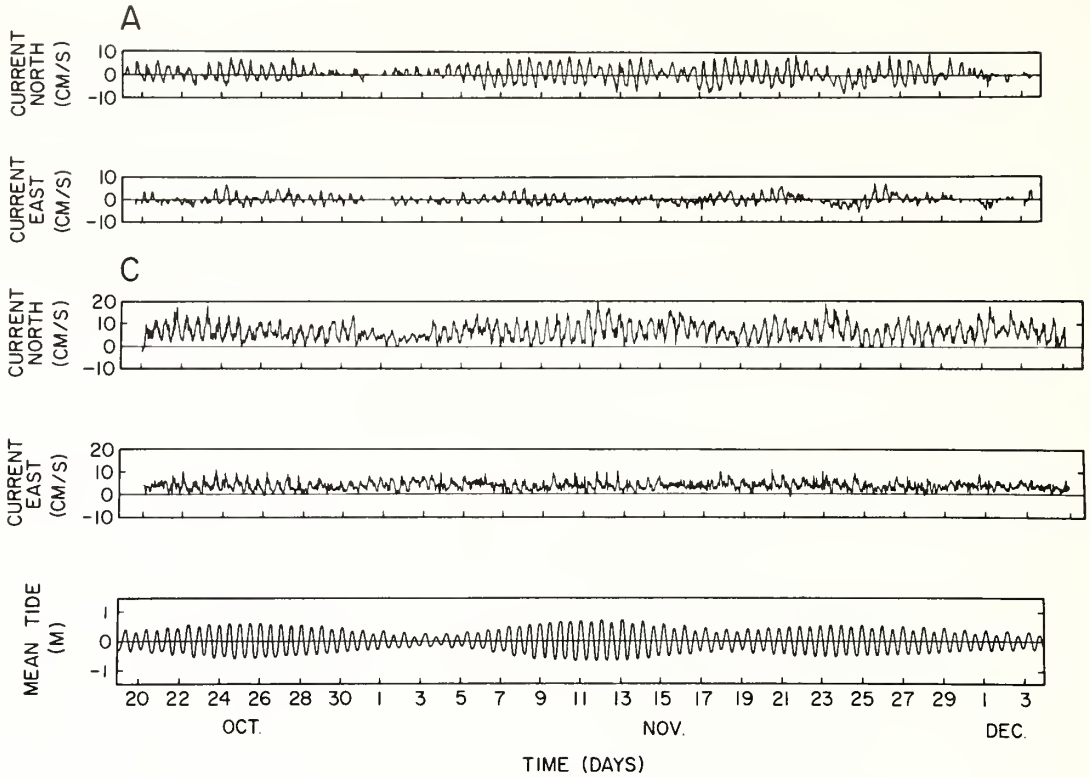

FIG. 2. Current direction and velocity profiles for stations A and C along with the tidal height profile for the same period predicted at Ponta Delgada.

and even then the bias amounts to at most 0.35 cm/s. The higher average speed at station C seems to reflect in part the narrowing of the rift floor at this location. The long period amplitude modulation evident in the tidal record over the 46 day period (tidal frequencies beating against each other) is reflected in the current measurements (Fig. 2).

In November 1972, J. Phillips (personal communication) made a number of short duration (45–49 h) current measurements in the same general area of the rift valley. His observations indicated that current velocities were relatively low (ranging from 2.6 cm/s (0.05 knots) to 14.9 cm/s (0.29 knots)), just as we have reported. He too recorded basically a unidirectional flow to the north and northeast at a site adjacent (0.75 km southeast) to our station C. From this comparison it might be cautiously stated that the current velocity and direction seems to be persistent, at least for this time of the year.

Discussion

In order to compare tidal components in records A and C, we have taken the raw data minus a 25 hour running average, and least squares fit that residual at five tidal frequencies. In Table 1, we have provided the tidal ellipse parameters for these components plus the velocity means for the unfiltered data. From this can be noted: (1) the near linear nature of the semidiurnal components and their orientation similar to the direction of the rift valley, (2) the relatively small (down by a factor of 10 from the principal semidiurnal contribution) and more circular diurnal tidal currents, (3) the high coherence of the semidiurnal tidal currents registered at the two meters, and (4) the extreme difference in the nonoscillatory velocity contribution which causes the vast dissimilarity in the progressive vector diagrams.

In order to uncover additional periodic components in the current records, the data from

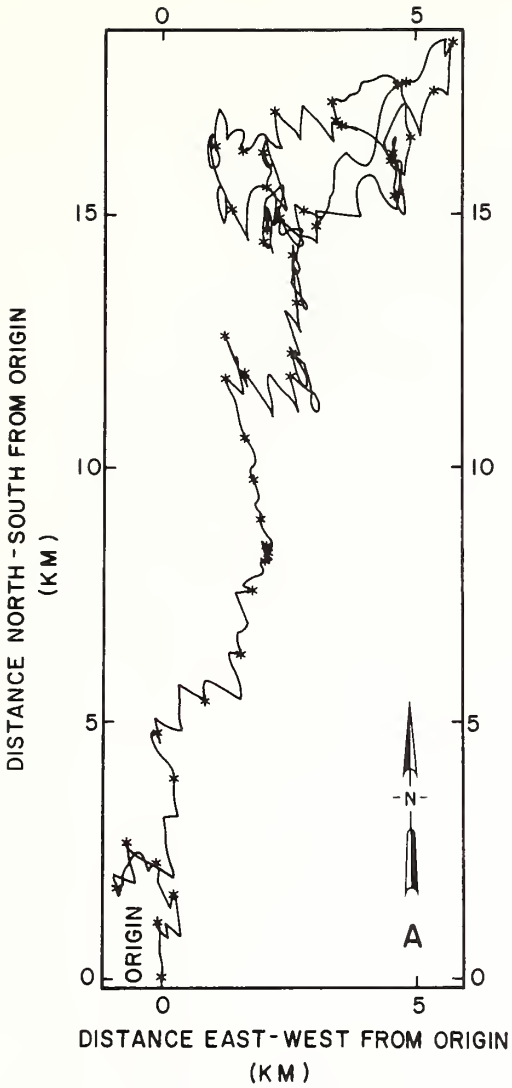

FIG. 3. Progressive vector diagram for Station A.

meters (A) and (C) were further subjected to spectral analysis. Figure 5 represents these results for meter (A). Because that meter is observed to have stalled in the first third of the record, the spectrum represents information contained in the last two-thirds of the record only. We have choosen a polarized spectral analysis as suggested by Gonella (1972) in order to sharpen a possible inertial frequency contribution. As is the convention, negative frequencies are clockwise components while the positive frequencies represent an anticlockwise rotational flow.

In order to remove scatter in the spectrum and at the same time resolve some of the low frequency contributions, we have 'decimated' (Blackman and Tukey 1958) the record by a factor of 16 and have used a Hanning spectral window on the resulting spectral averages. Because we have forced the information into the lower end of the spectrum, we have run the risk of alaising higher frequencies. The smallest resolvable period in this analysis is a fairly large 5.33 h. Mitigating information, we think, comes from a pilot analysis we performed using a Bartlett filter (Jenkins and Watts 1968) in which we found no peaks in the high frequency end of the spectrum and a rapid energy fall off. We have removed the average from the data before Fourier transforming.

Turning to the results of the analysis, we find domination of the spectrum by the semi-diurnal tidal current which Fig. 2 also shows. The near equality of those spectral peaks is another demonstration of the near linearity of those tidal components, while the apparent disparity in the height of the small diurnal components again suggest circularity of the tidal ellipse. The inertial period at this latitude is 20.0 h, and there is indeed a clockwise peak at 20.0 h, albeit relatively small.

Aside from the very low frequency peaks about which we make no comment, and the semidiurnal tides, the next most energetic contribution is the anticlockwise component near 6.2 h. This will be recognized as the product of nonlinear interactions of the semidiurnal components with themselves (first harmonics) or with each other. The small but recognizable peaks in both sides of the spectrum at 7.7 h, are believed to be the result of inertial/semidiurnal tidal interaction. It should be noted that it is the large amplitude of the semidiurnal tidal currents which cause many of these nonlinear interactions to rise above the background. Somewhat puzzling are the anticlockwise tidal side peaks at 11.1 and 14.6 h, which we do not believe are artifacts of the analysis.

From the pilot spectral analysis for both meters where the high frequencies ($> 1/5.33$h) were allowed, we found meter (A) observed a near $-5/3$ power law behavior similar to that reported by Webster (1972) from the western Atlantic whereas meter (C) demonstrated a near -1 frequency dependence. Neither (A) or (C) meters observed the preferred -2 dependence of Kolmogorov (1941).

TABLE 1. Tidal ellipse parameters

Period	Meter A					Meter C				
	Semimajor Axis	Semiminor Axis	Orientation	Ellipticity	Rotation	Semimajor Axis	Semiminor Axis	Orientation	Ellipticity	Rotation
$T = 12.0$	1.20	0.10	−14°	0.08	+	0.78	0.10	−6°	0.14	−
$T = 12.42$	3.15	0.33	−16°	0.10	−	3.63	0.93	−10°	0.25	−
$T = 12.66$	0.86	0.05	− 4°	0.06	+	1.19	0.14	−20°	0.12	+
$T = 23.93$	0.37	0.15	+ 3°	0.42	−	0.43	0.06	− 3°	0.15	+
$T = 25.82$	0.22	0.13	+ 4°	0.60	−	0.12	0.03	+57°	0.29	+
$T = \infty$	0.43	0.0	+12°	0.0	+	7.90	0.0	+30°	0.0	+

NOTES: The ellipticity is $|b/a|$ where a and b are the semimajor and semiminor axes respectively, both given in cm/s. The orientation angle is that of the major axis measured in degrees from north, and the sense of rotation is + for anticlockwise movement. The period is given in hours. All text and figure references are made to magnetic north. The notation $T = \infty$ denotes the zero frequency velocity component of the currents, *i.e.*, the velocity mean.

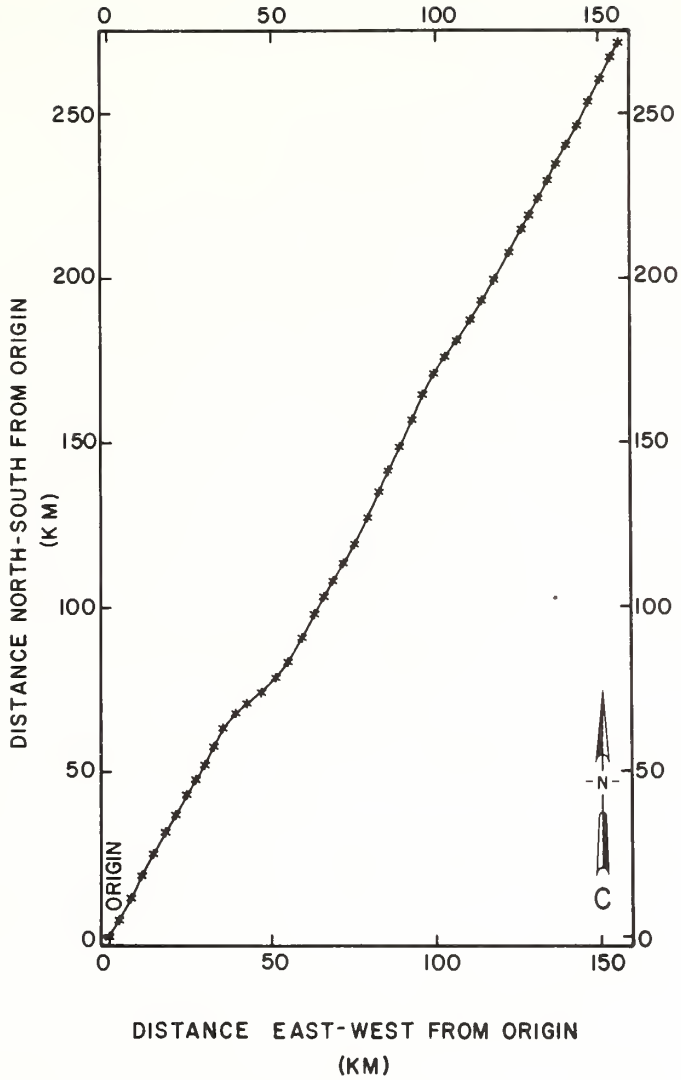

FIG. 4. Progressive vector diagram for Station C. For all intents and purposes the progressive vector plot for Station B is the same as that for Station C.

Summary

Current measurements made in the rift valley of the Mid-Atlantic Ridge indicate that the general flow regime is to the northeast, approximating the topographic trend of the ridge itself. Reversals in flow direction occurred consistently along the western margin of the valley where the valley floor is 4–5 km wide. A more or less unidirectional flow to the northeast prevailed throughout the period of observation in the axial zone of the valley. This anomalous flow pattern is perhaps attributable to the influence of local topography in the vicinity of the current meters. Mean current velocities at station C in the narrower section of the rift-valley floor were also found to be higher by a factor of three than those at station A. The topography within the rift valley of the Mid-Atlantic Ridge does appear to

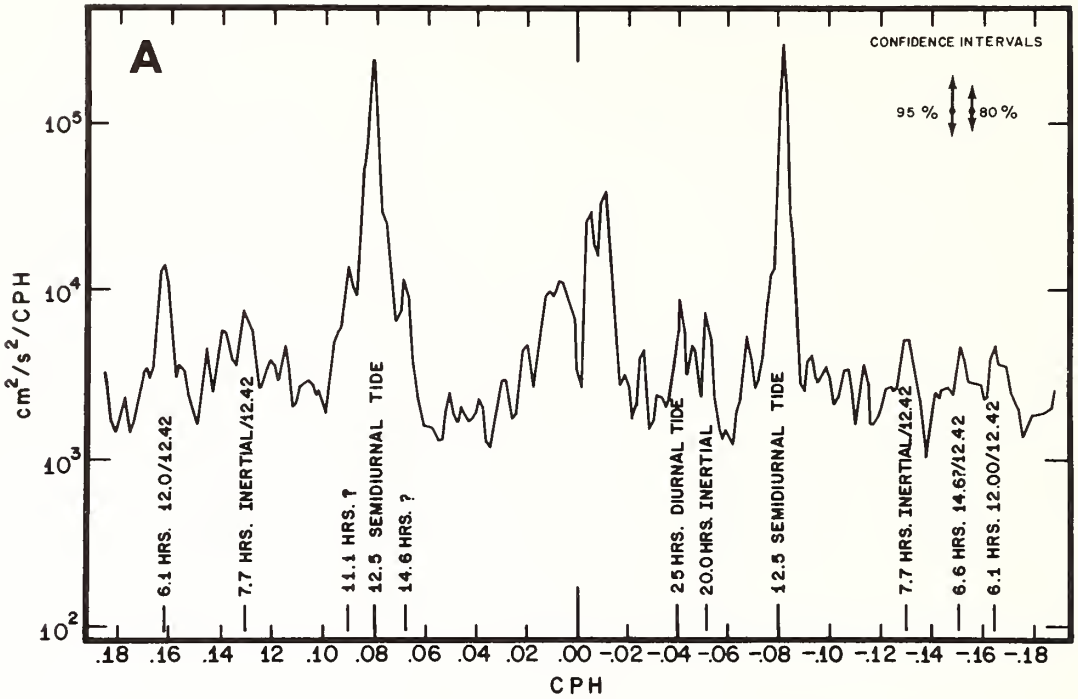

FIG. 5. A rotary component spectrum for the currents observed at mooring A. The right hand side (negative frequencies) represents clockwise components, the left hand side (positive frequencies) represents the anticlockwise components.

strongly influence the near-bottom current regime, although the currents seem to be of small amplitude.

Acknowledgments

We wish to thank the officers and crew of the USNS MIZAR and USNS LYNCH and particularly George Lapiene, Atlantic Oceanographic and Meteorological Labs, Donald Koelsch, Woods Hole Oceanographic Institution, James McGrath, Naval Research Lab, and Patrick Taylor, Naval Oceanographic Office for their assistance during the field phase of this study. We also acknowledge with many thanks the assistance of Thomas Clarke in processing the data and the critical review of our manuscript by N. P. Fofonoff.

BLACKMAN, R. B. and TUKEY, J. W. 1958. The measurement of power spectra. Dover, New York, New York.

GARNER, D. M. 1972. Flow through the Charlie–Gibbs fracture zone, Mid-Atlantic Ridge. Can. J. Earth Sci. **9**, pp. 116–121.

GONELLA, J. 1972. A rotary-component method for analyzing meteorological and oceanographic vector time series. Deep-Sea Res. **19**, pp. 833–846.

KOLMOGOROV, A. N. 1941. The local structure of turbulence in an incompressible fluid at very large reynolds numbers. Dokl. Akad. Nauk. SSSR **30**, (4), pp. 299–303.

JENKINS, G. M. and WATTS, D. G. 1968. Spectral analysis and its applications. Holden-Day, San Francisco, California.

NATIONAL OCEAN SURVEY. 1972. Tidal tables, 1973 (high and low water predictions); Europe and the West Coast of Africa. U.S. Dept. of Commerce, Rockville, Md.

NEEDHAM, H. D. and FRANCHETEAU, J. 1974. Some characteristics of the rift valley in the Atlantic Ocean near 36°48′ north. Earth Planet. Sci. Lett. **22**, pp. 29–43.

WEBSTER, F. 1969. Turbulence spectra in the ocean. Deep-Sea Res., Supp. **16**, pp. 357–368.

WÜST, G. 1933. Das Bodenwasser und die Gleiderun der Atlantischen Tiefsee, die Stratosphäre des Atlantischen Ozeans. Dent. Atlantische Expedition "Meteor", 1925–1927, Wiss. Ergeb., **7**(1).

Reprinted from: *Journal of Geophysical Research 80*, No. 15, 1953-1956.

Possible Bottom Current Response to Surface Winds in the Hudson Shelf Channel

J. W. Lavelle, G. H. Keller, and T. L. Clarke

NOAA Atlantic Oceanographic and Meteorological Laboratories, Miami, Florida 33149

Current measurements made in the Hudson Shelf Channel during the summer of 1973 show essentially channel axial bottom current even though the channel aspect ratio is small in the area of measurement. Although the current record is of short duration, correlation of water movement with surface winds is suggested by the data. The sense of summertime nontidal bottom flow in the channel (up or down channel) would appear to be controlled by the surface wind direction (offshore or onshore). These results would suggest the likelihood of net down-channel flow during the summer months.

Introduction

The New York Bight, defined as that area of the continental shelf bounded by Long Island on the north and New Jersey on the east, is dominated topographically in the near-shore region by the Hudson Shelf Channel. The channel itself is the drowned ancestral Hudson River Channel and leads southward for some 24 km from the present bight apex and then southeastward to the vicinity of the Hudson Submarine Canyon. In order to gain some insight into the circulation system of the bight and more particularly the flow regime in the upper portion of the Hudson Shelf Channel, current measurements were made in the summer of 1973 with a single bottom-mounted current meter. The meter, recording over an 11-day period before internal failure, was located (40°9.7′N, 73°41.2′W) approximately 45 km south of Long Island and 27 km east of New Jersey in the channel axis, where the water depth measured 62 m. The location of the axis was determined with a fathometer during a cross-channel transect.

Surprising though it may seem, understanding of the circulation system in the bight is still relatively poor. Although there have been several surface and bottom drifter studies made, comparatively few reports of direct current measurements are yet available for this area [*Charnell et al.*, 1972]. Further offshore but physiographically related to the channel is the Hudson Submarine Canyon, where summertime bottom current measurements were recently recorded [*Keller et al.*, 1973]. In that investigation, axial currents of sufficient magnitude to move coarse sediment were observed, but the length of the observations precluded correlations with possible forcing agents. Those measurements were made more than 100 km from the present site in much deeper water with greater relief.

In another recent and important study, measurements of currents at a site southeast of Block Island showed a strong correlation with prevailing meteorological conditions [*Beardsley and Butman*, 1974]. Documentation of the role surface winds play in the movement of shelf water has been made in other recent literature [*Huyer and Pattullo*, 1972; *Cannon et al.*, 1972; *Cannon*, 1972]. These earlier studies caused us to look to the wind as a possible driving mechanism for the small nontidal currents observed at the channel site.

With current measurements sampled every 10 min by a Geodyne 100-C internally recording Savonius rotor current meter positioned 1 m above the bottom and using weather records kept by the Coast Guard at Ambrose Tower and at Barnegat Light, New Jersey, we are able to show that the currents are axial in the channel during the recording period and suggest that the sense of flow (up or down channel) may be controlled to a large extent in the summertime by the prevailing surface winds. We present current and wind observations in some detail in the following section.

Copyright © 1975 by the American Geophysical Union.

Comparison of Winds and Currents

The data taken over the 11-day interval (August 3, 1973, at 0700 to August 14, 1973, at 0700) at 10-min intervals are given in component form in Figure 1, the solid line representing the raw data. In order to remove energy at diurnal tidal periods and below we have smoothed the data with a 25-hour boxcar averaging window, and that result is plotted as a dashed line. The highest recorded velocity (11.5 cm/s) occurred on August 9. The average speed over the 11-day period was 2.5 cm/s. On occasion the actual current speed fell below 1 cm/s, and the meter stalled.

It is evident from the record that currents during this period were heavily tidally influenced, although the tidal component generally is no larger in magnitude than the nontidal component. In order to appreciate tidal constituents we have made a least squares fit of the raw data minus the 25-hour running average at five tidal periods (T = 25.82, 23.93, 12.66, 12.42, and 12.00 hours) and have reconstructed the tidal current contribution as the dot-dash line in Figure 1. The M_2 semidiurnal component dominates with a 2.6-cm/s contribution, although the ringing tidal record demonstrates the significant role of the other tidal constituents.

In Figure 2 the progressive vector diagram demonstrates the near one-dimensional nature of the flow. The trend of the channel axis in this area is roughly 135°, as is the resultant flow direction in the diagram. The total 11-day excursion amounts to 8.8 km down channel. The most prominent feature is the 4-day southeast pulse beginning midday on August 7, during which the average down-channel flow amounted to nearly 4 cm/s.

Wind data taken at Ambrose Tower, some 34 km north-northwest of the site, and at Barnegat Light, New Jersey, some 56 km south-southwest of the site, are presented in Figures 3 and 4. At Ambrose Tower a log of meteorological and sea conditions is regularly kept, providing six wind velocity and pressure recordings per day over the study period. In the upper panels of Figure 3 the points represent the Ambrose Tower raw data in component form, and the solid line represents a 25-hour average. In the lower panels, irregularly kept wind estimates from Barnegat Light (points) as well as a hand-drawn

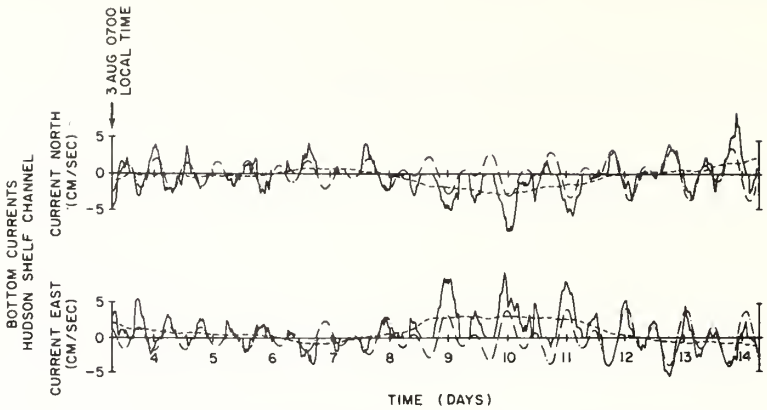

Fig. 1. Bottom current measurements (solid line) taken in the Hudson Shelf Channel from 0700 on August 3 to 0700 on August 14, 1973. The dashed line represents a 25-hour running average of the same data. The dot-dash line represents a least squares tidal fit to the currents.

average (solid line) are presented. At Ambrose Tower the wind record is clearly modulated by diurnal solar heating, although the predominant feature is the south-southwest wind beginning on August 7. The strongest winds recorded were 14.4 m/s on August 10, while the 5-day average amounted to 6.7 m/s. At Barnegat Light, south-southwest winds were evident from midday on August 7, with one interruption on August 10, until midday on August 11, when the wind began to rotate to the west.

Although the wind data are not as accurate or as frequent as we would like for the second station, there seems to be some coherence in meteorological records. We think that it is reasonable to assume that in their coherent aspects the wind data reflect a regional pattern, inclusive of the current meter site. Besides the south wind evident over 4 days in the center of the record, a west wind was evident over roughly a 2-day period near August 5 and 2-day period beginning August 12.

Turning now to the coherence between the wind and current meter data, we point out the correspondence between major features of the progressive vector diagrams (Figures 2 and 4). The residual bottom current began a trend down channel after midday August 7 and continued until the middle of August 11. The surface winds showed considerable strength from the south-southwest on August 7 until roughly midday on August 11, when the wind came from the west, that is, during the same interval as the down-channel flow.

The two periods of lighter west winds previously mentioned, beginning August 5 and 12, seem to be reflected in the current record as up-channel flows. During the first part of the observation period (August 3 at 0700 to August 5 at 0700) there was also a down-channel flow with a southwest wind.

If the correlation is as we propose, there would appear to be some hysteresis in the response of the system to the forcing. While the tidal currents are of the same magnitude as the residual currents and therefore the source of some masking, there appears to be considerably more lag in setting up a flow than in its decay. For example, the up-channel flow on August 12 may have required a half day of offshore winds to begin up-channel flow, while the down-channel flow of August 11 relaxed almost immediately to the shift in wind direction. The limited data that we have are clearly insufficient to support

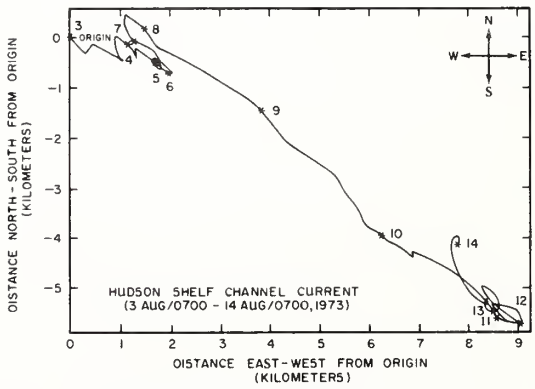

Fig. 2. Progressive vector diagram of the bottom currents in the upper Hudson Shelf Channel.

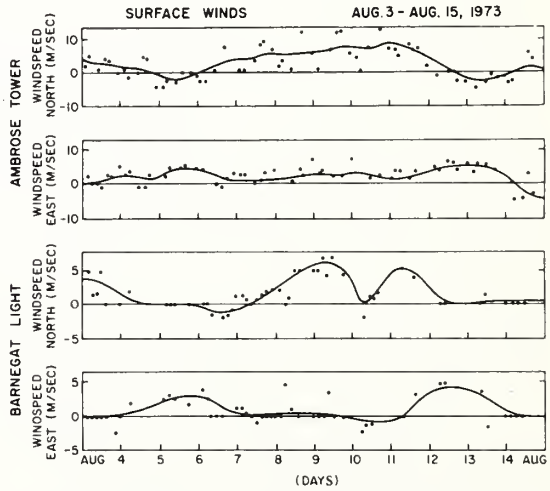

Fig. 3. Upper panels represent wind velocity components measured at Ambrose Tower with a 25-hour boxcar average (solid line) superimposed. The lower panels are velocity component estimates from the log at Barnegat Light, New Jersey, with a hand-drawn average. Directions expressed in this plot are directions toward which the wind is blowing.

anything more detailed than the broad correlation that we have proposed above.

In the Block Island work, *Beardsley and Butman* [1974] suggested that a northeast wind blowing parallel to the Long Island barrier can cause a relatively intense geostrophic flow to the west. We think that the correlation that we suggest is the result of the same basic mechanisms, although they are now operating on a highly stratified water column rather than the well-mixed condition existing during the late winter and early spring months. We may be seeing a situation of onshore winds leading to setup along the coast and bottom seaward flow, while offshore winds may cause some setdown and a compensating flow up channel. The correlation in this case could be dependent on the stratification extant in the bight during the summer months.

CONCLUSIONS

From these observations we think there is reason to suggest a correlation between flow in the axis of the Hudson Shelf Channel and the prevailing surface winds. During the summer period, winds which blow onshore (south-southwest or south) seem to produce down-channel flow, while winds blowing offshore (west or northwest) appear to cause a current reversal and a net up-channel current. In both cases the strength of the wind-induced flow is comparable to the tidal currents. The evidence begins to appear for sustained (>1.5 days) and reasonably high winds (>5 m/s). For winds of highly variable direction, no significant signature in the channel flow should be observed. If the stratification of the bight is a requisite ingredient for the flow, it would be reasonable to expect a correlation of this kind beginning in June and continuing through September.

It is informative to look at the mean meteorological conditions prevailing during the June–September months in the bight area. In a summary of meteorological conditions for American ports [*Brower et al.*, 1972], monthly mean wind speeds and directions are compiled for the offshore Sandy Hook, New Jersey, area. There, mean winds are shown to come out of the south or southwest from May through September at an average velocity of 5 m/s. The remaining months of the year, the winds are from the northwest at slightly higher average speeds. With this wind direction over the June–September period of high stratification a net down-channel flow from June through September could be expected. This same general result, summertime down-axis flow, was suggested in unrelated observations by *Keller et al.* [1973] in the Hudson Submarine Canyon.

Again we would like to mention the rectilinear nature of the tidal and residual currents during the measurements. While the Hudson Shelf Channel in the vicinity of the observation has a depth to width ratio of only 10^{-2}, the flow moves essentially up and down the channel axis, a result suggesting some topographic control.

Finally, we would like to point to two recent studies made of the sediments in the Hudson Shelf Channel. In work on the organic material and carbohydrate concentrations in the channel, P. G. Hatcher and L. E. Keister (personal communication, 1974) were able to observe distribution of materials whose apparent source was the sewage sludge dumping site of New York City, which lies at the channel head. Organic distributions at points sampled across the channel have maxima corresponding to the channel axis. Concentrations are highest near the source, as could be expected, but extend down the channel some 100 km following the bottom contours.

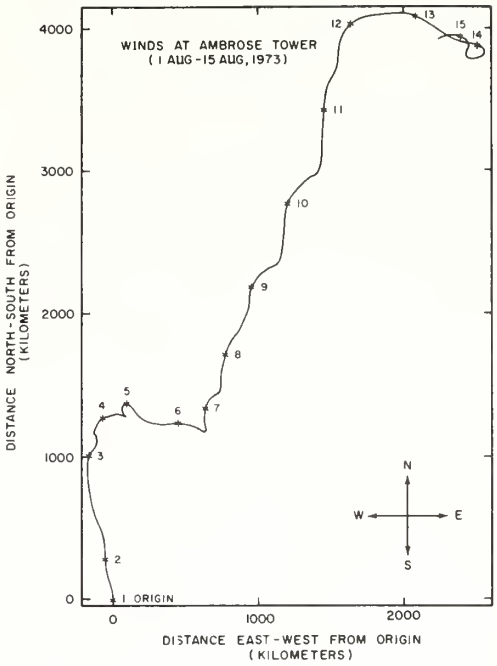

Fig. 4. Progressive vector diagram for the wind measured at Ambrose Tower.

Anomalous organic carbon concentrations are also found in the Hudson Submarine Canyon [*Keller*, 1973]. In a slightly earlier study of the heavy metal contaminants in the surficial sediments of the bight, *Carmody et al.* [1973] found anomalously high concentrations of trace metals following the Hudson Shelf Channel axis and extending to 30 km from the dump site. Both observations may be additional evidence for a consistent, if not considerable, bottom transport down the channel axis.

While the suggestion of wind-forced axial flow in the Hudson Shelf Channel is based on just one 11-day suite of observations, we think it can serve as a useful working hypothesis for additional and lengthier observations. There may indeed be a general transport down the channel and out through the canyon at certain times of the year, but verification awaits further measurements.

Acknowledgments. The authors would like to thank George Lapiene for his contributions to the engineering and field efforts involved in these measurements. We also acknowledge the helpful critique of the manuscript by Donald Hansen and Robert Charnell. This work was supported in part by NOAA's New York Marine Ecosystem Analysis Program (Mesa).

REFERENCES

Beardsley, R., and B. Butman, Circulation on the New England continental shelf: Response to strong winter storms, *Geophys. Res. Lett.*, *1*, 181–184, 1974.

Brower, W. A., D. D. Sisk, and R. G. Quayle, Environmental guide for seven U.S. ports and harbor approaches, report, p. 55, NOAA Environ. Data Serv., Nat. Clim. Center, Asheville, N. C., 1972.

Cannon, G. A., Wind effects on currents observed in Juan de Fuca submarine canyon, *J. Phys. Oceanogr.*, *2*, 281–285, 1972.

Cannon, G. A., N. P. Laird, and T. Ryan, Currents observed in Juan de Fuca submarine canyon and vicinity, 1971, *Tech. Rep. ERL 252-POL14*, Nat. Ocean. and Atmos. Admin., Boulder, Colo., 1972.

Carmody, D. J., J. B. Pearce, and W. E. Yasso, Trace metals in sediments of New York Bight, *Mar. Pollut. Bull.*, *4*, 132–135, 1973.
Charnell, R., D. Hansen, and R. Wickland, Surface and bottom water movement in New York Bight, The Effects of Waste Disposal in the New York Bight, report, Coastal Eng. Res. Center, Washington, D. C., 1972.
Huyer, A., and J. Pattullo, A comparison between wind and current observations over the continental shelf off Oregon, summer 1969, *J. Geophys. Res.*, *77*, 3215–3219, 1972.
Keller, G. H., Sedimentary dynamics within the Hudson Submarine Canyon, Procès-Verbaux Relations Sédimentaires entre Estuaires et Plateaux Continentaux, p. 49, Inst. de Géol. du Bassin d'Aquitaine, Bordeaux, France, 1973.
Keller, G., D. Lambert, G. Rowe, and N. Staresinic, Bottom currents in the Hudson Canyon, *Science*, *180*, 181–183, 1973.

(Received August 6, 1974;
accepted February 13, 1975.)

Reprinted from: *American Geophysical Union, Fall Annual Meeting 56*, No. 12, 1003.

TRACER OBSERVATIONS OF SAND TRANSPORT ON THE LONG ISLAND INNER SHELF

J.M. Lavelle
D.J.P. Swift (both at: Atlantic Oceanographic and Meteorological Laboratories, NOAA, 15 Rickenbacker Causeway, Miami, Fla. 33149)
H.R. Brashear
F.N. Case (both at: Oak Ridge National Laboratory, operated for ERDA by Union Carbide Corporation, Oak Ridge, Tennessee 37830)

We have observed both spring-summer and fall-winter sand transport in two experiments on the Long Island Inner Shelf at water depths of 20 to 24 meters using a radioisotope sand tracer system. Dispersion patterns of the tagged material, medium to fine sand with a mean diameter of 0.125 mm, sampled biweekly over both 70-day experiments, support the hypothesis of wintertime storm activity as the principal agent of shelf sand transport. In the late spring and early summer, movement is primarily diffusive in nature, extending 200 meters from the injection point, while late fall-winter patterns have strong advective features, including an ellipsoidal smear of material extending approximately 1200 meters longshore after the passage of several "northeasters." Near-bottom current observations made with Savonius rotor sensors show: a doubling of peak near-bottom velocities from approximately 30 to 60 cm/sec, from the first to the second experiment; and the dominance of westward storm flow along the Long Island Inner Shelf in transporting sand.

Reprinted from: *Journal of Geophysical Research 80*, No. 23, 3307-3314.

Crest of the Mid-Atlantic Ridge at 26°N

BONNIE A. MCGREGOR[1] AND PETER A. RONA

NOAA Atlantic Oceanographic and Meteorological Laboratories, Miami, Florida 33149

A relatively detailed investigation of the Mid-Atlantic Ridge crest at 26°N was conducted by using narrow-beam bathymetric data, total earth's magnetic field measurements, and underwater photographs. The Mid-Atlantic Ridge crest at 26°N appears to be hydrothermally active. The structural setting of this area is conducive to the occurrence of hydrothermal deposits. The walls of the rift valley are extensively faulted with blocks and steps ranging in size from kilometers to meters in width and relief. Underwater photographs show hydrothermal manganese associated with interpreted fault steps at depths between 3100 and 2500 m on the east wall, suggesting that the faults provide avenues for hydrothermal fluids. Small topographic highs in the floor of the rift valley are the sites of relatively recent volcanism and are believed to represent the top of an active dike emplacement zone. Bathymetric trend directions for this portion of the ridge crest are complex in comparison with plate rotation predicted trends for the Mid-Atlantic Ridge. The bathymetric grain is a function of processes active in the rift valley.

INTRODUCTION

During the 1972 trans-Atlantic geotraverse (TAG) program of the NOAA Atlantic Oceanographic and Meteorological Laboratories a geological and geophysical study of an area 180 km by 180 km of the crest of the Mid-Atlantic Ridge between 25°N and 27°N was carried out (Figure 1) [*Rona et al.*, 1973, 1975*b*]. As a continuation of this program in 1973, a relatively detailed study was made of an area 75 km by 55 km (area outlined in Figure 1) centering on the TAG hydrothermal field [*R. Scott et al.*, 1974], which was identified during the 1972 TAG program [*M. Scott et al.*, 1974]. This paper reports results of the detailed study, the objectives of which were (1) to define the geomorphologic features present on a slow-spreading midoceanic ridge, (2) to establish the relationship of these features to axial rift processes, and (3) to determine the structural framework associated with the hydrothermal mineral deposit. In the detailed study area, northwest-southeast track lines oriented perpendicular to the trend of the rift valley are 2 km apart, and the northeast-southwest lines parallel to the rift valley are 3.5 km apart (Figure 2). Narrow-beam echo-sounding data and total earth's magnetic field measurements were collected continuously along the track lines positioned by satellite navigation. Supplemental bathymetric data from the 10- and 20-km line-spaced survey (Figure 1) of the 1972 field season were also used. Small-scale features of the order of 1 m are revealed in a transect of stereophotographs made from the floor to the top of the east wall of the rift valley.

The general setting for this area is a portion of ridge crest in the central North Atlantic between two major fracture zones, the Kane at 24.7°N and the Atlantis at 30°N. The oldest sea floor studied in the detailed area is slightly older than 3 m.y. based on a 1.2-cm/yr spreading rate [*Lattimore et al.*, 1974].

BATHYMETRY

The general bathymetry of the Mid-Atlantic Ridge is shown in Figure 1. The rift valley is composed of a series of closed basins trending N25°E. Three transverse valleys spaced 30 km apart appear as deep basins on both the east and the west sides of the rift valley. These basins intersect the rift valley with a different trend on either side, 90° on the east and 60° on the west [*Rona et al.*, 1973, 1975*b*]. The rift valley widens and deepens at the intersection of these transverse valleys. Two oblique-trending transverse valleys are present on the west side of the ridge, and in each case a side lobe of the rift valley with a trend due north occurs such that the transverse valley trends are perpendicular to these north-south rift trends. Figure 3 is a schematic drawing of the previously discussed trends. Shaded areas are visible bathymetric trends, and dashed lines are trends that are less obvious but are present. According to *Johnson and Vogt* [1973], the Mid-Atlantic Ridge between 47° and 51°N can be divided into rift segments 30 km in length with either normal-trending (north-south) or oblique-trending axes. At 26°N the rift has a normal and an oblique trend in the same segment. The different trends may suggest minor adjustments in spreading direction for small blocks of sea floor.

The east wall of the rift valley located at 26°06'N, 44°45'W is the site of the TAG hydrothermal field described by *R. Scott et al.* [1974]. The detailed bathymetry of the ridge crest in this area is shown in Figure 4, the heavy 3500-m contour outlining the rift valley. Three of the transverse valleys intersect the rift in this area, two on the west and one on the east. Where the transverse valley trends are orthogonal to the rift southeast of the axis, the flanking valleys in the rift mountains parallel the N25°E trend of the rift axis. Where the transverse valley trends are oblique to the main rift trend northwest of the axis, the flanking valleys parallel the north-trending lobe or segment in the rift valley (Figure 4). The flanking valleys appear to form by isolating portions of the rift valley as shown on the southeast side of the rift at 25°55'N, 44°45'W (Figure 4), where discontinuous highs are beginning to isolate the 3500-m basin to the east of the rift. A similar feature appears to be forming at 26°15'N on the west side of the rift.

The axis of the rift valley within the detailed study area has two deep basins containing small linear topographic highs. One is located at the northern end of the southern basin, and the other is marked by the closed 4000-m contour in the northern basin (profiles 10–16 and 20–22 in Figures 4 and 5). Both features are 200–300 m high and are believed to be the site of recent volcanism. Fresh basaltic glass was recovered from the high in the northern basin (R. Scott, personal communication, 1974). Similar features were found in the Famous area to the north between 36° and 37°N [*Macdonald et al.*, 1974; *Needham and Francheteau*, 1974].

The east wall of the rift at 26°06'N, 44°45'W is higher than the west wall, and the rift valley narrows in this area. Large

[1] Also at Rosenstiel School of Marine and Atmospheric Science, University of Miami, Miami, Florida 33149.

Copyright © 1975 by the American Geophysical Union.

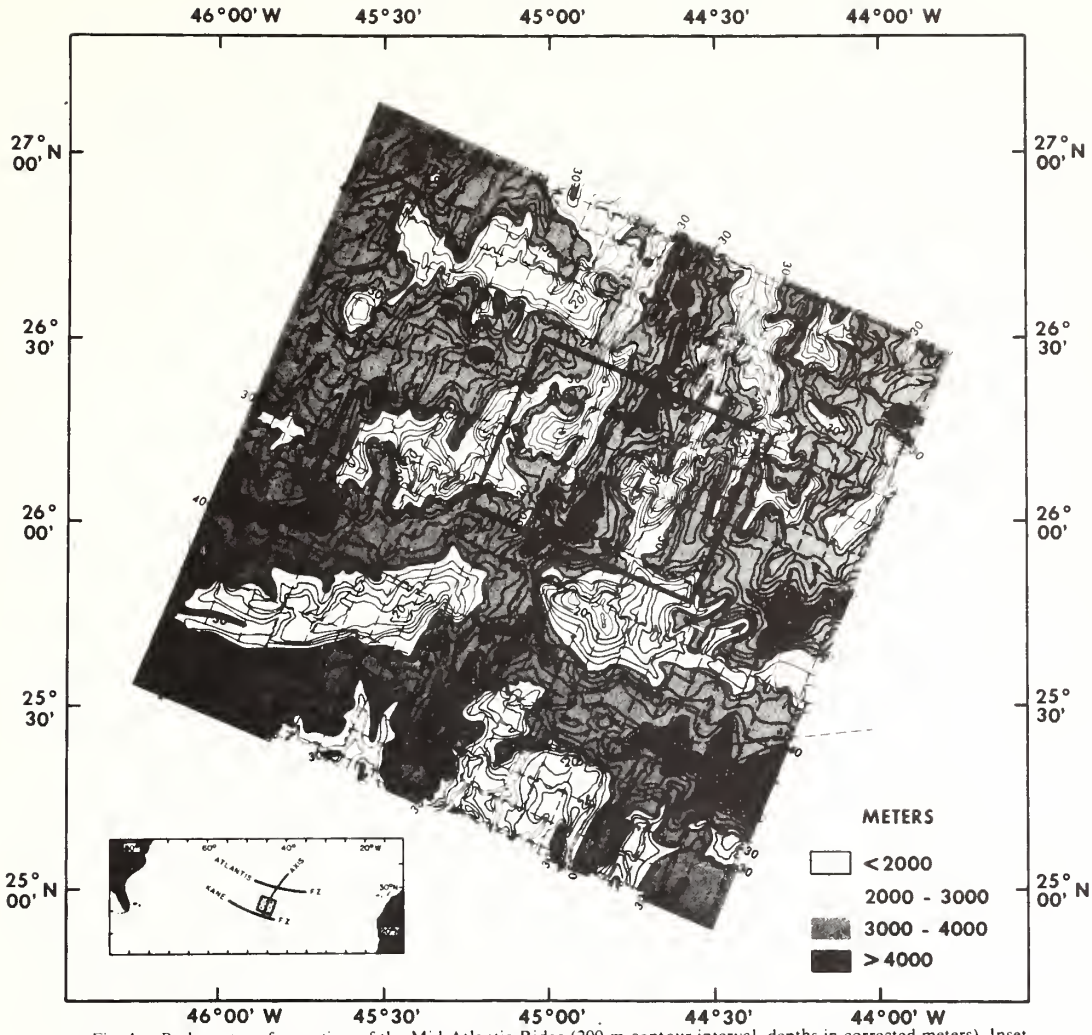

Fig. 1. Bathymetry of a portion of the Mid-Atlantic Ridge (200-m contour interval, depths in corrected meters). Inset shows general location of area. Outlined box is location of detailed study area shown in Figure 3. Dots are earthquake epicenter positions. Heavy 3600-m contour outlines the rift valley. Bathymetric map is from *Rona et al.* [1975*b*].

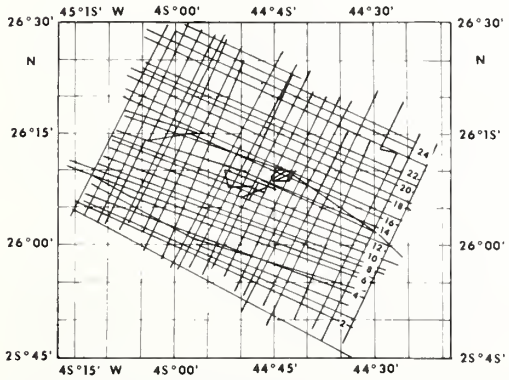

Fig. 2. Track lines from TAG phase 3, 1973. Track lines are data control for Figure 4, and index numbers are track locations for Figure 5.

blocks in the rift walls are apparent on the narrow-beam echo-sounding profiles and can be correlated for several kilometers along strike (arrows in profiles 4–8 of Figure 5). They are believed to have a fault origin, resembling fault blocks shown by *Atwater and Mudie* [1973] on the Gorda Rise. Suggested faults are indicated on Figure 5. The two peaks making up the east wall of the rift (profile 14) can be traced continuously from profile 4 to profile 20 (dashed line). Their elevation appears to be a function of the fault displacement, these blocks also being associated with the TAG hydrothermal field.

At least two scales of fault-derived features are present in the area: (1) those of the order of several kilometers with a minimum size of 0.4 km, visible on narrow-beam echo-sounding profiles, and (2) those of the order of meters, which can only be seen with bottom photography.

Underwater Photography

A transect of underwater photographs reveals the small-scale features and detailed structure of the east wall. Two

camera runs, each being of approximately 5-hour duration, are shown in relation to the bathymetry (Figure 6). Two underwater survey cameras in stereographic configuration were used with 35-mm negative movie film in each camera. Pictures were taken automatically every 8 s, providing overlap of adjacent photographs, while the cameras were maintained approximately 5 m above the bottom, at ship's speeds between 0.5 and 1 knot (0.25–0.5 m/s). During camera traverse 1, pictures of the bottom were taken continuously, whereas during camera traverse 2, a weak pinger return from the camera necessitated pulling clear of the bottom for an interval to identify the pinger and bottom returns.

Because of the large number of photographs obtained, one camera per run was selected, every third photograph scanned, and the percentage of bottom type recorded following the technique used by *Moore and Fiske* [1969]. Five categories of bottom type were identified as being significant for interpretation of the structure of the rift wall: (1) pillows, indicating lava flows, (2) talus, angular debris from gravel to boulder size, (3) breccia, cemented angular and subangular fragments, (4) sediment, composed of silt and sand, and (5) hydrothermal manganese deposit (Figure 7). A total of 1800 photographs from the two stations were scanned. Because of the volume of data the percentage of bottom types was averaged over approximately 15-min intervals and plotted as bar graphs (Figure 6). Also shown in Figure 6 are locations of three dredge hauls with percentage of total material dredged (TAG leg 3, 1972, and leg 4, 1973, cruise report, R. Scott, personal communication). The dredge hauls help identify some of the relationships and material present in the photographs. Sediment is present over most of the rift wall, although it may be only a few centimeters thick. Pillow basalts are found capping the top of this east wall and associated with a step on the wall at approximately 3000 m. This step was the site of a temperature increase in the bottom water [*Rona et al.*, 1975*a*]. Hydrothermal manganese having a layered appearance was photographed along both traverses between 2500 and 3100 m, blanketing the talus, and from the dredged material was found as a matrix filling interstices and cementing the talus. Talus is abundant over most of the wall. The spatial relationship of bottom types gives an indication of the structure of the wall. A sequence of sediment, talus, and breccia repeating itself suggests the presence of a terrace or step in the wall, sediment on the outer portion and talus plus breccia close to the wall implying a scarp as the source of the talus. The pinger and bottom trace, while they maintain the camera 5 m off the bottom, also confirm the presence of steps or terraces. On those portions of the camera runs that were made approximately perpendicular to the contours, the number of possible steps in the wall could be counted. Camera traverse 1 from 2800 to 2400 m had 10 such steps varying in width between 30 and 400 m with 40 m of average relief between each step to account for 400 m of relief of the wall. Smaller steps are present in the breccia between 2500 and 2400 m and in a small region of the pillow basalts at the top of the wall, as the camera periodically had to be raised between times of level towing while being maintained at approximately 5 m off the bottom. The size of these steps was of the order of 10 m wide and 10 m high. In the region of pillow basalts these steps probably represent the edge of lava flows and are constructional features. During camera traverse 2, between depths of 3400 and 3100 m, four steps were identified by bottom type sequence. The steps varied in width between 100 and 300 m, each being separated by 75 m of average relief. If the correlation of bottom type with structure is correct, the wall consists of many steps. The association of the hydrothermal manganese where it is present with talus and breccia at the juncture of the steps and wall suggests that the steps may be fault-controlled, the fault zone providing a conduit for hydrothermal solutions [*R. Scott et al.*, 1974; *McGregor et al.*, 1974*a*].

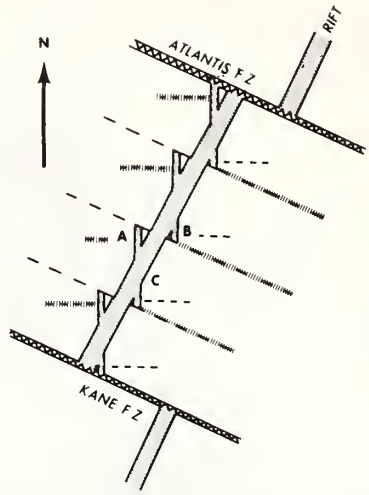

Fig. 3. Schematic drawing of the ridge crest and topographic trends. A and B are north-south trending rift segments, and C represents N25°E rift segments. Hatched bands are main transverse valley trends. All these trend directions make up the topographic fabric of the rift.

Also present in the photographs was evidence of bottom current activity confined above 3000 m. *Globigerina* ooze in some places appears to have a lag deposit of debris, which in some cases is manganese-coated pteropods similar to those seen in the Famous area (G. Keller, personal communication, 1974). Oscillation ripple marks with varying wavelengths up to 0.6 m, amplitudes about 2 cm, and varying orientations indicate that current direction is probably controlled by topography. In some instances, slight drift of the sediment cloud stirred up by impact of the camera's compass on the bottom was to the north. A large number of siliceous sponges are present on camera traverse 1 at depths between 2350 and 2900 m, where a solid substrate facilitates their attachment. The sponges have a concave side (Figure 7), and in general, this side faces south. If these sponges orient to maximize feeding efficiency, the concave side may be expected to be directed toward the current. This would imply a current flow to the north, which is in agreement with observations from the rift valley to the north at 36°–37°N [*Keller et al.*, 1975]. Although ripple marks were present, no strong bottom currents occurred during the camera transects, as is evidenced by the lack of dispersion of the sediment cloud formed by the camera's compass in most cases.

Magnetic Anomalies

Total earth's magnetic field measurements were made along the ship's tracks shown in Figure 2, the numbered tracks referring to the profiles in Figure 5. The international geomagnetic reference field 1965 coefficients [*International Association of Geomagnetism and Aeronomy (IUGG) Commission 2*, 1969] were used to reduce the data, with a 400-γ adjustment to the reference field based on the American world chart 1970 model [*Hurwitz*, 1970]. The large positive anomaly in the center of

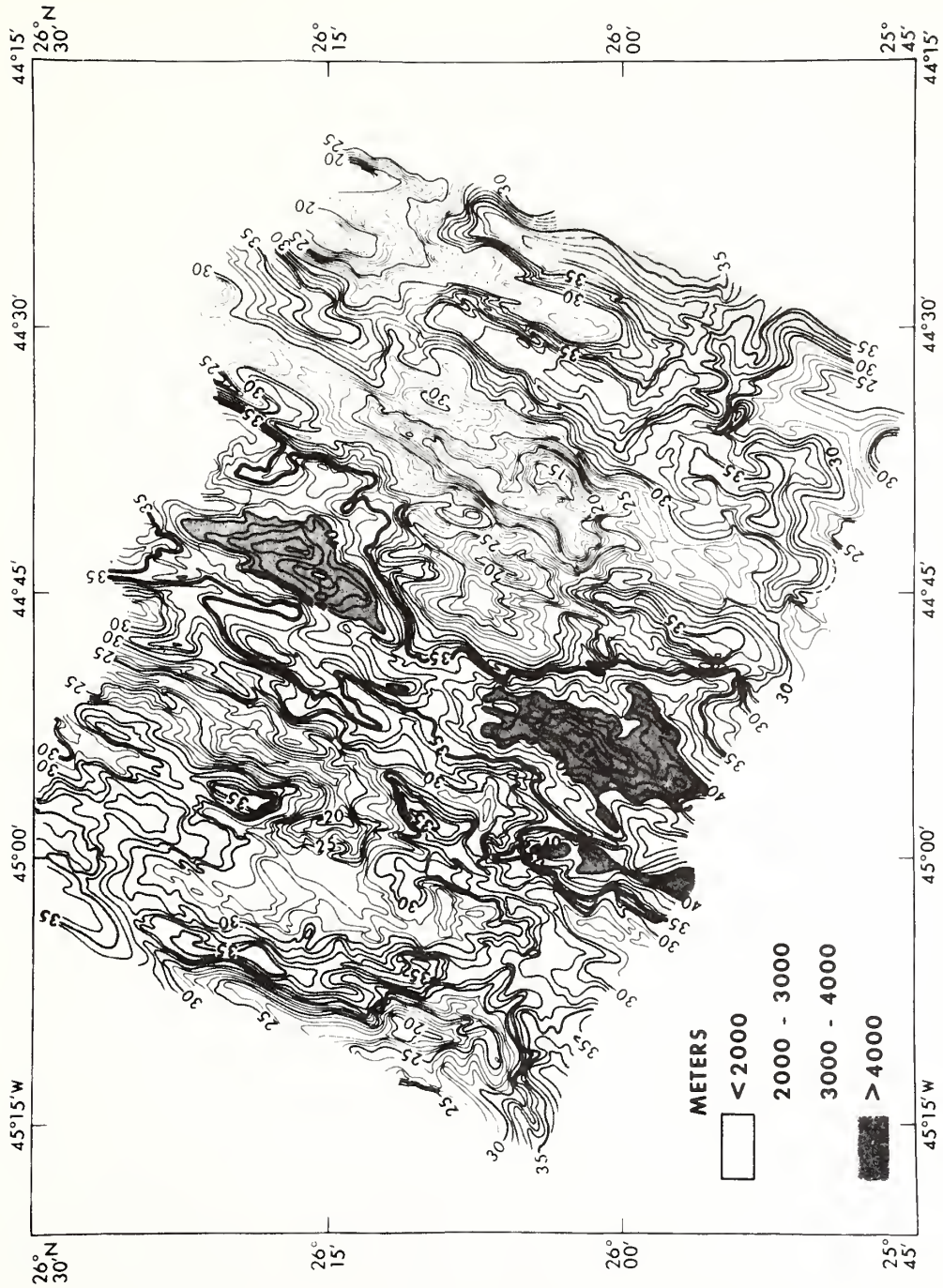

Fig. 4. Bathymetry of the Mid-Atlantic Ridge in hundreds of meters, depths being corrected for sound velocity [*Matthews*, 1939]. See outlined box in Figure 1 for location of this detailed bathymetry on general ridge area. Track lines are shown in Figure 2.

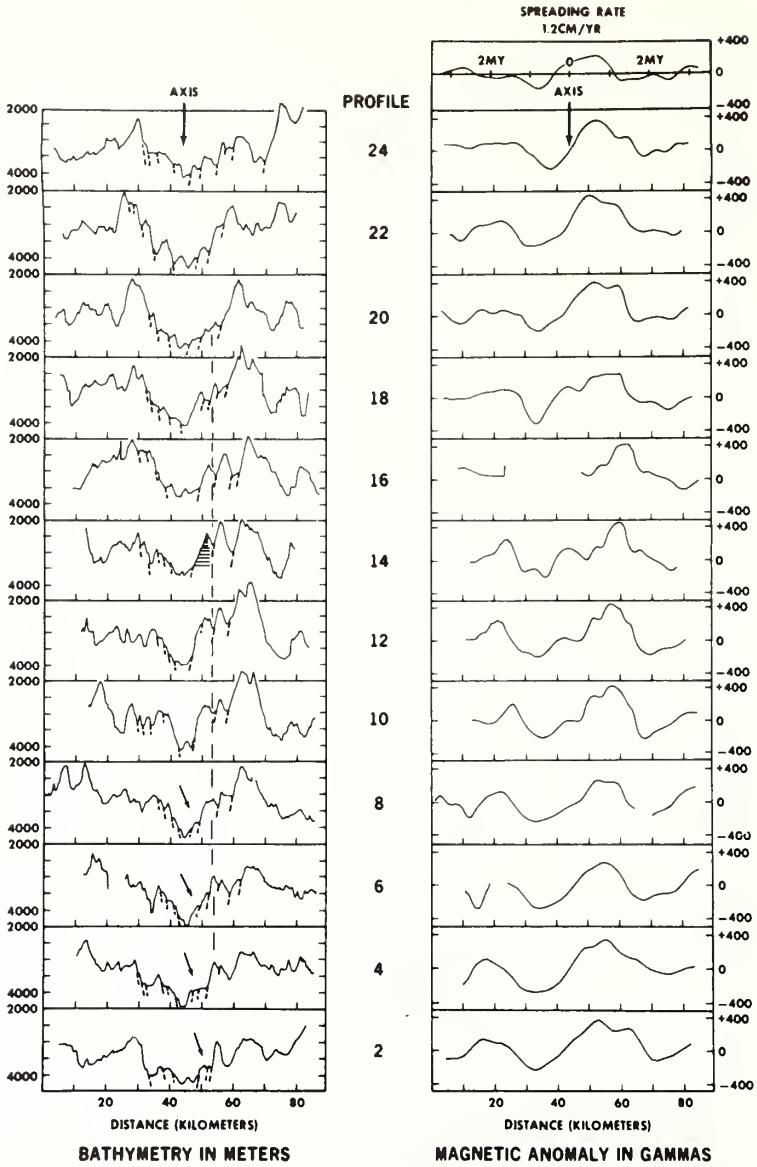

Fig. 5. Bathymetric and magnetic profiles orthogonal (NW-SE) to the ridge. See Figure 2 for location. Large arrows indicate axis of the rift valley. On profile 14, short lines indicate location of 10-m steps, and long lines indicate 100- to 300-m steps determined from photographic transects. Small arrows indicate fault blocks. Dashed line correlates large fault-controlled block in the east wall. Possible fault zones are suggested.

each profile (Figure 5) is the axial anomaly. A magnetic model for the area assuming a constant spreading rate of 1.2 cm/yr [*Lattimore et al.*, 1974] is shown in Figure 5. The oldest sea floor in the detailed study area is about 3 m.y. old.

A significant feature of the magnetics is the different character of the axial anomaly in the area of the TAG hydrothermal field. A low is present in the axial anomaly decreasing in prominence from profile 14 north and south to profiles 20 and 8. The source of this magnetic anomaly is a portion of sea floor with reduced intensity of remanent magnetization [*McGregor*, 1974; *McGregor et al.*, 1974*b*]. Since this is the site of the hydrothermal deposit and a bottom water temperature anomaly [*Rona et al.*, 1975*a*], hydrothermal alteration of the basalt and reduction of the intensity of remanent magnetization are expectable. Alteration of basalts by hydrothermal activity has been shown to reduce the magnetic susceptibility and intensity of remanent magnetization [*Luyendyk and Melson*, 1967; *Watkins and Paster*, 1971]. In addition to the hydrothermal manganese, altered basalts were dredged, including greenstones and zeolitized rocks (TAG leg 4, 1973, cruise report, R. Scott, personal communication). The Reykjanes Peninsula of Iceland, a hydrothermal area, also has a prominent magnetic low caused by the hydrothermal alteration of basalt [*Björnsson et al.*, 1972].

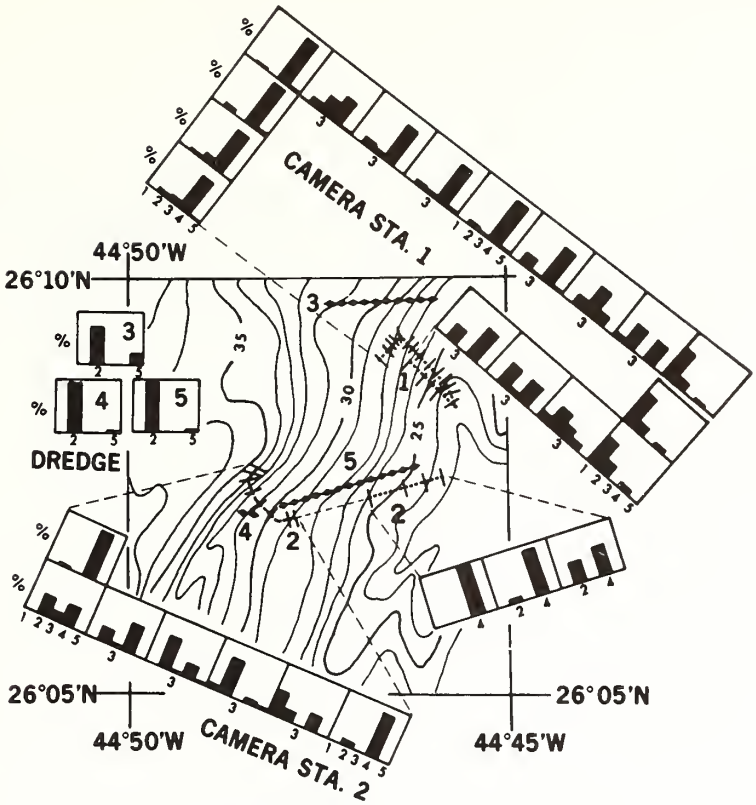

Fig. 6. Bathymetry, in hundreds of meters, of a portion of the east wall. Positions of two camera stations (heavy dashed lines) and three dredge stations (diamond pattern) are shown. Bar graphs are percentages of bottom type present along each camera run averaged over approximately 15 min of time. Bottom types are (1) pillow basalts, indicating flows, (2) talus, (3) breccia, (4) sediment, silt, and sand, and (5) hydrothermal manganese.

Computer modeling studies were undertaken to interpret the magnetic anomaly pattern present on the Mid-Atlantic Ridge at 26°N [*McGregor*, 1974; *McGregor et al.*, 1974*b*]. Variations in the intensity of magnetization parallel to the ridge crest were found, a low in the magnetization being correlated with an extensively faulted region in the east wall of the rift valley.

Earthquake Activity

The relationship of bathymetry and earthquake epicenter locations is shown in Figure 1, with the epicenter data from the NOAA National Geophysical and Solar Terrestrial Data Center Hypocenter Data File (C. A. von Hake, personal communication, 1973). Eighteen events from 1953 to 1973 and one from 1937 occurred in the area with magnitudes between 4.0 and 5.0. The plotted epicenters have an uncertainty in location of 20 km. In spite of the uncertainty it is useful where detailed bathymetry is available to look for any associations.

Within the study area the northern half of the rift is much more active than the southern half. Many epicenters appear to be associated with the wide, deep basins in the rift at the intersection of the transverse valleys. Some epicenters appear to be associated with the rift mountains, but this apparent association may reflect the uncertainty of location determinations. Coarse-grained gabbro dredged at 26°15'N, 44°20'W (R. Scott, personal communication, 1974) suggests exposure of a magma chamber. Such exposure is most probably related to faulting.

A detailed microearthquake survey between 36° and 37°N [*Spindel et al.*, 1974] shows that activity is associated with rift walls and is related to faulting. In the area 25°–27°N, detailed seismic monitoring was not done, but from the large-magnitude earthquake epicenters (magnitude of about 5 on the Richter scale), favoring of the east wall for the zone of activity was suggested. Of the 18 events shown in Figure 1, only three would not lie along the east wall (these would lie in the rift valley), a maximum error in position of 20 km being assumed. Conversely, of those 18 events, even with a maximum error in position being assumed, four can reside only under the east wall. North of the Azores triple junction between 47° and 51°N, *Johnson and Vogt* [1973] found that the epicenters, in spite of the error in position, still favored the west side of the rift.

The significance of earthquake swarms as indicators of possible hydrothermal or magmatic activity was suggested by *Sykes* [1970]. Earthquake swarms are present on the ridge crest at 28.4° and 31.4°N [*Sykes*, 1970], suggesting possible locations for additional detailed studies to be done.

Conclusion

Detailed studies are essential to defining the structure of ridges and to understanding rift processes. This portion of the

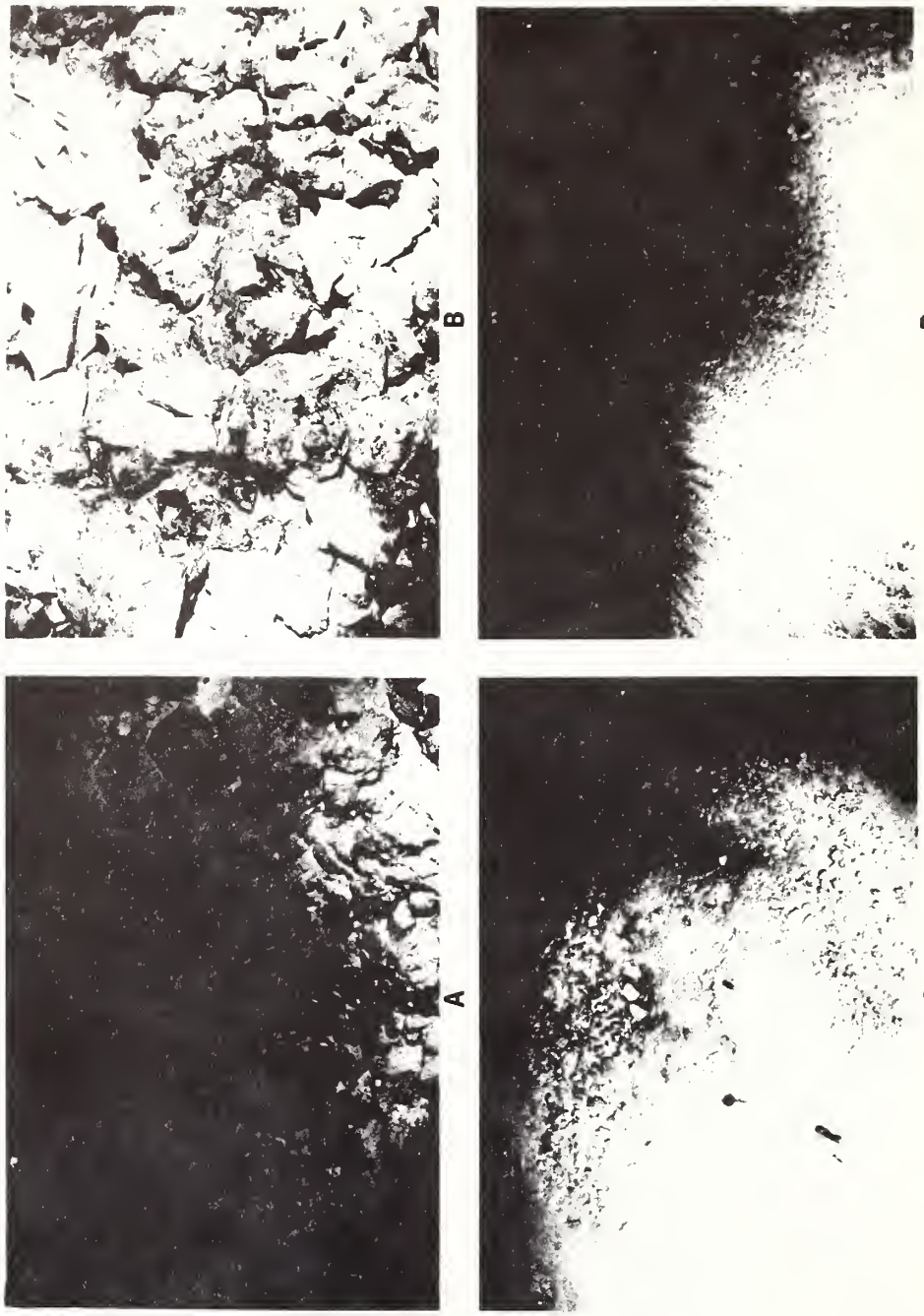

Fig. 7. Underwater photographs of bottom type categories plotted in Figure 5. Field of view is 6 × 4 m. (*a*) Pillow basalts at approximately 2400-m depth. (*b*) Talus at 3200-m depth. (*c*) Breccia and hydrothermal manganese (lower left and central portion of photograph) at 2600-m depth. Silica sponges are light areas casting dark shadows. (*d*) Ripple-marked sediment. Water depth is 2550 m.

Mid-Atlantic Ridge (25°–26°N), with its associated slow spreading rate, is extensively faulted. Fault blocks vary in size from tens of meters to kilometers in width and relief. The TAG hydrothermal field is associated with fault steps 30–300 m in width on the east wall as well as with large faulted blocks, suggesting that the fault zones provide an avenue for hydrothermal fluids. Hydrothermal manganese, identified from dredged specimens [*M. Scott et al.*, 1974], was photographed blanketing talus at depths between 3100 and 2500 m. Small steps, about 10 m in width and relief, occur at the top of the east wall of the rift.

Topographic features at 26°N bear certain similarities to those reported on other portions of the Mid-Atlantic Ridge between 36° and 37°N and between 47° and 51°N. The rift valley is composed of a series of discontinuous deep basins, with small linear topographic highs in the floor of the rift valley which are the site of recent volcanism and are believed to be the zone of active dike emplacement. The topographic fabric is complex in comparison with that predicted by plate tectonic theory. The rift valley itself is composed of two trend directions, topographic trends being a function of the portion of the rift valley from which they originated.

Seismicity and magnetic anomaly patterns may be useful in locating areas where tectonic processes are conducive to the occurrence of hydrothermal activity.

Acknowledgments. We gratefully acknowledge Dale C. Krause for his invaluable assistance in establishing the objectives and models tested by phase 3 of the NOAA-TAG 1973 field work. We thank Louis W. Butler, Mahlon M. Ball, and George H. Keller for enlightening discussions and review of the manuscript. We also thank J. William Lavelle for providing computer programing assistance, Sam A. Bush for assisting in the data reduction, and Martin R. Fisk for calculating magnetic field values. We express our appreciation to Charles A. Lauter, Jr., whose preparation and operation of the deep-sea camera made the photographic transects a success. L. L. Posey, W. S. Simmons, and the other officers and crew of the NOAA ship *Researcher* provided cooperation and diligence in executing the survey. Funds for the study were provided by the National Oceanic and Atmospheric Administration.

References

Atwater, T., and J. D. Mudie, Detailed near-bottom geophysical study of the Gorda Rise, *J. Geophys. Res., 78,* 8665–8686, 1973.

Björnsson, S., S. Arnorsson, and J. Tomasson, Economic evaluation of Reykjanes thermal brine area, Iceland, *Amer. Ass. Petrol. Geol. Bull., 56,* 2380–2391, 1972.

Hurwitz, L., Mathematical model of the 1970 geomagnetic field (abstract), *Eos Trans. AGU, 51,* 269, 1970.

International Association of Geomagnetism and Aeronomy (IUGG) Commission 2, Working Group 4, International geomagnetic reference field 1965.0, *J. Geophys. Res., 74,* 4407–4408, 1969.

Johnson, G. L., and P. R. Vogt, Mid-Atlantic Ridge from 47° to 51°N, *Geol. Soc. Amer. Bull., 84,* 3443–3462, 1973.

Keller, G. H., S. H. Anderson, and J. W. Lavelle, Near-bottom currents in the mid-Atlantic Ridge rift valley, *Can. J. Earth Sci., 12,* 703–710, 1975.

Lattimore, R. K., P. A. Rona, and O. E. DeWald, Magnetic anomaly sequence in the central North Atlantic, *J. Geophys. Res., 79,* 1207–1209, 1974.

Luyendyk, B. P., and W. G. Melson, Magnetic properties and petrology of rocks near the crest of the Mid-Atlantic Ridge, *Nature, 215,* 147–149, 1967.

Macdonald, K. C., B. P. Luyendyk, F. N. Spiess, and J. D. Mudie, Near bottom geophysical studies of the Famous rift valley, Mid-Atlantic Ridge (abstract), *Eos Trans. AGU, 55,* 446, 1974.

Matthews, D. J., Tables of the velocity of sound in pure water and sea water for use in echo-sounding and sound ranging, *Publ. H.D. 282,* 52 pp., Admiralty Hydrogr. Dep., London, 1939.

McGregor, B. A., Crest of Mid-Atlantic Ridge at 26°N: Topographic and magnetic patterns, Ph.D. thesis, Univ. of Miami, Coral Gables, Fla., 1974.

McGregor, B. A., P. A. Rona, and D. C. Krause, Crest of Mid-Atlantic Ridge at 26°N (abstract), *Eos Trans. AGU, 55,* 293, 1974*a*.

McGregor, B. A., C. G. A. Harrison, and P. A. Rona, Magnetic anomalies on the Mid-Atlantic Ridge crest at 26°N, *Geol. Soc. Amer. Abstr. Annu. Meet., 6,* 863, 1974*b*.

Moore, J. G., and R. S. Fiske, Volcanic substructure inferred from dredge samples and ocean-bottom photographs, Hawaii, *Geol. Soc. Amer. Bull., 80,* 1191–1202, 1969.

Needham, H. D., and J. Francheteau, Some characteristics of the rift valley in the Atlantic Ocean near 36°48′ north, *Earth Planet. Sci. Lett., 22,* 29–43, 1974.

Rona, P. A., R. N. Harbison, B. G. Bassinger, L. W. Butler, and R. B. Scott, Asymmetical bathymetry of the Mid-Atlantic Ridge at 26°N latitude (abstract), *Eos Trans. AGU, 54,* 243, 1973.

Rona, P. A., B. A. McGregor, P. R. Betzer, G. W. Bolger, and D. C. Krause, Anomalous water temperature over Mid-Atlantic ridge crest at 26° north latitude, *Deep Sea Res.*, in press, 1975*a*.

Rona, P. A., R. N. Harbison, B. G. Bassinger, R. B. Scott, and A. J. Nalwalk, Tectonic fabric and hydrothermal activity of Mid-Atlantic Ridge crest (26°N), *Geol. Soc. Amer. Bull.*, in press, 1975*b*.

Scott, M. R., R. B. Scott, A. J. Nalwalk, P. A. Rona, and L. W. Butler, Hydrothermal manganese in the median valley of the Mid-Atlantic Ridge, *Geophys. Res. Lett., 1,* 355–358, 1974.

Scott, R. B., P. A. Rona, B. A. McGregor, and M. R. Scott, The TAG hydrothermal field, *Nature, 251,* 301–302, 1974.

Spindel, R. C., S. B. Davis, K. C. Macdonald, R. P. Porter, and J. D. Phillips, Microearthquake survey of median valley of the Mid-Atlantic Ridge at 36°30′N. *Nature, 248,* 577–579, 1974.

Sykes, L. R., Earthquake swarms and sea floor spreading, *J. Geophys. Res., 75,* 6598–6611, 1970.

Watkins, N. D., and T. P. Paster, The magnetic properties of igneous rocks from the ocean floor, *Phil. Trans. Roy. Soc. London, Ser. A, 268,* 507–550, 1971.

(Received September 26, 1974;
revised January 30, 1975;
accepted February 20, 1975.)

Reprinted from: *EOS 56*, No. 6, 382.

SEISMIC PROFILES ALONG THE U.S. NORTHEAST COAST CONTINENTAL MARGIN

B.A. McGregor (NOAA, Atlantic Oceanographic and Meteorological Laboratories, Miami, Florida 33149)
G.H. Keller (NOAA, Atlantic Oceanographic and Meteorological Laboratories, Miami, Florida 33149)
R.H. Bennett (NOAA, Atlantic Oceanographic and Meteorological Laboratories, Miami, Florida 33149)

Twenty-seven hundred kilometers of seismic reflection profiles were collected between Hydrographer and Wilmington Canyons parallel to the continental margin on the outer shelf, middle slope, lower slope, and continental rise. On the slope and in the canyons extensive slumping has occurred. A stratified block separating twin canyons southwest of Block Canyon appears to be tilted. A wedge of sediment, probably Tertiary in age, with many reflectors thickens to the southwest between Alvin and Hudson Canyons. The slope in this area is cut by several large canyons whereas in the vicinity of Hydrographer Canyon and from Hudson to Wilmington Canyon the slope is extremely dissected with many small valleys. Reflecting horizons are continuous, parallel to the margin. Pronounced horizons in many places appear to control the morphology. Unconformities are abundant on the margin indicating varying depositional and erosional environments. On the rise a buried depression extends from Hudson to Lindenkohl Canyon.

Reprinted from: *Geological Society of America Annual Meetings, Abstracts with Programs* 7, No. 7, 1196.

IMPACT STRUCTURES ON LANDSAT IMAGERY

McHone, John F. Jr., Department of Geology, University of Illinois, Urbana, Illinois 61801; and Dietz, Robert S., National Oceanic and Atmospheric Administration, Miami, Florida 33149

Satellite generated imagery (LANDSAT 1:1,000,000) offers a "new look" at terrestrial meteorite craters and astroblemes (ancient impact scars). We have compiled an atlas of known impact sites from such images and, by comparison, selected other geologic features of possible extraterrestrial origin. Considering the plethora of endogenic circular geologic structures, the identification of an exogenic impact scar still requires field evidence of shock metamorphism; nevertheless some structures can be almost certainly recognised as astroblemes from LANDSAT imagery alone (e.g. Araguainha Ring in Mato Grosso, Brazil).

Established impact sites of the world are resolved by LANDSAT into five different styles: (1) large annular grabens (Manicouagan); (2) bull's eye patterns composed of concentric disks (Araguainha); (3) ghost rings (Gosses Bluff); (4) bleached rings (Barringer and Lonar craters); and (5) deep, as indicated by delayed freezing, circular lakes, commonly with central islands, in glaciated Precambrian shields (Clearwater Lakes, Mistastin, Lappajarvi).

A probable satellite-detected astrobleme is the Oman Ring (19°55'N, 56°58'E) in the Arabian Peninsula. This ghost ring structure, brought to our attention by Nicolas Short of NASA, is 6 km in diameter with a 2 km wide central dome.

Another probable site is Ozero El'gygytgyn (67°30'N, 172°05'E) in north eastern Siberia. A crater lake 14 km across, the feature resembles New Quebec crater in Canada but is much larger and more maturely eroded. Imagery shows the rudely circular shoreline to be enclosed by highly circular geomorphology bearing a definite rim along at least the north edge. Origin by impact in the early Quaternary or late Pliocene seems indicated.

Representative images of several other known and suspected impact sites have been selected for discussion.

Reprinted from: *Meteoritics 10*, No. 3, 209-214.

ON THE TERRESTRIAL ORIGIN OF THE TEPEXITL CRATER, MEXICO

Lucrecia Maupomé
Instituto de Astronomía, UNAM
México 20, D. F.
and
Centro de Investigación, IPN
México 14, D. F.
Román Alvarez
Instituto de Geofísica, UNAM
México 20, D. F.
Susan W. Kieffer
Dept. of Geology, University of California
Los Angeles, CA 90024
Robert S. Dietz
National Oceanic and Atmospheric Administration
Miami, FL 33149

The possibility of a meteoritic origin for Tepexitl crater in Mexico was proposed by Maupomé (1974), owing to the evident explosive origin of the crater, its circularity and its strong topographical resemblance to Wolf Creek crater, to the Pretoria Salt Pan, and to some lunar craters.

Located in Zacatepec plain, the crater is a bowl-shaped, nearly circular structure with a complete rim, Fig. 1a and 1b; its present depth averages 75 m from the top of the rim to the flat floor. Its measured diameters vary from 1180 m to 966 m. The rim varies in height above the crater floor from 57 m on the north to 92 m on the south. At the top the width is 2 to 5 m; the outer slopes are about 15° and the inner walls have slopes of about 27°. The crater has an inner ridge along the SE radius extending from the top of the rim to nearly the center of the crater. Tepexitl is located at 19°13′ N, 97°26′ W, in the NE part of the State of Puebla. The area is within the Mexican Volcanic Belt (Quaternary volcanism) and contains maars, calderas, volcanic cones, limestone outcrops and intrusive ryholitic domes. There are, however, few geological studies published on the area and those available cover it only partially (Ordóñez, 1905 and 1906; Ohngemach 1973). Tepexitl apparently had not been formerly described in the literature.

Geophysical studies were initiated in order to test the hypothesis of meteoritical origin (Alvarez *et al.*, 1975); aeromagnetometry and ground magnetometry surveys were carried out over volcanic cones, calderas, and Tepexitl, in order to study geophysically determinable differences. Such initial surveys yielded favorable results in support of an impact origin for Tepexitl since its magnetic response did not show the presence of a magnetic dipole detected at the majority of the other structures, thus suggesting a different origin for this crater.

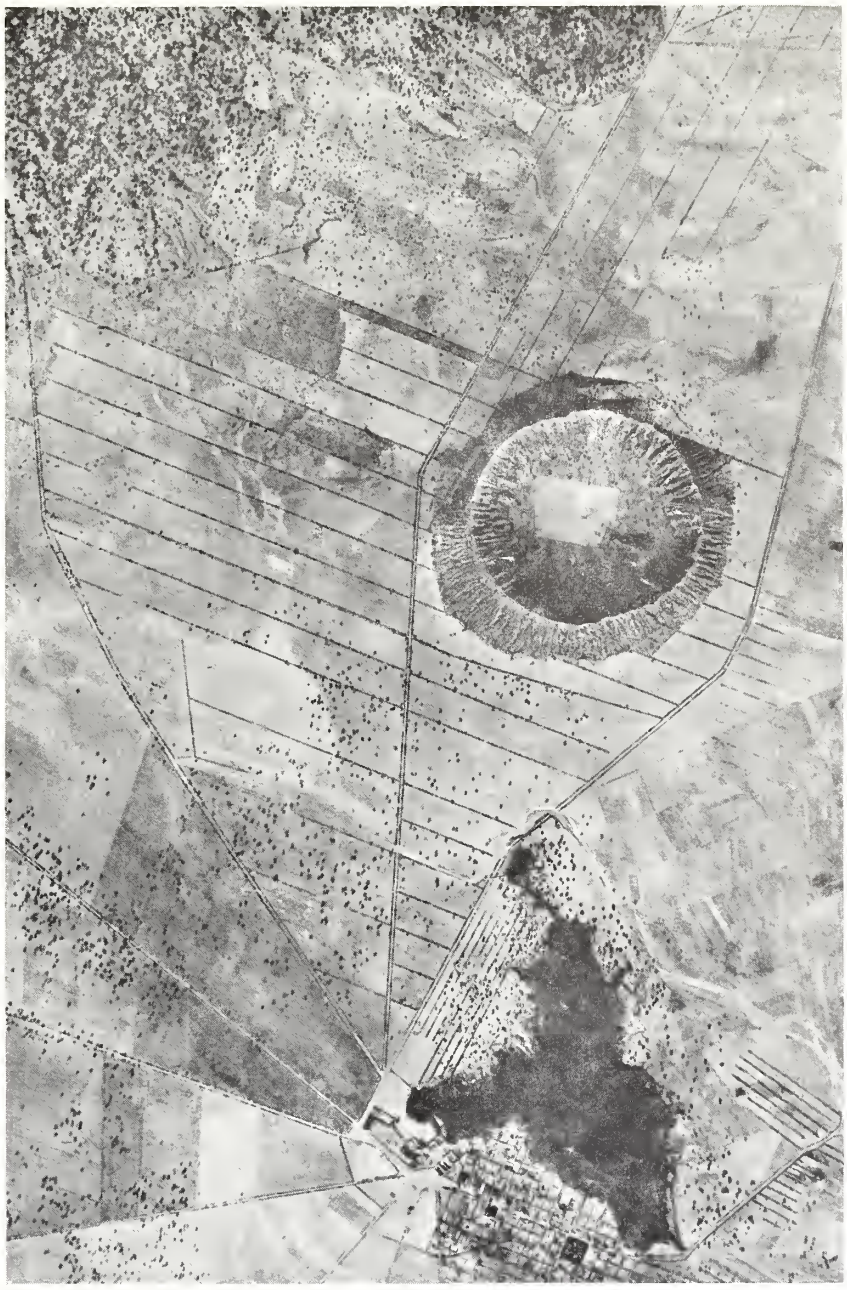

Fig. 1a Aerial view of Tepexitl, the inner ridge is in the SE quadrant. North is to the top. (Fig. 4, Plate 6, Maupomé 1974).

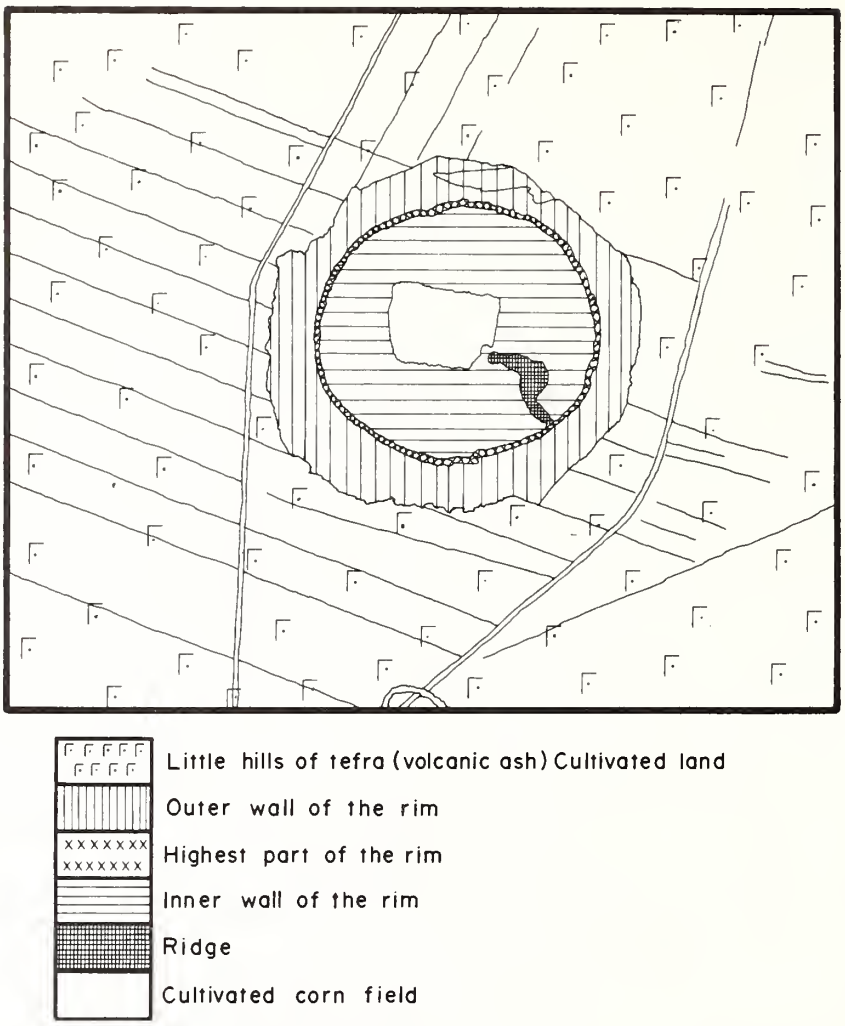

Fig. 1b Elements of the crater (Fig. 6, Maupomé, 1974).

Closer geological studies have indicated, however, that the origin of the structure is definitely volcanic. The crater is an ash ring composed primarily of volcanic glass (vitric) fragments. These were apparently ejected fairly cold as there is no evidence of welding of the ash into a welded tuff.

Although the crater floor has a depression below the regional level, the volume of the rim exceeds the volume of the bowl, indicating that there has been addition of material to the neighboring surface. This is unlike a

meteorite crater where the volume of the ejecta is essentially equal to the volume of the hole since the volume of the impacting missile is negligible in comparison.

The crater wall is made up mostly of dip-slope beds which retain their initial dips, dipping both outward and inward with respect to the rim crest. There is no evidence of inverted or overturned stratigraphy. Beds described earlier by Maupomé (1974) as "overturned" are in fact "draped" over the inside of the crater wall; these, however, are not stratigraphically overturned beds. In addition, at this crater there is no uplifted country rock showing a quaquaversal dip. In fact, no country rocks are seen at all in the rim. The rim is entirely constructional, made up of volcanic ash, which is contrary to the expectation if it were an impact crater.

Further arguments against the impact concept are that we found no meteorites, no shatter coning (Dietz, 1946b), no rock flour, and no rocks which could be interpreted as probably shock metamorphosed. However, some percussion fractures, plumose fracture, and slickensiding were noted, in addition to some scouring which may have been due to the moving ash clouds. There is no fracturing, however, that we can associate with the type of shock generated by a meteorite explosion.

The following model proposed for the volcanic origin of Tepexitl is based upon the stratigraphy of the crater. The oldest units exposed are unwelded white ash beds of rhyolitic composition, Table 1. In all there are

Table 1
Composition of rocks from Tepexitl (Tepx) and Tepeyahualco (Tlco)*

Compounds (%)	Tepx (black)	Tepx (grey)	Tlco (white-grey)
SiO_2	74.15	73.68	73.03
Al_2O_3	14.05	14.00	13.83
CaO	0.70	0.73	0.50
Na_2O	4.05	4.19	4.16
K_2O	4.05	4.11	4.02
Fe as Fe_2O_3	1.21	1.16	0.69
MgO	0.07	0.06	0.08
TiO_2	0.08	0.08	0.02
(H_2O)	1.17	1.83	3.17
Total	99.59	99.84	99.50

*Tepeyahualco is a complex explosion crater, located 20 km to the north of Tepexitl. The compositions shown in these columns may be characteristic of many of the young volcanic features in this region.

perhaps 50 of these ash units in the crater wall. In several gullies it is possible to see beds draped over the rim in a continuous bend. It appears that the surrounding valley was covered by a Pleistocene lake at the creation of Tepexitl. This lake may have provided the water necessary to generate phreatic explosions above a shallow magma reservoir.

Magma probably entered the region under Tepexitl and, at shallow depth, either reached the level of the ground water table or came in contact with lake water. A vent opened through the basement which, in this region, is limestone.

Since the crater is slightly elongated in the NW-SE direction, the initial vent may have been slightly elongated in this direction. The more violent periods of eruption produced ash beds dipping outward from the crater. The less violent eruptions (implying a smaller vent) allowed beds to be draped over the rim.

An obsidian plug of rhyolitic composition choked the vent leading to a period of quiescence during which this plug cooled and solidified. Subsequent eruptions, probably driven by more water entering the magma until pressure was sufficient to ream out much of the obsidian plug, resulted in the deposition of a unit containing obsidian blocks as the vent reopened. As the eruption continued, ashes were deposited on top of the obsidian blocks. This last stage of eruption appeared to have tapped the deeper parts of the reservoir, culminating with the transport of limestone xenoliths and alluvial cobbles to the surface.

The last eruption was possibly off-center because the obsidian plug would have been substantially stronger than the volcanic ejecta and crater fill. We infer that this last eruption was off-center toward the south because: 1, the south rim is 35 m higher than the north rim – the extra 35 m of height consists of the last-deposited beds; 2, draped beds are missing in the southern sector, presumably scraped off by the final eruption – the draped beds are preserved on all other sectors; 3, the anomalous ridge in the southeast is a constructional unit, containing abundant large obsidian blocks from the obsidian plug.

In conclusion, the following evidence is against an impact origin for Tepexitl: 1, no meteorites were found; 2, no shatter cones were discovered; 3, we could identify no shock metamorphosed rocks; 4, the rim is entirely composed of ash with no uplifted quaquaversally dipping country rock; 5, there are no overturned beds or overturned flap; 6, ejected blocks are of small size, the largest observed being about 1 m^3; 7, the ejected material is entirely volcanic; 8, the volume of the rim exceeds that portion of the crater which is depressed below the regional level, so that new material has been added to the earth's surface; 9, there is no evidence of a central dome or ring syncline; and, 10, there is no suevite (impact-melt rock) as would contain cored bombs, polymict breccia, etc.

The small mass of the moon and its low internal pressure make volcanism unlikely on the moon (Dietz, 1946a). Furthermore, generatical similarity among Tepexitl and moon's craters can be readily discarded in view of the exceedingly anhydrous lunar environment which would obviously prevent the occurrence of shallow phreatic explosions.

REFERENCES

Alvarez, R., L. Maupomé and A. Tejera, 1975. Aeromagnetometry and Ground Magnetometry of Volcanic Structures in Puebla, Mexico (in preparation).

Dietz, R.S., 1946a. The Meteoritic Impact Origin of the Moon's Surface Features. *The Journal of Geology, Vol. LIV*, 6, 359-375.

Dietz, R.S., 1946b. Geological Structures Possibly Related to Lunar Craters. *Popular Astronomy, Vol. LIV*, 9, 1-3.

Maupomé, L., 1974. Possible meteorite crater in Mexico. *Rev. Mex. Astron. y Astrofis.* 1, 81-86.

Ohngemach, D., 1973. Análisis Polínico de los Sedimentos del Pleistoceno Reciente y del Holoceno en la Región Puebla-Tlaxcala. *Communicaciones*, Fund. Alemana Inv. Cient. 7, 47-49.

Ordóñez, E., 1905. Los Xalapascos del Estado de Puebla (la. parte, México: Imprenta y Fototipía de la Secretaría de Fomento).

Ordóñez, E., 1906, Los Xalapascos del Estado de Puebla (2a. parte, México: Imprenta y Fototipía de la Secretaría de Fomento).

Manuscript received 7/1/75

Reprinted from: *Meteoritics 10*, No. 4, 454-455.

TEPEXITL CRATER, MEXICO: NOT METEORITIC

Lucrecia Maupomé*, Román Alvarez**, Susan W. Kieffer***
Robert S. Dietz****,
*Instituto de Astronomía, UNAM México 20, D.F. and
Centro de Investigación, IPN México 14, D.F.
**Instituto de Geofísica, UNAM México 20, D.F.
***University of California, Los Angeles, CA 90024
****National Ocean. and Atmos. Adm., Miami, FL

Although previously described as a possible meteorite crater (L. Maupomé, *Revista Mexicana de Astronomía y Astrofísica, V. 1*, 1974), Tepexitl crater (19°13'N, 97°26'W) is definitely volcanic. It should not be included on any list of possible terrestrial impact sites. Tepexitl crater, east of Puebla, México, and in the Mexican Volcanic Belt, is 1.2 km across and averages 75 m deep below its rim. Our examination reveals that Tepexitl is an ash ring built by successive magmatic phreatic eruptions of rhyolitic vitric ash. The remarkably symmetric ash ring suggest that the explosions were of the "gun-barrel" type formed under calm wind conditions. The associated magma chamber must have been shallow as only limestone and alluvial gravel xenoliths were ejected without any deep crustal or sub-crustal rocks. Abundant ground water or possibly a shallow lake presumably fueled these steam explosions. Tepexitl is but one of a score of volcanic crater-form features in the region. Although it has some unique aspects, which initially suggested that it might be an impact site, it is definitely a member of this regional family of volcanic explosion craters, maars and collapse features. The following evidence opposes an impact origin: 1, no meteorites were found; 2, no shatter cones were discovered; 3, we could identify no shock metamorphosed rocks; 4, the rim is entirely composed of ash with no uplifted quaquaversally dipping country rock; 5, there are no overturned beds or overturned flap; 6, ejected blocks are of small size, the largest observed being about 1 m^3; 7, the ejected material is entirely volcanic; 8, the volume of the rim far exceeds that portion of the crater which is depressed below the regional level, so that much new material has been added to the earth's surface; 9, there is no evidence of a central dome or ring syncline; and 10, there is no suevite, impact melt rock.

Reprinted from: *Marine Geology 18*, 47-69.

MORPHOLOGY AND SEDIMENTARY PROCESSES IN AND AROUND TORTUGAS AND AGASSIZ SEA VALLEYS, SOUTHERN STRAITS OF FLORIDA

LARRY L. MINTER[1], GEORGE H. KELLER[1] and THOMAS E. PYLE[2]

[1] *Atlantic Oceanographic and Meteorological Laboratories, National Oceanic and Atmospheric Administration, Miami, Fla. (U.S.A.)*
[2] *Marine Science Institute, University of South Florida, St. Petersburg, Fla. (U.S.A.)*

(Received June 17, 1974; accepted for publication July 24, 1974)

ABSTRACT

Minter, L. L., Keller, G. H. and Pyle, T. E., 1975. Morphology and sedimentary processes in and around Tortugas and Agassiz Sea Valleys, southern Straits of Florida. Mar. Geol., 18: 47—69.

Continuous seismic reflection profiling and new bathymetry data in the southern Straits of Florida over an area dominated by the Tortugas and Agassiz Valley systems have allowed a more detailed analysis of the morphology and sedimentary processes active in this region. Four dives in the submersible DSV "Alvin" supplement the seismic and bathymetric data.

The continental slope in the study area can be divided into two physiographic provinces: (I) an irregular topography controlled by the Florida Escarpment west of Tortugas Valley; and (II) the remainder of the continental slope which contains the majority of features under investigation. Seismic data indicate that the valleys are being filled shoreward of 290 fathoms (530 m) by a wedge of prograding sediments derived from the Florida shelf.

The morphology of the two valley systems reflects probable differences of origin. Tortugas Valley appears to have originated coincident with the eastern terminus of the Florida Escarpment and province-I-type topography. The Agassiz valleys may have an origin associated with jointing patterns observed by divers aboard DSV "Alvin". Current meter readings and bottom photographs from "Alvin" indicate that currents are relatively sluggish and not very effective in the transport of sediment within the valleys. An area of undulations west of Pourtales Terrace was investigated and concluded to be erosional in origin.

Slumping appears to have played a large part in shaping many features in the study area. The bottom morphology and sediment distribution on the continental slope and in the axis of the Straits of Florida suggest that bottom currents are active in shaping the entire area.

INTRODUCTION

The southern Straits of Florida separate the Florida-Bahama Platform, an extensive carbonate environment, from the crystalline and terrigenous sedi-

mentary rocks of Cuba (Hurley, 1964). The southern Straits extend from the Gulf of Mexico on the west to Cay Sal Bank on the east, where the easterly flowing Florida Current turns northward to enter the northern Straits of Florida.

An intensive study of an area in the southern Straits of Florida (Fig.1) was undertaken for the purpose of investigating the unusual bottom morphology noted in earlier studies (Jordan and Stewart, 1961; Jordan et al., 1964; Malloy and Hurley, 1970). The submarine topography of this area is dominated by the Tortugas and Agassiz Valleys which were recognized, named, and classified as two separate systems by Jordan and Stewart (1961). For the purpose of identification, a meridian at 82° 50′ W is considered to separate the Tortugas Valley and its associated tributary system from the Agassiz Valley system lying farther to the east. All of these valleys are unusual in that their relief increases in the downslope direction, unlike most submarine valleys whose heads display the greatest relief. The anomalous character of the valleys, which do not cross the continental shelf, but head

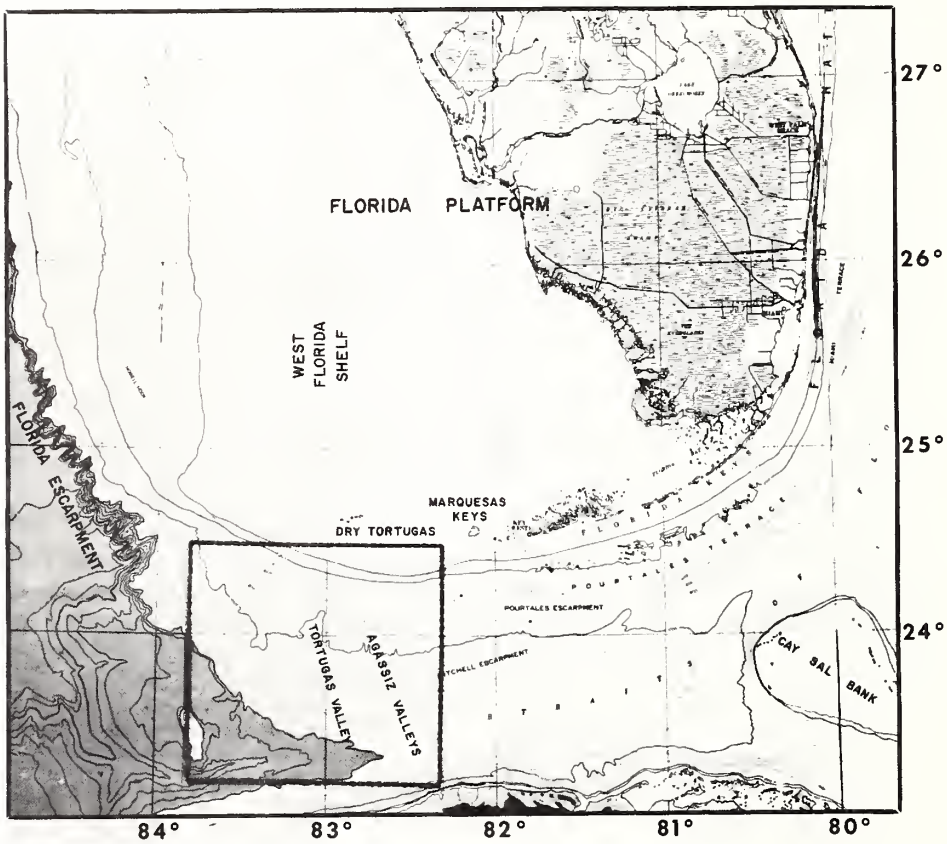

Fig.1. Location map showing regional features and area of study within dashed box. (From Uchupi, 1966a.)

in water depths of about 300 fathoms (549 m), has led to the hypothesis that the heads of these valleys are being infilled with recent sediments transported south and westward around the western end of the Marquesas Keys, located 35 km west of Key West, Florida (Fig.1), (Jordan and Stewart, 1961; Jordan, 1962). Another region of particular interest in the study area is a series of bottom undulations in the vicinity of latitude 24°16′N and longitude 82°22′W (Fig.2).

The bathymetric map presented here (Fig.2) is based on soundings made by the USC & GSS "Hydrographer" from 1952 to 1960. The previous studies mentioned above were either lacking in detailed soundings or did not include the complete area of study; consequently, a new base map was constructed. A portion of Kofoed and Jordan's (1964) bathymetry of the Tortugas Terrace was used to complete a small area lacking in sounding density (Fig.3, block A).

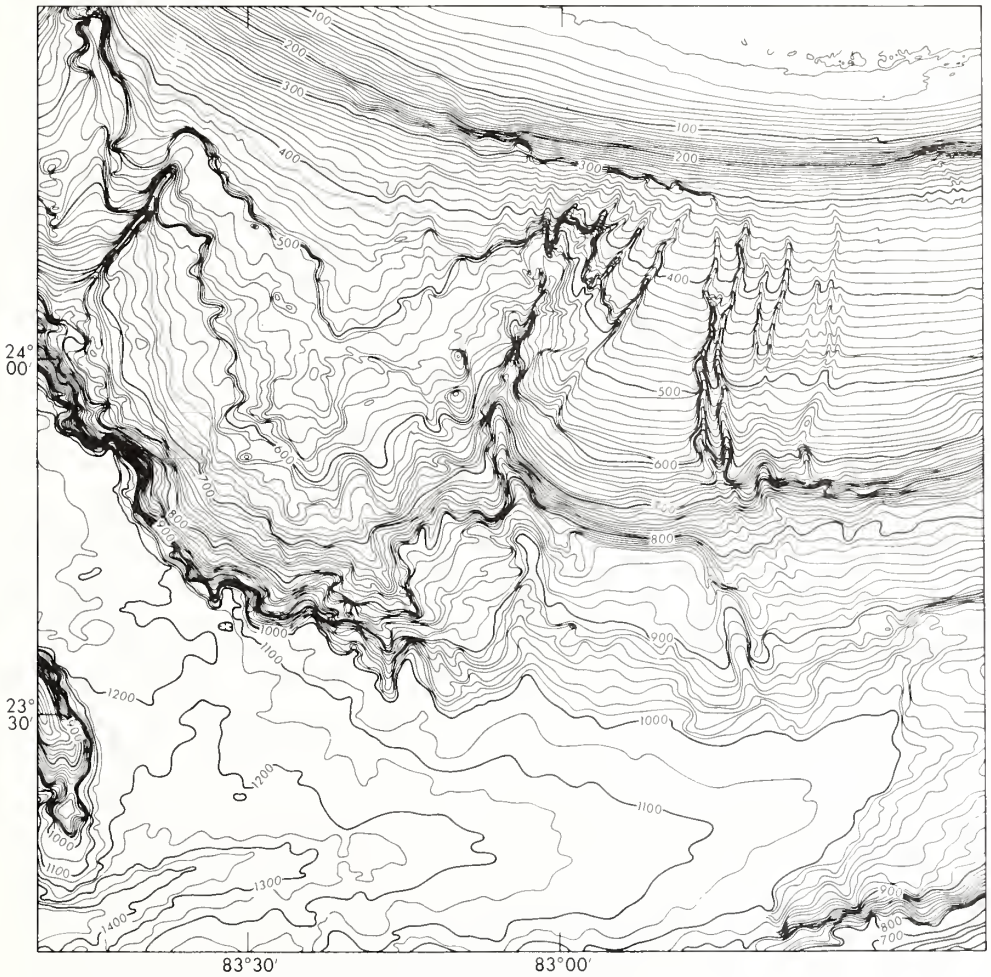

Fig. 2. Bathymetric map of study area. Contours in fathoms.

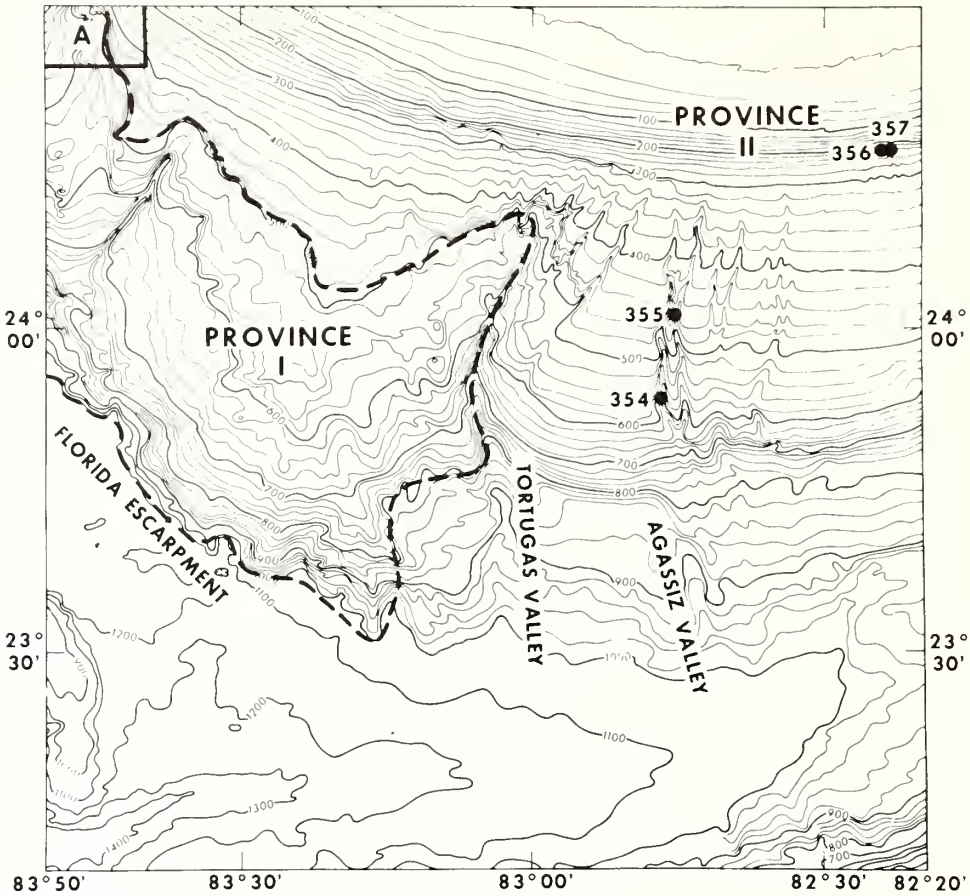

Fig.3. Bathymetric map showing physiographic provinces, position of Florida Escarpment in the study area and location of DSV "Alvin" dive sites. (Block A after Kofoed and Jordan, 1964.)

Seismic data consist of 10 cubic inch (163.9 cm^3) air gun and 3.5 kHz profiles run by NOAA's Atlantic Oceanographic and Meteorological Laboratories (AOML) in October of 1971, sparker profiles (160,000 joules) produced by the U.S. Naval Oceanographic Office from the USNS "Kane" in 1969, and 3.5 kHz profiles from the University of South Florida aboard RV "Eastward" in September of 1971. A total of nearly 1500 km of seismic lines were run (Fig.4).

In conjunction with the seismic work we also made four dives with the deep-sea submersible DSV "Alvin". Two dives were into two of the Agassiz valleys and two were made in the area of bottom undulations west of Pourtales Terrace. During the dives numerous bottom photographs and current meter readings were obtained. Short sediment cores of about 30 cm were recovered from each dive site.

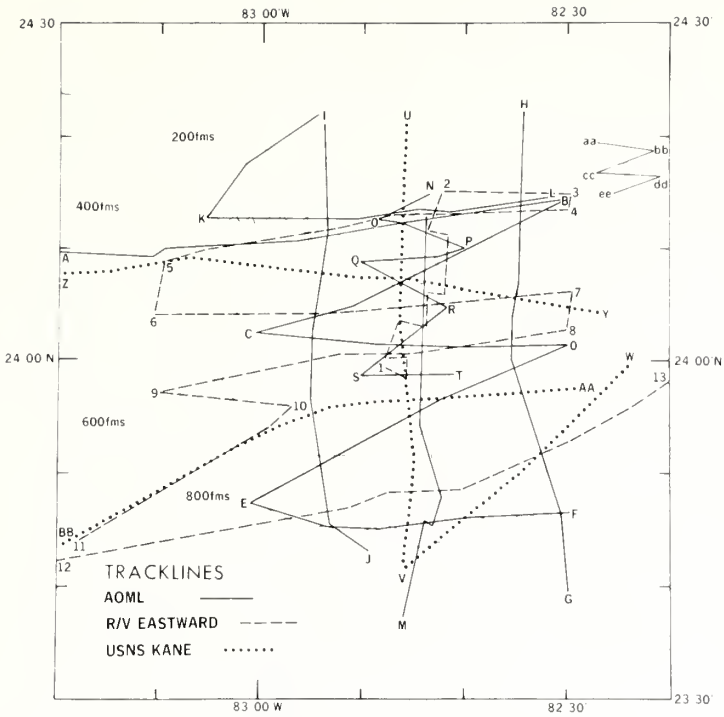

Fig.4. Chart showing position of tracklines used during study.

REGIONAL GEOLOGY

Morphology

The southern Straits of Florida are asymmetrical in cross-section due to the steeper slopes of the Cuban side of the trough. The narrowest portion, between Key West and mainland Cuba, is 154 km wide and the length of the southern Straits from 84°00′W longitude to Cay Sal Bank is approximately 347 km.

Morphological differences between the continental slopes of southern Florida and northern Cuba are readily apparent from previously published bathymetric maps (see Malloy and Hurley, 1970, fig.3). The Cuban slopes exhibit steep escarpments indented by numerous embayments which result in a complex topography. West of 81°17′W there is essentially no continental shelf along the northern coast of Cuba.

The Florida margin reveals a wide continental shelf west of the peninsula and a moderately wide shelf, approximately 62 km, from southern Florida across Florida Bay to the shelf break. Just below the shelf break and paralleling the lower Florida Keys is the Pourtales Terrace, a prominent feature of the southern Straits of Florida. Descriptions of the terrace and its geological setting have been presented by several investigators (Jordan, 1954;

Jordan and Stewart, 1961; Jordan et al., 1964; Malloy and Hurley, 1970; Gomberg, 1973), and will not be discussed here.

The Pourtales Escarpment forms the seaward edge of the Pourtales Terrace, displaying a relief of as much as 150 fathoms (275 m) in places. At the base of the escarpment the bottom flattens and begins a gentle slope toward the axis of the Straits. This gently dipping bottom is interrupted by another scarp, the Mitchell Escarpment, which separates the continental slope from the axis of the southern Straits of Florida.

The Florida Escarpment, which marks the outer limits of the west Florida continental slope, can be traced around the Florida Platform and eastward into the study area (Fig.1). The escarpment decreases in relief and depth to its base as it changes trend from south to southeast on entering the southern Straits. From the published bathymetry it can be seen that the continental slope south of 27°N between about 440 fathoms (805 m) and the base of the Florida Escarpment is of an irregular nature (Jordan and Stewart, 1959; Uchupi, 1966b). Embayments, valleys, isolated hills, and other rugged features are noted by irregular isobaths on the lower continental slope. Similar topography extends part way into the study area and can be seen between 440 fathoms (805 m) and the base of the Florida Escarpment eastward to 83°15′W (Fig.2). The escarpment also terminates at this point.

The axial trough of the southern Straits is a westerly dipping channel. Hurley (1964) has suggested that this gradient is due to sediment moving south and west through the Straits, just opposite the flow of the Florida Current. The existence of ripple marks indicative of southward flow along the bottom has been observed in the northern Straits of Florida (Hurley and Fink, 1963). Neumann and Ball (1970) and Düing and Johnson (1971) confirm these observations in portions of the northern Straits. As will be discussed later, bottom currents were observed at 235 fathoms (430 m) flowing in a westerly direction in the southern Straits during this study. A sediment "fan" entering the Gulf of Mexico from the southern Straits is considered by Hurley (1964) as possibly representing bottom transport by westerly moving currents. Seismic data of Pyle and Antoine (1973) show this "fan" to be a topographic feature with outcrops of reflectors at the edge of the sediment body. They interpret the "fan" as being primarily the result of erosional and not depositional processes.

Structure

Origin of the southern Straits of Florida has been a question for debate among geologists for many years. Agassiz (1888) suggested that the entire Straits of Florida were formed by erosion due to the flow of the Florida Current. Other investigators have ascribed them to graben faulting, subsidence and marginal upbuilding, and non-deposition or erosion coupled with reef growth of upbuilding (Pressler, 1947; Uchupi, 1966a; Antoine and Pyle, 1970). Due to the configuration of the southern Straits, Malloy and Hurley (1970) and Pyle and Antoine (1973) postulated a half-graben theory, with

downfaulting on the Cuban side and a generally smooth rise on the Florida side.

Faulting has been suggested as the probable cause for the Pourtales and Mitchell escarpments (Jordan and Stewart, 1961; Jordan et al., 1964; Uchupi, 1966a). Malloy and Hurley (1970) and Pyle and Antoine (1973) see evidence for faulting along the Mitchell Escarpment but feel that the Pourtales Escarpment may be the result of sediment deposition against the steeper face of an upbuilding reef front. Little work has been completed along the nothern coast of Cuba, however, Khudoley (1967) has shown the probable association of the steep Cuban slopes with some fault zones on the island.

The Florida Escarpment has been considered of fault origin by numerous workers (Jordan, 1951; Greenman and Le Blanc, 1956; Jordan and Stewart, 1959). However, magnetic data of Heirtzler et al. (1966), and Gough (1967) indicate that faulting has not occurred in the basement rocks. Antoine et al. (1967), Uchupi (1967), Uchupi and Emery (1968), and Bryant et al. (1969) believe the escarpment is due to upbuilding of carbonate banks during Cretaceous time along the outer edge of a subsiding continental block.

The topographic irregularities noted above the Florida Escarpment have been considered a result of faulting, lateral folding, and landslide features by Jordan and Stewart (1959) and large-scale, post-Lower Cretaceous erosion by Antoine and Pyle (1970) along the outer edges of upbuilding reefs along the scarp edge. The smoother upper continental slope appears to have formed by sediment upbuilding and outbuilding once the reefs died and subsided (Uchupi, 1967).

LOCAL GEOLOGY

The study area is an area of transition between the Gulf of Mexico and the Florida Straits (Fig.1). Here, too, the Florida continental slope of the southern Straits continually changes its strike from east—west to northwest—southeast as the southwestern edge of the Florida Platform is approached.

For descriptive purposes the bathymetry may be divided into two contrasting sections, the axis and the continental slope of the southern Straits. The axis of the Straits is defined as that area below the continental slope break. East of 83°15′W the boundary is determined by onlapping sediments of the axis of the Straits over the steeper dipping continental-slope sediments (Fig.5D). West of this point the continental slope-axis boundary is delimited by the base of the Florida Escarpment.

Axis of Straits

For the most part the axis of the southern Straits is contoured in 50-fathom (91-m) intervals on Fig.2. East of 83°15′W, or the terminus of the Florida Escarpment, a 10-fathom (18-m) interval was used to a depth of 1000 fathoms (1829 m) so as to better delineate several features of interest, most notably the lower Tortugas and Agassiz valleys. The lower sections of

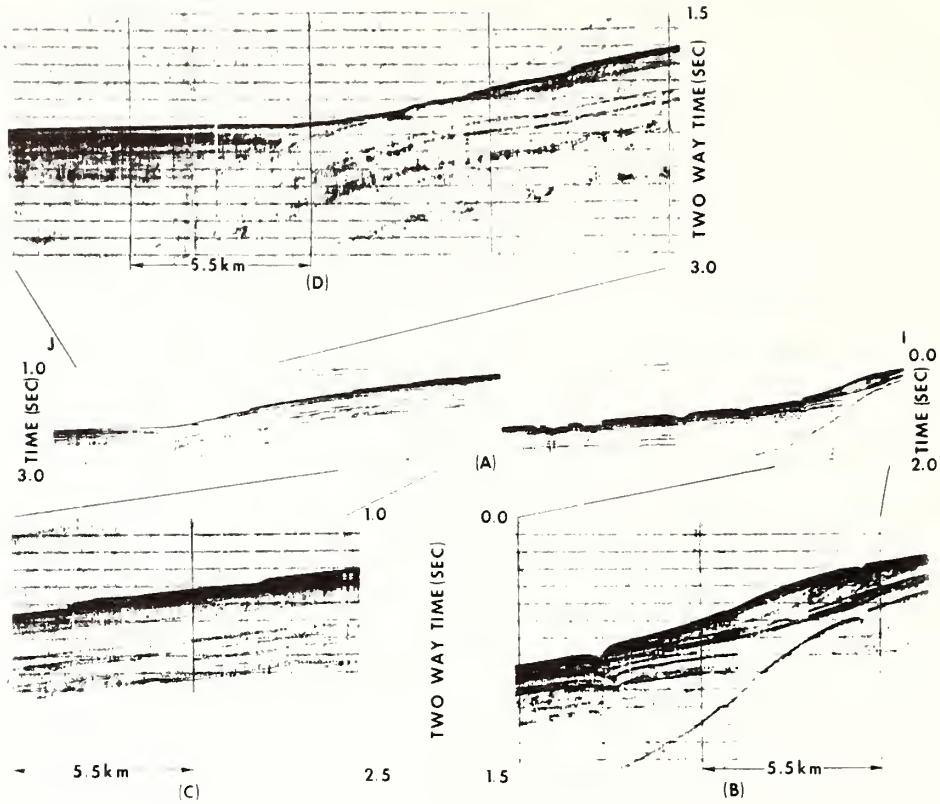

Fig.5. A. Entire line *I-J*. B. Prograding continental shelf above Tortugas Valley showing foreset bedding. The upper escarpment and probable reverse fault structure can be seen at the base of the prograding strata. C. Enlargement of "step-like" features. D. Axis-continental slope boundary east of Tortugas Valley. Distance between horizontal lines is equal to 40 fathoms (73 m).

these valleys are here defined as those portions which exist in the axis of the Straits while the upper valleys are on the continental slope.

The sediments of the axis are younger than those of the outer continental slope as can be seen by Fig.5D. Here the axial sediments butt against the steeper dipping continental slope beds and overlay the continuing sequence of continental-slope deposits. The appearance of the zone of contact here between the slope and axis deposits does not indicate that the axis is receiving sediments from the continental slope. The sharp contact and the flat-lying appearance of the axis beds are more indicative of deposition perpendicular to the continental slope, or in an east—west direction. Bottom current activity, although poorly known in the Straits of Florida, is probably of great importance in shaping the axial as well as the continental-slope deposits.

Continental slope

From bathymetry alone the continental slope in the study area can be divided into two physiographic provinces (Fig.3): (I) the irregular topography from 440 fathoms (805 m) to the base of the Florida Escarpment west of Tortugas Valley; and (II) the remainder of the continental slope in Fig.2.

Province I. The upper Tortugas Valley defines the easternmost extent of this province. Along the valley axis at 880 fathoms (1609 m) the transition from the upper to lower Tortugas Valley coincides with a westward shift of 20 km of the province boundary away from the valley (Fig.3). The boundary, at the 800-fathom (1463-m) isobath at this distance from the lower valley, then turns south and crosses the maximum slope of the area to 1000 fathoms (1829 m) depth. This marks the position considered the termination of the Florida Escarpment.

The continental slope of province I is not as well covered by seismic profiling as is province II. However, the seismic data available in province I reveal a differing configuration of the subsurface continental slope sediments. Line *AA-BB* is most interesting since it provides the best penetration of the subsurface. As can be seen in Fig.6, the surface of the continental slope east of Tortugas Valley (province II) is conformable, to the depth of penetration, with the deeper beds. West of the valley in province I structural deformities can be seen in the subsurface. Irregular bottom features, faulting, and warping of the beds are apparent. A major unnamed valley can be seen near the western edge of province I (Fig.2). The subsurface structure appears to be the controlling factor of the present continental slope morphology in province I.

Province II. The continental slope in province II includes the majority of features under investigation in this study. The Tortugas and Agassiz valley systems and the area of undulations west of Pourtales Terrace are the most pronounced and will be discussed in later sections. Other features of interest in province II are described below.

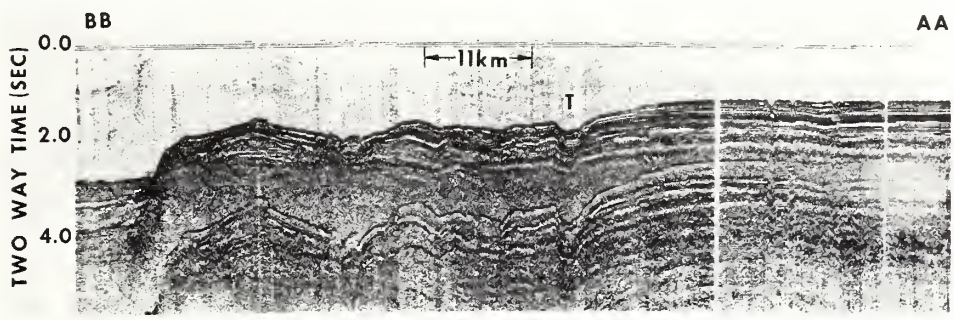

Fig.6. Line *AA-BB* relating province-I-type topography west of Tortugas Valley (*T*) on the left to province-II-type topography east of the valley. 2.0 seconds travel time equals 800 fathoms (1463 m) depth.

The continental-shelf break in the study area occurs at about 40 fathoms (73 m) (Fig.2). The average gradient of the sea floor below the break is 25 m/km or 1.5°. At about 100 fathoms (183 m) the bottom slope increases and at 140 fathoms (256 m) it reaches 3°. The reason for this increase is that progradation of material from the shelf has resulted in an outbuilding of the shelf edge which can be clearly seen in seismic profiles (Figs.5B, 7). Deposition of this nature has been noted in the Florida Straits and around the Florida Platform (Uchupi, 1966a; Rona and Clay, 1966; Uchupi and Emery, 1968; Bryant et al., 1969; Malloy and Hurley, 1970). Uchupi and Emery (1967) have also noted this pattern on the Atlantic continental margin.

Seismic profiles reveal a prograding sequence exhibiting foreset and bottomset beds. Jordan and Stewart (1961) have postulated that great amounts of sediment are being transported from Florida Bay and the west coast of Florida onto the continental slope west of the Marquesas Keys, enough to account for the smooth slopes from 25 (46 m) to 300 fathoms (549 m). Milligan (1962) has suggested that some sediment is also being introduced from the Gulf of Mexico by the Florida Current. The smoothness of the upper continental slope may be the result of the Florida Current touching bottom at this depth as described by Jordan et al. (1964). D. N. Gomberg (personal communication, 1974) has concluded that the Florida Current is active in an easterly flowing direction, at times, to a depth of at least 120 fathoms (200 m).

Below the prograding sequence of the upper continental slope, the sea floor east of Tortugas Valley is remarkably flat with slopes of less than 1° to a depth of about 540 fathoms (988 m). No discontinuities of the continental slope can be detected other than the valleys. At 540 fathoms (988 m) the gradient of the continental slope progressively increases until the slope break is reached. The maximum gradient noted is 4° near the base of the continental slope on both sides of the Agassiz valley system (Fig.2). Between the Tortugas and Agassiz valleys the slope break occurs at 850 fathoms (1554 m). East of the Agassiz valleys the break has decreased in depth to 780 fathoms (1426 m).

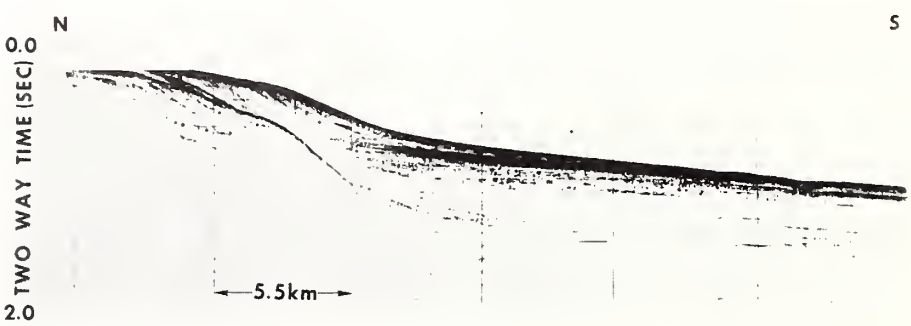

Fig.7. Prograding shelf sequence above Agassiz valleys along line *H-G*. Note absence of upper escarpment at this position. Depth between horizontal lines equals 40 fathoms (73 m).

Coincident with the increase in slope at 540 fathoms (988 m) between the two valley systems, a series of step-like features are observed on sub-bottom profiles *I-J* and *D-E* (Figs.5C, 8). A series of at least five and possibly six steps can be detected on the continental slope. The relief of the steps is relatively constant, on the order of 10—12 fathoms (18—22 m), and four of them can be tentatively correlated across the area by their depth from differing profiles.

The origin of these step-like features is probably related to the increased slope just above the shallowest step. The beds beneath the steps appear to be continuous on the seismic records, therefore faulting is ruled out. It is possible that, as the Florida slope subsided, the outer continental slope subsided more rapidly, creating zones of weakness in the upper strata. These weaker zones may then have slumped along their lineations, thus producing the "steps".

PROMINENT FEATURES

Three prominent areas in the study region constitute the principal objectives of the study: (1) The Tortugas valley system; (2) the Agassiz valley system; and (3) the area of bottom undulations near the western end of Pourtales Terrace. The primary object of the study was to investigate the morphology of these features and to attempt to understand their formation and the dynamic processes presently associated with these features.

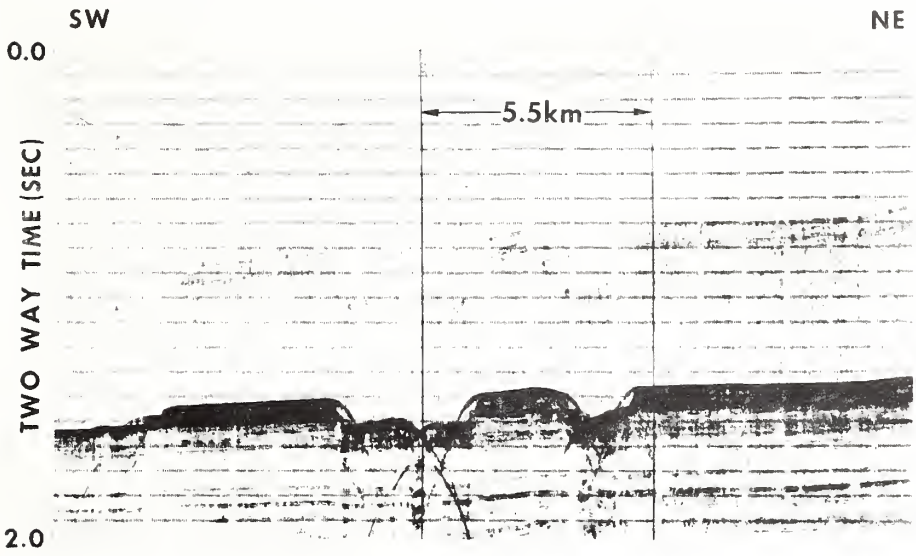

Fig.8. The two westernmost valleys along line *D-E*. Note apparent slumping in valley on right and possible secondary channel in the valley at left. Farther to southwest are additional "step-like" features. Vertical distance between horizontal lines is 40 fathoms (73 m).

Tortugas valley system

The Tortugas valley system is composed of the major Tortugas Valley and at least nine tributary valleys (Fig.2). Two local escarpments, one at 280 fathoms (512 m) and the other at about 440 fathoms (805 m), are major features within the system. The visible length of the entire Tortugas system is about 93 km, slightly more than half of that distance being on the continental slope.

Tributary Valleys. The Tortugas tributary valleys appear to be governed by the two escarpments. The narrow, steep-walled tributary valleys originate at the base of the upper escarpment at a depth of 310 fathoms (567 m) (Fig.2). From this locality the valleys run courses which are perpendicular to the regional slope. With the exception of the easternmost valley, which apparently does not enter the Tortugas head, the tributary courses are generally difficult to define once they pass seaward of the lower escarpment. Jordan and Stewart (1961) consider the easternmost valley to be younger than the Tortugas Valley because of its alignment with the maximum slope of the surface beds, which they believe postdate the formation of the Tortugas Valley.

Bathymetry reveals that the tributary valleys change their morphological characteristics as they transgress downslope (Fig.2). Near the base of the upper escarpment the tributaries are relatively shallow topographical expressions, but as they progress downslope toward the Tortugas Valley head, the width/depth ratio decreases rapidly. Near the lower scarp the valleys show near vertical walls with narrow widths. These deep channels dissipate as the lower scarp is crossed.

The Tortugas tributary valleys show evidence that they have maintained their position on the continental slope while the walls have been built up (Fig.9). The situation may possibly be much like that described off Cape Hatteras where Rona (1970) suggests that the intercanyon areas and valley walls are being deposited while currents act to keep the channels open. Some of the tributary valleys can be seen to possess fill while others are relatively clean. This implies that sweeping of the valleys is intermittent, or perhaps that some of the valleys are inactive now and are being filled.

Escarpments. The two escarpments in the Tortugas valley system, as mentioned above, define the limits of the Tortugas tributary valleys. Along lines *I-J* and *U-V* (Figs.5B, 10) the upper escarpment is visible at a depth of about 280 fathoms (512 m). This escarpment can be seen in Fig.2 and has a maximum relief of 30 fathoms (55 m). Line *I-J* (Fig.5B) provides the only evidence as to the possible origin of the scarp. This profile reveals that reverse faulting may have occurred with the bottomset beds of the prograding sequence overriding the seaward sediments at depth.

The lower escarpment, which begins at about 440 fathoms (805 m), is considered here to define the northern limits of the Tortugas Valley since the

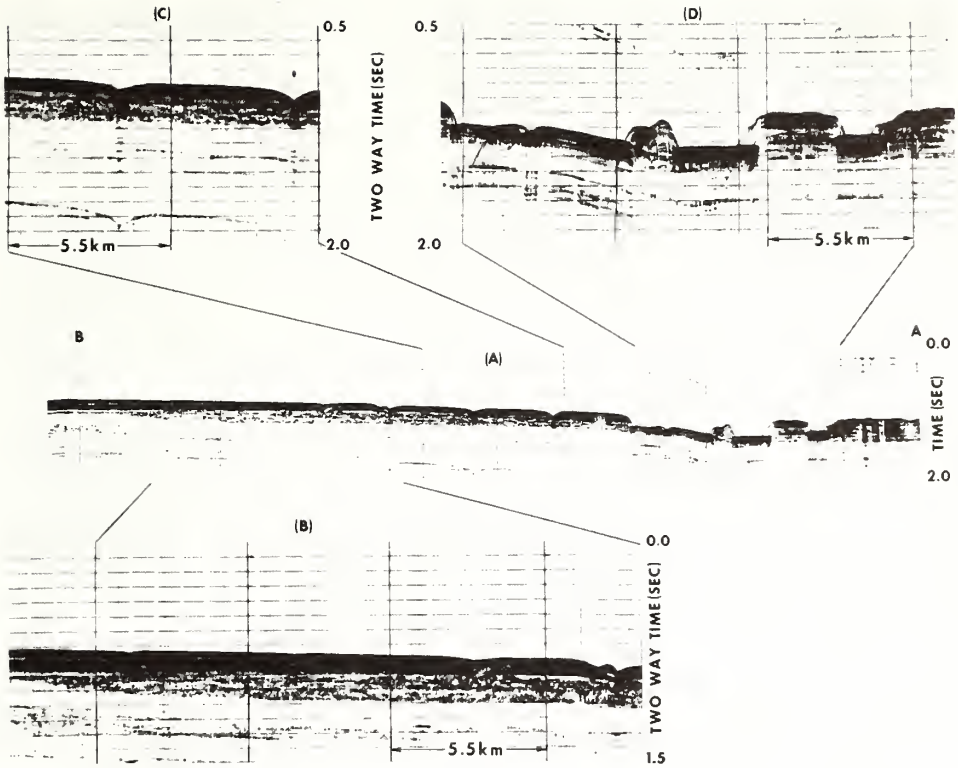

Fig.9. A. Complete line *A-B*. B. Section showing buried Agassiz valleys and upper escarpment at extreme right. C. Tortugas tributary valleys below upper escarpment. Note the building up of the channel walls and intercanyon areas while valleys have maintained their position. The same process can be observed in the subsurface along section B. D. Section across upper head of Tortugas Valley. The large valley at right is not delineated well by bathymetry. A buried valley can be seen to the right of this valley. 40 fathoms (73 m) between horizontal lines.

main valley cannot be traced shoreward of the scarp's position. Relief along the lower escarpment varies from 90 fathoms (165 m) near the west end to 40 fathoms (73 m) at the eastern end (Fig.2).

The depth and shape of the lower escarpment suggest a relationship associated with both the Florida Escarpment and the Tortugas Valley. The depth at which the lower escarpment originates is the upper limit of province-I-type topography. Additional scarps can be seen to the west of this escarpment at the same depth (Fig.2). The shape of the escarpment around the head of Tortugas Valley implies a genetic relation to the valley head. Two possible explanations of origin can be deduced from this information:(1) the scarp represents the eastern upper end of province-I-type topography; or (2) the scarp has been formed around the Tortugas Valley head. Seismic profiles reveal no evidence of fault origin for this escarpment.

It has already been shown that the Tortugas Valley marks the eastern end

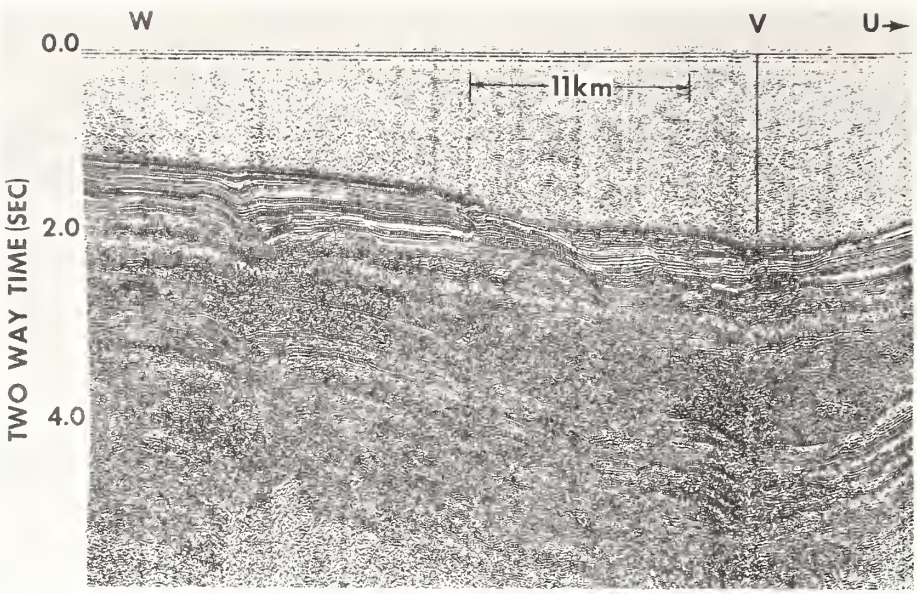

Fig.10. Seismic record along line *U-V-W*. Note blocky material on the surface to left of point *V*. This material is considered to be a slump mass derived from the continental shelf toward point *W*. 2.0 sec. travel time corresponds to 800 fathoms (1463 m) depth.

of province-I-type topography. That the escarpment transgresses into province-II-type topography argues against it being a result of upper province-I irregularities. Also, since the escarpment forms an approximate semi-circle around the Tortugas Valley head, it is felt that the second explanation is more plausible.

It is probable that this scarp was initiated as a slump scar by slow creep of the continental slope sediments into the head of Tortugas Valley. The tributary valleys are younger than the scarp and continental slope, as evidenced by their perpendicularity to both the maximum slope of the continental slope above the escarpment and the escarpment itself. Most of the tributary valleys never cut deep enough into the continental slope to reach the base of the escarpment and, therefore, appear to terminate at the escarpment.

Tortugas Valley. Tortugas Valley originates in what appears to be a pseudo bowl-like area bordered by the steep escarpment at 440 fathoms (805 m) to the north. Below the escarpment gently dipping beds converge to form a steep V-shaped trough with a minimum relief of 40 fathoms (73 m) from the top of the valley walls. The average gradient of the valley is 13 m/km (Jordan and Stewart, 1961). In contrast to the tributary valleys, the major valley broadens downslope. This broadening is accompanied by a gentle curve to the east. Along this curving section the walls of the valley are relatively steep. At a depth of 880 fathoms (1609 m) there is a rapid decrease in wall height which corresponds to the transgression of the valley from off the continental slope

into the axis of the Straits. The lower Tortugas Valley can be seen to be wider and shallower than the upper valley (Fig.2), perhaps due to a difference in sediment characteristics between the continental slope and axis as suggested by the continental slope-axis boundary (Fig.5D).

Profiles crossing the upper part of Tortugas Valley reveal several changes taking place in a downslope direction (Figs.6, 11). The channel becomes wider and deeper with depth. Along lines *AA-BB* and *10-11* (Figs.6, 11C) the bottom of the channel can initially be seen without sidewall reflection interference. From these profiles it appears that faulting and slumping are important factors in the present morphology of the valley. Profile *AA-BB*

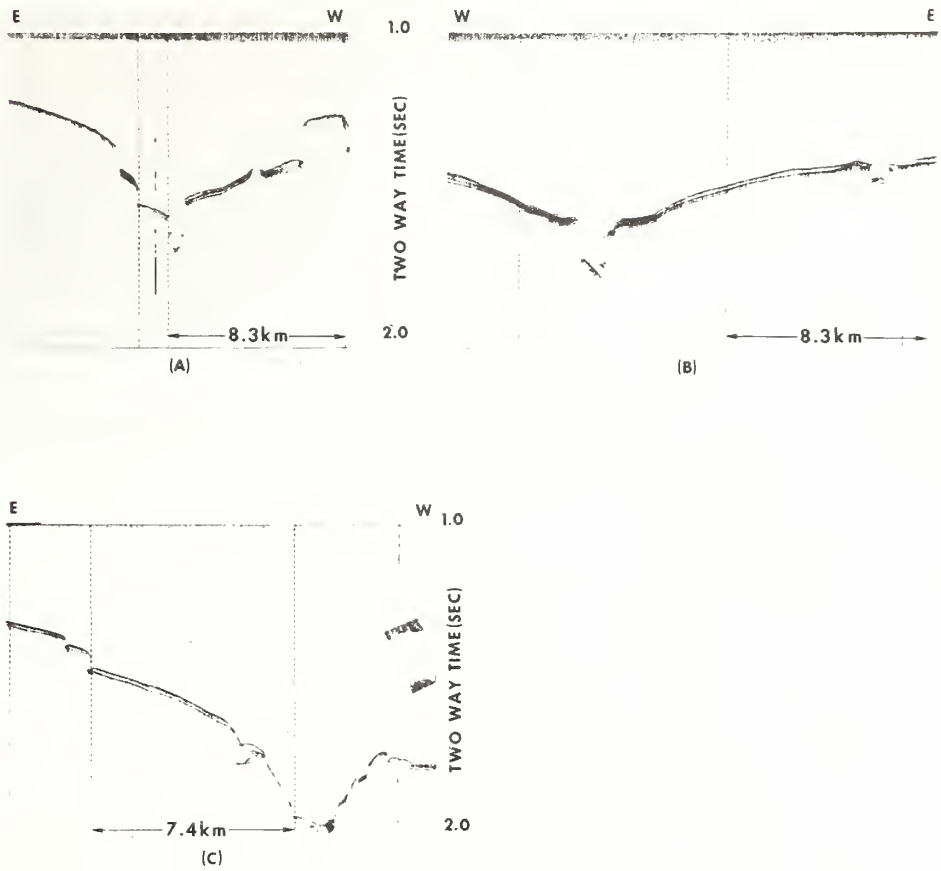

Fig.11. 3.5 kHz profiles across Tortugas Valley showing changing characteristics of the valley downslope. A. Portion of line *8-9*. Valley walls are very steep. An unidentified valley exhibiting natural levees can be seen west of the main channel. B. Crossing of Tortugas Valley along line *9-10*. Valley is wider than in A. The easternmost tributary valley can be seen east of the main valley. C. Tortugas Valley along line *10-11*. "Step-like" features can be seen on the eastern side. Notice apparent slumping along valley walls and orientation of bedding planes in the axis suggesting mass movement. 2.0 sec. travel time equals 800 fathoms (1463 m) depth.

(Fig.6) appears to show faulting along both sides of the valley in the subsurface. Line *10-11* (Fig.11C) shows evidence of fault blocks on the surface as well as slump features along the western side of the channel bottom and the eastern channel wall.

The origin of the Tortugas valley system is considered to be related to its position in respect to the Florida Escarpment. The escarpment can be traced no farther eastward than 83°15′W. The typical irregular topography above the Florida Escarpment, physiographic province I (Fig.3), can be seen to extend eastward to the upper Tortugas Valley. As seen from Fig.6, the deformed sediments west of the valley are in marked contrast to the conformable units to the east. It is probable that this transition line may then have been a zone of weakness, thus a likely place for the valley to form.

Agassiz valleys system

The Agassiz valleys, as a system, consist of at least ten north—south trending valleys on the Florida continental slope and a lower main valley which exists in the axis of the Straits (Fig.2). The lineal extent of the system, about 95 km, closely approximates that of the Tortugas valley system.

In addition to the bathymetric and seismic profiling work in the area, two dives (numbers 354 and 355) in the submersible DSV "Alvin" were undertaken in the two westernmost valleys of the Agassiz system (Fig.3). Each dive lasted about 6 hours

As Jordan and Stewart (1961) noted, the Agassiz valleys do not have the dendritic pattern of the Tortugas system but maintain nearly parallel trends throughout most of their length. However, at least three pairs of the valleys do appear to merge to form single channels. The two easternmost valleys merge at 490 fathoms (896 m), the westernmost two valleys merge at about 640 fathoms (1170 m), and the two valleys just east of these also unite at 490 fathoms (896 m) (Fig.2).

The escarpment which coincides with the heads of the Tortugas tributary valleys does not extend eastward to the Agassiz valleys although both systems seem to originate at about the same isobath (290 fathoms; 530 m). Seismic profile *A-B* (Fig.9B) reveals that the heads of the Agassiz valleys are being filled in at this depth. A profile downslope, *D-E*, shows the changing patterns of the valley morphology (Fig.8). All of the valleys tend to increase in relief downslope to the 520-fathom (951-m) isobath. Below this depth only three valleys remain visible (Fig.2). The three valleys continue their increasing relief to 650 fathoms (1189 m) where they terminate abruptly.

South of the Agassiz valleys and below 640 fathoms (1170 m), isobaths are generally irregular and not consistent with the surrounding submarine topography (Fig.2). Profile *V-W* (Fig.10) suggests a possible explanation. Between point *V* and 780 fathoms (1426 m), or 1.95 sec., the surface of the axis deposits is not smooth and continuous but displays a disorderly structure. At 780 fathoms (1426 m), or 1.95 sec. in Fig.10, the smooth dipping continental-slope beds are seen emerging from beneath the sediment fill. It

appears that this zone of irregular topography and substrate may be a localized slump mass, having initiated on the continental slope and transgressed out onto the axis of the Florida Straits. Initiation of such a slump would account for the sudden termination of the valleys at 650 fathoms (1189 m). Another valley heading at 600 fathoms (1097 m) between the two "slump" terminated valleys continues its path farther downslope than the 650-fathom (1189-m) contour. The fact that this valley has a wide, rounded head and a different appearance than the other valleys suggests that it is anomalous to the other valleys. It may be a younger feature formed after the slumping occurred.

The lower Agassiz Valley begins at a depth of 850 fathoms (1554 m) and crosses the axis to a depth of 990 fathoms (1810 m) (Fig.2). The width and axial gradient of this valley are very similar to those of the lower Tortugas Valley, and it seems reasonable to assume that the relationship of the lower valley to the upper valleys of each system is similar; they are the axial transgressions of the valleys which cross the continental slope. The relationship between the lower Tortugas Valley and the upper valley system is obvious from Fig.2, but the lower Agassiz Valley has no such tie.

A solution to this anomaly can be presented if we conclude that the two westernmost valleys of the Agassiz valley system were terminated by a local slump at 650 fathoms (1189 m). Upslope projection of the lower Agassiz Valley is found to coincide with the downslope projection of the two western valleys (Fig.2). It would seem justifiable to presume that these two upper valleys merged and were connected to the lower Agassiz Valley prior to the slumping which obliterated all evidence of the one time valley connections between 650 (1189 m) and 850 fathoms (1554 m).

Two dives with DSV "Alvin" reveal some of the differences in bottom morphology at various locations along the two westernmost Agassiz valleys. Dive 355 reached bottom at 477 fathoms (873 m) in the second valley from the west (Fig.3). Observers described the area as a gently undulating bottom, not anything like a valley, and having the appearance of a field blanketed in snow. Fine gray carbonate mud, silty-clay, makes up the bulk of the sediment, the remainder being mostly pelagic foraminifers, pteropod fragments, ostracods, and some sponge spicules. The bottom is relatively flat with no indications of scour marks or striations, suggesting that currents are playing a very minor role in transporting sediments along the bottom at this location. A number of pits of burrowing organisms and tracks, probably those of crabs, also appear undisturbed in the fine bottom deposits. No rock outcrops were seen in the area. The sea floor adjacent to the valley had an appearance similar to the axis.

Dive 354 reached the bottom at 607 fathoms (1110 m) in the axis of the westernmost valley (Fig.3). The bottom morphology differed from that of dive 355 in many respects. Slabs of chalky limestone, too friable to sample, were found in the canyon axis, as were boulders of hard rock 2—3 m in diameter. A small ridge could be seen extending across the valley axis. At the ridge crest a semi-consolidated brownish gray rock protruded through the mud cover of the valley floor.

The walls of the valley at this location were 55 fathoms (100 m) above the valley floor. The upper portions were vertical rock, too hard to be sampled, which appeared to be coralline. The lower halves of the walls had slopes of 20°—30°. Distinct contacts could be noted where the walls began to appear V-shaped, indicating a possible strata change at this level. However, observers felt that the cause of this contact may have been due to sedimentation and talus accumulation from above.

The vertical walls trend in a north—south direction and have the appearance of being fault or joint controlled due to their straight alignment. Observers aboard "Alvin" believed that jointing could be seen in the limestone walls. Subsequent inspection of seismic line *D-E* (Fig.8), which crosses the valley near the position of dive 354, and other profiles over the Agassiz valleys reveal no indication of faulting, although slumping is recognizable on the records.

Dive 354 revealed some channel axis characteristics similar to dive 355. Bottom conditions appeared to be depositional rather than erosional. Again photographs supported the suggestion that the valleys are filling as no scour marks or striations could be detected. Observers aboard "Alvin" noted material being introduced into the valley axis over the edge of the walls. This movement of sediment outside the valleys, although of unknown velocity and direction, is indicative of bottom currents which are probably aiding in shaping the general sedimentation pattern of the entire study area. This is also a direct observation of one method of valley fill in addition to fallout of fine material in suspension and tests of organisms.

Dives 355 and 354 provided short-term current measurements that aid in the interpretation of sediment transport within the valleys. Three bottom current readings were taken on dive 355 with values ranging from 0—9.2 cm/sec. (0.18 knots). The current flow was always to the south in the valleys. Dive 354 made one current meter reading of 2.5 cm/sec. (0.05 knots) downcanyon. These readings, together with the photographs, indicate little transport within the valleys.

Sediments of dive 354 at 607 fathoms (1110 m) recovered by the "Alvin" corer were slightly different than those farther upslope on dive 355. The deeper sediments contained a greater amount of pelagic foraminifers than those farther upslope. This should be expected as the carbonate muds, some of which originate from shore, decrease in a seaward direction and the fallout of foraminifers becomes a more important source of sediments.

Local slumping has probably played an important role in the introduction of sediments into the valleys at the position of dive 354. The large blocks of limestone and boulders described by divers aboard "Alvin" are probably part of the walls which have broken off along jointing planes. That these features are being covered by fine sediments suggests that the current meter readings, although of only short duration, are representative of current activity in the valleys today. However, short-term current readings must be regarded with skepticism as the valleys may be periodically scoured or filled.

The Agassiz valleys, between 320 (585 m) and 450 fathoms (823 m), show

the same evidence of maintaining their position on the continental slope while the walls and intercanyon areas have built up as the Tortugas tributary valleys. The aforementioned suggestion by Rona (1970) is concluded to be the same for both systems. This pattern can be seen in the Agassiz valleys in the subsurface of line *A-B* (Fig.9B) although the channels are now being filled by flat-lying sediments derived from progradation of the shelf edge.

Although firm conclusions as to the origin of Agassiz valleys cannot be made at this time, the best evidence is probably provided by observers aboard the submersible DSV "Alvin". They noted jointing patterns in the walls of the valley on dive 354 and it is possible that these jointing planes produced zones of weakness in the rock which were later eroded to form the valleys. Their straight alignment along the continental slope is suggestive of some type of structural control.

Undulation area

An area of slight undulations located at the western end of Pourtales Terrace, 24°16′N and 82°23′W (Fig.2) has been investigated by Jordan and Stewart (1961) and Jordan et al. (1964). Both works have described the morphology of the features, noting that they are asymmetrical in cross-section with the steep sides facing east. The crest to crest length varies from 900 m to 1150 m and the crest to trough depths range from 7 (13 m) to 15 (27 m) fathoms. Like the valley systems, the undulations trend parallel to the regional slope.

Jordan and Stewart (1961) considered these features to be step faults associated with faulting on the southern edge of the Pourtales Terrace. Jordan et al. (1964) see no evidence in seismic profiles to support the fault hypothesis nor do we. They suggest that the undulations are giant sand waves created by an easterly flowing bottom current associated with the swift-moving surface flow of the Florida Current. Their evidence can be seen in their fig.16. This figure shows a westerly thickening of unconsolidated bottom sediments at the western edge of the Pourtales Terrace indicating that an eastward setting current has been active in sediment transport over this end of the terrace.

Seismic profiles and the results of two dives (numbers 356 and 357; Fig.3) by DSV "Alvin" were used in an attempt to determine what processes are active in the area today. Profile *aa-bb* was run in an approximate west to east direction (Fig.4). A strong reflector below the surface strata is apparently the western extension of the Pourtales Terrace buried beneath a westerly thickening overburden (Fig.12). Line *bb-cc* was run nearly perpendicular to the undulations (Fig.4). Again westerly sediment thickening can be seen above a strong basement reflector (Fig.12), supporting Jordan et al.'s (1964) contention that an easterly flowing current was responsible for covering the western end of the Pourtales Terrace.

A total of seven current measurements were taken on dives 356 and 357 in this area. The range of values was 9.2 cm/sec. (0.18 knots) to 23.4 cm/sec.

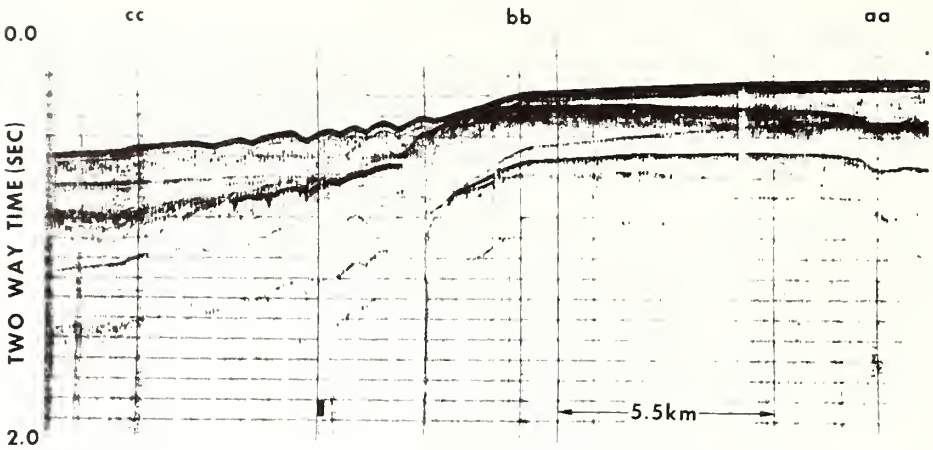

Fig.12. Lines *aa-bb* and *bb-cc*. A strong reflector 0.1 to 0.2 sec. below surface along *aa-bb* is probably the buried western end of Pourtales Terrace. Sediment thickening is to west. Undulations west of Pourtales Terrace seen in cross-section along *bb-cc*. Strong reflector can be seen 0.2 to 0.3 sec. below undulations. Features appear erosional. Vertical distance between horizontal lines equals 40 fathoms (73 m) depth.

(0.43 knots) all in a westerly direction with one exception, an 11.4 cm/sec. (0.24 knots) flow to the south in the trough of one undulation. The depth of both dives was approximately 235 fathoms (430 m). The observations of D. N. Gomberg (personal communication, 1974) and the results of these current measurements indicate that bottom flow reverses somewhere between 120 (200 m) and 235 fathoms (430 m). From seismic data it would appear that the prominent direction of flow is, or has been in the past, toward the east over the entire depth range (Fig.12). This information suggests that bottom currents do reverse at times in the southern Straits. The depth range over which these currents reverse cannot be defined by present data, but is most likely greater than the aforementioned range. No attempt at relating southerly flow in the northern Straits and westerly flow in the southern Straits has been attempted from these measurements.

The southerly flowing current measurement leaves open the possibility that these undulations are valley or erosional features. Although easterly flowing currents are responsible for covering the western end of Pourtales Terrace it does not appear that these features are sand waves as suggested by Jordan et al. (1964). From Fig.12 it can be seen that the axes of the undulations are considerably lower than the depth of the surrounding continental slope. The crests are a little, if any, higher than the local topography. Farther downslope seismic profiles show them to be lower. For these reasons it seems unacceptable to conclude that the features are depositional in origin. The fact that they incise the prograding sediment mass is evidence of their youth relative to the Tortugas and Agassiz valleys. Submersible pictures and observers' reports indicate that this area is one of present deposition.

Evidence is not conclusive as to their origin and more data, especially concerning currents, need to be gathered before further speculation is warranted.

The sediments obtained from dives 356 and 357 differed from those of 354 and 355 in particle size and content. Sediments of the undulation area are coarser than those in the valleys, as would be expected if they were being derived mainly from shoreward sources. Sponge spicules are more abundant and diverse as well as mollusc fragments and bits of coral. Foraminifera and pteropod fragments are still abundant but are of less proportion to the sand-size fraction of the sediments than in the deeper water samples.

CONCLUSIONS

The area of investigation is one of transition from a relatively narrow strait to a deep ocean basin. The new bathymetric map (Fig.2) and seismic profiles reveal the relationship between and the possible origin of several morphologic features. Of primary interest are the Tortugas and Agassiz valley systems. The Tortugas tributary valleys and the Agassiz valleys are aligned with the maximum slope and may have formed contemporaneously.

The southern Florida continental-shelf edge has been built out and upward resulting in the filling of the head of the Agassiz valleys shoreward of 290 fathoms (530 m). The Tortugas tributary valleys originate at the base of an apparent fault-controlled escarpment at the base of the prograding material from the shelf edge. Undulations incising this prograding sequence are believed to be erosional in origin.

The Florida Escarpment has been shown to be associated with a unique morphology between approximately 440 fathoms (805 m) to its base from 27°N to its termination at 83°15′W longitude. Above this depth the continental slope is generally smooth with few irregularities.

Bottom currents are probably playing a large role in the shaping of the continental slope and axial sediments. Bottom currents between 120 (220 m) and 235 fathoms (430 m) apparently reverse at times and it is probable that this depth interval may be greater. Over-all, the study area is considered to be one of deposition, although some erosional processes, mainly slumping, appear to have been important in the formation of a number of features. Some valleys may also have intermittent scour. The full extent to which erosional processes are active today require additional study.

ACKNOWLEDGEMENTS

The writers acknowledge with many thanks the officers and crews of the RV "Lulu", RV "Gosnold", RV "Eastward" and DSV "Alvin" for their most valuable assistance. Support in the field operations by George Lapiene and Douglas Lambert (AOML); F. Kelly (RV "Eastward"); D. Wallace, V. Maynard, R. Clingan, J. McCarthy and P. Jones (USF); A. Ekdale, E. McHuron and J. McCrevey (Rice); and G. Griffin (University of Florida) are gratefully acknowledged. Funds for the AOML field operation were provided by the

NOAA, Manned Undersea Science and Technology Office. RV "Eastward" time was made available to the University of South Florida by NSF through the Oceanographic Program of the Duke University Marine Laboratory.

REFERENCES

Agassiz, A., 1888. Three Cruises of the Blake. Houghton, Mifflin, New York, N.Y., 314 pp.

Antoine, J., Bryant, W. R. and Jones, B., 1967. Structural features of continental shelf, slope, and scarp, northeastern Gulf of Mexico. Bull. Am. Assoc. Petrol. Geologists, 51:257—262.

Antoine, J. W. and Pyle, T. E., 1970. Crustal studies in the Gulf of Mexico. Tectonophysics, 10:477—494.

Bryant, W. R., Meyerhoff, A. A., Brown, N. K., Furrer, M. A., Pyle, T. E. and Antoine, J. W., 1969. Escarpments, reef trends, and diapiric structures, eastern Gulf of Mexico. Bull. Am. Assoc. Petrol. Geologists, 53:2506—2542.

Düing, W. and Johnson, D., 1971. Southward flow under the Florida current. Science, 173:428—430.

Gomberg, D. N., 1973. Drowning of the Floridian Platform margin and formation of a condensed sedimentary sequence. Geol. Soc. Am. Bull., Abstr. Progr., p.640.

Gough, D. I., 1967. Magnetic anomalies and crustal structure in eastern Gulf of Mexico. Bull. Am. Assoc. Petrol. Geologists, 51:200—211.

Greenman, N. N. and Le Blanc, R. J., 1956. Recent marine sediments and environments of northwest Gulf of Mexico. Bull. Am. Assoc. Petrol. Geologists, 40:813—847.

Heirtzler, J. R., Burckle, L. H. and Peter, G., 1966. Magnetic anomalies in the Gulf of Mexico. J. Geophys. Res., 71:519—526.

Hurley, R. J., 1964. Bathymetry of the Straits of Florida and the Bahama Islands, Southern Straits of Florida. Bull. Mar. Sci. Gulf Carib., 14:373—380.

Hurley, R. J. and Fink, L. K., 1963. Ripple marks show that countercurrent exists in Florida Straits. Science, 139:603—605.

Jordan, G. F., 1951. Continental slope off Apalachicola River, Florida. Bull. Am. Assoc. Petrol. Geologists, 35:1878—1933.

Jordan, G. F., 1954. Large sinkholes in Straits of Florida. Bull. Am. Assoc. Petrol. Geologists, 38:1810—1817.

Jordan, G. F., 1962. Submarine physiography of the U.S. continental margins. U.S. Dept. Comm. Tech. Bull., 18:28 pp.

Jordan, G. F. and Stewart, H. B., 1959. Continental slope off southwest Florida. Bull. Am. Assoc. Petrol. Geologists, 43:974—991.

Jordan, G. F. and Stewart, H. B., 1961. Submarine topography of the western Straits of Florida. Geol. Soc. Am. Bull., 72:1051—1058.

Jordan, G. F., Malloy, R. J. and Kofoed, J. W., 1964. Bathymetry and geology of Pourtales Terrace, Florida. Mar. Geol., 1:259—287.

Khudoley, K. M., 1967. Principal features of Cuban geology. Bull. Am. Assoc. Petrol. Geologists, 51:668—677.

Kofoed, J. W. and Jordan, G. F., 1964. Isolated fault scarps on the continental slope off southwest Florida. Southeastern Geol., 5:69—77.

Malloy, R. J. and Hurley, R. J., 1970. Geomorphology and geologic structure: Straits of Florida. Geol. Soc. Am. Bull., 81:1947—1972.

Milligan, D. B., 1962. Marine Geology of the Florida Straits. Thesis, Florida State Univ., Tallahassee, Florida, 120 pp.

Neumann, A. C. and Ball, M. M., 1970. Submersible observations in the Straits of Florida: geology and bottom currents. Geol. Soc. Am. Bull., 81:2861—2874.

Pressler, E. D., 1947. Geology and occurrence of oil in Florida. Bull. Am. Assoc. Petrol. Geologists, 31:1851—1862.

Pyle, T. E. and Antoine, J. W., 1973. Structure of the west Florida Platform, Gulf of Mexico. Texas A and M Univ., Tech. Rept., 73-7-T: 168 pp.

Rona, P. A., 1970. Submarine canyon origin on upper continental slope off Cape Hatteras. J. Geol., 78:141—152.

Rona, P. A. and Clay, C. S., 1966. Continuous seismic profiles of the continental terrace off southeast Florida. Geol. Soc. Am. Bull., 77:31—44.

Uchupi, E., 1966a. Shallow structure of the Straits of Florida. Science, 153:529—531.

Uchupi, E., 1966b. Map showing relation of land and submarine topography DeSoto Canyon to Great Bahama Bank. U.S. Geol. Surv., Misc. Geol. Inv. Map I-475, 1 sheet.

Uchupi, E., 1967. Bathymetry of the Gulf of Mexico. Trans. Gulf Coast Assoc. Geol. Soc., 17:161—172.

Uchupi, E. and Emery, K. O., 1967. Structure of continental margin off Atlantic coast of United States. Bull. Am. Assoc. Petrol. Geologists, 51:223—234.

Uchupi, E. and Emery, K. O., 1968. Structure of continental margin off Gulf coast of United States. Bull. Am. Assoc. Petrol. Geologists, 52:1162—1193.

Reprinted from: *Florida Scientist 38*, Supplement 1, 13-14.

Substrate Mapping by Sidescan Sonar R.W. PENMENTER, W.L. Stubblefield, D.J.P. Swift, Atlantic Oceanographic & Meteorological Laboratories, Marine Geology & Geophysics Laboratory, 15 Rickenbacker Causeway, Miami, Florida 33149.

--Sonographs (sidescan sonar records) of the continental shelf floor off New York were used to determine the texture of bottom sediment. Nine sites in the New York Bight apex each approximately 150 by 300 m, were selected for study. The sites picked were either characteristic of important bottom sediment types, or straddled facies boundaries. Sonographs were made of each study area and grab samples collected every 15 m along a transect down the center of each area. Raydist navigation was used. Comparison of sonographs and grab sample data indicates that in some cases, changes in bottom texture finer than the standard Wentworth size classes may be resolved on the sonograph as variations in the intensity and character of the record. In areas where texture changes abruptly, the facies boundary is readily discernable on the sonograph. Such sidescan sonar records calibrated by grab samples are efficient tools for quickly mapping bottom sediment textures over large areas of the sea floor.

Reprinted from: *Geotechnique 25*, No. 2, 229-238.

Differential piezometer probe for an in situ measurement of sea-floor pore-pressure

A. F. RICHARDS*, K. ØIEN†, G. H. KELLER‡ and J. Y. LAI§

A telemetering differential piezometer was designed and constructed at the Norwegian Geotechnical Institute to measure a minimum differential pressure (pore-pressure referenced to hydrostatic pressure) of 34 kPa and a maximum pressure of 294 kPa in water depths of up to 500 m. An emplacement system was built at the University of Illinois. One successful in situ test in the Wilkinson Basin, in a water depth of 274 m, yielded a maximum excess pore-pressure of 59 kPa after the probe was driven about 3·2 m into the silty-clay bottom. An excess pore-pressure of 9·8 kPa was measured 5–10 h after emplacement of the probe. Implications of excess pore-pressures cyclically generated by storm and internal wave loading of sea-floor soils is discussed. It is concluded that a better understanding of submarine slope stability through the use of the effective stress principle should now be possible by measuring pore-pressure in situ.

Un télémètre/piézomètre différentiel fut projeté et construit à l'institut Géotechnique Norvégien, afin de mesurer une pression différentielle minimum (pression interstitielle se rapportant à la pression hydrostatique) de 34 kPa et une pression maximum de 294 kPa dans des profondeurs d'eau atteignants jusqu'à 500 m. Un système de mise en place fut construit à l'université d'Illinois. Le succès d'un test in situ dans le bassin de Wilkinson, dans une profondeur d'eau de 274 m, produisit une pression interstitielle avec un excès maximum de 59 kPa, après avoir enfoncé la sonde d'environ 3·2 m dans le fond de l'argile limoneuse. Un excès de pression interstitielle de 9·8 kPa fut mesuré cinq à dix heures après la mise en place de la sonde. On discute des conséquences d'excès de pression interstitielle engendrés d'une façon cyclique par la tempête et par le chargement interne de sols provenant du fond de la mer, produit par les vagues. On conclut qu'une meilleure compréhension de la stabilité sous-marine d'une pente par l'utilisation du principe de contrainte effective, devrait maintenant être possible, en mesurant la pression différentielle in situ.

More than a decade ago it was proposed that the likely relationship between excess pore-water pressure in cohesive sediments and potential submarine slides, slumps, and possibly turbidity currents could be investigated by the in situ measurement of pore-pressure in sea-floor sediments (Richards, 1962). Negotiations with the Norwegian Geotechnical Institute (NGI) in 1964–5 led to the acquisition by the University of Illinois, Urbana, of two differential piezometer probes and a counter-computer in 1966. This Paper describes the probe system that was built around these units and the results of its limited testing at sea in 1967.

Previously, the system was mentioned by Richards (1968) and Richards and Keller (1968). One test was very briefly summarized by Lai *et al.* (1968).

DIFFERENTIAL PIEZOMETER SYSTEM

Principal of operation and specifications

The magnitude of hydrostatic pressure increases linearly by about one decibar (10 kPa) per metre of sea-water depth. Thus, the measurement of very small pressures above or below hydrostatic in water depths of several hundred metres is difficult. The measurement of only

* Marine Geotechnical Laboratory, Lehigh University, Bethlehem, Pennsylvania.
† Norwegian Geotechnical Institute, Tåsen, Norway.
‡ NOAA, Atlantic Oceanographic and Meteorological Laborities, Miami, Florida.
§ Manila, Philippines.

the small difference in pore-pressures greater or less than hydrostatic in cohesive sea-floor sediments is relatively easy. This latter relationship is schematically shown in Fig. 1, which illustrates the 274 m water depth occurring at the principal test site that will be discussed later.

The piezometer was designed to measure a minimum differential pressure of less than 0·35 kg/cm^2 (34 kPa) and a maximum of 2 kg/cm^2 (196 kPa) from hydrostatic; after construction the maximum was found to reach 3 kg/cm^2 (294 kPa). Accuracy of the system during calibration testing was about $\pm 63{\cdot}5$ g/cm^2 ($\pm 6{\cdot}2$ kPa). The design working depth was 500 m, equivalent to a hydrostatic pressure of 50 kg/cm^2 (4·9 MPa). It was estimated that by utilizing the free-fall method the probe might penetrate up to 20 m below the bottom under its own weight.

The measuring principle is shown in Fig. 2. A pressure differential is measured between the hydrostatic pressure, u_2, and the pore-water pressure, u_1. The pressures are transmitted in water-saturated tubes. One long plastic tube extends from the u_2 bourdon tube, through the weight stand, to above the water–sediment interface. The pore-pressure in the sediments surrounding the porous bronze filter at the tip of the probe is transmitted through a second plastic tube to the u_1 bourdon tube. Any difference in pore-pressure relative to the reference hydrostatic pressure deflects the bourdon tubes, shown in Fig. 3, causing a change in tension and hence the change in frequency of the vibrating wires that are clamped to the end of each tube. The relationship between the vibrating wires and electro-magnets is shown in Fig. 4. A linear relationship exists between the magnitude of the differential pressure and the change in the difference of the squares of the frequencies of the vibrating wires. The vibration frequencies are telemetered over an electrical logging cable to the ship. Aboard the ship an electronic frequency counter and computer displays the squares of the frequencies of the vibrating wires and the difference between the squares (Fig. 2). A block diagram of the principal components in the counter-computer is shown in Fig. 5.

Weight stand

In Urbana, a weight stand was constructed 3·66 m long from the base of the support cone to the bail (Fig. 6). A 0·95 m long stainless steel tube separated the base of the support cone and the top of the piezometer. The entire probe system was 4·9 m long, tip to bail.

Lead weights were cast having diameters of 15 and 20 cm. A few of the larger diameter weights were placed at the bottom of the weight stand to make the hole in the sea floor sufficiently large to reduce wall friction upon probe retrieval. The entire probe system, when fully weighted for deployment, had a maximum weight of nearly 570 kg in air.

SEA TESTS

Operational procedures

The entire probe system (Fig. 6) was prepared for deployment in the summer of 1966; however, because the scheduled ship unexpectedly could not be made available, the tests were postponed one year. The probe system was deployed a number of times during June 1967 in the Wilkinson Basin, Gulf of Maine, which is located about 125 km east of Boston. In this basin, from the bottom surface to a depth of about 3 m, the average properties of the normally consolidated silty clays are: $w = 163$, $w_L = 124$, $w_P = 47$ and $\gamma_{sat} = 1{\cdot}33$ Mg/m^3. At the bottom of the basin the water temperature was only 5–6°C (Schopf, 1967). Consequently, after assembly, the tip of the probe was packed in ice for 0·5–1 h each time before it was lowered to the sea floor.

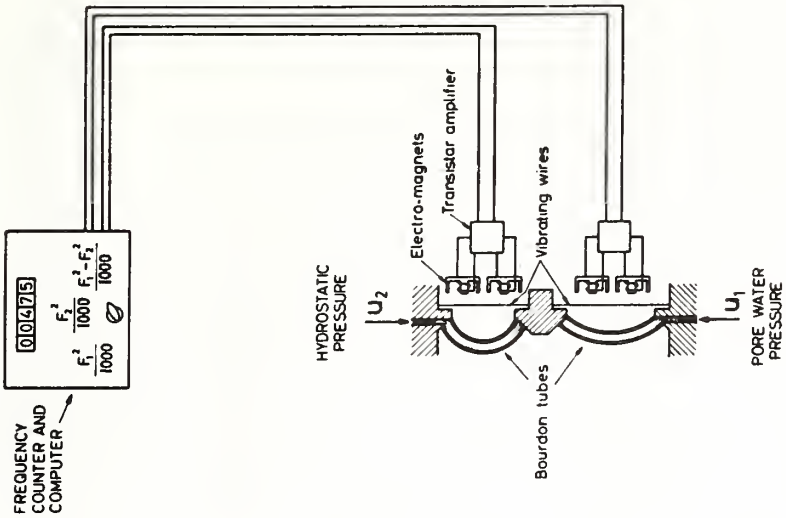

Fig. 2. NGI–Illinois differential piezometer measurement principle

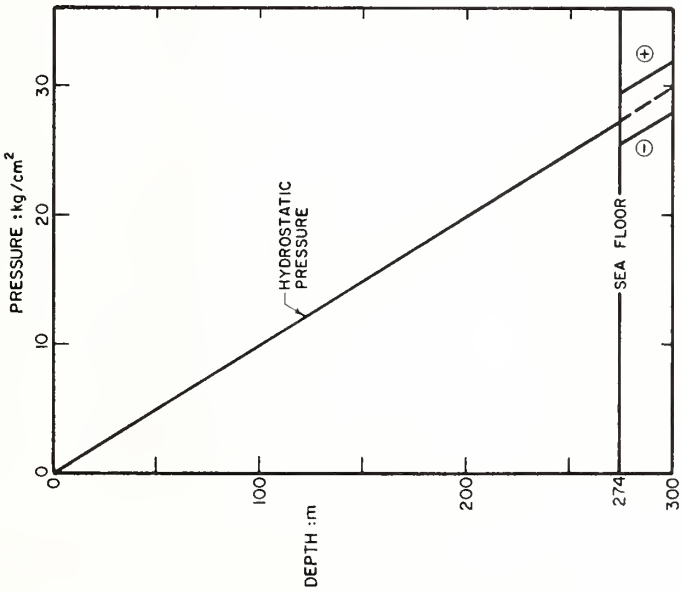

Fig. 1. Schematic representation of linear increase of hydrostatic pressure at test site in the Wilkinson Basin and differential pressure range of ± 2 kg/cm^2 (196 kPa) greater than and less than hydrostatic that could be measured by probe

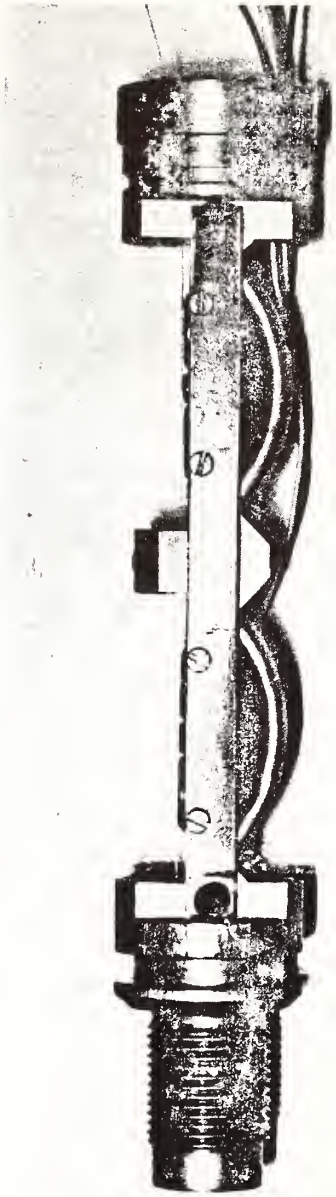

Fig. 3. Detail of bourdon gauges

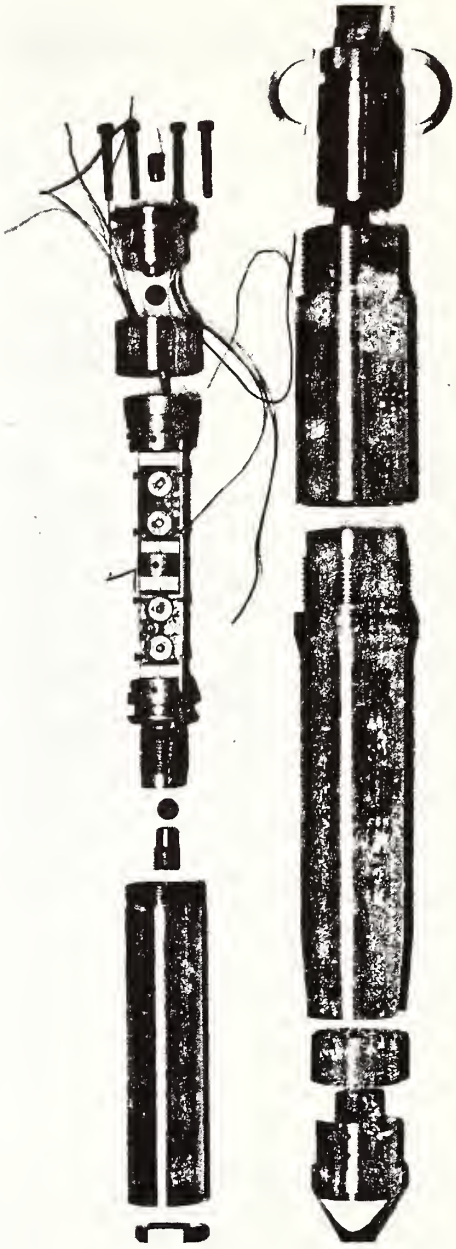

Fig. 4. Detail of electro-magnet and vibrating-wire assembly (left) and entire probe tip (right), which is 37·5 cm long

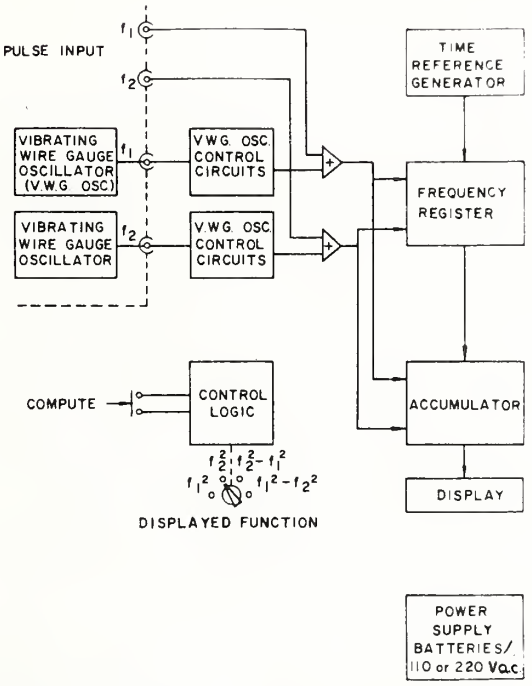

Fig. 5. Block diagram of the electronic counter-computer

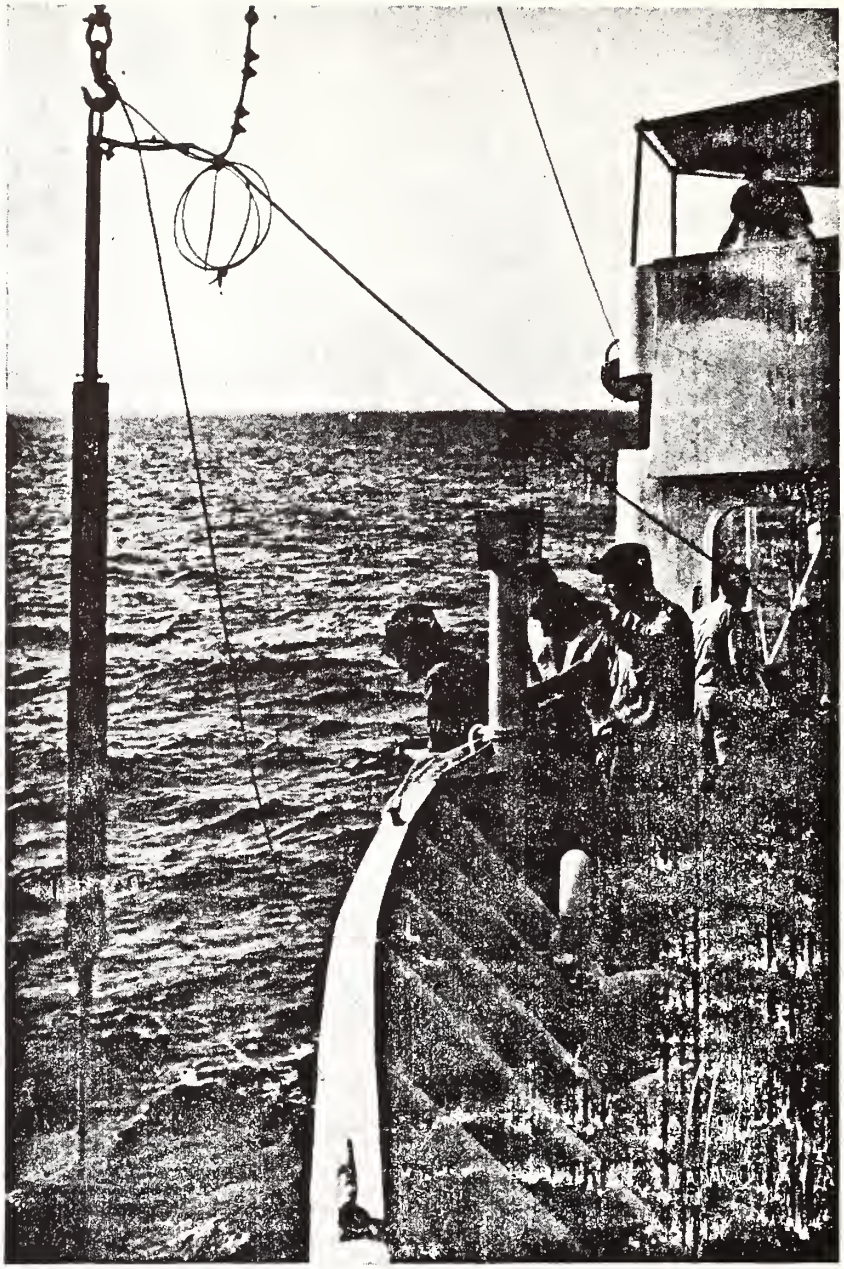

Fig. 6. Telemetering NGI–Illinois differential-piezometer probe system hanging over side of NOAA Survey Ship *Davidson*, June 1967. The probe is 4·9 m long

The following operational procedure was followed after the probe was lowered. It was held a short distance above the sea floor until the zero reading remained steady, indicating that ambient temperature and pressure equilibrium had been attained. The probe was then raised several metres above the bottom to gain potential energy, and then dropped into the bottom by allowing the winch to freewheel. The free-fall method (see Richards, 1973) could not be utilized during the 1967 testing at sea. While the probe was in the sediment, changes in the vibrating wire frequencies were recorded. After the readings stabilized, the probe was pulled out of the bottom and the zero reading again recorded to determine if any changes had occurred.

It was intended that the penetration depth would be measured in a comparable manner to that used to determine the penetration depth of the NGI Torpedo sampler (Richards, 1973). This method would consist of echo-ranging on a hollow acoustic reflector attached by a line to the bail of the probe. In operation, the length of the line was to be sufficiently long to ensure that the reflector was always located above the bottom. However, due to a misunderstanding on the last lowering, the required co-ordination of effort was not maintained and this method could not be used. There is no reason to believe that the method would not be successful if it were properly used, in light of the comparable operational experience obtained in Norway.

RESULTS

Only one full test was completed at sea. Problems with connectors, cable failures, and other difficulties unrelated to the functioning of the probe system consumed the remaining available time for testing. Fig. 7 records the dissipation of excess pore-pressures generated when the probe was emplaced on 12 June, 1967, an estimated 3·6 m below the bottom in a water depth of 274 m at latitude 42° 35·1′ north and longitude 69° 36·8′ west. The lack of measurements between 80 and 306 minutes occurred because one of the vibrating wires stopped vibrating, presumably because of an intermittent connexion in a pair of mating electrical plugs that had partly pulled apart.

DISCUSSION

In the interpretation of the data (Fig. 8), the following assumptions have been made:

(*a*) the probe actually was at the estimated depth below the bottom;
(*b*) all the excess pore-pressure generated by the probe emplacement was dissipated in the ten hour measurement interval;
(*c*) only pore-water entered the porous bronze filter, i.e. there was no water leakage to the porous filter from an elevation higher than the filter;
(*d*) free gas was not present in the soil at the time of the measurement.

The first assumption is not critical; either a greater or a lesser depth would not significantly change the conclusions if the other assumptions were valid.

Although Fig. 7 shows little change in the magnitude of excess pore-pressure sensed during the last 5 h the probe was in place, it may be debated whether all of the excess pore-pressure generated by driving the probe into the bottom was dissipated during the relatively short time interval monitored. An interval at least three to five times longer would have permitted a more valid assessment of whether excess pore-pressure existed at the approximate depth and location tested. The length of time is dependent on the depth of penetration, consolidation characteristics of the sediment, and other factors. This uncertainty cannot be resolved from the data presented. It is therefore concluded that while the measurement is suggestive, it is by no means conclusive.

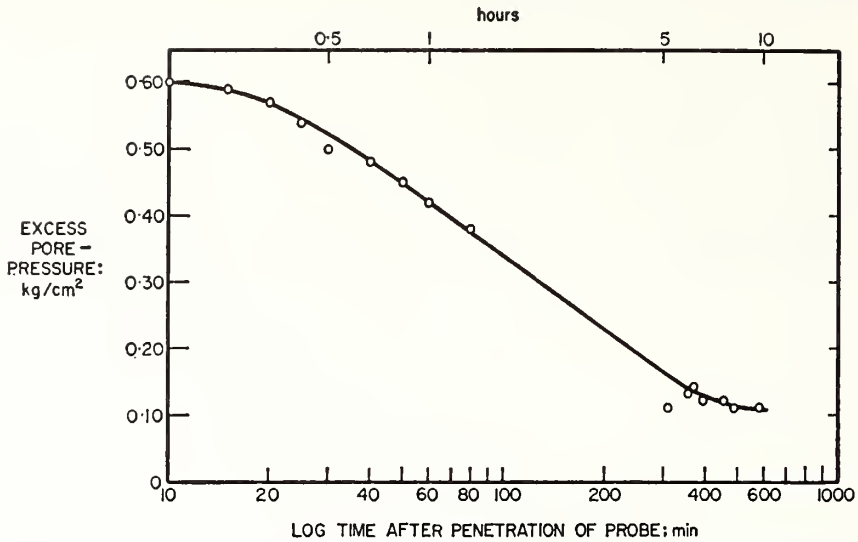

Fig. 7. Measured values of excess pore-pressure against log time after penetration and eye-fitted curve for 12 June, 1967 test

The third assumption is believed valid considering the design of the probe tip, the distance of the tip to the base of the weight stand, the method of emplacement, and the low permeability of the silty clay indicated by the mean grain size being less than 2 μm.

Whether or not gas was present in the soil is not known for certain. Free gas has not been observed in cores raised from the deeper parts of the Wilkinson Basin. The soil in the vicinity of the test site is exceptionally transparent to acoustic energy from echo sounders, which suggests that free gas probably was not present in the soil at the test site.

SUBSEQUENT STUDIES

Since this investigation, a number of developments have occurred that are relevant to the future use of differential piezometers. Morgenstern (1967) assessed submarine slumping and the formation of turbidity currents in terms of effective stress; he clearly recognized the importance of excess pore-pressures. Sangrey *et al.* (1969) interpreted soil behaviour under repeated loading in terms of effective stress; they concluded that the build-up of pore-pressure was critical in bringing the soil to the effective stress failure envelope. Henkel (1970) postulated that differential loading by waves could cause submarine soil failure seaward of the Mississippi River Delta. Wilson and Greenwood (1974) reported that cyclically loaded soil samples failed at stresses less than the compressive strength of the soils obtained from standard strength tests. The theme of slides induced by cyclical storm wave pressure loading was amplified by Bea (1971), Wright and Dunham (1972), Mitchell *et al.* (1973), Bea and Arnold (1973), Bea and Bernard (1973) and others. Southard and Cacchione (1972), in discussing earlier laboratory and theoretical work by Cacchione, hypothesized that internal waves may break on the outer continental shelf and upper continental slope, which also could cause cyclical loading. Bea (1974) wrote that side-looking sonar records of the shelf edge immediately after hurricane Camille showed mysterious 'ripples' that disappeared 4·8–6·4 km shoreward of the shelf-break. He hypothesized that these ripples may have resulted from internal waves breaking at the edge of the shelf.

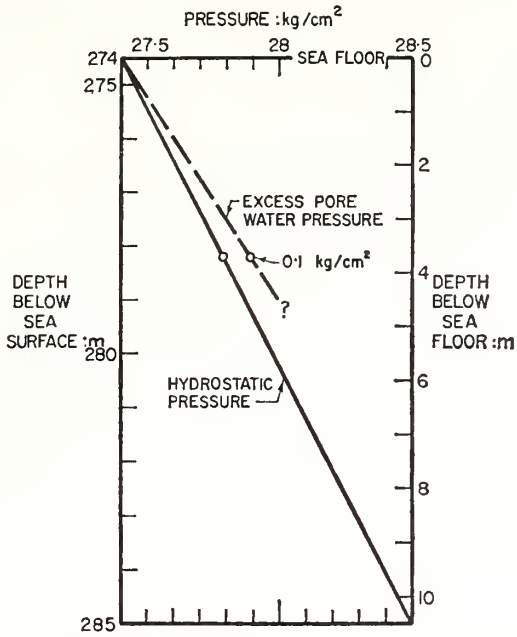

Fig. 8. Interpretation of results of the test shown in Fig. 7

The time appears appropriate to measure the pore-pressure in situ; to compute the total stress by conventional means or from in situ nuclear densitometer measurements (Hirst *et al.*, 1975); and to derive the effective stress actually existing in the floor of the ocean, particularly in areas susceptible to storm or internal wave loading. A knowledge of the total, effective and pore-water stress in sea-floor soils will significantly contribute to an understanding of submarine slope stability.

CONCLUSIONS

The NGI–Illinois differential piezometer probe system was successfully operated at a depth of 278 m below the sea surface, which corresponds to a hydrostatic pressure of about 27 kg/cm^2 (2·65 MPa).

A maximum excess pore-pressure of 0·6 kg/cm^2 (59 kPa), resulting from driving the probe approximately 3·2 m into the bottom, was measured immediately following emplacement.

There was little change in the 0·1 kg/cm^2 (9·8 kPa) magnitude of excess pore-pressure measured between five and ten hours after emplacement.

While the magnitude of apparent excess pore-pressure remaining after nearly ten hours indicates that a small excess pore-pressure existed in sediments believed to be normally consolidated, the time interval was insufficiently long to permit a more definite assessment to be made. It is possible that this apparent excess pore-pressure might have been largely or entirely dissipated if the pore-pressure was monitored for a considerably longer time after the emplacement of the probe.

The free-fall, probe-emplacing method was not tested. Consequently, the maximum depth in which this probe may be emplaced in soft cohesive sediments was not determined.

The bourdon gauge pressure sensing system performed adequately. However, the use of bellows, differential pressure transducers, or other more sensitive transducers probably would

result in a more accurate measuring system. A bellows differential piezometer was built at the NGI after the bourdon gauge units were delivered; it has not been tested at sea. A differential conductance piezometer has been designed, but not built, at the Marine Geotechnical Laboratory.

With the technology existing to measure pore-pressure in situ on the ocean floor, a better understanding of submarine slope stability is now possible. A knowledge of pore-pressure also will significantly contribute to long-term engineering investigations utilizing the effective stress principle.

ACKNOWLEDGEMENTS

Tests at sea were made from the NOAA Survey Ship *Davidson*, Lt Cdr W. Jeffers commanding. At the University of Illinois, Professor V. J. McDonald and Mr J. Sterner ably assisted in electrical-electronic maintenance and operation. Mr R. G. Bea, Shell Oil Company, is thanked for his constructive review of this Paper. This investigation was performed under Office of Naval Research contract NONR 3985(09), NR 081-260, to the University of Illinois. The Paper was written under the sponsorship of ONR contract N00014-67-A-0370-0005, NR 083-248, to Lehigh University.

REFERENCES

Bea, R. G. (1971). How sea-floor slides affect offshore structures. *Oil and Gas Jnl* **48**, 88–92.

Bea, R. G. (1974). Private communication.

Bea, R. G. & Arnold, P. (1973). Movements and forces developed by wave-induced slides in soft clays. *Preprints Offshore Tech. Conf.* **2**, 731–742.

Bea, R. G. & Bernard, H. A. (1973). Movements of bottom soils in the Mississippi delta offshore. *Offshore Louisiana Oil and Gas Fields. Lafayette Geol. Soc. and New Orleans Geol. Soc.*, 13–28.

Henkel, D. J. (1970). The role of waves in causing submarine landslides. *Géotechnique* **20**, 75–80.

Hirst, T. J., Burton, B. S., Perlow, M., Jr, Richards, A. F. & Van Sciver, W. J. (1975). Improved in situ gamma-ray transmission densitometer for marine sediments. *Ocean Eng.* **3**, May.

Lai, J. Y., Richards, A. F. & Keller, G. H. (1968). In place measurement of excess pore pressure in Gulf of Maine clays (abstract). *Am. Geophy. Union Trans.* **49**, 221.

Mitchell, R. J., Tsui, K. K. & Sangrey, D. A. (1973). Failure of submarine slopes under wave action. *Proc. 13th Coastal Eng. Conf.* **2**, 1515–1541. New York: American Society of Civil Engineers.

Morgenstern, N. R. (1967). Submarine slumping and the initiation of turbidity current. *Marine geotechnique*, 189–220. Urbana: University Illinois Press.

Richards, A. F. (1962). Unpublished report to Royal Norwegian Council of Scientific and Industrial Research.

Richards, A. F. (1968). Discussion to session 1, shear strength of soft clay. *Proc. Geotech. Conf., Oslo* **2**, 131–133. Oslo: Norwegian Geotechnical Institute.

Richards, A. F. (1973). Geotechnical properties of submarine soils, Oslofjorden and vicinity, Norway. *Norwegian Geotech. Inst. Tech. Rept 13*, 107 pp.

Richards, A. F. & Keller, G. H. (1968). Measurement of shear strength, bulk density, and pore pressure in recent marine sediments by in situ probes: results of 1967 shallow water tests (abstract). *Am. Assoc. Petroleum Geol. Bull. 52*, 547.

Sangrey, D. A., Henkel, D. J. & Esrig, M. I. (1969). The effective stress response of a saturated clay soil to repeated loading. *Canad. Geotech. Jnl* **6**, 241–252.

Schopf, T. J. M. (1967). Bottom-water temperatures on the continental shelf off New England *US Geol. Survey Prof. Paper 575-D*, D192–197.

Southard, J. B. & Cacchione, D. A. (1972). Experiments on bottom sediment movement by breaking internal waves. *Shelf sediment transport: process and pattern*, 85–97. Stroudsburg, Pa: Dowden, Hutchinson and Ross.

Wilson, N. E. & Greenwood, J. R. (1974). Pore pressures and strains after repeated loading of saturated clay. *Canad. Geotech. Jnl* **11**, 269–277.

Wright, S. G. & Dunham, R. S. (1972). Bottom stability under wave induced loading. *Preprints Offshore Tech. Conf.* **1**, 853–862.

Reprinted from: *Journal of Geology 83*, No. 4, 536.

Sonographs of the Sea Floor. By R. H. Belderson, N. H. Kenyon, A. H. Stride, and A. R. Stubbs. Amsterdam: Elsevier Publishing Company, 1972. 185 pages, 163 figures. $27.75.

"Sonograph" is a term used by the authors to describe the records made by side-scan sonar. Side-scan sonar is a technique developed over the past 15 years to determine the shape of the ocean bottom and is finding new applications in biology, oceanography, and engineering. The side-scan technique is a variation of echo sounding in which the sonar transducer is directed oblique instead of normal to the ocean bottom. Sonographs of the ocean bottom have been compared to oblique aerial photographs of the land with the important difference that the sonograph is an acoustic rather than an optical picture. The authors briefly consider the acoustics of side-scan sonar and concentrate their considerable collective experience on the interpretation of sonographs. They present a picture atlas of 163 sonographs from the collection of the British National Institute of Oceanography. The atlas is divided into 109 geological sonographs (continental shelf, upper continental slope, deepsea floor) and 64 other sonographs (marine life, sea effects, man-made objects). The sonographs are clearly reproduced on 22 by 30.5 cm ($8\frac{1}{2}$ by 12 inch) pages. Each is accompanied by a brief description and a line drawing which differentiates data from acoustic effects and gives overall dimensions of the area ensonified. A problem in the use of the sonographs presented is that their widths are slightly nonlinear because distance to scattering features is a slant-range; techniques have subsequently been developed to convert slant-range to true-range display. Most of the sonographs were made by towing the instrument package within tens of meters of the ocean bottom on a cable suspended from a ship proceeding at a speed of about 1 knot. These sonographs have a slant-range of less than 1 km and show small-scale geological, biological, and engineering features. Ten of the sonographs were made with an instrument called GLORIA (from Geological Long Range Inclined Asdic) with a slant-range up to 22 km which is towed near the ocean surface from a ship at speeds up to 7 knots. The resolution of features is roughly one thousandth of the range. The book is useful as a manual of interpretation for everyone using side-scan sonar and anyone interested in the capabilities of side-scan sonar for geological, biological, oceanographic, and engineering applications. A list of 120 references covering the physical principles, instrumentation, and application of side-scan sonar between 1954 and 1971 is included.

Peter A. Rona
National Oceanic and Atmospheric Administration

Reprinted from: *Science 190*, No. 4213, 422.

Minerals and Plate Tectonics

In his article, "Minerals and plate tectonics (II): Seawater and ore formation" (Research News, 12 Sept., p. 868), Allen L. Hammond cites examples of active hydrothermal systems known on the sea floor. An additional documented example is the TAG hydrothermal field (*1*), discovered on the crest of the Mid-Atlantic Ridge at 26°N by the Trans-Atlantic Geotraverse (TAG) project of the National Oceanic and Atmospheric Administration. Manganese oxide of hydrothermal origin (*2*) present on one wall of the rift valley (*3*) is inferred to have been deposited by hot (*4*), metal-enriched (*5*), aqueous solutions discharging from fractures in the sea floor (*6*). The existence of such sub-sea floor hydrothermal systems at sites along oceanic ridges indicates that hydrothermal activity may concentrate metals in oceanic crust throughout the opening of an ocean basin, from the Red Sea stage to the Atlantic Ocean stage, by sea floor spreading about a divergent plate boundary.

PETER A. RONA

Atlantic Oceanographic and Meteorological Laboratories, National Oceanic and Atmospheric Administration, Miami, Florida 33149

References

1. R. B. Scott, P. A. Rona, B. A. McGregor, M. R. Scott, *Nature (Lond.)* **251**, 301 (1974).
2. M. R. Scott, R. B. Scott, P. A. Rona, L. W. Butler, A. J. Nalwalk, *Geophys. Res. Lett.* **1**, 355 (1974).
3. B. A. McGregor and P. A. Rona, *J. Geophys. Res.* **80**, 3307 (1975).
4. P. A. Rona, B. A. McGregor, P. R. Betzer, D. C. Krause, *Deep-Sea Res.*, in press.
5. P. R. Betzer, G. W. Bolger, B. A. McGregor, P. A. Rona, *EOS, Am. Geophys. Union Trans.* **55**, 293 (1974).
6. P. A. Rona, R. N. Harbison, B. G. Bassinger, R. B. Scott, A. J. Nalwalk, *Geol. Soc. Am. Bull.*, in press.

Reprinted from: Proc. Offshore Technology Conference,
Paper No. OTC 2317, 713-715.

THIS PRESENTATION IS SUBJECT TO CORRECTION

Relation of Offshore and Onshore Mineral Resources to Plate Tectonics

By

Peter A. Rona, NOAA

©Copyright 1975

Offshore Technology Conference on behalf of the American Institute of Mining, Metallurgical, and Petroleum Engineers, Inc. (Society of Mining Engineers, The Metallurgical Society and Society of Petroleum Engineers), American Association of Petroleum Geologists, American Institute of Chemical Engineers, American Society of Civil Engineers, American Society of Mechanical Engineers, Institute of Electrical and Electronics Engineers, Marine Technology Society, Society of Exploration Geophysicists, and Society of Naval Architects and Marine Engineers.

This paper was prepared for presentation at the Seventh Annual Offshore Technology Conference to be held in Houston, Tex., May 5-8, 1975. Permission to copy is restricted to an abstract of not more than 300 words. Illustrations may not be copied. Such use of an abstract should contain conspicuous acknowledgment of where and by whom the paper is presented.

ABSTRACT

The Pacific and Atlantic are natural laboratories to study relations between mineral resources and plate tectonics. The distribution of mineral deposits about convergent lithospheric plate boundaries may be best observed in the Pacific. The Pacific is surrounded by convergent plate boundaries where oceanic crust is consumed by subduction along Benioff zones. Areas of offshore petroleum potential are associated with the convergent plate boundaries which create oceanic trenches along the eastern Pacific and small ocean basins along the western Pacific. Precious, base, iron and ferro-alloy metal deposits occur onshore from the convergent plate boundaries on continents in the eastern Pacific and on island arcs and continents in the western Pacific. The distribution of mineral deposits about divergent plate boundaries is less known than about convergent plate boundaries because the former are submerged oceanic ridges. The Atlantic is bisected by the Mid-Atlantic Ridge where oceanic crust is created by sea floor spreading. Certain metals are being concentrated in oceanic crust at divergent plate boundaries by hydrothermal processes. The TAG Hydrothermal Field, an active hydrothermal area discovered by the NOAA Trans-Atlantic Geotraverse (TAG) on the Mid-Atlantic Ridge at 26°N, is providing information of how metals are concentrated in oceanic crust at divergent plate boundaries. Present models which treat the relation between mineral deposits and lithospheric plate boundaries are largely interpretive, explaining the observed distribution of deposits. The development of these models may lead to the discovery of new deposits both offshore and onshore.

References and illustrations at end of paper.

INTRODUCTION

The Atlantic is an opening ocean basin that is inferred to have been growing wider at a rate of several centimeters per year for approximately the past 200,000,000 years. The Pacific is a closing ocean basin that is inferred to have been diminishing in size at a rate comparable to that of the opening of the Atlantic. The contrasting histories of the Atlantic and Pacific are explained according to the theory of plate tectonics in terms of motions of lithospheric plates (Fig. 1) about divergent and convergent plate boundaries (Fig. 2). The occurrence of mineral deposits including petroleum may be related to plate motions and, in particular, to geological processes associated with the boundaries between the plates. Differences in plate motions have resulted in different distributions of minerals in the Atlantic and Pacific regions that may be characteristic of divergent and convergent plate boundaries.

DIVERGENT PLATE BOUNDARIES

Relations between the opening of an ocean basin about a divergent plate boundary and the occurrence of mineral deposits may be inferred from the development of the Atlantic as follows:

1. At an early stage of opening following continental rifting a sea is formed with its circulation restricted by tectonic conditions and by the positions of the surrounding continents[1]. Conditions in this sea favor both the accumulation of organic matter that may become petroleum and of rock salt that may subsequently form domes to trap the petroleum[2]. Metalliferous sediments and possibly massive stratabound sulfide bodies are concentrated by hydrothermal processes at the divergent plate boundary. An example of this early stage of opening is the Red Sea[3].

2. Widespread metalliferous sediments immediately overlying basalt of the ocean basins indicate that hydrothermal activity at a divergent plate boundary may continue as the ocean basin opens[4-6].

3. The recent discovery of the TAG Hydrothermal Field by the NOAA Trans-Atlantic Geotraverse (TAG) project, where metal oxides and possibly sulfides are being deposited on the Mid-Atlantic Ridge at 26°N, indicates that hydrothermal processes may concentrate metals in oceanic lithosphere at a divergent plate boundary from early (Red Sea) to advanced (Atlantic Ocean) stages of opening[7,8].

CONVERGENT PLATE BOUNDARIES

The Pacific Ocean basin is inferred to be closing as a consequence of consumption of oceanic lithosphere at convergent plate boundaries around three-fourths of its perimeter. Relations between the consumption of an ocean basin at a convergent plate boundary and the occurrence of mineral deposits may be inferred from the Pacific[9], as follows:

1. The structural framework at a convergent plate boundary expressed as an oceanic trench or an island arc that delineates a marginal basin creates conditions that favor the development of offshore petroleum.

2. The subduction of oceanic lithosphere along a Benioff zone at a convergent plate boundary is genetically related to the occurrence of iron and ferro-alloy, base, and precious metal deposits, such as those distributed along the continental margins and island arcs of the Pacific[10-12].

SUMMARY

A model depicts processes at divergent and convergent plate boundaries of the Atlantic and Pacific (Fig. 3). Petroleum is related to early stages of opening of an ocean basin about a divergent plate boundary and to basins formed at convergent plate boundaries. Certain iron and ferro-alloy, base, and precious metals are concentrated in oceanic lithosphere by hydrothermal processes at a divergent plate boundary from early to advanced growth stages of an ocean basin. The metals undergo further concentration when the oceanic lithosphere is subducted at a convergent plate boundary. The metals are deposited along the convergent boundary where they are most accessible for exploitation.

REFERENCES

1. Rona, P.A.: "Possible Salt Domes in the Deep Atlantic off Northwest Africa," Nature (1969) 224, 141-143.
2. Rona, P.A.: "Comparison of Continental Margins of Eastern North America at Cape Hatteras and Northwestern Africa at Cap Blanc," Bull. Am. Assoc. Pet. Geologists (1970) 54, 129-157.
3. Hutchinson, R.W. and Engels, G.G.: "Tectonic Evolution in the Southern Red Sea and its Possible Significance to Older Rifted Continental Margins," Geol. Soc. Am. Bull. (1972) 83, 2989-3002.
4. Böstrom, K. and Peterson, M.N.A.: "Origin of Aluminum-Poor Ferromanganoan Sediments in Areas of High Heat Flow on the East Pacific Rise," Mar. Geol. (1969) 7, 427-477.
5. Dymond, J., Corliss, J.B., Heath, G.R., Field, C.W., Dash, E.J., and Veeh, H.H.: "Origin of Metalliferous Sediments from the Pacific Ocean," Geol. Soc. Am. Bull. (1973) 84, 3355-3372.
6. von der Borch, C.C., Nesteroff, W.D., and Galehouse, J.S.: "Iron-Rich Sediments Cored During Leg 8 of the Deep Sea Drilling Project," In, Tracey, J.I. Jr., et al.(eds.), Initial Reports of the Deep Sea Drilling Project (1971) 8, 725-819.
7. Scott, R.B., Rona, P.A., McGregor, B.A., and Scott, M.R.: "The TAG Hydrothermal Field," Nature (1974) 251, 301-302.
8. Scott, M.R., Scott, R.B., Rona, P.A., Butler, L.W., and Nalwalk, A.J.: " Rapidly Accumulating Manganese Deposit from the Median Valley of the Mid-Atlantic Ridge," Geophys. Res. Letters (1974) 1, 355-358.
9. Rona, P.A., and Neuman, L.D.: "Plate Tectonics and Mineral Resources of the Pacific," Bull. Am. Assoc. Pet. Geologists (1974) 58, 1456.

10. Sawkins, F.: "Sulfide Ore Bodies in Relation to Plate Tectonics," J. Geol. (1972) 80, 377-397.
11. Sillitoe, R.H.: "Relation of Metal Provinces in Western America to Subduction of Oceanic Lithosphere," Geol. Soc. Am. Bull. (1972) 83, 813-818.
12. Mitchell, A.G.H.: "Metallogenic Belts and Angle of Dip of Benioff Zones," Nature Phys. Sci. (1973) 245, 49-52.
13. Le Pichon, X.: "Sea Floor Spreading and Continental Drift," J. Geophys. Res. (1968) 73, 3661-3697.
14. Rona, P.A.: "New Evidence for Seabed Resources from Global Tectonics," Ocean Management (1973) 1, 145-159.
15. Isacks, B., Oliver, J., and Sykes, L.R.: "Seismology and the New Global Tectonics," J. Geophys. Res. (1968) 73, 5855-5899.
16. Rona, P.A.: "Plate Tectonics and Mineral Resources," Scientific American (July 1973) 229, 86-95.

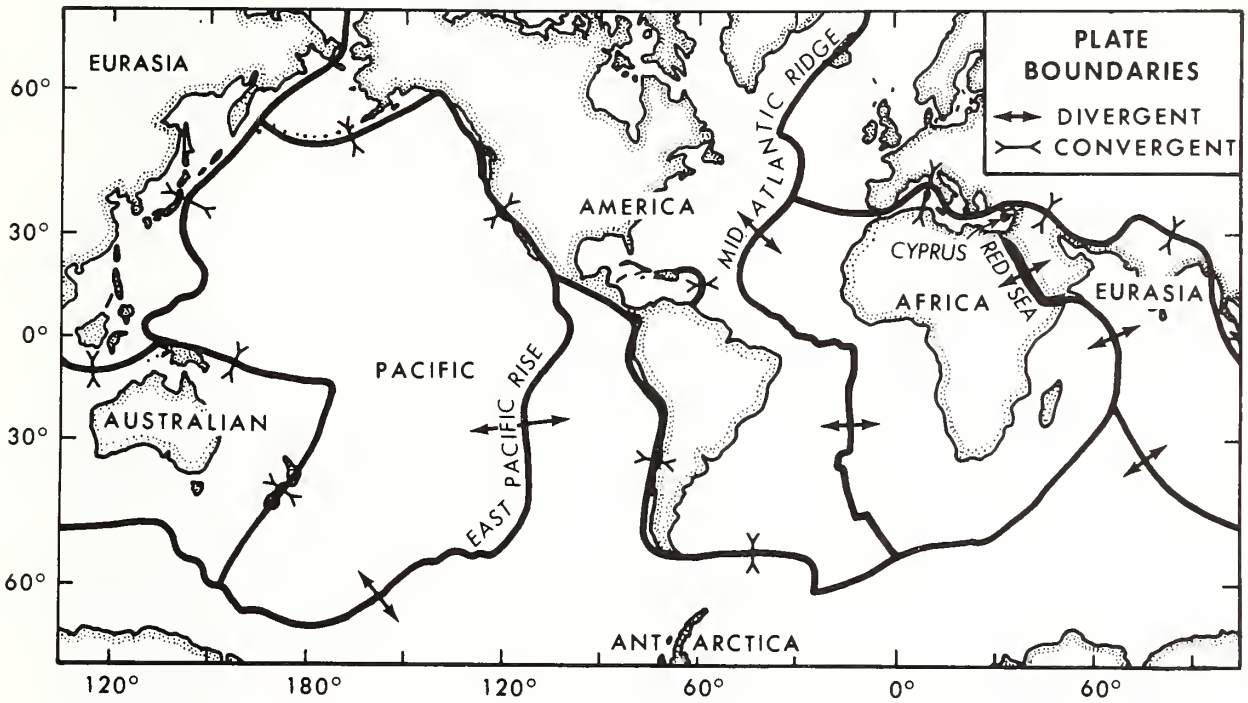

Fig. 1 - Boundaries of six principal lithospheric plates[13,14]. Divergent plate boundaries where lithosphere is created and convergent plate boundaries where lithosphere is destroyed are indicated.

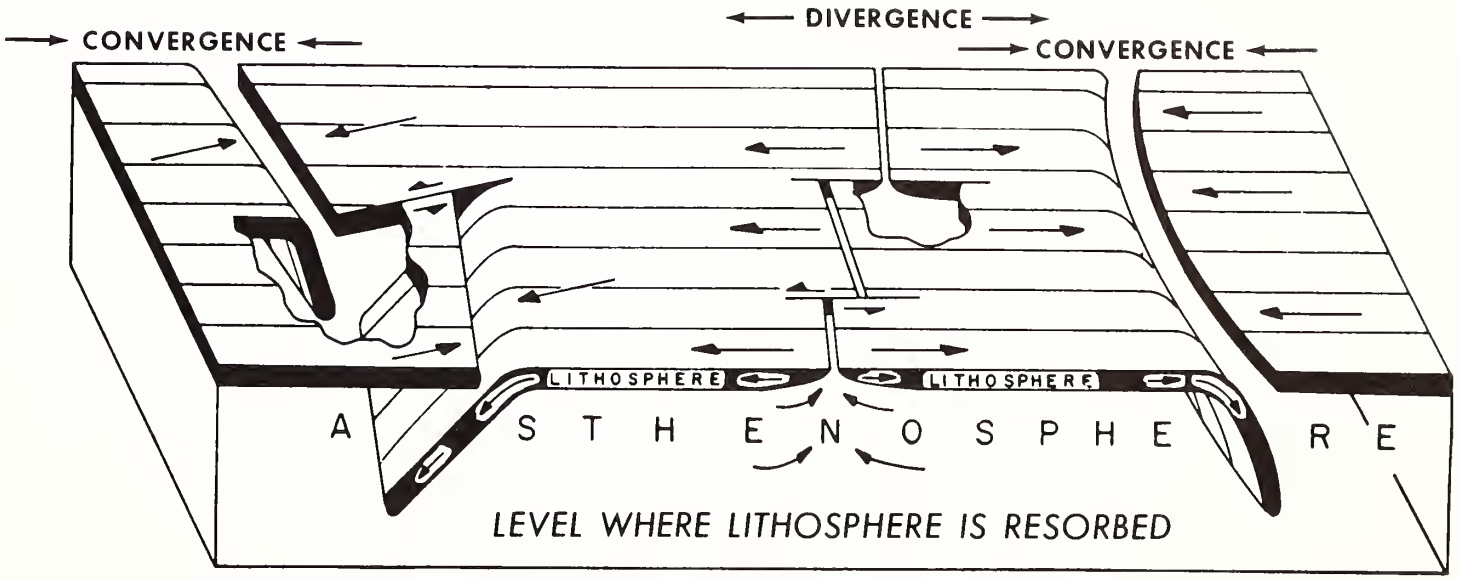

Fig. 2 - Diagrammatic representation of how divergent and convergent plate boundaries work[15,14]. Lithospheric plates about 100 kilometers thick (60 miles) move like conveyor belts from an oceanic ridge (divergent plate boundaries) and are subducted along a Benioff zone beneath an oceanic trench (convergent plate boundary). A third type of plate boundary, a transform boundary, accomodates horizontal plate motions.

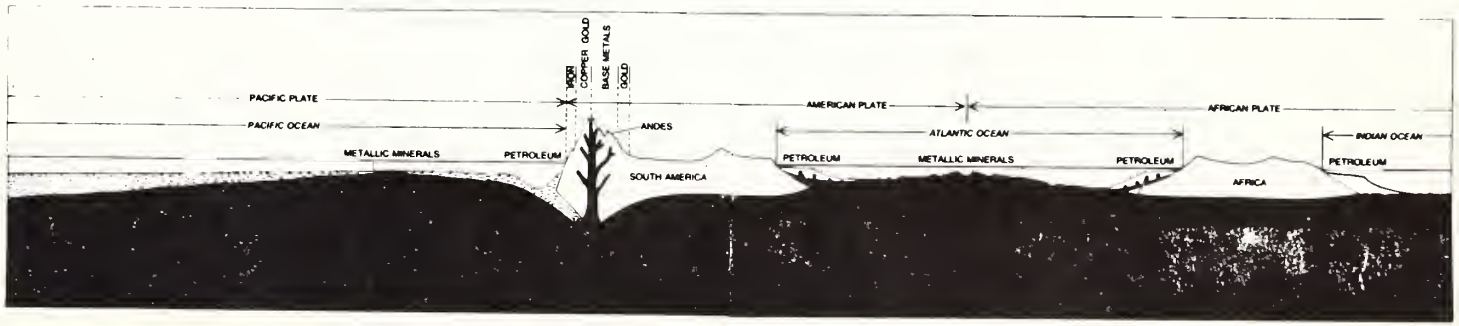

Fig. 3 - A model using a diagrammatic east-west cross-section of the Atlantic and Pacific regions to show the relation of petroleum and metals to divergent and convergent plate boundaries[16].

Reprinted from: Proc. International Symposium on Continental Margins of Atlantic Type, Brazil, 1-15.

SALT DEPOSITS OF THE EASTERN AND WESTERN ATLANTIC

Peter A. Rona
Atlantic Oceanographic and Meteorological Laboratories
National Oceanic and Atmospheric Administration
Miami, Florida, U.S.A.

ABSTRACT

Sufficient information is available from onshore and offshore geological surveys and drilling to relate the distribution of evaporites in time and space to the development of the Atlantic. Evaporites had long been recognized in marginal basins of the Atlantic but their seaward extent was thought to be restricted by shelf-edge barriers. The discovery of salt deposits in the Atlantic ocean basin beneath the continental rise indicated that the real restrictions on evaporite deposition were the tectonic setting produced by the rifting of the continents and the configuration of the Atlantic Sea during early stages of drift. Questions raised include distinctions between salt deposits of Atlantic marginal basins and ocean basin, shallow versus deep water evaporites, and the relation of the salt deposits to horizontal (sea floor spreading) and to vertical (rifting, subsidence, and eustacy) movements. The Atlantic exhibits a classic distribution pattern of evaporites of an opening ocean basin.

Reprinted from: *Encounter with the Earth*, edited by L.F. Laporte, Canfield Press, San Francisco, Ca, 83-86.

Viewpoint **Peter A. Rona**

Peter A. Rona is a research scientist with the National Oceanic and Atmospheric Administration, Miami, Florida. Dr. Rona's recent work has been on the possible link between plate tectonics and economically valuable mineral deposits. In this Viewpoint Dr. Rona reviews the geologic factors controlling such deposits along plate boundaries.

Learning Where to Look for Mineral Resources

The revolutionary advance in our understanding of internal processes of the earth made during the past ten years is leading to economic returns through the discovery of new mineral resources. The problem of exploring the earth's crust for mineral deposits is the proverbial one of searching

for a needle in a haystack. Just as the needle is tiny relative to the size of the haystack, so petroleum and metal deposits are small relative to the volume of the earth's crust. Many valuable mineral deposits occupy areas less than that of a city block. The problem of discovering a deposit, like that of finding the needle in the haystack, is facilitated by knowing where to look. In the past we have found only the most accessible deposits on the continents, largely by trial and error, without a real understanding of why and where the deposits occurred. As a result of our increased understanding of internal processes of the earth we are gaining insights that tell us where to probe for new sources.

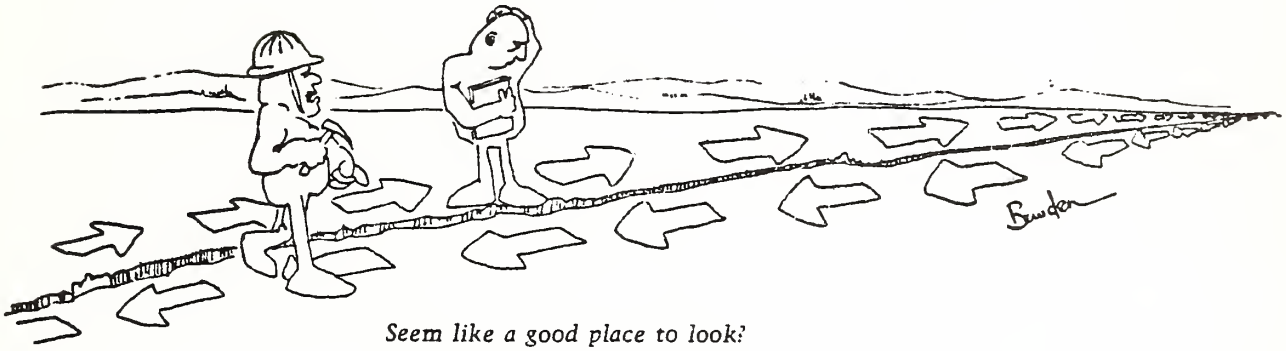

Seem like a good place to look?

How do internal processes control mineral deposits? An important clue is the observation that many minerals lie along the boundaries between the plates that divide the earth's crust (Figure 3-1). Petroleum and various base and noble metals occur along the margins of the Pacific Ocean, which are plate boundaries. These deposits include the metal provinces of western North and South America, and the petroleum of Indonesia and the west coast of the United States. We are exploring the plate boundaries submerged beneath the ocean along midoceanic ridges and have found that overlying sediments are enriched in various metals and that solid metal deposits appear at certain sites along the Mid-Atlantic Ridge. For this reason we suspect that metal deposits including copper, manganese, iron, nickel, lead, zinc, chromium, cobalt, uranium, and gold may be present at sites on midoceanic ridges. We do not think that midoceanic ridges contain any petroleum. Sediments on the floor of the Red Sea, where a plate boundary lies between Africa and Eurasia, are enriched in iron, zinc, copper, lead, silver, and gold. Sediments full of organic matter that may eventually become petroleum are preserved at the margins of the Red Sea.

Why should certain mineral deposits be concentrated along plate boundaries? Plate boundaries are where the geologic action takes place. As crustal material is being created at divergent plate boundaries and is being destroyed at convergent plate boundaries, processes are working to concen-

trate minerals in deposits along the boundaries. The metals that appear at divergent plate boundaries on midoceanic ridges and in the Red Sea are being deposited from hot solutions that concentrate metals from the rocks lying at these boundaries (Figure 3–2a). The metals at convergent plate boundaries around the Pacific Ocean are also deposited from hot solutions rich in metals possibly derived from the melting of the Pacific plate as it plunges beneath the adjacent continents (Figure 3–2b).

Many mineral deposits lie in areas far from present plate boundaries. To understand the reason for the location of these deposits, we must consider how the sizes, shapes, and positions of the continents and ocean basins have changed through time. For example, the Atlantic originated as a sea at an early stage in the development of the divergent plate boundary and widened into an ocean over a period of 200 million years. Various metals and organic matter may have accumulated in the Atlantic Sea, as they have in the present Red Sea, so that metal and petroleum deposits may be present at sites under the miles-thick sediments along the eastern and western margins of the Atlantic Ocean.

The separation of continents by continental drift about divergent plate boundaries may divide preexisting mineral provinces. Fitting the continents together in their positions prior to continental drift in a global jigsaw puzzle may reveal the continuity of certain mineral provinces between the continents. Diamonds found in northwest South America (Guyana and Venezuela) appear to have been derived from source rocks in west Africa (Liberia, Ivory Coast, and Ghana) when South America and Africa were joined prior to the opening of the Atlantic Ocean. Gold-bearing formations in these two regions of South America and Africa can be matched across the Atlantic. Metal provinces of southeast Africa, Southern India, and western Australia apparently match as well, agreeing with the positions of these continents when joined prior to continental drift.

Mineral deposits may also be present along former plate boundaries that are no longer active. Metal deposits of the Appalachian Mountains of southeastern North America and the Ural Mountains between Europe and Asia may have originated when these mountain ranges developed at former convergent plate boundaries. Still other mineral deposits within continents do not appear to conform either to present or former plate boundaries, and their origins remain problematic.

The patterns of mineral distribution that are emerging from our increased understanding of internal processes of the earth are guiding man's search for new mineral deposits. However, many factors should be kept in mind concerning mineral resources for the future. Nature is not manufacturing new mineral resources at plate boundaries as fast as man is depleting known mineral deposits. The rate of accumulation of metal deposits from hot solutions at midoceanic ridges is about 8 millionths of an inch per year (2 hundred-thousandths of a centimeter per year). The minimum time required to form petroleum from organic matter and

concentrate it into pools is of the order of tens of thousands of years. Many existing mineral deposits are inaccessible to us because they are too deeply buried in the crust to be detected and recovered by present technology; and when deposits are accessible, often the cost of production would be higher than the market value. Even with our increased understanding of where to look for new mineral deposits, evaluation of a new area of land or sea may require years of exploration and expenditure with uncertain outcome. Following the discovery of a valuable petroleum or metal deposit, five to ten years of developmental work are generally required before the prospect is ready for production. In conclusion, our greater understanding of the earth's internal processes can be expected to accelerate the discovery of mineral resources on the continents and in the ocean basins, but still offers us no promise of utopia.

Summary

The earth's present-day surface results from large-scale processes operating throughout its crust and upper mantle. The all-encompassing theory of plate tectonics explains the broad features and geologic activity that we observe on the face of the earth. Relatively thin, rigid plates move either by gravity or convection over the thicker, plastic upper mantle. Plate boundaries are marked by long, linear geologic features like mountain ranges, submarine basaltic ridges, volcano and earthquake zones, and deep sea trenches—depending on whether plates are moving together, moving away from each other, or slipping past one another.

Continents are thick slabs of lighter rocks floating more or less in isostatic balance on the denser, underlying mantle. Ocean basins are underlaid with thinner slabs of heavier rock resting on the mantle. Continents are regions of higher elevation continually eroding; ocean basins are areas of lower elevation that receive sediments deposited from the continents. As oceanic plates collide with continental plates, the oceanic sediments may be scraped off and piled against the continents or metamorphosed and granitized as they descend below the continent. Plate collisions also deform rocks by faulting and folding them.

Basaltic lavas continuously well up from the mantle and form long, linear ridges within the central portions of ocean basins along diverging plate boundaries. Plate movement away from the midoceanic ridges brings these mantle materials from the oceans and eventually adds them to the continents. Plates thus grow at their diverging boundaries and are consumed at converging ones. Consequently, throughout geologic history continents have grown with the continuous addition of mantle material and have shifted spatially as plate movement has carried them along.

Reprinted from: *Deep-Sea Research 22*, 611-618.

Anomalous water temperatures over Mid-Atlantic Ridge crest at 26° North latitude

PETER A. RONA,* BONNIE A. MCGREGOR,* PETER R. BETZER,† GEORGE W. BOLGER† and DALE C. KRAUSE‡

(*Received* 7 *August* 1974; *in revised form* 30 *January* 1975; *accepted* 24 *February* 1975)

Abstract—Two positive temperature anomalies with different characteristics were measured in the water over the walls of the rift valley of the Mid-Atlantic Ridge at 26°N latitude.

A water temperature profile parallel to the ocean bottom was made with three thermistors mounted in a 4 m long vertical array on a towed deep-sea camera over a hydrothermal mineral deposit, the TAG Hydrothermal Field, situated on the southeast wall of the rift valley. It revealed an abrupt anomaly of + 0·11°C associated with an inverse gradient of 8×10^{-3} °C m^{-1} within 20 m of the bottom along a horizontal distance of about 350 m between water depths of 3030 and 2950 m.

Over the northwest wall of the rift valley, a vertical water temperature profile measured with reversing thermometers revealed a relative warming of 0·20°C between 2000 m and the ocean bottom at 2508 m.

Either conductive transfer of heat or discharge of hydrothermal solutions from the ocean bottom could be the heat source for the observed temperature anomalies. The different geologic setting in the two areas suggests that the anomaly over the southeast wall is due to the discharge of hydrothermal solutions; that over the northwest wall to *in situ* conductive transfer of heat or possibly to the advection of a bolus of warm water into the area.

INTRODUCTION

MID-OCEANIC ridge systems are recognized as regions of considerable geologic activity. Large volumes of basic rock are intruded or extruded, fault systems displace sections of the crust, and the epicenters of shallow earthquakes are located at ridge crests. Although most of these processes occur over long time periods, they may at times measurably affect the physical–chemical environment of adjacent deep ocean waters (KNAUSS, 1962; LUBIMOVA, VON HERZEN and UDINTSEV, 1965). An interdisciplinary investigation of the environment of a hydrothermal mineral deposit on the Mid-Atlantic Ridge at 26°N was performed in the fall of 1973 (R. SCOTT, RONA, MCGREGOR and M. SCOTT, 1974; M. SCOTT, R. SCOTT, RONA, BUTLER and NALWALK, 1974). The investigation, part of the Trans-Atlantic Geotraverse (TAG) project of the National Oceanic and Atmospheric Administration, included the measurement of near-bottom water temperatures. This report summarizes data obtained from a deep-towed camera equipped with thermistors, from an STD (salinity, temperature, depth) system, and from standard hydrographic casts over the TAG Hydrothermal Field on the southeast wall of the rift valley and adjacent portions of the Mid-Atlantic Ridge crest (RONA, MCGREGOR, BETZER and KRAUSE, 1974).

INSTRUMENTATION

Water temperature measurements parallel to the ocean bottom were made with a system similar to that used to make heat flow measurements in the sea floor. It consisted of thermistor temperature probes (Fenwall part number K2365) and a thermoprobe recorder (modified Alpine model 323) mounted on the frame of a deep-sea camera. Three thermistor temperature probes were mounted at heights of 0, 3, and 4 m above the base of the camera frame. The thermistors were calibrated at the factory prior to the experiment and recalibrated at 0°C in an ice bath following the experiment; drift correction of the order of 0·01°C (2 Ω) was applied to the data. The accuracy of the thermistors is ± 0·01°C and their precision is ± 0·004°C. The output of each thermistor was recorded sequentially at an interval of 45 s. A tiltmeter in the thermoprobe recorder used mercury switches to measure inclination from the vertical in 15° increments. The instrument package included thermistors, recorder, two deep-sea cameras (EG & G model 207A), two light sources (EG & G model 208),

*National Oceanic and Atmospheric Administration, Atlantic Oceanographic and Meteorological Laboratories, 15 Rickenbacker Causeway, Miami, Florida 33149, U.S.A.

†Department of Marine Science, University of South Florida, St. Petersburg, Florida 33701, U.S.A.

‡Division of Oceanography, UNESCO, Paris, France.

and an acoustic pinger (EG & G model 220). It was towed at ship's speeds between 15 and 45 m min^{-1} and maintained at a distance of about 5 m above the ocean bottom by means of a hydraulically-controlled deep-sea winch. This distance was determined to an accuracy of 2 m by the acoustic pinger. The visible wire angle was nearly zero so that the water depth measured by the ship's narrow-beam echo sounder (6° total beamwidth) was used as the depth of the ocean bottom at the instrument package. The estimated accuracy of depth below sea level of the instrument package is ± 100 m with corresponding uncertainty in the computation of potential temperature.

Vertical profiles of water temperature and salinity were made with two techniques, an STD system (Plessey model 9040) and hydrocasts. The accuracy of the STD system is ± 0·02°C for temperature, ± 0·02‰ for salinity, and ± 10 m for depth, with a precision of ± 0·005°C, ± 0·001‰, and ± 1 m, respectively. The hydrocasts involved simultaneous temperature measurements on two protected reversing thermometers and a single unprotected reversing thermometer to estimated accuracies of ± 0·02°C, and ± 0·1°C, respectively; the temperatures presented are the average of the measurements on the two protected thermometers. Quadruplicate measurements of salinity were made on each of two water samples from each Niskin bottle. All of the analyses were carried out at sea in an air conditioned laboratory with a Beckman (Model RS7B) induction salinometer using standard Copenhagen water as a reference. The average between duplicate analyses of the same water sample was 0·005‰. An acoustic pinger was used to determine height above the bottom of the STD and the hydrocasts, both of which were lowered to about 15 m from the ocean bottom. *In situ* temperature measurements were converted to potential temperature following BRYDEN (1973). Primary navigational control was by a satellite navigational system.

RESULTS

Two profiles parallel to the ocean bottom were made with the thermistor temperature probes mounted on the deep-sea camera. Thermistor

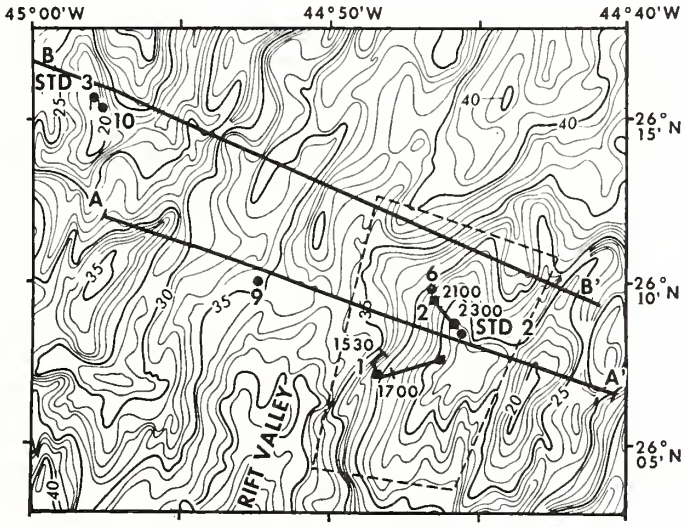

Fig. 1. Bathymetric map in hundreds of corrected meters of the area of investigation including the southeast and northwest walls of the rift valley of the Mid-Atlantic Ridge at 26°N based on a 2 × 4-km grid of narrow beam bathymetric profiles (MCGREGOR and RONA, in press). The TAG Hydrothermal Field is outlined by dashed lines (R. SCOTT, RONA, MCGREGOR and M. SCOTT, 1974). Locations are shown of thermistor profiles 1 and 2, hydrocast Stas. 6, 9 and 10, and STD profiles 2 and 3. Satellite fixes along thermistor profiles 1 and 2 are indicated by squares and times bracket temperature measurements listed in Table 1. Lines A–A′ and B–B′ are the locations of the bathymetric profiles shown in Figs. 5 and 6.

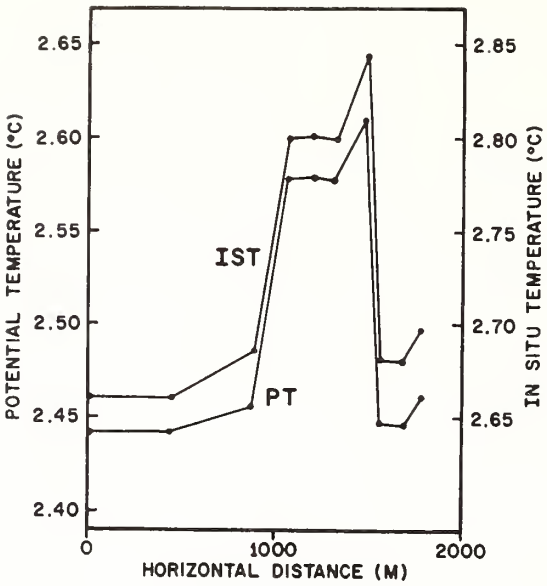

Fig. 2. Thermistor profile 1 of *in situ* (IST) and potential (PT) temperature between 2 and 20 m above the ocean bottom over a portion of the TAG Hydrothermal Field on the southeast wall (Fig. 1).

profile 1 (Figs. 1 and 2) is about 2 km long and crosses a portion of the TAG Hydrothermal Field on the southeast wall of the rift valley between depths of 3420 and 2910 m (Table 1). An abrupt increase of 0·16°C occurred while the instrument package was between 2 and 20 m above the ocean bottom along a horizontal distance of about 350 m between water depths of 3030 and 2950 m (Table 1). The water depths determined during thermistor profile 1 are corroborated by a relatively detailed isobath map (Fig. 1). The temperature increase attributable to adiabatic heating for the 80-m change in depth is about 0·05°C, as determined from an STD profile in an adjacent area, leaving a residual positive temperature anomaly of 0·11°C. Although the value of the temperature increase was taken from the lowermost thermistor, similar temperature increases were recorded on all three thermistors (Table 1). A temperature gradient of 8×10^{-3} °C m^{-1} warming toward the ocean bottom was measured over the 4-m long vertical thermistor array at the maximum of the temperature anomaly. This 0·11°C step-like positive temperature anomaly is equivalent to a

Table 1. *Temperatures measured along thermistor profiles* 1 *and* 2.

Thermistor profile 1 (Fig. 2)

Date	Time (GMT)	Depth of Bottom (m)	Distance of lowermost thermistor above bottom (m)	*In situ* temperature (°C) Thermistor position in vertical array (m above lowermost thermistor) 4	3	0
10 Oct. 1973	1530	3420	6	2.703	2.691	2.665
	1540	3410	8	2.706	2.693	2.665
	1550	3405	4	2.706	2.693	2.670
	1600	3400	4	2.706	2.693	2.667
	1610	3300	10	2.703	2.689	2.660
	1620	3120	11	2.700	2.688	2.660
	1630	3080	4	2.698	2.684	2.660
	1640	3030	2	2.726	2.715	2.686
	1644	3000	6	2.777	2.762	2.811
	1647	2990	20	2.789	2.769	2.819
	1650	2975	7	2.843	2.833	2.799
	1653	2960	6	2.860	2.853	2.845
	1655	2950	8	2.848	2.828	2.681
	1658	2920	10	2.709	2.702	2.681
	1700	2910	6	2.741	2.722	2.697

Table 1. *continued*

Thermistor profile 2

Date	Time (GMT)	Depth of Bottom (m)	Distance of lowermost thermistor above bottom (m)	*In situ* temperature (°C) Thermistor position in vertical array (m above lowermost thermistor) 4	3	0
8 Oct. 1973	2100	2800	2	2.936	2.929	2.895
	2110	2750	4	2.946	2.929	2.895
	2120	2700	8	2.951	2.929	2.914
	2130	2680	5	2.946	2.929	2.905
	2140	2620	10	2.946	2.939	2.914
	2150	2590	7	2.955	2.935	2.901
	2200	2520	8	2.942	2.929	2.905
	·2210	2500	4	2.951	2.939	2.914
	2220	2450	2	2.984	2.967	2.952
	2230	2400	9	3.012	2.977	2.943
	2240	2390	4	2.984	2.967	2.943
	2250	2380	11	3.003	2.986	2.990
	2300	2370	2	3.060	3.044	3.015

vertical rise and fall of the thermistor instrument package of about 300 m (estimated from Fig. 4) in horizontal distances of 100 and 50 m (Fig. 2). A vertical fluctuation of this magnitude is ruled out because no abrupt changes occurred in the ship's speed, the winch meter wheel readings, the bottom topography, or in the position of the camera relative to the bottom.

Thermistor profile 2 (Fig. 1) is 2·5 km long and traverses a portion of the TAG Hydrothermal Field. A gradual increase of 0·12°C was measured on the lowermost thermistor between 2 and 11 m above the bottom along a horizontal distance of 1·67 km between depths of 2800 and 2370 m (Table 1). The temperature increase was recorded on all three thermistors. Unlike the temperature increase registered along thermistor profile 1, this increase is wholly attributable to adiabatic heating for the 850-m change in depth as determined from an STD profile in the area.

Hydrocasts were made over the southeast wall (Sta. 6; 26°09′W: 44°47′W; Fig. 1), the median valley (Sta. 9; 26°10′N, 44°53′W; Fig. 1), and the northwest wall (Sta. 10; 26°15′N, 44°57′W; Fig. 1) of the Mid-Atlantic Ridge. The values of potential temperature calculated from reversing thermometers are similar at the three stations down to a depth of about 2000 m (Fig. 3). Below 2000 m the temperature profile over the southeast

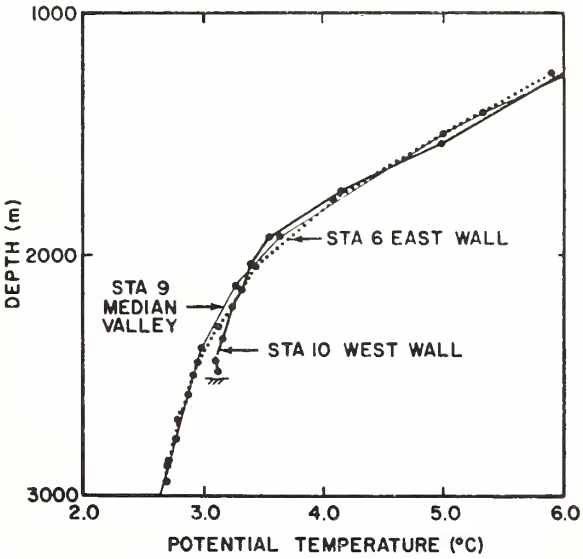

Fig. 3. Potential temperature profiles determined by reversing thermometers over the southeast (Sta. 6) and northwest walls (Sta. 10) of the rift valley (Sta. 9). Large dots are the depths of the reversing thermometers; the lowermost thermometers were about 15 m above the ocean bottom, shown beneath the profile at Sta. 10.

wall remains similar to the temperature profile in the rift valley while the temperature profile over the northwest wall attains a temperature 0·20°C warmer than the profile in the rift valley. The salinity distribution over the northwest wall was normal from 2000 to 2493 m, 15 m above the bottom (Sta. 10; Fig. 3).

STD profiles were made from the surface to within about 15 m of the ocean bottom on the southeast wall (STD 2; 26°08′N, 44°45′W; Figs. 1 and 4) and northwest wall (STD 3; 26°16′N, 44°58′W; Figs. 1 and 4) of the rift valley. Both STD profiles exhibit subadiabatic temperature gradients to a depth of about 2500 m where the gradient in STD 2 over the southeast wall becomes nearly adiabatic between 2500 m and the ocean bottom at about 2650 m. The adiabatic temperature gradient, using our measured values of temperature and pressure in the area investigated, was 1×10^{-5} °C m^{-1}.

DISCUSSION

Previous observations indicate the occurrence of relative warming and superadiabatic gradients of water at certain sites above or near mid-oceanic ridges (Knauss, 1962; Lister, 1963; Lubimova, von Herzen and Udintsev, 1965; Bodvarsson, Berg and Mesecar, 1967; Sclater and Klitgord, 1973; Williams, von Herzen, Sclater and Anderson, 1973). Two of the principal processes that may account for positive temperature anomalies are conductive transfer of heat through the ocean bottom and discharge of hydrothermal solutions from the ocean bottom into the overlying water column.

Evidence exists both for high conductive transfer of heat and for hydrothermal activity on the Mid-Atlantic Ridge at 26°N. High values of heat flow ranging between 2·0 and 8·6 HFU typical of oceanic ridges have been measured in sediments here (Langseth, Malone and Bookman, 1972). Suspended particulate matter recovered in hydrocasts beginning 15 m above the ocean bottom in this crestal region of the Mid-Atlantic Ridge contains anomalous concentrations of iron and manganese relative to suspended matter at corresponding depths in the adjacent Atlantic away from the ridge crest (Betzer,

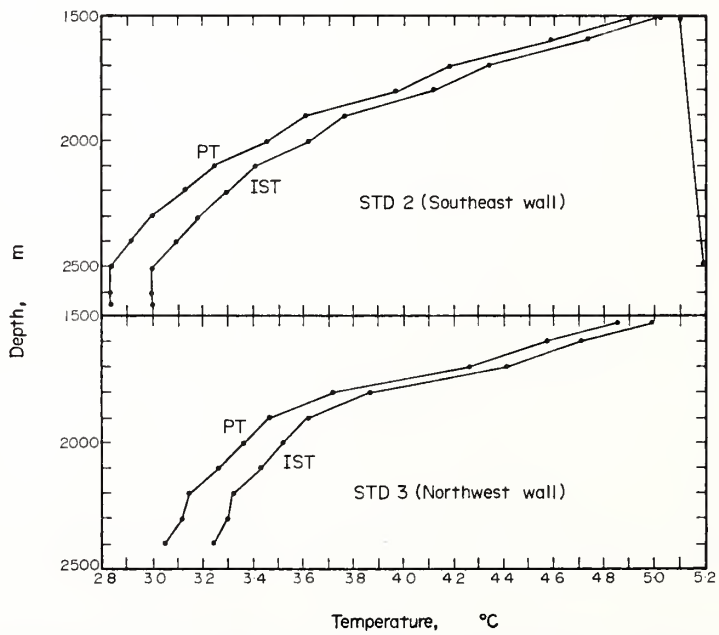

Fig. 4. STD profile 2 (Fig. 1) over the southeast wall and STD profile 3 (Fig. 1) over the northwest wall of the rift valley. The curve on the extreme right is the computed adiabatic gradient.

BOLGER, MCGREGOR and RONA, 1974). The aluminum content and Fe/Al ratios in near-bottom suspended materials over the ridge (2·6% and 1·5, respectively) differed markedly from ridge sediments (5·6% and 1·0, respectively). The aluminum content of near-bottom suspended matter did not increase over the ridge. It is apparent from these observations that the suspended material collected and analysed was not simply resuspended ridge sediments. Colloidal metal hydroxides have, of course, been observed to precipitate from hydrothermal solutions upon contact with the oxidizing oceanic environment (ZELENOV, 1964). The metal enrichment observed in the suspended particulate matter over the Mid-Atlantic Ridge is consistent with the hypothesis that hydrothermal exhalations account for the increase in sedimentary trace metal concentrations on oceanic ridges (BÖSTROM and PETERSON, 1966; CORLISS, 1971).

The processes responsible for the observed enrichment of particulate matter in metals would be expected to add silica and fluoride to near-bottom water. Contrary to expectation, no significant increases were found in either silica/chlorinity or fluoride/chlorinity ratios measured in the same near-bottom water samples from the Mid-Atlantic Ridge crest at 26°N (FANNING, BETZER, BOLGER, MILLER, MCGREGOR and RONA, 1974). These data indicate that, if hydrothermal solutions had been discharged from this region of the ridge crest, then the silica and fluoride had been diluted to near-background levels and only a small residual of metal-rich particulate matter remained in suspension.

Positive temperature anomalies were measured at sites over the southeast and northwest walls of the rift valley at 26°N. The regional evidence cited allows either conductive transfer of heat or hydrothermal discharge as a heat source for these anomalies; however, the geologic setting provides some insight into the nature of the individual anomalies. Over the TAG Hydrothermal Field on the southeast wall of the rift valley an abrupt and narrow temperature increase of 0·11°C accompanied by a gradient inversion was measured parallel to the ocean bottom in thermistor

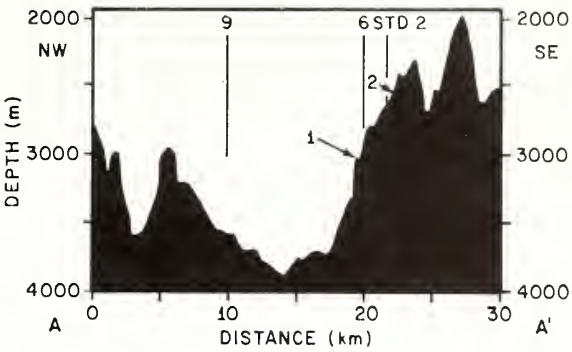

Fig. 5. Reproduction of narrow beam bathymetric profile A–A′ (Fig. 1) across the area investigated. Thermistor profiles 1 and 2, hydrocast Stas. 6 and 9, and STD profile 2, are projected on to the bathymetric profile.

profile 1 (Figs. 1 and 2). This temperature anomaly occurred in the vicinity of a step-like topographic level interpreted as a portion of fault block in the wall of the rift valley (Fig. 5) Bottom photographs made concurrently with the temperature increase reveal pillow lavas and basalt breccia with what appears to be hydrothermal material (MCGREGOR and RONA, in press). Identification of the material dredged from the site of the temperature anomaly as hydrothermal is based on the rapid rates of accumulation and purity of manganese oxides present (M. SCOTT, R. SCOTT, RONA, BUTLER and NALWALK, 1974). Sediment clouds induced by occasional impact of the camera compass in thin sediment patches in the vicinity of the temperature anomaly indicate that near-bottom oceanic currents were negligible during the period of thermistor profile 1. The narrow, abrupt character of this anomaly, as well as its occurrence at a site where hydrothermal material is abundant and where a fault zone may act as a conduit for hydrothermal solutions, favor interpretation that the anomaly resulted from hydrothermal discharge.

Over the northwest wall of the rift valley a hydrocast (Sta. 10) measured a relative temperature increase of 0·20°C in the lower 425 m of the water column (Figs. 1 and 3). No increase in either silica/chlorinity or fluoride/chlorinity ratios was found in water samples recovered concurrently with the temperature recording. Downward mixing of overlying water is ruled out as a source

for the temperature increase because the overlying water column is subadiabatic and therefore stable as determined by STD profile 3 (Figs. 1 and 4). Advection of a warmer water mass from the east or west is considered unlikely because the water was cooler at corresponding depths to the east in the rift valley (Figs. 1 and 3) and to the west in STD 3 (Fig. 6); this observation does not exclude the possibility of advection of warmer water as a bolus rather than as a laterally continuous water mass. Only a few fragments of basalt were recovered in seven attempts to dredge the northwest wall at the site of the temperature anomaly. Hydrothermal material dredged from the southeast wall at the TAG Hydrothermal Field is sufficiently friable so that, if present, it is likely that samples would have been recovered from the site dredged on the northwest wall. The absence of hydrothermal material from the site of the anomaly suggests either that the anomaly is due to *in situ* conductive transfer of heat, or to advection of a bolus of water which had already been warmed by conductive transfer or hydrothermal discharge.

The question remains why temperature anomalies were not observed at thermistor profile 2 and at Sta. 6 over the TAG Hydrothermal Field on the southeast wall of the rift valley (Figs. 1 and 3). The intermittent activity of oceanic currents inferred from the presence of ripple marks in thin sediment revealed by bottom photography and the lack of topographic closure create conditions which favor the rapid dissipation of heat. These conditions on the Mid-Atlantic Ridge at 26°N are in marked contrast to those at hydrothermal sites in the Red Sea (Degens and Ross, 1969). In the Red Sea, temperature increases of the order of 40°C were measured within tens of meters of the sea floor where hypersaline solutions discharge into enclosed basins (Ross, 1972). The most probable answer to the question posed is that spatial and temporal variations exist in the generation of temperature anomalies in near-bottom water and that these variations are related to the nature of the heat sources and to the movements of the water. Long-term temperature, salinity, and near-bottom current measurements over active oceanic ridges should help to determine the frequency and significance of heat fluxes to the deep ocean (Williams and von Herzen, 1974).

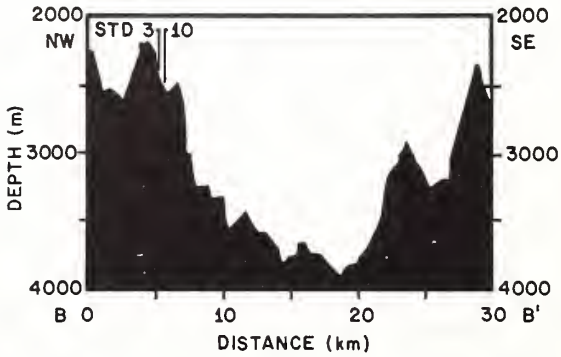

Fig. 6. Reproduction of narrow beam bathymetric profile B–B′ (Fig. 1) across the area investigated. Hydrocast Sta. 10 and STD profile 3 are projected on to the bathymetric profile.

Acknowledgements—Charles A. Lauter, Jr., of NOAA, assembled and operated the heat flow system which Dr. George Peter of NOAA loaned to us. Dr. Ants Leetmaa of NOAA advised us on the reduction and interpretation of temperature data and read the manuscript. Drs. Kendall Carder and Susan Betzer of the University of South Florida made helpful suggestions for improving the manuscript.

Captain Lavon L. Posey, Cdr. Walter S. Simmons, Lt. Paul M. Duernberger, and other officers and crew of the NOAA ship *Researcher* provided strong support.

This work was supported by NOAA and the Office of Naval Research under contract N 00014-72A-0363-0001 to the University of South Florida.

REFERENCES

Betzer P. R., G. W. Bolger, B. A. McGregor and P. R. Rona (1974) The Mid-Atlantic Ridge and its effect on the composition of particulate matter in the deep ocean. *American Geophysical Union Transactions, EOS*, **55**, 293.

Bodvarsson G., J. W. Berg, Jr. and R. S. Mesecar (1967) Vertical temperature gradient and eddy diffusivity above the ocean floor in an area west of the coast of Oregon. *Journal of Geophysical Research*, **72**, 2693–2694.

Böstrom K. and M. N. A. Peterson (1966) Precipitates from hydrothermal exhalations on the East Pacific Rise. *Economic Geology*, **61**, 1258–1265.

Bryden H. L. (1973) New polynomials for thermal expansion, adiabatic temperature gradient and potential temperature of sea water. *Deep-Sea Research*, **20**, 401–408.

CORLISS J. B. (1971) The origin of metal-bearing submarine hydrothermal solutions. *Journal of Geophysical Research*, **76**, 8128–8138.

DEGENS E. T. and D. A. ROSS, editors (1969) *Hot brines and recent heavy mineral deposits in the Red Sea*, Springer-Verlag, 600 pp.

FANNING K. A., P. R. BETZER, G. W. BOLGER, G. R. MILLER, B. A. MCGREGOR and P. R. RONA (1974) Silica and fluoride over the TAG Hydrothermal Field. *American Geophysical Union Transactions, EOS*, **55**, 293.

KNAUSS J. A. (1962) On some aspects of the deep circulation of the Pacific. *Journal of Geophysical Research*, 2493–3954.

LANGSETH M. G., JR., L. E. MALONE and C. A. BOOKMAN (1972) Sea floor geothermal measurements from *Vema* cruise 25: New York. Lamont-Doherty Geological Observatory, Technical Report 4, CU-4-72, Office of Naval Research Contract N00014-67-A-0108-0004, Technical Report 2, CU-2-72, National Science Foundation Grant GP5356, Technical Report 2, CU-2-72, National Science Foundation Grant GA1412, 159 pp.

LISTER C. R. B. (1963) Geothermal gradient measurement using a deep-sea corer. *Geophysical Journal*, **7**, 571–583.

LUBIMOVA E. A., R. VON HERZEN and G. B. UDINTSEV (1965) On heat transfer through the ocean floor. In: *Terrestrial heat flow*, W. H. K. LEE, editor, American Geophysical Union Geophysical Monograph **8**, pp. 78–86.

MCGREGOR B. A. and P. A. RONA (in press) Crest of Mid-Atlantic Ridge at 26°N. *Journal of Geophysical Research*.

RONA P. A., B. A. MCGREGOR, P. R. BETZER and D. C. KRAUSE (1974) Anomalous water temperatures over Mid-Atlantic Ridge crest at 26°N. *American Geophysical Union Transactions, EOS*, **55**, 293.

ROSS D. A. (1972) Red Sea hot brine area: revisited. *Science*, **175**, 1455–1457.

SCLATER J. G. and K. D. KLITGORD (1973) A detailed heat flow, topographic, and magnetic survey across the Galapagos spreading center at 86°W. *Journal of Geophysical Research*, **78**, 6951–6975.

SCOTT M. R., R. B. SCOTT, P. A. RONA, L. W. BUTLER and A. J. NALWALK (1974) Rapidly accumulating manganese deposit from the median valley of the Mid-Atlantic Ridge. *Geophysical Research Letters*, **1** (8), 355–358.

SCOTT R. B., P. A. RONA, B. A. MCGREGOR and M. R. SCOTT (1974) The TAG hydrothermal field. *Nature*, **251**, 301–302.

WILLIAMS D. L. and R. P. VON HERZEN (1974) Heat loss from the earth: new estimate. *Geology*, **2**, 327–328.

WILLIAMS D. L., R. P. VON HERZEN, J. G. SCLATER and R. N. ANDERSON (1973) Lithospheric cooling on the Galapagos spreading center, East Pacific. *American Geophysical Union Transactions, EOS*, **55**, 244.

ZELENOV K. K. (1964) Iron and manganese in exhalations from the submarine volcano of Banu Wuhu (Indonesia). *Doklady Akademii nauk SSSR*, **155**, 1317–1320.

Reprinted from: *Geological Society of America, Abstracts with Programs 7*, No. 7, 1263.

SUBMARINE HYDROTHERMAL ACTIVITY AND SEAFLOOR SPREADING AT 26°N, MAR

Scott, Robert B., Department of Geology, Texas A&M University, College Station, Texas 77843; Malpas, John, Department of Geology, Memorial University, St. Johns, Newfoundland, Canada; Udintsev, Gleb, Institute of Oceanology, USSR Academy of Sciences, Moscow, USSR; Rona, Peter A., NOAA-AOML, Miami, Fla., 33149

On a joint USSR-US cruise of the R/V KURCHATOV in 1975, hydrothermal deposits were found 18 km southeast of the rift valley in the direction of crustal spreading from the TAG hydrothermal field located on the eastern rift valley wall at 26°N, MAR. Veins of hydrothermal manganese oxides and analcite are within altered basalt talus. The talus is also encrusted with two layers of manganese oxides: a basal layer of hydrothermal manganese (40% Mn, 0.1% Fe, 550ppm Cu, 920ppm Ni, 50ppm Co, 2800 ppm Ba) that varies between 1 and 10 mm thick and an upper layer of hydrogenous ferromanganese (11.1% Mn, 16.4% Fe, 670ppm Cu, 1400ppm Ni, 1840ppm Co, 2000ppm Ba) that varies between 0.5 and 2 mm thick. The hydrothermal crust consists of birnessite that forms submetallic, grayish-brown laminations; from SEM studies the crust shows the typical boxwork of birnessite plates. In contrast, the hydrogenous layer is extremely botryoidal, amorphous to X-rays and shiny black; SEM studies show each botryoid to be massive, without any crystalline textures. The initiation of hydrogenous ferromanganese growths mark the end of local hydrothermal activity. Using a growth rate of 25 mm/my based upon the Cu+Ni+Co content, the hydrothermal activity lasted up to 0.25 my after the formation of the rift valley wall. Hydrothermal activity must persist along segments of the rift valley wall for periods of at least one my, forming strips of hydrothermally altered ocean crust. The hydrothermally affected segment of the rift valley wall forms the young end of a highland ridge that is transverse to the rift axis and parallel to the crustal spreading direction; an abnormal concentration of faults strike parallel to the rift axis and segment this ridge. Cold seawater enters these fault zones, reacts with hot basaltic rock and exits along similar fault zones, forming hydrothermal deposits.

Reprinted from: *Geological Society of America, Abstracts with Programs 7*, No. 7, 1285-1286.

TEMPORAL AND SPATIAL SUBSTRATE VARIATION IN THE NEW YORK BIGHT APEX

Stubblefield, W. L., Atlantic Oceanographic and Meteorological Laboratories, Miami, Florida 33149; Permenter, R. W., Atlantic Oceanographic and Meteorological Laboratories, Miami, Florida 33149, NOAA

Quarterly monitoring of selected areas in the New York Bight Apex, over a one and one-half year span, indicates a pronounced temporal and spatial variation within the upper few millimeters of the substrate. By means of sidescan sonar, bottom grab sampling, and bottom photography, bottoms ranging from coarse, clean sand to muddy, very-fine sand were observed. A temporal variation became apparent when the sampling stations were reoccupied with the aid of precision navigation. The monitoring, which included samples taken shortly before and after a decadal storm, suggests that the substrate mobility is most prevalent in the vicinity of Long Island and New Jersey shorelines and in Christiaensen Basin which marks the head of the Hudson Shelf Valley. Sidescan records from nearshore Long Island indicate development of sand wave-like forms during the winter and subsequent degradation during the summer months. The sand wave development is probably associated with the peak-flow events of the winter storms. The features are of negligible relief, and may be degraded by the action of bottom wave surge and benthic organisms. Christiaensen Basin, which is characterized by muddy, very-fine sand in its center, is the settling site for much of the sewage sludge material presently being dumped by New York City. Sidescan records show that the Basin is characterized by a patchy bottom pattern. The patches are irregular in shape, frequently elongated to the northwest and vary in shape and position between observations which support the suggestion of temporal mobility of the bottom sediments.

59

Reprinted from: *Journal of Sedimentary Petrology 45*, No. 1, 337-358.

SEDIMENT RESPONSE TO THE PRESENT HYDRAULIC REGIME ON THE CENTRAL NEW JERSEY SHELF[1]

WILLIAM L. STUBBLEFIELD, J. WILLIAM LAVELLE AND DONALD J. P. SWIFT
National Oceanic and Atmospheric Administration, Atlantic Oceanographic and Meterological Laboratories, 15 Rickenbacker Causeway, Miami, Florida 33149

THOMAS F. McKINNEY
Dames and Moore Inc., 14 Commerce Drive, Cranford, New Jersey 07016

ABSTRACT: Petrographic data, from vibracores and grab samples collected on the Central New Jersey Shelf, suggest a substrate still actively responding to the hydraulic regime. Radiocarbon dates of shell material from the ridge and swale topography indicates aggradation of the ridge's crest during the last 500 years and exposure of earlier Holocene material in the deeper troughs of the area. The samples from both the cores and the surficial samples were investigated for heavy mineral percentages and grain size analysis in addition to radiocarbon dating. The concentration of heavy minerals into disseminated bands, as observed in the vibracores, is compatible with sediment transport by sand ripples on the ridge's flanks. The grain size variation was subjectively analyzed by applying a Q-mode factor analysis which produced three distinct groupings of the grain size distribution. Each grouping is found to characterize a particular part of the ridge topography. Fine sand and moderate sorting occurs on the flanks, medium to fine sand and moderate sorting occurs on the crests whereas two populations are found in the troughs; coarse, poorly sorted sands and very fine, well sorted sands. This textural variation supports a hypothesis of up-flank rheologic and suspensive transport of medium and fine sand during intense storms and subsequent down-flank winnowing of fine sand during less intense meterological events. The radiocarbon dates indicate that size fractionation and heavy mineral concentrations are subsequent to isolation from a beach environment.

INTRODUCTION

This paper assesses petrographic and stratigraphic aspects of the central New Jersey Shelf as a guide to the origin of surficial sediments, and of the ridge and swale topography into which they are molded. Origins proposed for this topography include: (a) mainland and barrier beaches overstepped by a transgressive sea (Veatch and Smith, 1939; Shepard, 1963; Emery, 1966; Garrison and McMaster, 1966; Uchupi, 1970); (b) subaerial beach ridges dating from earlier Pleistocene stillstands (Sanders, 1962; Dietz, 1963; Kraft, 1971); (c) modern submarine ridges formed subsequent to the Holocene transgression (Schlee and Pratt, 1972; Duane, *et al.*, 1972); (d) drowned stream interfluves (McKinney and Friedman, 1970); and (e) formation at the foot of the shoreface with subsequent modification by the shelf hydraulic regime (Swift, *et al.*, 1972a).

This study is one of several detailed examinations of the continental shelf substrate in the New York Bight being pursued by NOAA's Miami-based Atlantic Oceanographic and Meteorological Laboratories in support of NOAA's Marine Ecosystem Analysis (MESA) program. The area was selected as a prominent offshore example of the ridge and swale topography of the Middle Atlantic Bight. This class of shelf floor topography is extensively fished for both surf clams (*Spisula*) and bottom fish, and is under increasing pressure for use as an ocean dumpsite. For both purposes, it is important to determine the stability of the substrate, and the pattern and rate of sediment transport. This particular study is concerned with present response of ridge and swale topography on the central New Jersey shelf to the hydraulic regime as indicated by analysis of grab samples and vibracores gathered by R/V VENTURE during July, 1972. The reader is referred to McKinney, *et al.* (1974) for an analysis based on side-scan records and submersible observations.

[1] Manuscript received January 10, 1974; revised September 23, 1974.

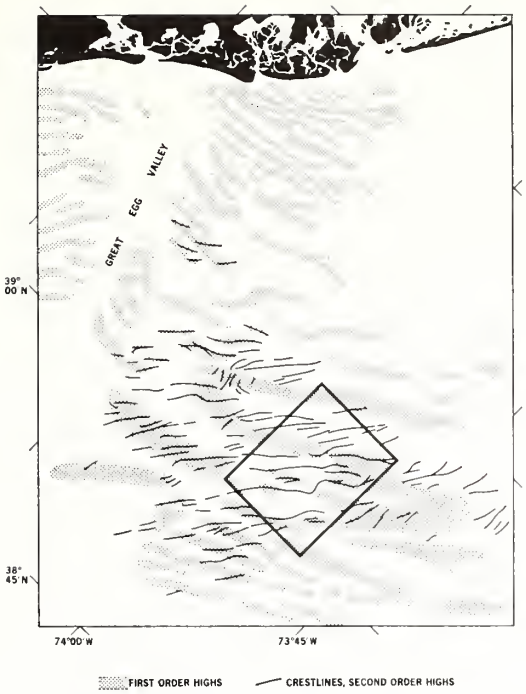

FIG. 1.—Index map of the New Jersey shelf with the study area outlined. The first order highs are shown as stippled areas and the crest line of the second order highs as solid lines (From McKinney, *et al.*, 1974).

Study Area

Fifty kilometers east-southeast of Atlantic City, New Jersey, on the central continental shelf, there exists a pronounced system of large scale ridges and swales at two characteristic wavelengths (Fig. 1). A third, small scale system consists of bands of contrasting sediment types with negligible relief (McKinney, *et al.*, 1974). These three features appear to be superimposed on a broad shoal-retreat massif, a constructional feature resulting from the retreat of a littoral drift depositional center associated with a retreating estuary mouth. Swift *et al.* (1972b) have related this massif with the ancestral Schuylkill River. McKinney, *et al.*, (1974) have inferred that the large first order ridges were initiated in a nearshore or estuary mouth environment, possibly tide dominated, while the second order forms were formed at a later period on the open shelf.

Examination of a 1:125,000 scales ESSA bathymetric map contoured at one-fathom intervals (Stearns, 1967), suggests that the first and second order ridge systems are oriented in a northeasterly direction averaging 54° for the first order system and 40° for the second (Fig. 1). Ridge spacing averages 3.1 km (1.9 nm) with the range varying from 1.2 km (0.75 nm) to 4.85 km (3 nm). Average side slopes are 0.4° with the minimum being 0.1° and a maximum of 0.9°.

METHODS

Field Methods

Grab samples were collected in an area bounded by 39°00′N and 39°10′N latitude; 73°45′W and 74°00′W longitude with navigation provided by dual, automatic tracking Loran A/C receivers. The grab samples were taken by a Shipek bottom sampler approximately every 0.8 km (0.5 nm) along LORAN lines 1.62 km (1 nm) apart (Fig. 2). A more dense sample net, transecting local topography and normal to the initial LORAN lines, was completed in the western sector of the sampling area. It is in this western sector that the maximum ridge slope is found.

Each sample was categorized as to crest, flank, and trough from Stearns (1967) bathymetric map. The classification of the samples was achieved by drawing cross sections normal to the regional bathymetry and dividing the ridge system into respective environments on the basis of change in slope. These environments, crest, flank, and trough, were identified throughout the sectors of the study area by particular depths which correspond to the change in slope. Each sample was associated with an environment by evaluation of that sample relative to its geographic position and depth. Position of sample relative to flank, crest, or trough was checked by comparison with the record of the fathometer which was left running and was annotated during the period of grab sampling. This approach affords an objective labelling of each sample relative to the ridge system.

In addition to the 191 grab samples collected, four vibracores were obtained. Core V-1 was taken on a crest, core V-2 from a trough, core V-3 from the lower reaches of a flank, and core V-4 represents the upper flank (Fig. 2). These four cores, from different parts of the ridge system, afford a total cumulative penetration relative to sea level of 15.6 m (Fig. 3).

Laboratory Techniques

The Shipek grab samples were split from a kilogram to approximately 60 gm using the random scoop technique suggested by Shepard and Young (1961), and were dry sieved using 3-inch U. S. Standard Sieve to separate the fraction coarser than 2 mm. The sand and silt

fraction was weighed on a top-loader Metler balance and placed in an ultrasonic water bath for a period of 1 to 3 hours depending on the amount of silt and clay present in the sand. The ultrasonic bath tends to disaggregate the finer particles (Gipson, 1963) and disperse both the silt/clay and sand size particles (Kravitz, 1966) allowing for a more complete separation of the silt/clay from the sand. The samples were wet sieved using a size 230 mesh to remove the silt/clay < 0.625 mm and dried. After drying, the samples were weighed to determine the weight percentage of silt/clay. The vast majority of the 191 samples contained less than 1% fines with only 3 samples exceeding 3% fines and 19 samples surpassing 2% concentration of fines.

The sand fraction was further reduced by splitting with a microsplitter to 10-gm samples and analyzed in regard to size distribution by a settling tube [Rapid Sediment Analyzer (RSA)], calibrated against sieves (Sanford and Swift, 1971). The RSA, when electronically coupled with a Hewlett-Packard 9810 calculator, prints out a grain size distribution in quarter phi units and the mean, standard deviation, skewness, and kurtosis of each sample. The values are derived by moment calculations based on a sand fraction recalculated to 100%. The silt-clay fraction was not included in the moment calculations in order to maintain a hydrodynamically similar sample, since the silt/clay material possesses values for incipient motion and entrainment velocity that differ widely from those of sand-size material.

Weight percent of heavy minerals was determined on selected sand fractions from both the Shipek grab samples and the vibracores. Since the heavier minerals are generally finer than 0.42 mm, the sand was sieved to this size so as to increase the percent of heavy minerals per sample. We were concerned with relative concentration among samples rather than an absolute measurement of concentration. The samples were dried, weighed, and placed in separatory funnels using tetrabromoethane ($CHBr_2$-$CHBr_2$) to effect separation. The heavy minerals were drained from the funnel, dried, weighed, and a weight percentage calculated (Table 1).

The four vibracores, after removal from the core barrel, were maintained in an upright position at approximately 5°C. The cores were transversely cut into 70 cm lengths and radiographed. The cores were then longitudinally split, immediately described for color, structure, lithology, faunal content, and photographed.

TABLE 1.—*Percent of heavy minerals in the sand*

V-1		V-4		Surficial	
Sample	%	Sample	%	Sample	%
75 cms	0.85	2 cms	2.27	19 (T)	15.16
85	1.14	10	4.29	22 (F)	3.92
95	6.64	20	1.63	24 (F)	4.34
100	3.74	40	1.86	26 (C)	7.99
133	0.04	45	1.31	28 (C)	4.21
140	1.35	50	4.98	30 (F)	5.34
150	1.54	60	5.13	38 (F)	4.50
160	1.19	70	2.43	40 (F)	3.90
170	0.24	80	3.30	42 (F)	4.99
175	0.40	90	4.35	48 (C)	22.09
185	0.17	100	2.12	58 (T)	39.4
195	1.18	110	3.97	73 (C)	6.18
		129	1.03	76 (T)	5.59
		130	4.33	80 (C)	4.54
		140	3.52	102 (C)	6.09
		160	4.78	103 (C)	6.46
		170	2.61	104 (C)	6.10
		180	1.87	112 (T)	5.39
		190	2.52		
		200	1.75		
		210	3.61		
		220	1.56		
		240	0.64		
		250	1.60		
		260	2.15		
		270	2.51		

The samples from a core are prefixed by a "V." The surficial sands are marked to reflect the part of the ridge system the sample was taken, *e.g.* Crest (C), Flank (F), or Trough (T).

One half of the split core was sampled every 10 cms within the sand units or at any observable grain size discontinuity and processed similarly to the grab samples in order to determine grain size distribution and related statistical parameters. The other half of the core was partially impregnated with CIBA epoxy #6005 and 6010 and CIBA hardeners #830 and 850 to a recipe of 4:4:1:3. The partial impregnation, in addition to providing archival material, facilitates the investigation of *in situ* grain size distribution as well as other sedimentary structures.

Shell material from cores V-2, V-3, and V-4 were radiocarbon dated by facilities at the Department of Geology, University of Miami, Florida. Samples were selected in an attempt to establish the Pleistocene-Holocene boundary and to determine if ridge aggradation has occurred subsequent to passage of the beach environment. See Table 2 for the samples, sample location, depth in the core, and radiocarbon dates.

Factor Analysis

To detect patterns in the regional distribution of grain size characteristics in the 191 grab

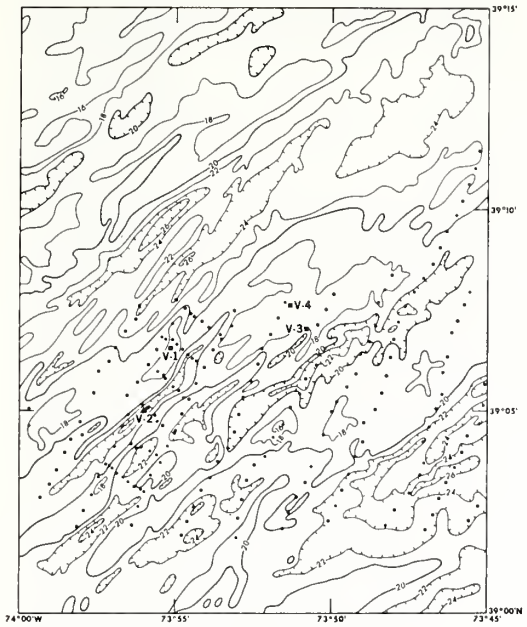

FIG. 2.—Bathymetry of the study area. The Shipek grab samples are shown as solid circles and the vibracores as squares. The core number appears beside the position.

samples, a Q-mode factor analysis was applied. Factor analysis, besides its inherent ability to process copious quantities of bulky data quickly, provides an objective approach to the interpretation. Factor analysis is rapidly becoming a common tool among sedimentologists and thus does not warrant a detailed discussion of techniques. Interested readers, however, are referred to the papers of Imbrie and Van Andel (1964) and Klovan (1966).

The data input consists of the grain size distribution of individual samples. For this study three eigenvalues were found to represent 94% of all sample interrelations. The remaining 6% are scattered among several eigenvalues and may be discarded as ambient noise. With the exception of three, all samples have a communality above 0.80 and the majority exceed 0.90, highly suggestive that a satisfactory grouping description is obtained for the bulk of the samples.

EVOLUTION OF THE STUDY AREA

Quaternary History Based on Radiocarbon Dating and Stratigraphy

The four vibracores from the study area (Fig. 2) provide an insight to its late Quaternary history. Radiocarbon dates of fauna found in the cores (Fig. 3) give maximum ages varying from less than 500 years B.P. for the ridge sand units to greater than 36,000 years B.P. for silty-clay beneath the surficial sands in the troughs. Using a date of approximately 16,000 years B.P. for the Pleistocene-Holocene boundary in this area (Emery and Uchupi, 1972), the cored part of the ridges are late Holocene, the surficial trough sands are middle Holocene, and the underlying silty clay (cores V-3 and V-2) is late Pleistocene. These dates and the lithologies of their matrices allow us to infer the late Quaternary history.

Radiocarbon dates, site elevation, and depth of core penetration suggest that cores V-2 and V-3, which represent late Pleistocene marine

TABLE 2.—*Radiocarbon dates of selected fauna from the study area*

Core	Position	Fauna dated	Depth below sea level	Apparent age (years B.P.)
V-2	39°05.1′N 73°55.6′W	*Mercenaria mercenaria*	45.63 m (83)	29,700 ± 650
V-2	Same	*Crassostrea virginica*	46.95 m (125)	32,150 ± 600
V-3	39°05.7′N 73°50.5′W	*Mercenaria mercenaria*	41.88 m (8)	10,950 ± 360
V-3	Same	*Ensis directus*	43.30 m (150)	22,035 ± 665
V-3	Same	*Mercenaria mercenaria*	44.30 m (250)	25,300 ± 1040 1200
V-3	Same	*Mercenaria mercenaria*	45.50 m (370)	> 36,000
V-4	39°06.9′N 73°31.3′W	*Placopecten magellanicus*	36.90 m (60)	< 500
V-4	Same	*Placopecten magellanicus*	37.55 m (125)	3,760 ± 70
Trough Sample #156	39°05.6′N 73°55.1′W	*Crassostrea virginica* *Mercenaria mercenaria*	44.00 m	10,050 ± 170

The depth from top of the core to the dated fauna, in centimeters, appears in parentheses beside Depth Below Sea Level.

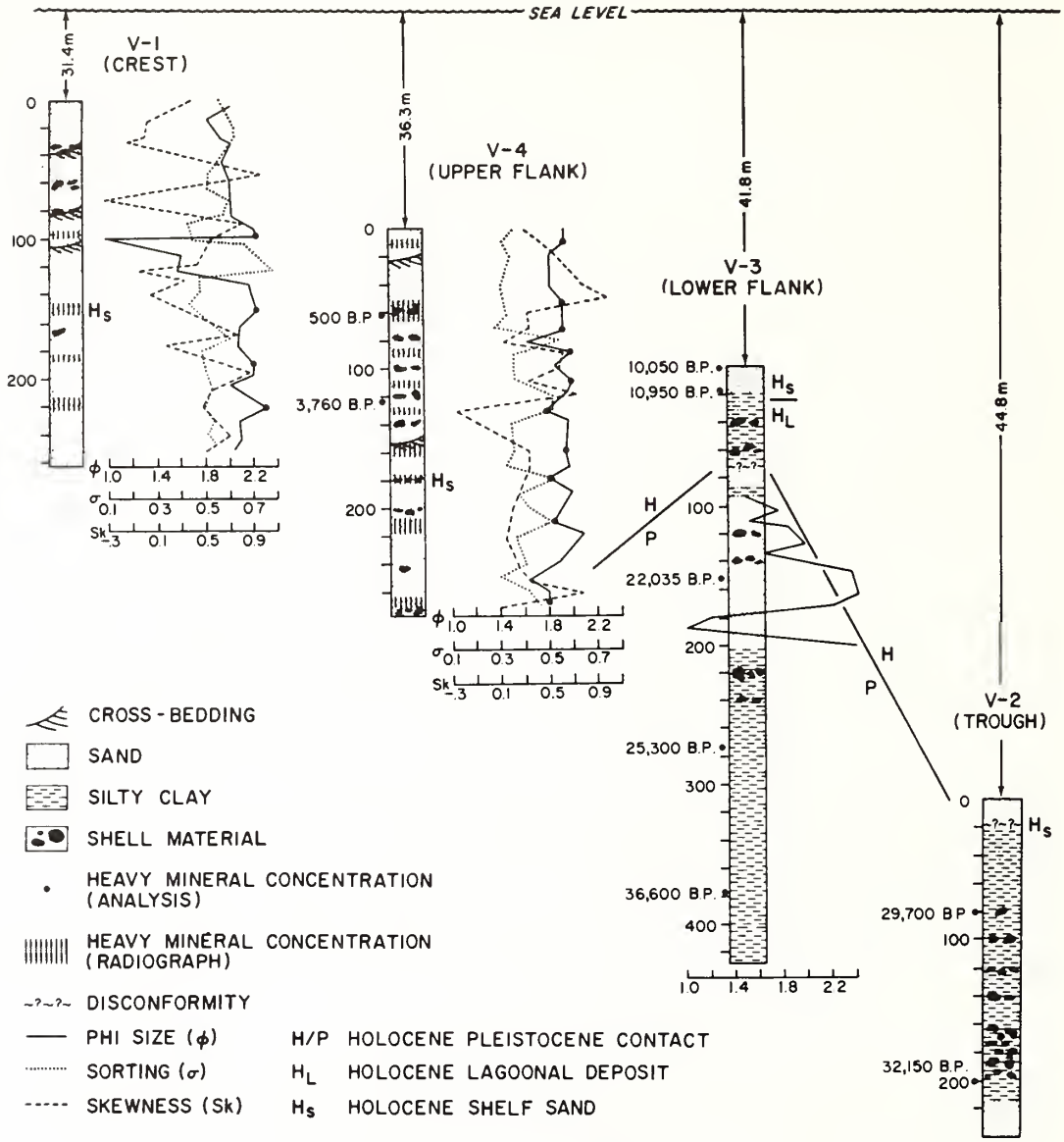

FIG. 3.—Lithic log of the 4 vibracores and mean grain size in quarter phi (ϕ) units within the sand. The standard deviation (σ), which is an indicator of sorting, and the skewness (Sk) are plotted for the crestal and upper flank cores. Heavy mineral concentrations in the sand are shown on both the lithic log and the mean grain size log. Vertical scale, in 20 cm intervals, is along the left edge of each core.

regression and early Holocene transgression, overlap by at least 1 m and should be correlative. The site of core V-3 is 5.6 km (3.48 n.m.) seaward of core V-2, but is 3 m shallower; it is on the lower flank of a ridge system while core V-2 is in a trough (Fig. 2). However, the sedimentary features of the cores offer little basis for a direct correlation.

The sandy silt of core V-2 and the middle sand zone and lower silty clay in core V-3 are Pleistocene in age. They are correlated with the late Wisconsin regression as dated by Milliman and Emery (1968). Dates of shelly, silty clay of core V-2 and the bioturbated lower silty clay of V-3 (Fig. 4), fall below the sea level curve of Milliman and Emery as indicated by Fig. 5. These units appear to have been deposited on a muddy inner shelf in advance of a

FIG. 4.—Bioturbation in the lower silty clay of core V-3. The interval shown is from 392 to 410 cms below the top of the core.

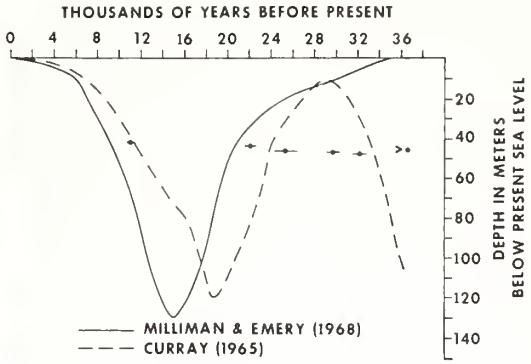

FIG. 5.—Comparison of data from this study with sea level curves proposed by Milliman and Emery (1968) and Curray (1965). The sea level curve suggested if a line were drawn through the dated samples from this study differs from that of other workers. This variance may be a product or regional differences in isostatic adjustment associated with the advance and retreat of the ice sheet.

prograding shoreline; which feature is perhaps indicated by the upward coarsening sand in the middle of core V-3 (Fig. 3). Radiocarbon dates and depths for this sand unit are close enough to the sea level curve of Milliman and Emery to qualify as nearshore deposits. The dates from the silty muds come from depths within the core that are 15 to 40 meters beneath the Milliman and Emery sea level curve (Fig. 5). These sands may have been deposited in deeper water, or their dates may reflect later subsidence of the New Jersey shelf as subcrustal material flowed northward during deglaciation (Emery and Uchupi, 1972).

Whereas evidence from this study suggests a local difference in sea level from that postulated by Milliman and Emery (1968) and Curray (1965), a statement based on only two cores is premature. If a local difference does exist, however, it may be an artifact of sampling localities; Curray (1965) used dated samples from the continental shelf of the Gulf of Mexico, whereas Milliman and Emery (1968) used a compilation of Atlantic Shelf data but with only one date between 24,000 and 36,000 years B.P. taken north of Cape Hatteras, North Carolina. A coring program scheduled in this area may resolve the apparent difference.

The upper silty clay of core V-3 is of questionable origin. If the 22,035 year old sand indeed marks seaward passage of the late Wisconsin shoreline, then the Pleistocene-Holocene boundary must occur between the sand and overlying clay. Physical examination of core V-3 suggests such a disconformity (Fig. 3). The clay would therefore mark the landward passage of the Holocene lagoonal belt.

The overlying surficial sand may have been deposited as the early Holocene barrier transgressed the lagoon. Analysis of denser coring nets on the New Jersey inner shelf (Stahl, *et al.*, 1974) shows that closer to the modern coast, basal barrier sands overlie lagoonal muds of Holocene age. However, the barrier sands

are only a meter or so thick as a consequence of erosional retreat of the shore face, which leveled the barrier superstructure and redistributed it as a nearshore marine sand sheet resting disconformably on the truncated barrier sands. The sharp contrast in core V-3 (Fig. 3) between the supposed lagoonal mud and the surficial sand may indicate that here the barrier veneer has been completely removed and that nearshore marine sands rest directly on the lagoonal clays. The inferred lagoonal deposit appears to be missing altogether in core V-4, suggesting that the Holocene disconformity has appreciable relief.

The date obtained for the upper surficial sand in core V-3 is on the upper margin of the Milliman and Emery (1968) sea level curve. If the date is valid, then the anomalously high position of the date (Fig. 5) may indicate that additional uplift other than glacial rebound has transpired, since isostatic compensation associated with deglaciation was complete by this time.

DEPOSITIONAL HISTORY OF THE HOLOCENE SAND SHEET AS INFERRED FROM CORE PETROGRAPHY

Grain Size Variation

The history of the continued aggradation of the Holocene sand sheet after the passage of the shoreline and the evolution of the ridge and swale topography must be contained in the flank core, V-4, and the crestal core, V-1 (Fig. 3). If the upper flank core V-4 is characteristic of the medial portion of the sand sheet and the crestal core, V-1, of its top, then the sheet has coarsened irregularly upwards from fine to medium sand (Fig. 3). The range of mean grain size does not appreciably overlap, however, it seems probable that there has been a lateral size segregation as well, with finer sands being preferentially deposited on the flanks.

The flank core, V-4, is remarkably uniform fine sand, with grain size varying between 0.234 mm and 0.166 mm (Fig. 3). The variation of grain size is not completely resolved by the 10-cm sampling interval as most sample points are maxima or minima. The maxima and minima presumably represent discrete depositional events, and the small range of grain size characteristics suggests that processes occurring during these events were quite uniform through time.

The crestal core is more variable, with a cross-bedded layer of medium to coarse shelly sand followed by an upward coarsening sequence in which additional cross-bedding occurs (Fig. 3). The horizons may represent storm events with associated appreciable bedload transport.

Heavy Mineral Deposits

A further insight into the depositional mechanisms associated with the Holocene sand sheet is afforded by the distribution of heavy mineral zones and their grain size characteristics. These zones produce clear bands on the radiograph of the cores. Subsequent sampling and heavy liquid separation revealed that the bands contained from 1.30 to 6.64% heavy minerals (Table 1).

No attempt was made to determine the mineral composition. However, a systematic relationship between the vertical distribution of heavy minerals and grain size characteristics was observed. In the crest core (V-1) and the upper part of the flank core (V-4), zones rich in heavy minerals were zones of finer sand, and a higher degree of sorting (lower standard deviations). In Figure 3, heavy mineral concentrations can be seen to occur at minima of these parameters. However, in the lower part of the flank core (core V-4), below 120 cms, heavy mineral concentrations occur in zones of coarser, less well sorted sand.

Everts (1972), in a recent detailed study of marine heavy mineral deposits, describes deposits of two types. Sharply defined heavy mineral laminae occurring on ocean beaches and bands of disseminated deposits forming on aggrading rippled surfaces. In the latter case subsequent ripple migration bypasses the light fraction, and heavies are deposited in the troughs to form a pavement beneath the moving ripples. This mechanism was observed in the field by Everts when the bed shear stress was approximately 0.6 times that required to maintain a uniformly flat bed of equivalent grain size under fluvial conditions. When bed shear exceeded this 0.6 limit, heavy minerals were entrained in the ripples and were no longer preferentially deposited in the troughs.

In Everts' study, disseminated deposits resulting from ripple migration were well sorted and positively skewed. Thus, the heavy mineral zones within the crestal core and upper 120 cms of the flank core (Fig. 3) are texturally compatible with Evert's proposed mechanism, while the lower part of the flank core (V-4) is not.

Stapor (1973) describes two distinct mechanisms of formation of heavy mineral deposits on the beaches of the northeastern Gulf of Mexico. The heavy mineral deposits on open beaches appear to result from a concentrating

TABLE 3.—*Components of the ridge and swale system and related parameters*

	$\bar{x}$	σ	Sk	K	Coarse	Fines	"A"	"B"	"C"
CREST	1.9 (.06)	0.47 (.06)	0.64 (.45)	1.58 (.64)	0.04 (0.03)	0.73 (0.39)	77	21	2
FLANK	2.19 (.47)	0.45 (.10)	0.23 (.45)	0.56 (.98)	0.43 (0.93)	1.43 (0.65)	83	11	6
TROUGH II	2.48 (.08)	0.39 (.04)	-0.01 (.37)	0.63 (.68)	0.18 (0.21)	2.03 (0.60)	97	2	1
TROUGH III	1.09 (.17)	0.78 (.07)	0.34 (.28)	0.90 (.44)	4.92 (2.36)	0.97 (0.57)	76	12	12

The trough samples are categorized as to factors II and III, fine and coarse fraction respectively. The labeling of the subpopulations follows Moss (1962).

$\bar{x}$ = Mean Grain Size.
σ = Standard deviation.
Sk = Skewness.
( ) = Standard deviation of the sample populations.
K= Kurtosis.
Coarse = Material coarser than -1.0ϕ.
Fines = Material finer than 4.0ϕ.

process which tended to remove the coarser particles from the quartz rich parent population, with the efficiency of coarse grain removal increasing with decreasing specific gravity. His conclusions were based on a comparison of grain diameters of the sample with settling velocity of equivalent diameters for each mineral species. Although Stapor does not specify, such selective removal of coarser grains would presumably result in a finer sand substrate exhibiting positive skewness described by Everts (1972) and ourselves.

Stapor also describes heavy mineral populations on "sheltered beaches," which apparently result from a concentrating process which tends to remove finer particles from the heavy mineral population. Samples of such a deposit would presumably be coarser and negatively skewed as in the case of the lower heavy mineral zones of core V-4.

Stapor's samples are from beaches and therefore, as clearly indicated by Everts (1972), cannot be directly compared with heavy mineral deposits found beneath mean low water. However, Stapor believes that the heavy mineral deposits of his "sheltered" Gulf beaches were concentrated on the shelf floor and were then delivered as slugs of heavy mineral-rich sand to the beaches. He suggests that the heavy mineral deposits of sheltered beaches were fine-truncated by asymmetrical wave surge on the shelf whereas the deposits of the open beaches were coarse-truncated in a higher energy environment where coarser grains on the depositional surface experienced greater dispersive pressure (see Bagnold, 1954), and hence a greater probability of entrainment.

The geographic connotations of Stapor's analysis are not directly applicable to the offshore cores of this study, and his evaluation of the responsible hydraulic mechanisms should be applied to our heavy mineral deposits with caution. However, it seems that two different concentrating mechanisms were operating during the formation of the heavy mineral bands in cores V-1 and V-4. Differential response to dispersive pressures experienced by grains on a current-swept depositional surface may indeed have been responsible for the coarse-truncated crestal deposits. In the case of the fine-truncated sands in the lower portion of core V-4, asymmetrical wave surge is a feasible mechanism, especially in that the seaward-sloping outer flank is presumably a dynamic analog of the regime of shoaling waves on the sloping shore face. This is particularly true during storm events when wave surge can penetrate that deep.

PRESENT HYDRAULIC PROCESSES AND SEDIMENT RESPONSE

Petrography of Surficial Sediments

Distribution of mean diameters.—The mean grain size of the sand fraction within the study area varies from 0.63 mm to 0.13 mm, corresponding to a range of coarse to fine sand on Wentworth's (1922) scale of particle size. The textural variation is considered relative to a particular part of the complete ridge system with each sample grouped as to crest, flank, or trough (see methods). The statistical moments of each separate grouping appears as part of Table 3. When the samples are plotted on Stearns (1967) bathymetric map, the textural variation appears to be a complex function of bathymetry (Fig. 6). This is especially apparent in the western

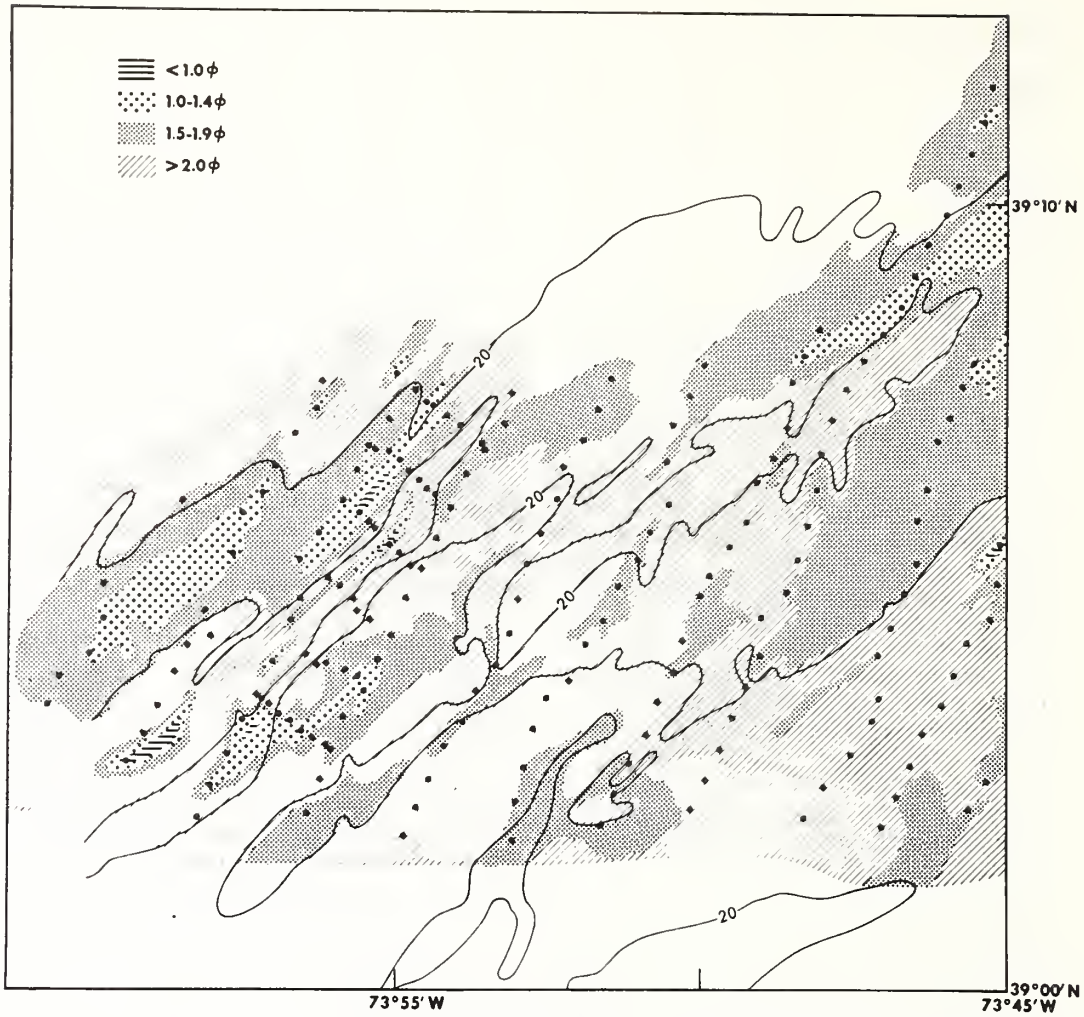

FIG. 6.—Isopleth map of the mean grain size of the study area in relation to the 20-fathom contour. Where control is poor, textural boundaries have been defined by depth, since depth has been independently shown to be a major control of grain size (Fig. 9).

sector of the study area where the grab sample net is sufficiently dense to deduce subtle trends in grain size facies.

The crestal sands are of medium grain size, well sorted (low standard deviation), and contains only a trace of a population larger than sand size (Table 3). The flank sands, when compared to the crestal sands, are finer, of comparable sorting, but possess a larger amount of the very coarse material. The trough sands, however, tend to be either fine or coarse. The fine trough sands are much finer than the flank sands and with a higher degree of sorting. The amount of granular size material (> 2.0 mm) in the fine trough sands is much greater than that on the crest but is somewhat less than that found on the flanks. The coarse sand is on the opposite end of the spectrum, as reflected in Table 3, and is atypical of any other part of the ridge system. The coarse sands have mean values on the coarse end of Wentworth's (1922) medium grain classification, sorting which is very poor (large standard deviation) and contains large amounts of material coarser than sand-size. In a few of the coarse trough sands the amount of material larger than 2.0 mm exceeds 20%.

This granule size material in the troughs appears as lag deposits of detritus, clay pebbles, and large fragmented pelecypods, primarily *Cras-*

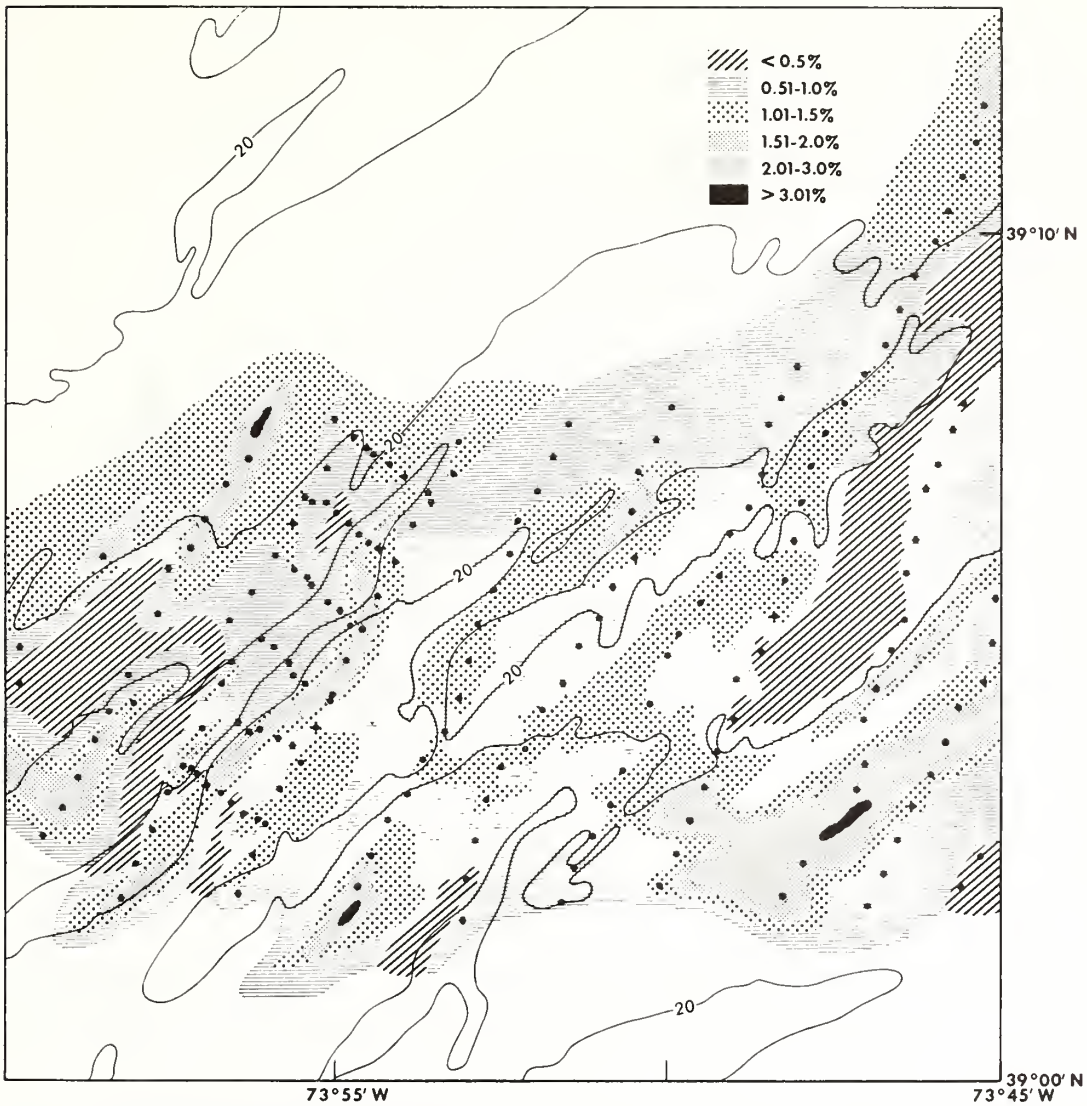

FIG. 7.—Isopleth map of material finer than sand size particles ($< 4.0\ \phi$) in relation to the 20-fathom contour. The solid dots represent grab sample stations. Note that the maximum percentage of fines is only in slight excess of 3%.

sostrea virginica and *Mercenaria mercenaria*. Radiocarbon determinations date this fauna as 10,050 years B.P. (Table 2).

Distribution of Fine Fraction.—The percent of material finer than 0.0625 mm in the samples is generally very low, with the maximum silt-clay fraction exceeding 3% in three samples, and only 9% of the samples contained in excess of 2% fine fraction. The percent of fines recorded for this study, however, exceed those quoted by Frank and Friedman (1973) for an area slightly north of our study area. The difference between the two investigations may be a product of laboratory techniques, since this study incorporated ultrasonic and wet sieving methods as a means of determining percent of fine material. However, a greater exposure of the silt-clay substrate in the study area may be the major contributor to the higher percent of fine fraction noted here.

The distribution of silt/clay material appears to be less rigidly controlled by bathymetry than the mean grain size. However, bathymetry does

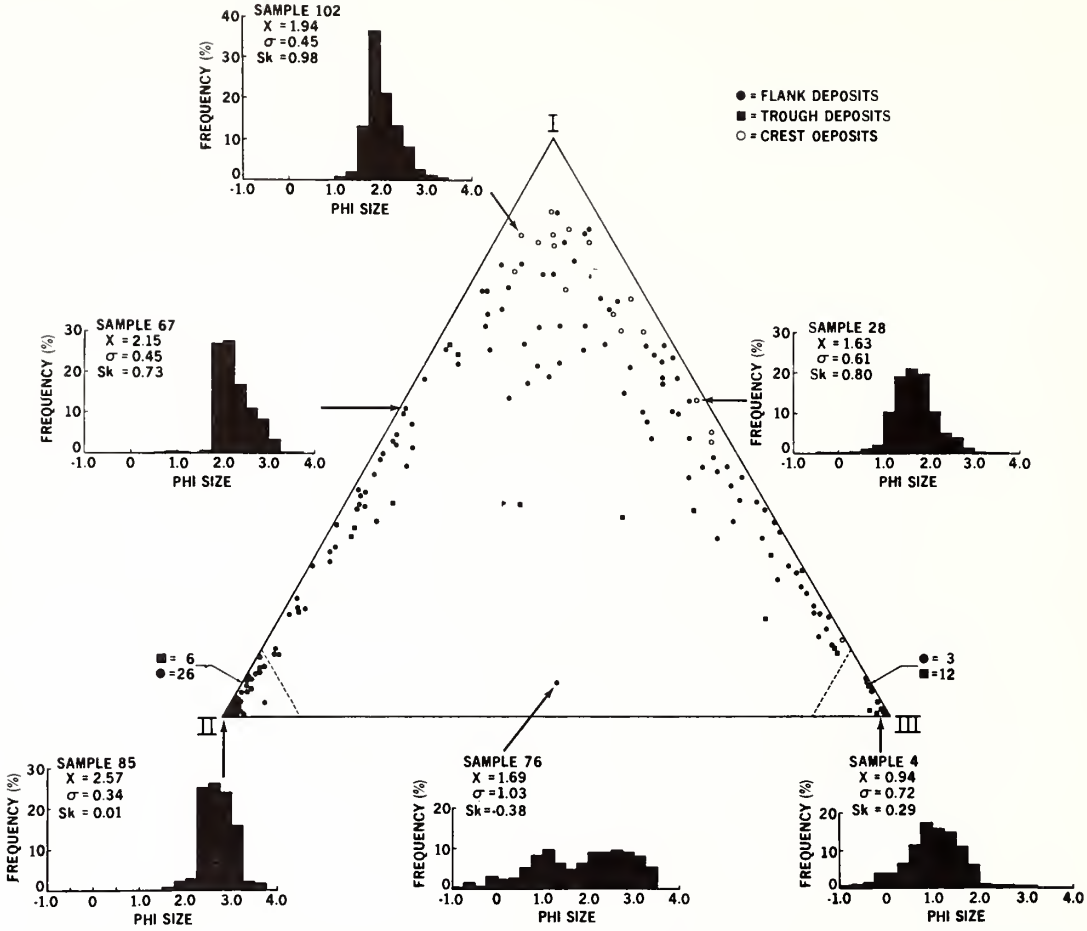

FIG. 8.—Normalized factor components of the surficial samples and associated histograms of representative samples. Factor I denotes the eigenvalue of greatest influence on all the samples, whereas factor III represents that of least influence. The samples are symbolized to indicate the part of the ridge system from which they were taken. The histograms display the mean grain size ($\overline{\chi}$), standard deviation (σ), and skewness (Sk) in addition to the size distribution.

exert some influence on the distribution as suggested by Figure 7 and Table 3. The greatest concentration of this fine fraction appears to be associated with the lower flanks and those troughs floored with fine sand, whereas the intermediate and low silt-clay values occur impartially on the crests, upper flanks, and troughs. Figure 7 indicates that the highest percent of silt-clays are found in silled basins or in the southwestern portion of the northeast-southwest troughs. The southwestern ends of the troughs are generally shoaler and more broad than the medial or northeastern sectors (Fig. 2).

Application of Factor Analysis.—Factor components, derived through factor analysis, are plotted on a ternary diagram (Fig. 8) with symbols to denote crest, flank, or trough samples. Figure 8 shows more clearly than the raw data of Table 3 the morphologic control of grain size. The crestal sands, containing predominately factor I sands, are intermediate in grain size with a moderately high sorting value as indicated by a low standard deviation (Table 3). Samples occasionally contain coarse population as indicated by high values for factor III, but do not appear to have an appreciable fine population. On the average, the flank sands are finer grained than the crestal sands but possess a comparable standard deviation. The trough sands display an obvious bimodality with coarse and fine sand samples, and a notable absence of medium factor I sands. The fine trough

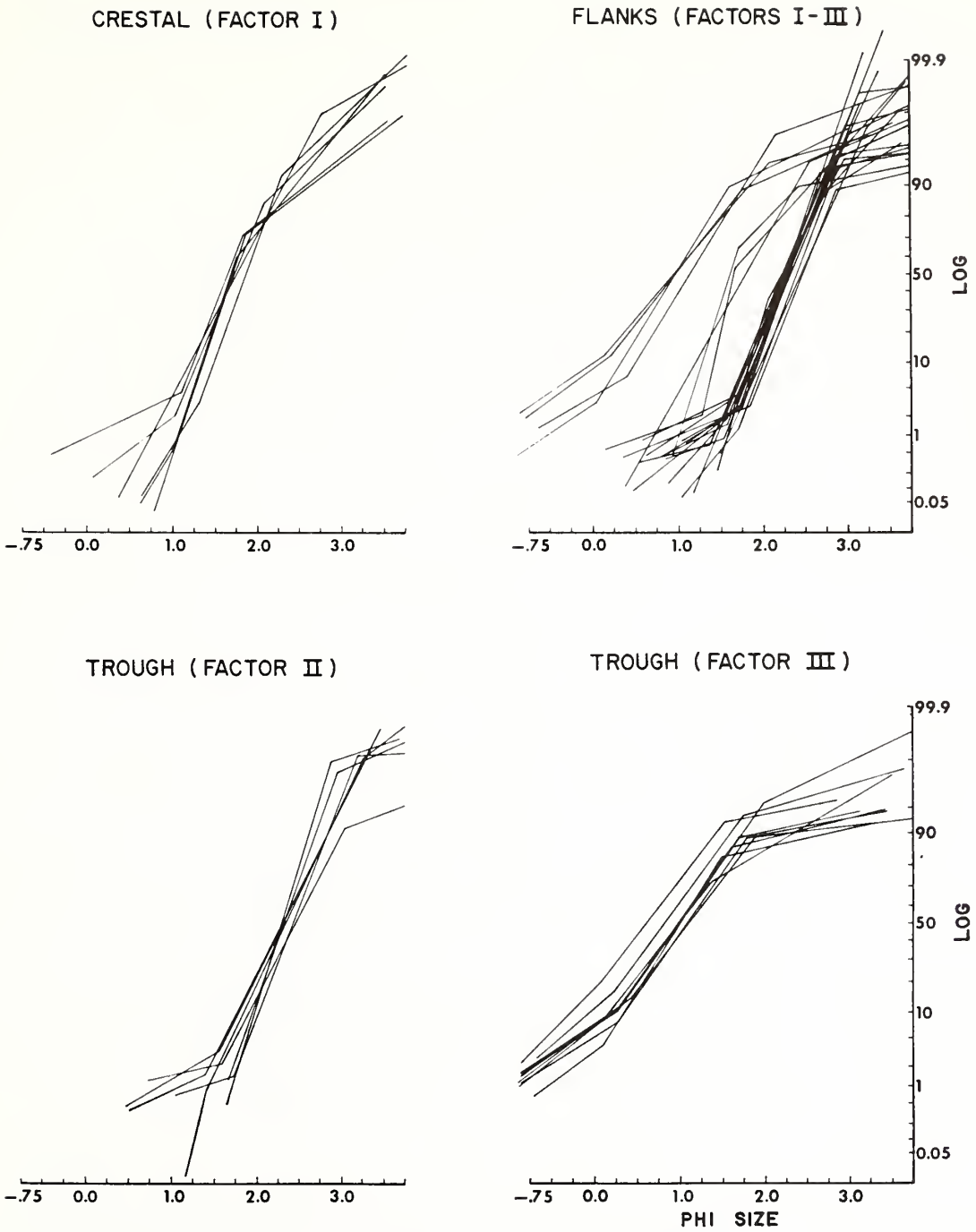

FIG. 9.—Cumulative frequency of the size distribution plotted on log-normal probability paper. The trough samples are divided into a fine (factor II) and coarse (factor III) fraction. The two apparent groupings within the flank sands are reflective of the fine and coarse fractions.

sands are finer than the average flank sand and possess a high degree of sorting (Table 3). The coarse sand fraction has a high standard deviation suggestive of poor sorting.

The three samples, which fail to plot either in the apices or along the baseline between factors II-I-III, are all trough sands and bimodal in respect to fine and coarse sands and have an extremely poor sorting value (Fig. 8). These samples are anomalous to the bulk of the samples and probably reflect sampling of fine-grained sand blanketing a lag of coarse sand fraction. These appear to be an admixture of both the coarse and fine sand populations observed in the troughs.

Samples which plot along only two of the baselines of a ternary diagram and cluster in two of the three apices have been noted by other workers. Imbrie and Van Andel (1964), in their discussion of factor analysis, attribute this plotting characteristic to sediment source. From previously presented argument, the sediment in this study is assumed to be reworking of a nearshore marine sand sheet, thus the source in this study is not the major contributing factor to the sample groupings. Klovan (1966) and Solahub and Klovan (1970) postulate that the grouping patterns reflect the energy spectrum. However, it is somewhat simplistic to describe the sample groupings solely on the basis of a local energy flux. The differing behavior of suspended load and bedload, and the nature of bed building process (Moss, 1972) are probably equally important.

Application of Subpopulation Analysis.—In order to deduce subpopulations from size distributions, and infer sample genesis, several workers have attempted to dissect frequency curves and cumulative frequencies on the basis of natural breaks or by comparing shape parameters to grain size. Proponents of each of these methods include Visher (1969), McKinney and Friedman (1970), and Moss (1962, 1963, 1972). Disagreement exists, however, on the accuracy of the various derivative techniques and the actual meaning of the subpopulations. Visher (1969), by plotting the cumulative frequency of the size distribution on log-normal probability paper (see Fig. 9), suggests that the three straight lines which usually develop may be directly equated to modes of sediment transport.

McKinney and Friedman (1970) incorporated a frequency curve dissection method suggested by Hald (1952). In this approach the grain size frequency is plotted on a log scale with the grain size on an arithmetic scale. At each break in slope of the parabola a new parabola is drawn so that a descending limb of each parabola passes through the slope break point. Ideally, three parabolas result, each representing a subpopulation. It is common, however, that only the "A" subpopulation is a parabola which indicates a normal distribution. The "B" subpopulation is generally positively skewed (a tail of fines) with the "C" subpopulation being negatively skewed (a tail of coarse material). McKinney and Friedman's interpretations agree basically with Visher but they include interstitial entrapment as a contributor to that subpopulation which Visher defined as a product of suspended transport.

Moss (1962, 1963) defined subpopulations by plotting three parameters of particle shape versus grain size and conducted extensive flume work (Moss, 1972) to test his findings. He concludes that three basic subpopulations exist. Following Moss' initial contribution, Visher (1969) had equated material emplaced by saltation to Moss' "A" subpopulation; suspended material to the "B" subpopulation; and material moved by tractive processes as Moss' "C" subpopulation. Moss (1972) contends, however, that the subpopulations are primarily indicative of bed-building processes and the bed regime and are only secondarily the result of the gross mode of transport. He considers saltation combined with packing processes to be responsible for the "framework population" or "A" subpopulation. Subpopulation "B" or "interstitial population" consists of the finer particles deposited interstitially into the "A" framework; suspended particles may in fact preferentially enter the framework, but only if they are available. When there is little suspension, both subpopulations "A" and "B" may be derived from bedload. Larger particles which move tractively over a bed of "A" comprise his subpopulation "C" or "contact population." As the bed regime varies from a fine ripple stage through coarse ripple, dune, and rheologic stages, the mean diameters and relative proportions of the subpopulations shift.

The relative percent of the subpopulations of New Jersey shelf samples, whether derived by either the cumulative curve or dissection of a frequency curve, appears to be in general agreement, with a correlation of 0.995 between these two methods. The technique suggested by Hald (1952) for frequency curve dissection, however, does result in slightly larger values for the two end subpopulations (the "B" and "C" populations of Moss, 1972) than does the cumulative curve method. Likewise the plot of shape versus

size indicates that the medial member, subpopulation "A," is smaller than suggested by the cumulative curves (see Fig. 16 in Moss, 1972). This variance is to be expected when different subjective methods of data reduction are compared.

The size distributions for this study were plotted as cumulative curves on log-normal probability paper (Fig. 9) so that subpopulations appear as distinct segments. The samples were grouped by location on crest, flanks, or troughs, with the trough samples divided into those possessing a high percentage of factors II or III. To aid in interpretation, the only samples considered were those containing a minimum of 90% of factors II or III or 80% of factor I (Fig. 8). The reason that samples with a smaller percentage of factor I were examined as compared to samples containing factors II and III is that no samples contained 90% of factor I. Subpopulations by percent weight are listed in Table 3, as indicated by inflections in cumulative curves. Our method of determination is different from that of Moss, but in order to maintain continuity with previous workers and to avoid overtaxing the literature with yet another classification system, the subpopulations are labelled to agree with Moss (1962).

The relative percent of the subpopulations varies among samples from the crest, flank, and trough. The crestal sands, with a minimum of 80% factor I, contain a surprisingly high percent of "B" subpopulation, relative to the other subpopulations. The trough sands, some of which are predominately fine factor II sands, and others, predominately coarse factor III, represent the two extremes in Table 3. The trough sands with a preponderance of factor II are nearly completely represented by the "A" subpopulation, whereas trough sands containing 90% or more of factor III have a substantial percent of "B" and "C" subpopulations. The flank sands, some of which include 90% of factor II, others 90% of factor III, and others with 80% of factor I, are generally intermediate in regard to subpopulations.

Application of CM Analysis.—Passega (1964) has drawn inferences concerning the transport mode and depositional regime of sands on the basis of plots of coarsest percentile (C) against medium percentile (M). Large suites of samples tend to produce a sigmoid scatter when so plotted. Passega has interpreted segments of the scatter as indicative of specific modes of transport (Fig. 10, first panel).

Sands from the central New Jersey shelf plot as a roughly linear scatter which diverges slightly from the C = M line (Fig. 10). When the points are identified by factor type, three en echelon sub-scatters with vertical boundaries are resolved (see "Flank" panel, Fig. 10). The factor II sands fit well into Passega's "suspension with some rolling" zone (Passega's wording), but the factor III and I sands do not fit as well.

Effect of Wave Surge on Size-Frequency Distributions.—In the following section an attempt is made to apply Moss' and Passega's concepts to the New Jersey shelf samples. It must be remembered that Moss took samples from rivers and flumes which were one or two framework grains thick and had been subjected to unidirectional flow. His conclusions were based on both size and shape parameters. He, and Passega apparently sieved their samples. Samples for this study were collected from the shelf's surface with a Shipek grab sampler whose average depth of penetration was 8 cm. The shelf samples have been subjected to a flow field in which a wave surge component and a unidirectional flow component are probably of subequal intensity. Samples were analyzed by means of a rapid sediment analyzer calibrated against sieves.

The most significant of these uncertainties in comparing the size characteristics of our samples against those of Moss and Passega may be the effect of wage surge in modifying the size frequency distribution. Numerous writers have described grain size distributions from marine environments experiencing wave surge (see review in McKinney and Friedman, 1970, p. 229, also Visher, 1969, p. 1083). However, descriptions of "marine sands from the wave zone" are contradictory and a comparison of papers suggests that there is no unique grain size curve for sands of this environment. Furthermore, most samples on which analysis were based were taken from the upper shoreface, in less than 10 m of water, a highly specialized hydraulic environment, characterized by intense, nearly continuous and often highly asymmetrical wave surge on an appreciable slope. At these shoal depths, friction tends to damp out wind-driven currents. Our samples were taken from deeper water, from a more subdued topography in which wave surge may be expected to penetrate to the sea floor mainly during storms, when unidirectional wind-driven flow may be expected to be most intense.

It seems probable, however, that the superposition of wave surge and unidirectional flow

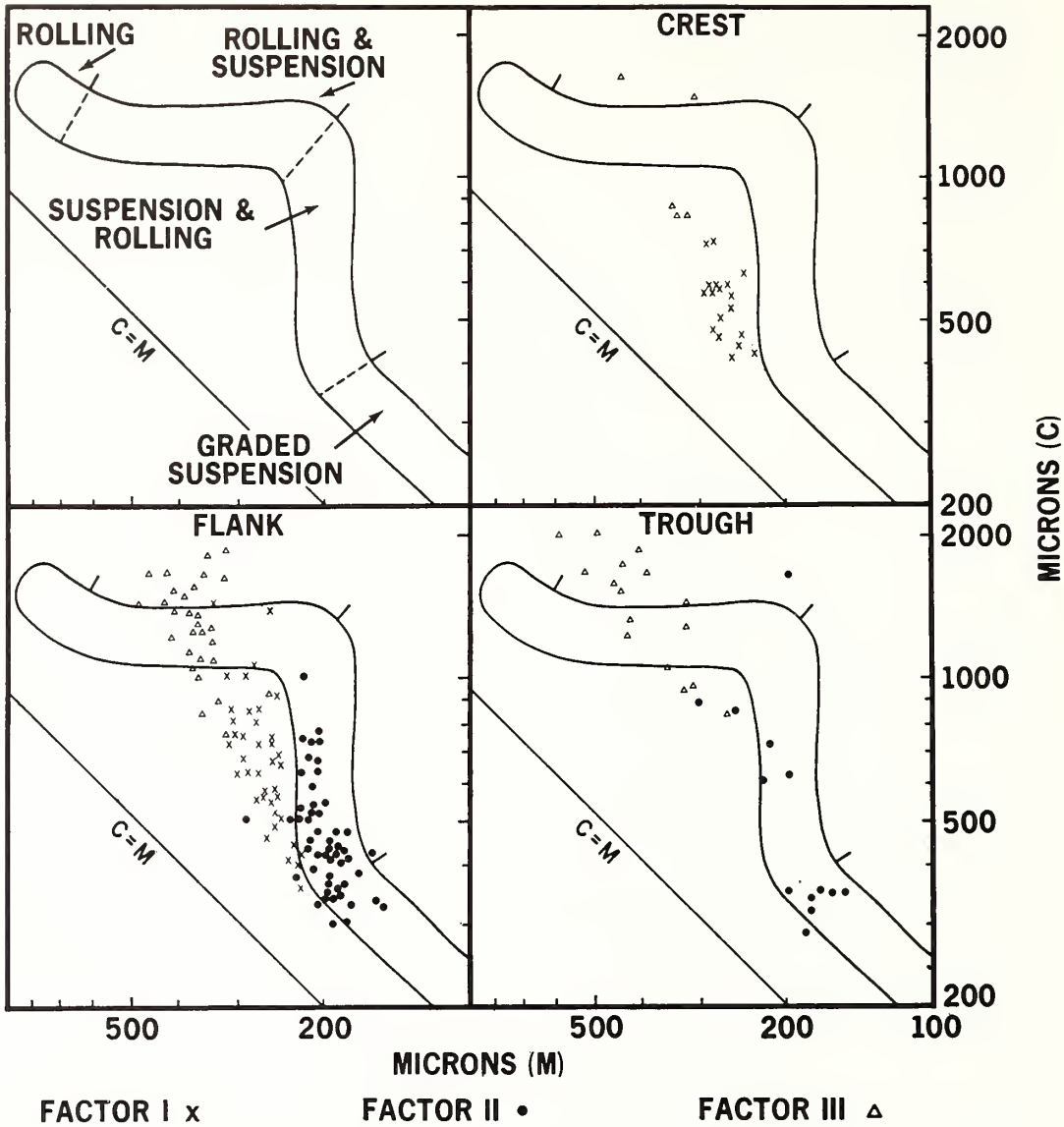

Fig. 10.—CM diagram after Passega (1964).

components during storms, resulting in pulsating flow, has modified grain size distributions of bottom sands to an extent detectable by Moss' and Passega's methods. As noted, our samples plot as a linear scatter on a CM diagram, rather than as Passega's sigmoid scatter. Passega (1964) explains the bend between the vertical pattern where suspension dominates and the horizontal pattern where rolling dominates, as due to a lack of particles in the size range between the maximum size that can be carried as a graded suspension and the optimum size for rolling. The vertical trend is described as the result of a decreasing quantity of the maximum suspensive size (M = constant), with an increasing admixture of rolling grains (C varies). As suspensive transport ceases to be significant, C becomes constant, while M varies.

The sigmoid scatter is characteristic of river sands (Passega, 1964). It is missing in Passega's plots of turbidite sands; these form a scatter parallel to C = M, similar to the graded suspension segment of Figure 10. It would appear that in a turbidity current there is no

"maximum suspensive size." We note that Passega's (1964, Passega *et al.*, 1967) examples of shelf sands either have too few points to give a coherent pattern, or else are so fine textured that they fall entirely into the uniform and graded suspension segments. During storm flow on the shelf, wave surge and unidirectional components of the flow field are probably subequal in intensity. Because of the sudden intensive suspension of sand during peak wave surge, there may be no sharp upper limit to the size that can be suspended and the nearly linear scatter in Figure 10 may in fact be characteristic of medium grained shelf sands.

Little consideration has been given to the lubricating effect of superimposed wave surge on the entrainment and transport of sand by unidirectional flow, whereby during peak surge, "a burst of sediment is thrown upward into the fluid from the region just downstream of each ripple crest [by the lee eddy] and upstream from the ripple crests by the high velocity and shear stress in these regions" (Kennedy and Locher, 1972). We tentatively infer that this process would permit rheologic flow of coarse sand and suspensive transport of fine sand at lower mean velocities (or coarser grades traveling by these modes at high mean velocities).

Trough Texture and Depositional Regime.—Depositional regimes may be inferred for the trough, flank, and ridge sands on the basis of Moss' and Passega's studies. Coarse factor III sands of the troughs are well endowed with both "B" and "C" subpopulations (Table 3). This suggests Moss' high intensity "rheologic" bed regime in which bed load travels as a dense cloud of colliding particles buoyed up by dispersive pressure, but pulled toward the bed by gravity. This stage corresponds to the "transition" of Southard and Bogachwal (1973), and their "upper flat bed sedimentation" represents this regime's full development. Moss' (1972) flume studies suggest this rheologic bed regime is a unique solution for the depositional regime of the coarse factor III sands of the troughs, since Moss was able to obtain a significant proportion of the "C" subpopulation only under the rheologic bed regime.

The factor III sands of the trough plot a little below, on, or more commonly a little above the "rolling and suspension" zone (Fig. 10). The scatter however, trends across this zone at a high angle, behavior that is more compatible with rheologic flow than with the dune regime in which rolling and suspension might occur together.

The fine factor II sands of the trough are less amenable to analysis by Moss' (1972) data. His flume studies suggest that with an "A" subpopulation sands finer than 0.25 mm can undergo only two bedload regimes as flow intensifies, the fine-ripple regime and the high intensity rheologic regime, before becoming entrained as suspended load. Both of these regimes are characterized by an abundant "B" subpopulation. Because grains do not project above the viscous sublayer in the fine-ripple regime, microturbulence is not generated over the bed or in the open interstices, and fine material from both suspension and bedload can pass copiously into the bed as a "B" population. When the flow intensifies, the fine sand transport goes directly into the rheologic stage where the dispersive pressure drives the fine sand into the interstices despite micro-turbulence, again resulting in a significant portion of "B" subpopulation. However the fine factor II trough sands have negligible "B" populations (Table 3).

We note that in the CM diagram (Fig. 10) the fine factor II sands of the troughs (and the much more abundant factor II sands of the flank) fall into the "suspension with some rolling" zone of Passega. We therefore tentatively infer that the texture of factor II sands reflects significant suspensive transport, a category not considered by Moss.

Crest Texture and Depositional Regime.—The medium factor I sands of the crest are problematical. According to Moss' studies, sands of this diameter may move in the coarse ripple regime, the dune regime, or the rheologic regime. The corresponding "B" subpopulations are low, moderate, and high. Factor I sands are the most enriched in "B"; thus Moss' (1962, 1963) studies suggest the rheologic regime, as do the grain size characteristics of the zones enriched in heavy minerals (see previous discussion). As noted above, the displacement of factor I sands from the normal CM pattern (Fig. 10) suggests a high intensity rheologic flow, or perturbation of the flow by wave surge, or both. However, the cross-bedded horizon observed in the crestal and upper flank cores indicates that the dune regime prevails during some transport events.

Flank Texture and Depositional Regime.—All three factor types occur in flanks, suggesting that both rheologic and suspensive transport events are the determinants of flank textures. Factor II sands are predominant, however, suggesting that this regime is subjected primarily

TABLE 4.—*Calculated transport of sediment during a 10 day period in June. Data from McClennen (1973)*

Sand size	Phi unit	% Exceedence (Shield's criterion)	Material moved per transverse meter (Laursen's total bedload formula)	
			Kilograms	Number of sand grains
Coarse sand	0.5 ϕ	13.19	207.98	11×10^8
Medium sand	1.5 ϕ	25.46	305.21	13×10^8
Fine sand	2.5 ϕ	25.46	267.59	92×10^8
Very fine sand	3.5 ϕ	25.46	180.38	50×10^8

The % Exceedence column reflects the artificiality introduced when considering current data only in 5 cm/sec intervals and not as a continuous function. The suggested quantity of sediment transport is based on Shield's (1936) function of critical velocity and Laursen's (1958) equation for total load concentration.

to suspensive transport events. This suggestion is supported by the CM diagram (Fig. 10) with the fine grained factor II sands plotting on the portion of Passega's (1964) diagram where transport is postulated to be via suspension and some rolling.

Model for Hydraulic Process and Substrate Response

Hydraulic Regime.—The stratigraphic and petrographic observations of ridge and swale sands do not provide a unique solution for the hydraulic regime that has distributed the sands. They do, however, provide constraints for deducing the nature of this regime. Baldly stated, our data lead us to infer that since the passage of the beach, the troughs of the ridge and swale system are subjected alternately to coarse, high intensity, bedload deposition and fine suspensive deposition; crests are uniquely subjected to a regime characterized by high intensity flow and suspensive deposition with an occasional interval of dune formation; and flanks are subject to all of these regimes at different times, with suspensive transport dominating.

These inferences must be considered relative to our scanty knowledge of the hydraulic climate of the central New Jersey shelf. During the summer, the water column is stratified and undergoes a southerly drift, partly as a baroclinic response to terrestrial runoff (Bumpus, 1973). Surface tidal current velocities are generally less than 20 cm/sec (Redfield, 1956), and the tides are therefore generally inadequate to move bottom sand.

During the fall, decreasing temperatures and the increased frequency of storms homogenizes the water column. During the months of December, January, and February, storms cross the New Jersey shelf approximately every ten days. Repeated episodes of intense northeast winds might be expected to drive shelf water landward, and where constrained by the shoreline, southward. Harrison and Pore (1967), have inferred that in deeper water a geostrophic component of flow, also southward, may occur in response to such a wind setup.

Whereas there are no published measurements of the winters' flow field, a partial documentation of the summer flow field velocity is available from limited current observations made by McClennen (1973). McClennen's "C" meter, 100 cms above the substrate, was deployed during a ten-day period of the quiet summer season, but seems to have caught a mild summer storm in which sustained velocities of 35 cm/sec occurred. The velocity record was used to calculate the percent of time that the threshold velocity was exceeded for four representative size classes of sand and the resulting transport, by mass and number of grains (Table 4). The figures should not be taken too literally as many assumptions are involved and the equations used (Shields, 1936; Laursen, 1958) are based on shallow, steady flow in flumes, but they suffice to show that significant transport occurs. Ten transport events of this magnitude per year would be able within several decades to transport, over the surface area of a ridge, an amount of sediment equal to the volume of the ridge, yet the ridges rest on a surface ten millennia old. We tentatively conclude that either the ridges are quite young, or else the flow field in the millennia since transgression has been structured in such a way as to maintain the ridges, otherwise they would have been degraded and flattened.

A mechanism capable of maintaining ridges may exist in the storm flow field, but very little is known about this subject. Current-parallel bedforms are generally attributed to

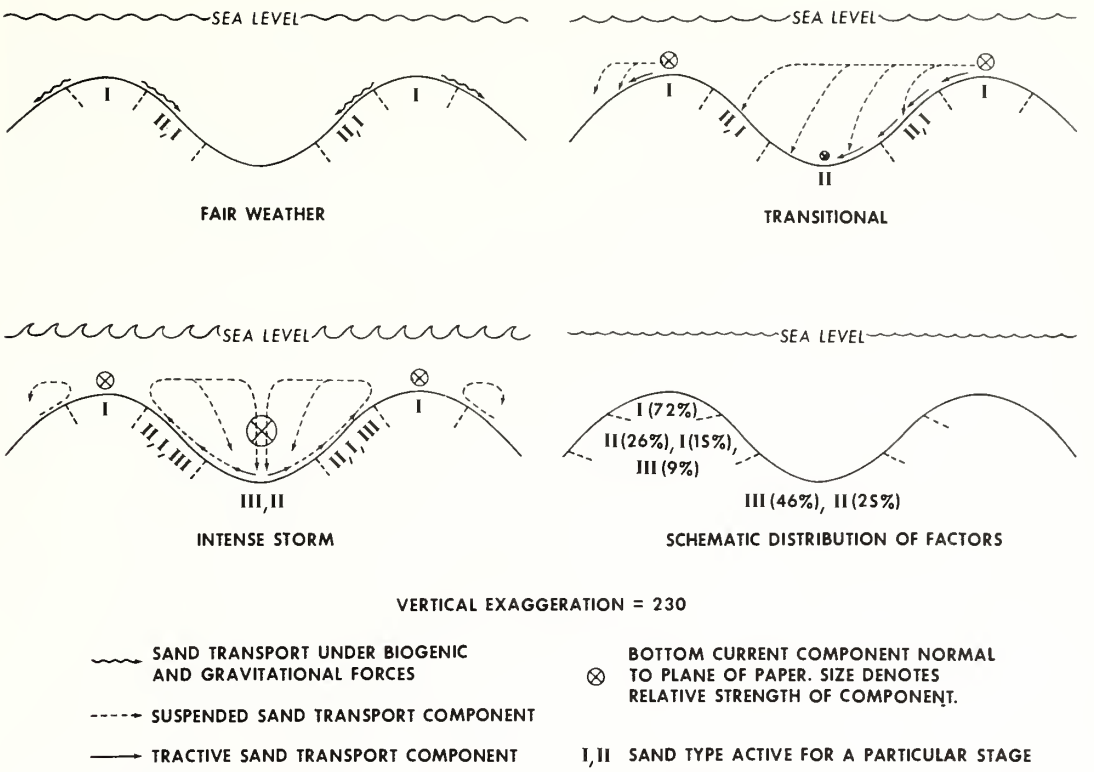

FIG. 11.—Model for sediment transport with no interpretation of internal structure intended. The numerals denote the percent of the three factor sands found on the crest, flank, or in the trough.

current-parallel perturbations in flow (Allen, 1968), and these are usually described as arrays of horizontal helical vortices, with alternately right-handed and left-handed rotation, so that a cell shares a rising limb with a cell on one side, and a descending limb with a cell on the other (Wilson, 1972). The secondary flow component is perhaps a few percent of the main flow; both components are most intense in the downwelling limbs.

The case is perhaps best documented on the sand seas of the world's deserts, where wind parallel sand dunes as large as the New Jersey shelf ridges have required up to 10 millennia to form (Wilson, 1972). Cloud streets are sometimes aligned with their crests (Hanna, 1969), and cloud streets are generally attributed to helical flow structure in the planetary boundary layer of the atmosphere (Brown, 1971), with clouds forming along the rising limbs of the half-cells. The tidal sand ridges of the southern bight of the North Sea have also been attributed to helical flow (Houbolt, 1968), although the situation is rendered complicated by residual ebb and flood currents (Huthnance, 1973). Theoretical studies (Faller, 1963; Faller and Kaylor, 1966) suggest that all large-scale flows on a rotating planet that are shallow relative to their depth (Ekman boundary layer flow) are unstable above critical Reynolds values, and that the instability tends to take the form of helical flow structure.

Coupling between such large scale flow cells and the ridge topography if it does occur, may be a sporadic phenomenon. Sidescan records from the study area (McKinney *et al.*, 1974) show a pervasive pattern of sand ribbon-like features occurring mainly in troughs. These are themselves probably the consequence of small-scale helical flow structure. The ribbons trend uniformly along the topography, making a 30° oblique angle with the trough axes. If this is a record of the last major storm, then this storm, or at least its last stage, does not appear to have had a flow direction appropriate for coupling, since the sand ribbons do not form herring bone patterns about trough axes.

Storm flow directions on continental shelves are variable (Sternberg and McManus, 1972, Fig. 78) and may rotate within a single storm.

If flow parallels topography during peak flow intensity, then flow cells could lock onto topography during this period, to scour troughs and aggrade crests. If the trend of second order ridges (Fig. 1) is determined by mean storm flow, then such coupling may be sufficiently frequent to maintain ridges.

Whereas no direct evidence exists for the perhaps chimerical helical flow, the petrography of the Holocene sands and their morphology and stratigraphy do indicate sediment transport normal to the ridges, as well as parallel to them. The pattern of transport, furthermore, appears to be time dependent, varying with the rigor of the hydraulic event (Fig. 11).

Substrate Response to High Intensity Flow.—The axial zones of coarse factor III sands on trough floors is attributed to a high intensity flow field, possibly of the nature described above, in which high velocity, wind-driven, surface flow converges over troughs, descends and diverges on the bottom. The regime is an erosive one; submersible dives (McKinney, *et al.*, 1974) show that zones of the thin factor III sands locally have been swept away, exposing ribbon-like windows of coarser shelly, pebbly sand. This lag deposit includes shells of *Crassostrea virginica* and *Mercenaria mercenaria* dated at 10,050 years B.P. These brackish water forms appear to have been scoured out of the underlying clayey substrate.

The texture of factor I sands of the crests appears to also form during high intensity flow. Core V-4 (Fig. 3) indicates that the high intensity regime of the crests is at least locally depositional. Radiocarbon dates from pelecypod shells (*Placopecten magellanicus*) show that this core has received over a meter of sand in the last 3,760 years, and 60 cm in the last 500 years.

During flow sufficiently intense to activate coarse factor III sands of the troughs and medium factor I sands of the crest, the fine factor II sands must also be activated. Their texture implies suspensive transport. The upslope coarsening of these sands, noted also by McKinney, *et al.* (1974), could result in part from high intensity flow events if trough divergence and crestal convergence of bottom flow are in fact associated with these events. Progressive sorting would result as bottom flow decelerates from the intense flow of the downwelling zone, to the more diffuse flow upwelling over crests. McKinney, *et al.* (1974), have noted that the sand ribbon-like patterns of trough floors locally extend into the finer sands of flanks. The bedforms develop up to 2 m of relief in this fine, deep substrate, and become widely spaced.

Substrate Response to Moderate Intensity Flow.—The presence of fine factor II trough sands and of medium, well sorted crestal sands which contain a negligible component of factor II requires a yet more complicated scheme. The ridge crests at 31 m depth must be activated much more frequently than the troughs at 45 m. Activation restricted to crests should result from long period swells (storm forerunners), waning of an intense storm, or from wind stress to short-lived for downward momentum transfer to reach the bottom during periods of partial stratification. Such activity might reasonably be expected to winnow the crests and deposit fine sand, silt, and clay on flanks and in troughs as a graded suspension (Fig. 11).

The finest sediments, when deposited, present hydraulically smooth surfaces whose grains do not protrude above the laminar sublayer, and in addition, tend to have some cohesiveness. Submersible dives have revealed widespread "rusty bottoms" during fair weather; sectors in which the sand-water interface has developed an algal film. As a consequence of these several mechanisms, a higher velocity is required to entrain these materials than to deposit them. This behavior probably explains why factor II sands extend across the margins of troughs whose axes appear to be subject to periodic high energy events.

Substrate Response to Fair Weather Regime.—During fair weather circulation, which must prevail the majority of the time, the ridge crests may undergo some surficial ripple sorting, but the deeper surfaces appear to be dominated by biologic activity (Fig. 11). Submersible observations indicate that sand dollars and stone crabs are abundant on the crests and upper flanks, and crabs are active on the lower flanks and in the troughs as well. Both rippling and benthic activity would presumably induce minor downslope transport.

CONCLUSION

Substantial evidence exists to suggest that the ridge and swale system in the central New Jersey shelf is actively responding to the modern hydraulic regime. Despite considerable evidence for mobility of the bottom sediment, the ridges and swales maintain their form. Troughs expose windows of coarse lag sands over prerecent substrate, indicating an erosional regime. The troughs show little evidence of sediment

accumulation, and many samples in fact present textural evidence indicative of high intensity flow. Ridge crests likewise present evidence of high intensity flow, but are at least locally aggradational, as a core has been dated to reveal a meter of aggradation in the last 3,760 years, and 60 cm in the last 500 years.

The petrographic and stratigraphic data presented do not provide a unique solution for the flow field that activates the surficial sediments of the central New Jersey shelf. They do, however, provide inferential constraints. The simplest model compatible with the data recognizes three stages of activity (Fig. 11). During fair weather circulation, the activity on the ridge system is mainly biogenic with sand dollars being prevalent on the crest and upper flank and crabs most active in the troughs.

A second stage of activity results from storms which fail to entrain the complete water column on the shelf, because wind velocities are not sufficiently intense or sustained or because the water column is too stratified. During such periods crests may undergo winnowing by wave surge and by the unidirectional component of the storm flow field. Factor I sand texture may be formed on crests, while factor II sand textures are formed on the flanks and troughs, when fine sands move off crests as bedload or graded suspension or both.

A third stage may be inferred to result from major storms, when the entire shelf water column is set into motion. Such movements may involve large scale secondary circulation with descent and divergence of high velocity surface water in the troughs. The troughs undergo scour, during which time the fine factor II sands develop their characteristic texture of abundant "B" and "C" subpopulations. Since pre-Recent substrate underlies trough axes at the depths of less than a meter where sampled, the trough bottom currents may diverge, thus sweeping out the troughs and returning sand to ridge flanks and crests. Some of this material may aggrade flanks and crests where factor II and I textures are respectively imprinted but the finer sand cannot undergo permanent deposition on the crests as wave surge is most intense here, and returns to the flanks and troughs as the storm wave surge and the mean flow return to the weaker intermediate stage of activity.

The resultant facies include medium grained sand on the crests, an admixture of grain-sizes on the flanks but with a preponderance of fine-grained sand, and both coarse and fine deposits in the troughs with little medium-grained sand present (Fig. 11). The ridges appear to be maintained by differential sediment transport with net upflank transport of medium sand, and net down flank transport of fine sand.

Modern sediment movement in the ridge and swale topography is confined to the outermost skin of sand; the cores may have been formed throughout much or all of the preceding period of Holocene transgression. However, it is inadvisable to call these features relict for this reason; all bedforms consist of active skins and inert cores. Large scale bedforms migrate much more slowly than small scale bedforms (Allen, 1968), and current parallel bedforms move yet more slowly since their migration is a response mainly to secondary components of flow. The criterion for bedform activity should not be age of the core, but instead whether or not the bedform's skin processes serve to maintain it.

ACKNOWLEDGMENTS

The authors are grateful to Dr. H. B. Stewart, Jr. and Dr. G. H. Keller for constructive criticism offered to this study. Special appreciation is extended to Sue O'Brien and David Senn for the illustrations. Dr. Don Moore, of the Rosenstiel School of Marine and Atmospheric Science, University of Miami, Florida, provided biological identification.

REFERENCES

Allen, J. R. L., 1968, The nature and origin of bedload hierarchies: Sedimentology, v. 10, p. 161–182.

Bagnold, R. A., 1954, Experiments on a gravity-free dispension of large solid in a Newtonian fluid under shear: Proc. Royal Soc. London, A 225, p. 49–63.

Brown, R. A., 1971, A secondary flow model for the planetary boundary layer: Jour. Atmospheric Sciences, v. 27, p. 742–757.

Bumpus, D. F., 1973, A description of the circulation on the continental shelf of the east coast of the United States: Progress in Oceanography, v. 6, chp. 4, p. 117–157.

Curray, Joseph R., 1965, Late Quaternary history continental shelves of the United States: *in* Wright, H. E., Jr., and D. G. Frey (*eds.*), the Quarternary of the United States; Princeton, N. J., Princeton Univ. Press, p. 723–735.

Dietz, R. S., 1963, Wave-base, marine profile of equilibrium and wave built terraces; a critical appraisal: Geol. Soc. America Bull., v. 74, p. 971–990.

Duane, D. B., M. E. Field, E. P. Meisburger, D. J. P. Swift, and S. J. Williams, 1972, Linear shoals on the Atlantic inner shelf, Florida to Long Island: *in* Swift, D. J. P., D. B. Duane, and O. H. Pilkey (*eds.*), Shelf Sediment Transport Process and Pattern; Dowen, Hutchinson, and Ross, Inc., Stroudsburg, Pa., p. 447–449.

Emery, K. O., 1966, Atlantic continental shelf and

slope of the United States geologic background. U. S. Geol. Survey Prof. Paper 529-A, p. 1–23.

———, AND E. UCHUPI, 1972, Western North Atlantic Ocean; Topography, Rocks, Structure; Water, Life, and Sediments: Am. Assoc. Petroleum Geologists Bull., Memoir 17, p. 532.

EVERTS, CRAIG H., 1972, Exploration for high energy marine placer sites: Univ. of Wisc. Sea Grant Technical Report 72-210, p. 179.

FALLER, A. J., 1963, An experimental study of the instability of the laminar Ekman boundary layer: Jour. Fluid Mech., v. 15, p. 560–576.

———, AND R. E. KAYLOR, 1966, A numerical study of the instability of the laminar Ekman boundary layer: Jour. Atmospheric Sci., v. 23, p. 466–480.

FRANK, W. M., AND G. M. FRIEDMAN, 1973, Continental Shelf Sediments off New Jersey: Jour. Sed. Petrology, v. 43, p. 224–237.

GARRISON, L. E., AND R. C. MCMASTER, 1966, Sediments and geomorphology of the continental shelf off southern New England: Marine Geology, v. 14, p. 273–289.

GIPSON, MACK, JR., 1963, Ultrasonic disaggregation of shale: Jour. Sed. Petrology, v. 33, p. 955–958.

HALD, A., 1952, Statistical Theory with Engineering Application, New York, John Wiley and son, 783 p.

HANNA, S., 1969, The formation of longitudinal sand dunes by large helical eddies in the atmosphere: Jour. Applied Meterology, v. 8, p. 874–883.

HARRISON, W., AND N. A. PORE, 1967, An approach to correlation and prediction in the drift-runoff-wind system: (In) Circulation of continental shelf waters off the Chesapeake Bight, ESSA Adm., Prof. Paper 3, p. 1–82.

HOUBOLT, J. J. H. C., (1968) Recent sediments in the southern bight of the North Sea: Geol. en Mijnbouw, v. 47, p. 245–273.

HUTHNANCE, J. M., 1973, Tidal current asymmetries over the Norfolk sandbanks: Estuarine and Coastal Marine Science, v. 1, p. 89–99.

IMBRIE, J., AND T. H. VAN ANDEL, 1964, Vector Analysis of Heavy Mineral Data: Geol. Soc. America Bull., v. 75, p. 1131–1156.

KENNEDY, J. F., AND F. A. LOCHER, 1972, Sediment suspension by waves: *in* Meyer, R. E. (*ed.*), Waves on Beaches and Resulting Sediment Transport: Academic Press, London.

KLOVAN, J. E., 1966, The use of factor analysis in determining depositional environments from grain size distribution: Jour. Sed. Petrology, v. 36, p. 115–125.

KRAFT, J. C., (1971) Sedimentary facies patterns and geologic history of a Holocene transgression: Geol. Soc. America. Bull., v. 82, p. 2131–2158.

KRAVITZ, H. H., 1966, Using an ultrasonic disruptor as an aid in wet sieving: Jour. Sed. Petrology, v. 36, p. 811–812.

LAURSEN, E. M., 1958, The total sediment load of streams: Proc. Amer. Soc. Civil Engineers, v. 84 (HY1), p. 1530–31 to 1530–33.

MCCLENNON, C. E., 1973, New Jersey continental shelf near bottom current meters records and recent sediment activity: Jour. Sed. Petrol., v. 43, No. 2, p. 371–380.

MCKINNEY, T. F., W. L. STUBBLEFIELD, AND D. J. P. SWIFT, 1974, Large scale current lineations on the Great Egg Shoal Retreat Massif, New Jersey Shelf: Investigations by sidescan sonar: Marine Geology, v. 17, p. 79–102.

———, AND G. M. FRIEDMAN, 1970, Continental shelf sediments of Long Island, New York: Jour. Sed. Petrology, v. 40, p. 213–248.

MILLIMAN, J. D., AND K. O. EMERY, 1968, Sea levels during the past 35,000 years: Science, v. 162, p. 1121–1123.

MOSS, A. J., 1962, The physical nature of common sandy and pebbly deposits (Part I): Am. Jour. Sci., v. 260, p. 337–373.

———, 1963, The physical nature of common sandy and pebbly deposits. (Part II): Am. Jour. Sci., v. 261, p. 297–343.

———, 1972, Bedload sediments: Sedimentology, v. 18, p. 159–219.

PASSEGA, R., 1964, Grain size representation by CM patterns as a geological tool: Jour. Sed. Petrology, v. 34, p. 830–847.

———, A. RIZZINI, AND G. BORGHETTI, 1967, Transport of sediments by waves, Adriatic coastal shelf, Italy: Am. Assoc. Petroleum Geologists Bull., v. 51, p. 1304–1319.

REDFIELD, A. C., 1956, The influence of the continental shelf on the tides of the Atlantic coast of the United States: Jour. Marine Res., v. 17, p. 432–448.

SANDERS, J. F., 1962, North-south trending submarine ridge composed of coarse sand off False Cape, Virginia: Abstr. Am. Assoc. Petrology Geologists Bull., v. 46, p. 278.

SANFORD, R. B., AND D. J. P. SWIFT, 1971, Comparison of sieving and settling techniques for size analysis, using a Benthos Rapid Sediment Analyzer: Sedimentology, v. 17, p. 257–267.

SCHLEE, J., AND R. PRATT, 1972, Atlantic continental shelf and slope of the United States: U. S. Geol. Survey Prof. Paper 529–H.

SHEPARD, F. P., 1963, Submarine Geology, New York, Harper and Row, 557 p.

———, AND R. YOUNG, 1961, Distinguishing between beach and dune sands: Jour. Sed. Petrology, v. 31, p. 196–214.

SHIELDS, A., 1936, Anwendung der ahnlichkeits mechanik und der turbulenzforsechung auf die Geschiebe Beweguna: Preussische Versuchanstalt fur Wasserbau und Schiffbau, Berlin.

SOLOHUB, J. T., AND J. E. KOLOVAN, 1970, Evaluation of grain-size parameters in lacustrine environments: Jour. Sed. Petrology, v. 40, p. 81–101.

SOUTHARD, J. B., AND L. A. BOGUCHWAL, 1973, Flume experiments on the transition from ripples to lower flat bed with increasing grain size: Jour. Sed. Petrology, v. 43, p. 1114–1121.

STAPOR, F. W., JR., 1973, Heavy mineral concentrating processes and density/size equilibrium in the marine and coastal dune sands of the Apolachiola, Florida, region: Jour. Sed. Petrology, v. 43, p. 396–407.

STAHL, L., J. KOCZAN, AND D. J. P. SWIFT, 1974, Anatomy of a shoreface-connected sand ridge on a New Jersey shelf: Implications for the genesis of the shelf surficial sand sheet: Marine Geology, v. 2, p. 117–120.

STERNBERG, R. W., AND D. A. MCMANUS, 1972, Implications of sediment dispersal from long-term bottom current measurements on the con-

tinental shelf of Washington: *in* Swift, D. J. P., D. B. Duane, and O. H. Pilkey (*eds.*), Shelf Sediment Transport: Process and Pattern: Dowden, Hutchinson and Ross, Stroudsburg, Pa., p. 181–195.

STERNS, F., 1967, "Bathymetric maps of the New York Bight, Atlantic Continental Shelf of the United States, Scale 1:125,000." National Ocean Survey, National Oceanic and Atmospheric Admin. Rockville, Md.

SWIFT, D. J. P., B. HOLLIDAY, N. AVIGNONE, AND G. SHIDELER, 1972a, Anatomy of a shorefaced ridge system, False Cape, Virginia: Marine Geology, v. 12, p. 59–84.

———, J. W. KOFOED, F. P. SAULSBURG, AND P. SEARS, 1972b, Holocene Evolution of the Shelf Surface, Central and Southern Atlantic Shelf of North America: *in* Swift, D. J. P., D. B. Duane, and O. H. Pilkey (*eds.*), Shelf Sediment Transport Process and Pattern; Dowden, Hutchinson and Ross, Inc., Stroudsburg, Pa., p. 499–575.

UCHUPI, E., 1970, Atlantic continental shelf and slope of the United States shallow structure: U. S. Geol. Survey Prof. Paper 529-I, 44 p.

VEATCH, A. C., AND P. A. SMITH, 1939, Atlantic submarine valleys of the United States and the Congo submarine valleys: Geol. Soc. America Spec. Papers no. 7, 101 p.

VISHER, G. S., 1969, Grain size distribution and depositional processes: Jour. Sed. Petrology, v. 39, p. 1074–1106.

WENTWORTH, C. K., 1922, A scale of scale and class terms for clastic sediments: Jour. Geology, v. 30, p. 377–392.

WILSON, I. G., 1972, Aeolian bedforms—their developments and origins: Sedimentology, v. 19, n. 3/4, p. 173–210.

Reprinted from: *Sedimentary Geology 14*, 1-43.

BARRIER-ISLAND GENESIS: EVIDENCE FROM THE CENTRAL ATLANTIC SHELF, EASTERN U.S.A.

DONALD J.P. SWIFT

Atlantic Oceanographic and Meteorological Laboratories, Miami, Fla. (U.S.A.)

(Submitted July 9, 1974; revised and accepted January 31, 1975)

ABSTRACT

Swift, D.J.P., 1975. Barrier-island genesis: evidence from the central Atlantic shelf, eastern U.S.A. Sediment. Geol., 14: 1—43.

Since most barrier systems appear to have retreated into their present positions from further out on the continental shelf, the continental shelf is a logical place in which to investigate barrier genesis. The Middle Atlantic Bight of North America, one of the best known shelf sectors, does not appear to contain any drowned barriers. Instead, a series of terraces bear on their surfaces a discontinuous carpet of lagoonal sediments beneath a discontinuous sand sheet formed by erosional barrier retreat. Scarps separating terraces are the lower shorefaces of stillstand barriers whose superstructures were destroyed when shoreface retreat resumed. Thus the "origin" of most barriers is that they have retreated in from the position of their immediate predecessors. Barrier genesis, in the classic sense of large-scale, coastwise spit progradation or mainland-beach detachment, could only have occurred at Late Wisconsin lowstand, when the sense of sea-level displacement was reversed. The relative roles of coastwise spit progradation and mainland-beach detachment depend on coastal relief and slope, with steep, rugged coasts favoring spit progradation at the expense of mainland-beach detachment. Since most major barrier systems form on flat coastal plains, it would appear that mainland-beach detachment is the more important mode of barrier formation.

During stillstands or periods of reduction in the rate of sea-level rise, coasts can more nearly approach their climax configuration, in which the shoreline is relatively straight, and the shoreface is well developed and of maximum possible slope. Coastal adjustments during such periods may require localized mainland-beach detachment and coastwise spit progradation, in order to attain such a configuration.

INTRODUCTION

Contemplation of the origin of barrier islands has long been one of the favorite pastimes of coastal geomorphologists. Schwartz's collection of significant papers on this topic (Schwartz, 1973) will no doubt stimulate a further flurry of interest of which this paper is perhaps an example. How can the present generation claim to add anything new? Perhaps we do have a

significant perspective inaccessible to our predecessors; those of us interested in shelf geology at this point in history have, thanks to technological advances, a far better collection of data from the shelf surface and subsurface — critical information if the uniformitarian principle is to be applied to the problem of barrier genesis during a transgression.

I would like to present a paradigm for a barrier island that I think is a helpful simplification; a barrier island is a littoral sand body consisting of (1) a shoreface maintained by the prevailing hydraulic regime, and (2) attached washover fans whose surfaces are modified by aeolian and by biological (including human) activity. Barriers are in some respects analogous to sand waves, which consist of a current-graded slope attached to an avalanche slope. If this viewpoint is accepted, then the beach and shoreface response surfaces are clearly the critical zones; the existence, geometry, and behavior of other parts of the barrier are dependent on the behavior of the shoreface. The delicate balance of this system, and the rapidity with which the system adjusts to human interference, has recently been documented in an intriguing case history by Dolan et al. (1973).

Some workers have described the origin of modern barriers in terms of their response to the Late Holocene reduction in the rate of sea-level rise (Curray, 1969, p. JC-II-16). Others have stressed that most barriers have reached their present positions by migration from more seaward positions (Otvos, 1970a,b; Dillon, 1970; Pierce and Colquhoun, 1970; Stapor, 1973). However, few seemed to have taken the concept of barrier migration to its logical uniformitarian conclusion.

To do so may require not only a change in the solution, but a change in the nature of the question being asked. If the conclusions of Stapor, Otvos, and Pierce and Colquhoun can be applied to the general case, then the question of how a barrier is initiated is in a sense, trivial. Firstly, if barriers have migrated into their present positions as a consequence of post Pleistocene sea-level rise, then the problem of genesis is transferred "out there" to some Late Holocene stillstand position on the shelf or perhaps to the shelf edge. Secondly, as Otvos and Stapor make very clear, migrating barriers are in a constant state of morphologic flux, with individual barrier islands and barrier spits continually undergoing expansion, contraction, fragmentation and integration. Thus a barrier system might have migrated to its present position from the shelf edge, but no two barrier islands or spits will necessarily have existed during the same fraction of this time interval. Those aspects of barrier behavior are also characteristic of smaller, simpler bed forms; the nature of the maintaining process of, say, current ripples, is more significant than the nature of the initiating process, since the sand-water interface is metastable when the critical-velocity threshold is achieved, and any small perturbation will begin the constructive feedback between flow and substrate. Likewise, in such systems the individual forms, ripples, are ephemeral with respect to the lifetime of the ripple train.

It therefore stands to reason that much of the evidence concerning the

genesis of the barriers of eastern North America must be sought on the Atlantic continental shelf surface (see Field and Duane, in preparation, for a related viewpoint). However, before examining this area, let us review elements of shoreface dynamics relevant to barrier formation.

SHOREFACE DYNAMICS

The shoreface as an equilibrium surface

The concept of the shoreface as a responsive interface between a substrate and a water column in a state of dynamic equilibrium with each other was first expressed in the geological literature in a highly deductive, qualitative way be Fenneman (1902) and Douglas Johnson (1919, p. 211).

Johnson states:

> "The essential nature of the shore profile . . . [is] that nice balance between the amount of work required to remove the debris and the ability of the waves to do removal work which we call "equilibrium". The subaqueous profile is steepest near land where the debris is coarsest and most abundant; and progressively more gentle further seaward where the debris has been ground finer and reduced in volume by the removal of part in suspension. At every point the slope is precisely of the steepness required to enable the amount of wave energy there developed to dispose of the volume to sediment there in transit."

Earlier, however, an Italian engineer, Cornaglia (1887) had observed a critical mechanism for the grading of the shoreface; depth and grain size on a point on the shoreface profile is determined by the Newtonian balance of forces on a sand grain; the value of the downslope component of gravitational force versus that of the net fluid force averaged over a wave cycle. Cornaglia's ideas were not available to workers in the United States until the Coastal Engineering Research Center (Anonymous, 1950) published an edited translation of an address by the Swedish coastal scientist, Munch-Peterson. U.S. workers developed the null-line concept, as it came to be called, into a complex numerical model for the shoreface equilibrium (summarized in Johnson and Eagleson, 1966). Further field work has shown that the null-line mechanism is only one of the processes controlling the shoreface equilibrium (Murray, 1967; Cook and Gorsline, 1972). The downslope gravitational component is probably not sufficiently intense over most of the shoreface for the null-line mechanism to be an adequate model of sedimentation. However, the structure of the wave-velocity field itself may induce a divergence of shore-normal sediment transport about a null line (Wells, 1967).

An adequate theory of shoreface sedimentation does not exist. However, no one who has watched a major storm strip away 50 m of beach, only to return the material in much the same configuration as before, can doubt that at least the upper shoreface exists in a state of equilibrium with the hydraulic regime.

Since the concept of equilibrium will be referred to again in this paper, it is important to define it carefully, and also stress the importance of the time scale of observation to the equilibrium concept. LeChatelier's principle is the most basic definition; an equilibrium system is one which when stressed, reacts in such a way as to relieve the stress. When "stressed" by a storm, a shoreface responds by widening and flattening through upper-shoreface erosion and offshore deposition. When fair weather returns, the lost sand (or its equivalent) also returns, to upper shoreface and beach storage. Systems whose characteristics oscillate about fixed values in this manner are systems in a state of homeostatic equilibrium. Whether or not a system can be described as an equilibrium system depends in part on its innate characteristics, but also on the time and space scales of observations. A coastal engineer is less likely than a geologist to find the term "equilibrium" applicable to the shoreface. The shoreface as he sees it is in a state of continual change and usually exhibits a slope intermediate between the extreme fair weather and storm profiles. The geologist is concerned with the long-term near configuration of the shoreface as observed over periods of years or decades. From his point of view, the response time of the shoreface to hydraulic change is instantaneous when compared with such long-term processes as the migration of the shoreline in response to sea-level rise. In these terms, the equilibrium concept is a useful one.

The shoreface and the sediment continuity equation

Our thought about this dynamic control zone on the forward surface of barrier islands has been clarified by the insistence of C.A.M. King in successive editions of her definitive text (most recently 1972) in considering the relative roles of onshore—offshore coastal transport, versus shore-parallel transport. This is implicitly the continuity concept of classical physics: to assess the coastal sediment budget, one considers a unit volume of a coastal water column (Fig. 1), and considers its imports and exports of water and sediment, through the faces of the box. These transport components are not merely convenient, but reflect the basic forcing mechanisms; the wave-driven longshore current and wind-driven coastal flow parallel to the beach on one hand, and upwelling and downwelling with associated coast-normal bottom transport, due to wave surge and wind and wave setup on the other hand.

The continuity relationship allows us to assess the relationship of the longshore sand flux to coastal progradation and retrogration. The sediment continuity equation is:

$$\frac{\partial \overline{C}}{\partial t} + \vec{\nabla} \cdot \vec{V}C = -\frac{\rho}{d}\left(\frac{\partial h}{\partial t}\right)$$

Where $\vec{V}$ is a vector velocity, $\overline{C}$ is average concentration of sediment, ρ is sediment density, d is water depth, h is height from baseline, and $\vec{\nabla}$ is the

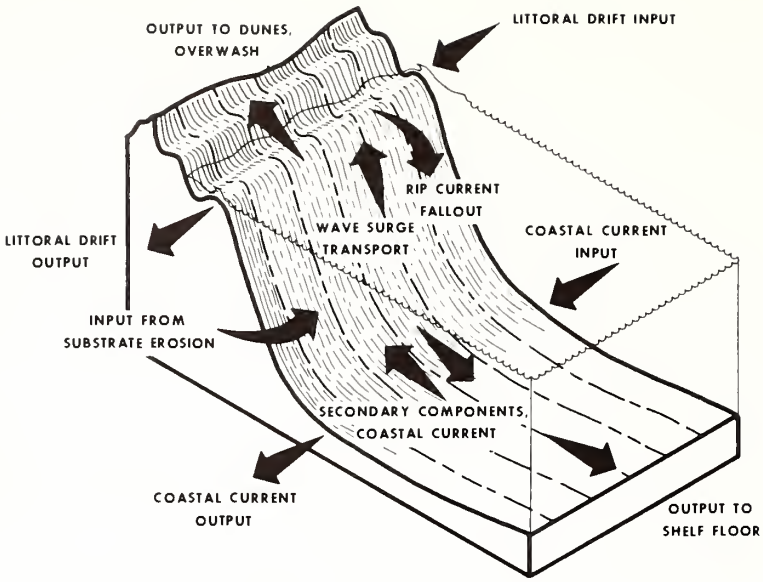

Fig. 1. The unit volume of coastal water column and its substrate. Arrows indicate components of sediment and water transport. Coast-parallel water movements are more intense than coast-normal movements, hence resultant transport vectors tend to make low angle with coast.

divergence, an operator indicating net difference. The equation states that time rate of change of sediment concentration, plus the net difference between sediment advected into the box and sediment advected out of the box, is proportional to the time rate of change of height of the water—sediment interface (aggradation or erosion). In other words, the shoreline tends to aggrade when the sediment-discharge gradient across the box is negative, or if the concentration of sediment is increased with time; erosion requires the reverse conditions.

May and Tanner (1973) have used a simplified version of the sediment continuity relationship in a model for the straightening of the coastline. With waves approaching normal to a coast composed of a series of headlands and bays, wave refraction will cause a greater wave-energy density (E) on the headland beaches (Fig. 2A) with a corresponding reduction of this characteristic on the bay beaches (Fig. 2B). However, the angle between wave crests and the beach will be greatest on the side of the headland. These relationships are indicated in a very schematic fashion in Fig. 2.

May and Tanner describe the longshore sediment transport rate as proportional to littoral power:

$$P_L = 0.5\, EC \sin 2\beta$$

where P_L is the longshore component of wave power, E is the wave-energy density (in Fig. 2A, proportional to the spacing of wave rays), C is wave-

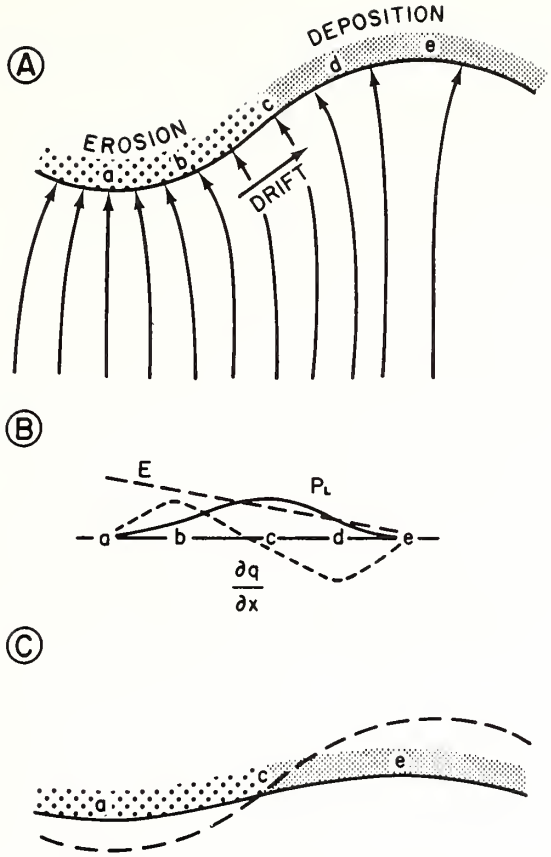

Fig. 2. Model for littoral sediment transport. A. Wave-refraction pattern with wave approach normal to coast. B. Resulting curves for energy density at the breaker. E (dimensions MT^{-2}); longshore component of littoral wave power P_L (dimensions MLT^{-3}); and the littoral-discharge gradient $\partial q/\partial x$ (dimensions L^2T^{-1}). C. Advanced state of coastal evolution. After May and Tanner, 1973.

phase velocity, and β is breaker angle. Thus the sand-transport rate is at a maximum between the point of maximum wave-energy density, a, and the point of maximum breaker angle, but much closer to the latter since on this gently embayed coastal model, the wave-energy density gradient is relatively flat (Fig. 2B).

In this two-dimensional situation, where only the longshore component of sand transport is considered, the sediment continuity equation reduces to:

$$\frac{\partial h}{\partial t} = -\epsilon \frac{\partial q}{\partial x}$$

where ϵ is a dimensional constant related to sediment porosity. The term $\partial q/\partial x$ is the rate of change of littoral drift discharge with distance along the

beach and varies as the derivative of P_L (Fig. 2B). The equation states that where the sand-discharge rate decreases along an isobath of the shoreface (negative $\partial q/\partial x$) the shoreface at a point along the isobath must build up at a rate proportional to the drop in discharge across that point. In Fig. 2, $\partial q/\partial x$ is positive from *a* to *c*, hence the shoreface off the headland must erode, and the headland shoreline retreat. Maximum erosion will occur at *b*, where the gradient is steepest. Between *c* and *e* it is negative, hence the bay shoreface must aggrade and the bay shoreline advance. Maximum deposition will occur at *d*.

If waves advance normal to this shoreline over a sufficiently long period of time, a very peculiar shoreline must result. It will be essentially a straight line normal to wave approach running through point *c*. However, a sliver-like peninsula will protrude at *a*, where $\partial q/\partial x = 0$, and a narrow re-entrant will occur at *e* where $\partial q/\partial x = 0$ also. In nature, however, the direction of wave approach varies, day by day around the mean orientation, and positions *a*

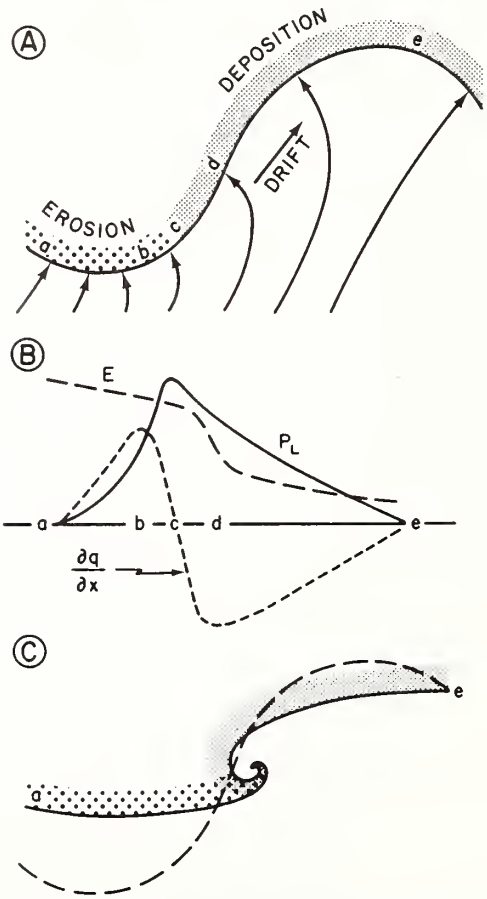

Fig. 3. Variant of littoral-transport model, with a more deeply embayed coast and an oblique direction of wave advance.

through e shift accordingly, hence such anomalies do not occur at the mean positions of a and e, and in our ideal model, a smooth, straight shoreline must result. The coast is shown in an intermediate stage of evolution in Fig. 2C.

It is interesting to consider a variant of this model, in which the degree of embayment of the coast is more extreme, and the mean direction of wave approach is at an angle to the coast (Fig. 3). Under these conditions, the decrease in wave-energy density from headland to bay head may no longer be nearly linear, but may be more nearly a step function. The littoral-discharge gradient is no longer primarily controlled by the breaker angle, but is strongly modified by the discontinuity in the wave-energy density. These relationships are very sensitive to the nature of the nearshore bathymetry, and become quite difficult to predict. They are presented in qualitative fashion in Fig. 3B. The main effect of the new configuration is the capture of the point of maximum littoral deposition, d, by the step in the wave-energy density distribution. Shoaling at this point may be sufficient to result in a discontinuity in the shoreface, in the form of a recurved spit which progrades into the bay, as the headland retreats and the bay-head beach advances (Fig. 3C).

The shoreface in profile

The unit-volume model can be simplified to a coast-normal profile to assess the consequences of landward and upward translation of the equilibrium profile in response to rising sea level. Bruun (1962; see also Schwartz, 1965, 1967, 1968) has shown that the geometry of such a translation requires shoreface erosion and a corresponding aggradation of the adjacent sea floor, assuming $\partial q/\partial x = 0$ parallel to the coast through the unit volume (Fig. 4A). Moody (1964, pp. 142—154) has described landward profile translation on the Delaware Coast, as induced by storm sedimentation. The barrier steepens over a period of years towards the ideal wave-graded profile, by both upper-shoreface aggradation and lower-shoreface erosion. During periods of fair weather, the landward asymmetry of fair-weather wave surge traps sand on the upper shoreface, resulting in a trend towards increasing sand storage in the shoreface and beach prism. Mild storms erode the shoreface; but upper-shoreface deficits tend to be made up. This trend is abruptly terminated by a major storm which results in massive shoreface and beach erosion, a markedly flattened gradient, and landward profile translation on the order of tens of meters. The cycle then begins anew.

Thus the longterm behavior of the shoreface during a marine transgression, whether retrogradation or progradation, depends on the balance between fair-weather accumulation and storm erosion over the observational interval. If erosion predominates, the mean trajectory of the shoreface must be landwards and upwards (Fig. 4A). The barrier superstructure may retreat in cyclic, tank-tread fashion, by a process of storm washover of sand, its burial, and re-emergence at the upper shoreface. Debris from the eroding

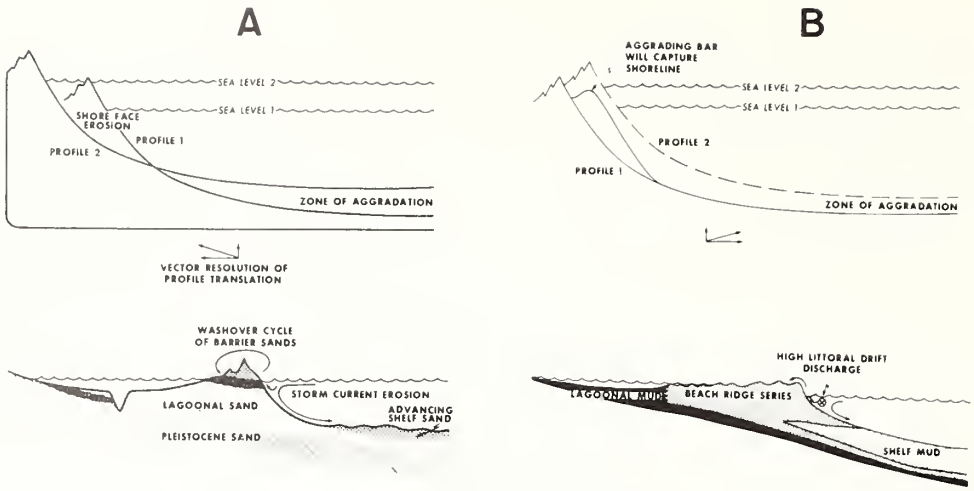

Fig. 4. A. Erosional shoreface retreat, after Bruun, 1962. On an unconsolidated coast, a rise of sea level results in shoreface erosion, and concomitant aggradation of the inner-shelf floor as long as coastwise sand exports equal or exceed coastwise sand imports. B. Depositional advance of the shoreface, in response to an excess of coastwise sand imports over exports. After Curray et al., 1969.

lower shoreface will accumulate beneath the rising lower limb of the profile on the adjacent sea floor. The transfer process is poorly understood. Transfer from the shoreface to the adjacent shelf floor probably occurs during storms when the coastal boundary of the storm flow field takes the form of a down-welling jet flowing along the contours of the shoreface, in response to coastal-wind setup (Swift et al., in press). However, if sedimentation predominates over erosion on the shoreface, the profile will translate seaward and upward, usually by means of the cyclic outward growth of beach ridges (Curray et al., 1969; Fig. 4B this paper).

A word on the factors controlling the steepness and curvature of the profile is in order at this point. Grain size is the most obvious control (Bascom, 1951); the coarser the sediment supplied to the coast, the steeper the shoreface profiles. Shorefaces built on shingle may attain 30° slopes near the beach; shorefaces of sand are rarely more than 10° at their steepest, while shorefaces on muddy coasts are so flat as to be virtually indistinguishable from the inner shelf. Sediment input and the wave climate also affect the shape of the profile. In general, inner shelves experiencing a higher influx of sediment and a lower wave-energy flux per unit area of the bottom are flatter, while inner shelves with a lower influx of sediment and a higher wave-energy flux per unit area of the bottom are steeper (Wright and Coleman, 1972). Due to the complex interdependence of the process variables, cause and effect are difficult to ascertain; on a steeper shelf, for instance, grain size is coarser because the steeper slope results in more energy being released per unit area of the bottom; more energy is released because the

coarser grain size results in a higher effective angle of repose. Or starvation of the profile will result in steepening, with a resultant higher energy flux and coarsening of its surface (Langford-Smith and Thom, 1969).

The relationship between the rate of sea-level displacement and the shape of the profile requires some thought. A number of workers have assumed that rapidly translating coasts are in a state of disequilibrium, and that equilibrium can only be realized on very slowly translating or stillstand coasts. This view results from an inadequate appreciation of the equilibrium concept and is tantamount to stating that only chemical reactions that have gone to completion are equilibrium reactions.

It is important to distinguish clearly between the concept of coastal maturity on one hand, and the concept of coastal equilibrium on the other. Davis (in Johnson, 1919) has assembled a spectrum of coastal types which suggests that the coastal profile passes through stages of "youth, maturity, and old age" in which the profile becomes increasingly flatter, until a final profile of static equilibrium is reached — ultimate wave base, in which the continental platform has been shaved off to a level below which further marine erosion occurs so slowly as to be negligible. The scheme is unrealistic in that it fails to recognize the continuous nature and mutual dependence of the process variables of an equilibrium system. Some of these stages will occur as transient states after the sudden rejuvenation of a tectonic coast. But as the profile becomes increasingly mature, its rate of change decreases, until it attains the equilibrium configuration required by existing rates of such other process variables as sediment input and eustatic sea-level change. At this point the profile must continue to translate according to the Bruun (1962) model of parallel shoreface retreat (Fig. 4A), until the rate of one or another variable changes again.

Only in such cases of relatively rapid tectonism may hysteresis, or lagged response occur. Strictly speaking, the term "disequilibrium" should be applied only to such cases. Slower changes in a process variable will allow continuous and compensating adjustment of profile, and while its shape changes, the profile is at all times in equilibrium. Coastal disequilibrium tends to be more apparent on rocky coasts, because of the greater response time of the indurated substrate, and because such coasts are more likely to be subject to tectonism.

Consequently, the effect of the rate of sea-level displacement in the equilibrium profile must depend on the initial slope of the substrate. On low coasts, where the initial slope is flatter than the maximum potential slope of the equilibrium profile, then the more rapid the sea-level displacement, the flatter the resulting equilibrium profile (see for instance Van Straaten, 1965). This relationship may be viewed as a function of work done on a substrate to build the optimum shoreface. As a coast advances more rapidly, successive shorelines experience the energy flux of the regime of shoaling waves for shorter periods of time and the resulting profile is flat (immature). If, however, a coast undergoes stillstand, the climax, or fully mature configu-

ration can develop, which is the steepest profile possible for the available grain size of sand, rate of sediment influx and hydraulic climate.

On high, rocky coasts, however, the initial slope of the substrate may be steeper than mean, or even the maximum slope of the steepest profile permitted by these variables. Under such circumstances, the more rapidly transiting shorelines, since these do the least work, have the least-modified and hence steepest (most immature) profiles, while the most slowly moving shorelines are the most modified and hence flattest profiles.

Variation in curvature of the shoreface, plus variation in the angle of translation of the shoreface lead to a variety of possible modes of translation. Fig. 5 illustrates some possible scenarios. In Fig. 5A, the coast is undergoing Bruun erosional retreat, as in Fig. 4A. The trajectory of shoreface-

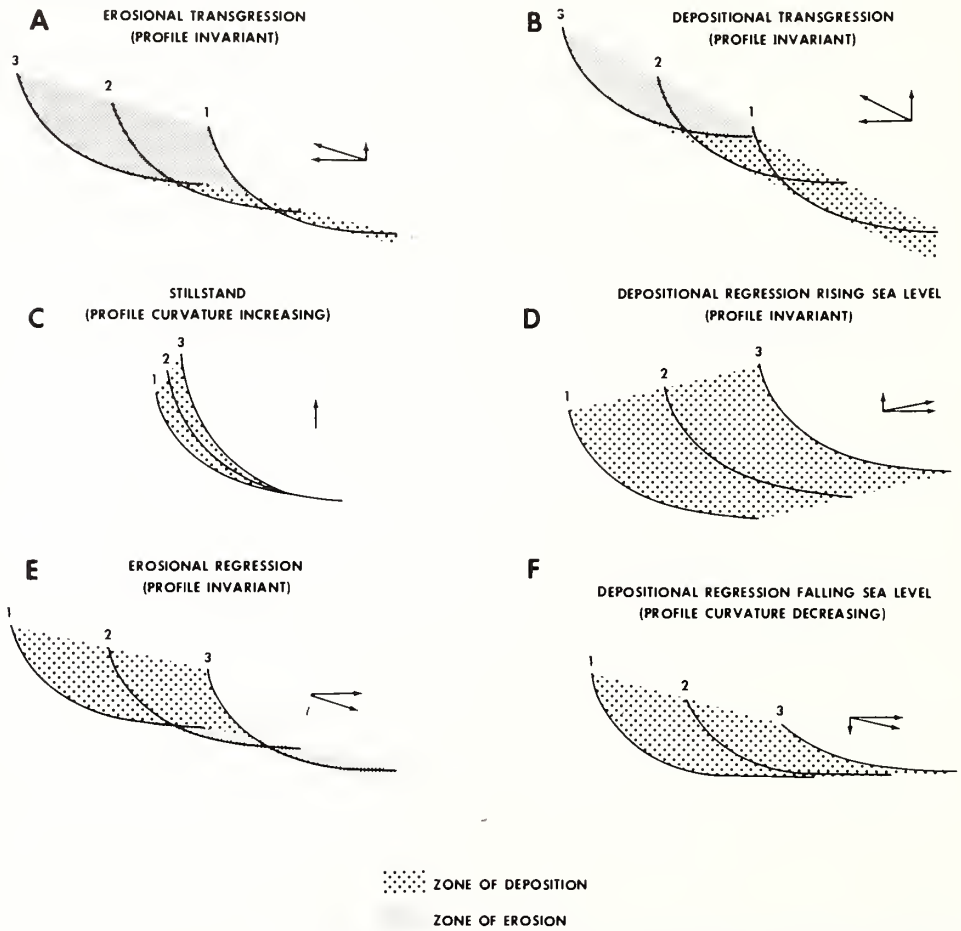

Fig. 5. Modes of shoreface translation as a function of (1) direction of profile translation and (2) change in profile curvature. Envelopes of erosion and aggradation are shown. Terms from Curray, 1964.

profile translation is parallel to the surface being transgressed. River sand is trapped in the throats of estuaries. Littoral-discharge gradients are positive along most parts of the coast. Most modern retreating coasts fall into this category.

In Fig. 5B, the rate of sea-level rise has decreased. Estuary mouths have adjusted to their tidal discharge, and are capable of bypassing sand. The littoral-drift gradient is still positive but is more gentle, hence shoreface erosion is less severe. The trajectory of shoreface-profile translation diverges from the surface being transgressed, and the back-barrier zone becomes a widening expanse of marshes or lagoons. The transgressing shoreface no longer destroys all back-barrier deposits as in Fig. 4A, as these deposits are now much thicker and the shoreface merely translates through their upper portion. Basal back-barrier deposits may be found beneath a thick layer of shelf-floor sand, that has accumulated seaward of the shoreface. As the widening belt of marshes and lagoons taps more of the river sediment, less is fed to the outer beaches, the trajectory of profile translation ceases to diverge from the surface being transgressed, and the oceanic shoreline and inner lagoonal shoreline transgress at more or less the same rate. The Lumbee Group of the Cretaceous coastal plain of North and South Carolina was probably formed in this manner (Swift and Heron, 1969).

In Fig. 5C, sea-level rise has decreased. There is sufficient input of sand into the littoral-drift system to cause the upper shoreface to prograde, steepening the profile. The Late Holocene reduction in the rate of sea-level rise of 4,000—7,000 years ago may have had this effect on portions of the world's coasts.

In Fig. 5D, a markedly greater injection of river sand into the coastal drift nourishes the entire shoreface. The profile translates upwards and outwards. The Costa de Nayarit (Curray et al., 1969) is a classic example of such a coast.

In Fig. 5E, sea level is falling. The Bruun process is reserved and the shoreface profile translates seaward down the sloping shelf surface. The upper shoreface progrades. The lower shoreface and inner-shelf floor subject to intensified wave action by a shoaling water column, erode. In Fig. 5F, sea level is falling, but there is a sufficient input of mobile fine sediment that both the shoreface and inner-shelf sectors aggrade.

The shoreface in plan view

Coastal straightening. A characteristic of the equilibrium shoreface surface that as much as any mechanism is the basic "cause" of barrier islands is its innate tendency toward two-dimensionality; its tendency to be defined by a series of nearly identical profiles in the downdrift direction. The equilibrium shoreface does not "want" a lateral boundary, since the wave and current field to which it responds does not generally have one. The initial conditions during a period of coastal sedimentation may however include such discon-

tinuities; as in the case of a coast of appreciable relief (bay—headland coast) beginning transgression.

On such a coast shoreface surfaces will tend to be incised into the seaward margins of promontories exposed to oceanic waves, and will propagate by constructional means in the downdrift direction as long as material is available with which to build, and a foundation is available to build on. The basic mechanism is presented in schematic fashion in Fig. 3.

Where the shoreline curves landward into a bay, the longshore component of littoral wave power decreases, and $\partial q/\partial x$ is negative. The shoreface at that point must aggrade until $\partial q/\partial x$ approaches zero at that point, and the zone of negative $\partial q/\partial x$ has moved downdrift. We give the lateral propagation of the shoreface into coastal voids the descriptive term "spit building by coastwise progradation" (Gilbert, 1890; Fisher, 1968).

However, the tendency of the shoreface to maintain lateral continuity also acts to prevent discontinuities as well as to seal them off after they have formed. In order to illustrate this, we may consider another set of initial conditions; a low coastal plain with wide, shallow valleys after a prolonged stillstand during which processes of coastal straightening by headland truncation and spit-building have gone to completion. Bay-head beaches have prograded to the position of adjacent headlands, or have been sealed off by spits and filled in by marshes. Fig. 2 is a better model from which to deduce the consequences for this set of initial conditions. As this coastline submerges, the water, seeking its own level, would invade valleys more rapidly than headlands could be cut back. The oceanic shoreline, however, would not follow, for if it should start to bulge into the flooding stream valleys, the bulge would become a zone of negative $\partial q/\partial x$; hence the rate of sedimentation would increase to compensate for any incipient bulge. The shoreface would translate more nearly vertically than landward at this sector, until continuity along the coast would be restored. The beach and dune, nourished by littoral drift, would be able to grow upwards at the same rate as sea-level rise, but the swale behind the dune would not. Shallow water bodies would extend into these swales from the sides of estuaries. Thus a straight or nearly straight oceanic shoreline must detach from an irregular inner shoreline, and be separated from it by a lagoon of varying width. This process of mainland-beach detachment was first proposed by McGee (1890), and later described in detail by Hoyt (1967) and Hails and Hoyt (1968).

Coastal rotation. In addition to straightening the coast by infilling or inhibiting bays, the trend of the coast towards equilibrium in plan view may involve rotation of coastal segments into preferred orientations with respect to prevailing waves. In order for such rotation to transpire the coastal segment must be a more or less closed system with respect to littoral drift. The simplest case is a groin field, whose groins extend seaward through the zone of maximum wave action, so that drift between groins tends to accumulate against the downdrift groin while the upper end of the compartment, starved

by the updrift groin, tends to retreat. Pocket beaches, between rocky headlands, behave in a similar manner, tending to rotate into a normal orientation with respect to prevailing wave orthogonals.

If the initial angle between the prevailing wave direction and the coastline is less than 50°, then an equilibrium alignment at less than normal orientation may prevail. Davies (1973; p. 173) has noted that many beaches tend to build parallel to the line of maximum drift, which lies in the region of about 40°—50° to the direction of wave approach. A homeostatic equilibrium tends to prevail for such beaches. Any increase in beach angle causes a reduction in the beach-parallel component of littoral wave power while a decrease in beach angle causes a reduction in wave-energy density and therefore a reduction in total littoral wave power. Davies refers to such an oblique equilibrium alignment as a *drift alignment.* Large-scale coastal segments generally cannot rotate very far. As the downdrift sector finds itself in progressively deeper water, there is more surface area of shoreface to nourish, and more and more sand is required for each angular unit of rotation. The extent to which rotation transpires probably also depends on the rate of sea-level rise or fall; with a slowly rising sea-level, for instance, equilibrium might be reached at a beach-wave angle closer to the climax configuration, than in the case of a more rapid rise of sea level.

Coastal compartments not captured by the drift alignment will proceed to the *swash alignment* (Davies, 1958) or alignment normal to wave orthogonals. The adjustment is a feedback process, since as orientation of the shoreface shifts, the pattern of refraction of surface wave trains which induces the shift must also change.

Straight swash coasts are inherently unstable, so that slight initial variations of substrate configuration tend to initiate a constructive feedback, until the coast stabilizes in a series of wave-like forms, such as the cuspate forelands of the Carolina coast, or as an alternation of swash and drift segments, such as the offset coasts of successive zetaform beaches (Davies, 1973, p. 136).

Shoreface maintenance and barrier formation

Barrier island formation by upward growth. We have arrived at two time-honored mechanisms for barrier formation by a consideration of shoreface dynamics. Before considering the relative roles of coastwise spit progradation and mainland-beach detachment, we should consider a third basic mechanism, namely De Beaumont's (1845; in Schwartz, 1973) initiation and upward growth of offshore bars. In a sense, this is a special case of the mainland-beach detachment hypothesis in that it stresses onshore—offshore sediment transport, versus coastwise sediment transport. There are two basic problems associated with this mode of barrier formation that have been faced with varying degrees of success by its proponents.

The first concerns initial conditions. Johnson (1919) solved this by requir-

ing a previous withdrawal of the sea, such that at time zero, a metastable condition prevails, in that the sea-floor slope is gentler than that required by the equilibrium profile. However, as previously noted, the response time of the shoreface is instantaneous with respect to even glacioeustatic sea-level fluctuations. Prograding shorelines continue to maintain shorefaces as they prograde, generally by the cyclic formation of closely spaced beach ridges (Fig. 4B). The result of stillstand passing into regression may be the expansion of the stillstand barrier into a beach-ridge plain tens of kilometers wide (Curray et al., 1969). As many authors have noted, a beach ridge is not the same thing as a barrier. Beach ridges are generally much narrower than barriers (on the order of 50 m versus perhaps 500 m for a barrier; Curray, 1969), although the largest beach ridges are as large as narrow barriers. Beach ridge "lagoons" are usually marshy swales no wider than the ridges themselves (Curray, 1969). Barrier surfaces may consist of beach-ridge complexes, but these sequences have been tacked on to the forward face of a much larger feature — the barrier foundation. The subaerial surface of the Atlantic coastal plain is webbed with such beach-ridge plains between successive high stand barrier systems (Oaks and Coch, 1963; Colquhoun, 1969), demonstrating the general inadequacy of a prograding shoreline to build an offshore barrier and wide lagoon according to Johnson's method. In genetic terms, beach ridges (or if the influx of fine sediment is sufficient, cheniers) appear to be the response of prograding shorelines to shoreface processes, while barriers are the response of stillstand or retrograding shorelines.

The second and closely related problem associated with the upbuilding-bar hypothesis is the inadequacy of known mechanisms of swash-bar formation for building barriers of appropriate scale and distance from shore. Break-point bars are small-scale features which form beneath the breaker, on mainland beaches and on barriers. On retrograding coasts, they tend to form as storms wane, then migrate onshore as swash bars (intertidal bars) during the ensuing fair-weather period, to weld to the beach (King, 1972). On prograding coasts, break-point bars are stabilized by accretion on their seaward faces, become swash bars, then during periods of neap tide, may build high enough to become the new shoreline and initiate dunes (Curray, 1969). The resulting feature, however, is a beach ridge, not a barrier island.

The only other available mechanism appears to be intertidal swash platforms associated with the ebb-tidal deltas of estuary mouth or tidal-inlet shoals (Oertel, 1972). These are commonly shore-normal, levee-like structures, but the "new barrier island" figured by Shepard (1973, fig. 7b) from the Gulf Coast of Florida may be of this origin since it closes off a tidal inlet. This small feature appears to represent a new superstructure element formed on an existing barrier platform.

Otvos (1970a) advocates the emergence of offshore bars as a mechanism for generating barrier islands. His "subsurface evidence", however, is ambiguous, in that bore-hole spacing is not shown, and criteria for distinguishing barrier subenvironments are not discussed. In any case, his cross-sections

cannot distinguish between the offshore initiation and emergence of barrier islands, and their lateral migration in the direction of drift, which he so clearly describes and figures (Otvos, 1970a, fig. 3). Hoyt's (1967) conclusions appear to be still valid: ". . . minor barriers may form from bars, but the observed cases have been small, short-lived features formed close to the shoreline, and can hardly be compared with the major features under discussion."

Coastwise spit progradation vs. mainland-beach detachment. Much of the debate concerning origin of barriers deals with the relative importance of spit-building versus mainland-beach detachment (Fisher, 1968; Hoyt, 1967, 1968, 1970; Otvos, 1970a,b). The problem can be fully answered only by careful study of the field evidence, and as noted by several authors (Otvos, 1970a,b; Pierce and Colquhoun, 1970) the evidence has frequently been destroyed by landward migration of the barriers. However, it is possible, in the time-honored deductive fashion of coastal morphologists, to consider the conditions most favorable to these two modes of barrier formation. Spits are certainly characteristic of coasts of high relief undergoing rapid transgression as described above (see papers in Schwartz, 1973). It seems probable that under such conditions mainland-beach detachment would be severely inhibited. Even allowing for ideal initial conditions with a classic coast of old age (Fig. 6), where alluvial fans are flushed with truncated headlands, detached mainland beaches would have a limited capability for survival. With signifi-

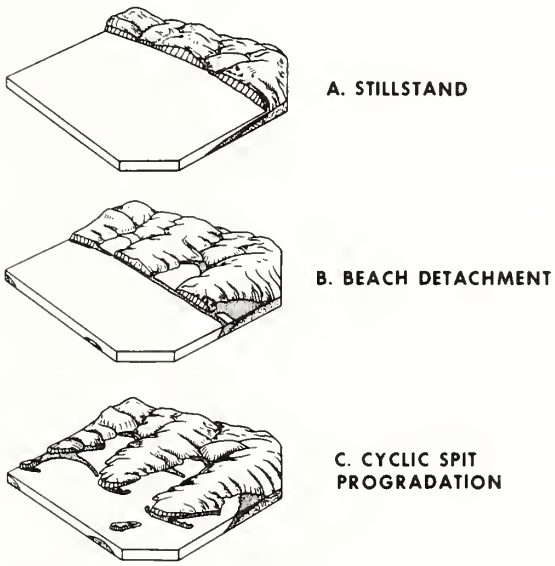

Fig. 6. Evolution of the shoreface as a rugged coast passes from stillstand to transgression. A mature configuration is replaced by a transient state of mainland-beach detachment, then by a quasi steady-state regime of cyclic spit building. Johnson's (1919) stages of coastal maturity — portrayed in reverse sequence!

cant relief, the submarine valley floors adjacent to retreating headlands must lie in increasingly deeper water after the onset of transgression. As the submarine surface area of the barrier requiring nourishment increases, the capacity of littoral drift to nourish it may eventually be exceeded. As this point is approached, storm washover will cause the barrier to retreat until equilibrium is restored, a position which may be well inland from the tips of headlands. Both littoral wave power and sediment supply may be deficient in these inland positions, further jeopardizing the survival of the barrier. As the loop of the barrier into the bay becomes extreme, sediment supply from headlands is liable to capture by secondary spits formed during storms. These may prograde out toward the drowned valley thalweg until capacity is again exceeded and their tips are stabilized; further movement being limited to retreat coupled with that of the headland to which they are attached.

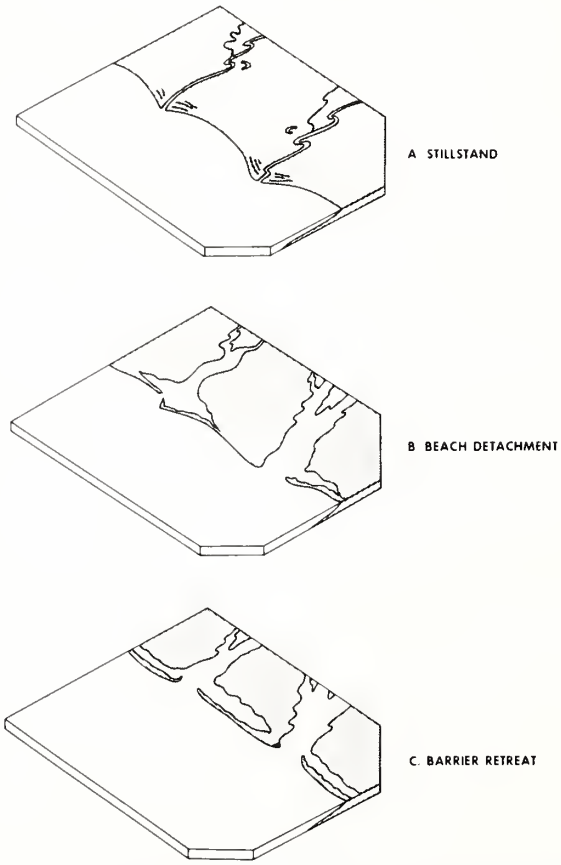

Fig. 7. Evolution of the shoreface as a low coast passes from stillstand to transgression. A mature coastal configuration passes via mainland-beach detachment into a steady-state regime of barrier retreat.

Finally the survival or primary barriers on such a coast would be limited by the tendency of submerging headlands to form islands. A spit tied to a promontory that becomes an island can retreat no further if a drowned tributary valley lies landward of it, but must instead be overstepped. The few unequivocal examples of transgressed barriers on the shelf floor appear to be overstepped, rock-tied spits (McMaster and Garrison, 1967; Nevesskii, 1969).

On the other hand, transgression of a coast of very subdued relief — such as is the case for most coastal plains — would tend to promote mainland-beach detachment at the expense of spit formation, given initial conditions of a straight coast (Fig. 7). The depth of water in which detached bay-mouth barriers would be built would be less, because the relief would be less. Littoral drift would be generally adequate to nourish the lesser submarine surface area of the barrier face. The upper, erosional zone of the shoreface (Fig. 4A) would be more likely to extend down into the pre-recent substrate (Fig. 8); hence erosion of the inner-shelf floor would become as important a source of sand for the barrier as the erosion of adjacent headlands. With a rise in sea level, valley-front dune lines would grow upward. Rivermouths, initially deltaic, would flood as estuaries, while lagoons would creep behind the beaches toward the headlands on either side. Coastal discontinuities

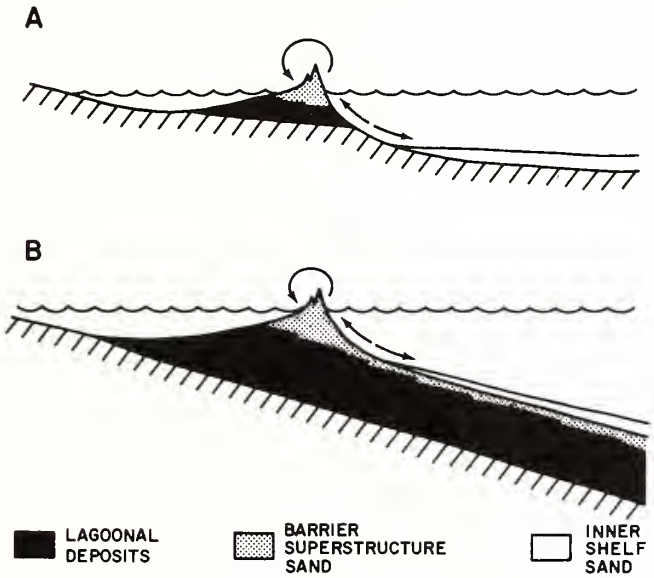

Fig. 8. Contrasting sand budgets. A. Of a barrier built on a gentle submarine gradient as in Fig. 6. B. On a steep submarine gradient as in Fig. 5. In A, zone of shoreface erosion penetrates to pre-recent substrate, which becomes "income" for barrier nourishment. In B, the barrier may only "borrow" from its own "capital" through shoreface erosion, and the heavy expenditure involved in paving the shelf with sand during barrier retreat may "bankrupt" the retreating barrier, which must either accelerate its retreat, or be overstepped. In either case shoreface continuity is liable to be broken, resulting in cyclic spit building.

sufficient to induce coastwise spit progradation would be unlikely to occur, except in special cases to be discussed later.

Thus, on a low, initially straight coast, barrier spits and barrier islands would preferentially form by mainland-beach detachment, rather than by coastwise progradation.

HOLOCENE BARRIER MIGRATION, MIDDLE ATLANTIC BIGHT OF NORTH AMERICA

Evidence from the shelf floor

In order to illustrate the preceeding inferences, let us consider the Holocene barriers of the Middle Atlantic Bight, keeping always in mind that: (1) barriers are response elements in water column—substrate systems in states of dynamic equilibrium; (2) the response times of barriers to such process variables as wave climate and sand supply is instantaneous relative to such "geologic" process variables as the rate of sea-level rise; and (3) in such closely coupled, migrating systems, there are continuous small-scale adjustments to local values of process variables; hence the pattern of the barrier system is instantly changing.

Let us start with the Late Wisconsin lowstand. As sea level dropped to this position, the coast must have had a somewhat different complexion than does the present coast; prograding coasts tend to consist of coalescing deltas; or if rivers are widely separated, of deltas alternating with beach ridge or chenier plains. Deltas themselves tend to consist of distributaries webbed with these features. This Late Pleistocene, progradational fabric is well preserved on the modern subaerial coastal plain (Oaks and Coch, 1963; Colquhoun, 1969). Even on the prograding Late Wisconsin coast there locally may have been true barriers; larger-scale forms with lagoons behind them many times wider than inter-beach ridge swales. These would have formed where the rate of coastal sedimentation locally decreased due to the migration of river mouths, in a manner analogous to the destructional phase of delta building (Scruton, 1960).

The present submarine morphology of the Middle Atlantic Bight suggests that the shelf edge during the Late Wisconsin lowstand (of perhaps 15,000 years ago; Milliman and Emery, 1968) consisted of a series of deltas (Fig. 9), now recognizable as oval terraces with seaward convex scarps falling away before them, and much gentler seaward concave slopes rising behind them (Swift et al., 1972b).

At maximum lowstand, with sea level falling in excess of 125 m, the deltas would have been dissected, with gullys feeding into submarine canyons, and the steep upper-slope gradient would probably have suppressed extensive barrier and spit formation. Here perhaps is time zero for the formation of Holocene barriers on the Atlantic coast.

We must next ask ourselves what would happen as the sea came up over

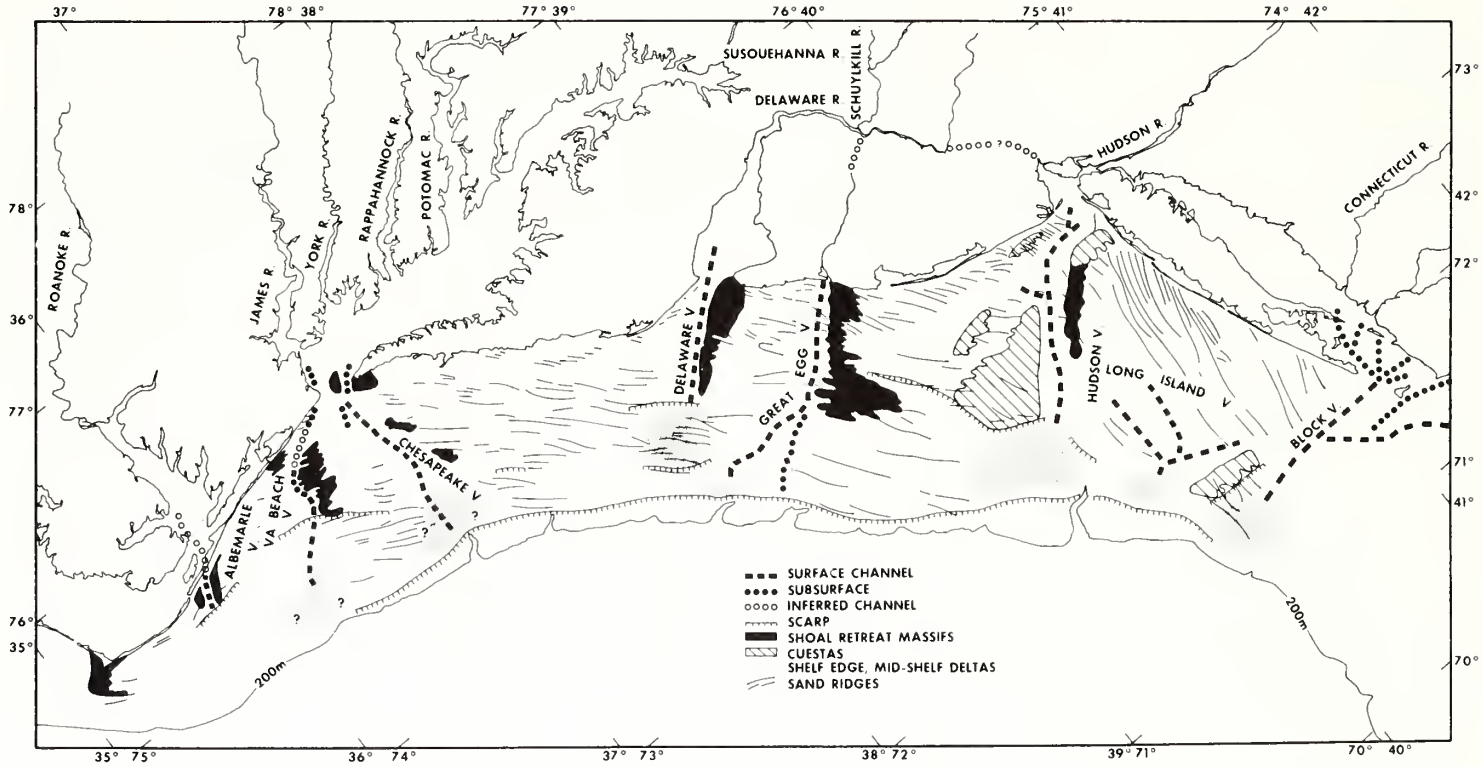

Fig. 9. Geomorphic framework of the Middle Atlantic Bight. From Swift and Sears, 1974.

the shelf edge. The reasoning presented in the previous section would lead us to infer that conditions would be ideal for essentially simultaneous formation of barriers along the length of the Middle Atlantic Bight. The primary mechanism would be mainland-beach detachment, since the shoreline would be constrained to be straight by virtue of being the shelf edge, and the land behind it would be flat, by virtue of being a deltaic outer coastal plan.

From here on in the "origin" of the barrier system at each stage (with some exceptions to be noted later) is simply that it migrated in from the preceeding stage; once a barrier has migrated a unit width, it becomes meaningless to ask whether its origin is detachment or coastline progradation.

It is becoming apparent that the Holocene barrier system has left little or no trace of its migration across the shelf. The discontinuous sheet of clean sand veneering the shelf surface contains neither structures nor fauna that are unique to barrier environment; instead an inner-shelf lithosome appears to rest directly and disconformably on back-barrier deposits (Shideler et al., 1972; Stahl et al., 1973; Sheridan et al., 1974; Stubblefield et al., 1975; Fig. 10, this paper) without the intervention of barrier superstructure deposits. When a beach fauna is found, it is as a lag deposit *between* the sand sheet and the underlying back-barrier deposits (Fischer, 1961; Field, 1974). The

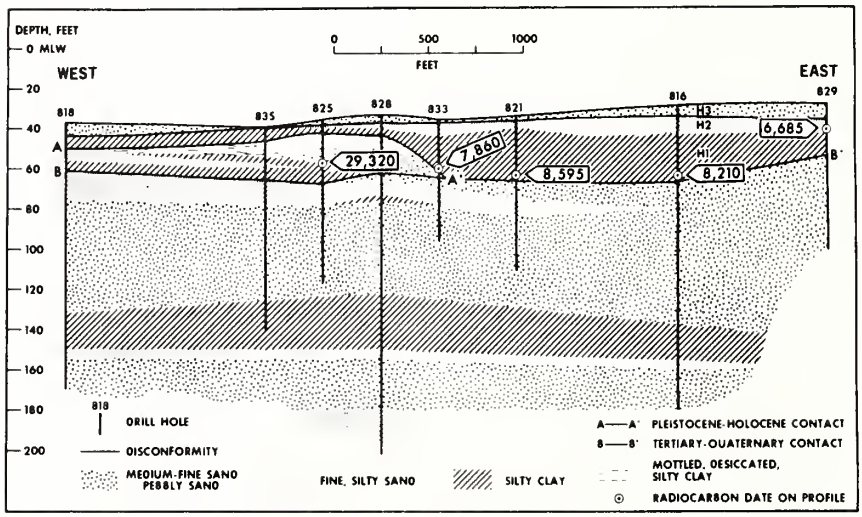

Fig. 10. Stratigraphy of the New Jersey coast five miles offshore from Beach Haven Inlet, illustrating the "lagoonal carpet". Shoreface retreat has continuously destroyed the superstructure of the retreating barrier. Initial transgressive deposits of lagoonal mud (*H1*) and overwash sand (*H2*) are separated from the marine-debris sheet (*H3*) by a disconformity. Central portion of lagoonal deposit was probably deposited by a landward-migrating tidal channel, trending into the page, resulting in seaward-facing cut bank of Pleistocene clay between drill holes 828 and 833. This situation is intermediate between Fig. 8A and 8B. Lagoonal carpet is discontinuous, and substrate sand is locally released into modern coastal transport system. From Stahl et al., 1973.

surficial sand sheet would thus appear to be the product of erosional shoreface retreat, as illustrated in Fig. 4A.

The ridge and swale topography of the Middle Atlantic Bight superficially resembles a prograding subaerial strand plain, but the age relationships are reversed. Shells collected from the surface are progressively younger in a landward direction, rather than older (Merrill et al., 1965). The ridge topography does not generally meet Gilbert's (1890) stairstep criterion for a submarine strand plain formed during shoreline retreat. Gilbert pointed out in this case, the toe of each barrier must lie at the altitude of the top of the barrier immediately seaward. But in the Middle Atlantic Bight, topographic profiles across broad sectors of ridge topography are gently inclined polyharmonic curves, rather than step functions. Inner-shelf ridge fields can be traced directly into shorefaces (Duane et al., 1972) where they appear to be forming in response to boundary flow of the storm flow-field (Swift et al., 1973). The ridge topography, however, appears to be "contagious"; it appears on shoal-retreat massifs (low, shelf-transverse highs that are retreat paths of littoral-drift convergences) where it has not been initiated by shoreface processes (Swift and Sears, 1974, especially fig. 19). Textural evidence suggests that the surficial sands of central-shelf ridge fields are continuing to respond to storm flow- events (McKinney et al., 1974; Stubblefield et al., 1975).

Apparent shoreline morphology of the stairstep variety *does* occur in the Middle Atlantic Bight, in the form of a series of terraces and scarps (Fig. 9; Emery and Uchupi, 1972, fig. 21; McClennen and McMaster, 1971). The terrace—scarp sequence has a wavelength in the order of tens of kilometers; the ridge topography with spacings of 2—4 km occurs on the terrace surfaces. It is difficult, however, to attribute the stairstep sequence to saltatory overstep of barriers (Curray, 1964, p. 199), where the surf zone is "captured" by the lagoonal beach as the barrier founders, since the supposed drowned lagoons are mantled by the characteristic sand sheet of erosional shoreface retreat. Instead, the shorelines must reflect a more complex process (Fig. 11) whereby periodic stillstand caused the vertical component of shoreface translation to increase at the expense of the horizontal component, resulting in stillstand or even progradation (see Fig. 5C). Such stillstands would have been due to glacioeustatic sea-level fluctuations, regional or local fluctuations in sediment supply, or all three effects. During such periods, the shoreface may attain its climax configuration by means of straightening and rotation of coastal compartments. Carver (1971) has noted that in North America's Southern Atlantic Bight, stillstand positions are marked by distinctive heavy-mineral zones enriched in the more labile species. Carver suggests that during stillstand, littoral-drift compartments became integrated with each other, and with a stream net capable of delivering the enriched piedmont mineral suite, in addition to the more limited, mature suite reworked from coastal-plain strata.

At the conclusion of a stillstand, the equilibrium response of the barrier

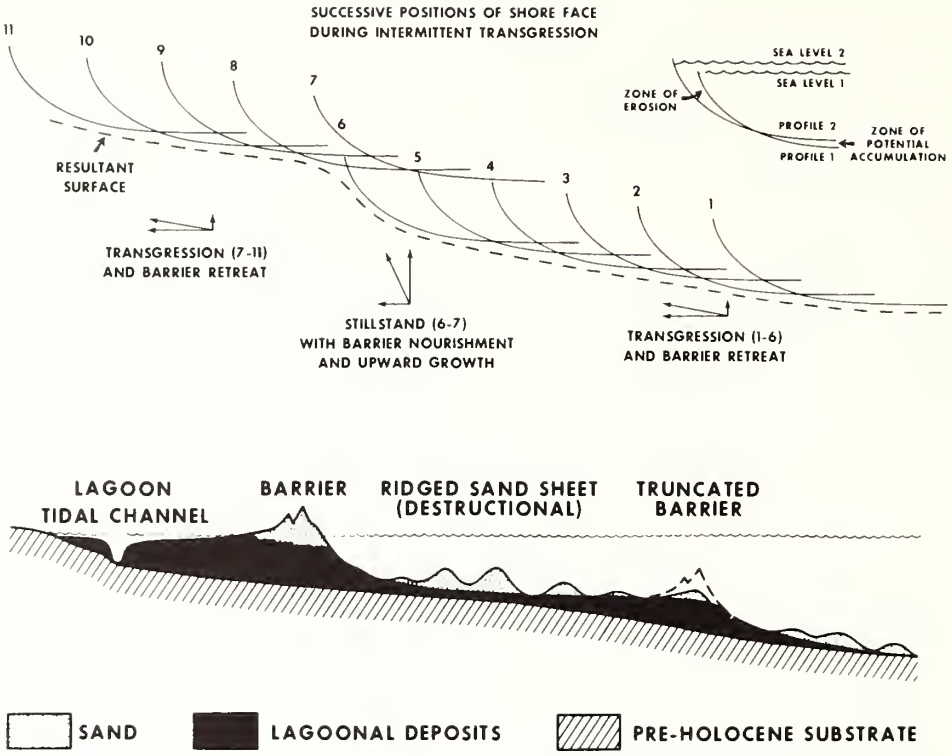

Fig. 11. Formation of a shelf scarp. Stillstand and upward profile translation is followed by a resumption of transgression, truncating stillstand barrier.

system to renewed sea-level rise would be a resumption of erosional shoreface retreat, if the principles set forth in the preceeding section are accepted. The superstructure of the stillstand barrier would be sheared off, and a residual sand sheet would be generated by erosional shoreface retreat on the surface behind it.

Sand ridges locally perched on terrace edges may represent local overstep of barriers. They should be viewed with suspicion, however, particularly if associated with linear closed lows along the bottom of the scarp. Close correlation of the loci of maximum crestal aggradation and maximum trough scour is characteristic of the ridge topography, and such perched ridges may be of secondary origin, due to bottom-current convergence in the storm flowfield, localized along the scarp. Thus the scarp of the Middle Atlantic Bight may be more accurately described as the truncated remnants of lower shorefaces, than as former shorelines.

Resumption of transgression of a mature coast after stillstand may duplicate initial conditions, with barriers formed by mainland-beach detachment along the length of the coast.

Emery (1967) has attempted to reconstruct the Holocene shoreline histo-

ry of the Atlantic Shelf by comparing rates of sea-level rise and slope of the shelf at the shoreline against time. He is concerned with the relative areal extent of estuaries versus lagoons. He infers that estuaries were dominant as the shoreline came up over the steep, dissected upper slope, decreased in extent as the shoreline traversed the flat central shelf, and increased again as the shoreline climbed the steeper, incised inner shelf. His criteria for estuarine development, namely relief and regional slope, are those described earlier as those promoting coastwise spit progradation at the expense of mainland-beach detachment. However, as noted earlier, it is doubtful if spit progradation was ever dominant in view of the generally flat nature of the shelf.

Evidence from the modern shoreline

We appear to be presently experiencing near stillstand conditions as a consequence of a tenfold reduction in the rate of sea-level rise, relative to values prior to 4,000 B.P. (Milliman and Emery, 1968), and we can, therefore, observe aspects of stillstand not readily determined from the drowned scarps of the shelf. Estuary-mouth morphology of the Middle Atlantic Bight has changed markedly in the last few millenia. Shelf valleys have been largely decoupled from estuary mouths; only the Delaware Shelf Valley may be still traced directly into its modern generating zone (Swift, 1973; Swift and Sears, 1974). A trend towards the integration of coastal compartments has been accomplished by reduction or elimination of the ancestral Albermarle, Virginia Beach (ancestral James?), and Great Egg (ancestral Schuylkill?) estuaries (Swift and Sears, 1974; Fig. 9, this paper). A striking asymmetry of coastal compartments has developed (or perhaps has been merely intensified), resulting in a repeating motif along the length of the Middle Atlantic Bight (Fig. 12). Its subaerial expression from north or east to west or south consists of a cuspate or recurved spit on the northeast end, followed by the mainland beach of a truncated headland, then a south-trending spit, followed by a barrier-island chain. The asymmetry may reflect the attempt of the coastal compartments to rotate into a position corresponding more closely to a drift alignment. Interestingly, these compartments appear to have experienced difficulty in rotating as units (if this is indeed the correct explanation for their asymmetry), and the compartments have developed discontinuities, a barrier overlap inlet at Fire Island, a broad bulge at Atlantic City, and a barrier overlap inlet evolving into a cuspate foreland at Chincoteague. Thus rotation during stillstand may counteract the general trend toward coastal integration, and locally induce coastwise spit progradation.

Modification of the coastal superstructure appears to be closely coupled with modification of the shoreface and inner shelf. The steep, erosional shorefaces at the north ends of the coastal compartments give way to broad, gentle, constructional shorefaces, suggesting a nearly closed system, in which south-trending storm contour currents have aggraded the shoreface to the

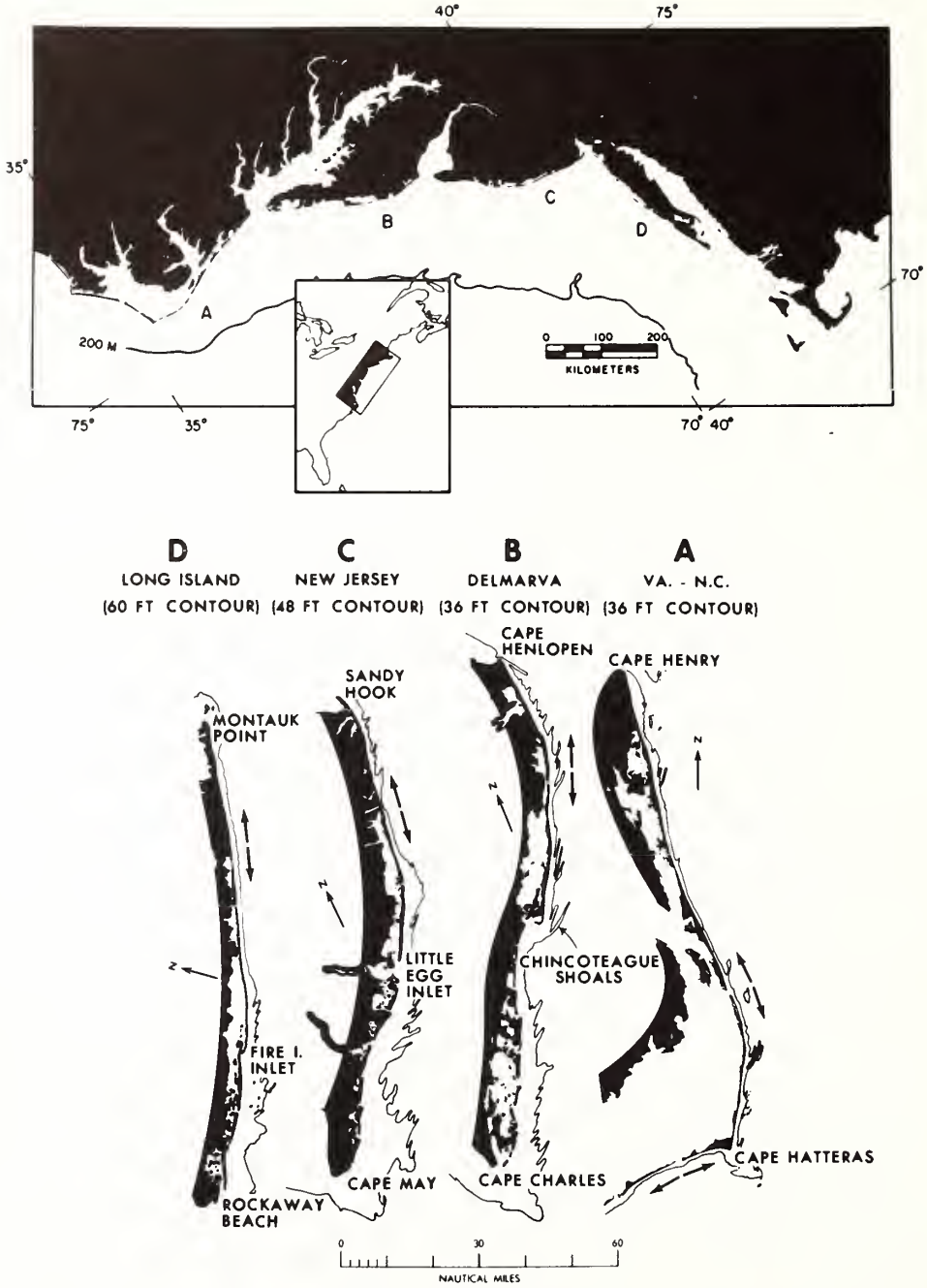

Fig. 12. Coastal compartments of the Middle Atlantic Bight. From Duane et al., 1972.

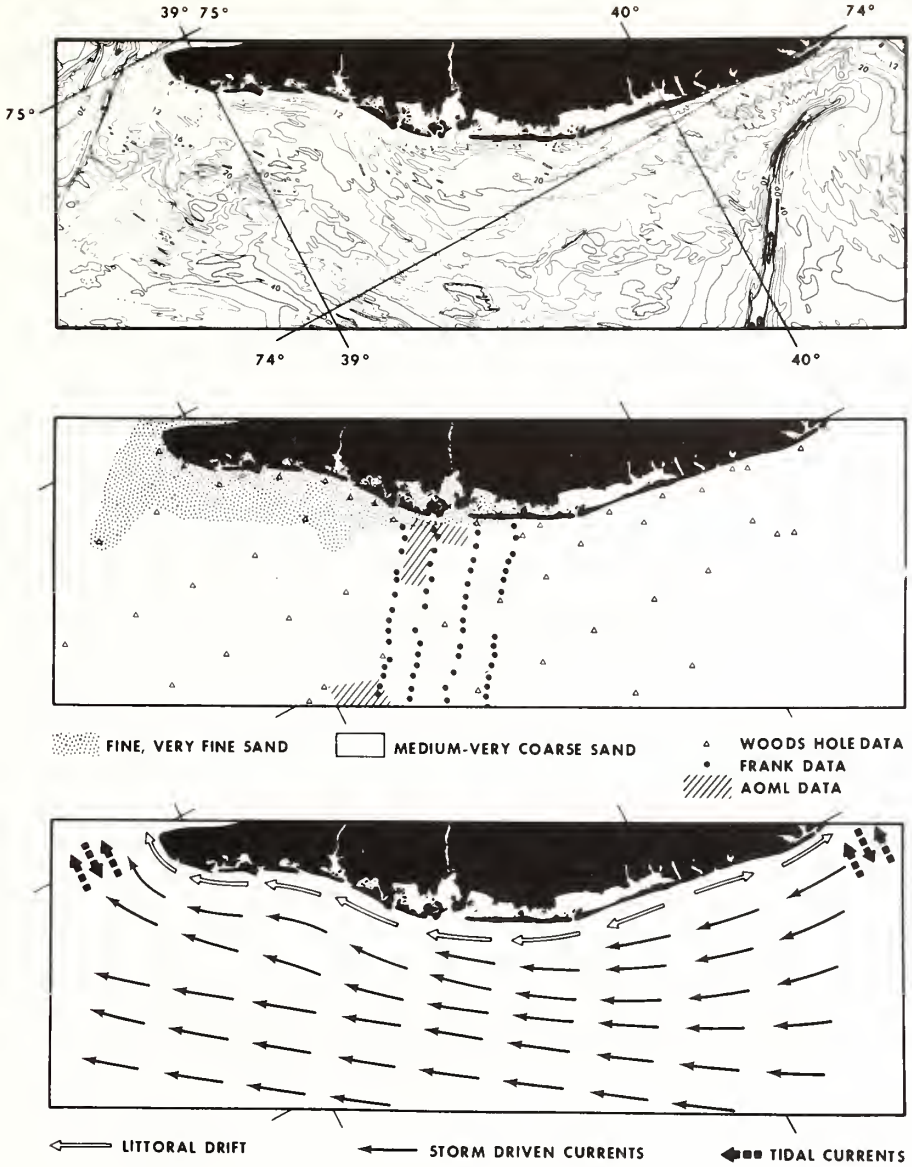

Fig. 13. Topography (Uchupi, 1970), surficial grain size distribution (Hathaway, 1970; Frank and Friedman, 1972; Stubblefield et al., 1974), and hypothetical pattern of sediment transport for the New Jersey coastal compartment. In the central panel, the fine sand province may be equated to a dominately aggradational zone, while the medium to very coarse province may be equated to a neutral to erosional zone. In the bottom panel, a possible pattern of storm flow and resultant sand transport is based on grain-size gradients, and on the trend of ridge morphology (evidence reviewed in Swift et al., 1972b, pp. 561—567).

south at the expense of the shoreface to the north (Figs. 13—15). The schematic flow patterns in the bottom panels of these figures are not based on detailed information, and merely serve to indicate that with a regional pattern of southwesterly storm flow (Beardsley and Butman, 1974), coastal flow would tend to converge with the shore along the northeastern ends of

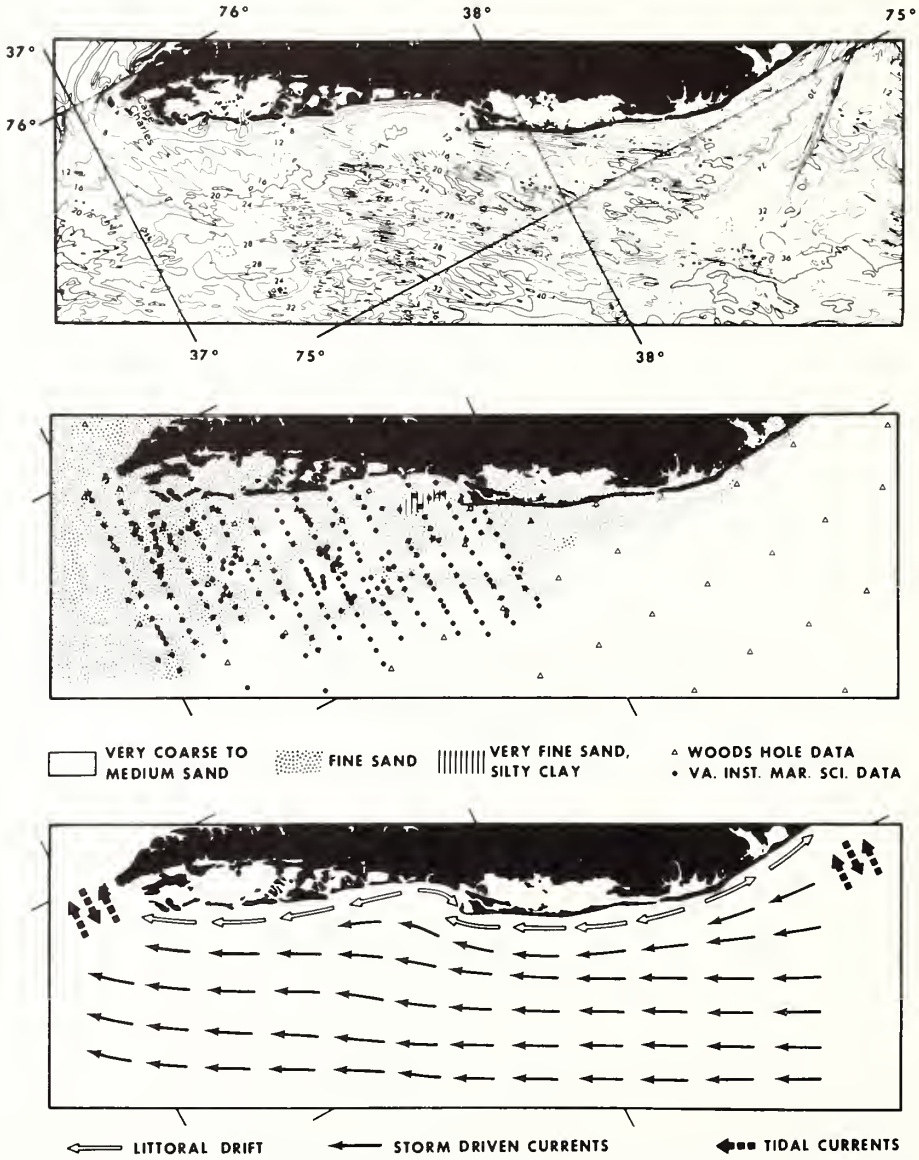

Fig. 14. Topography (Uchupi, 1970), grain-size distribution (Nichols, 1973; Hathaway, 1970), and hypothetical pattern of sediment transport in the Delmarva coastal compartment. Interpretations as in Fig. 13.

the coastal compartments, and diverge from the shore along the compartment's southwestern ends.

Littoral-drift divergences are located toward the centers of the coastal compartments rather than on the mainland-beach sector (Fig. 12), hence the south-trending spits must be fed by the inner shelf, rather than mainland-

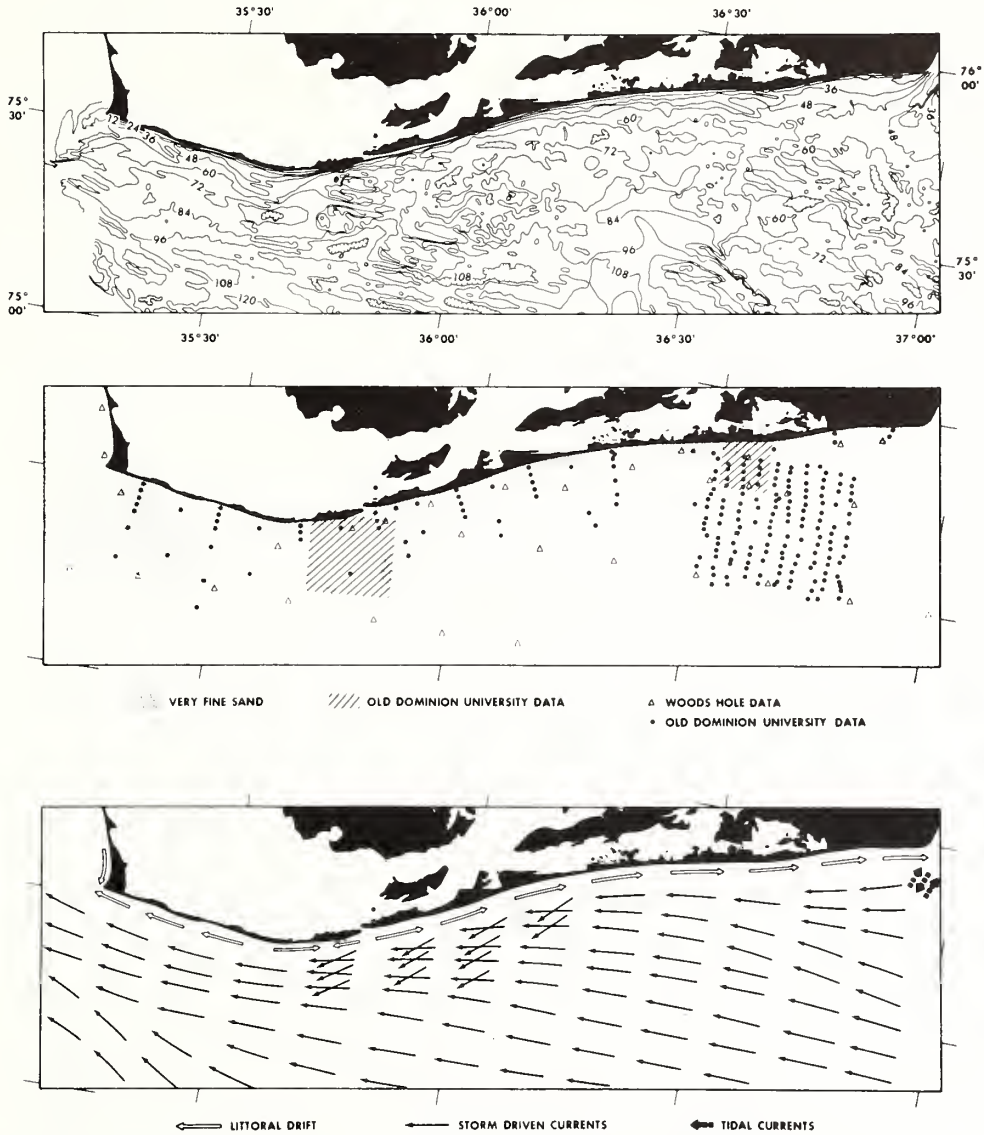

Fig. 15. Topography (Goldsmith, 1973), surficial grain-size distribution (Swift et al., 1971, 1972a; Shideler et al., 1972; Sears, 1973; Hathaway, 1970), and hypothetical pattern of sediment transport for the Virginia—northern North Carolina coast. For further resolution of relationship of transport pattern, see Fig. 17.

beach erosion, and a simple coastwise-progradation origin for the barrier systems seems unlikely. In the case of the New Jersey coastal compartment, this conclusion is reinforced by heavy-mineral studies of McMaster (1954) which indicate a series of mineralogical provinces, rather than a single source for the entire compartment. Berm grain sizes of the New Jersey and at least a portion of the Delmarva coastal compartments become finer toward the south (Fig. 16), in harmony with grain size on the inner shelf (Figs. 15—16). The pattern suggests that the flux of fine shelf sand towards the distal ends of the coastal compartments has resulted in nourishment of the beach as well as aggradation of the inner shelf. The situation on the Virginia—northern North Carolina coastal compartment is not as clear cut. Inner-shelf grain size becomes finer toward the south, but this trend is interrupted by a major

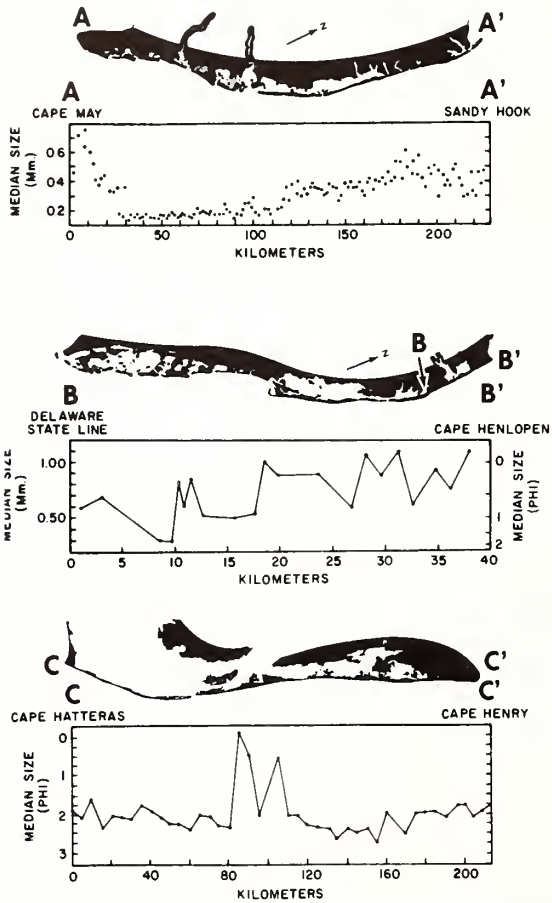

Fig. 16. Median diameters of berm grain sizes for a New Jersey coast (McMaster, 1954), Delaware coast (Anonymous, 1956), and Virginia—northern North Carolina coast (Swift et al., 1971).

coarse anomaly at the site of the buried Albermarle channel (see later discussion). Grain size becomes coarser to the south of this site, probably because of intensification of the wave climate toward Cape Hatteras (Tanner, 1960).

EVOLUTION OF THE NORTHERN NORTH CAROLINA—VIRGINIA COAST

Earlier studies of coastal morphogenesis

The northern North Carolina—Virginia coastal compartment (Fig. 17), one of the better known, illustrates many of the problems involved in under-

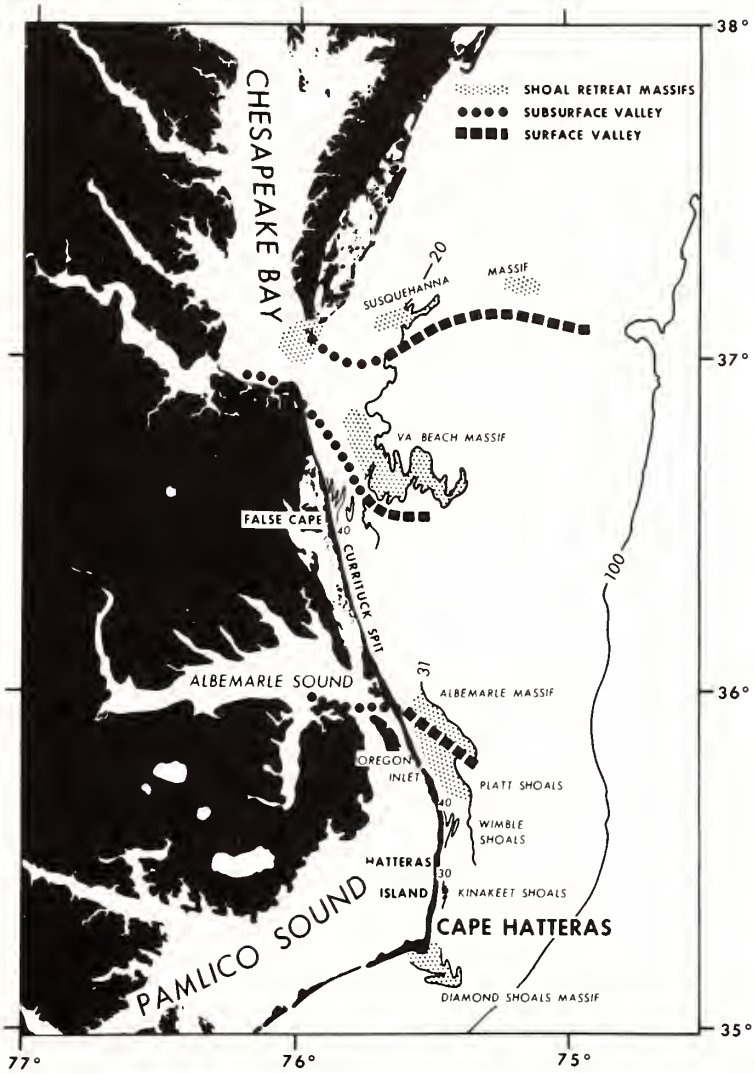

Fig. 17. Regional morphology and place names of Virginia—northern North Carolina coast.

standing barrier genesis. Johnson (1919) used this sector to illustrate his thesis of barrier genesis by coastal emergence, but as shown by Fisher (1973), his geometrical analysis was based on premises of dubious value.

Fisher (1967), and Pierce and Colquhoun (1970), have stressed the reorganization of the shoreline towards a more nearly climax configuration attendant on the Late Holocene reduction in the rate of sea-level rise. Pierce and

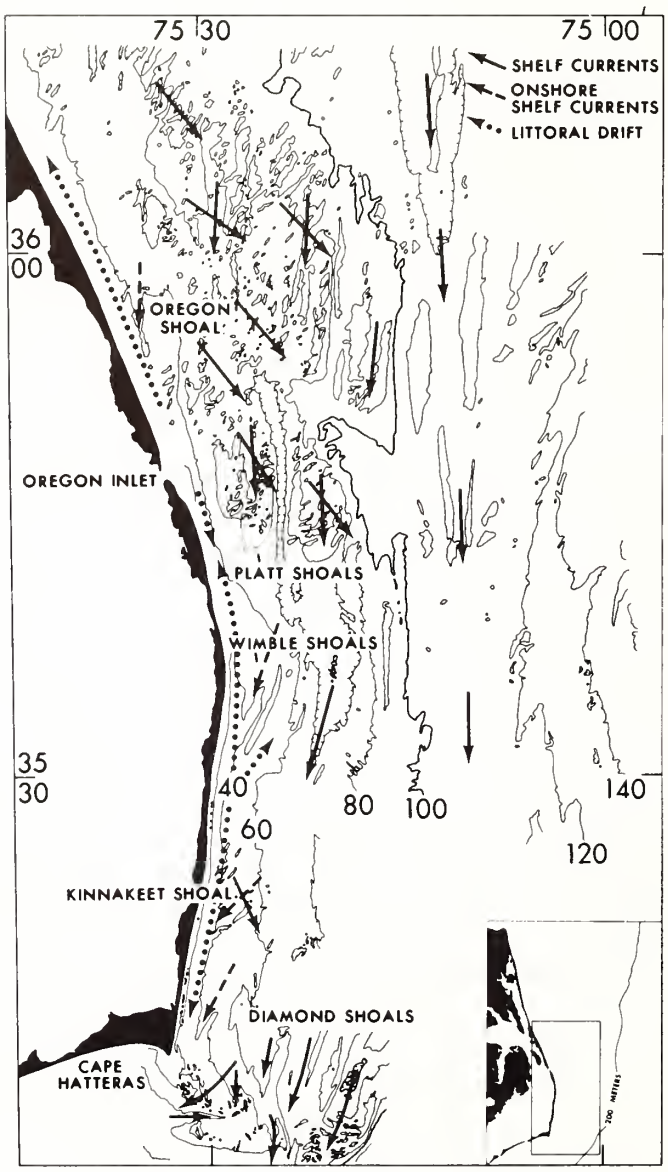

Fig. 18. Morphology of the northern North Carolina shelf, and possible relation to direction of sediment transport. See text for explanation.

Colquhoun note that the highly irregular mainland coast of Pamlico Sound renders unlikely Fisher's (1967, 1968) hypothesis that the Carolina barrier system formed by simple coastwise progradation. They postulate that instead the "primary" Late Holocene barrier system was formed by reoccupation and detachment of a pre-existing Late Wisconsin barrier (inner lagoonal shoreline north of Albermarle sound, lagoonal island north of Oregon Inlet, Fig. 18) but that the bulk of the present barrier is a secondary system formed seaward of the primary system by southward spit progradation coupled with landward retreat.

This scenario causes as many problems as it solves. As noted by Fisher (1967) the south section of "secondary" barrier does preserve beach-ridge sets which tend obliquely across the island. However this pattern is as compatible with southward inlet migration (Hoyt and Henry, 1967) as it is with spit progradation. Pierce (1968) has shown that at least a third of the sand required to balance the present sand budget of this sector must be coming from inner-shelf erosion, a source compatible with a detachment or landward migration origin.

Perhaps the worst problem with a purely coastwise-progradation origin for the southern barrier system is the vast shoal extending seaward from Cape Hatteras. It appears to be a shoal-retreat massif, marking the retreat path of the littoral-drift convergence at the Hatteras cuspate foreland during the Holocene transgression (Swift et al., 1972b, pp. 525—533, 548—522). Both the cuspate foreland and the shoal-retreat massif are aggrading on their south sides, and eroding on their north sides (Fisher, 1967, fig. 32; Swift et al., 1972b, fig. 212). They are therefore shifting southwards, but it is difficult to see how the shoals would shift to the extent required by Pierce and Colquhoun's scheme of coastwise progradation and still retain their identity. At any rate, the presence of this vast sand ridge indicates that retreating Cape Hatteras has been a sink rather than a source for littoral drift throughout Holocene time.

Evidence from the inner shelf

Source problems complicate the picture for the northern section of supposedly secondary barrier as well. Littoral drift diverges from the vicinity of Oregon Inlet towards both ends of the compartment (Figs. 12, 15), hence erosion of the shoreface, not erosion north of Currituck Spit must be the main source of sand to nourish the barrier system. The morphology of the inner shelf may serve as a guide to the direction, if not rate, of shelf floor sediment transport (Fig. 18). Interaction of the shelf floor with the storm flow field has molded the shelf floor into a ridge and swale topography during the course of the Holocene transgression (Swift et al., 1974). Medium and coarse sand has been swept into ridges whose alignment is inferred to be close to that of peak storm flow. The intervening troughs expose Pleistocene substrate in their up-current ends, and shoal in the assumed down-current

direction. The maintaining mechanism may be an ordering of the storm flow field into helical flow cells, although the direct measurements required to test this hypothesis have yet to be performed. Near shore, in the Oregon Inlet sector, ridge crests bear sand waves (Figs. 18, 19) whose orientation suggests an obliquely offshore flow component, perhaps associated with regional wind set-up during storms. Both ridges and sand waves are molded into the former estuary mouth shoal associated with the ancestral Albemarle River (see later discussion). It is not clear whether flow events activating the two sets of bed forms occur simultaneously, although they conceivably could; in Ekman boundary layer flow, helical flow cells may be oriented to the right of the geostrophic flow direction; the angle increases with mean flow intensity (Lilly, 1966). At any rate, the ridges in this area have maintained their relief over the past century; trough floors have aggraded towards their southern ends, but ridge crests have aggraded more (Sears, 1973).

Along the coast, shoreface-connected ridge systems (False Cape, Oregon Shoal, Wimble Shoal, Kinnakeet Shoal; Figs. 17, 18) appear to serve as conduits for fine sand with which the shoreface is nourished. At False Cape,

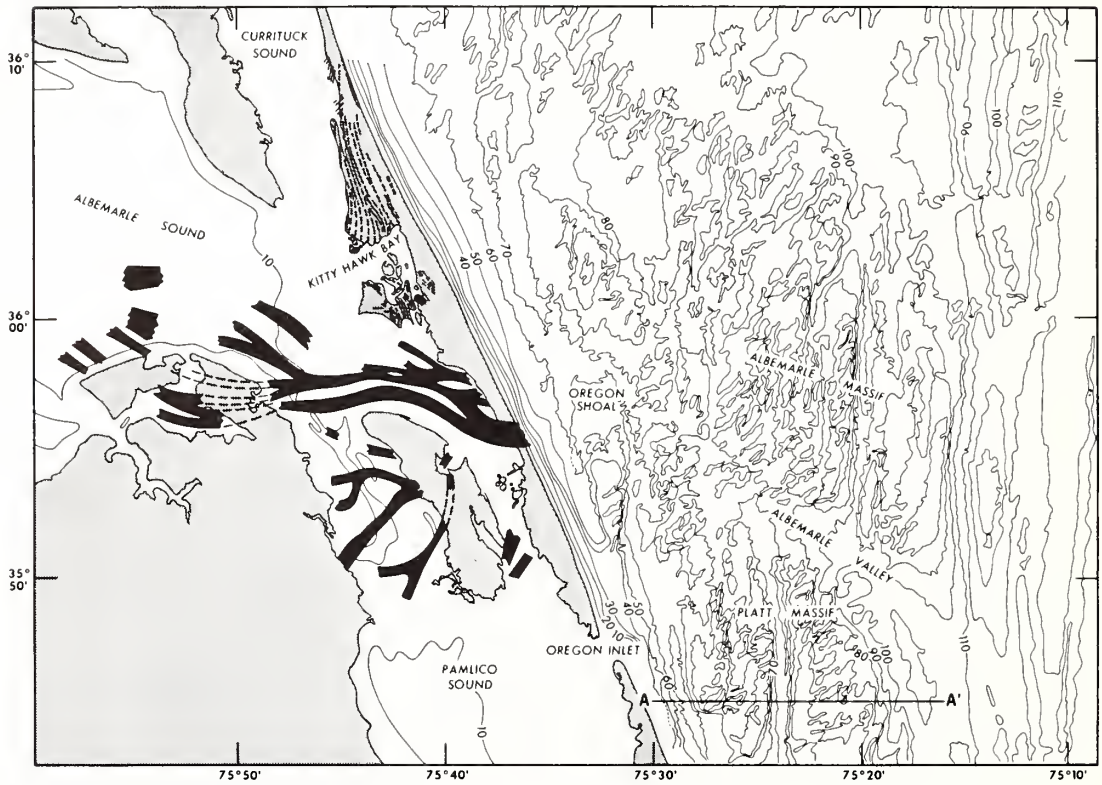

Fig. 19. Albemarle sector of Carolina coast. Subsurface channels from O'Connor et al., 1972; beach ridges from Fisher, 1967. Contours in feet.

the shoreface south of the ridge has aggraded up to 3 m and berm grain size has been depressed for several kilometers downdrift (Swift et al., 1975). These shoreface-connected ridge systems occur at bends in the barrier chain, suggesting that they serve to stabilize its segments.

South of Wimble Shoals, the inner shelf becomes smooth and featureless, and the fine sand blanket, heretofore confined to the upper shoreface, expands across the inner shelf floor (Fig. 15). Seismic work suggests that the Holocene sand sheet thickens, and the Holocene-Pleistocene contact may be no longer resolved (Shideler and Swift, 1972). This zone appears to be a sink for fine sand swept out of the ridge topography to the north.

Sub-Recent evolution of the Virginia—northern North Carolina coast

There is some evidence for restructuring of the Virginia—northern North Carolina barrier system, but the transition may have been more continuous than the primary barrier—secondary barrier sequence envisioned by Pierce and Colquhoun (1970). Shelf-floor highs off Kitty Hawk and Virginia Beach appear to be shoal-retreat massifs, generated by the retreat of estuary-mouth shoals associated with the ancestral Albemarle and James rivers, respectively (Swift and Sears, 1974), between 11,000 and 4,400 and 5,600 years ago (Sears, 1973). They must predate the barrier system in its present configuration, since the Albemarle shelf valley passes under Currituck spit (Fig. 19), and the Virginian Beach shelf valley passes under the cuspate spit of Cape Henry (Fig. 17). The morphologic transformation of estuary-mouth shoal into shoal-retreat massif is presented in a schematic way in Fig. 20.

The closest analog for coastal configuration north of Cape Hatteras during the period of estuary-mouth retreat would be the present estuarine coast of the Georgia Bight (Henry and Hoyt, 1968), with its sequence of arcuate estuary mouth shoals. The Georgia coast does possess a Holocene barrier system (stabilized in most areas on the forward face of a Pleistocene still-stand barrier system). The lagoons are quite narrow, however, and most of the discharge of the estuaries passes directly through the tidal inlets that are also estuary mouths.

The course of events which lead to formation of the modern coast are probably unknowable, in the sense of a unique solution. However, the available evidence suggests the following scenario. At the onset of the Late Holocene reduction in the rate of sea-level rise, the barriers began to grow upward, as a consequence of the vertical component of shoreface translation increasing over the horizontal component (Fig. 5C). This would have transpired because lower shoreface and inner-shelf erosion continued to feed sand to the barrier at the same rate as before.

It is possible to place some constraints on the exchange of sand between barrier face and adjacent shelf as the barriers moved into their present position. A comparison of shoreface profiles from Cape Henry to Cape Hatteras shows that an angular (and probably mainly erosional) inflection between

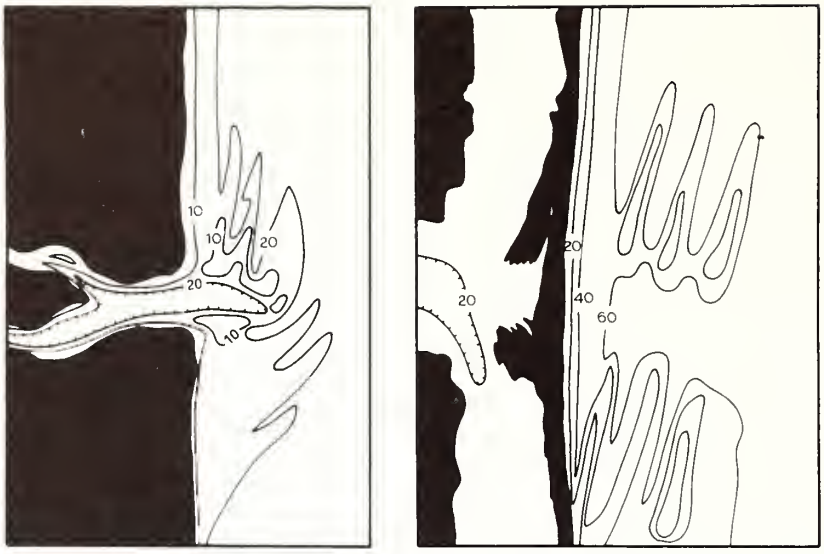

Fig. 20. Schematic diagram illustrating the evolution of an estuary mouth shoal into a shoal-retreat massif. Modeled after the Platt shoals sector (Fig. 19). This former estuary mouth is anomalous in that the massifs occur in both sides of the shelf valley, and do not extend very far out on the shelf. Depth in feet.

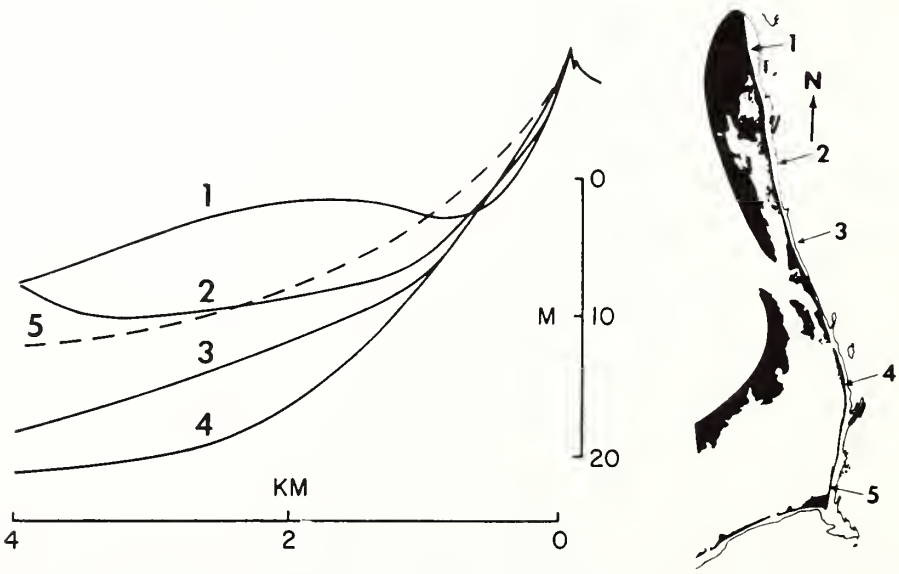

Fig. 21. Profiles of the Virginia—northern North Carolina shoreface. From National Ocean Survey 1200 series charts.

shoreface and inner shelf lies at successively greater depths to the south (Fig. 21). The deepest inflection point occurs just south of Platt Shoals (profile 4), where vibracoring indicates an absence of Holocene cover and suggests perhaps 6 m of erosion of the Pleistocene substrate (Sears, 1973). The deepening trend is reversed at the southernmost profile immediately north of Cape Hatteras. Here, adjacent to a sector of shelf aggradation, profile 5 is smoothly exponential and probably constructional in origin.

Schemes for three different modes of barrier retreat which are compatible with these observations are presented in Fig. 22. The diagram suggests that after the late Holocene reduction in the rate of sea-level rise (between periods *T3* and *T4*) the vertical component of shoreface translation increased. At the north end of the coastal compartment, sand eroded from the shoreface either went to build up the barrier superstructure or was swept out to the inner-shelf floor, and was bypassed south. Below Oregon inlet, the shelf floor may actually have undergone erosion. Further south, the trajectory of

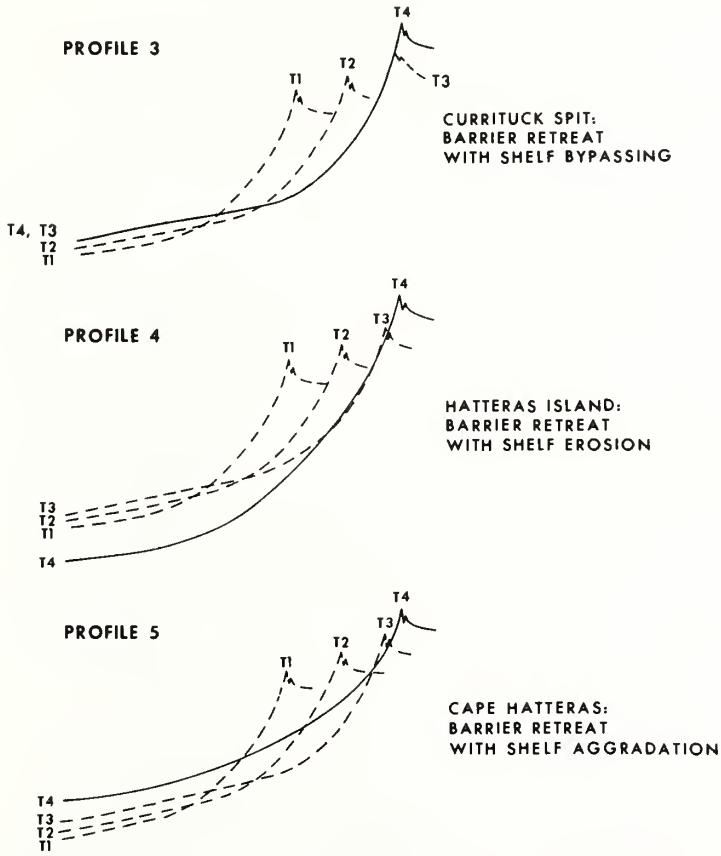

Fig. 22. Transgressional schemes for the Virginia—northern North Carolina coast. See text for explanation.

shoreface translation paralleled the upper shoreface, and both the inner shelf and barrier superstructure aggraded.

The result of dominantly upward barrier growth would have been a widening of the Pamlico Sound—Roanoke Sound lagoonal system. The northernmost lagoon, Currituck Sound, would have begun to creep northward behind Currituck Spit detaching successive sections of mainland beach. The process is presumably still occurring today, and Back Bay of Currituck Sound is probably as good an example as we will ever have of mainland-beach detachment (Fig. 23). The highly irregular, scalloped nature of the shoreline and island are characteristic of salt-marsh surfaces where compaction and sea-level

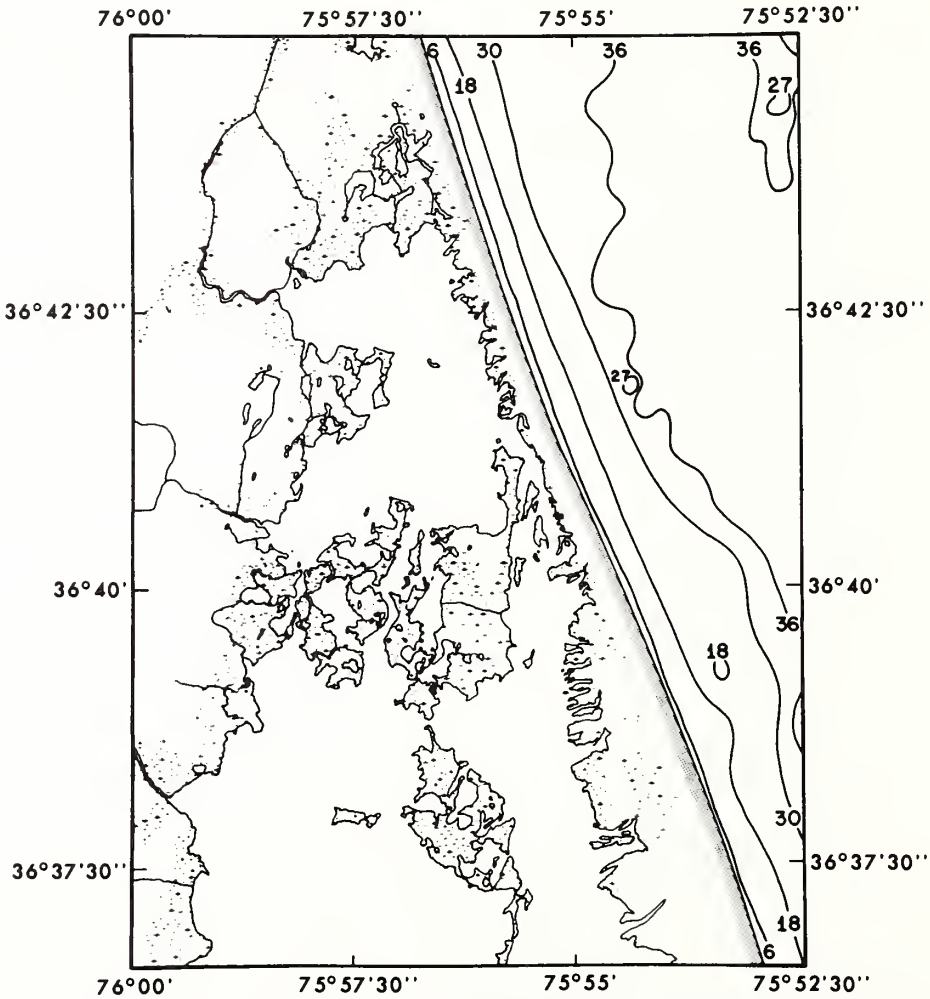

Fig. 23. Back Bay, Virginia coast, a probable modern example of mainland-beach detachment.

rise are balanced by aggradation. Ponds and scallops develop due to constructive feedback between wave fetch and marginal erosion.

Flooding of Chesapeake Bay at the onset to coastal stabilization led to the piracy of the James estuary by the Chesapeake trunk estuary, and the growth of Cape Henry as a cuspate spit over the former James channel (Fig. 17).

There seems to be little need to call on large-scale coastwise spit progradation in this scenario. The present barriers are directly the result of landward migration, as they are underlain by lagoonal deposits (Pierce and Colquhoun, 1971, fig. 3). The early barriers would presumably have experienced the same wave climate, would have had the same access to an inner-shelf sediment source, and would have been migrating over the same nearly flat coastal plain; it is difficult to see why the earlier Holocene barrier system would have been sufficiently irregular to trigger a major episode of spit building as the rate of sea-level rise decreased. The trend of the Carolina coast is close to the swash alignment; there is no evidence for spit formation associated with the rotation of barrier segments, as at the more northerly trending Chincoteague sector of the Delmarva coast.

CONCLUSIONS

A consideration of shoreface dynamics, plus examination of the Central Atlantic Shelf surface has permitted a reassessment of barrier island and barrier spit genesis.

It is helpful to regard a barrier as a large-scale, composite sand body, consisting of a wave and current graded shoreface, attached to washover fans. The response of this system to changes in the hydraulic regime is instantaneous, with respect to such long term phenomena as sea-level rise.

The lagoonal carpet of the Central Atlantic Shelf indicates that the modern barriers have retreated to their present positions from the shelf edge, during the post-glacial transgression. Thus the immediate genesis of most central Atlantic barriers is a retreat in from the position of its immediate predecessor. The ultimate "cause" of barriers is the behavior of the shoreface, whose equilibrium response to the hydraulic regime is a concave-up surface. Since the oceanic shoreface must be straight, there will tend to be two shorelines, for water seeking its own level will flood back-barrier lows between headlands. During transgression individual spits and islands may come and go and lagoons will fluctuate in width, but once initiated, a barrier system will retreat as a steady-state phenomenon, as long as the variables controlling its behavior remain constant.

Barrier "genesis" in the classical sense of mainland-beach detachment or coastwise spit progradation can only occur on a large scale when a regression passes through stillstand into transgression. The relative roles of mainland-beach detachment and coastwise spit progradation depend on the configuration of the substrate, with spit building favored by greater relief and regional

slope. Mainland-beach detachment is favored by low flat coasts, where wave erosion extends far enough down the shoreface to tap the barrier's substrate as a source of sediment. Since most long continuous barrier systems occur on low flat coasts, they were by this logic initially formed by mainland-beach detachment, before retrograding to their present positions. Stillstands result in periods of upward barrier growth. With renewed transgression, however, barrier retreat resumes. The resulting shelf-floor scarp is not truly a drowned shoreline, but merely the lower half of the stillstand shoreface; the barrier superstructure having been destroyed by erosional shoreface retreat.

During stillstands, or at reductions in the rate of sea-level rise, the coastal equilibrium may tend towards its climax configuration. The process may involve rotation of coastal segments toward an orientation normal to prevailing wave orthogonals. Discontinuities may develop, in the form of barrier overlap inlets. This is an important form of coastwise spit progradation on low barrier coasts, but it is doubtful whether it is a predominant barrier-forming process.

REFERENCES

Anonymous, 1950. Munch-Petersons littoral drift formula. Beach Erosion Board Bull., 4: 1—31.

Anonymous, 1956. Delaware coast from Kitts Hummock to Fenwick Island, beach erosion control study. U.S. Corps of Engineers, Philadelphia District, 47 pp.

Bascom, W.N., 1951. The relationship between sand size and beach face slope. Trans. Am. Geophys. Union, 32: 868—874.

Beardsley, R.C. and Butman, B., 1974. Circulation on the New England Continental Shelf: Response to strong winter storms. Geophys. Res. Lett., 1: 181—184.

Bruun, P., 1962. Sealevel rise as a cause of shore erosion. J. Waterw. Harbors Div. Am. Soc. Civ. Eng. Proc., 88: 117—130.

Carver, R.E., 1971. Holocene and Late Pleistocene sediment sources, continental shelf off Brunswick, Georgia. J. Sediment. Petrol., 41: 372—525.

Colquhoun, D.J., 1969. Coastal plain terraces in the Carolinas and Georgia, U.S.A. In: Quaternary Geology and Climate. Natl. Acad. Sci. Publ., 1701: 150—162.

Cook, D.O. and Gorsline, D.S., 1972. Field observations of sand transport by shoaling waves. Mar. Geol., 13: 31—55.

Cornaglia, P., 1887. Sul Regime della Spiagge e sulla Regulazione dei Porţi. Turin.

Curray, J.R., 1964. Transgressions and regressions. In: R.L. Miller (Editor), Papers in Marine Geology — Shepard Commemorative Volume. MacMillan, New York, N.Y., pp. 175—203.

Curray, J.R., 1969. Shore zone sand bodies: barriers, cheniers, and beach ridges. In: D.J. Stanley (Editor), The New Concepts of Continental Margin Sedimentation. American Geological Institute, Washington, D.C., pp. JC-II-1—JC-II-19.

Curray, J.R., Emmel, F.J. and Crampton, P.J.S. 1969. Lagunas costeras, un simposio. In: Mem. Simp. Int. Lagunas Costeras. UNAM-UNESCO, Nov. 28—30, 1967, Mexico, D.F., pp. 63—100.

Davies, J.L., 1958. Wave refraction and the evolution of curved shorelines. Geogr. Stud., 5: 1—14.

Davies, J.L., 1973. Geographical Variation in Coastal Development. Hafner, New York, N.Y., 204 pp.

Dillon, W.P., 1970. Submergence effects on a Rhode Island barrier and lagoon and inferences in migration of barriers. J. Geol., 78: 94—106.

Dolan, R., Godfrey, P.J. and Odum, W.E., 1973. Man's impact on the barrier islands of North Carolina. Am. Sci., 61: 152—162.

Duane, D.B., Field, M.E., Meisburger, E.P., Swift, D.J.P. and Williams, S.J., 1972. Linear shoals on the Atlantic inner continental shelf, Florida to Long Island. In: D.J.P. Swift, D.B. Duane and O.H. Pilkey (Editors), Shelf Sediment Transport: Process and Pattern. Dowden, Hutchinson and Ross, Stroudsburg, Pa., pp. 447—499.

Emery, K.O., 1967. Estuaries and lagoons in relation to continental shelves. In: G.H. Lauff (Editor), Estuaries. Am. Assoc. Adv. Sci. Publ., 83: 757 pp.

Emery, K.O. and Uchupi, E., 1972. Western North Atlantic ocean: topography, rocks, structure, water, life, and sediments. Am. Assoc. Pet. Geol. Mem., 17: 532 pp.

Fenneman, N.M., 1902. Development of the profile of equilibrium of the subaqueous shore terrace. J. Geol., 10: 1—32.

Field, M.E., 1974. Buried strandline deposits on the central Florida inner continental shelf. Geol. Soc. Am. Bull., 85: 57—60.

Field, M. and Duane, D., in preparation. Post Pleistocene events on the inner continental shelf, and the origin of barrier islands.

Fischer, A.J., 1961. Stratigraphic record of transgressing seas in the light of sedimentation on the Atlantic Coast of New Jersey. Am. Assoc. Pet. Geol. Bull., 45: 1656—1660.

Fisher, J.J., 1967. Development pattern of relict beach ridges, Outer Banks barrier chain, North Carolina. Thesis, Univ. North Carolina, Durham, N.C., 250 pp., unpublished.

Fisher, J.J., 1968. Barrier island formation: discussion. Geol. Soc. Am. Bull., 79: 1421—1426.

Fisher, J.J., 1973. Bathymetric projected profiles and the origin of barrier islands — Johnson's shorelines of emergence, revisited. In: D.R. Coates (Editor), Coastal Geomorphology. State Univ. N.Y., Binghamton, N.Y., pp. 161—180.

Frank, W.M. and Friedman, G.M., 1973. Continental shelf sediments off New Jersey, J. Sediment. Petrol., 43: 224—237.

Gilbert, G.K., 1890. Lake Bonneville. U.S. Geol. Surv. Monogr., 1: 438 pp.

Goldsmith, V.G., Sutton, C.H. and Davis, J.S., 1973. Bathymetry of the Virginian Sea, Part I Chesapeake Bight (map). Virginia Institute of Marine Science, Gloucester Point, Va.

Hails, J.R. and Hoyt, J.H., 1968. Barrier development on submerged coasts: problems of sea level changes from a study of the Atlantic Coastal Plain of Georgia and part of the East Australian Coast. Z. Geomorphol., 7: 24—55.

Hathaway, J.C., 1971. Data file, continental margin program, Atlantic coast of the United States, 2. Samples collection and analytical data. Woods Hole Oceanographic Institution reference 71—15, U.S. Geol. Surv., Woods Hole, Mass., 496 pp.

Henry, V.J. and Hoyt, J.H., 1968. Quaternary paralic and shelf sediments of Georgia. Southeast. Geol., 9: 195—214.

Hoyt, J.H., 1967. Barrier island formation. Geol. Soc. Am. Bull., 78: 1125—1136.

Hoyt, J.H., 1968. Barrier island formation: reply. Geol. Soc. Am. Bull., 79: 1427—1431.

Hoyt, J.H., 1970. Development and migration of barrier islands, northern Gulf of Mexico, discussion. Geol. Soc. Am. Bull., 81: 3779—3782.

Hoyt, J.H. and Henry, V.J., 1967. Influence of island migration on barrier island sedimentation. Geol. Soc. Am. Bull., 78: 77—86.

Johnson, D., 1938. Shore Processes and Shoreline Development. Wiley, New York, N.Y., 2nd ed., 1st ed. published in 1919.

Johnson, J.W. and Eagleson, P.S., 1966. Coastal Processes. In: A.J. Ippen (Editor), Estuary and Coastline Hydrodynamics. McGraw-Hill, New York, N.Y., pp. 404—492.

King, C.A.M., 1972. Beaches and Coasts. St. Martins, New York, N.Y., 2nd ed., 570 pp.

Langford-Smith, T. and Thom, B.G., 1969. New South Wales coastal morphology. J. Geol. Soc. Aust., 16: 572—680.

Lilly, D.K., 1966. On the instability of Ekman boundary flow. J. Atmos. Sci., 23: 481—494.

May, J.P. and Tanner, W.F., 1973. The littoral power gradient and shoreline changes. In: D.R. Coates (Editor), Publications in Geomorphology. State Univ. N.Y., Binghamton, N.Y., 404 pp.

McClennen. C.E. and McMaster, R.L., 1971. Probable Holocene transgressive effects on the geomorphic features of the continental shelf off New Jersey, United States. Marit. Sediment., 7: 69—72.

McGee, W.D., 1890. Encroachments of the sea. The Forum, 9: 437—449.

McKinney, T.F., Stubblefield, W.L. and Swift, D.J.P., 1974. Large-scale current lineations on the central New Jersey shelf: investigations by side-scan sonar. Mar. Geol., 17: 79—102.

McMaster, R.L., 1954. Petrography and Genesis of the New Jersey Beach Sands. N.J. State Dep. Conserv. Econ. Dev., Trenton, N.J., 239 pp.

McMaster, R.L. and Garrison, L.E., 1967. A submerged Holocene shoreline near Block Island, Rhode Island. J. Geol., 75: 335—340.

Merrill, A.S., Emery, K.O. and Rubin, M., 1965. Oyster shells on the Atlantic continental shelf. Science, 147: 395—400.

Milliman, J.P. and Emery, K.O., 1968. Sealevels during the past 35,000 years. Science, 162: 1121—1123.

Moody, D.W., 1964. Coastal morphology and processes in relation to the development of submarine sand ridges off Bethany Beach, Delaware. Thesis, Johns Hopkins Univ., Baltimore, Md., 167 pp.

Murray, S.P., 1967. Control of grain dispersion by particle size and wave state. J. Geol., 75: 613—634.

Nevesskii, E.N., 1969. Some data on the postglacial evolution of K Bay and the accumulation of bottom sediments within it. p. 92—110, In: V.V. Longinov (Editor), Dynamics and Morphology of Seacoasts. Akademiya Nauk SSSR Trudy Instituta Okeanologii v. 48, 371 p. Translated from Russian by Israel Program for Scientific Translations; reproduced by the Clearinghouse for Federal Scientific and Technical Information, Springfield, Virginia.

Nichols, M.M., 1972. Inner shelf sediments off Chesapeake Bay. I, General lithology and composition. Va. Inst. Mar. Sci. Spec. Sci. Rep., 64: 20 pp.

Oaks Jr., R.Q. and Coch, N.K., 1963. Pleistocene sea levels, southeastern Virginia. Science, 140: 979—983.

O'Connor, M.P., Riggs, S.R. and Winston, D., 1972. Recent estuarine sediment history in the Roanoke Island area, North Carolina. In: B.W. Nelson (Editor), Environmental Framework of Coastal Plain Estuaries. Geol. Soc. Am. Mem., 133: 453—464.

Oertel, G.F., 1972. Sediment transport of estuary entrance shoals and the formation of swash platforms. J. Sediment. Petrol., 42: 854—863.

Otvos, E.G., 1970a. Development and migration of barrier islands, northern Gulf of Mexico. Geol. Soc. Am. Bull., 81: 241—246.

Otvos, E.G., 1970b. Development and migration of barrier islands, northern Gulf of Mexico: reply. Geol. Soc. Am. Bull., 81: 3783—3788.

Pierce, J.W., 1968. Sediment budget along a barrier island chain. Sediment. Geol., 3: 5—16.

Pierce, J.W., 1970. Tidal inlets and washover fans. J. Geol., 78: 230—234.

Pierce, J.W. and Colquhoun, D.J., 1970. Holocene evolution of a portion of the North Carolina coast. Geol. Soc. Am. Bull., 81: 3697—3714.

Schwartz, M.L., 1965. Laboratory study of sealevel rise as a cause of shore erosion. J. Geol., 73: 528—534.

Schwartz, M.L., 1967. The Bruun theory of sealevel rise as a cause of shore erosion. J. Geol., 75: 76—92.

Schwartz, M.L., 1968. The scale of shore erosion. J. Geol., 76: 508—517.

Schwartz, M.L., 1973. Barrier Islands. Dowden, Hutchinson and Ross, Stroudsburg, Pa., 451 pp.

Scruton, P.C., 1960. Delta building and the Deltaic sequence. In: R.P. Shepard, F.B. Phleger and T.J. Van Andel (Editors), Recent Sediments, Northwest Gulf of Mexico. Am. Assoc. Pet. Geol., pp. 82—102.

Sears, P.C., 1973. Evolution of Platt Shoals, Northern North Carolina Shelf: Inferences from Areal Geology. Thesis, Old Dominion Univ., Norfolk, Va., 82 pp.

Shepard, F.P., 1973. Submarine Geology. Harper and Row, New York, N.Y., 3rd ed., 517 pp.

Sheridan, R.E., Dill Jr., C.E. and Kraft, J.C., 1974. Holocene sedimentary environment of the Atlantic inner shelf off Delaware. Geol. Soc. Am. Bull., 85: 1319—1328.

Shideler, G.L. and Swift, D.J.P., 1972. Seismic reconnaissance of Post Miocene deposits. Middle Atlantic continental shelf, Cape Henry, Virginia to Cape Hatteras, North Carolina. Mar. Geol., 12: 165—185.

Shideler, G.L., Swift, D.J.P., Johnson, G.H. and Holliday, B.W., 1972. Late Quaternary stratigraphy of the inner Virginia continental shelf: a proposed standard section. Geol. Soc. Am. Bull., 83: 1787—1804.

Stahl, L., Koczan, J. and Swift, D., 1974. Anatomy of a shoreface-connected ridge system on the New Jersey shelf: implications for the genesis of the shelf surficial sand sheet. Geol. Soc. Am. Bull., 2: 117—120.

Stapor, F., 1973. History and sand budgets of the barrier island system in the Panama City, Florida, region. Mar. Geol., 14: 277—286.

Stubblefield, W.L., Dicken, M. and Swift, D.J.P., (1974). Reconnaissance of bottom sediments on the inner and central New Jersey Shelf. MESA Report No. 1, U.S. Government Printing Office, Washington, D.C., 39 pp.

Stubblefield, W.L., Lavelle, J.W., McKinney, T.F. and Swift, D.J.P., 1975. Sediment response to the hydraulic regime on the central New Jersey shelf. J. Sediment. Petrol., in press.

Swift, D.J.P., 1973. Delaware shelf valley: estuary retreat path, not drowned river valley. Geol. Soc. Am. Bull., 84: 2743—2748.

Swift, D.J.P., Duane, D.B. and McKinney, T., 1974. Ridge and swale topography of the Middle Atlantic Bight: secular response to Holocene hydraulic regime. Mar. Geol., 15: 227—247.

Swift, D.J.P. and Heron Jr., S.D., 1969, Stratigraphy of the Carolina cretaceous. Southeast. Geol., 10: 201—240.

Swift, D.J.P., Holliday, B., Avignone, N. and Shideler, G., 1972a. Anatomy of a shoreface ridge system, False Cape, Virginia. Mar. Geol., 12: 59—84.

Swift, D.J.P., Kofoed, J.W., Saulsbury, F.P. and Sears, P., 1972b. Holocene evolution of the shelf surface, central and southern Atlantic coast of North America. p. 499—574. In: D.J.P. Swift, D.B. Duane, O.H. Pilkey (Editors), Shelf Sediment Transport: Process and Pattern. Dowden, Hutchinson and Ross, Stroudburg, Pa., pp. 499—574.

Swift, D.J.P., Sanford, R.B., Dill Jr., C.E. and Avignone, N.F., 1971. Textural differentiation on the shoreface during erosional retreat of an unconsolidated coast, Cape Henry to Cape Hatteras, western North Atlantic shelf. Sedimentology, 16: 221—250.

Swift, D.J.P. and Sears, P., 1974. Estuarine and littoral patterns in the surficial sand sheet, central and southern Atlantic shelf of North America. In: G.P. Allen (Editor), Shelf and Estuarine Sedimentation: a Symposium. Univ. Bordeaux, Institut de Geologie du Bassin d'Aquitaine, Talence.

Swift, D.J.P., Shideler, G.L., Holliday, B.W., McHone, J. and Sears, P., 1975. Distribution and genesis of inner continental shelf sands, Cape Henry to Cape Hatteras. Coastal Engineering Research Center Tech. Memo., in press.

Tanner, W.F., 1960. Florida coastal classification. Trans. Gulf Coast Assoc. Geol. Soc., 10: 259—266.

Uchupi, E., 1970. Atlantic continental shelf and slope of the United States: shallow

structure. U.S. Geol. Surv. Prof. Pap., 529 (1): 44 pp.
Van Straaten, L.M.J.U., 1965. Coastal barrier deposits in south and north Holland — in particular in the area around Scheveningen and IJmuiden. Meded. Geol. Sticht. N.S., 17: 41—75.
Wells, D.R., 1967. Beach Equilibrium and second order wave theory. J. Geophys. Res., 72: 497—509.
Wright, L.D. and Coleman, J.M., 1972. River delta morphology: wave climate and the role of the subaqueous profile. Science, 176: 282—284.

Reprinted from: Sedimentary Mechanics, IX International Congress of Sedimentology, Nice, France, Theme VI, 193-198.

Response of the Shelf Floor to Geostrophic Storm Currents, Middle Atlantic Bight of North America

by Donald J.P. Swift
Geological Oceanographer, National Oceanic and Atmospheric Administration, Atlantic Oceanographic and Meteorological Laboratories, Miami, Florida, USA.

RIDGE AND SWALE TOPOGRAPHY

A key response of the floor of the Middle Atlantic Bight to its hydraulic climate is the ridge and swale topography. Sand ridges are up to 10 m high, tens of km long, 2-4 km apart, and have side slopes of a degree or less (Fig. 1). The ridges make a northward opening angle with the adjacent shoreline of 0° to 35° (1, 2).

On the inner shelf, ridges locally extend into the shoreface, merging with it in depths as shoal as 4 m. Inner shelf ridges generally have steeper and finer grained seaward flanks (1). They tend to migrate slowly offshore and to the south, extending their crestlines so as to maintain contact with the shoreface, which is itself undergoing erosional retreat in response to postglacial sealevel rise. Eventually, however, they become isolated and stranded on the deepening shelf floor.

Fields of ridges formed by erosional retreat of the shoreface can be traced seawards for tens of km. Individual ridges retain their relief and distinctive grain size patterns after the departure of their nearshore generating zone. In particular, troughs continue to penetrate through the sand sheet produced by erosional retreat of the shoreface, exposing the sandy gravel that veneers the underlying early Holocene and Pleistocene silty clays and fine silty sands (3). Locally, incision of troughs has

---

[1] Swift, D.J.P., Duane, D.B., and Pilkey, O.H., 1972. Shelf Sediment Transport: Process and Pattern. Dowden, Hutchinson and Ross, Stroudsburg, Pa.,

[2] Swift, D.J.P., Duane, D.B., and McKinney, T.F., 1973. Marine Geology, 15:227-247.

[3] Stubblefield, W.L., Lavelle, J.W., McKinney, T.F., and Swift, D.J.P., in press. Jour. Sed. Petrol., March, 1975.

continued into the older deposits themselves (4).

Ridges also appear that do not seem to have formed in the nearshore zone. Shelf valleys in the Middle Atlantic Bight tend to be bordered on their north flanks by shoal retreat massifs; the retreat paths of the littoral drift depositional centers of estuary mouths (Fig. 1). The north sides and crests of the massifs are commonly serrated by ridge patterns trending across the massifs.

SAND RIBBONS, LINEAR EROSIONAL WINDOWS, AND SAND WAVES

Sidescan sonar studies reveal a widespread pattern of sand ribbons and linear erosional windows of negligible relief (Fig. 2). These features are 2 to 20 m wide, and several hundred meters long. When they occur in sets, they may be 20 to 70 m apart (5). They occur most frequently where the surficial sands are a meter or less thick. A common pattern consists of wide, flat-topped sand ribbons, separated by much narrower, notch-like erosional windows in which the basal Holocene gravel is exposed. Such windows frequently occur alone. The ribbon and window patterns tend to parallel the regional contours, but locally cross contours at angles up to 20°. The features may be symmetrical in plan view, or may have more sharply defined landward or seaward sides. Nearshore, they tend to form northward opening angles with the trend of the shoreline. Here ribbons tend to have more sharply defined seaward margins, while windows tend to have more sharply defined landward margins.

At the southern end of the Middle Atlantic Bight where the shelf floor shoals and narrows, fields of sandwaves occur. At Platt Shoals (Fig. 3),

---

[4] Stubblefield, W.L., and Swift, D.J.P., 1974. Abstracts with Programs. Geol. Soc. Amer., 6:976.

[5] McKinney, T.F., Stubblefield, W.L., and Swift, D.J.P., 1974. Marine Geology, 17:79-102.

flat-topped sandwaves 2-5 m high with spacings of 200 to 500 m occur on sand ridge crests. The southward facing slopes are steeper, shorter, and finer grained, but are rarely at the angle of repose. The sandwaves are not quite normal to the shoreline; the northward opening angle tends to be acute as though the responsible flow had an offshore component.

GEOSTROPHIC STORM FLOWS

It is far easier to describe the morphologic and textural patterns of the Middle Atlantic Bight than it is to explain them, due to the paucity of hydraulic observations. However, recent studies suggest that the forcing mechanism is a geostrophic response of the water column to winter storms.

A recent study by Beardsley and Butman (6) shows that not every storm results in such coupling. They observed strong, sustained response only when the storm cell rested in the Middle Atlantic Bight, so that the isobars of the storm paralleled the isobaths of the shelf floor. Under these conditions downshelf winds drove surface water onshore via the mechanism of Ekman transport, and the resulting set-up of shelf water against the coast caused a shelf-wide southward geostrophic flow, with mid-depth velocities on the order of 30-45 cm sec^{-1}

COASTAL BOUNDARY OF THE STORM FLOW FIELD

While the apparent southward sense of sand transport in the Middle Atlantic Bight may be thus accounted for, the "signature" of such geostrophic flows, in the form of ridge fields and sand ribbon patterns remains enigmatic. There are, however, some aspects of coastal geostrophic flows which may shed some light on the formation of these features. One such aspect is the probable nature of the coastal boundary of a southward geostrophic flow. When such a flow attains approximate equilibrium, land-

---

[6] Beardsley, R.C., and Butman, B., 1974. Geo. Res. Letters, 1:181-184.

ward transport in the surface Ekman layer is balanced by seaward return flow in the bottom Ekman layer. In the nearshore zone of downwelling, the two boundary layers overlap. In shallow water, the coriolis term is not significant in the equation of motion and the water accelerates downcoast in response to wind stress, until the pressure and friction terms balance. The result is a downwelling coastal jet (Fig. 4). This coastal pattern of storm flow is responsible for aggrading the inner shelf floor at the expense of the retreating shoreface. It is probably also intimately involved in the formation of shoreface-connected sand ridges during erosional shoreface retreat. Limited observations suggest that downwelling and flow acceleration tend to be localized in the troughs behind shoreface-connected ridges.

CELLULAR FLOW STRUCTURE IN GEOSTROPHIC FLOWS

Under conditions of peak storm flow, the upper and lower boundary layers may overlap far out onto the shelf. Theoretical and experimental studies (7, 8, 9) indicate that such boundary layer flow becomes unstable above a critical Reynolds number. However, because the unstable flow is still subject to the Coriolis effect, the instability is not random but ordered. It takes the form of alternate flow-parallel bands of downwelling and upwelling. These are linked by horizontal helical vortices with alternating right and left hand sense of rotation.

This mechanism is similar to, and perhaps identical with, Langmuir circulation. It has been suggested that the upper mixed layer of the ocean is maintained by wind-driven Langmuir circulation and that at least large Langmuir cells are in fact Ekman instabilities (8). The

---

[7]Faller, A.J., 1963. Jour. Fluid Mech., 15:560-576.

[8]Faller, A.J., 1971. Ann. Review Ecology and Systematics, 2:201-233.

[9]Faller, A.J., and Kaylor, R.B., 1966. Jour. Atmos. Sci., 23:466-480.

diameter of the flow cells is believed to be the depth to which the cells have eroded the underlying stratified water. It is a matter of observation on the Atlantic continental shelf that during the late fall, as storm intensity and frequency increase, the surface mixed layer becomes thicker and thicker, until it rests on the shelf floor.

It is tempting to view the sand ribbons and linear erosional windows of the Middle Atlantic Bight, and also the large scale sand ridge topography, as responses to such cellular flow structure. The smaller sand ribbons may result from cellular flow in relatively thin bottom Ekman layer, while sand ridges may be responses to peak flow, when top and bottom Ekman layers overlap across much of the shelf. The several spatial scales of sand ridges may be correlated with the several simultaneous scales of flow cells observed in laboratory experiments (9). The larger scales of sand ridge topography would require exceedingly flat flow cells, even with a fully developed Ekman layer, with depth to width ratios of 1:12 to 1:250. However, Faller and Kaylor note ratios of 1:12 for "type I" flow cells, and "much greater" depth to width ratios for the larger "type II" flow cells.

Langmuir (10) has noted that the downwelling zones of Langmuir cells, which receive the wind-driven, high velocity surface water, are much more sharply defined than the upwelling zones, which serve mainly to complete continuity in the manner of "ground" in electrical circuitry. In extremely flat flow cells, most of the "stretch" would occur in the diffuse upwelling zones. An excess of downwelling over upwelling velocity might also account for the notch-like nature of some erosional windows, and of some troughs between sand ridges.

Sand ribbons and sand ridges would also presumably differ in their temporal as well as spatial scales of formation. Sand ribbons would presumably be a response to a single flow event, or perhaps a season of flow events;

---

[10]Langmuir, I., 1925. Science, 87:119-123.

sand ridges would be the consequence of brief periods of substrate-flow coupling repeated over decades, centuries, or millenia.

The tendency towards sharper seaward contacts of sand ribbons, sharper landward contacts of erosional windows, and steeper seaward flanks of sand ridges is also compatible with geostrophic flow theory. Geostrophic flows driven by coastal set-up must experience a secondary circulation in which surface water moves onshore, and bottom water moves offshore. However, if cellular flow structure is fully developed, this mean secondary circulation must be suppressed. Instead, flow cells whose sense of rotation is the same as that of mean flow would be enhanced, which every alternate cell, rotating in the opposite sense, would be inhibited (Fig. 5). Such asymmetry of flow cells would lead to the observed asymmetry of bedforms.

Thus the apparent regional nature of sand transport on the Middle Atlantic Bight and also the patterns of bedforms appear to fit a comprehensive theory of southward sand transport by geostrophic flows. However, it may be no coincidence that this apparently simple model is presented at a time when almost no direct observations of substrate response to hydraulic process are available. There are other characteristics of large scale, unbounded flows which may serve to explain the observed bedform patterns, either in the absence of the proposed geostrophic flow mechanisms, or as complementary mechanisms. In particular, sand ridge topographies may be maintained if the ridges are aligned with the mean flow direction, but there is a considerable variance in flow direction for successive flow events, so that most flows trend at some angle across the grain of the topography. These mechanisms have been discussed in detail by others (11, 12).

---

[11] Smith, J.D., 1969. Jour. Geology, 77:39-55.

[12] Huthnance, J.M., 1972. Estuar. Coastal Mar. Sci., 1:89-99.

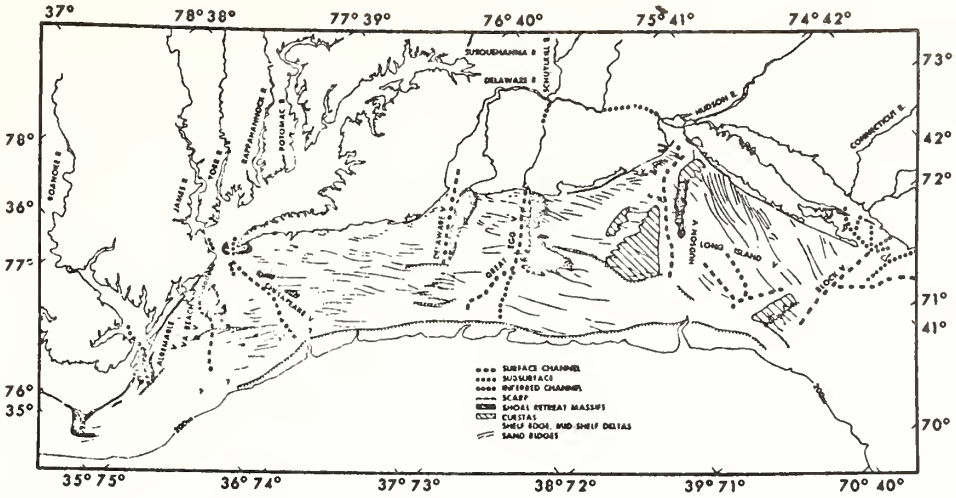

Fig. 1. Morphologic framework of the Middle Atlantic Bight.

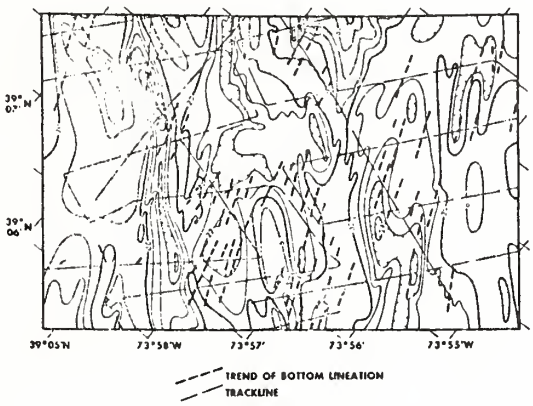

Fig. 2. Pattern of sand ribbons and erosional windows north of the Great Egg Shelf Valley. Depth in fathoms. From (5).

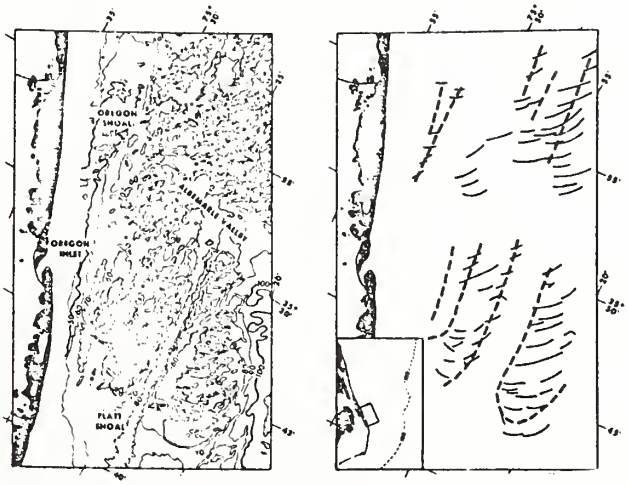

Fig. 3. Sandwaves atop sand ridges in the vicinity of the Albermarle Shelf Valley. Depth in feet.

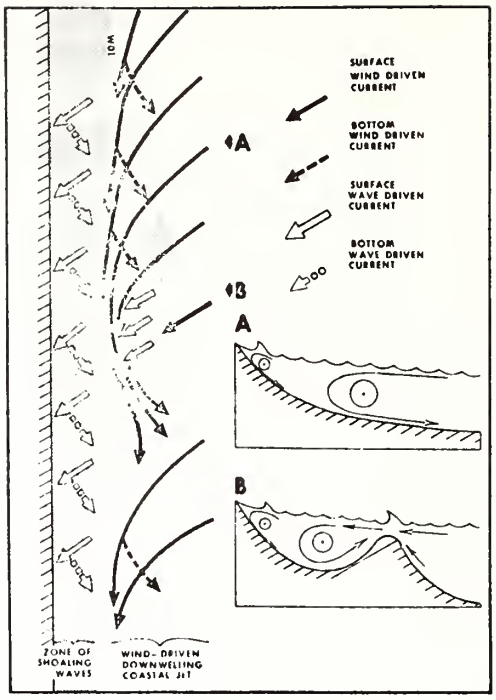

Fig. 4. A model for the coastal boundary of the storm flow field in the vicinity of a shoreface-connected ridge. Compare with Fig. 3.

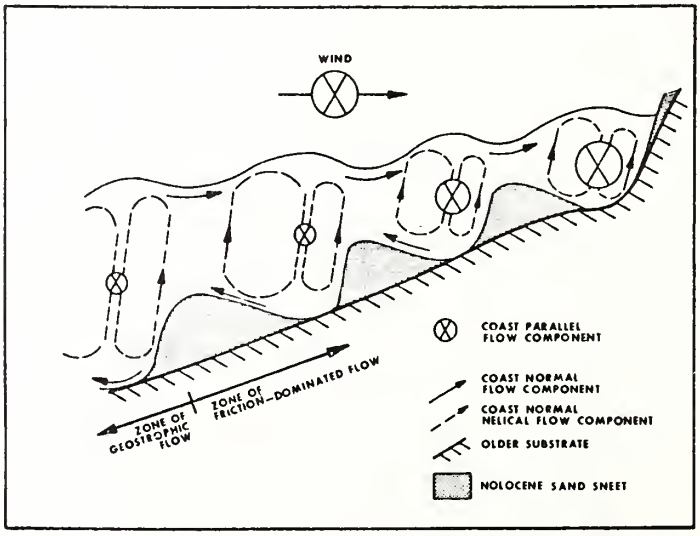

Fig. 5. A model for cellular storm flow. Note extreme vertical exaggeration; cells would have height to width ratios of at least 1:15.

Reprinted from: *Marine Geology 18*, 105-134.

TIDAL SAND RIDGES AND SHOAL-RETREAT MASSIFS

DONALD J. P. SWIFT

Atlantic Oceanographic and Meteorological Laboratories, Miami, Fla. (U.S.A.)

(Received June 10, 1974; accepted November 1, 1974)

ABSTRACT

Swift, D. J. P., 1974. Tidal sand ridges and shoal-retreat massifs. *Mar. Geol.*, 18:105—134.

In 1963, Off defined a bedform type which he described as rhythmic linear sand bodies caused by tidal currents. He figured twelve examples from around the world. Since then, the morphology and dynamics of sand transport in one of these areas, the tidal shelf seas around Great Britain, have undergone intensive study. The tidal sand ridges emerge as anomalies, in that they do not fit into the sequence of morphologic provinces which characterize the major sediment transport paths.

It is suggested here that the ridge fields are analogous to the shoal-retreat massifs of the Middle Atlantic Bight in that they have been inherited from a nearshore regime during the course of the Holocene transgression. Shoal-retreat massifs are low, broad, shelf-transverse sand bodies which mark the retreat paths of coastal depocenters associated with littoral drift convergences. Two main types of shoal-retreat massifs in the Middle Atlantic Bight are: (1) estuarine shoal-retreat massifs; and (2) cape shoal-retreat massifs.

Two similar classes of shoal-retreat massifs may develop in tidal shelf seas, but the mechanism is somewhat different. Class-1 tidal massifs are tidal ridge fields whose ridges were hydraulically packaged in an estuarine environment. If, upon transgression, they find themselves in a broad tidal bight which continues to funnel tidal flow, the ridges may survive for long distances out into the bight. The ridge fields of the Southern Bight of the North Sea may have undergone such an evolution.

Class-2 tidal massifs occur off promontories in tidal seas that are swept by the edge waves generated by amphidromic tidal systems. Here the debris of shoreface erosion tends to be stored as shoreface-connected, tide-maintained ridges. Such ridges are also pre-adapted to survive with modification for long distances out on the associated shelf, as the water column deepens during a marine transgression.

INTRODUCTION

Sediment genesis and dispersal on a storm-dominated shelf

The extremely detailed bathymetric maps available for the Atlantic shelf of North America, together with supplementary information on surficial sediments and shallow structure, have resulted in a clear picture of the mechanisms by which the Holocene surficial sand sheet was formed (Swift et al., 1972, 1974; Swift and Sears, 1974). The sand sheet is the blanket of debris produced by the erosional translation of the more steeply inclined

shoreface scarp into the flat coastal plain terrace during the Holocene transgression. The surficial sand is thus relict in the sense that it is derived from the underlying substrate. However, size frequency distributions of its samples generally reflect Holocene depositional mechanisms rather than earlier ones (Stubblefield et al., 1974). The term autochthonous is therefore preferred as a descriptor for the mode of sedimentation, since the term relict implies inherited rather than equilibrium textures (Curray, 1965; Swift et al., 1971). Autochthonous sedimentation, wherein the shelf cannibalizes its own substrate, may be contrasted with allochthonous sedimentation where the bulk of the surficial sediment is of recent fluvial origin, as in the case of the Niger shelf (Allen, 1965).

Holocene fluvial and lagoonal sediments and Pleistocene sediments pass through an "energy fence" (Allen, 1965) of landward asymmetrical wave surge on the retrograding shoreface by one of two modes. In shoreface bypassing, sediments eroded from the retreating shoreface are shifted downcurrent (generally southward on the Atlantic shelf) by littoral drift, and by inner shelf storm currents during periods of strong onshore winds, and tends to be deposited just seaward of the shoreface, to form the leading edge of the shelf surficial sand sheet (Fig.1).

Material retained for longer periods of time in the coastal transport system is ultimately deposited at littoral drift convergences, a mode termed downdrift bypassing. Sand shoals form at such convergences and translate landward with the retrograding shoreline. The low, shelf-transverse sand ridges which mark their retreat paths have been termed shoal-retreat massifs (massif in the sense of a topographic high composed of smaller scale highs; Swift et al., 1972; Fig.2 this paper).

The surficial sand sheet of the Atlantic continental shelf exhibits a variety of morphologic—stratigraphic patterns, reflecting differing coastal regimes, and varying patterns of shoreface and downdrift bypassing (Swift and Sears, 1974). In the Middle Atlantic Bight with its deeply incised, widely spaced estuaries and moderate wave regime, shoal-retreat massifs that are the retreat paths of estuary-mouth shoals alternate with the thinner shoreface retreat blankets of the coastal compartments. Both are overprinted with a ridge and swale topography (Swift et al., 1974), a response of the surficial sand sheet to the storm flow field (Fig.3). Ridges may form at the foot of the retreating shoreface and be detached as the transgression continues, or may be impressed directly on shoal-retreat massifs.

Off North and South Carolina, the more intense wave regime has created a series of cuspate forelands. As a consequence of the littoral drift convergences associated with the foreland apices, cape shoal-retreat massifs alternate with shoreface retreat blankets (Swift et al., 1972). To the south as the scale and spacing of forelands decrease, the massifs tend to overlap, and the resulting sand sheet is more accurately described as a cape shoal-retreat blanket. This sector has likewise been overprinted with a ridge and swale. topography (Fig.4).

The Atlantic shelf of North America is a storm-dominated shelf. It does

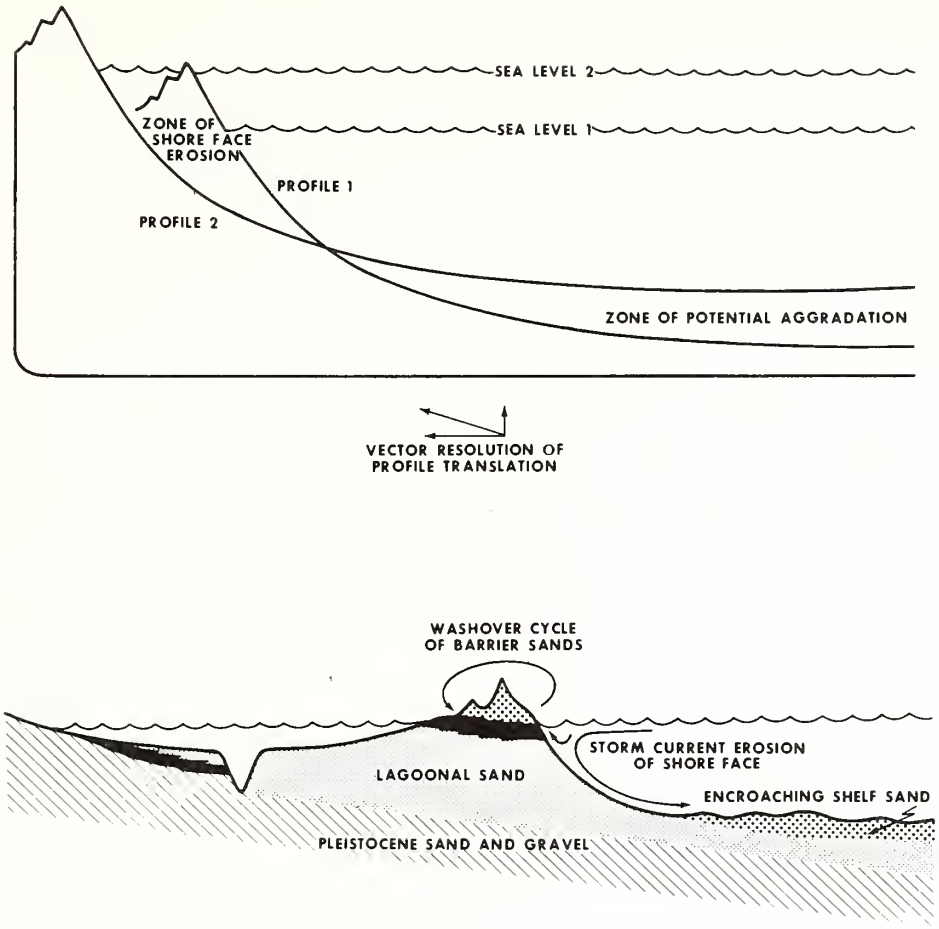

Fig.1. Shoreface bypassing. Landward and upward translation of the shoreface profile results in shoreface erosion and concomitant deposition of debris as the leading edge of the transgressive shelf sand sheet (Swift et al., 1974.)

not experience the sustained wave intensity of coasts in the lee of the prevailing westerlies such as the California or Irish coasts. Except in the Gulf of Main, in the Georgia Bight, and in the mouths of estuaries, tidal currents are not sufficiently amplified to significantly modify bottom topography.

Sediment genesis and dispersal on a tidal shelf

As noted by Stride (1963), Belderson and Stride (1966), Belderson et al. (1971) and Kenyon and Stride (1970) the fabric of the surficial sand sheet of tide-dominated shelves is rather different. Sedimentation in their study area, the shelf around the British Isles, may still be inferred to be autochthonous at least with respect to sand, since estuary mouths are sinks rather than sources with respect to marine sand, even in the case of estuarine

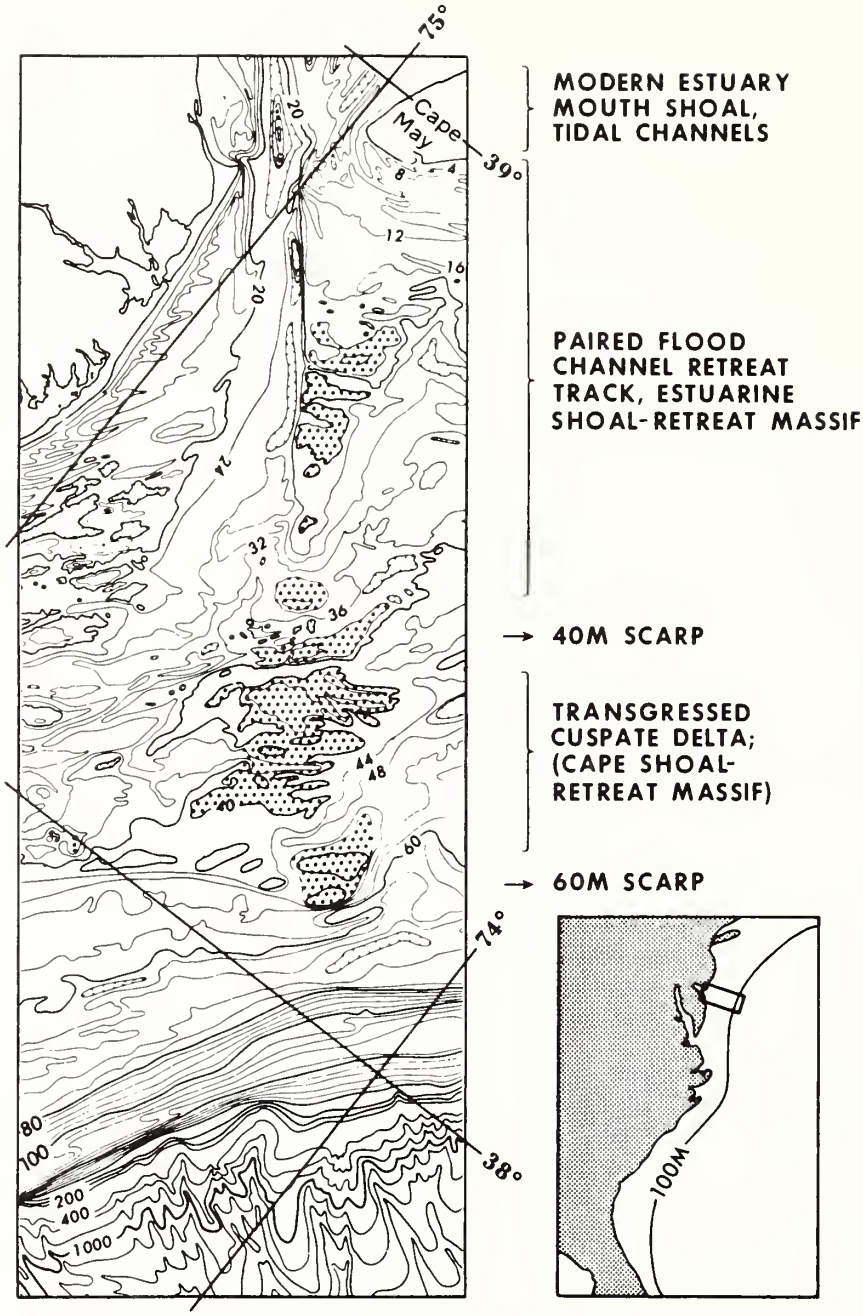

Fig.2. Downdrift bypassing. Littoral drift from the New Jersey coastal compartment to the north has been delivered to the mouth of Delaware Bay during its retreat across the shelf in response to postglacial sea-level rise. The retreat path of this littoral drift depositional center forms a low, shelf-transverse ridge, or shoal-retreat massif. (From Swift, 1973.)

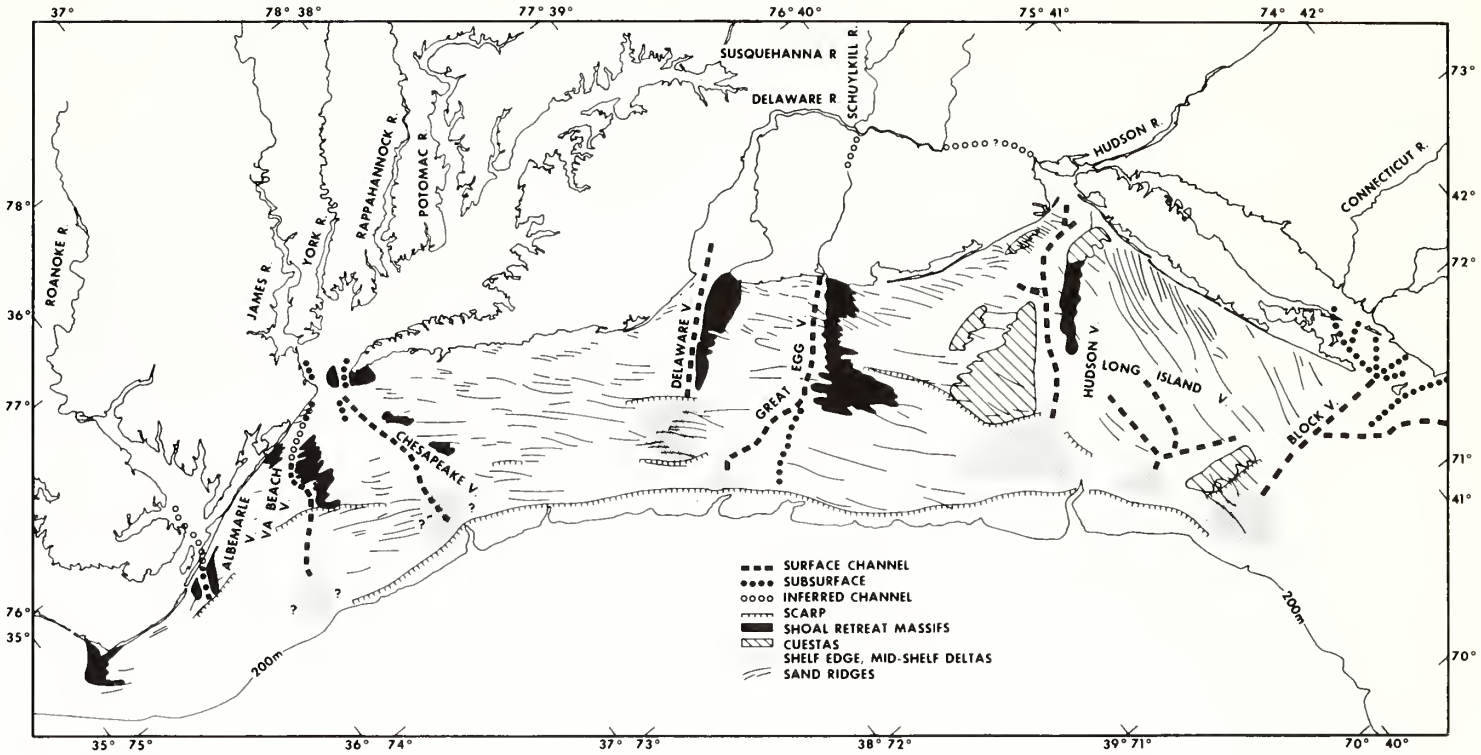

Fig.3. Morphologic framework of the Middle Atlantic bight, North America, showing pattern of estuarine shoal-retreat massifs, and overprinted pattern of ridge and swale topography. (From Swift and Sears, 1974.)

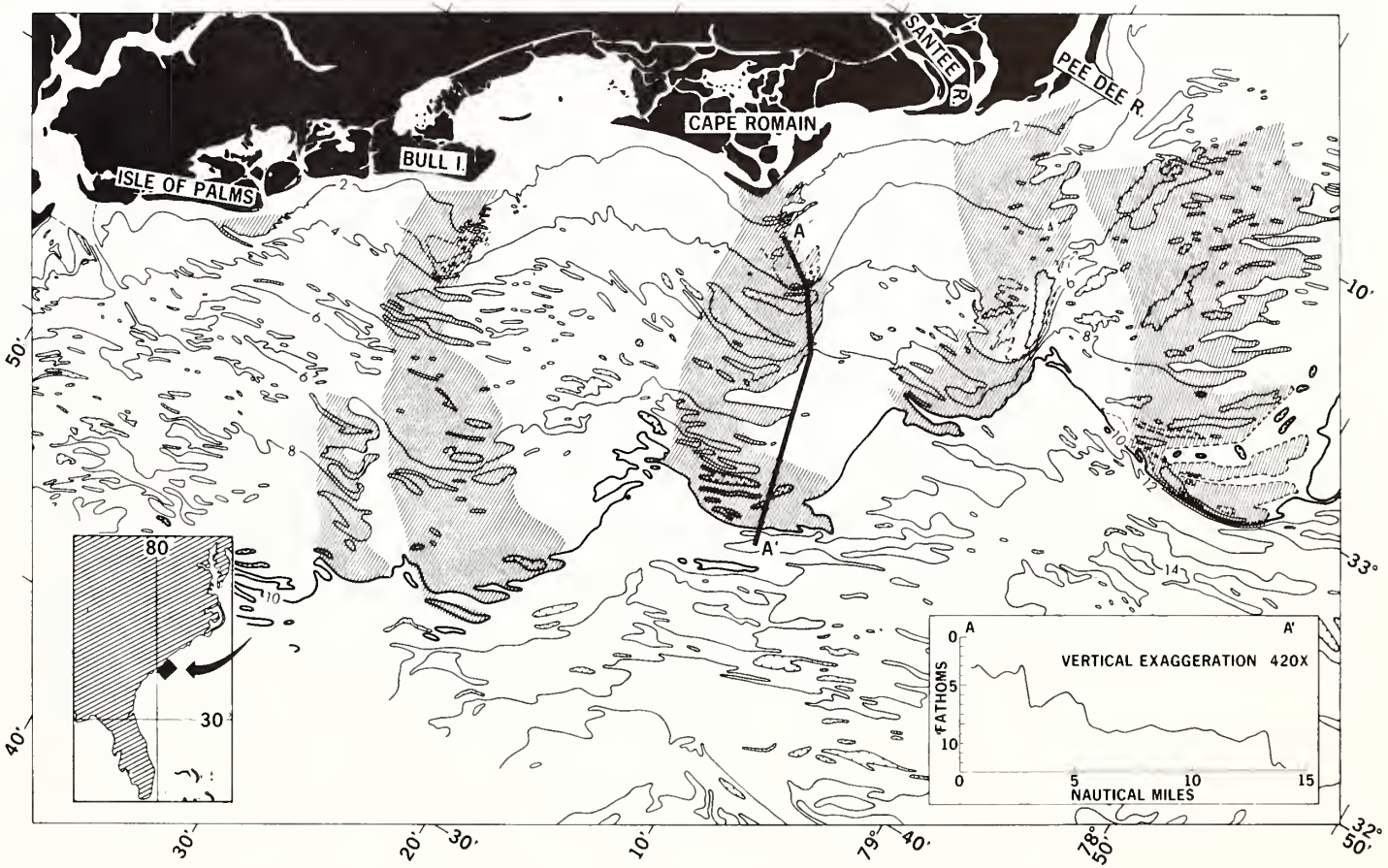

Fig. 4. Cuspate forelands of the Carolina coast and associated shoal-retreat massifs. Note overprinting by ridge and swale topography. (From Swift et al., 1972.)

mouths of the Rhine distributaries (Oomkens and Terwindt, 1960). Shoreface bypassing has apparently been the dominant mechanism of supply (Belderson and Stride, 1966). However, the more intense hydraulic climate of the tide-swept shelf of Great Britain appears to be capable of erasing most traces of earlier coastal environments from the sea floor. Instead the British workers report a complex systematic pattern on sea floor sediment dispersal (Fig.5) in which sand streams move through a succession of textural and morphologic facies down the gradient of mid-tide velocities (Fig.6). Dominant bedforms include erosional furrows (Stride, 1973), sand ribbons (Kenyon, 1970b), sand waves (Stride, 1970), and patchy sand sheets (Kenyon, 1970b), in order of decreasing mid-tide velocities.

TIDE-MAINTAINED SAND RIDGES

Categories of tidal ridges

A rather striking large-scale bedform that does not appear to be accounted for in their scheme is the current-parallel tidal sand ridge. Off (1963) has shown that these features have a world-wide distribution on shelf sectors in which the tide has undergone resonant amplification (Off, 1963; Fig.7 this paper).

Most of the tidal ridge fields figured by Off tend to fall into two categories. A first category consists of ridges in embayments, or the mouths of embayments. This class of ridge is generally parallel to the axis of the embayment and normal, or oblique, to the regional trend of the shoreline.

A second class of ridges occurs off capes and promontories. The ridges tend to be coast-parallel, but the ridge field as a whole tends to be elongated normal to shore. A third class, not figured, tends to occur on shelf edges where they intercept oceanic tidal streams. The first two classes occur together in the Southern Bight of the North Sea (Fig.7D; the Norfolk ridge field trends seaward from the Norfolk Promontory, while the Dutch, Flemish, and Thames ridge fields occupy the funnel-shaped Southern Bight of the North Sea.

Sand storage and stability of tidal ridges

These ridges are anomalous with respect to the scheme of tidal transport paths of Stride, Belderson, and Kenyon in two respects. Firstly, they appear to occupy no preferred location with respect to the facies sequence of the transport paths. Secondly, unlike the bedforms of the transport paths, they appear to be largely closed systems. Tidal transport paths, as described by British workers, start from "bedload partings," or zones of divergence of bottom sediment transport, and end in bedload convergences or over the shelf edge. The proximal sand ribbons and distal sand waves of these transport paths are in a sense hydraulically maintained sediment traps, in which grains undergo prolonged residence in their intermittent journey down the

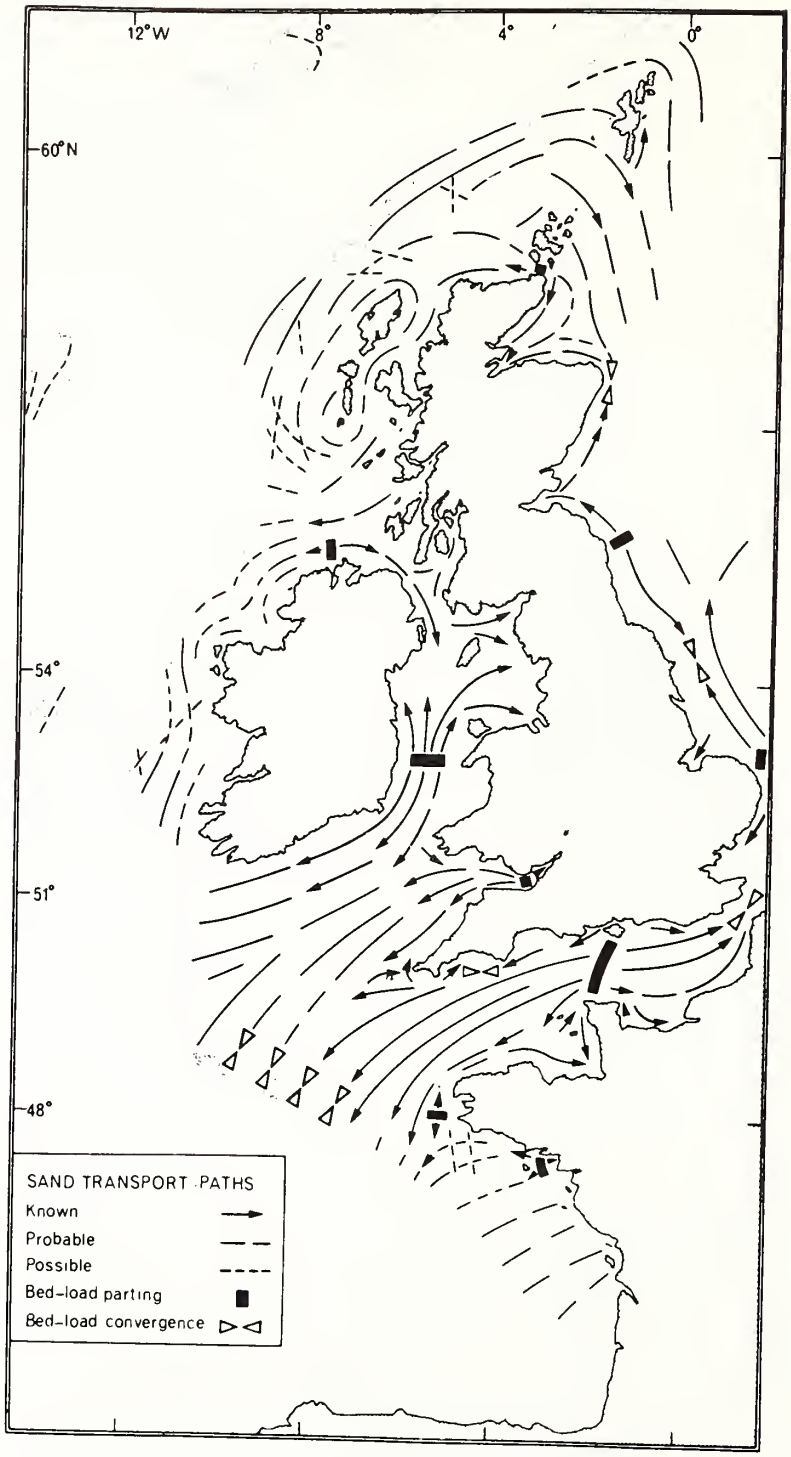

Fig.5. Pattern of sediment transport around the British Isles. (From Kenyon and Stride, 1970.)

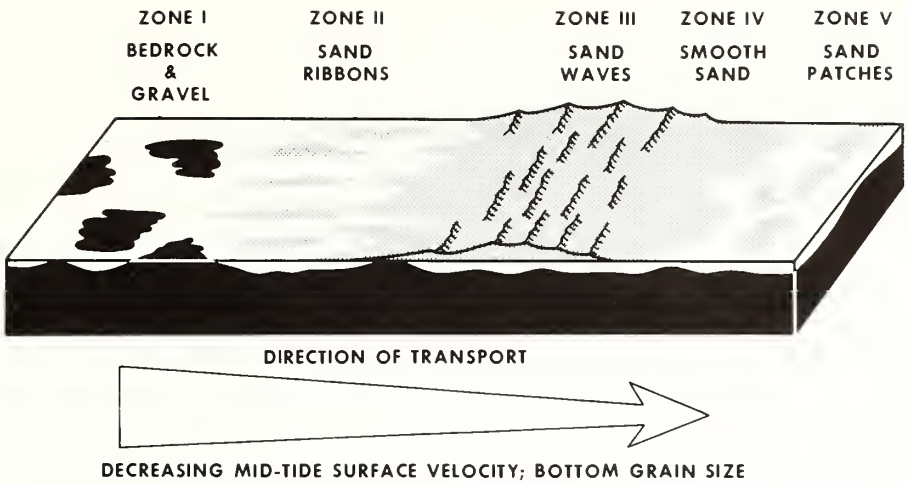

Fig.6. Succession of morphologic provinces along a tidal transport path, based on Belderson et al., 1971.

transport path. Sand ribbons are hypothesized to be zones of temporary deposition beneath bottom convergences due to secondary flow cells in the tidal stream (Allen, 1970). Sand waves are known to advance tank-tread fashion, due to deposition on the slip face, burial, erosion on the upcurrent side and redeposition on the slipface (Allen, 1968a).

Tidal sand ridges appear to be hydraulically maintained sand traps of a higher order of efficiency. As noted by Houbolt (1968; Fig.8 this paper), and by Caston (1970), Caston and Stride (1970), the tidal sand ridges of the North Sea tend to be partitions separating tidal currents with a dominantly flood discharge on one side from tidal currents with a dominantly ebb discharge on the other; the ridges are as a consequence sand circulation cells which comprise closed or nearly closed loops in the sediment transport system. This characteristic is clearly indicated by bedform patterns. Sandwaves tend to climb obliquely up both sides of the ridge, with their orthogonals meeting head on along the crest; or if the ridge is asymmetrical in cross-section (Fig.8 above) they move obliquely up the gentle side only; however, grain orientation on the steeper side suggests that sand here moves with the opposite sense.

Caston (1970) notes that the stability of tidal sand ridges extends to larger-scale ridge patterns. Ridges may migrate laterally due to stronger residual tidal flows on one side than on the other. However, different segments tend to migrate at different rates, so that a side-slipping ridge will become offset, then sigmoid as two internal channels develop, and finally split into three parallel ridges (Fig.8A—D). Ridge evolution is thus cyclic rather than linear. Rates of side-slipping and ridge evolution are slow, however, and ridge stability is sufficient that the course of 17th-century

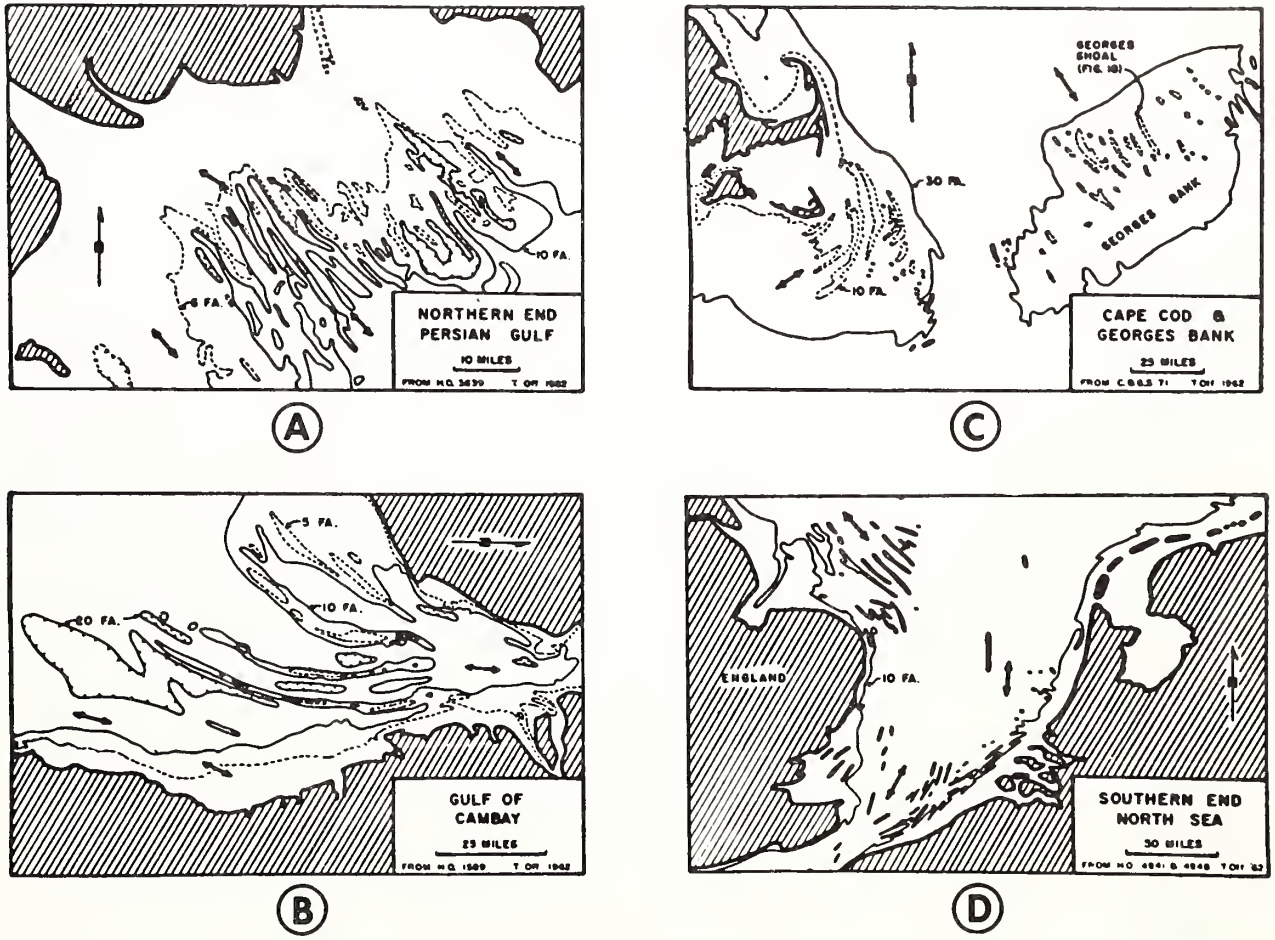

Fig. 7. Examples of tidal ridge fields in the mouths of embayments and on open coasts. Double-ended arrows indicate sense of tidal flow. (From Off, 1963.)

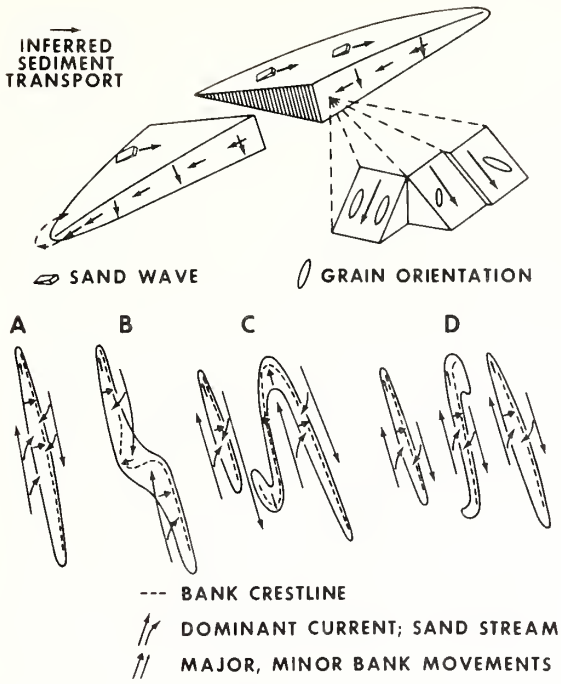

Fig.8. Morphologic patterns in tidal ridge fields. Above: structure of Well Bank, Norfolk ridge field, from Houbolt, 1968. Below: cyclic evolution of Norfolk ridges, from Caston, 1970.

Dutch naval battles may be traced on modern maps (Brouwer, 1964). The galleons and caravels had to avoid the same ridges that atomic submarines manoeuver about today. Such stability is probably characteristic of all large-scale current-parallel bedforms. Wilson (1973) has calculated that the great wind-parallel dunes of the sand-sea deserts may have taken ten thousand years to attain their present size. Their rates of migration are so slow that oases between ridges can migrate with the ridges.

Ridges that have required much of the duration of the Holocene to develop must have been affected by the secular changes in Holocene climate (for desert ridges) and Holocene sealevel (for tidal shelf ridges). It seems reasonable, therefore, to examine tidal ridge fields to see if this is a class of tidal shelf topography whose formation is contingent on shoreline migration. The most landward occurrence of tidal sand ridges is within tidal estuaries. A logical course of study is therefore a consideration of estuarine ridges and their associated flow fields, and comparison of these features with the ridges and flow fields of associated shelf sectors, to see if initially estuarine ridges may have survived transgression to become shelf ridges during the Holocene transgression.

SHELF RIDGES FROM ESTUARINE RIDGES

Estuarine flow

The cross-sectional area of river channels is a power function of river discharge (Leopold et al., 1964). Where rivers enter the sea, a salt wedge intrudes beneath the fluvial jet, whose discharge is amplified by entrainment of the underlying, more salty water, resulting in two-layer (estuarine) circulation. Most rivers enter tidal seas. River mouth discharge is increased by the volume of the reversing tidal flow which propagates for some distance upstream. The estuarine (two-layer) circulation that is residual to the tidal cycle is itself increased by the efficient tidal mixing. Thus a river mouth whose channel is in equilibrium with total discharge must expand rapidly through the tide-influenced zone toward the sea.

At the river mouth proper, a variety of processes conspire to construct an arcuate, seaward-convex sand shoal (Fig.9). The most fundamental factor is the hydrodynamic continuity relationship; expansion of the fluvial jet results in rapid deceleration and loss of capacity, and sediment is deposited in the form of a shoal. Estuarine circulation also plays a role; river mouth morphology and the circulation interact, so that the crest of the shoal becomes the leading edge of the salt wedge during flood stage; or if the tidal

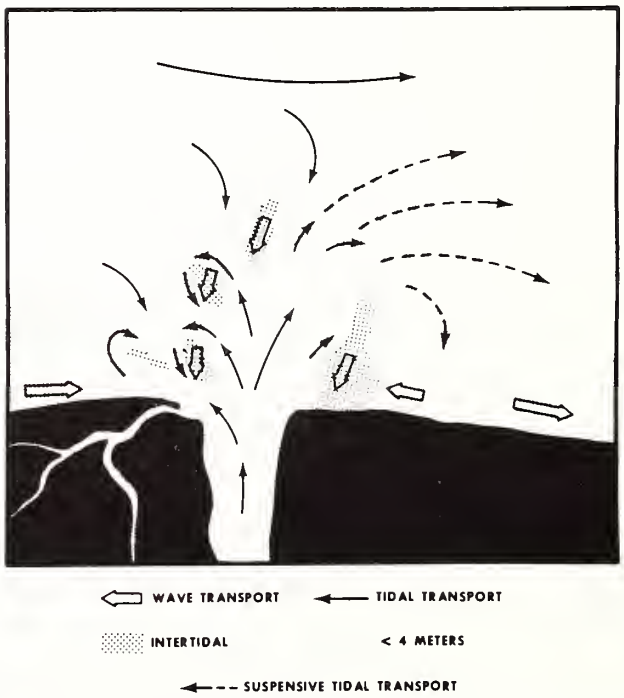

Fig.9. Sediment transport patterns on an estuary-mouth shoal. (After Oertel, 1972.)

component of river mouth discharge is very large, the spring ebb-tide terminus of the salt wedge; or both (Moore, 1970). The crest of the shoal thus becomes a bottom current convergence during periods of maximum sediment transport, and hence a reservoir for sand storage. A third major process maintaining the river mouth shoal is littoral drift, which is diverted seaward along the shoal crest and also serves to nourish it.

Sediment storage in river mouth shoals is mediated by the behavior of the tidal wave as it passes over the shoal crest. The tide within the estuary is retarded by friction and is out of phase with the shelf tide; it continues to ebb after the shelf tide has already begun to flood. The two water masses tend to interpenetrate, with the main ebb jet passing out over the center of the shoal, and the oceanic tide flooding on either side of it. The response of the shoal surface to this repeated flow pattern is an interdigitation of ebb and flood dominated channels, separated by a discontinuous, zig-zag system of sand banks (Ludwick, 1974b). Since opposite sides of these banks experience flow residual to the tidal cycle in opposite directions, each bank becomes a sand circulation cell or closed loop in the sand transport system (Fig.9). As such it is a hydrodynamic trap for sand supplied by littoral drift and tends to build up into the intertidal zone as a wave-dominated swash platform (Oertel, 1972).

Despite the relatively rapid postglacial rise in sea level, some river mouths have been able to maintain equilibrium channels, as deltas (prograding river mouths) or as equilibrium estuaries (slowly retrograding river mouths; see Fig.10A, B). Most, however, have not. Disequilibrium estuaries have resulted whenever aggradation of the estuary floor (in mm yr^{-1}) has been less than the rate of sea-level rise, so that before any given segment of channel could close down to the lower limiting cross-sectional area required for fluvial and tidal discharge the main shoreline had passed it by.

Such "drowned" or disequilibrium estuaries are generally more nearly funnel-shaped, rather than trumpet-shaped, as are the equilibrium forms. As a consequence of their higher ratio of salt water to fluvial discharge, their river-mouth shoals are retracted into the throat of the estuary and the interpenetration of ebb and flood channels becomes marked (Fig.10C).

With a yet further increase of tidal over fluvial discharge such a coastal indentation may no longer be appropriately called an estuary, but simply a bay. Large bays experiencing high tidal ranges may build a tide flat — tidal channel complex at their heads as a consequence of net landward sediment transport by the shoaling tidal wave (for instance, the German bight of the North Sea — Reineck, 1970). These deposits are the functional equivalent of the tide-molded deposits of a disequilibrium estuary.

Transgressive evolution of an estuary

Ridge initiation in the upper estuary. Many of the tidal ridge systems figured by Off appear to be active wide-mouth estuary or tidal-gulf morphologies. Other examples are probably explicable in terms of landward translation

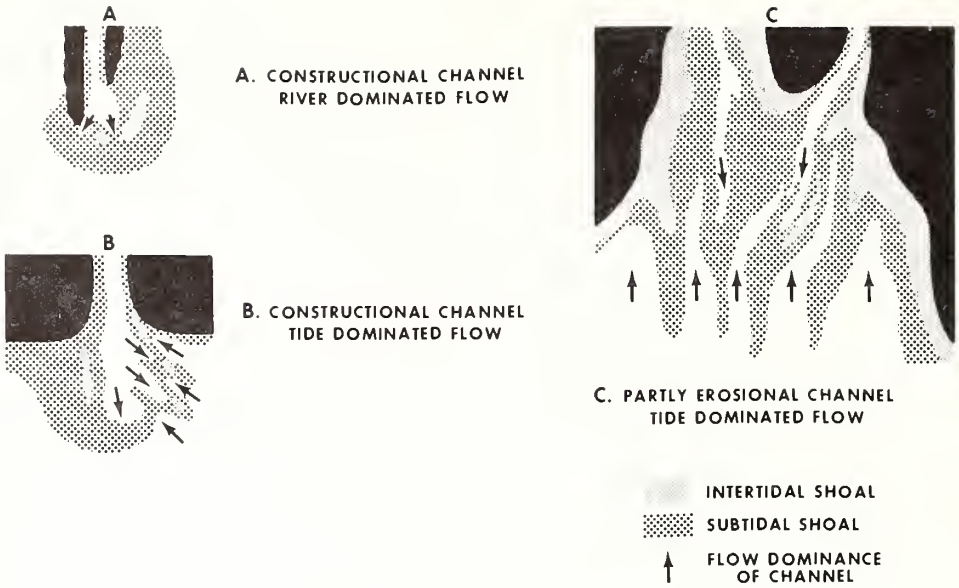

Fig.10. Varieties of river-mouth morphology.

of nearshore marine environments in response to the postglacial rise in sea level, with concomitant restructuring of estuarine ridge fields as shelf ridge fields. In order to understand such a transition, it is necessary to trace the evolution of a tidal ridge in a wide-mouth (disequilibrium) estuary during the course of a transgression, from its first emergence at the head of the estuary, through the estuary mouth, on to the adjacent shelf.

Kraft et al. (1974) have attempted to trace the transgressive history of the mouth of Delaware Bay by equating a series of transects across the modern bay with the time series of profiles that would be expected at a single point during transgression (Fig.11). Here ridges first appear as subaqueous tidal levees on the edge of tidal flats marginal to tidal channels. Unlike the tidal sand ridges of open shelf seas these ridges migrate away from their steep sides (Weil et al., 1974). As transgression proceeds, the channels service a larger and larger tidal prism, and tend to widen. The effect on the levees is erosion on the steep, channel-facing side, and aggradation on the gently sloping side facing away from the channel. The origin of these tidal levees (as well as the origin of river levees) requires some thought.

It seems probable that channeled flow, both in bankful stage (as in a river) and with overbank flow (as in a flooded river or tidal estuary), experiences a secondary circulation in the form of a double helical flow cell, with a common descending limb in mid-channel (Jeffreys, 1929; Leopold et al., 1964, p.283; Wilson, 1973); at bends the pattern is deformed into a single helix. The mechanism is poorly understood. In flumes with rectangular cross-sections a somewhat more complex secondary flow pattern has been attributed to the unequal distribution of Reynolds (turbulent) stress components

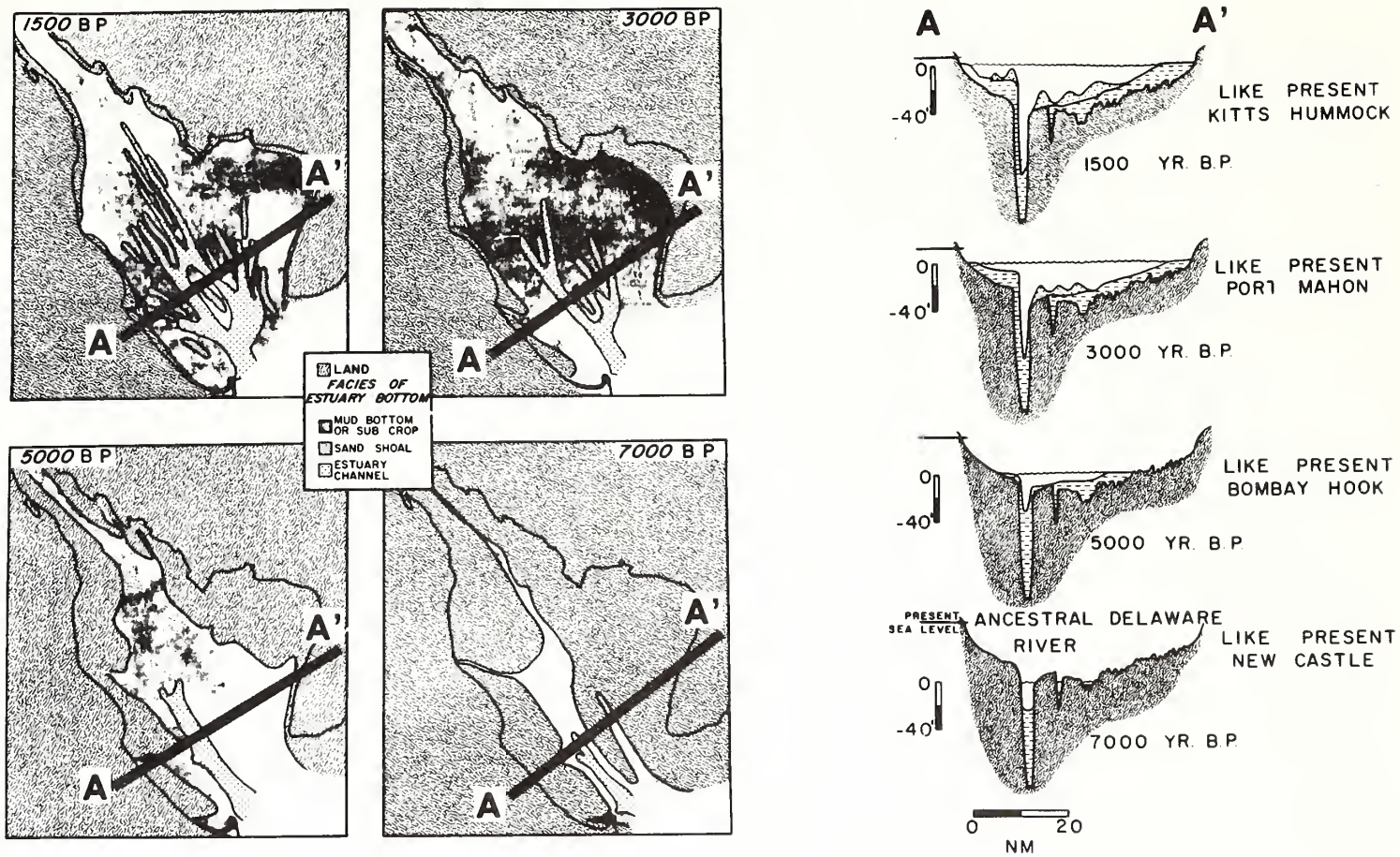

Fig.11. Holocene evolution of a single section through Delaware Bay as inferred from successive downbay sections. Cross-sections on right are modern cross-sections, which are inferred to be equivalent to the time series that would appear at the single transect shown in the panels at left. (From Kraft et al., 1974.)

(Kennedy and Fulton, 1961; Gessner, 1973), resulting in secondary flow directed at flume corners. Bagnold (1966) suggests that in natural channels the asymmetric exchange of momentum between the bottom boundary flow and the core flow may generate an elevated free surface and a pressure field capable of driving bottom flow divergence. Such a secondary component of channel flow would result in a bottom current divergence and would be conducive to the formation of marginal levees.

Weil et al. (1974) have attributed the submarine levees of Delaware Bay tidal channels to density-driven secondary flow associated with the tidal cycle (Fig.12). They note that the tide floods more rapidly in the channel axes, where the deeper water column is less retarded by bottom friction. Hence during the first part of the flood period, fingers of denser, faster water extend up channel axes. Weil et al. suggest that the "pressure gradients resulting from cross-shoal density and velocity contrasts induce and contribute to secondary flow out of the deeper channel, up the steep face of the levee, and across its crest". The shoal that they studied had more intense ebb flow on the gentle side than on the steep side, and Weil et al. infer that a similar pattern of secondary flow would occur on the ebb (Fig.12B), as "higher current velocities develop on the gentle side of the shoal and the ebbing denser bottom waters are overridden by faster flowing, less dense surface waters".

Ridge modification in the lower estuary. Upper estuary channels tend to be ebb-dominated (greater ebb discharge; see Fig.13) perhaps because the upper estuary water mass tends to flood along isobaths, but to ebb normal to them, under the added impetus of gravity. Further down estuary, as levees begin to build, the interfluves tend to become flood-dominated channels in their own right, although the sense of dominance of channel and interfluves may locally be reversed (Fig.12C). As previously noted, retardation of the tidal wave in the estuary results in a phase lag across the estuary-mouth shoal, causing in turn an interdigitation of ebb and flood channels, separated by partition ridges, across the crest of the shoal. Studies by Ludwick (1974a) at the mouth of Chesapeake Bay suggest that downwelling and bottom current divergences characterize flow in these channels as well (Fig.14). However, downwelling and bottom divergence are restricted to the flood tide. Ludwick (1974a) suggests that they are inhibited on the ebb by the greater stratification of water flowing from the inner estuary. If so, it may be the consequence of the more basic helical flow mechanism associated with rivers (see above) rather than of the density-driven mechanism (Weil et al., 1974); although in Fig.11 this latter mechanism is modelled more convincingly for the flood than for the ebb. While the model of Kraft et al. calls for a steady landward migration of the ebb—flood channel system of the Delaware estuary-mouth shoal during the Holocene transgression, Ludwick (1974b) believes that the analogous Chesapeake Bay mouth shoal has grown across the bay mouth as a zig-zag submarine spit since the Late-Holocene reduction in the rate of sea-level rise. Spit growth, he suggests, has been fed

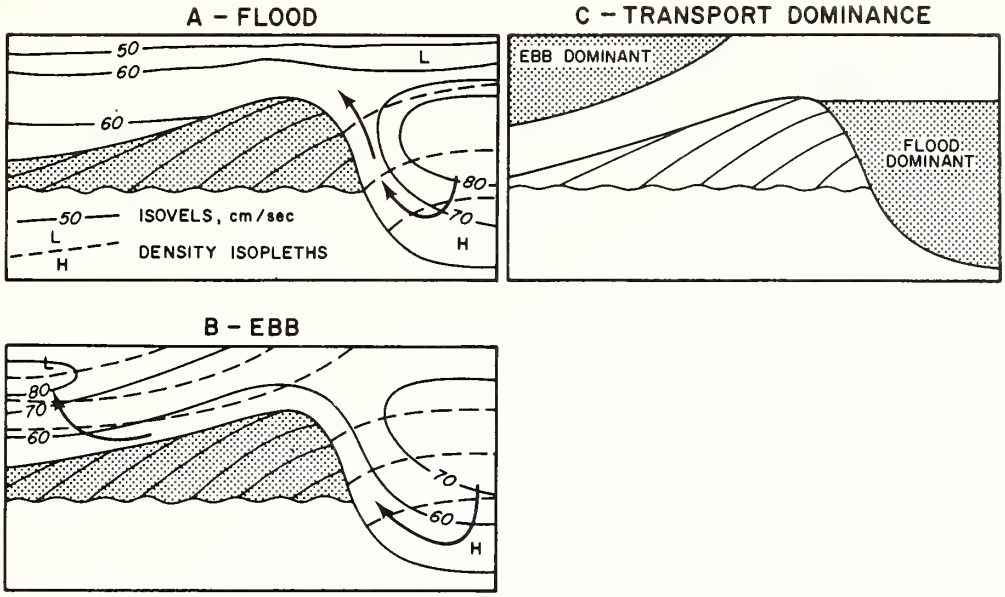

Fig.12. Schematic diagrams illustrating a possible mechanism for maintaining a submarine tidal levee. See text for explanation. (After Weil et al., 1974).

by the littoral drift input of the adjacent Delmarva coastal compartment, with the zig-zag spit alternately capturing the flood-dominated flanking flow and the ebb-dominated axial flow.

Thus ridges initiated in the upper estuary may undergo a complex evolution as successive estuary environments and associated flow regimes pass over them. Individual ridges may maintain their integrity through this process or be replaced by related forms maintained by somewhat different mechanisms.

Modification of ridge morphology intensifies as the regional shoreline passes, and the lower estuarine regime is replaced by an open shelf regime. If the wave climate is intense, then the outer surface of the estuary-mouth shoal is beveled by erosional shoreface retreat in a fashion similar to that transpiring on the adjacent mainland coast. The north side of the Delaware Bay mouth shoal, depositional center for the littoral drift of the New Jersey coastal compartment, has left a retreat path across the Delaware shelf in the form of a low, subdued ridge (shoal-retreat massif; Fig.2). It continues to retain a weakly developed ridge topography impressed upon it, but ridge orientation, away from the shore-normal ridges of the estuary mouth, has rotated into parallelism with the coastwise trend of storm flow on the shelf.

Ridge modification on the adjacent shelf. In wide-mouth estuaries which open into broader tidal bights (for instance, the modern Thames estuary, which opens into the Southern Bight of the North Sea; Fig.5D, 12), ridges

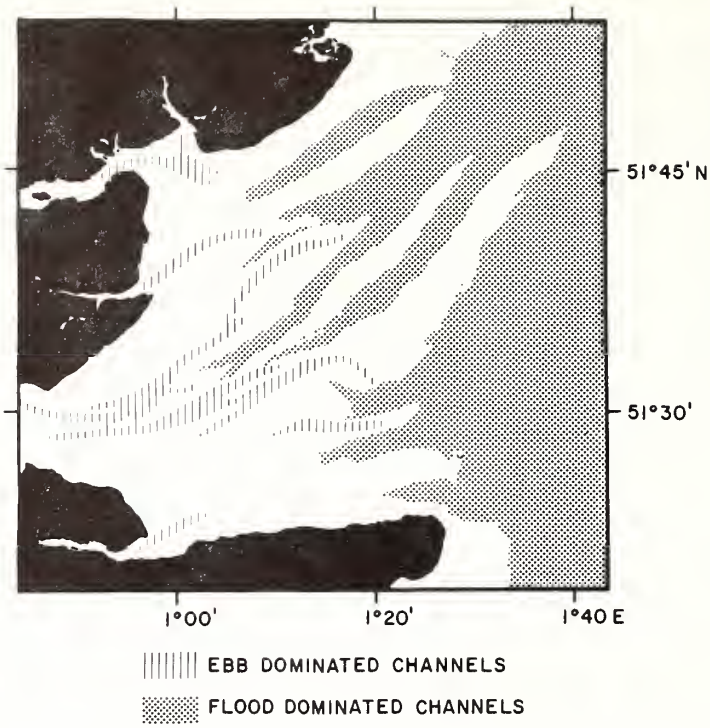

Fig.13. Ebb—flood channel morphology of the outer Thames estuary. (Modified from Robinson, 1956.)

initiated in the estuary mouths might be expected to survive for long periods after transgression as a consequence of the reduced wave climate, if the orientation of the tidal ellipse does not change markedly. But ridges which have been hydraulically packaged as estuary-mouth partitions must now respond to the rotary tidal regime of the open shelf. The two main hydraulic flow patterns cited for ridge maintenance, helical flow cells and interdigitation of ebb- and flood-dominated flows, appear to continue to play significant roles in the maintenance of ridges by open shelf tidal flow, but the forcing mechanisms may be somewhat different (Fig.15). On the estuary-mouth shoal the "unit cell" of which the topography is built appears to be an ebb—flood channel couplet, separated by a z-shaped partition ridge. The ebb channel shoals seaward and terminates in an ebb sinus, while the flood channel shoals landward, terminating in a flood sinus (Ludwick, 1970, 1974b). Seaward of the shoal crest, this pattern must break down, as here each channel must be a seaward extension of a flood channel (see Fig.9B), an inherently unstable pattern (Robinson, 1956).

As the crest of the estuary-mouth shoal recedes due to continued transgression, the pattern tends to change from one of well defined channels separated by partition ridges to one of doubly terminated ridges, whose intervening lows comprise an anastomosing system of less well defined chan-

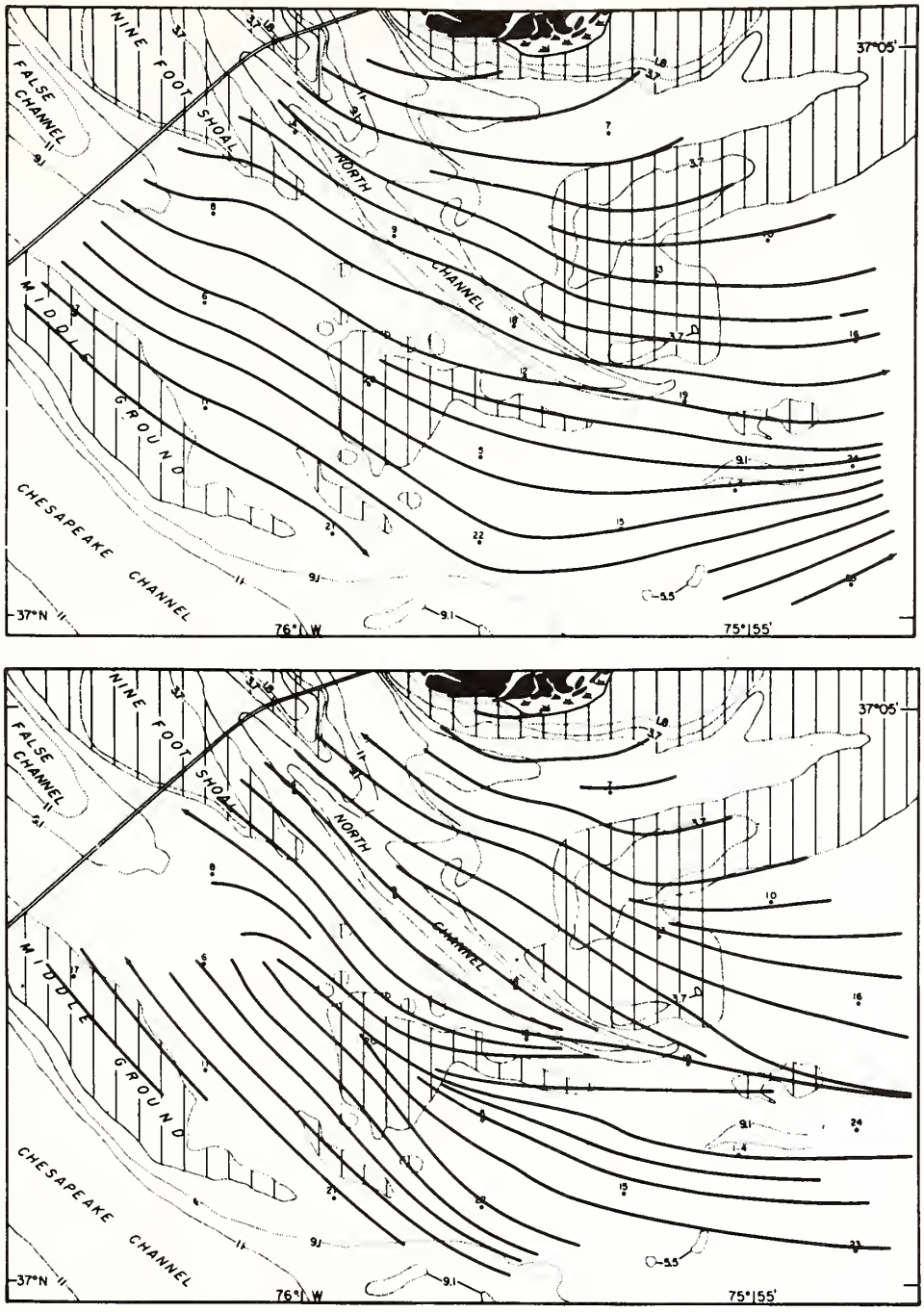

Fig.14. Ebb-directed (above) and flood-directed (below) sediment transport at the bed, north side of Chesapeake Bay mouth. Stream-lines are for the sediment transport vector, $\tau_0 u_{100}$; see Ludwick, 1974 for computations. Depths in meters. Vertically ruled areas (shoaler than 5.5 m) are the shoals marginal to an interdigitating ebb—flood channel system. (From Ludwick, 1974.)

nels (see Outer Thames estuary in Houbolt, 1968, end paper map). On such openwork shelf ridge systems, ebb and flood sinuses still occur, but as minor zig-zags or bifurcations of ridges. Channels between main ridges are themselves divided into ebb dominant and flood dominant sides (Caston and Stride, 1970; Fig.15 this paper). All channels have the same sense of shear. Thus the ridges are sand circulation cells, but the sense of circulation is the same from ridge to ridge, instead of alternating between clockwise and counter clockwise as on the estuary-mouth shoal.

Huthnance (1973) attributes this open-shelf flow pattern to interaction of the ridges with the shelf tide. His model considers a rectilinear reversing tide whose flow directions make an oblique angle with the ridge axis. The cross-ridge component of flow must accelerate over the ridge crest for continuity reasons. The ridge-parallel component of flow must decrease up the up-current flank as the water column shoals, and influence of friction becomes proportionately greater. However, because high velocity fluid is being transported into the shoal region, the decrease in the ridge-parallel flow component lags behind the decrease in depth. On the down-current flank, the restoration of the ridge-parallel flow to ambient velocity is similarly lagged. When the tide changes, up-current and down-current flanks reverse roles. When flow is averaged over the tidal cycle, a clockwise pattern of residual around the ridge results (or counter clockwise, depending on whether the oblique, reversing tidal stream is sinistral or dextral with respect to the ridge). Huthnance proposes a second mechanism whereby in the Northern Hemisphere, coriolis force also results in clockwise circulation.

Huthnance's mechanisms are interesting, but the requirement that there be a significant angle between the axis of the tidal stream and that of the

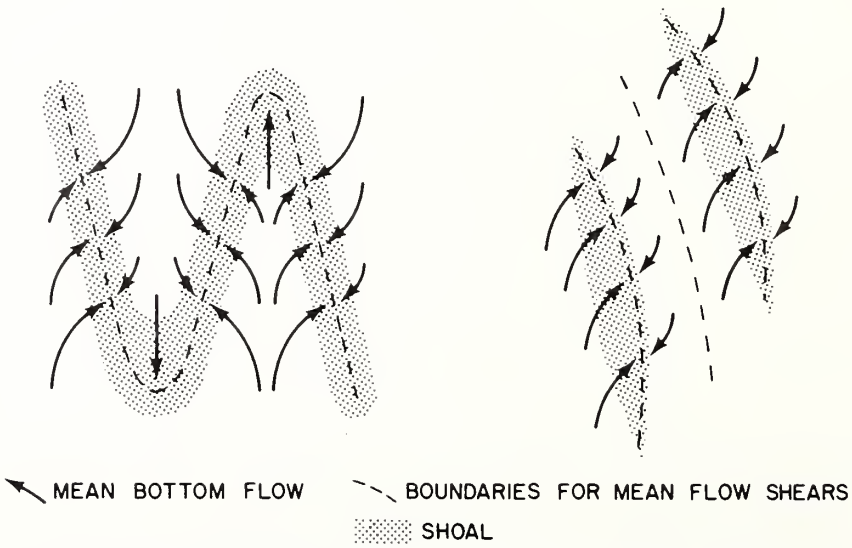

Fig.15. Residual current patterns around estuarine and open-shelf ridges.

ridge is problematic. The ridges are a response element within the flow field-substrate system, not an independent forcing element. It seems doubtful that ridges of cohesionless sand could maintain a significant angle with the tidal stream for any length of time, unless it were somehow an equilibrium response to flow. Smith (1969) notes that tidal sand ridges might be expected to orient themselves parallel to the long axis of the tidal ellipse, as the sand body would then be at a small angle of attack throughout most of the high velocity part of the tidal cycle. According to slender body theory the cross-shoal component of flow during this period can be considered to be two-dimensional, and driven by the cross-shoal pressure gradient. It would thus sweep sand first up one side and then up the other as the tide rotated.

Possibly the dilemma is resolved by the lag effect cited by Postma (1967; Fig.16 this paper) and Stride (1973). Due to a lag in the entrainment of sand, the period of maximum sand transport is believed to lag behind maximum flood flow, and again behind maximum ebb flow. The result should be to align the response element (sand ridge) obliquely across the major axis of the tidal ellipse.

In the large scale, unbounded flows of the open shelf, helical flow structure may continue by mechanisms other than, or in addition to, those operating in river channels and estuaries. Since shelf flow fields are shallow relative to their extent, and occur on a rotating planet, they comprise Ekman boundary flows, whose velocity profiles, above the logarithmic boundary layer, should be upward-expanding Ekman spirals, as a consequence of frictional retardation of the flow by the sea floor. Above critical Reynolds numbers, such flow becomes unstable (Faller, 1963; Faller and Kaylor, 1966; Faller, 1971). However, the instabilities occur within the Ekman field; hence are ordered, not random, and in fact take the form of arrays of horizontal helical flow cells, with adjacent cells rotating in the opposite sense. Such helically structured flow, driven by the semi-diurnal tide, may

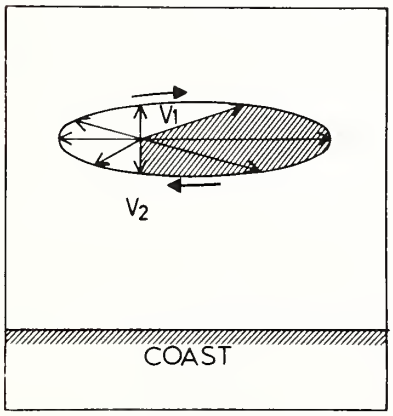

Fig.16. Lag effects in a rotating tide. Sand entrainment starts at velocity *V1*, and continues through velocity *V2*. (From Postma, 1967.)

couple with shelf-ridge topographies such as those of the Southern Bight of the North Sea, as has been suggested by Houbolt (1968).

To summarize the above considerations, it seems probable that tidal sand ridges may be packaged by a confined estuarine or bay flow regime of reversing tides in a form that will permit them to survive transgression and adapt to a tidal shelf environment. The Southern Bight of the North Sea may provide a case history of such a transition, with the Thames estuary still actively generating ridges, and the Flemish and Zeeland ridge fields and other ridge fields of the Southern Bight marking early zones of ridge generation in a somewhat more confined, estuary-like flow regime, prior to the cutting of the Straights of Dover (Fig.7D).

TIDAL SHOAL-RETREAT MASSIFS OF OPEN COASTS

Ridge-generating processes of open tidal coasts

The estuary to tidal bight transition is less useful as an explanation of several other major ridge fields of tidal shelves, because they may be traced landward to open coasts, rather than into estuaries. One well-studied example, the coast of southeast England, is characterized by a remarkable capacity for subtidal storage of sand. Spits extend across stream mouths, but otherwise the coast is a bluffed mainland coast in which the attempt of the wave regime to build barriers has been inhibited, apparently by the competition of subtidal sand bodies for the debris of shoreface erosion.

The shoreline of southeast England, like most unconsolidated shorelines, is separated from the gently dipping shelf floor by a more steeply dipping shoreface, a surface in equilibrium with the hydraulic climate (Fenneman, 1902; Swift et al., 1974). The upper shoreface appears to be a response to the regime of shoaling waves. King (1972, p.156) has described swash bars which migrate up through the intertidal zone to weld to the beach on the coast of southeast England. The lower shoreface, however, experiences mid-tide surface velocities in excess of 100 cm/sec (2 kn) and is instead tide-dominated. As a consequence of the amphidromic tidal regime of the North Sea, the tidal wave passes south along the coast as a progressive edge wave. Shallow-water distortion of the tidal wave results in a strong flood residual, oriented south, parallel to the coast.

The shoreface has responded to the tidal regime by deforming into a series of accretionary bulges, whose subaerial expressions are known as *nesses* (Robinson, 1966; Fig.17 this paper). The nesses tend to be connected to submarine sand ridges which extend obliquely upcoast and seaward. As a consequence of their orientation with respect to the coastal tidal wave, the channels landward of them are flood-dominated, while their seaward sides are ebb-dominated. The coast of southeastern England is retreating at rates generally in excess of a meter a year (King, 1972, pp.470—474) and each ridge crest must serve as a zone of bottom current convergence on which is

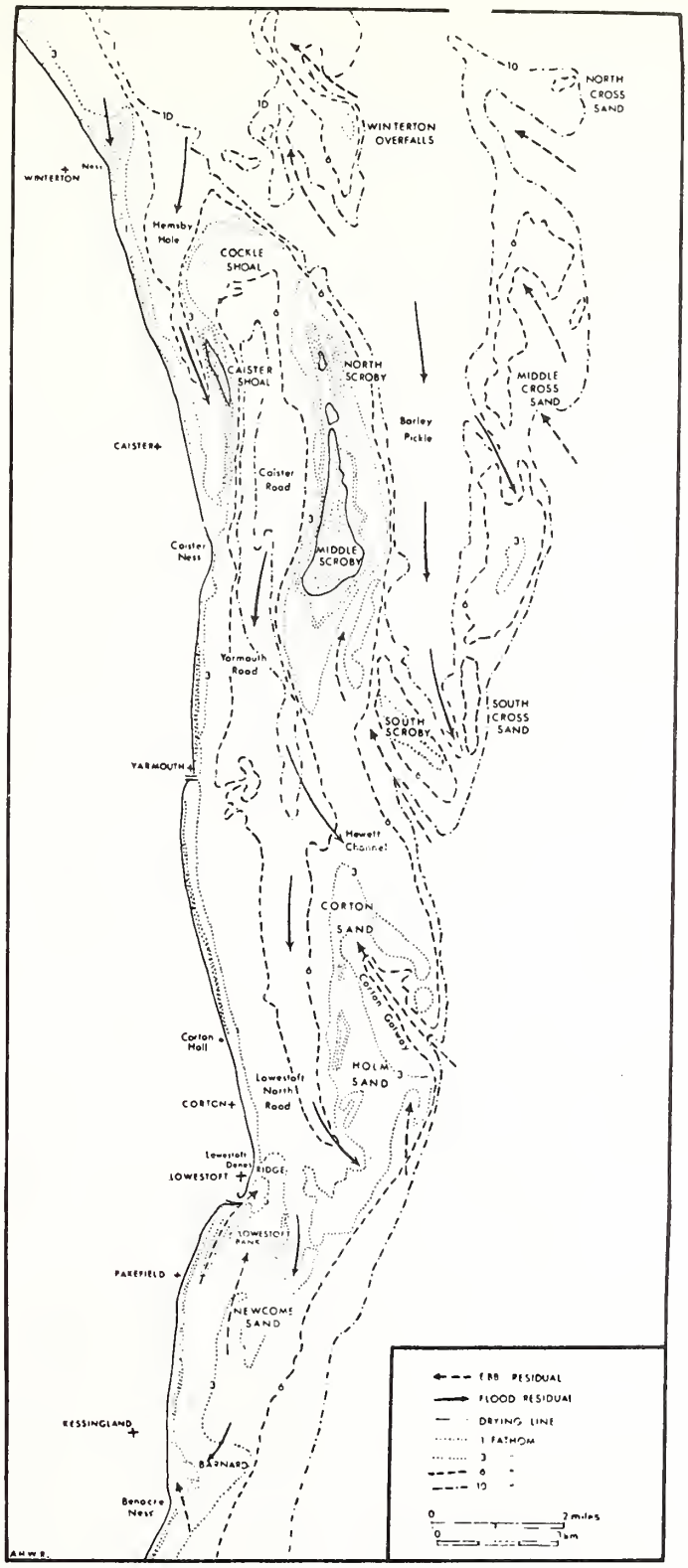

Fig.17. Shoreface-connected, tide-maintained ridges of the Norfolk coast. (From Robinson, 1966.)

deposited material eroded from the upcoast shoreface, and also from the downcoast shoreface in the zone of reverse drift behind the ness.

Historical records examined by Robinson indicate that the nesses tend to migrate downcoast. Their downcoast migration, coupled with landward translation of the shoreface, appears to have left a poorly organized sequence of detached tidal ridges on the adjacent inner shelf, in a manner similar to the detachment of storm-generated ridges described from the North American shelf (Swift et al., 1974).

The Norfolk ridge field as a shoal-retreat massif

It is important to remember that a bedform is only half of a closely coupled feedback system, in which a perturbation in the flow field maintains a perturbation in the substrate, and vice versa. The detached offshore ridges (Fig.18) are "relict" in the sense that they were born in the somewhat different regime and geometry of the shoreface. They are, however, equilibrium features in that they continue to induce the flow perturbation that originally induced them; otherwise they could not remain as ridges of unconsolidated sand in the face of such high velocities. As the ridges are traced seaward across Fig.18 to the offshore ridge field a systematic change is, however, apparent; ridge spacing and amplitude increases. This is in accord with Allen's (1968b) contention that the wavelength of large-scale bedforms is proportional to flow depth. Like estuarine ridges, the Norfolk ridges pass through the transition of Fig.15, from ebb—flood channel couplets to sand cells with the same sense of circulation (Caston and Stride, 1970; Huthnance, 1973). Ridges out to, but not including Hewitt Ridges tend to be sigmoidal in plan view and are subject to Caston's (1970) scheme of cyclic evolution (Fig.6). Seaward of this limit, ebb—flood channel systems are not apparent. Since ebb—flood channel systems are a wave-phase lag phenomenon, the transition may occur at a characteristic Froude number.

Nantucket shoals ridge field as a shoal-retreat massif

The apparent evolutionary sequence of shoreface-connected ridges, sigmoidal inner-shelf ridges, and arcuate outer-shelf ridges of the Norfolk ridge field suggest that it is a shoal-retreat massif, marking the retreat path of the coastal tidal regime of the Norfolk salient across 90 km of the North Sea floor. As such, it is probably not a unique phenomenon. The great ridge field of Nantucket shoals (Fig.19) on the U.S. Atlantic shelf may be an analogous case. Here mid-tide flood velocities regularly attain 100—200 cm/sec (2—4 kn; Atlantic Coastal Pilot). There is a continuous sequence of shoal-transverse tidal ridges up the axis of the shoal towards Nantucket Island. The sequence is completed by a series of shoreface-connected ridges on the seaward margin of Nantucket Island (shading denoting shoreface-connected ridges in Fig.19 is based on ESSA map 0708N-52 with 1 fathom resolution). As in the case of the Norfolk ridge field, ridge spacing

and amplitude increases steadily in a seaward direction through this sequence. The ridges exhibit seaward asymmetry, as do the Norfolk ridges. The Nantucket map is sufficiently detailed to resolve the sandwave pattern as well as the coarser pattern of ridges. Sandwaves are normal to trough axes, but climb obliquely up the landward flanks of ridges to swing into parallelism with the crest. Paired ebb and flood sinuses occur locally (arrows, Fig.19) as in the inner Norfolk ridges. However, the asymptotic relationship of sand-

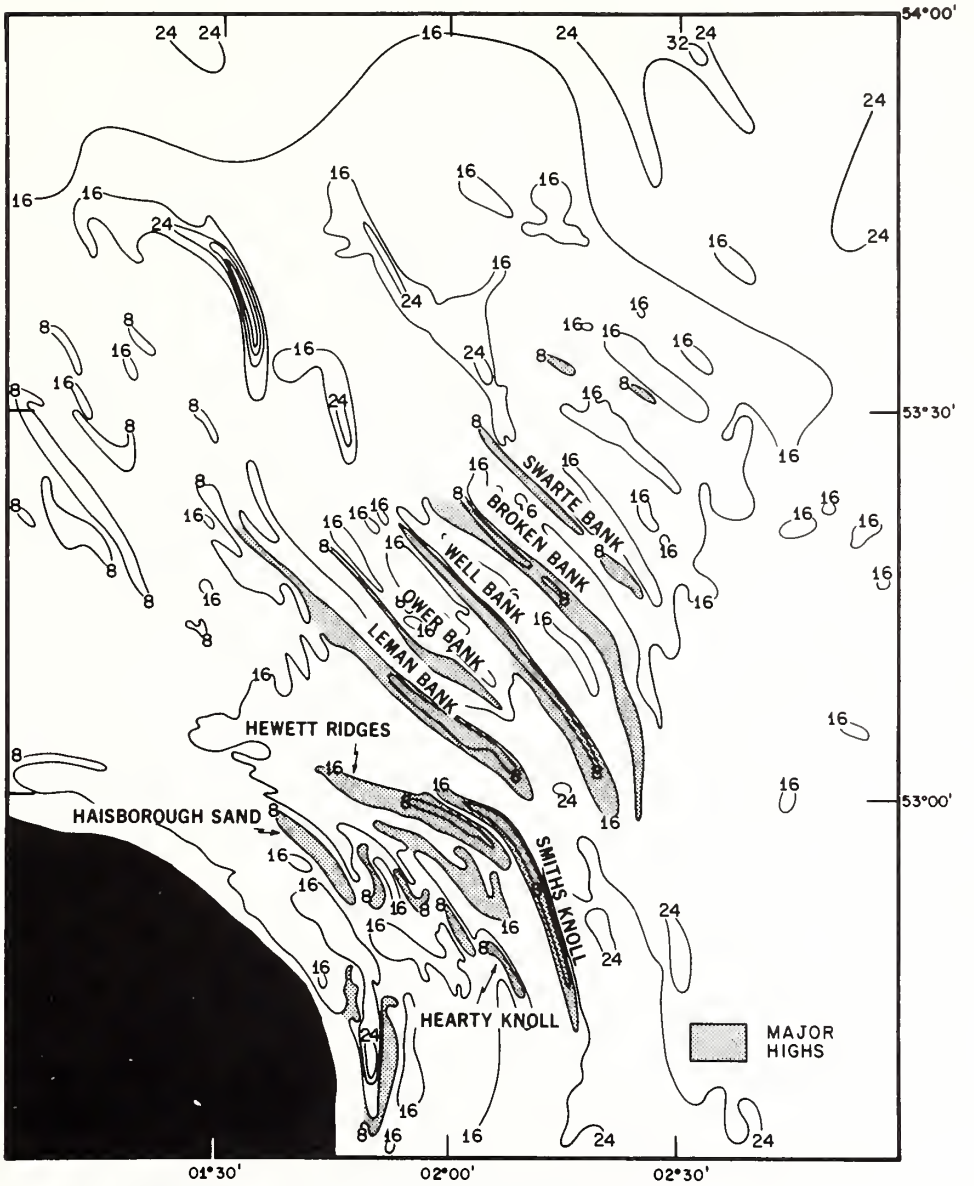

Fig.18. The Norfolk ridge field. (From Houbolt, 1968.)

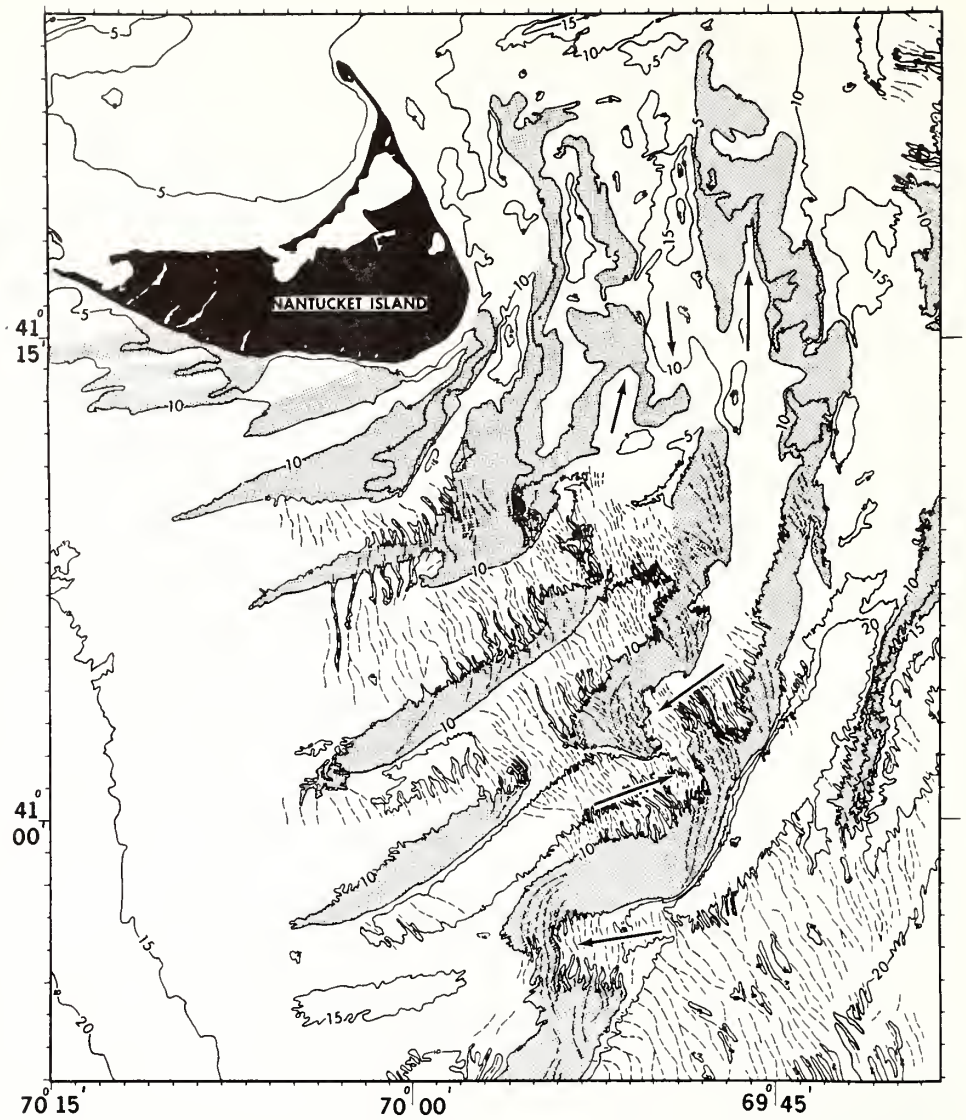

Fig.19. Nantucket shoals ridge field. Arrows indicate sense of residual flow in major ebb—flood sinus couplets, as inferred from morphology. From C & GS map 0708N-53. Dashed lines are the positions of sand-wave crests inferred from the 1 fathom contours of the original map.

waves to the crests of asymmetric ridges suggests that most ridges are of the open-shelf type, with each ridge having the same sense of residual current circulation around it (Fig.15).

As indicated by its sea-truncated drainage pattern, Nantucket Island is the remnant of a much larger subaerial surface, the ancestral Nantucket

peninsula. The spatial series of ridges apparent in Fig.19 may be viewed on uniformitarian grounds, as equivalent to a time series. This equation suggests that as the Nantucket shoreface has undergone erosional retreat, the resulting debris has been packaged as shoreface-connected ridges, which in turn have evolved in response to a deepening flow field.

REFERENCES

Allen, J. R. L., 1965. Late Quaternary Niger Delta and adjacent areas: sedimentary environment and lithofacies. Am. Assoc. Pet. Geol. Bull., 49: 547—600.

Allen, J. R. L., 1968a. Current Ripples. North-Holland, Amsterdam, 433 pp.

Allen, J. R. L., 1968b. The nature and origin of bedform hierarchies. Sedimentology, 10: 161—182.

Bagnold, R. A., 1966. An approach to the sediment transport problem from general physics. U.S. Geol. Surv. Prof. Pap., 422—1, 37 pp.

Belderson, R. H. and Stride, A. H., 1966. Tidal current fashioning of a basal bed. Mar. Geol., 4: 237—257.

Belderson, R. H., Kenyon, N. H. and Stride, A. H., 1971. Holocene sediments on the continental shelf west of the British Isles. In: F. M. Delany, ICSU/SCOR Working Party 31 Symposium, Cambridge, 1970, pp.157—170.

Brouwer, J. E. J., 1964. The North Sea. In: L. P. Stamp (Editor), The North Sea and the law of the Continental Shelf. World Land Use Survey Occ. Pap., 5, 41 pp.

Caston, V. N. D., 1970. Linear sand banks in the southern North Sea. Sedimentology, 18: 63—78.

Caston, V. N. D. and Stride, A. H., 1970. Tidal sand movement between some linear sand banks in the North Sea off northeast Norfolk. Mar. Geol., 9: M38—M42.

Curray, J. R., 1965. The Quaternary of the United States. In: H. E. Wright Jr. and D. G. Frey (Editors), The Quaternary of the United States. Princeton University Press, Princeton, N. J., pp.723—735.

Faller, A. J., 1963. An experimental study of the instability of the laminar Ekman boundary layer. J. Fluid Mech., 15: 560—576.

Faller, A. J., 1971. Oceanic turbulence and the Langmuir circulations. Ann. Rev. Ecol. Syst., 2: 201—235.

Faller, A. J. and Kaylor, R. E., 1966. A numerical study of the instability of the laminar Ekman boundary layer. J. Atmos. Sci., 23: 466—480.

Fenneman, N. M., 1902. Development of the profile of equilibrium of the subaqueous shore terrace. J. Geol., 10: 1—32.

Gessner, F. B., 1973. The origin of turbulent secondary flow along a corner. J. Fluid Mech., 58: 1—25.

Houbolt, J. J. H. C., 1968. Recent sediments in the southern bight of the North Sea. Geol. Mijnbouw, 47: 245—273.

Huthnance, J. M., 1973. Tidal current asymmetries over the Norfolk sandbanks. Estuarine Coastal Mar. Sci., 1: 89—99.

Jeffreys, H., 1929. On the transverse circulation in streams. Proc. Camb. Phil. Soc., 25: 20—25.

Johnson, D. W., 1919. Shore Processes and Shoreline Development. Hafner, New York, N.Y. 1965 facsimile, 584 pp.

Kennedy, J. and Fulton Jr., J. F., 1961. The effect of secondary currents upon the capacity of a straight open channel. Trans. EIC, 5: 12—18.

Kenyon, N. H., 1970a. The origin of some transverse sand patches in the Celtic Sea. Geol. Mag., 107: 389—394.

Kenyon, N. H., 1970b. Sand ribbons of European tidal seas. Mar. Gel., 9: 25—39.

Kenyon, N. H. and Stride, A. H., 1970. The tide-swept continental shelf sediments between the Shetland Isles and France. Sedimentology, 14: 159—175.

King, C. A. M., 1972. Beaches and Coasts, St. Martin's Press, New York, N.Y., 570 pp.
Kraft, J. C., Sheridan, R. E., Moose, R. D., Strom, R. N. and Wiel, C. B., 1974. Middle—Late Holocene evolution of the morphology of a drowned estuary system. In: G. Allen (Editor), Estuary and Shelf Sedimentation: a Symposium. University of Bordeaux. (in press).
Leopold, L. B., Wolman, M. Gordon, and Miller, J. P., 1964. Fluvial Processes in Geomorphology. W. H. Freeman, San Francisco, Calif., 522 pp.
Ludwick, J. C., 1970. Sand waves and tidal channels in the entrance to Chesapeake Bay. Inst. Oceanography, Old Dominion Univ., Tech. Rep. 1, 7 pp.
Ludwick, J. C., 1974a. Tidal currents, sediment transport, and sandbanks in Chesapeake Bay entrance, Virginia. In: M. O. Hayes (Editor), Int. Estuarine Conf. Proc., 2nd, Myrtle Beach, S. C., Oct. 15—18, 1973, in press.
Ludwick, J. C., 1974b. Tidal currents and zig-zag shoals in a wide estuary entrance. Geol. Soc. Am. Bull., 85: 717—726.
Moore, G. T., 1970. Role of salt wedge in bar finger sand and delta development. Am. Assoc. Pet. Geol. Bull., 54: 326—333.
O'Brien, M.P., 1931. Estuary tidal prisms related to entrance areas. J. Civ. Eng., 1: 738—743.
Oertel, G. F., 1972. Sediment transport of estuary entrance shoals and the formation of swash platforms. J. Sed. Petrol., 42: 858—863.
Off, T., 1963. Rhythmic linear sand bodies caused by tidal currents. Am. Assoc. Pet. Geol. Bull., 47: 324—341.
Oomkens, F. and Terwindt, J. H. J., 1960. Inshore estuarine sediments in the Haringvliet (Netherlands). Geol. Mijnbouw, 39: 701—710.
Postma, H., 1967. Sediment transport and sedimentation in the estuarine environment. In: G. H. Lauff (Editor), Estuaries. Am. Assoc. Adv. Sci., Washington, D.C., 757 pp.
Reineck, H. E., 1970. Marine Sandkörper, rezent und fossil. Geol. Rundsch., 60: 302—321.
Robinson, A. H. W., 1956. The submarine morphology of certain port approach channel systems. Inst. Navig. J., 9: 20—46.
Robinson, A. H. W., 1966. Residual currents in relation to shoreline evolution of the East Anglian coast. Mar. Geol., 4: 57—84.
Smith, J. D., 1969. Geomorphology of a sand ridge. J. Geol., 77: 39—55.
Stride, A. H., 1963. Current swept sea floors near the southern half of Great Britain. Q. J. Geol. Soc. Lond., 119: 175—199.
Stride, A. H., 1970. Shape and size trends for sand waves in a depositional zone of the North Sea. Geol. Mag., 107: 469—477.
Stride, A. H., 1973. Interchange of sand between coast and shelf in European tidal seas (abstract). In: Abstracts, Symposium on Estuarine and Shelf Sedimentation, Bordeaux, July, 1972, p.97.
Stride, A. H., Belderson, R. H. and Kenyon, N.H., 1972. Longitudinal furrows and depositional sand bodies of the English Channel. Mém. Bur. Rech. Géol. Minières, 79: 233—244.
Stubblefield, W. L., Lavelle, J. W., McKinney, T. F. and Swift, D. J. P., 1974. Sediment response to the hydraulic regime on the central New Jersey shelf. J. Sed. Petrol., in press.
Swift, D. J. P., 1973. Delaware Shelf Valley: estuary retreat path, not drowned river valley. Geol. Soc. Am. Bull., 84: 2743—2748.
Swift, D. J. P. and McMullen, R. M., 1968. Preliminary studies of intertidal sand bodies in the Minas Basin, Bay of Fundy, Nova Scotia. Can. J. Earth Sci., 5: 175—183.
Swift, D. J. P. and Sears, P., 1974. Estuarine and littoral patterns in the surficial sand sheet, central and southern Atlantic shelf of North America. In: G. P. Allen (Editor) Estuary and Shelf Sedimentation: a Symposium. University of Bordeaux, Talence, 1973, in press.
Swift, D. J. P., Stanley, D. J. and Curray, J. R., 1971. Relict sediments, a reconsideration. J. Geol., 79: 322—346.

Swift, D. J. P., Kofoed, J. W., Saulsbury, F. P. and Sears, P., 1972. Holocene evolution of the shelf surface, central and southern Atlantic coast of North America. In: D. J. P. Swift, D. B. Duane, and O. H. Pilkey (Editors), Shelf Sediment Transport: Process and Pattern. Dowden, Hutchinson and Ross, Stroudsburg, Pa., pp.499—574.

Swift, D. J. P., Duane, D. B. and McKinney, T., 1974. Ridge and swale topography of the Middle Atlantic Bight: secular response to Holocene hydraulic regime. Mar. Geol., 15: 227—247.

Swift, D. J. P., Lavelle, J. W. and McHone, J., 1975. Maintenance of the coastal equilibrium profile: Some data from the Middle Atlantic Bight, U.S.A. Sedimentology, in press.

Weil, C. B., Moose, R. D. and Sheridan, R. E., 1974. A model for the evolution of linear tidal built sand ridges in Delaware Bay, U.S.A. In: G. Allen (Editor), Estuary and Shelf Sedimentation: a Symposium. University of Bordeaux, Talence, 1973, in press.

Wilson, I. G., 1972. Aeolian bedforms — their development and origins. Sedimentology, 19: 173—210.

Wilson, I. G., 1973. Equilibrium cross-section of meandering and braided rivers. Nature, 241: 393—394.

63 Reprinted from: Mid-Atlantic Shelf/New York Bight ASLO Symposium, 65-66.

Donald J.P. Swift, George L. Freeland, Peter E. Gadd, J. William Lavelle and William L. Stubblefield
NOAA/AOML, 15 Rickenbacker Causeway, Miami, Florida 33149

MORPHOLOGIC EVOLUTION AND SAND TRANSPORT IN THE NEW YORK BIGHT

The New York Bight is a roughly pentagonal sector of North America's Middle Atlantic Bight (Fig. 1). It is divided into a series of compartments by transverse shelf valleys, including the Block, Long Island, Hudson, North New Jersey, Great Egg, and Delaware Shelf Valleys (1). These features were incised repeatedly into the shelf surface by rivers during Pleistocene low stands of the sea, although not always in the same position. At the onset of the Holocene transgression the valleys served as retreat paths for estuaries, and they are consequently partly or largely filled with estuarine deposits. As the shoreline passed over a given segment of the buried channel, the channel was in many cases partially re-excavated by estuary mouth scour, while its northern margin tended to be aggraded by littoral drift from the adjacent coastal compartment.

As a result of this diverse activity, shelf valley morphology may be quite complex. The shelf valleys themselves are in many cases the retreat paths of estuary mouth scour trenches and do not everywhere directly overlie the buried river-cut channel. They may be flanked by shoal retreat massifs; the retreat paths of estuary mouth shoals. Shelf valleys commonly extend seaward into mid-shelf or shelf-edge deltas. The Holocene transgression appears to have been intermittent in nature, and during stillstands, scarps were locally cut into the shelf surface.

The plateau-like interfluves between shelf valleys also underwent considerable modification during the Holocene transgression. At any given time, the nearshore hydraulic climate tended to maintain an inner shelf profile, of more steeply dipping shoreface, and more gently sloping shelf floor. As sealevel rose, this profile was translated landward by means of storm erosion of the shoreface. The eroded sand moved along the coast under the impetus of wind- and wave-driven littoral currents, to be deposited at the tips of spits or in estuary mouth shoals. However, during this process, much of it leaked out onto the adjacent shelf floor. As a result, the shelf floor has been veneered with 0-10 m of sand of primarily local origin.

Modification of the shelf floor did not cease with passage of the shoreline. As a consequence of its geometry, the Middle Atlantic Bight between Cape Cod and Cape Hatteras is subjected to an unusually rigorous hydraulic climate (2). The storm tracks of mid-latitude lows tend to pass northward along the length of the Bight. Many storms nest for an interval in the Bight, so that the isobars of atmospheric pressure parallel the isobaths of the shelf surface, and intense northeast winds blow down the entire arc of the Bight. The result of this "scale-matching" phenomenon is a strong geostrophic coupling between wind and water flow, so that the shelf water column may translate uniformly southward in slab-like fashion at mid-depth speeds in excess of 30 cm sec^{-1}, for periods up to several days. Within a few km of the beach a coastal jet may form in response to direct wind stress. Flows up to 60 cm sec^{-1} have been observed in this nearshore zone (as measured by Savonius rotor meters 1 m off the bottom; [3]).

Comparison of current meter records with the dispersal patterns of sand labeled with a radioisotope (Fig. 2) indicates that the transport of sand on the shelf occurs in intense bursts, when storms accelerate near bottom (1-2 m) flow above a threshold of 20 cm sec^{-1}. Transport events may last for hours or days, and are commonly separated by days to weeks of quiescence. Transport is generally parallel to isobaths, and may trend either southwesterly or northeasterly, depending on the prevailing direction of the flow event. During the period November 11 to January 31, a single intense flow associated with a 3-day "northeaster" drove labeled fine sand for 1200 m to the west of the injection point along the Long Island inner shelf. Calculations of fluid power expended on the sea floor suggest that this northeaster induced a greater volume of sand transport on the sea floor than did the sum of the eight other flow events of the observation period (3).

The effect of this regime on the shelf floor is various. Wave oscillation ripples and trains of sandwaves up to 1 m high may be seen after storm flows. Sand and gravel ribbons up to 50 m wide by a km long may also appear. However, the most striking response of the sea floor to storm flows is a ridge and swale topography, of sand ridges up to 10 m high, 2-4 km apart, and with side slopes less than a degree. Ridge crests may be traced for tens of km, converging to the south with the shoreline at angles of 15 to 35°.

Unlike smaller scale bedforms which appear to be responses to a single flow event or season of events, the ridges appear to be long term, time-averaged responses. Ridges on the Central New Jersey Shelf yield successively older dates with depth, that span the duration of the Holocene transgression. On the New Jersey and Long Island coasts, ridges appear to be presently forming at the foot of the shoreface. Ridge sequences may be traced as far as 20 km offshore in apparent genetic sequence. The ridges appear to be responses to the wind-sheared flow of the inner shelf, but the formative mechanism is not clear. Storm flow is predominantly southward and seaward, obliquely over the ridge crests, and there is local evidence that nearshore ridges migrate very slowly offshore and downcoast, extending their crestlines to keep contact with the retreating shoreline as they do so (4). Shifts of a unit width in 50 or more years have been noted, although the actual movement may have been confined to a few major storms. Seismic studies of ridges on the Central New Jersey shelf indicate that ridge modification continues even after contact with the retreating shoreline is finally broken; troughs continue to be scoured, crests aggraded, and ridge positions slowly shift.

(1)Swift, D.J.P., Kofoed, J.W., Saulsbury, F.P. and Sears, P., 1972. Shelf Sediment Transport: Process and Pattern. Dowden, Hutchinson and Ross, Stroudsburg, Pa., p. 499-574.
(2)Beardsley, R.C. and Butman, B., 1974. Geophys. Res. Letters, 1:181-184.
(3)Lavelle, J.W. and others. Paper submitted to Geophys. Res. Letters.
(4)Moody, D.W., 1964. Ph.D. Thesis, Johns Hopkins University, 167p.

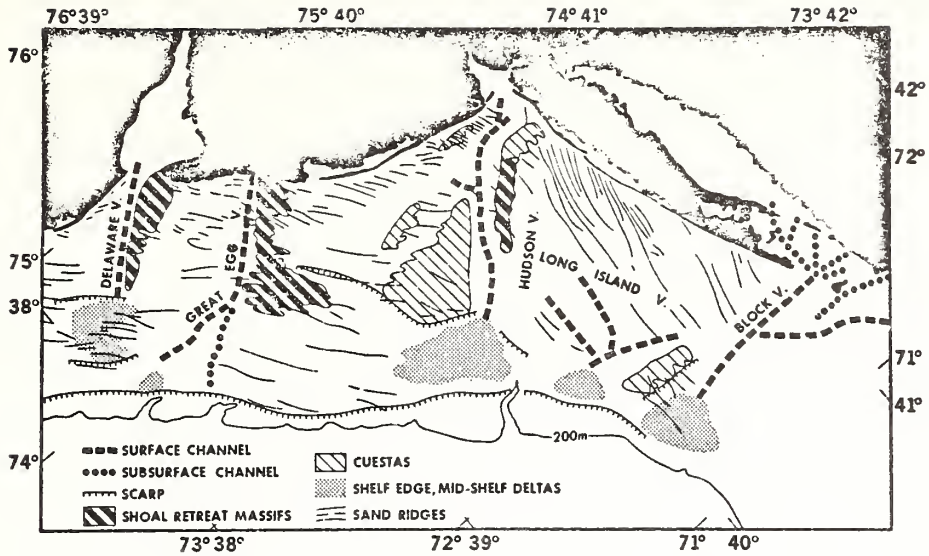

Fig. 1. Morphologic framework of the New York shelf surface.

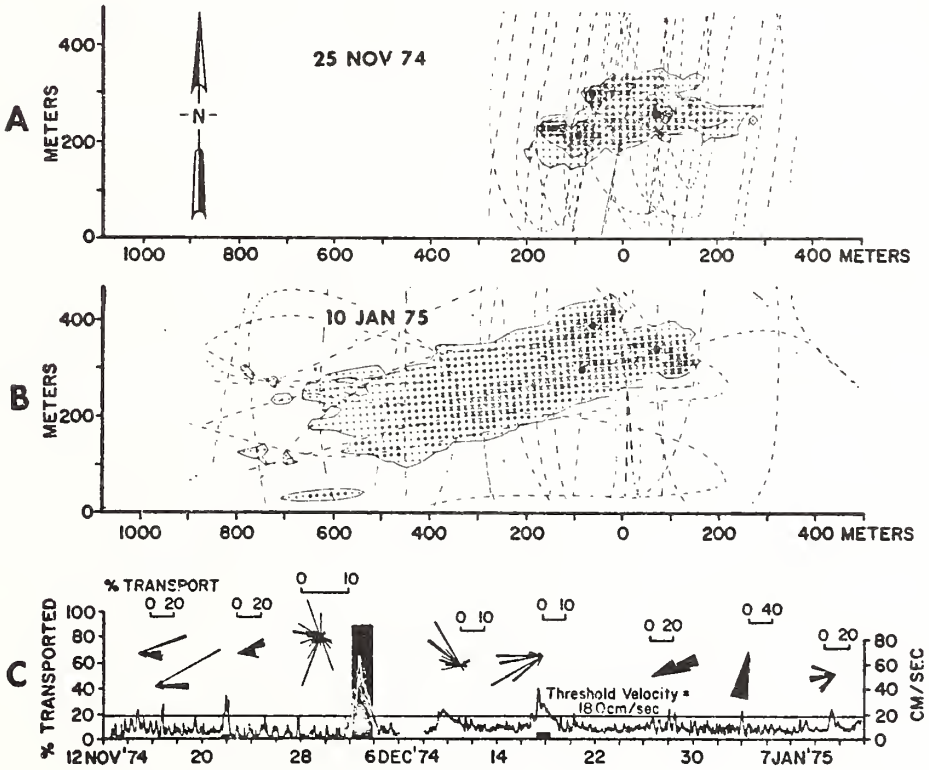

Fig. 2. Tracer dispersal experiment off Jones Beach, Long Island. A, B: dispersal patterns. 60 g of native sand labeled with Ru^{103} were emplaced at each of the black dots on 12 November 1974. Intensity of pattern varies with intensity of signal as recorded by towed scintillometer (dashed tracklines). Data have been corrected for background and for decay. C: time-velocity record (jagged line). Vertical bars are relative estimates of sand transported during flow events. Height is proportional to percent of total transport over duration of record, as determined by $(U_{100} - U_{th})^3$ where U_{th} is threshold speed. Width of bar is proportional to duration of event. Roses similarly indicate percent transport and duration by direction class.

Reprinted from: NOAA Technical Report ERL 316-AOML 16, 45 p.

U.S. DEPARTMENT OF COMMERCE
Frederick B. Dent, Secretary

NATIONAL OCEANIC AND ATMOSPHERIC ADMINISTRATION
Robert M. White, Administrator
ENVIRONMENTAL RESEARCH LABORATORIES
Wilmot N. Hess, Director

NOAA TECHNICAL REPORT ERL 316-AOML 16

The Initial Water Circulation and Waves Induced by an Airflow

W. L. McLEISH
G. E. PUTLAND

BOULDER, COLO.
February 1975

For sale by the Superintendent of Documents, U. S. Government Printing Office, Washington, D. C. 20402

CONTENTS

		Page
	ABSTRACT	1
I.	INTRODUCTION	1
II.	EXPERIMENTAL METHODS	2
III.	DATA ANALYSIS	7
IV.	OBSERVATIONS	9
V.	DISCUSSION	39
VI.	CONCLUSIONS	43
VII.	ACKNOWLEDGMENTS	43
VIII.	REFERENCES	44

THE INITIAL WATER CIRCULATION AND WAVES INDUCED BY AN AIRFLOW

W. L. McLeish and G. E. Putland

ABSTRACT

The early water circulation and waves under an airflow were examined in laboratory experiments. At a particular fetch or time, a waterflow undergoes a laminar-turbulent transition through an intermediate circulation pattern. Simultaneously the first, capillary-gravity waves undergo a correlated characteristic transition leading to separate capillary and gravity waves, and the wave energy increases markedly. Some of the energy of the current is transferred to the waves during the transition. A viscous sublayer lies at the surface above a turbulent flow, but is thinner than a corresponding sublayer at a solid boundary.

I. INTRODUCTION

The ocean surface is of major significance to sea-air interaction studies because many quantities enter and leave the ocean only through the surface. Unique mechanisms of transport dominate near it and often control the rates of transfers. Because of these mechanisms, properties of water near the surface are particularly sensitive to variations in exchange rates. As a result of these aspects of ocean processes, understanding and monitoring several air-sea interactions can be furthered through a study of the layer of water adjacent to the surface.

The present report examined the early patterns of water waves and flow in a wind-water tunnel. Mean water-velocity profiles very near the

surface were obtained with bubble tracers, deeper profiles in the main waterflow were measured with a submerged hot-film anemometer, and wave heights were recorded by a wave gage. Photographs showed the distinctive initial wave patterns, and an infrared radiation thermometer identified vertical mixing produced by water turbulence. The initial growths of wind-generated water current and waves were found to have interrelated characteristics not considered in present theories of sea-air interaction. In addition, a viscous sublayer adjacent to the surface above water turbulence was demonstrated, but found to be thinner than the corresponding sublayer at a solid boundary. The thinner water boundary layer implies less resistance to the transport of water properties to the surface than at a solid boundary.

II. EXPERIMENTAL METHODS

The basic construction of the wind-water tunnel was described by McLeish _et al_. (1971). A blower drew a smooth airflow over a 90- by 600-cm water surface. A plastic foam air filter was later installed, and a curved sheet of metal was used to damp waves at the downwind end of the tank. The water circulation appeared to approach equilibrium after a few minutes of operation. Some experiments examined effects of starting the airflow, either slowly by switching on the blower or rapidly by releasing the exhaust door while the blower was turning at full speed. The latter procedure caused noticeable water vibrations when the blocked blower was running and a seiche in the tank when the door slammed open. Some air leaked by the closed blower exhaust door.

The water was filtered to reduce scattered light in photographs and softened to prevent scale formation on the electrolysis wire in bubble photography experiments. In addition, hydrochloric acid was added to give a 0.04-percent concentration to increase the electrical conductivity of the water. While the air was flowing, the water surface was continuously cleaned by flowing over a barrier at the downwind end. The water level was maintained near the level of the entrance duct by continuous refilling during experiments. The room was kept dark between experiments to retard biological growth so that the water had to be changed only rarely. The water temperature was generally between the dry- and wet-bulb temperatures of the air.

Motions of water near the moving surface were measured by photographing clouds of microscopic hydrogen bubbles generated by electrolysis on a thin vertical wire through the surface. The quality of the bubble patterns was highly variable and depended largely on the condition of the wire surface and on the electrical pulses. Considerable efforts were required to develop adequate techniques for these measurements. A 0.001" gold alloy or platinum wire was soldered as a short extension to a copper wire support and inserted vertically into the water to a depth of a few millimeters. The lower end of the wire was free. The surface of the wire could be cleaned with aqua regia to give fair bubble patterns, but platinizing the wire surface or oscillating the wire with a vibrator was of no value. The performance of the wire surface could best be enhanced through electrolysis at a high rate. Application of -160 V to a wire submerged a short distance removed the

outer surface within a minute, and the remaining wire gave improved bubble patterns. One short section of wire was completely dissolved in 5 min of this treatment.

The electrical power supply unit provided negative 0 to 160 V d.c. pulses with an on-time fraction of 5 to 95 percent at 1/2 to 200 pulses per second and 200 mA current. An adjustable spike was produced at the beginning of each pulse. A negative 0 to 6 V bias was applied to the wire between pulses. Each pulse triggered a single photograph by a cine camera. A frequency counter recorded the pulse rate. The minimum overvoltage necessary for photography was used in the electrical pulses, and a negative bias barely generating bubbles was maintained between pulses. A pulse voltage of 2 to 5 V, with an on-time fraction of 20 to 50 percent and a fairly broad spike of 10 V, was often used. The resistance of the wire and water circuit during a pulse was on the order of 1,000 Ω. As many as 50 distinct bubble lines per second could be produced.

A 35-mm 16-fps cine camera viewed the bubble pattern crosswind at an upward angle of about 1/7 and with an image scale of 1:1. Light from a 5,000-W bulb on the opposite side of the tank was focused by a Fresnel lens and traveled slightly upwind and slightly upward through the water to the bubble area. The pulse that triggered each photograph was recorded with a six-channel light-beam oscillograph along with water height.

Figure 1 shows bubble-line patterns in a nearly laminar flow just upstream of the formation of steep waves. The merging of the lines downstream is attributed to cross-stream motion and not bubble rise

Figure 1. Bubble lines and surface reflections. The width of the photograph represents 24 mm in the direction of the flow. A curved line of bubbles is just leaving the electrolysis wire on the left, and the surface reflection gives a symmetry about a horizontal line. The vertical out-of-focus white line is the wire of a wave gage.

because the reflections are well separated, although ragged. However, only the newest two lines were used in the analysis. The bases of bubble lines appear to rise in this frame, but the mean motion was slightly downward.

The photograph of bubble lines in figure 2 was obtained in fully turbulent flow downstream. In general, the entire reflections and bubble lines were visible. However, because of irregularities of the reflections, only regions near the surface were used in the analysis.

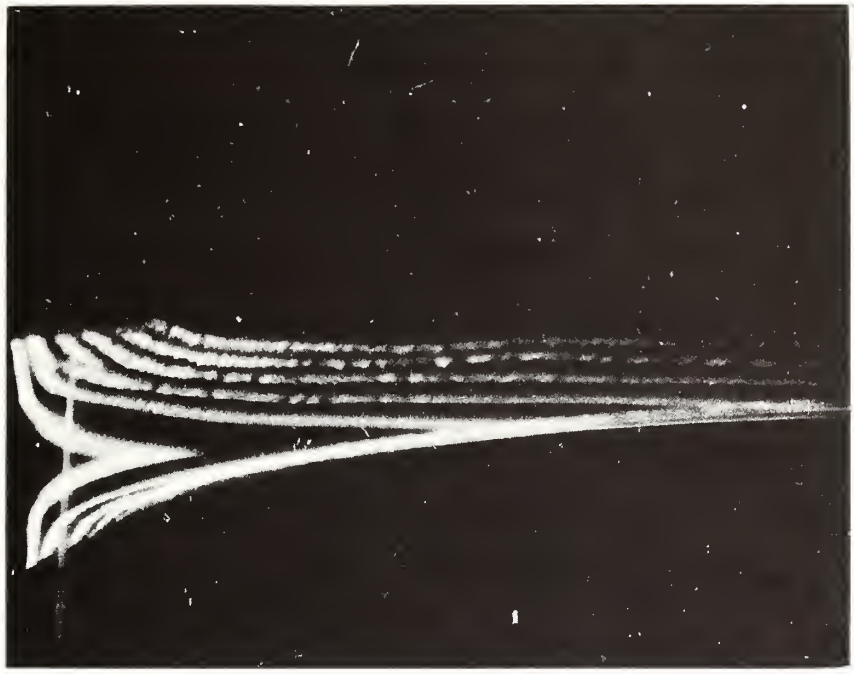

Figure 2. Bubble lines and surface reflections. The scene was rotated through the alinement of relay mirrors. The straightness of the image of a wave gage wire shows that the water surface was nearly level.

Hot-film anemometers recorded velocities in the air and in the water. These data are Eulerian in nature, in contrast with the bubble-tracer measurements which are Lagrangian and include wave currents.

Water heights were recorded with a wave gage similar to one described by Hires (1968). The frequency response of this instrument was not tested directly; however, its performance beneath wind waves was compared with that of a submerged hot-film anemometer. In one experiment, the wave gage recorded 17 wave crests/sec while the anemometer recorded 19 velocity maxima/sec. In another experiment, 17 wave crests/sec were measured with 21 velocity maxima/sec. Because the

anemometer response was biased toward high frequency waves, it appears that the wave gage was capable of recording water waves near these frequencies.

In addition, a true rms voltmeter and an infrared radiation thermometer were used in some experiments, and compacted surface films, floating dust, and dye streaks were studied in others. Photographic and visual observations of the initial waveforms were best made with the room darkened, the water surface illuminated from within the air entrance duct, and the waveforms viewed from the downwind end of the tank near the water surface.

III. DATA ANALYSIS

Enlarged projections of the first two free-drifting bubble lines and their surface reflections (see figs. 1 and 2) were traced onto paper, and the tracings were digitized. The data were analyzed by a computer through rotation of axes, determination of the depth of each reading by interpolation between the direct and reflected images, a second interpolation to fixed depths, subtraction between the two bubble lines, and averaging a number of frames. In addition, the apparent height of the midpoint between a point on a bubble line and its reflection was used to calculate a mean crosswind velocity V where the waves were not steep. The mean difference in depths of the bases of the two bubble lines in a single frame was also calculated. Errors in the calculation caused by slopes of the water surface were reduced by

averaging several measurements. Unreadable frames were omitted; and the experiment was discarded if there were several unreadable frames.

It is difficult to estimate the accuracy of the bubble measurements. The equipment was designed to measure positions to 0.01 cm, but greater errors could have arisen in interpreting the photographs. Buoyant rise of the bubbles would lead to further errors, but the rise rate calculated for 25-μ diameter bubbles--according to the modified Stokes equation $W = g\rho a^2/3\mu$--gave a vertical rise between frames of only 0.004 cm. Interference to the flow by the wire decreases the water velocity, but the results of Schraub et al. (1964) indicated this error in the present measurements to be negligible. Acceleration, or spinup, of the water circulation may not have progressed to an equilibrium in these experiments, and the velocity profiles represent relative, not absolute, velocities.

One experiment (fig. 6 below) was performed among steep waves that gave significant rotations to the bubble-line patterns. Mean water velocities were calculated first by rotating the axes so that the surface intersections of the two bubble lines appeared at the same height and again by rotating so that the average of the two bubble-line-plus-reflection images was upright. The mean absolute difference in rotation was 9°, but the mean surface velocities differed by only 3 percent.

Chart records containing other measurements were digitized and the data averaged. Wave records often had smooth envelopes which could be analyzed separately. The envelope widths, calculated as wave energy,

were compared with measurements from the true rms voltmeter. The data from wave envelopes showed faster and greater rises and falls in wave energy than did the voltmeter. In addition, the wave envelopes were so traced as not to include any seiche or other low frequency waves present in the tank.

Photographs of the upwind water surface show that the initial steep waves occurred as short-crested dimples moving downstream in somewhat irregular rows. A wave or water current recording at one point might or might not be in a wave row at a particular time. Because a wave row remained in one position for a few seconds, averages were extended in experiments within the rows.

Wave energy was calculated in erg/cm^2 according to

$$E_{total} = 2 \cdot E_{potential} = \rho g \overline{\eta^2}$$

where η^2 is the variance of water height fluctuations. This equation is accurate only for gravity waves; however, the energy of capillary waves is small generally in comparison with that of gravity waves.

IV. OBSERVATIONS

Figures 3 through 6 show mean water-velocity profiles near the surface obtained from bubble photographs. Figure 3 was derived from a series including figure 1, and figure 6 was derived from a series including figure 2. The accompanying table 1 gives the experimental conditions. Empirically fitted exponential curves $U = a e^{-bz}$ were drawn in figures 3 through 5 to illustrate the smoothness of the data. The

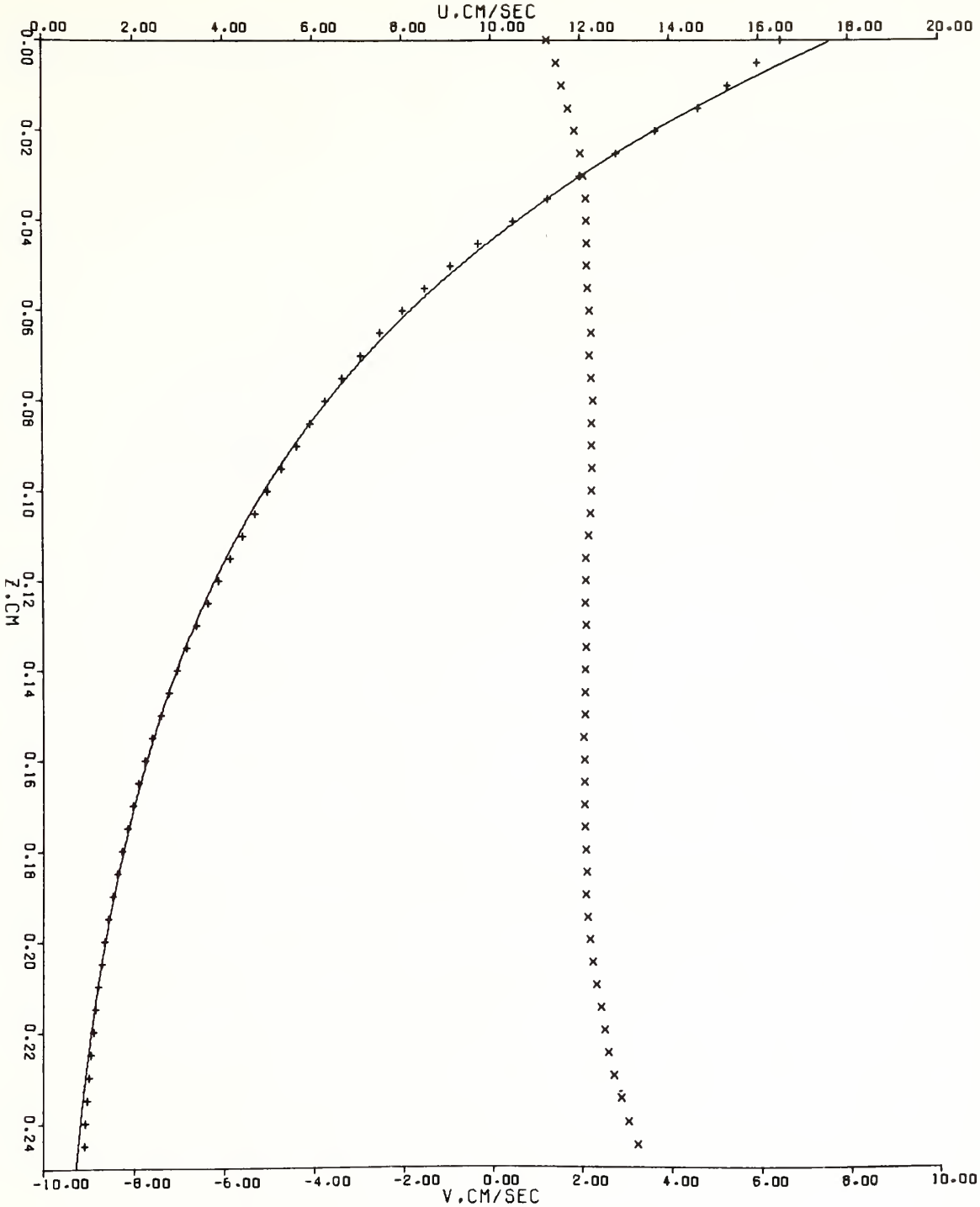

Figure 3. Mean water-velocity profile. Downstream (+) and cross-stream (x) velocity components were derived from bubble lines. The solid line is the rms best-fit exponential curve to the downstream data.

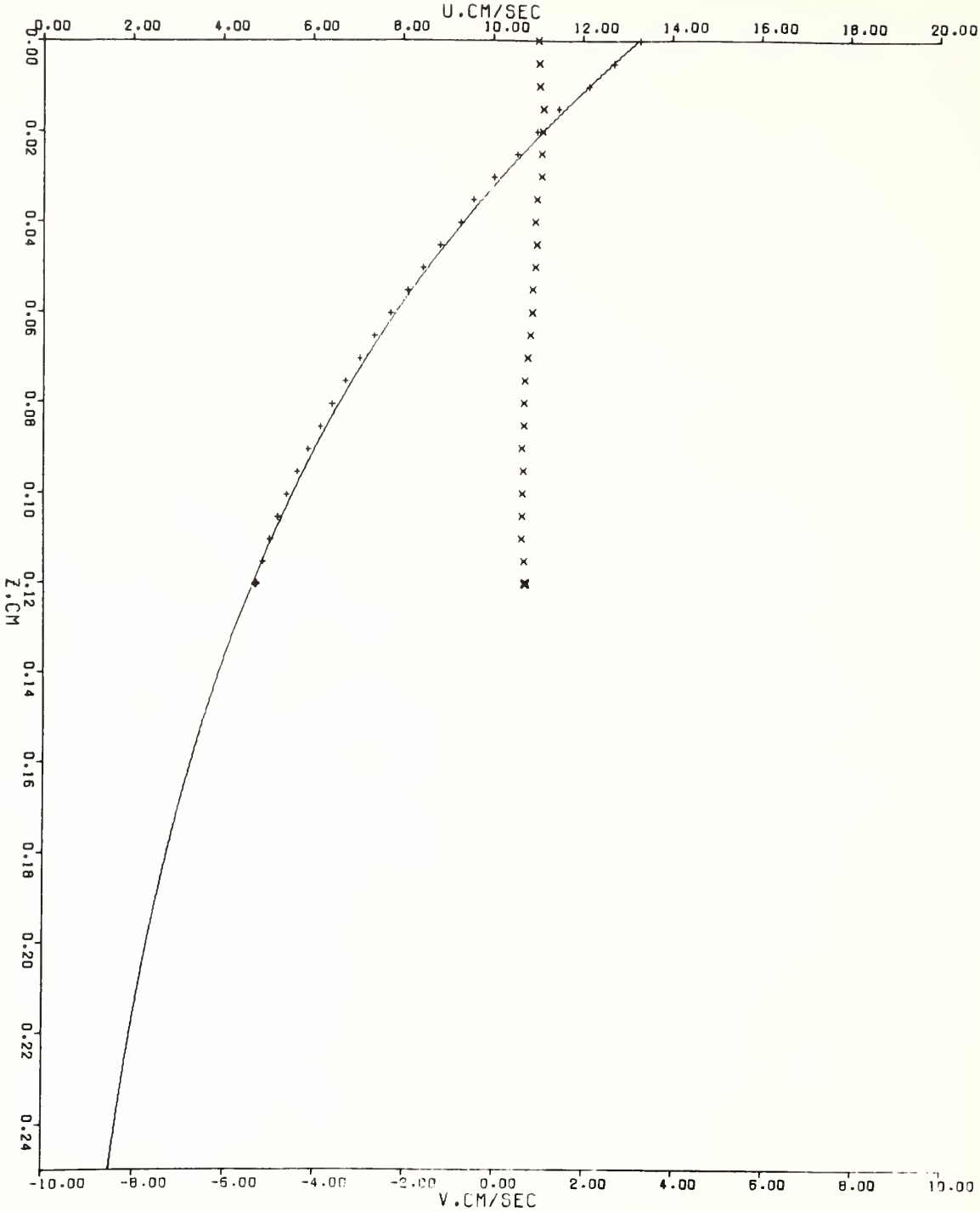

Figure 4. Mean water-velocity profile. Downstream (+) and cross-stream (x) velocity components were derived from bubble lines. The solid line is the rms best-fit exponential curve to the downstream data.

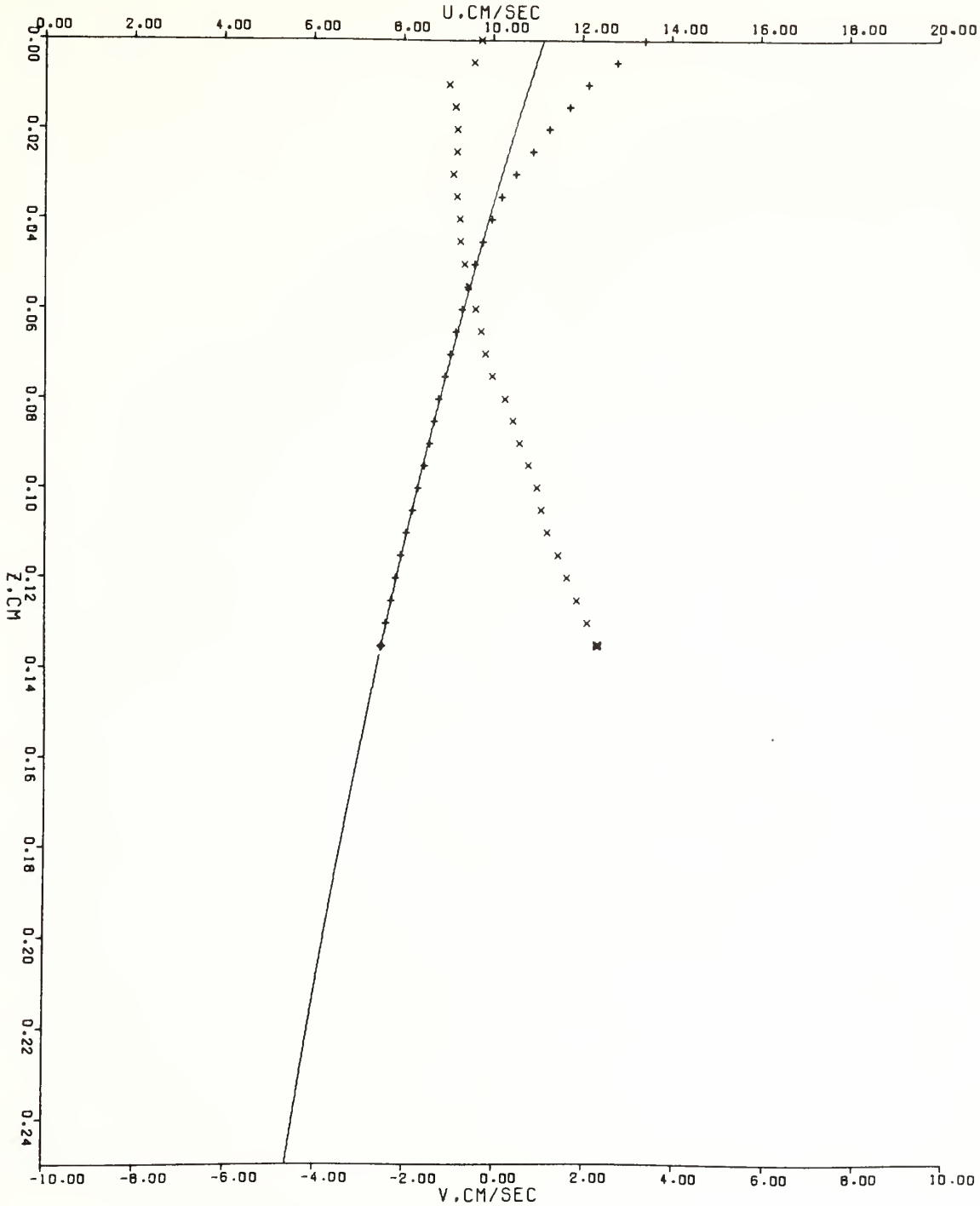

Figure 5. Mean water-velocity profile. Downstream (+) and cross-stream (x) velocity components were derived from bubble lines. The solid line is an exponential curve fitting the deeper downstream data.

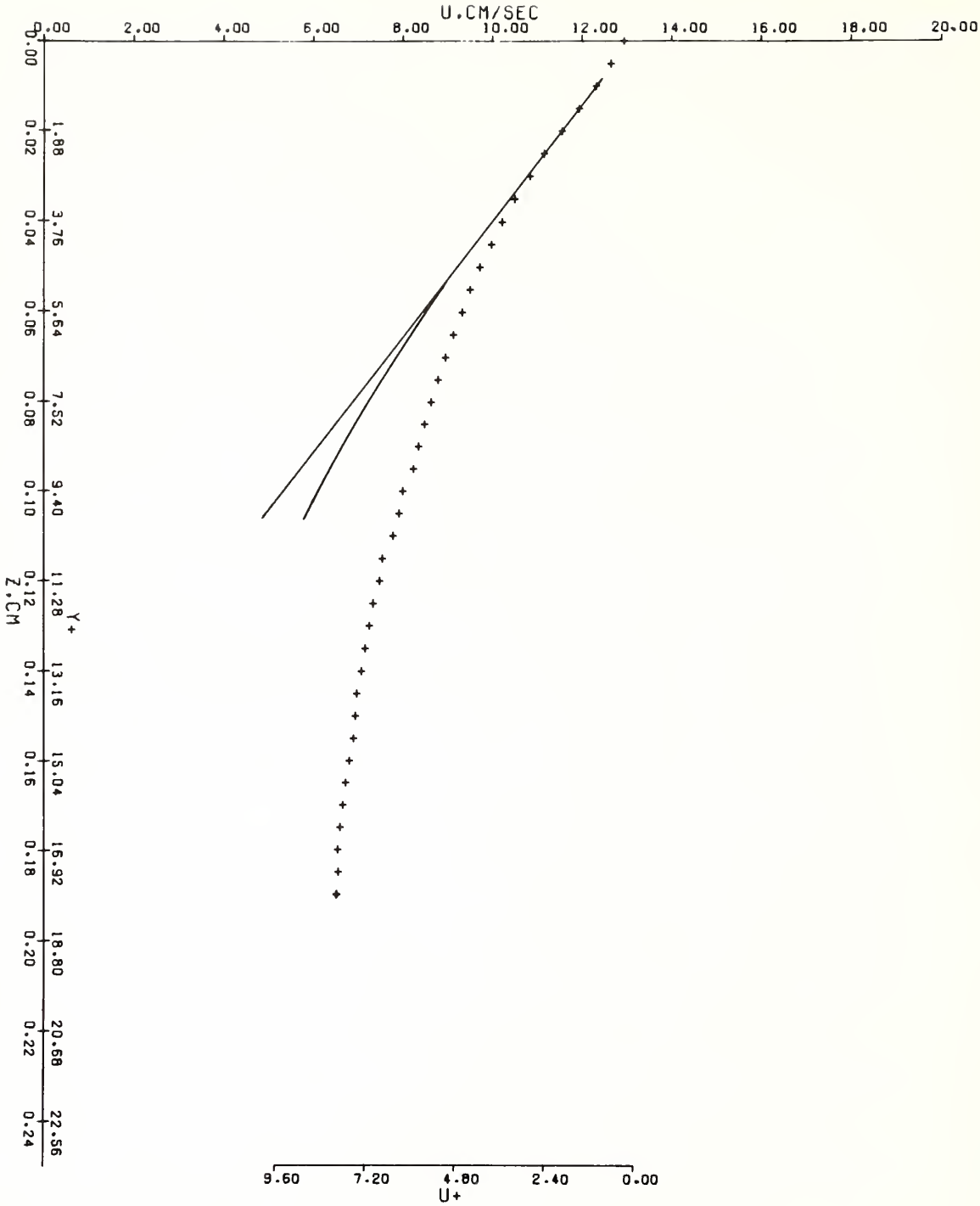

Figure 6. Downstream component of mean water-velocity profile. The straight line is fitted to the slope near the surface, and the curved departure represents the profile at a solid boundary in dimensionless units Y+ and U+.

Table 1. Water Velocity Measurements from Bubble Photographs

Figure	3	4	5	6
Number of frames analyzed	46	11	17	37
Duration of experiment, sec	3.5	10	26	4.3
U_a, cm/sec	900	550	600	550
Fetch, cm	24	25	69	382
Location	early wave rows	above wave rows	within wave rows	below wave rows
Best exponential fit				
a, cm/sec	18.3	13.6	—	—
b, cm^{-1}	12.4	8.6	—	—
rms ϵ, cm/sec	0.15	0.15	—	—
$\overline{W}$, cm	-0.017	-0.002	+0.005	-0.056
Stress, dynes/cm^2	2.0	1.0	1.2	0.7

curve in figure 5 approximates only a portion of the profile. The best exponential fit and the rms departure of the mean velocity values from the fit were obtained with a computer. The mean depth difference between the bases of successive bubble lines is given in the table as $\overline{W}$ where a positive value represents a mean rise. The surface stress τ_0 was calculated from the exponential curves in figures 3 and 4 and from the smoothed surface velocity gradient in figures 5 and 6. The longer durations in figures 4 and 5 resulted from analyzing only 1 frame/sec. Another analysis of the run in figure 6, not presented, extended over 85 sec but gave a profile similar to that shown in the figure.

The bubble-line photographs allow measurements of water velocity very near the surface, even among waves of some steepness, although the accuracies in figures 5 and 6 were decreased by wave shapes. The mean velocity profiles in figure 3 were obtained in the early laminar-turbulent zone where the flow was largely laminar in nature. The downstream velocity component U fit a smooth curve well. The cross-stream component V also fit a smooth curve, although it was offset. Both profiles showed departures near the surface, attributed to airflow interference by equipment mounted asymmetrically above the bubble wire. The buoyancy-induced vertical motion between frames was small.

The velocities in figure 3 fluctuated rapidly between frames. The rms fluctuation at a depth was about 15 percent of the mean velocity at that depth. The depth-averaged variance, reduced by the number of frames in the average, led to a calculated rms fluctuation of the average of 0.16 cm/sec, comparable to the observed rms departure of the mean

profile from the fitted smooth curve. The correlation of fluctuations at depth with the surface fluctuations showed a rapid decrease with depth, reaching a value of 0.5 at a depth of 0.035 cm, then remaining near 0.3 to 0.4 at greater depths. Because the theoretical correlation caused by sinusoidal water waves is unity at all depths, the shape of the correlation curve indicates very shallow, rapid fluctuations possibly caused by fluctuations in air stress. The kurtosis of the frequency distribution of surface fluctuations was -0.2, compared with 0 for a normal distribution and with -1.2 for a uniform distribution. This value is in accord with the possibility that the surface fluctuations were largely turbulent in origin.

A mean surface stress of 2.0 dynes/cm^2 was indicated by the surface shear in figure 3. It appears that the stress was not constant with fetch, but was disturbed by an irregularity at the upwind edge of the water. This is supported by observations of changes in the fetch at which the waveforms underwent transition when the water level was changed slightly.

The data in figure 4 were obtained at a lower airspeed well before transition so that the flow was solely a developing laminar boundary layer. The profile fit a smooth curve well, with a calculated stress of 1.0 dynes/cm^2. Figure 5 was obtained within the laminar-turbulent transition shown by the wave patterns and is of an intermediate shape not fitting a simple analytic curve. The indicated stress is close to that in figure 4.

Figure 6 was obtained well downstream where both the circulation and the waves represented the little-changing pattern of development beyond the early transition. A straight line representing the surface shear is included, and a curve is drawn to show the departure from a linear profile observed in a turbulent transition layer at a solid boundary. This curve was calculated using the observed surface stress and average measurements from graphs of turbulent boundary-flow profiles given by Mellor and Herring (1969) and by Kline et al. (1967) in nondimensional form. The viscous sublayer at the free surface is roughly one-half as thick as at a solid boundary. The different thickness may indicate that the value of von Karman's constant k is larger in turbulence at a free boundary. Also, the indicated surface stress supported by water shear is less than upstream, although other measurements indicate the total stress to be greater. The decrease might be attributed to the effects of waves on momentum transport.

Figure 7 shows mean water velocity measured by a hot-film anemometer at different depths as a function of fetch with a midstream airspeed of 850 cm/sec. Mean water velocities obtained from a submerged hot-film anemometer extend to greater depths than do the bubble-line photographs, although such data are not available near a wavy surface. The "zero" depth readings here were obtained at the minimum continuously submerged depth of the probe. The dip in the "zero" depth plot was found in two additional series of measurements. The water velocities in figure 7 show an initial rise in surface water velocity

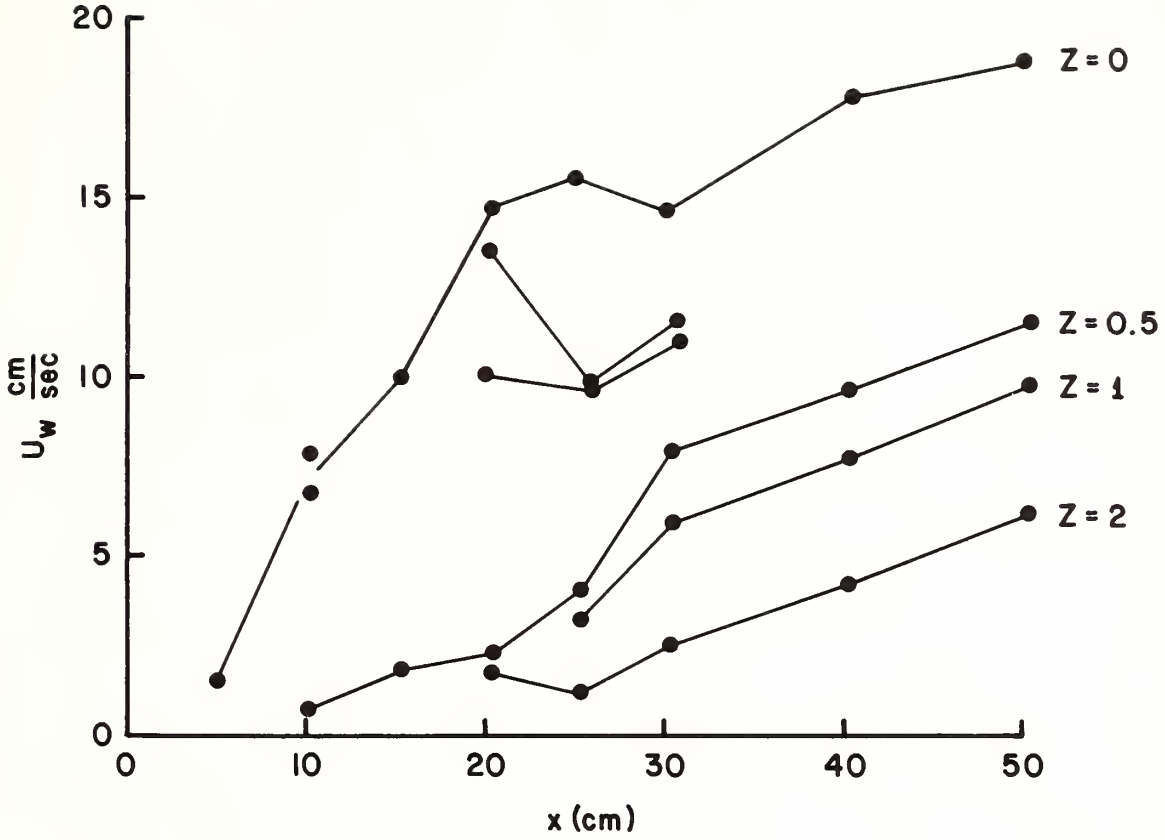

Figure 7. Mean water velocity versus fetch at different depths.

and deeper increases farther downstream, as expected for a developing laminar boundary layer. A dip in surface velocity and a rapid acceleration below mark the beginning of vertical mixing by turbulence and occur at the rapid growth of waves.

Another set of these measurements is contoured in figure 8 as a vertical longitudinal section of water velocity. A laminar boundary layer developed to a depth of 0.5 cm in the first 20 cm of fetch. Then the near-surface velocity decreased between 25 and 35 cm of fetch while the flow below accelerated rapidly. Farther downstream, the mean velocities increased again as a turbulent boundary layer. The onset of vertical mixing is most clearly demonstrated in the velocity difference between the surface and a depth of 0.5 cm. The mean difference was 11 cm/sec at a fetch of 20 cm and 4 cm/sec at 30 cm of fetch.

Figure 9 contains two sets of measurements of wave energy versus fetch with an airspeed of 850 cm/sec. A nearly fixed position identified at the beginning of each wave row is referred to as a "source point." The fetches of the source points and the approximate ends of wave rows are shown. Two different high-pass filters nominally passing frequencies greater than 1 and 10 Hz were used in the rms voltmeter for these experiments. This figure shows drastic changes in wave energy at the locations of the water current changes. The two plots of wave energy versus fetch show very little growth before the source points at a fetch of about 15 cm, rapid growth to a fetch of 25 to 30 cm, and then slower growth as if approaching a saturation.

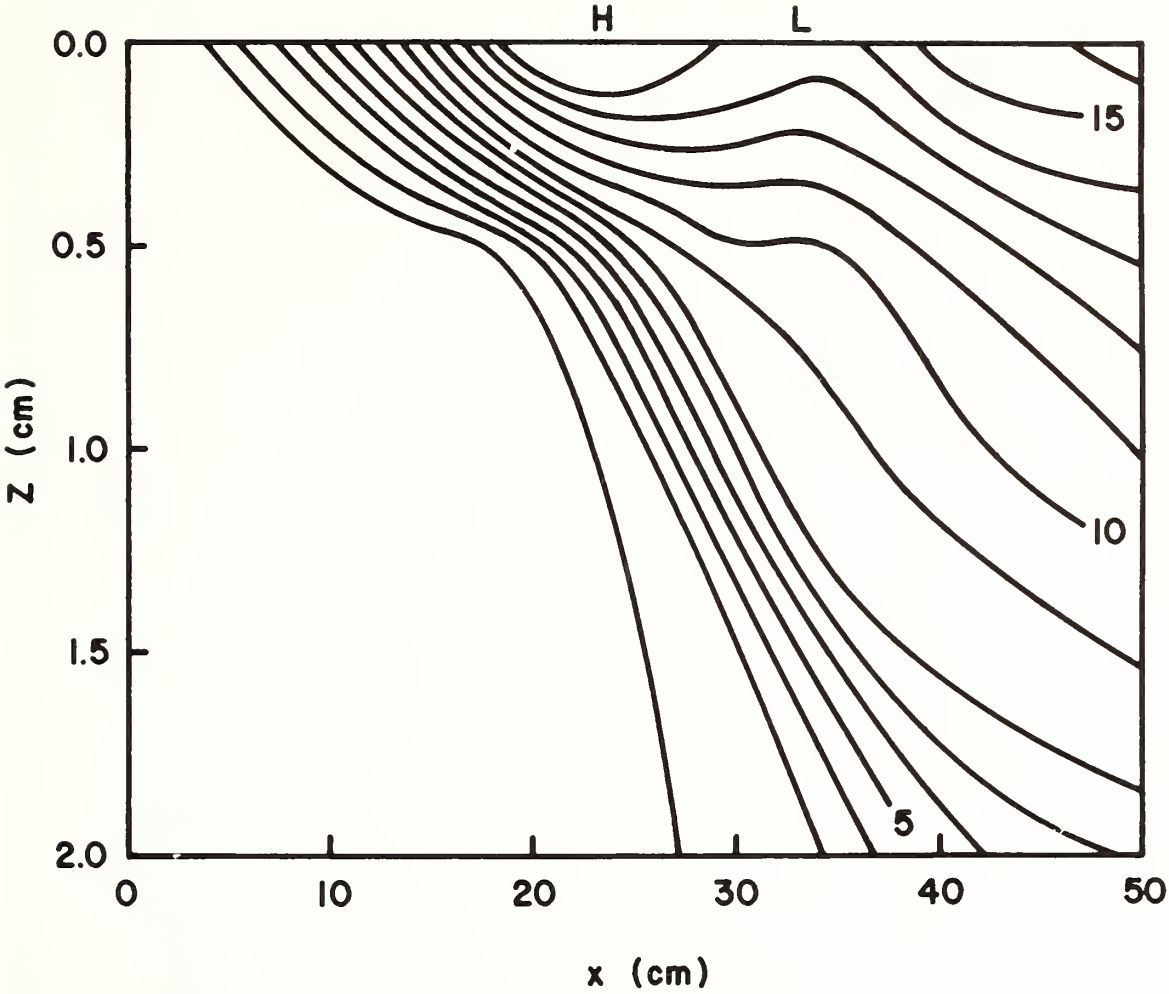

Figure 8. Vertical longitudinal section of water velocity. The contour interval is 1 cm/sec.

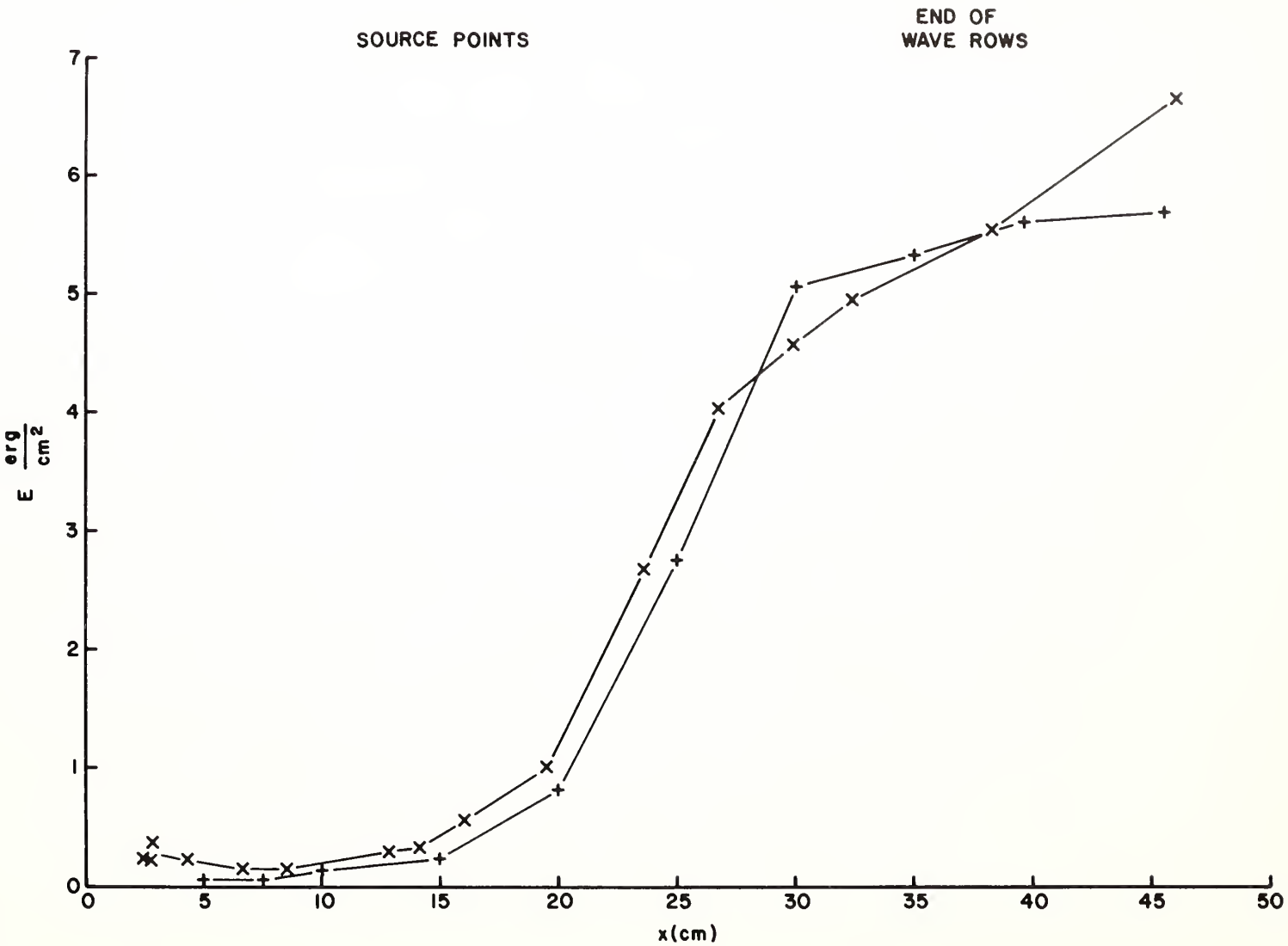

Figure 9. Wave energy versus fetch. The data marked (+) were less filtered than the other.

Wave energy at the same airspeed passed by a sharp high-pass filter with a cutoff at 8 Hz is shown in figure 10. There is a distinct maximum in wave energy at a fetch of 35 cm. The energy at this fetch was nearly as great as the less filtered values in figure 9. After the initial wave development, the filtered high-frequency wave energy was nearly constant to a fetch of at least 400 cm, although the lower frequency waves were seen to be much greater. The capillary-gravity waves grew and approached saturation before lower frequency waves developed significantly.

Figure 11 shows wave energy at a fetch of 400 cm as a function of time as the airflow was increased suddenly. Air leakage over the water surface before opening the blower, and possibly motor vibration, led to very small amplitude waves with a frequency of 2 crests/sec. These apparently did not play a role in the further development of the wave field. Only slight wave growth occurred during the first 15 sec of fast airflow; the waves had a frequency of 15 crests/sec. The rate of wave energy growth next increased abruptly to a peak in energy. Approximately 95 percent of the wave energy at the peak arose during the period of rapid growth. The crest frequency of the rapidly growing waves was only 7 crests/sec. The wave energy then decreased to about 10 percent of the peak. Repeated experiments give somewhat different results, but the pattern of wave growth described here was found repeatedly.

The measurements of wave energy at different fetches in figures 9 and 10 were replotted on a semilogarithmic graph in figure 12. The

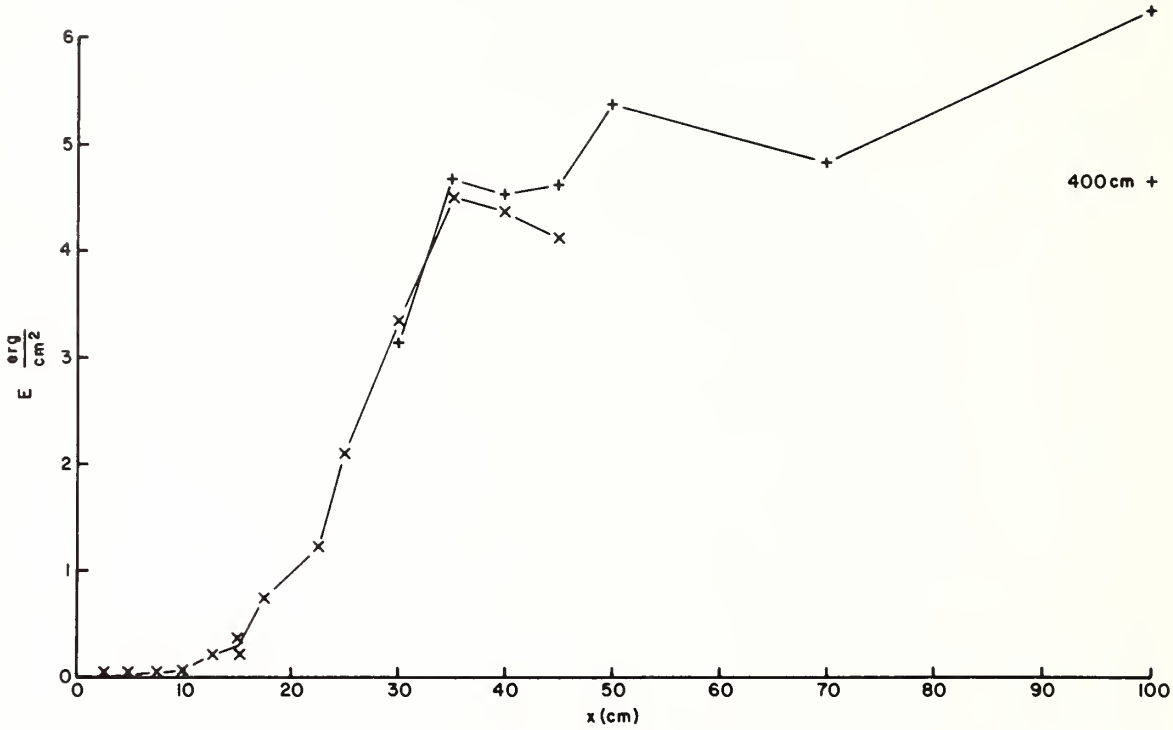

Figure 10. Filtered wave energy versus fetch.

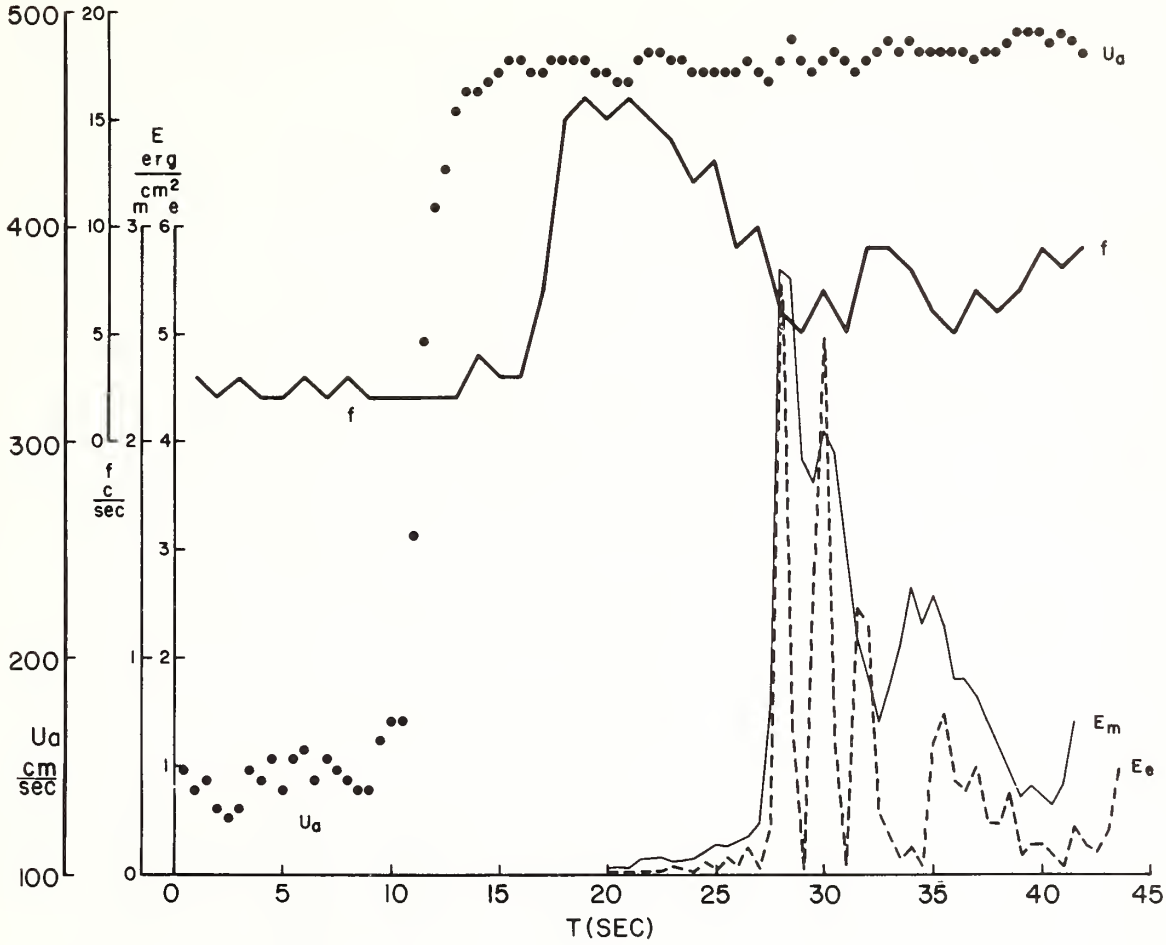

Figure 11. Wave energy versus time after the start of increased airflow. The wave energy was measured with a meter (E_m) and calculated from the width of the wave envelope (E_e). Airspeed (U_a) and crest frequency (f) are also plotted.

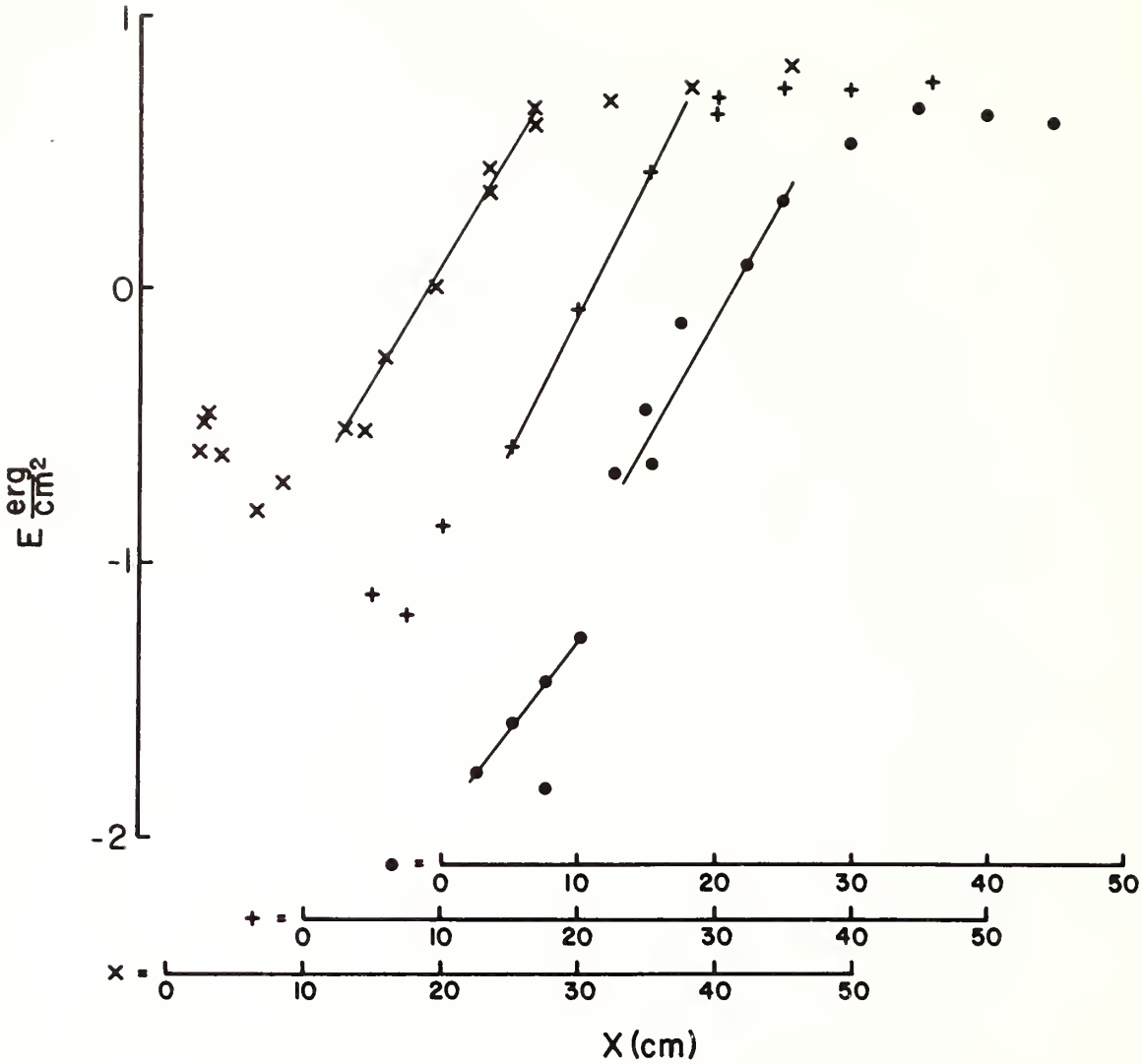

Figure 12. Wave energy versus fetch during three experiments in figures 9 and 10.

measurements of wave energy versus time in figures 11 and 15 were replotted in figure 13. Line segments were drawn to show linear sections of the plots. The very different energy levels in figure 13 are attributed to the different airspeeds. The plot of wave energy versus fetch in figure 12 shows that approximately 90 to 95 percent of the wave growth occurred in an exponential manner between about 15 and 25 to 30 cm of fetch. In the less filtered data, the early wave growth was obscured by unrelated lower frequency waves, but the plot of filtered data shows an earlier exponential growth stage of small amplitude waves. Similarly, the replot of wave energy versus time shown in figure 13 shows two stages of exponential wave growth. The waves in the first, minor stage were found to have a frequency near 15 crests/sec, and those in the major stage had a frequency near 7 crests/sec.

Figure 14 contains hot-film anemometer measurements of water velocities at a depth of 0.2 cm and a fetch of 50 cm as the airflow was started slowly. The normalized square of the width of the velocity fluctuation envelope and the airspeed were also plotted. This figure shows that when the airflow increased gradually, the water velocity increased rapidly; but it decreased abruptly as the steep waves developed. The velocity decrease may be associated with the dips in surface velocity in figures 7 and 8.

A similar experiment with a fetch of 365 cm, a velocity probe depth of 0.3 cm, a wave gage, and a rapidly started airflow is shown in figure 15. The water velocity probe gave erratic readings when the

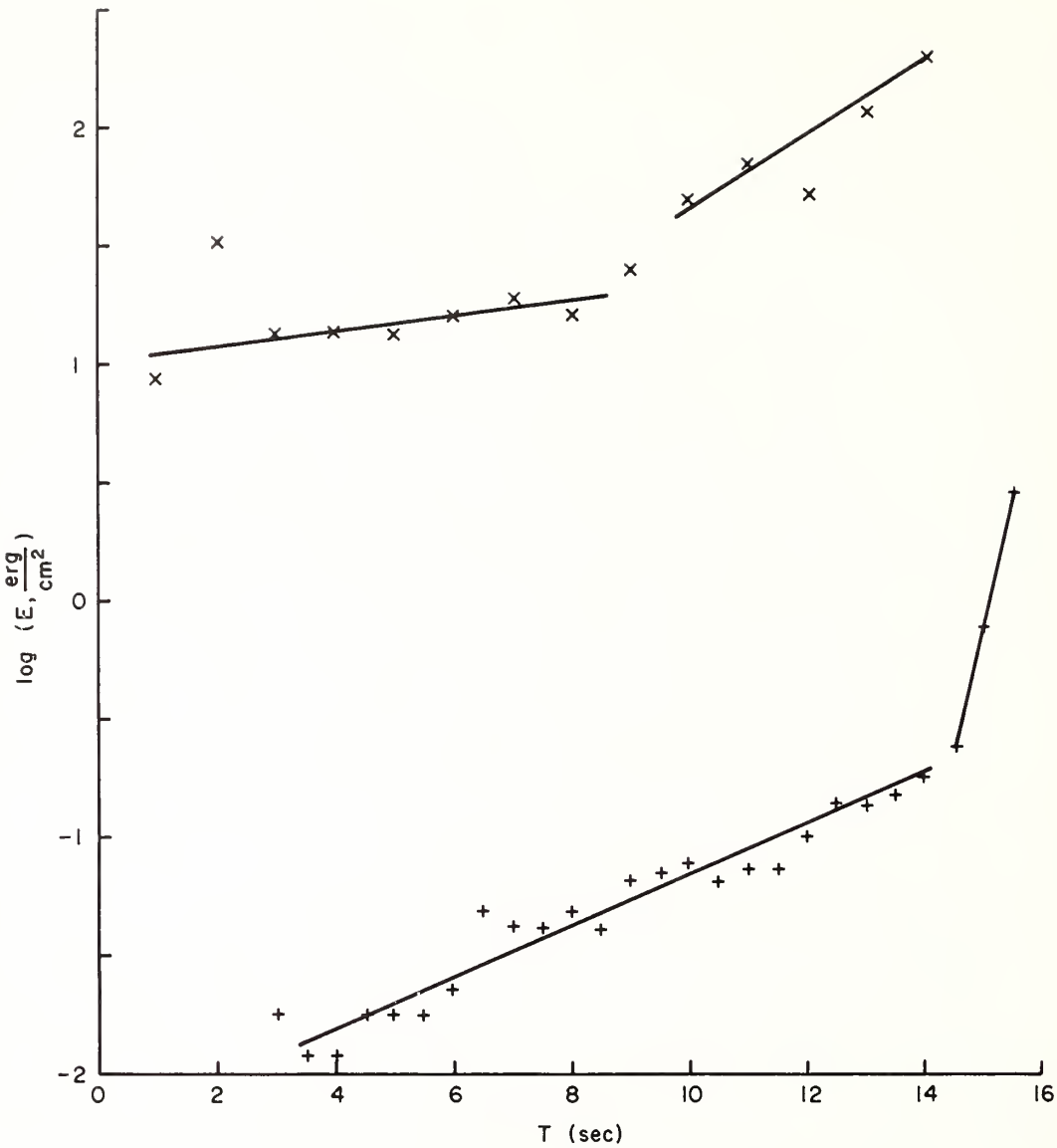

Figure 13. Wave energy versus time. Data are replotted from figures 11 (+) and 15 (x).

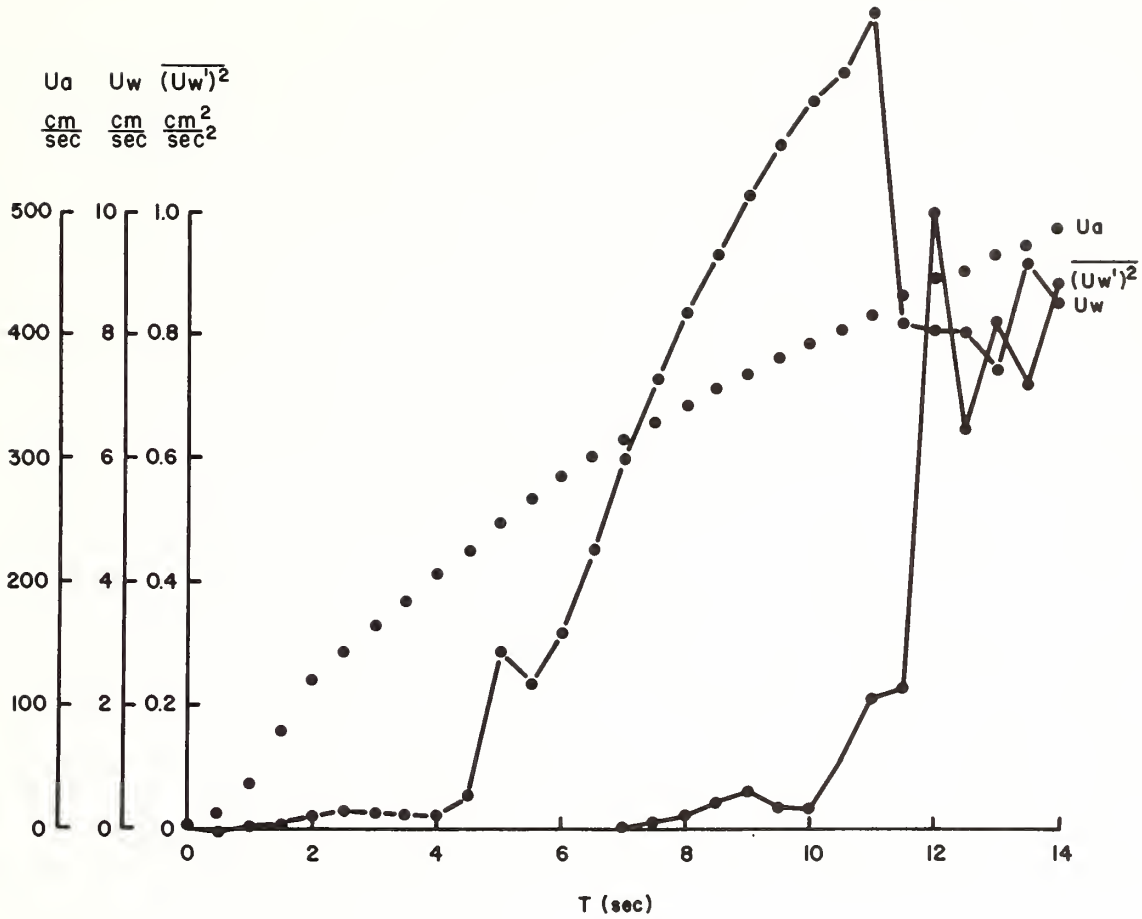

Figure 14. Near-surface water velocity versus time. The short-term average velocity U_w (dashed line), the square of the velocity fluctuations $(U_w')^2$ (continuous line), and the airspeed U_a (dots) are shown.

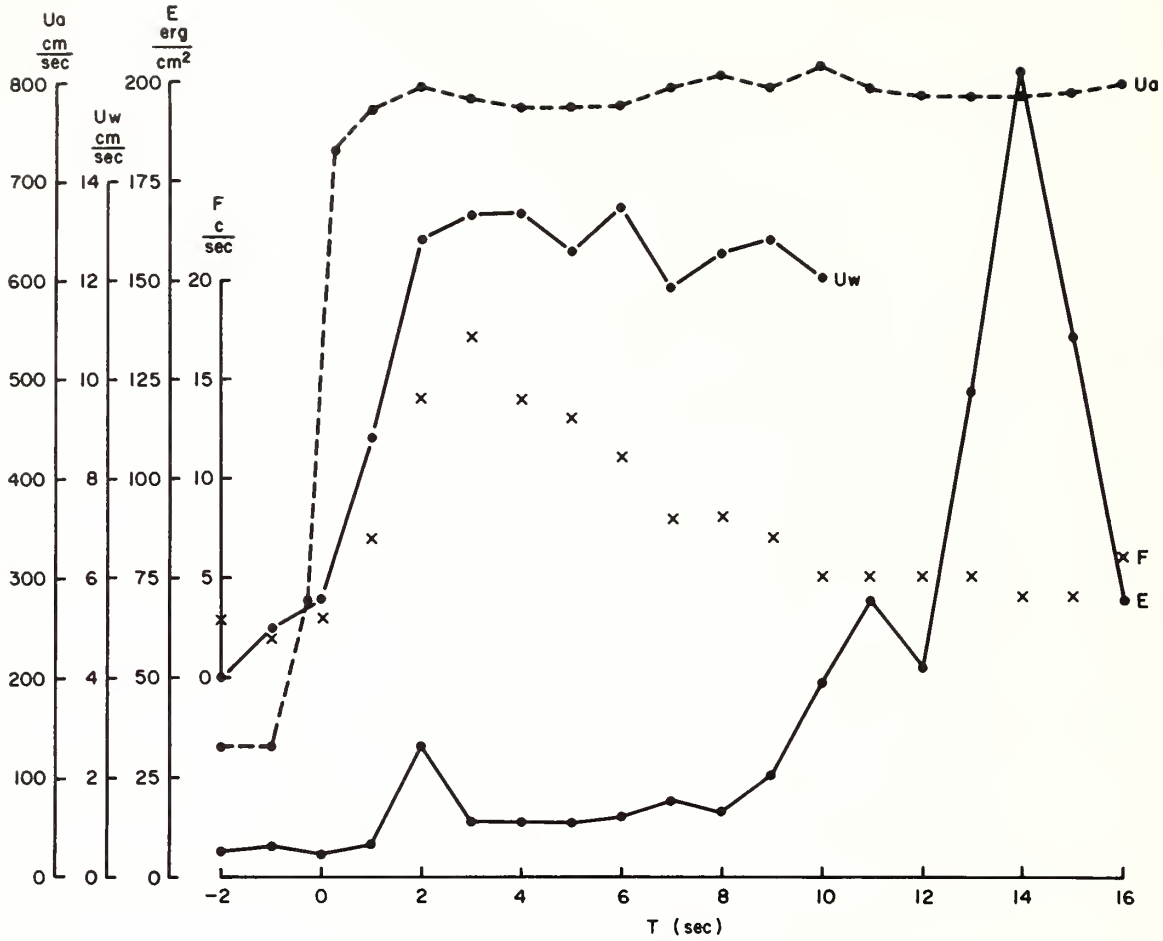

Figure 15. Near-surface water velocity and wave energy versus time. The mean velocity (U_w) is interrupted as the wave energy (E) increases. Airspeed (U_a) and wave crest frequency (F) are included.

waves appeared. Wave energy was calculated from the width of the wave envelope, and the frequency plot represents numbers of wave crests. The near-surface velocity rose rapidly when the fast airflow began, and only later did significant waves appear. In experiments in which the velocity probe was at a depth of 0.5 cm or greater, the increase in velocity was delayed until the steep waves appeared.

In a different but similar wind tunnel installation, an infrared radiation thermometer viewed a 30-cm diameter circular area of the water surface at a fetch of 150 cm and a maximum airspeed of 600 cm/sec. Figure 16 shows the surface temperature changes when the blower was turned on. The water surface temperature changes are consistent with the changes in water circulation described above. The water surface temperature decreased as the airflow developed, rose suddenly as steep waves appeared in the measurement area, and then became steady at an intermediate value. The rise in surface temperature is taken to represent the beginning of vertical mixing indicated in figures 7 and 8.

In addition, the difference between surface and bulk water temperatures was recorded using the infrared radiation thermometer mounted above a water surface at a fetch of 190 cm at different airspeeds. As the airspeed increased, the line of source points moved upstream past the radiometer, and the water surface there became rough. Figure 17 shows a series of measurements over smooth and rough surfaces and a second more detailed series over a rough surface. The variation in surface temperature depression at a single fetch with airspeed further

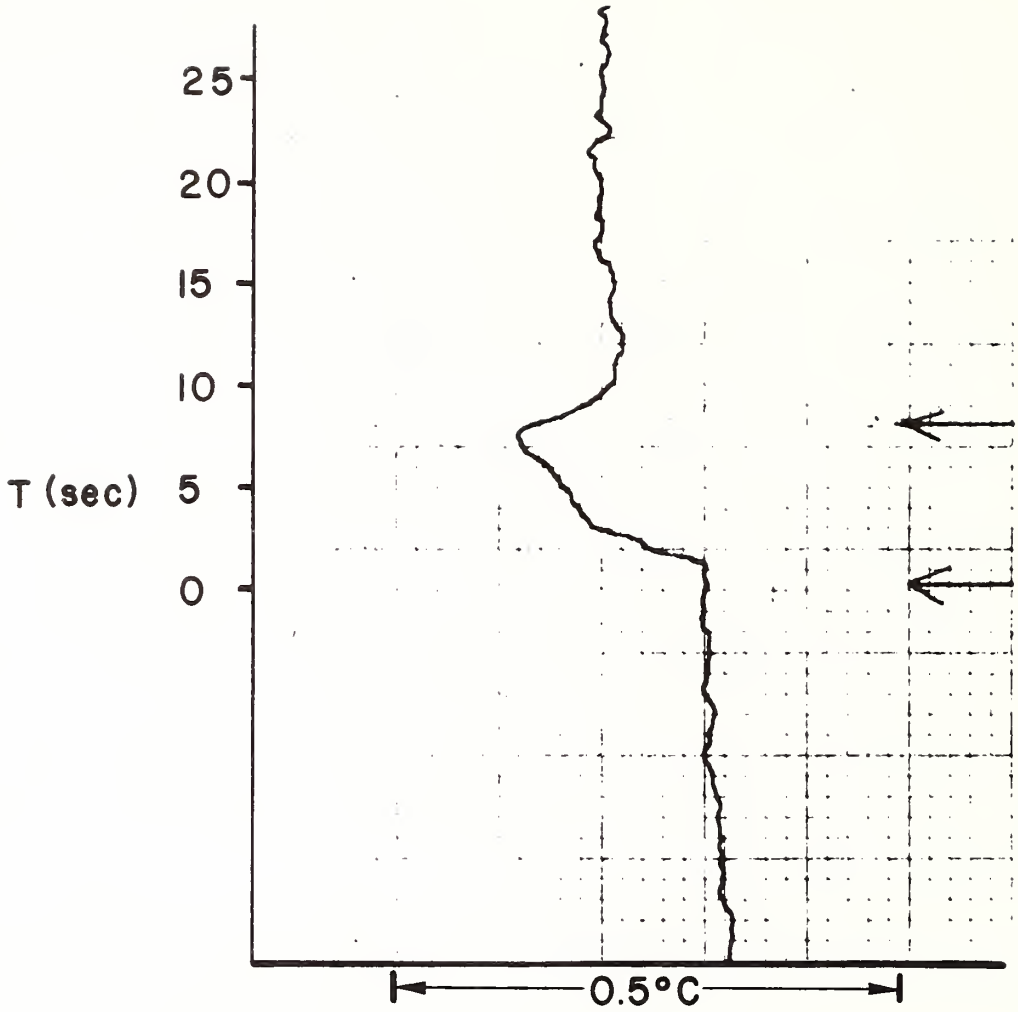

Figure 16. Water surface temperatures versus time after an airflow began. Arrows mark the start of the airflow and also show the time that the water surface beneath the radiometer became rough.

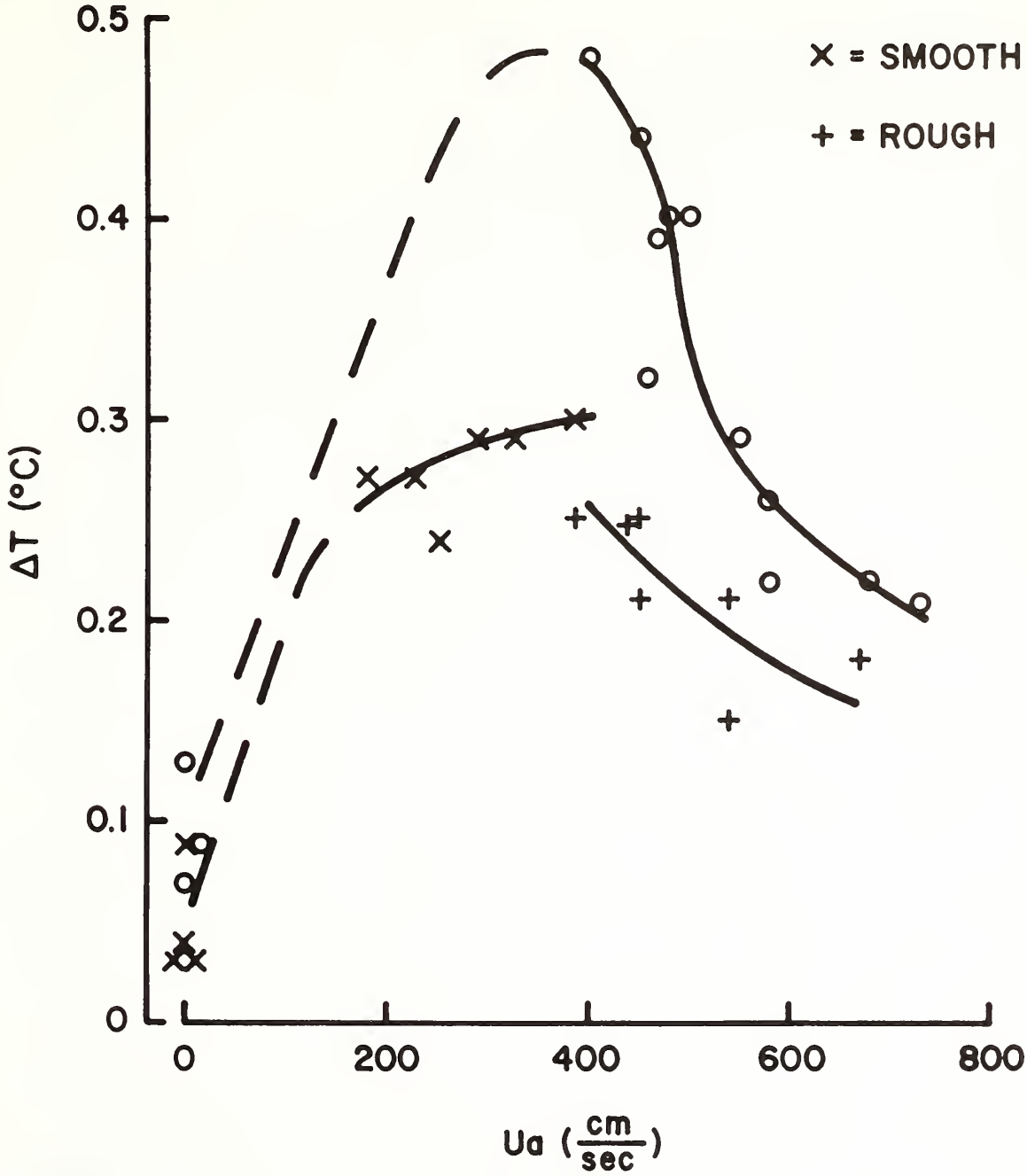

Figure 17. Two series of measurements of water surface temperature depression versus airspeed. In one series, the surface was characterized as either smooth or rough during each measurement.

demonstrates changes in water circulation at the transition. Although there is a gap in the data at low airspeeds, the data show the depression to increase with airspeed where the surface was smooth, the appearance of an apparent discontinuity, and then a lessening of the depression with airspeed above the rough surface. The waveform transition was within the measurement area at the discontinuity in the temperature depression curve. A second, higher set of readings shows the shape of the temperature depression curve downstream of the transition to be concave, opposite to the shape of the curve upstream.

The photograph in figure 18 shows the initial wind waves on a water surface. The width of the scene was about 90 cm. The small-amplitude water waves were regular and long-crested. Rapidly growing waves developed only well downstream, had short-crested "dimple" shapes, and were mostly in rows alined along the direction of the airflow. Irregular larger waves formed downstream of the wave rows.

Figure 19 is a nearly vertical photograph of the water surface where the steep waves first appeared. The regular precursor waves had a wavelength of about 1.8 cm. Dimple-shaped waves developed from the troughs of the precursor waves.

The oblique photograph in figure 20 is a 0.5-sec time exposure of the surface reflection of a floodlamp on the same region of a water surface. The time exposure demonstrates that succeeding dimples formed in the same location, and each followed the previous one to give rows of dimples with bands of smooth water between. The source points of the

Figure 18. Upwind portion of a water surface disturbed by an airflow.

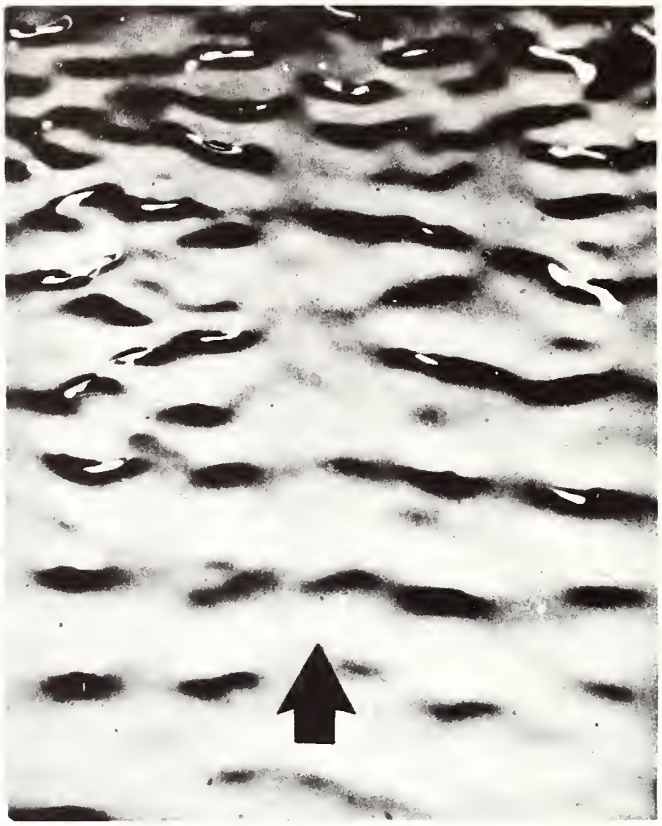

Figure 19. Initial wind waves. The length of the arrow represents 1.8 cm. Bright spots in the dark wave troughs resulted from multiple reflections.

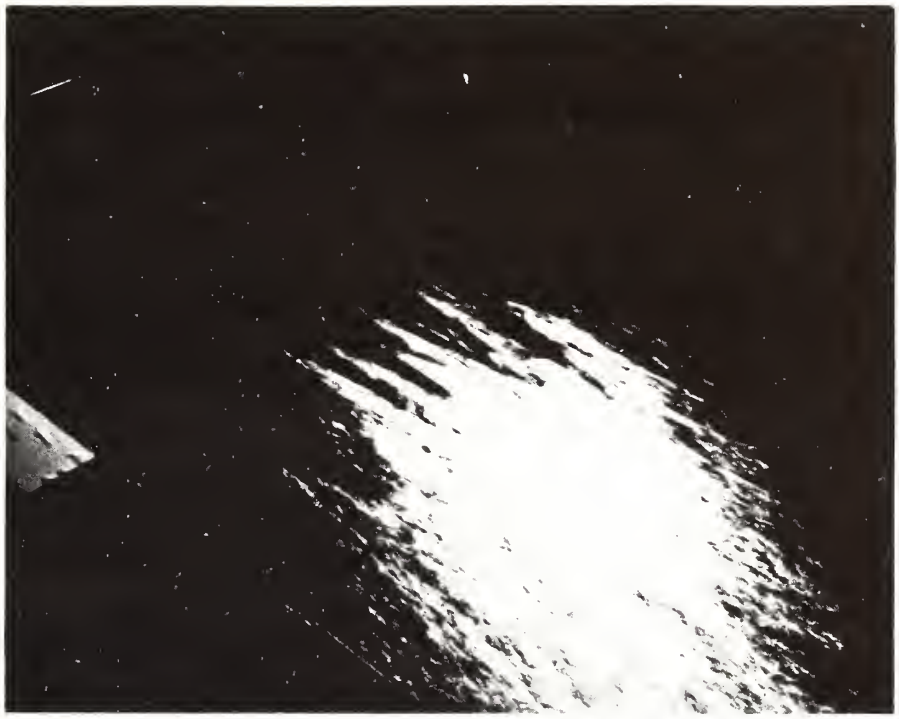

Figure 20. Time exposure of transitional waves in rows. The diameter of the area of reflection was about 50 cm. The light bands in the upwind portion of the reflection were given by steep, short-crested waves moving downwind; the dark bands between them were regions of smooth water.

steep waves remained in one position for several seconds before shifting rather abruptly to a new configuration.

Figure 21 shows the variation in fetch of source points with airspeed as observed by eye. The mean fetch as well as the mean crosswind separation varied approximately as the reciprocal of the square of the airspeed. The fetch was less with more turbulent airflows and also varied with water level. As the level was raised and water overflowed into the entrance duct, the source points moved upstream and passed into the entrance duct when the water depth in the duct was on the order of 0.2 to 0.3 cm. When alternatively a false bottom was installed in the tank to give shallow water depths, the fetch to source points and the initial waves appeared to be affected only at depths of less than 0.3 cm.

A drop of fluorescein dye solution falling a short distance onto the upwind surface of water beneath a slow airflow separated into a patch of surface film and a subsurface blob connected by a thin streak of dye. The surface film drifted downstream and separated into patches on the surface passing between wave rows. The dye streak became stretched downstream between two wave rows and appeared to undergo rotation about a longitudinal axis. When the dye encountered the edge of a compacted surface film, it moved as if the compacted film were a solid boundary. Floating dust particles also showed these surface circulations.

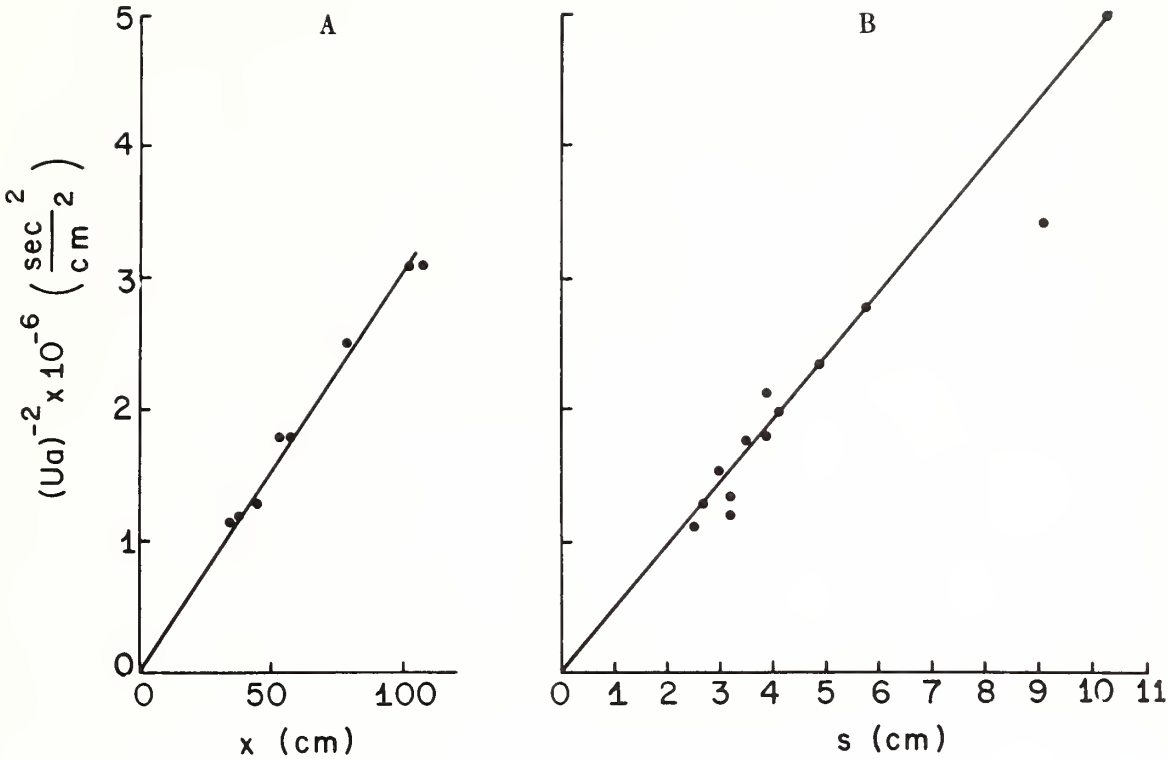

Figure 21. Fetch of source points (a) and traverse spacing (b) versus airspeed.

V. DISCUSSION

The present experiments furnish a description of the intermediate patterns of wave and current flow during the development of wind waves and wind-driven water turbulence. Different stages in the development of waves and current preceded the appearance of the gravity and capillary wave pattern characteristic of wind waves and water turbulence. In most respects, the upstream patterns at different fetches with a steady airflow were duplicated at a fixed fetch downstream when an airflow was started abruptly, and the two situations are combined in a description of the major features of wave and current development.

The first developing waves were regular with long crests. In these experiments, the wave length was near 1.8 cm and the frequency was near 15 Hz, about that of capillary-gravity waves of minimum phase speed. The energy of these precursor waves increased with fetch sometimes to a value near 0.2 to 0.3 ergs/cm, approximately 5 percent of the wave energy after the next growth phase. With a steady airflow, the form of the early wave energy growth was obscured by reflected and other unrelated waves on the surface, but the energy through a high-pass filter increased exponentially. These other waves were absent when the airflow was started abruptly, and the first growth rate was clearly seen to be exponential. A laminar boundary layer with a smooth velocity profile developed in the water.

The transition between the first and second phases of wave development was marked by a transverse line of source points on the water

surface, each of which emitted a rapid series of steep, dimple-shaped waves. Each dimple developed from the trough of a small-amplitude precursor wave. For some distance downstream of the source points, the dimples tended to travel in rows parallel to the direction of the airflow. When the airflow was started abruptly and after several seconds of development of precursor waves, the row of source points appeared at the appropriate fetch in the upwind portion of the water tank. The transition from precursor waves to dimples in rows moved rapidly down the tank, possibly at the airspeed, so that rows of dimples momentarily covered nearly the entire water surface.

The transition region also had an exponential increase in wave energy. The growth factor was more than 10 times greater than previously measured when the airflow was started abruptly, and most of the wave growth occurred during this phase. The wave frequency decreased by about one-half before the waves became highly irregular. The wave amplitudes decreased after this phase and later developed again. With an abruptly increasing airflow, the steep transition waves appeared to be in packets.

The pattern of rows of dimples continued until a wave energy of about 5 erg/cm^2 was attained. The waves then developed, apparently through some intermediate patterns, to long-crested, separate gravity and capillary waves. With further development, the gravity and capillary waves continuously showed greater differences in frequency; the gravity waves increased in amplitude while the capillary waves appeared

to be saturated in energy. The final pattern was characteristic of wind waves on larger, open bodies of water.

In all cases, the waveform transition was accompanied by a transition from a laminar waterflow to turbulence. Particles floating on the surface and dye within the upper water indicated shallow longitudinal water vortexes with surface convergences between the rows of waves. The depth region of significant currents increased from less than 0.5 to more than 2 cm, and the surface speed decreased slightly over a short distance. The water surface temperature reflected this flow change. At successively greater airspeeds, the surface temperature at one position decreased (when the water was being cooled by the air) at a decreasing rate; but the temperature increased with airspeed after the transition, again at a decreasing rate. When the airflow was started abruptly, the water surface began to cool; but at the appearance of steep waves the surface warmed abruptly, and the temperature became constant at an intermediate value.

The velocity profile in the turbulent flow region (fig. 6) shows a linear region near the surface. This is believed to be the first direct demonstration of a viscous sublayer in water at the free surface. The viscous sublayer is significantly thinner at a free surface than at a solid wall. The difference could result in part from the less restrictive boundary condition at the air-water interface.

The relation between the fetch to the wave source points and the airspeed is in accord with a general relation between air stress τ and

transition fetch x_c of current and waves obtained through a dimensional analysis. Several quantities appear in the analysis, but considerations of the mechanisms reduce the number of independent quantities. Stress and viscosity υ are considered to act only upon water currents, with density ρ, as in the combination $\tau/\rho\upsilon$. Surface tension Γ and gravity g act with density only to propagate capillary-gravity waves, and a ratio having dimensions of velocity can be written $(\Gamma g/\rho)^{1/4}$. One form of dimensionless ratio of the pertinent quantities is $\pi = \frac{\tau x_c}{\rho\upsilon(\Gamma g/\rho)^{1/4}}$. Some previous laboratory studies have found stress approximately proportional to the square of the airspeed (e.g., Shemdin, 1972) so that transition fetch may vary as the reciprocal of the square of the airspeed. The relation τx_c = constant implies that the kinetic energy of the flow at transition has a fixed value. The variation of transition fetch with the smoothness of the intersection at the bottom of the air entrance duct and the water surface demonstrated a variation in stress as did the fetch dependence on the turbulence in the air. However, observations that the fetch was not affected by bottom depth at depths greater than a few millimeters illustrate the shallowness of the circulation determining the transition.

Water velocity shear near the surface leads to an interaction between the flow and waves at transition. Some shear persists downstream, and some interaction must continue throughout a rough water surface. The correlation between waves and current may have implications to problems of air-sea interaction. The Miles and Phillips theories of wind-wave generation treat only the influence of air pressure (Kinsman, 1965)

and do not pertain to a waterflow-mediated generation of initial steep waves. Longuet-Higgins (1969) suggested that major waves grow by energy transfer from short waves, but gave no further suggestion of the means of short wave growth. Additional study of the energy transfer from water current to waves appears desirable. Also exchange rates between the sea and atmosphere frequently are limited by the rate of diffusion across the viscous sublayer in the water. The thickness of the layer thus partly controls the exchange rate, and this thickness is less than in corresponding flows at a solid boundary. Further, current theories of laminar-turbulent transition at a solid boundary cannot apply near a free surface.

VI. CONCLUSIONS

The initial growth of steep waves beneath an airflow proceeds by a unique mechanism involving three-dimensional wave shapes and an interaction with the shear flow of the water near the surface. Water turbulence near the surface is modified by the waves and the free motions of the surface. A viscous sublayer exists beneath the water surface, but is thinner than near a solid boundary.

VII. ACKNOWLEDGMENTS

William Everard designed and constructed the special electronic equipment. Figures 16 through 21 were obtained while at the Scripps Institution of Oceanography, La Jolla, Calif.

VIII. REFERENCES

Hires, R. I. (1968), An experimental study of wind-wave interactions, Reference 68-5, Chesapeake Bay Institute, The Johns Hopkins Univ., Baltimore, Md., 169 pp.

Kinsman, B. (1965), Wind Waves: Their Generation and Propagation on the Ocean Surface, Prentice-Hall, Englewood Cliffs, N. J., 676 pp.

Kline, S. J., W. C. Reynolds, F. A. Schraub, and P. W. Runstadler (1967), The structure of turbulent boundary layers, Fig. 9b, J. Fluid Mechanics, 30 (Pt. 4):741-773.

Longuet-Higgins, M. S. (1969), A nonlinear mechanism for the generation of sea waves, Proc. Roy. Soc. A 311:371-389.

McLeish, W., R. A. Berles, W. H. Everard, and G. E. Putland (1971), The SAIL 6-m wind-water tunnel facility, NOAA Tech. Memo. ERL AOML-12, Environmental Research Labs., Miami, Fla., 19 pp.

Mellor, G. L., and H. J. Herring (1969), Two methods of calculating turbulent boundary layer behavior based on numerical solutions of the equations of motion, Fig. 3a, in Proceedings Computation of Turbulent Boundary Layers--1968 AFOSR-IFP Stanford Conference, Vol. 1., eds. S. J. Kline, M. V. Morkovin, G. Sovran, and D. J. Cockrell, Thermosciences Div., Dept. of Mechanical Engineering, Stanford Univ., Palo Alto, Calif., pp. 331-345.

Schraub, F. A., S. J. Kline, J. Henry, P. W. Runstadler, Jr., and A. Littell (1964), Use of hydrogen bubbles for quantitative determination of time dependent velocity fields in low speed water flows, Report MD-10, Div. of Engineering Mechanics, Stanford Univ., Palo Alto, Calif., 66 pp.

Shemdin, O. H. (1972), Wind generated current and phase speed of wind waves, J. Phys. Oceanogr., 2:411-419.

Reprinted from: *Journal of Physical Oceanography 5*, No. 3, 516-518.

Measurements of Wind-Driven Flow Profiles in the Top Millimeter of Water

William McLeish and Gerald E. Putland

Atlantic Oceanographic and Meteorological Laboratories, NOAA, Miami, Fla. 33149

(Manuscript received 13 January 1975, in revised form 4 February 1975)

ABSTRACT

Shapes of mean water velocity profiles measured with microscopic bubble tracers in developing laminar flows are recognizably different from those in a turbulent flow. A previously deduced viscous sublayer occurs at the surface, although it is thinner than an analogous sublayer computed for a solid boundary. The differing thickness leads in part to decreased surface temperatures at slicks.

1. Sublayers at a water surface

A cold surface layer is often found at the ocean surface, almost always so at night. McAlister (1964) suggested that within this boundary layer there must be a conductive sublayer with a nearly linear temperature profile. His measurements with a specialized infrared radiometer at low wind speed indicated a conductive heat flow from the sea in approximate agreement with the total heat flow estimated from measurements in the air. Later, Timofeev (1966) asserted that the boundary layer exists only when the water surface is relatively smooth and disappears at higher wind speeds. However, further radiometric measurements by McAlister and McLeish (1969) demonstrated the existence of a conductive sublayer in laboratory experiments at moderate air speeds, and McAlister *et al.* (1971) measured the total heat flow from the ocean by this technique. Since the turbulent water motions advecting heat also transport momentum, the existence of a conductive sublayer also implies a viscous sublayer. The viscous sublayer in water should be about twice as thick as the conductive sublayer (Wu, 1971). Information on the thickness of these sublayers at a water surface is necessary to measure ocean temperature and heat flow radiometrically and to predict exchanges of various materials between the atmosphere and the ocean.

Measurements showing boundary layer thickness at a water surface have not been found among previous studies. The radiometric measurements in a conductive sublayer indicate only a minimum thickness, not its total thickness. Velocity profile measurements at 0.1 cm depth intervals by McAlister and McLeish (1969) had insufficient resolution to show a linear surface region. Laboratory velocity profiles by Wu (1968) appeared linear but fitted calculated logarithmic profiles satisfying the experimental conditions and so do not indicate viscous sublayers.

Accepting the general assumption that boundary layers over a solid surface and the air-sea interface are similar, Wu (1971) calculated the thicknesses of conductive and viscous sublayers as a function of wind velocity. Katsaros and Businger (1973) made further calculations concerning the determination of heat flow from the ocean using radiometric measurements. In both papers, the authors emphasized the need for measurements to determine the flow structure near the surface. The present study furnished mean water velocity profiles very near the surface in both laminar and turbulent laboratory flows. The viscous sublayer at a free surface is considerably thinner than at a solid boundary.

2. Velocity profiles in the upper water

Profiles of velocity in the top millimeter of water in a wind-water tunnel have been measured from cine photographs of clouds of microscopic hydrogen bubble tracers. Experimental methods were described by McLeish and Putland (1975). The buoyant rise of the bubbles was small, and the bubbles were photographed shortly after release. By using neutrally buoyant markers, the bias errors of floating tracers in an irregular flow described by McLeish (1968) were avoided. Laminar and turbulent regions of the water surface could be distinguished with the bubble patterns, by the mixing of dye streaks, and, it has been found, through the shapes of the waves. The present depth interval of 0.005 cm between measurements provides several velocity readings within the depth region in which a linear viscous sublayer might be expected.

Fig. 1 shows downwind U and crosswind V mean water velocity profiles in the upstream region beneath

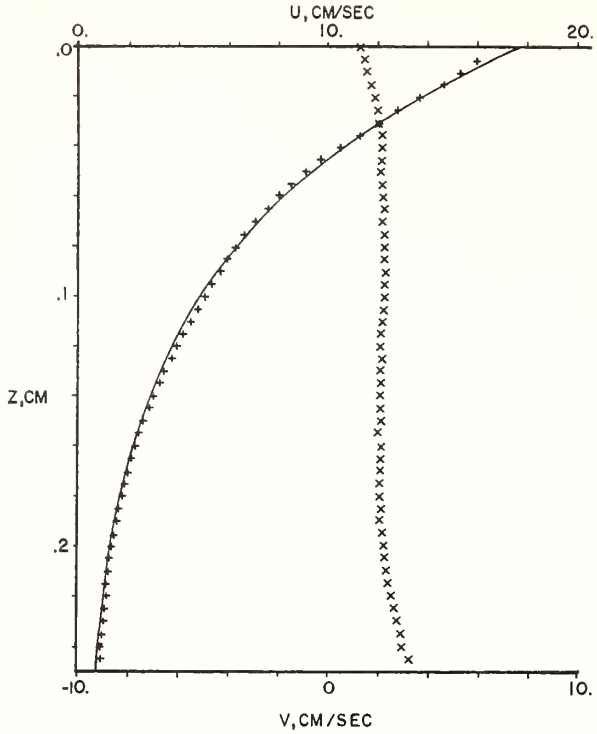

FIG. 1. Water velocity profile in an essentially laminar flow, + downwind and × crosswind. The fitted line is an exponential curve.

an air flow with a midstream velocity of 900 cm s^{-1}. The water flow there was essentially laminar but beginning a transition to turbulent flow. An exponential curve fitted the U readings well, although such a curve is not necessarily characteristic of a developing laminar boundary layer. In fact, Kunishi (1963) reported transient laminar velocity profiles with a different exponential shape. Instead, the fitted curve illustrates the precision of the individual measurements. In particular, an apparently erroneous mean velocity defect is seen in the upper 2–3 readings that might have been caused by air flow interference of equipment mounted asymmetrically in the air above the measurement area. The fitted curve indicates a surface shear from which a stress of 2.0 dyn cm^{-2} was calculated. Calculations based on estimated wave parameters indicated that the wave drift current was small. The crosswind velocity profile, although offset, shows generally little variation with depth.

The velocity fluctuations in Fig. 1 were rapid, and the rms value at a depth was roughly 15% of the mean value there. The depth-averaged variance, reduced by the number of photographs, was similar to the variance of the differences between the mean values and the fitted curve. These departures, then, could be random fluctuations. The correlation between fluctuations at a depth and at the surface

$$\overline{(U'(z)U'(0)}/\{\overline{[U'(z)]^2}\,\overline{[U'(0)]^2}\}^{\frac{1}{2}}$$

decreased to a value of 0.5 at a depth of only 0.035 cm and remained near 0.3–0.4 below. Since the vertical correlation of wave motions should remain unity, the rapid decrease in correlation with depth suggests that wave orbital motions were largely removed by the $\frac{1}{16}$ s averaging between photographs. Furthermore, the kurtosis of the frequency distribution of surface velocity fluctuations was −0.2, as compared with zero with a normal distribution (turbulence) and −1.2 for a uniform distribution (approximately, waves). Rough estimates indicate that turbulent fluctuations in the air flow could cause the very shallow water velocity fluctuations.

The velocity profiles in Fig. 2 represent fully laminar flow with an air speed of 550 cm s^{-1}. The shape of the profiles were similar to those in Fig. 1, although the surface shear indicated a stress of only 1.0 dyn cm^{-2}.

Fig. 3 was obtained at the same air speed as Fig. 2 but downstream where the water flow was fully turbulent. The overall shear in the turbulent boundary layer was considerably less, and the shear zone was thinner than in the laminar flow case. Although the water surface was much rougher than upstream, the indicated stress was less, 0.7 dyn cm^{-2}. The linear portion of the profile at the surface represents a viscous sublayer. This was thinner than the computed profile at a solid boundary with the same stress, as represented in Fig. 3 by a straight line and a departing curved line. The curved line was derived from nondimensional

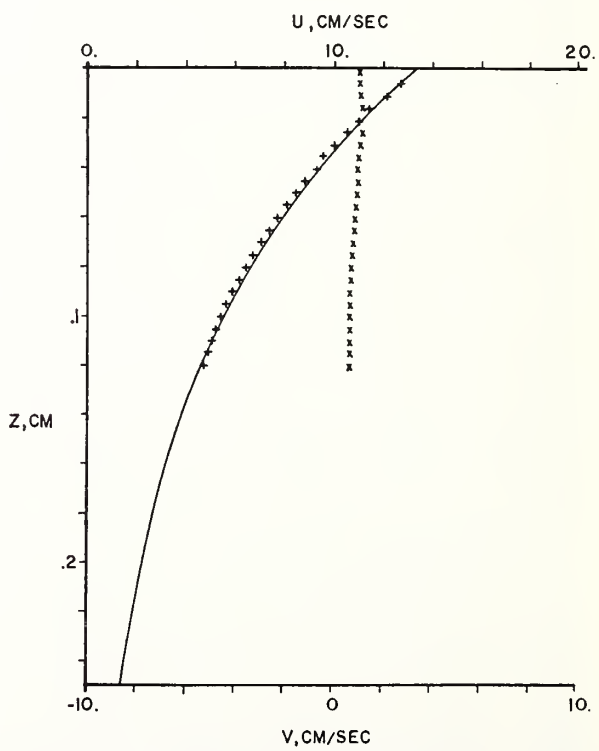

FIG. 2. Water velocity profile in a fully laminar flow, + downwind and × crosswind. The fitted line is an exponential curve.

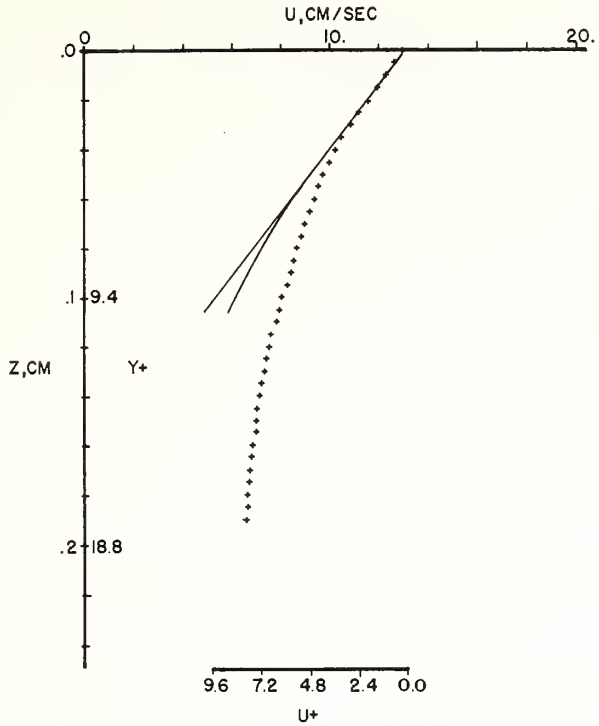

FIG. 3. Water velocity profile in a turbulent flow. The straight line fits the surface slope, and the curved departing line follows the mean profile at a solid boundary.

values by Kline *et al.* (1967) and by Mellor and Herring (1969, see Fig. 3a).

3. Discussion

The linear surface segment in Fig. 3 is believed to represent the first direct measurement of a viscous sublayer at a water surface. Although thinner than at a solid boundary, the viscous sublayer supports the previous evidence for a conductive sublayer sufficiently thick for radiometric heat flow measurements with moderate wind speeds.

Ocean slicks commonly are cooler than the adjacent water surface and, at certain scales and times, represent the dominant surface temperature fluctuations at sea (McLeish, 1970). This effect can be attributed in part to the horizontal rigidity of a slick. A slick acts on the water turbulence below much as does a solid boundary. The conductive sublayer beneath a slick, then, is thicker than elsewhere and, in hindering the normal loss of heat from the sea, gives an increased surface temperature depression. Reduced air stress on the smooth surface at a slick also gives increased sublayer thickness.

The thickness of the viscous sublayer at a free surface is determined in part by the horizontal water motions occurring there and can differ from that at a solid boundary. The present observations indicate that previous estimates of sublayer thickness based on an analogy to a layer at a solid boundary are of the correct order of magnitude but could be improved substantially through direct profile measurements.

Acknowledgments. We are indebted to Mr. F. Ostapoff, Dr. C. Thacker and Ms. S. Worthem for comments on the manuscript.

REFERENCES

Katsaros, K. B., and J. A. Businger, 1973: Comments on the determination of the total heat flux from the sea with a two-wavelength radiometer system as developed by McAlister. *J. Geophys. Res.*, **78**, 1964–1970.

Kline, S. J., W. C. Reynolds, F. A. Schraub and W. C. Runstadler, 1967: The structure of turbulent boundary layers. *J. Fluid Mech.*, **30**, 741–773.

Kunishi, H., 1963: An experimental study on the generation and growth of wind waves. *Disaster Prev. Res. Inst. Kyoto Univ. Bull.*, No. 61.

McAlister, E. D., 1964: Infrared optical techniques applied to oceanography, 1, Measurement of total heat flow from the sea surface. *Appl. Opt.*, **3**, 609–612.

——, and W. McLeish, 1969: Heat transfer in the top millimeter of the ocean. *J. Geophys. Res.*, **74**, 3408–3414.

——, ——, and E. A. Corduan, 1971: Airborne measurements of the total heat flux from the sea during BOMEX. *J. Geophys. Res.*, **76**, 4172–4180.

McLeish, W., 1968: On the mechanisms of wind-slick generation. *Deep Sea Res.*, **15**, 461–469.

——, 1970: Spatial spectra of ocean surface temperature. *J. Geophys. Res.*, **75**, 6872–6877.

——, and G. E. Putland, 1975: The initial water circulation and waves induced by an air flow. NOAA Tech. Rept. ERL 316-AOML 16. [Available from Superintendent of Documents, Washington, D. C.]

Mellor, G. L., and H. J. Herring, 1969: Two methods of calculating turbulent boundary layer behavior based on numerical solutions of the equations of motion. *Proc. Computation of Turbulent Boundary Layers—1968 AFOSR-IFP Stanford Conference*, S. J. Kline, M. V. Morkovin, G. Sovran and D. J. Cockrell, Eds., Thermosci. Div., Dept. Mech. Eng., Stanford University, 331–345.

Timofeev, Yu. M., 1966: Thermal sounding of surface water layers by means of thermal radiation. *Izv. Atmos. Oceanic Phys.*, **2**, 772–774.

Wu, J., 1968: Laboratory studies of wind-wave interactions. *J. Fluid Mech.*, **34**, 91–112.

——, 1971: An estimation of oceanic thermal-sublayer thickness. *J. Phys. Oceanogr.*, **1**, 284–286.

Reprinted from: Preliminary Scientific Results of the GARP Atlantic Tropical Experiment, prepared by the International Scientific and Management Group (ISMG) of the World Meteorological Organization, Volume II, GATE Report No. 14, 392-397.

Preliminary Analysis of Ocean Internal Wave Observations by Acoustic Soundings

Feodor Ostapoff, John Proni, and Ron Sellers

Atlantic Oceanographic and Meteorlogical Laboratories
NOAA, Miami, Florida

INTRODUCTION

One of the major objectives of the Oceanographic Sub-program (GATE Report No. 8, 1974) is to "concentrate on the physics of small scale processes including studies of surface waves, internal waves, oceanic fronts, and the development of the mixed layer."

In order to achieve this goal, it is necessary to observe perturbations at the bottom of the mixed-layer and in the upper thermocline (R. Pollard, 1974; Kraus and Ostapoff, 1974).

One of the first attempts to accomplish this goal in the open ocean was made during Phase III of GATE in the C-Scale array on board the R. V. COLUMBUS ISELIN. In addition to direct measurements by moored current meter systems and towed CTD/STD sensors, indirect acoustic sensing techniques have been applied. This preliminary note gives a brief description of the sensing technique and the first results of an intercomparison experiment during GATE between the acoustic record and a corresponding STD time series. An example will also be presented illustrating the application of the data to the analysis of the observations obtained during the joint roving operations between DISCOVERY and ISELIN, as well as QUADRA, DISCOVERY, and ISELIN.

TECHNIQUE

An acoustic transducer mounted in a towing fish was operated in such a mode that simultaneous STD profiles or time series as well as towed STD profiles were feasible. The transducer operates at 20 KHz with a pulse duration of 2.2 msec. and a repetition rate of .75 sec. (Proni and Apel, 1974). The beam width is approximately 12° by 18° (to the half power points). Figure 1 shows an example of the sonar record obtained on September 19 showing wave-like motion at the top of the thermocline. Heavy slanted lines are sonar reflections from the STD which was profiling down to 100 meters. In a sense, the acoustic technique as applied here to ocean phenomena is quite similar to the acoustic echo sounder techniques used in studies of the atmospheric boundary layer (Little, 1969; Frisch and Clifford, 1974). It is important to realize that this technique does not require biological scatterers to be present such as in the deep-scattering layer (DSL); but that density fluctuations in a layered fluid are sufficient to produce a higher acoustic scattering cross-section (Proni and Apel, 1974; Little, 1969; Apel, Proni, Byrne, and Sellers, 1974).

PRELIMINARY RESULTS

Sections of the acoustic record (as seen in Figure 1) have been analyzed for the time period during which the STD instrument was held at a constant depth of 45 meters. This level corresponds to the first solid scattering return on the acoustic record.

The acoustic record was then scaled by eye and digitized. Figure 2 shows the undulations of the scattering layer (dashed curve) at about 45 meters for a 45-minute period. The solid line represents the temperature record from the STD. It should be noted that at this level the density field is more or less determined by temperature, because at this level the salinity goes through a broad maximum.

It is evident from Figure 2 that the temperature fluctuations are approximately 180° out of phase with the fluctuation of the acoustic scattering layer as it should be if these fluctuations represent internal waves. As the layer is lifted, the temperature decreases and vice versa. Moreover, the double amplitude for the waves on the right hand side of the top

curves can be determined from the vertical temperature distribution, i.e.

$$\delta T / \frac{\Delta T}{\Delta Z} \simeq 11.5 \text{ meters}$$

where $\delta T = 3.2^{o}C$ from the time series and $\Delta T/\Delta Z = 0.28^{o}r$ from the STD cast. This compares to an estimated double amplitude from the acoustic record of ~ 12.5m.

The lower curves in Figure 2 simply indicate the phase relationships, since the acoustic record at 45m depth was difficult to read and another scattering layer at 65 meters was chosen for this analysis. This is justified because for periods of several minutes the acoustic record shows that these layers move up and down in phase. However, a comparison of the amplitudes is not possible with this information.

Spectral analysis shows that in the upper time series in Figure 2 most energy lies in a period band of 9-17 minutes, with a smaller peak at 17 minutes, while in the lower record around 7-8 minutes.

The R. V. COLUMBUS ISELIN recorded some 160 hours of acoustic data in various modes: 1. While steaming jointly with DISCOVERY and QUADRA during the batfish operation. 2. While in free drift mode. 3. While hovering over a cyclesonde buoy. It is intended to digitize the acoustic data which also were recorded on magnetic tape and to process the data objectively by computers. This analysis will be carried out jointly with our British and Canadian colleagues in the study of the upper ocean dynamics.

REFERENCES

Apel, J. R., J. R. Proni, M. H. Byrne, and R. L. Sellers, 1974: Near Simultaneous Observations of Intermittent Internal Waves from Ship and Spacecraft. (Submitted for publication in Geoph. Res. Letters)

Frisch, A. S. and S. F. Clifford, 1974: A Study of Convection Capped by a Stable Layer Using Doppler Radar and Acoustic Echo Sounders. JAS, Vol. 31, No. 6, pp. 1622-1628.

Kraus, E. B. and F. Ostapoff, 1974: AS-II: Mesoscale Phenomena in the Boundary Layers of the Ocean and the Marine Atmospheres. EOS, Trans. AGU, Vol. 55, No. 8, pp. 763-764.

Little, C. G., 1964: Acoustic Methods for the Remote Probing of the Lower Atmosphere. Proc. IEEE, Vol. 57, No. 4, pp. 571-578.

Pollard, R., 1974: Wind-driven Deepening of the Oceanic Mixing Layer. Presented at the IAMAP-IAPSO combined First Special Assemblies, Melbourne, Australia, 14-25 January 1974.

Proni, J. R. and J. R. Apel, 1974: On the Use of High-frequency Acoustics for the Study of Internal Waves and Microstructures. (Accepted for publication in JGR)

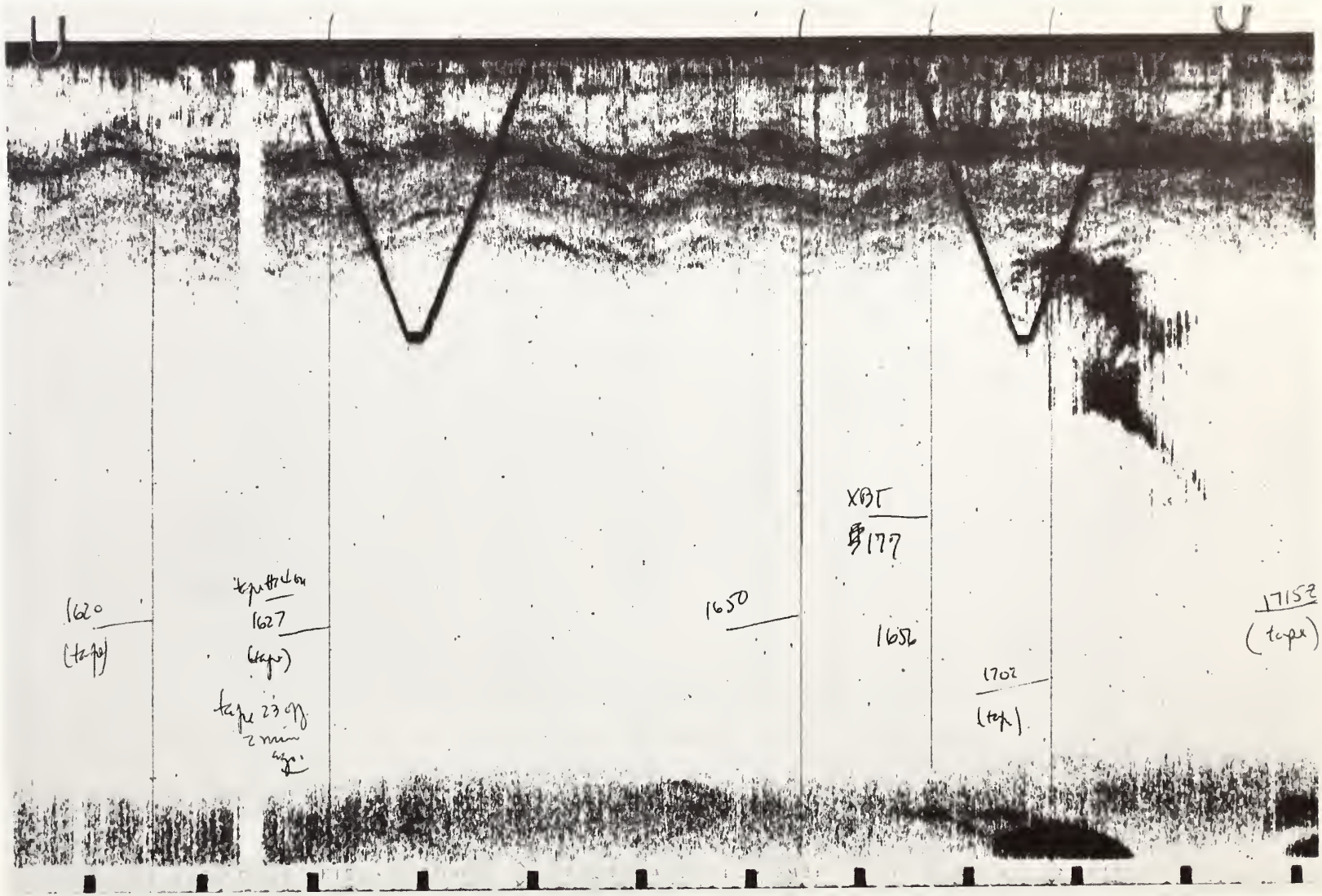

Figure 1: Section of analogue record of the acoustic sounding device used on the R. V. Iselin during phase 3 of GATE. Heavy solid lines represent the acoustic return of the STD (salinity-temperature-depth) instrument. Vertical full scale about 225 meters.

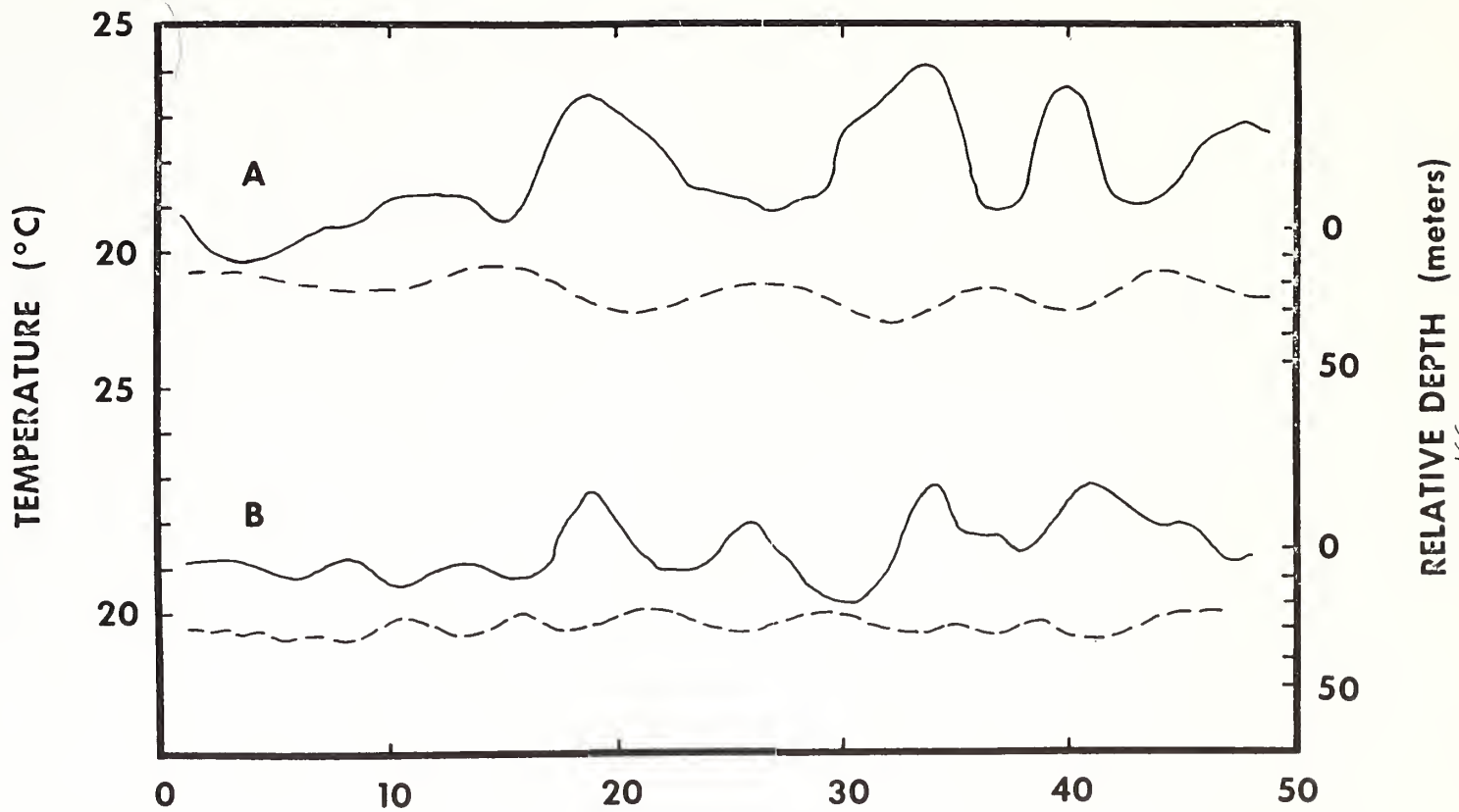

Figure 2: Time series (total record length ~ 50 minutes each) of temperature (solid curve) and acoustic scattering layer (broken curve). A. Both parameters at ~ 45 meters of depth. B. Temperature at about 48 meters and scattering layer at 65 meters.

67 Reprinted from: Proceedings of the NASA Earth Resources Survey Symposium, Houston, Texas, June 1975, Vol. 1-C, 1911-1936.

A COMPARISON OF SKYLAB S-193 AND AIRCRAFT VIEWS OF SURFACE ROUGHNESS AND A LOOK TOWARD SEASAT

M-2

By Duncan Ross, Sea-Air Interaction Laboratory, National Oceanic and Atmospheric Administration, Atlantic Oceanographic and Meteorological Laboratories, Miami, Florida

ABSTRACT

An extensive aircraft underflight program was conducted along the Skylab groundpath for the purpose of documenting wind, wave, and atmospheric conditions affecting the amplitude of the active and passive microwave signatures. The S-193 microwave system senses a roughness parameter at the ocean surface that is proportional to the surface windspeed. The exact relationship between the wind and this roughness parameter is the subject of continuing investigations.

In the case of the active portion of the system, the intensity of off-nadir backscatter from the ocean is thought to be primarily determined by the amplitude of short gravity/capillary waves and has been shown to be strongly a function of azimuth relative to the surface wind direction. The passive side of the instrument senses the naturally emitted (and reflected) microwave energy and is proportional to the RMS slope and percent foam coverage of the ocean.

NOAA, NASA, and USAF aircraft were equipped with a variety of environmental sensors in an attempt to specify the surface conditions affecting the satellite sensors as well as active and passive microwave sensors intended to calibrate the Skylab instrument. The aircraft program is described, and some comparisons of satellite and aircraft results are presented. The principal result of the comparison of active radar is that direct inferences of the surface windspeed are possible, but subject to considerable scatter, and that this scatter appears to be due to interaction between long gravity and short Bragg waves and backscatter due to rain as well as errors in correcting for azimuth dependence. It is shown that σ_0 for incidence angles of $\approx 50°$ increases both with windspeed and with increasing energy level of the high-frequency gravity waves that, themselves, are proportional to both the local wind and fetch in a manner that is not uniquely determined by the windspeed.

An unforeseen opportunity to observe a Pacific hurricane by both Skylab and NOAA aircraft has contributed to the development of a simplified wave forecasting scheme applicable to hurricanes, and more general conditions, which combines the better qualities of both spectral and height/period forecasting techniques. The implication of this result to the SEASAT program is that quite large data inputs in both the time and space domain can be handled using existing computers and should produce a forecast of comparable or superior quality to existing spectral techniques, but in shorter time steps. Horizontal polarization data obtained by the aircraft in Hurricane Ava, and in other experiments, which led to this development are presented.

INTRODUCTION

The S-193 experiment aboard Skylab was intended to test the concept of remote determination of surface wind conditions on a worldwide basis as an aid to improved environmental forecasts. A part of this experiment included an aircraft underflight program to calibrate and validate the inference of surface wind conditions from the satellite measurements of radar backscatter, σ_0, and upwelling naturally emitted microwave energy, T_a.

A number of significant developments have evolved as a result of this combination of satellite and aircraft studies of the environment, which will be touched upon herein. It is impossible, however, to discuss in depth all aspects included in the scope of this program. Results presented here are preliminary, and some conclusions may be modified as additional data sets are considered. The reader is, therefore, asked to be tolerant of missing details and tentative conclusions that, hopefully, will be firmed up in future reports.

AIRCRAFT INSTRUMENTATION

The aircraft measurements were obtained from instrumented NOAA, NASA, and USAF C130 aircraft. All aircraft were equipped with a basic environmental package consisting of an inertial platform for windspeed determination, a Barnes Infrared Radiometer for sea surface temperatures, a laser wave profiler for wave measurements, a Cambridge Dew Point Hygrometer, a Rosemount Air Temperature Probe, and a vertical camera for white-cap photography. The NOAA C130 was additionally equipped with a three-frequency passive microwave system at K_u (14.5 GHz), X (8.35 GHz), and L (1.8 GHz) bands. This system was used for dual polarization measurements at X and K_u bands and horizontal polarization measurements at L-band. Because the NOAA aircraft was not available for the third launch period, a cooperative arrangement with the Air Force 53rd Weather Reconnaissance Squadron of the Air Weather Service was negotiated by NOAA, and the inertial platform, laser, microwave, and camera systems were transferred to the Air Force C130 for the SL-4 underflight program. Figure 1 shows the NOAA C130 aircraft with passive microwave antennas extended to the in-flight operating position.

The NASA JSC C130 aircraft was similarly equipped except that the microwave system was both active and passive (time-shared) and centered only at 13.5 GHz. The NASA aircraft participated in the underflight program during all three launch periods.

SATELLITE INSTRUMENTATION

Skylab S-193 Instrument. The S-193 experiment aboard Skylab consists of an instrument capable of operation in one of three modes: (1) short pulse altimetry, (2) radar backscatter, and (3) a passive radiometer mode. The instrument is a single-frequency device centered at 13 GHz (K_u band). In the so-called RADSCAT configuration, the instrument alternately switches between the active and passive mode. It is capable of scanning in the along-track and across-track directions, and thus obtains dual polarization measurements of radar backscattering cross section, σ_0, and

upwelling naturally emitted microwave energy, which is directly proportional to the apparent, or antenna, temperature T_a, as a function of incidence angle.

Radar Backscatter. The mechanisms responsible for determining the level of radar energy backscattered by the ocean surface are primarily, but not limited to, the amplitude of resonant Bragg waves for incidence angles between about 30° and 80°, and the RMS slope distribution for near vertical incidence angles (Wright, 1968; Valenzuela, 1968). The Bragg condition is defined as

$$\frac{2\pi}{\lambda_{water}} = K_B = K_0 \cos \theta_1 + K_0 \cos \theta_2$$

where θ_1 and θ_2 are the incident and scattering angles, $K_0 = 2\pi/\lambda$ microwave. In the case of S-193, these waves correspond to cm wavelength ocean waves. The detailed behavior of Bragg waves and also their effect on backscatter has been the subject of considerable study in laboratory experiments in recent years (cf. Rouse and Moore, 1972; Duncan, Keller, and Wright, 1974; Keller, Larson, and Wright,1974; Keller and Wright, 1975; Reece and Shemdin, 1974; and many others). The principal result of these studies is that the backscattered doppler radar spectrum for a particular radar frequency and incidence angle is not a unique function of windspeed but rather is, to some degree, a function of fetch, duration, and presence of swell as well as wind speed.

The Wave Spectrum. It has been suggested that the S-193 RADSCAT data are affected by both long and short ocean waves. In the following sections, an attempt will be made to evaluate S-193 data in terms of the wave spectrum. A brief description of the spectrum and its behavior during growth and swell situations is therefore appropriate.

Wave conditions can be fully described by the two-dimensional energy spectrum, $A^2(f,\theta)$, and integration over direction (θ) and frequency, f, yields the total energy

$$E = \int_0^{\infty} \int_{-\pi}^{\pi} [A(f,\theta)]^2 \, d\theta df$$

which is proportional to mean surface displacement, $2\sigma^2$.

For a wind blowing off a shoreline, the fetch is defined simply as the distance from shore to the downwind measurement site. Figure 2 presents the behavior of the one-dimensional energy spectrum for seven fetch locations during offshore wind conditions as observed in the JONSWAP experiment (Hasselmann et. al., 1973). The inset of Figure 2 depicts the meaning of the five parameters suggested by Hasselmann et. al. as convenient for describing the important characteristics of the spectrum. It can be seen from this figure that the peak frequency, f_m, grows and migrates toward lower frequencies as fetch increases. Hasselman et. al. found that the sharpness parameter, γ, and the width parameters σ_a, σ_b, are essentially independent of fetch. The Phillips parameter, α, however, generally decreased with increasing fetch. The behavior of the spectral scale parameters can also be represented

conveniently in nondimensional form by incorporation of the local windspeed, U_{10}, and gravity. Thus, Figure 3 presents the behavior of nondimensional energy

$$\tilde{E} = \frac{Eg^2}{U_{10}^4}$$

and nondimensional frequency

$$\tilde{f}_m = \frac{f_m U_{10}}{g}$$

versus nondimensional fetch

$$\tilde{X} = \frac{xg}{U_{10}^2}.$$

Nondimensionalization in this manner has properly accounted for the windspeed dependence of the behavior of total energy and peak frequency with fetch. The interrelationship between α, $\tilde{E}$, and $\tilde{f}_m$ is therefore apparent and was studied in detail by Hasselmann et. al. (1975). They proposed $\tilde{f}_m$ as a convenient means of describing the stage of development of the wave spectrum in an average sense. Figures 4 and 5 from this study show the behavior of $\tilde{E}$ and α with respect to $\tilde{f}_m$ and $\tilde{X}$. The lines denoted

$$C_\omega = 10^{-3}$$

and

$$C_\omega = 10^{-5}$$

are representative of the momentum entering the wave field (Hasselmann et. al., 1973), with an approximate mean value of

$$C_\omega \approx 10^{-4},$$

or about 20 percent of the total momentum transferred to the ocean by the wind. Variations about the mean are attributed to changes in the local wind conditions. An example of varying the wind by a factor of 1.5 for a particular f_m is included in the figures.

RESULTS

Because the principal purpose of the S-193 experiment was to remotely infer surface wind conditions, it is appropriate to first consider examples of the data from a typical pass as a prelude to more extensive analysis of the complete data set. Figure 6 presents the results of a pass in the Gulf of Mexico during SL-2 and is a typical example of variable low windspeed conditions. The S-193 active radar backscattering cross sections, (σ_0), and passive microwave antenna temperature, T_a, for horizontal polarization and an incidence angle of 50° are shown plotted as a function of latitude along with the surface wind conditions as determined from the NOAA aircraft underflight.

Considerable variability can be seen for σ_0, especially around 19° and 22° N. The data for those latitudes less than 23°, however, were not corrected for azimuth dependence and therefore show scatter due to changes in wind direction as well as speed. The higher latitudes, however, are of most interest because they were accompanied by extensive ground truth. It can be seen that the surface winds decreased significantly between 24° and 26° N, while σ_0 decreased only slightly between 24° and 25.5° N and actually increased at 26° N. The horizontally polarized antenna temperature agrees well with aircraft determinations and also increases significantly at 26° N. Because of the presence of many rain showers observed by the aircraft to be in the area of 26° N, these increases are tentatively attributed to this factor. This pass, therefore, implies significant corrections would normally be required to account for the presence of rain.

During SL-2, a unique opportunity to observe high wind conditions developed with the appearance of a hurricane in the eastern Pacific southwest of Acapulco, Mexico (Ross et. al., 1974). As plans were being formulated for observing the storm with the S-193 system, the NOAA C130 aircraft deployed on the 6th of June to Acapulco, refueled, and flew a 7.5-hour mission into the storm. Figure 7 is a NOAA-2 composite satellite view of Hurricane Ava showing the flight track of Skylab as it conducted a data pass with S-193 operating in the side-looking solar inertial mode. Unfortunately, the storm was rapidly moving away from the subsatellite track and it was not possible to obtain measurements in the region of maximum winds. Figure 8 is an example of active and passive measurements of Ava obtained at incidence angles of 42.5° and 50.5° along with estimates of surface winds obtained during the aircraft penetration and rainfall rates estimated from the NIMBUS-5 satellite 19.35 passive microwave system (Wilheit, 1972). It can be seen from this figure that there is an increase in σ_0 and T_a in the higher wind areas of the storm with the highest antenna temperature occurring in the zone of heavy rainfall.

High wind conditions were also obtained during the third launch period. Figure 9 shows the subsatellite track for data obtained on the 9th of January at incidence angles of 0° and ± ≈50° along with the NOAA surface analysis for 1800Z. This situation is particularly interesting because the windspeed varied from 7.5 to 30 m/sec from the beginning to the end of the sampling period with little rainfall reported except in the region of the front. Figure 10 presents the variation in σ_0 and T_a for +47.6° and -50.5° incidence angle along with surface winds estimated from an isotach analysis based mainly on ship reports and the NASA JSC aircraft measurements. A qualitative comparison of these data sets, together with that from Hurricane Ava and the June 11 pass in the Gulf of Mexico, strongly suggests a first-order dependency on surface wind conditions but with scatter.

Unfortunately, due to damage to the S-193 antenna occurring during an SL-3 extravehicular excursion, the antenna pattern was altered in an unknown fashion. It is therefore risky to include the 9 January data set with those obtained during SL-2 when calculating windspeed dependency. This case was therefore treated separately and is shown plotted against windspeed in Figure 11. σ_0 and T_a data obtained during SL-2 are shown in Figure 12 plotted against windspeed. These data sets are restricted to those data passes described above, which were accompanied by an aircraft underflight. Aircraft-determined antenna temperatures included show good agreement with S-193. The surface winds attached to each satellite data point are judged to be accurate to about 1 to 3 m/sec in the case of SL-2 and 3 to 5 m/sec in the case of the SL-4 pass of 9 January. The judgment of accuracy includes the effects of mesoscale variability in the local wind conditions and inaccuracies associated with aircraft-determined winds and ship reports in the case of

the 9 January data. Unfortunately, no study is known to the author that compares ship reports (mostly visual estimates) to continuously recorded and calibrated winds averaged over 10 to 30 minutes. Therefore, one is left with a judgment.

DISCUSSION

The above data sets strongly suggest a useful first-order relationship between surface winds for both σ_0 and T_a subject to some degree of scatter. There are several sources of errors in both parameters contributing to the scatter that crops up in the processing. In addition, there may be errors due to invalid atmospheric assumptions (or errors in the corrections required for a particular assumption), random errors in inferring the 10-meter windspeed from aircraft measurements, as well as natural variability in local wind conditions. The above errors inherent to this data set probably cannot be reduced any further.

One potential source of error that can be addressed, however, lies in the lack of uniqueness of the active or passive signature due to the variability in possible wave conditions that may be present for a given windspeed. Reece and Shemdin (1974), in a study conducted in a wave tank, showed that the high-frequency waves, for a particular fetch, are windspeed dependent, but the absolute energy level for a particular windspeed is reduced with the addition of a low-frequency component (swell) and that the amount of the reduction is proportional to the amplitude of the low-frequency component. Mitsuyasu (1971) showed similar reduction in the high-frequency gravity region of the wave spectrum with the introduction of swell. Hasselmann et. al. (1973), showed that the Phillips constant (α) (Phillips, 1958), which determines the energy level of the f^{-5} region of the wave spectrum, decreases with increasing nondimensional fetch as discussed earlier. In order to assess the possible importance of the gravity wave spectrum in this data set, it is desirable to consider σ_0 as a function of some observable parameter of the wave field that varies with fetch in a well-behaved and predictable manner.

The nondimensional peak frequency, $\tilde{f}_m$, was shown earlier to be a particularly useful parameter that well describes the stage of development of the wave spectrum. Aircraft measurements of the wave spectrum were used directly to specify $\tilde{f}_m$ for Skylab data sets obtained on 5 and 11 June 1973. The data for Hurricane Ava, however, present a special problem because the aircraft measurements were not obtained at the exact subsatellite point. In order to specify the peak frequency, it was desirable to develop some technique of estimating these parameters from the aircraft data set. The hurricane wind fields are circular in nature, however, and the fetch relationship needed to infer $\tilde{f}_m$ is ambiguous and arbitrary. Furthermore, the position of the aircraft measurements relative to the eye of the hurricane were concentrated in the rear quadrant, whereas most of the satellite positions were to the right of the hurricane center. Figure 13, however, presents some of the wave data obtained, plotted along with spectra from the North Sea measured under similar wind conditions, but fetch limited, and in the North Atlantic during fully developed conditions. The resemblance between the spectra is striking. The most significant feature of the Ava spectra, however, is the general lack of "swell," which would appear as a secondary peak in the spectrum. This is especially significant when the unidirectional assumption required in processing the aircraft data is considered. Because we assume all waves are moving in a direction parallel to the aircraft flight track, swell from some other direction is moved toward lower frequencies in the mapping process to fixed coordinates, leading to an unrealistic "broad"

appearance to the spectrum with multiple peaks. Hurricane Ava was a superhurricane by any criteria and had a record low pressure for eastern Pacific storms of 914 millibars. Fortunately, another such storm of which wave measurements have recently become available was Hurricane Camille, one of the worst hurricanes to ever strike the coast of the United States as it went ashore near Mobile, Alabama, in August of 1969. Camille's eye dimensions, maximum winds, forward velocity, and central pressure were virtually identical to those of Hurricane Ava. Measurements of wave conditions in relatively deep water were obtained by a consortium of oil companies. Some of the data were reported recently (Patterson, 1974, and Hamilton and Ward, 1974) and were used in this study. Figure 14 presents the relative positions of Camille and Ava wave data to the eye and wind field of Ava as determined from the NOAA aircraft flight. It is fortunate that Camille was so similar to Ava as the windspeeds measured on the oil company platform were biased low because of poor anemometer exposure for a storm approaching in the direction of Camille. Ava's winds were therefore used to specify the Camille wind field, which avoids the difficulty of introducing another empirically based technique to specify 10-meter anemometer winds. The wave data from Camille and Ava were then nondimensionalized and plotted against the nondimensional radial distance from the eye and are presented in Figure 15. It can be seen that a simple power law reasonably well describes the radial behavior of both $\tilde{E}$ and $\tilde{f}_m$. Nondimensional peak frequencies for the Ava data set were therefore calculated from the expression.

$$\tilde{f}_m = 1.6\tilde{R}^{-.25}$$

where

$$\tilde{R} = \frac{rg}{U_{10}^2}$$

and r is the particular radial distance from the subsatellite point to the eye of Ava. The Ava data set was then combined with data from 5 and 11 June 1973 and is shown in Figure 16. It can be seen that σ_0 varies considerably with $\tilde{f}_m$. It can be argued that, because the windspeed is included in the calculation of $\tilde{f}_m$, it is difficult to correctly separate the windspeed dependency from stage of development. To aid in this separation of dependencies, a multiple regression analysis was performed according to the equation

$$Z = a_0 + a_1x + a_2y$$

letting $Z = \sigma_0$, $x = U_{10}$, and $y = \tilde{f}_m$. The constants a_0, a_1, and a_2 were found to be -29.5, 0.20, and 59.4, respectively. Such a dependency on $\tilde{f}_m$ is much greater than expected or would be predicted on the basis of wave tank experiments cited earlier. The same multiple regression analysis was performed on the 9 January data set, based on hindcast $\tilde{f}_m$, for 47.6° incidence angle, and yielded values of -15.7, 0.39, and 17.5 for the same constants. The hindcast performed assumed limited fetch, but unlimited duration, and the rather low wave heights reported suggest an underestimate for the values of $\tilde{f}_m$ for the higher winds. Also possible is a bias in the case of the hurricane data set due to backscatter from rain. The 9 January data set, however, seems to confirm a fetch dependency and both sets considered together suggest that controlled high-wind, variable-fetch experiments should be performed to accurately infer high winds from measurements of σ_0.

A similar treatment of the fetch effect in the case of the passive microwave measurements is also indicated and is underway.

RELATION TO SEASAT

The success of the simplified approach suggested by Hasselmann et. al. (1975) for specifying the evolution of the wave spectrum depends on successful parameterization of the nonlinear interactions that control the exchange of energy within the spectrum that, in turn, are very sensitive to local gustiness in the surface wind conditions. However, because it is not necessary to deal with the entire directional spectrum for each grid point in a numerical forecast scheme, it will be possible to increase the density of grid points and decrease the time steps involved in forecasting waves. For example, a typical spectral model consisting of 17 frequencies and 15 directions for 512 grid points in the North Atlantic requires 130 000 storage locations, whereas the simplified approach, expanded to account for two swell systems, can increase the grid density to 5012 and require only 30 072 locations. Such a forecasting approach is needed for rapid assimilation of satellite data and will likely be in operation by the time the SEASAT satellite is launched. At this time, the First Global GARP Experiment will also be underway and provide a unique opportunity to test the SEASAT concept.

CONCLUSIONS

The Skylab S-193 experiment has proved that active and passive microwave sensors can be used to infer surface winds but are subject to scatter and a decreasing sensitivity with increasing windspeed in the case of the active radar, and bias due to rainfall with little sensitivity to lower windspeeds in the case of passive microwave signatures. These results, therefore, suggest that combined active and passive systems with a weighted averaging process (employing polarization dependencies) being used to infer the local wind might reduce some of the scatter due to random errors and should be tested with Skylab data. The results further suggest that a parameterization of the wave spectrum may be necessary in order to further reduce the scatter in σ_0. The Skylab data set contains most of the data needed to test these hypotheses and could lead to satellite determination of both the windspeed <u>and</u> surface wave spectrum by judicious use of active and multifrequency passive microwave systems.

ACKNOWLEDGMENTS

The author is grateful to the many people in the satellite and aircraft program which comprised the Skylab experiment. Special thanks are due the NOAA C130 crew for expertly conducting 500 foot flight tracks in one of the most severe hurricanes of record, and the NASA JSC and USAF air crews for low-level flights into severe winter storms (especially the Air Force loadmaster who finally closed a balky cargo door allowing a planned high-altitude pressurized return to shore during one occasion). Finally, the accuracy and extent of passive microwave data collected by the NOAA and USAF aircraft is due to the diligence and competence of the Naval Research Laboratory and is greatly appreciated.

REFERENCES

Barnett, T. P., and J. C. Wilkerson (1967), On the generation of ocean wind waves as inferred from airborne radar measurements of fetch-limited spectra. J. Mar. Res. 25, 292.

Duncan, J. R., W. C. Keller, and J. W. Wright (1974), Fetch and wind speed dependence of Doppler spectra. Radio Science 9, No. 10, 809-819.

Hamilton, R. C., and E. G. Ward (1974), Ocean data gathering program-quality and reduction of data. Offshore Technology Conference Proceedings, OTC 2108-A, 750-756.

Hasselmann, K., T. P. Barnett, E. Bouws, H. Carlson, D. E. Cartwright, K. Enke, J. A. Ewing, H. Gienapp, D. E. Hasselmann, P. Kruseman, A. Meerburg, P. Muller, D. J. Olbers, K. Richter, W. Sell, and H. Walden (1973), Measurements of wind-wave growth and swell decay during the Joint North Sea Wave Project (JONSWAP), Deutsche Hydrogr. Z., Suppl. A(8°), No. 12.

Hasselmann, K., D. B. Ross, P. Mueller, and W. Sell (1975), A Parametrical Wave Prediction Model, submitted to Journal of Physical Oceanography.

Keller, W. C., T. R. Larson, and J. W. Wright (1974), Mean speeds of wind waves at short fetch. Radio Science 9, No. 12, 1091-1100.

Keller, W. C., and J. W. Wright (1975), Microwave scattering and the straining of wind-generated waves. Radio Science 10, No. 2, 139-147.

Mitsuyasu, H. (1971), Observations of the wind and waves in Hakata Bay. Rep. Res. Inst. Appl. Mech., Kyushu University, 19:37-74.

Patterson, M. M. (1974), Oceanographic Data from Hurricane Camille. Offshore Technology Conference Proceedings, OTC 2109.

Phillips, O. M. (1958), The equilibrium range in the spectrum of wind generated waves. J. Fluid Mech. 4(4), 426-434.

Pierson, W. J., and L. Moskowitz (1964), A proposed spectral form for fully developed wind seas based on the similarity theory of S. A. Kitaigorodskii. J. Geophys. Res. 69, 5181-5190.

Reece, A. M., and O. H. Shemdin (1974), Modulation of capillary waves by long waves. Symposium on Ocean Wave Measurement and Analysis, Amer. Soc. Civil Eng., New Orleans, Louisiana.

Ross, D., B. Au, W. Brown, and J. McFadden (1974), A remote sensing study of Pacific Hurricane Ava. Ninth International Symposium on Remote Sensing of Environment Proceedings, 15-19 April, 163-180.

Ross, D., and V. Cardone (1974), Observations of oceanic whitecaps and their relation to remote measurements of surface wind speed. J. Geophys. Res. 79, No. 3, 444-452.

Rouse, J. W., and R. K. Moore (1972), Measured surface spectrum dependence of back-scattering from rough surface. IEEE Trans. Antennas Propagat., AP-20, 211-213.

Valenzuela, G. R. (1968), Scattering of electromagnetic waves from a tilted, slightly rough surface. Radio Science 3, 1057-1066.

Wilheit, T. (1972), Nimbus-5 Users Guide, NASA Goddard Space Flight Center, Washington D.C.

Wright, J. W. (1968), A new model for sea clutter, IEEE Trans. Antennas Propagat., AP-16, 217-223.

Figure 1. The NOAA C130 aircraft show passive microwave sensors in the extended position.

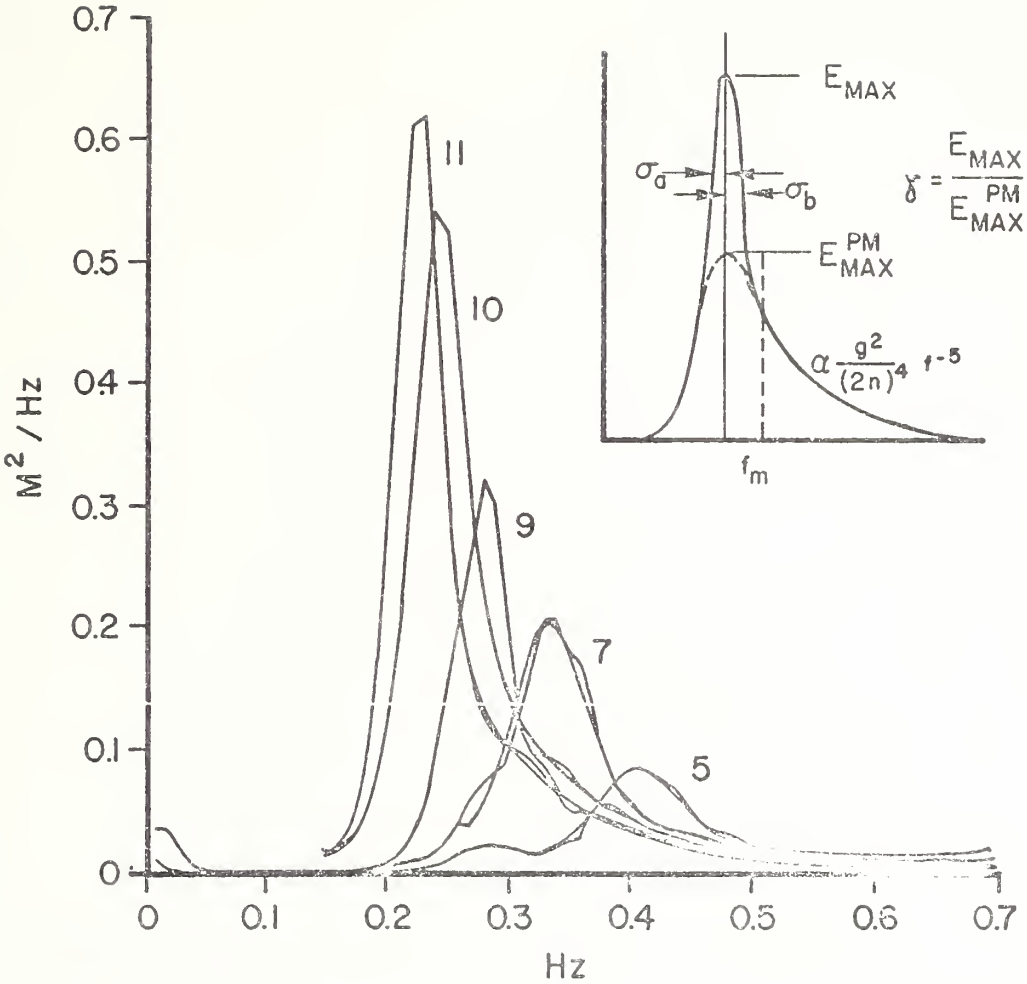

Figure 2. Growth of wave spectra for offshore wind conditions during JONSWAP-69. Fetch increases from Station 5 through Station 11. Three shape parameters σ_a, σ_b, and γ, and the scale parameters f_m and α suggested by Hasselmann are shown in the inset. γ is simply the ratio of the energy at f_m to that which would be predicted by the Pierson-Moskowitz (1964) form of the spectrum.

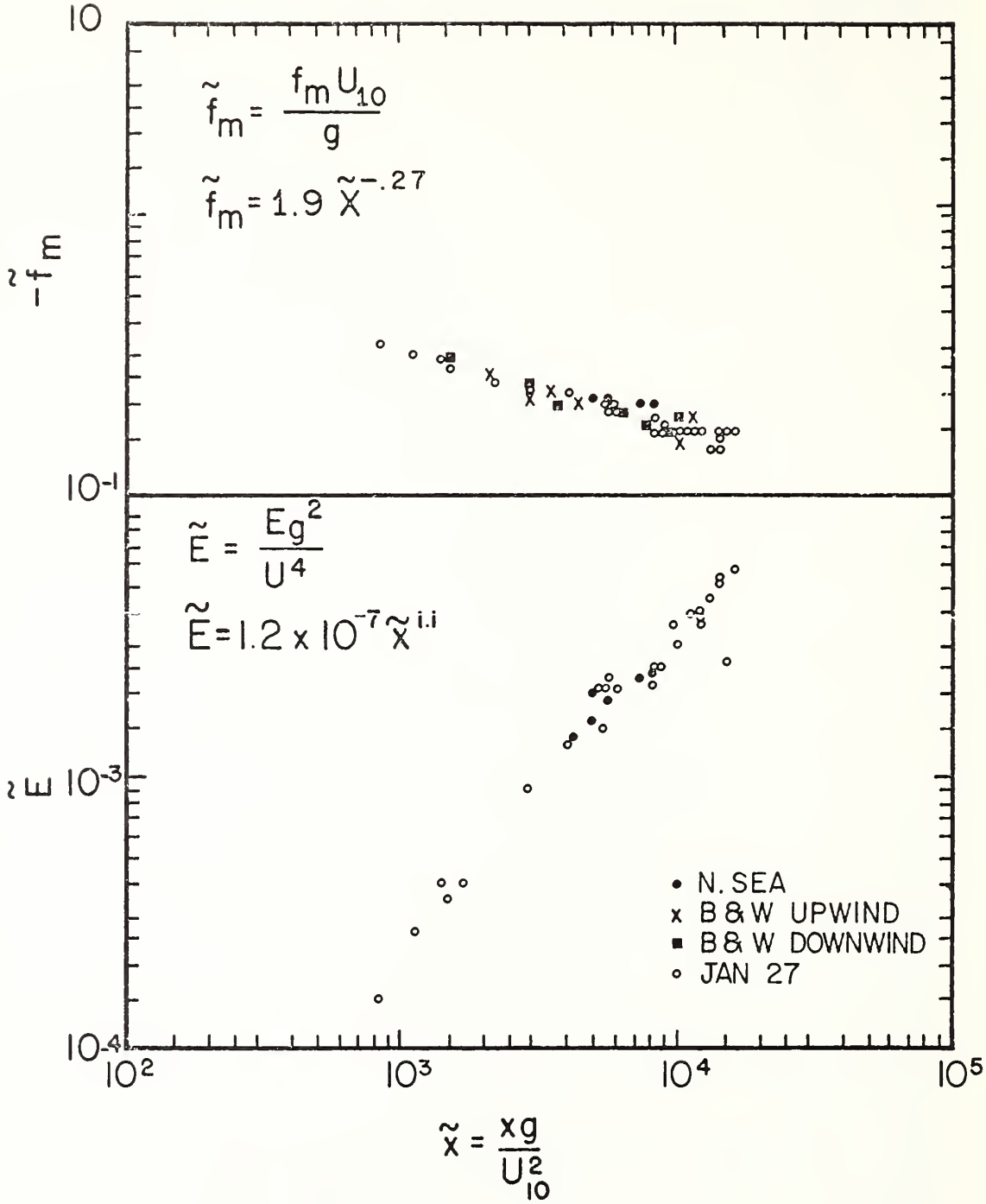

Figure 3. Dimensionless parameters $\tilde{E}$ and $\tilde{f}_m$ versus dimensionless fetch $\tilde{X}$ for high wind-speeds (15 to 25 m/sec) as determined by aircraft experiments in the North Sea and off Cape Fear, N. C., on 27 January (Ross and Cardone, 1974, and Barnett and Wilkerson, 1969).

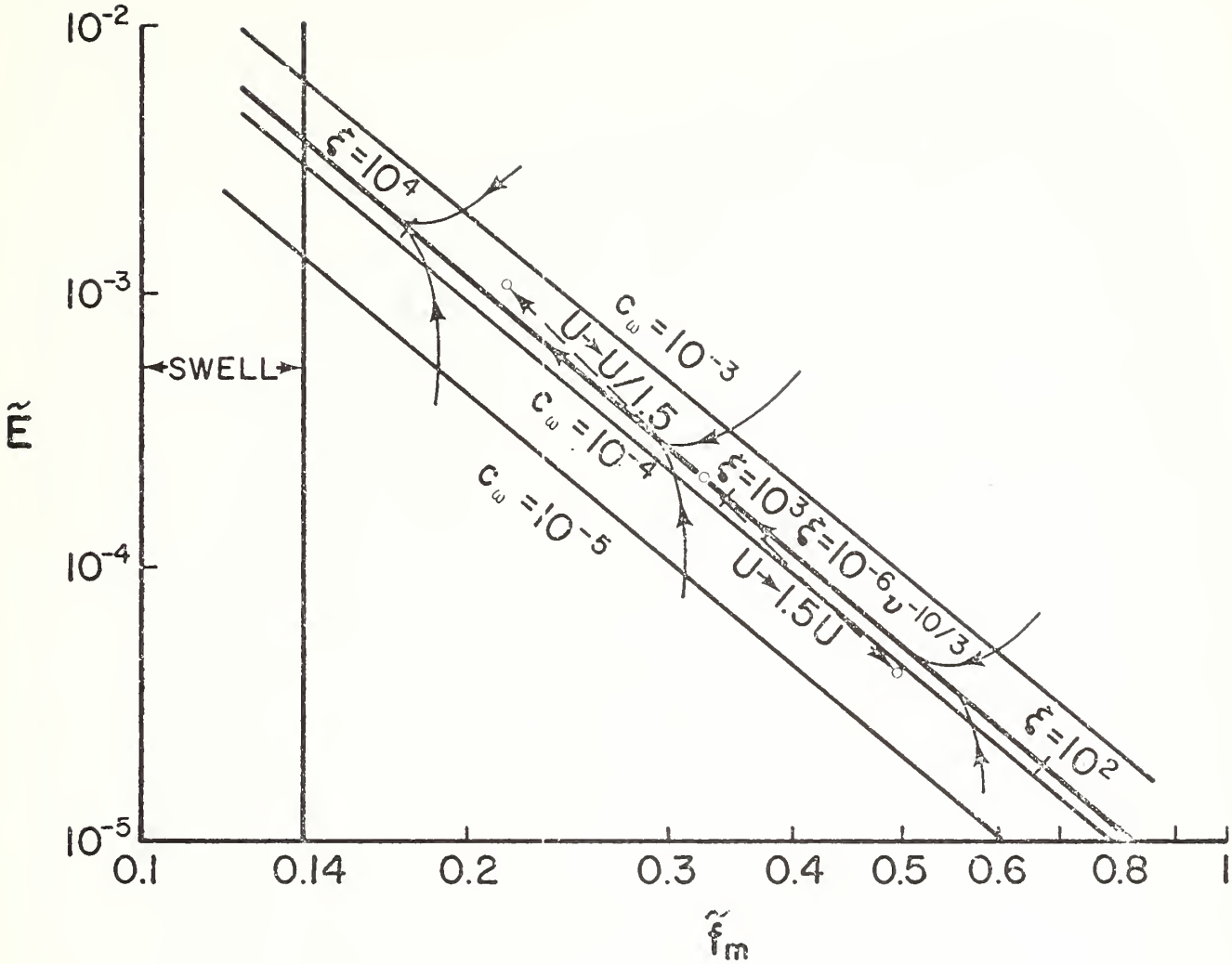

Figure 4. The behavior of $\tilde{E}$ and $\tilde{f}_m$ during growth. A sudden change of windspeed by a factor of 1.5 results in a departure from the mean followed by readjustment to mean condition along the curved lines indicated. Nondimensional fetch relationships $\tilde{X} = E = \frac{xg}{U_{10}^2}$ for particular $\tilde{f}_m$ are included. The upper and lower boundaries ($C_\omega = 10^{-3}$ and $C_\omega = 10^{-5}$) represent the limits of momentum being transferred to the wave spectrum.

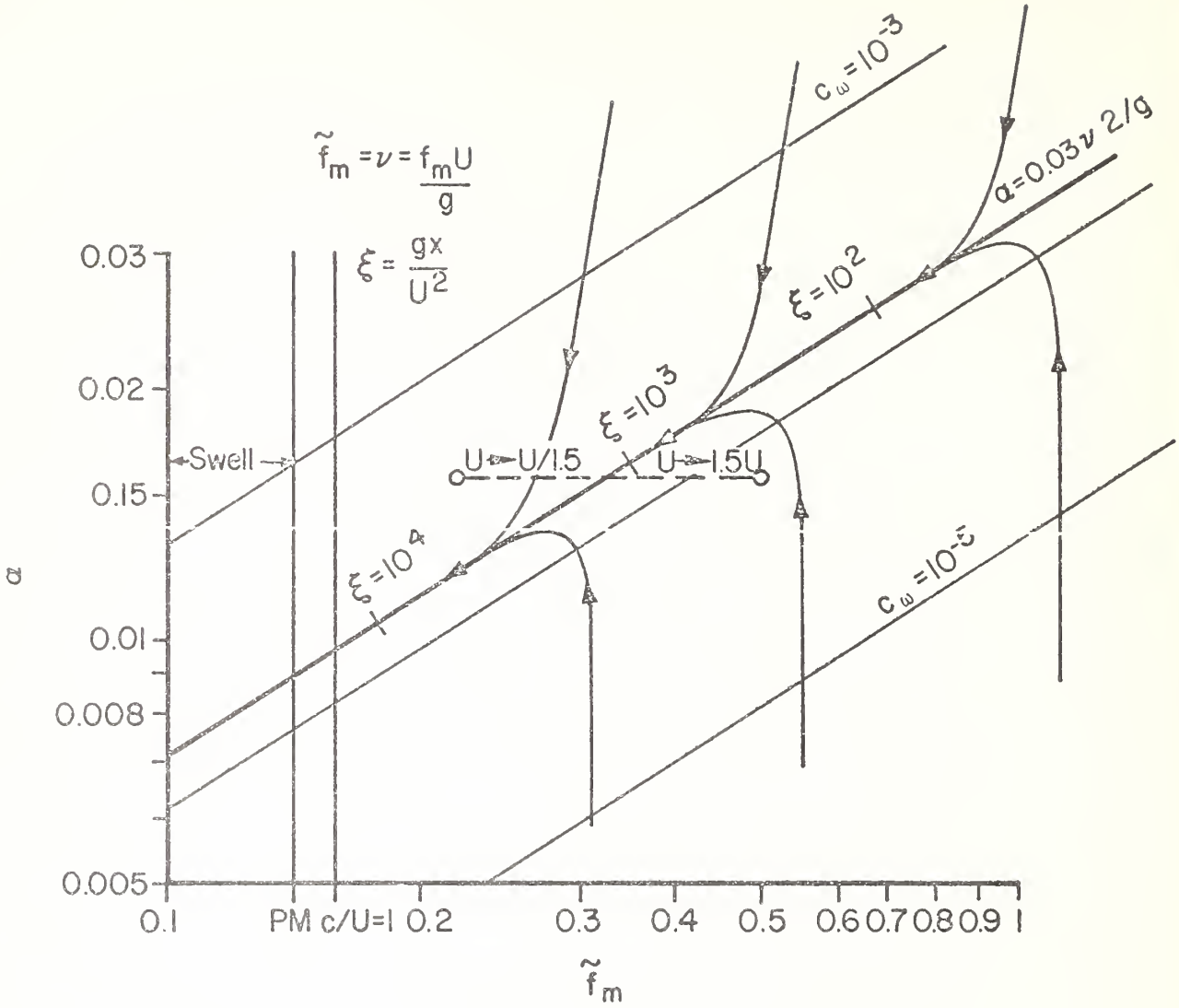

Figure 5. The Phillips parameter α versus $\tilde{f}_m$. Corresponding fetches ξ are indicated by the tick marks. The behavior of α during readjustment to a change in local wind (U) conditions is along the curved lines.

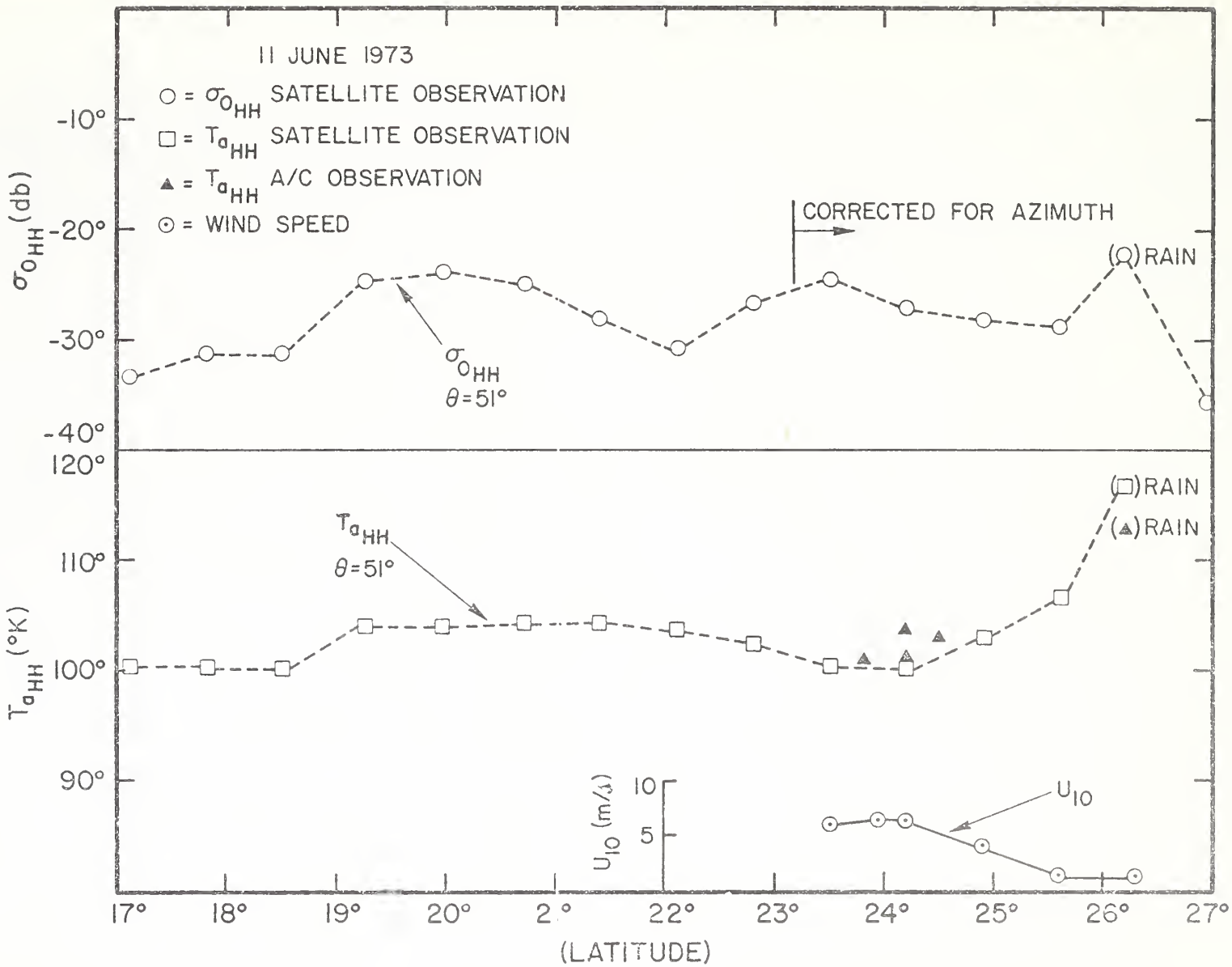

Figure 6. Skylab pass of 11 June in the Gulf of Mexico.

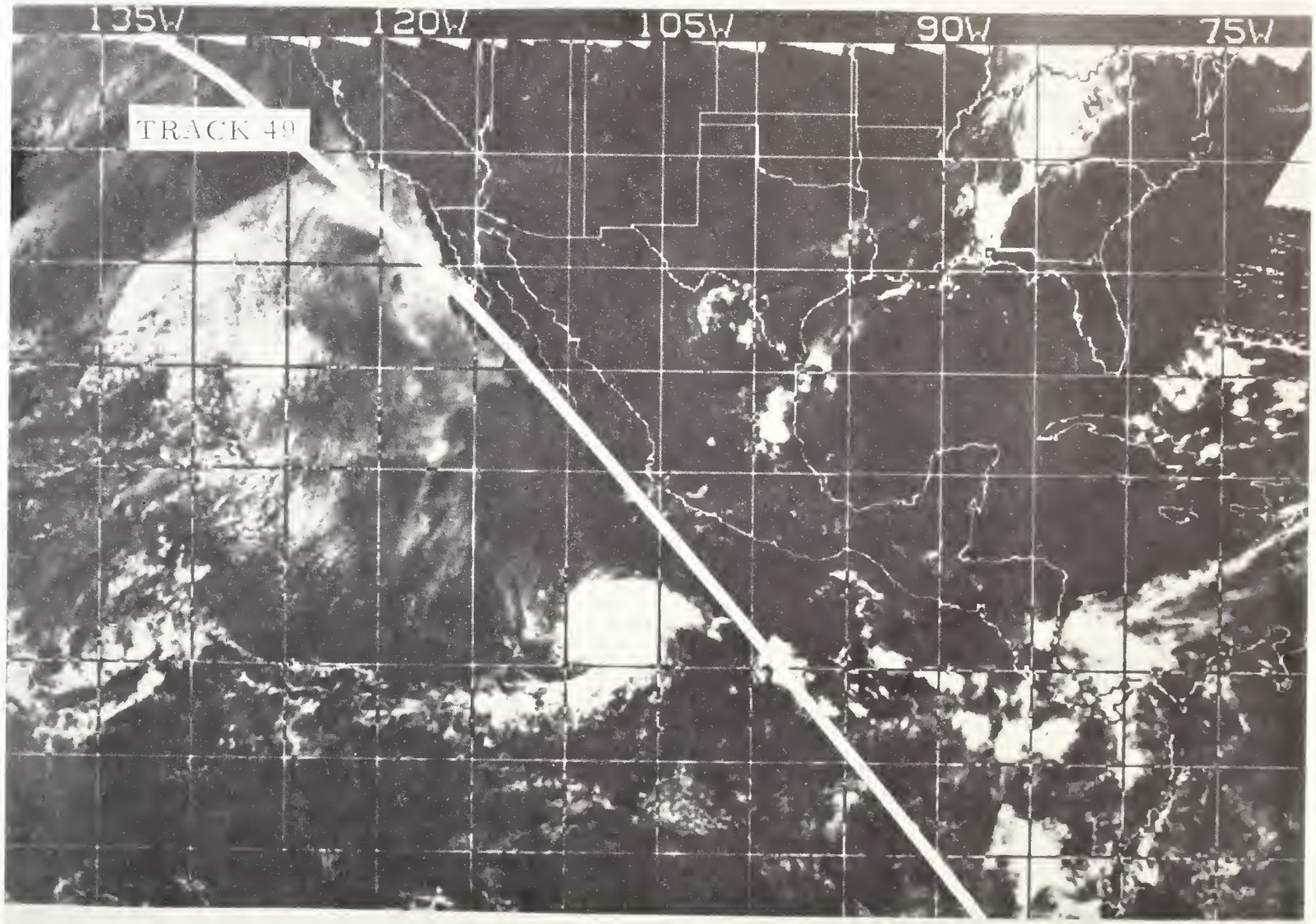

HURRICANE AVA, JUNE 6, 1973, NOAA 2 COMPOSITE

Figure 7. Hurricane Ava, June 6, 1973, NOAA-2 composite showing track of Skylab satellite.

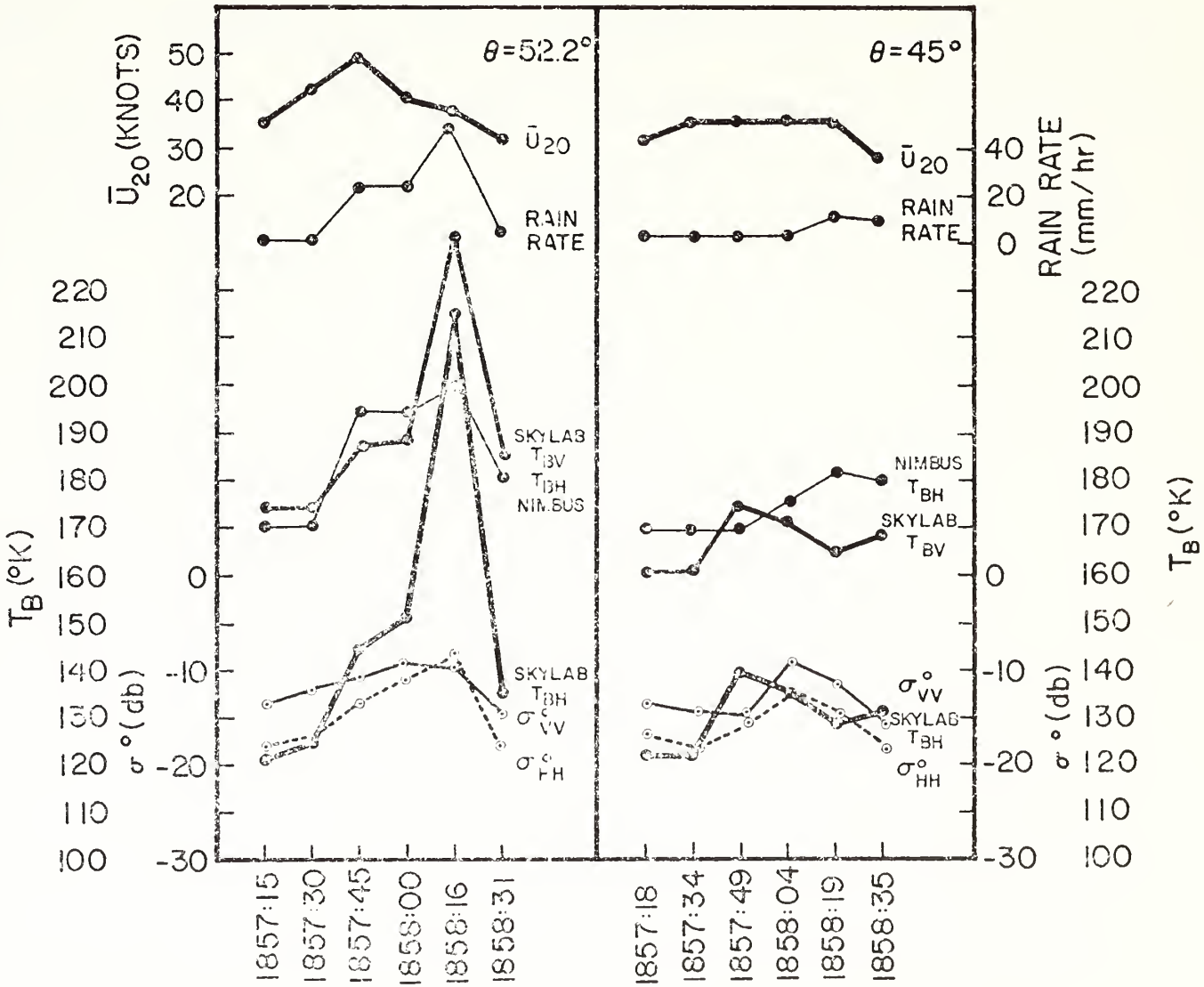

Figure 8. Skylab and NIMBUS-E data in Hurricane Ava.

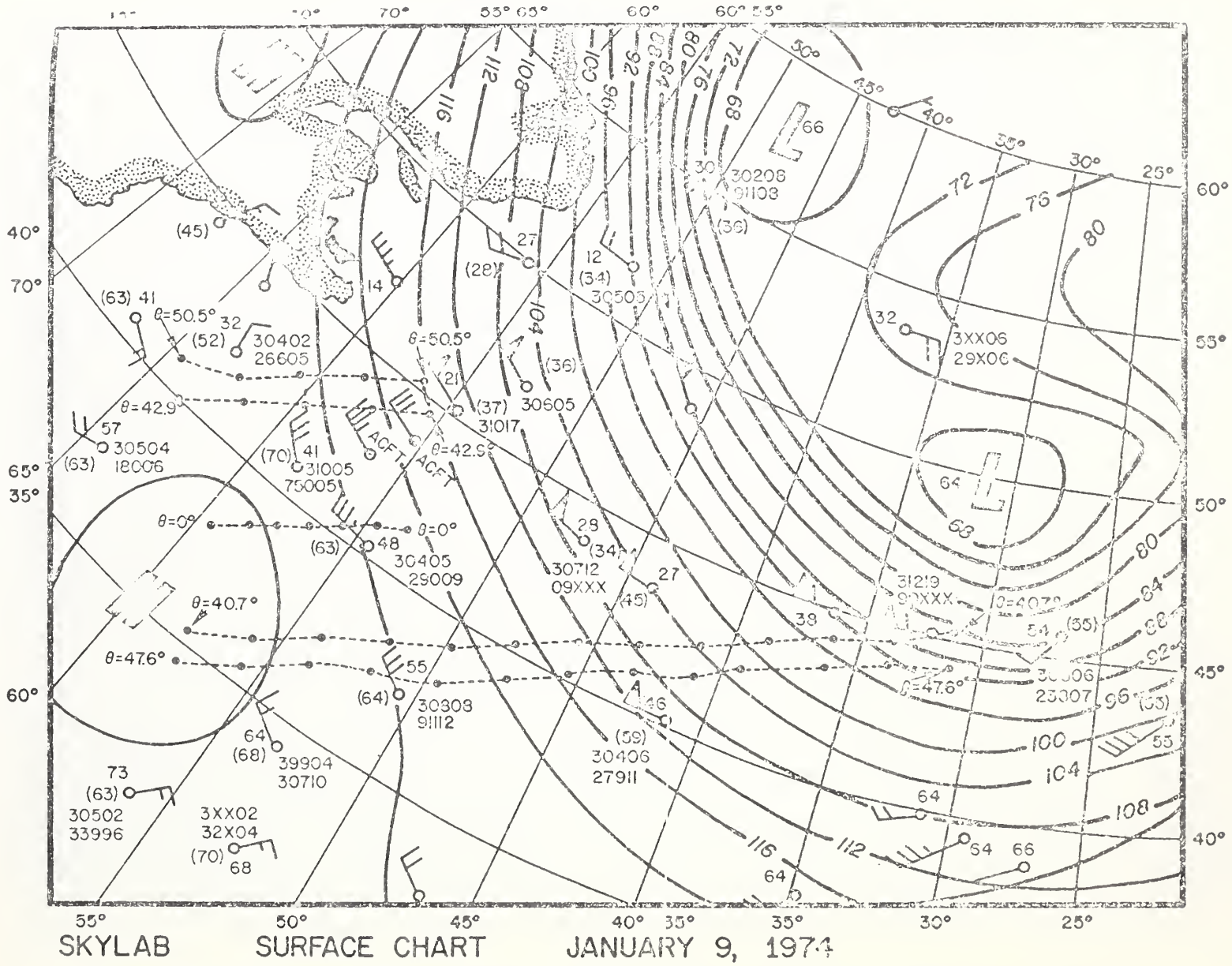

Figure 9. Surface meteorological analysis for 9 January 1974 pass. Subsatellite positions of S-193 under study are shown for the indicated incidence angles.

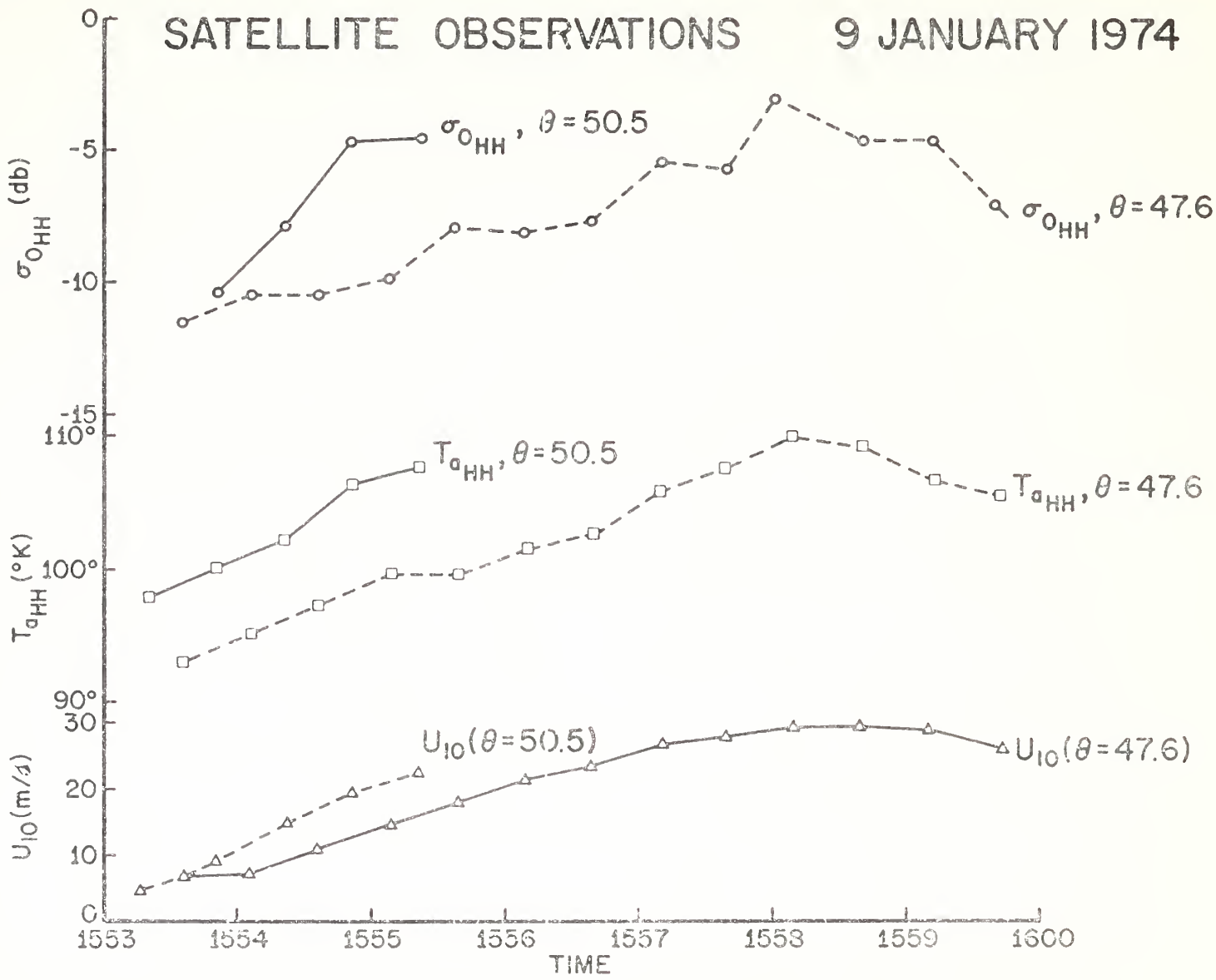

Figure 10. S-193 data during the 9 January pass along with surface winds determined from the surface analysis.

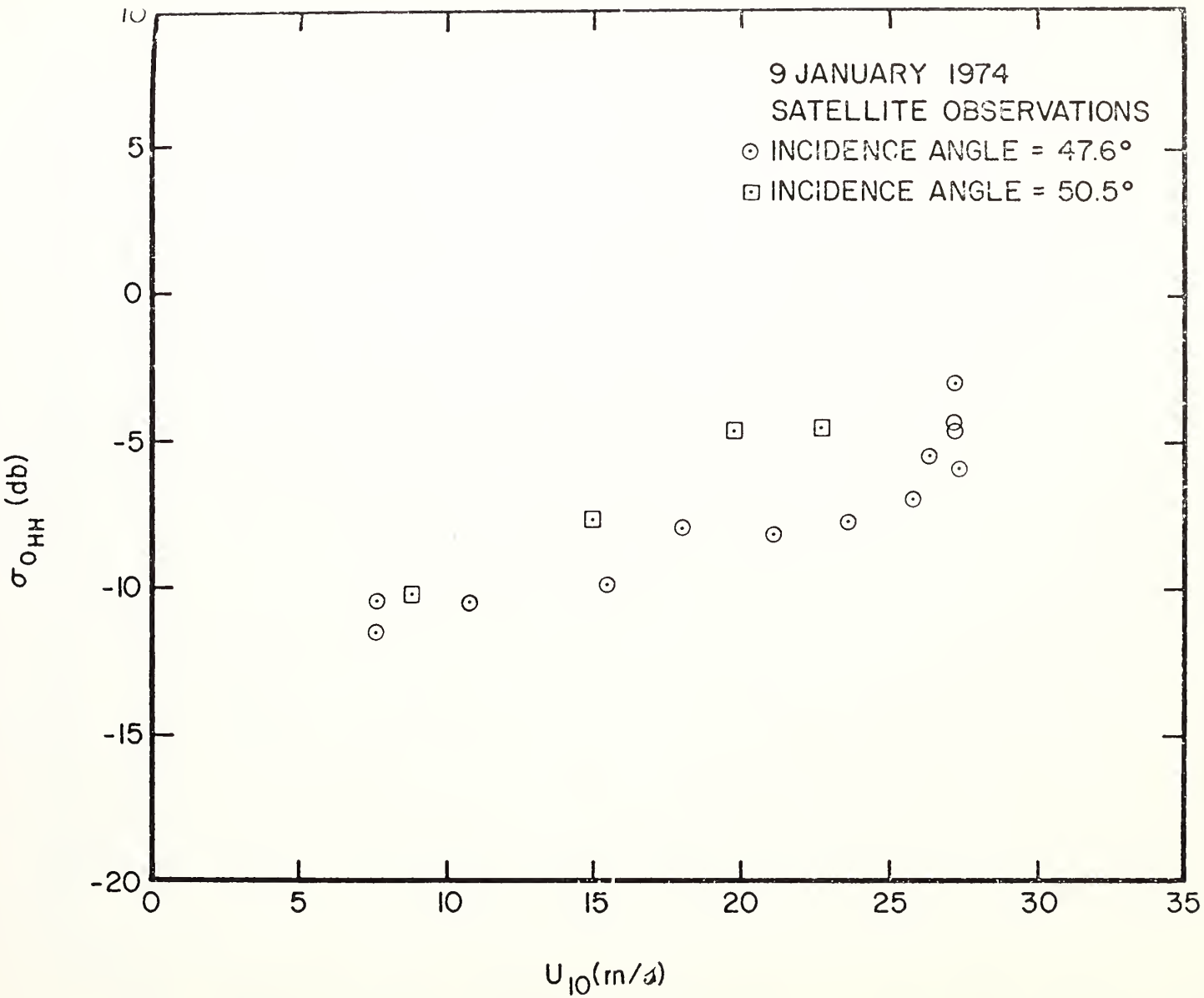

Figure 11. Radar backscatter, σ_0 versus windspeed for 9 January.

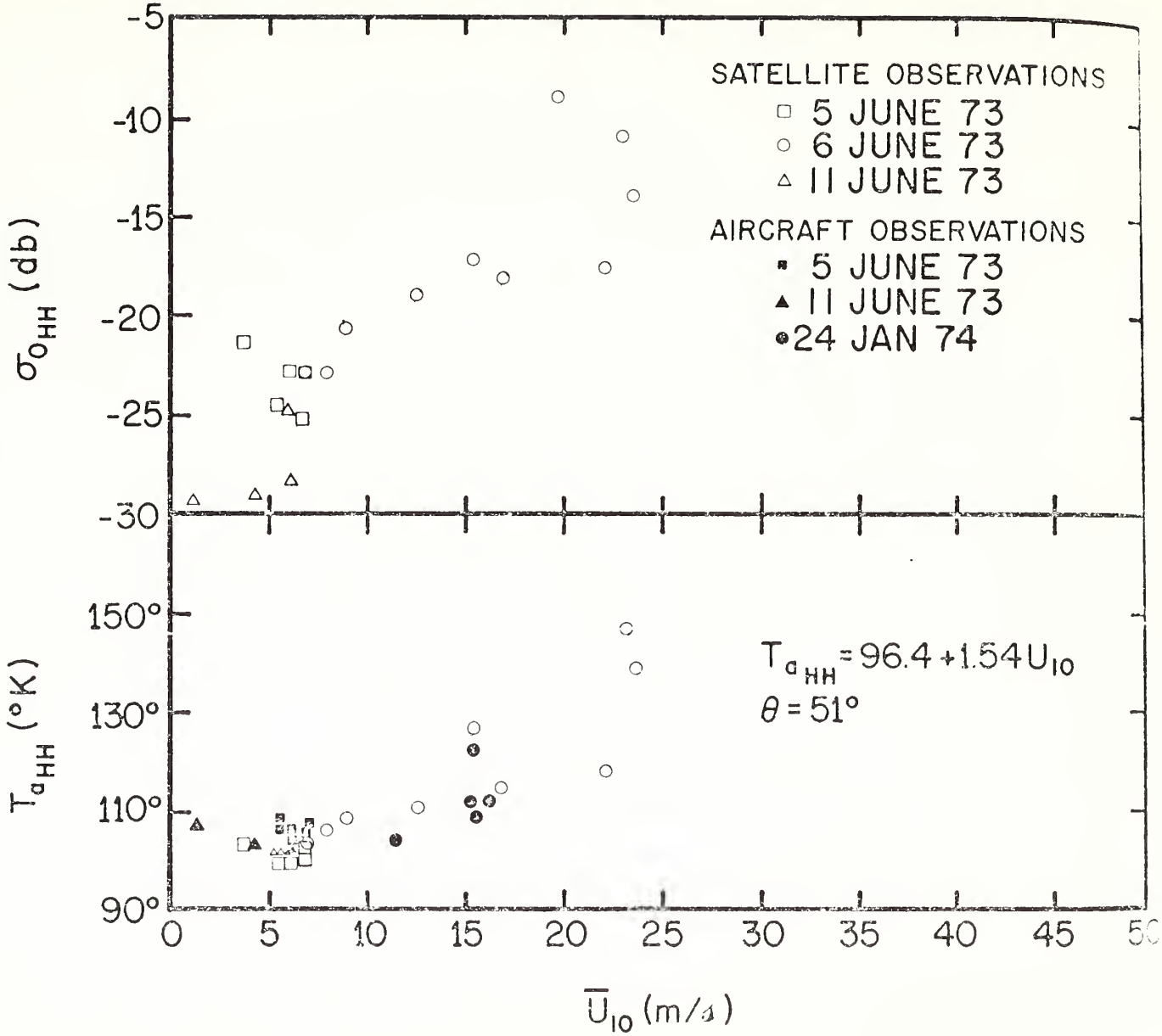

Figure 12. Radar backscatter and antenna temperature versus windspeed during SL-2.

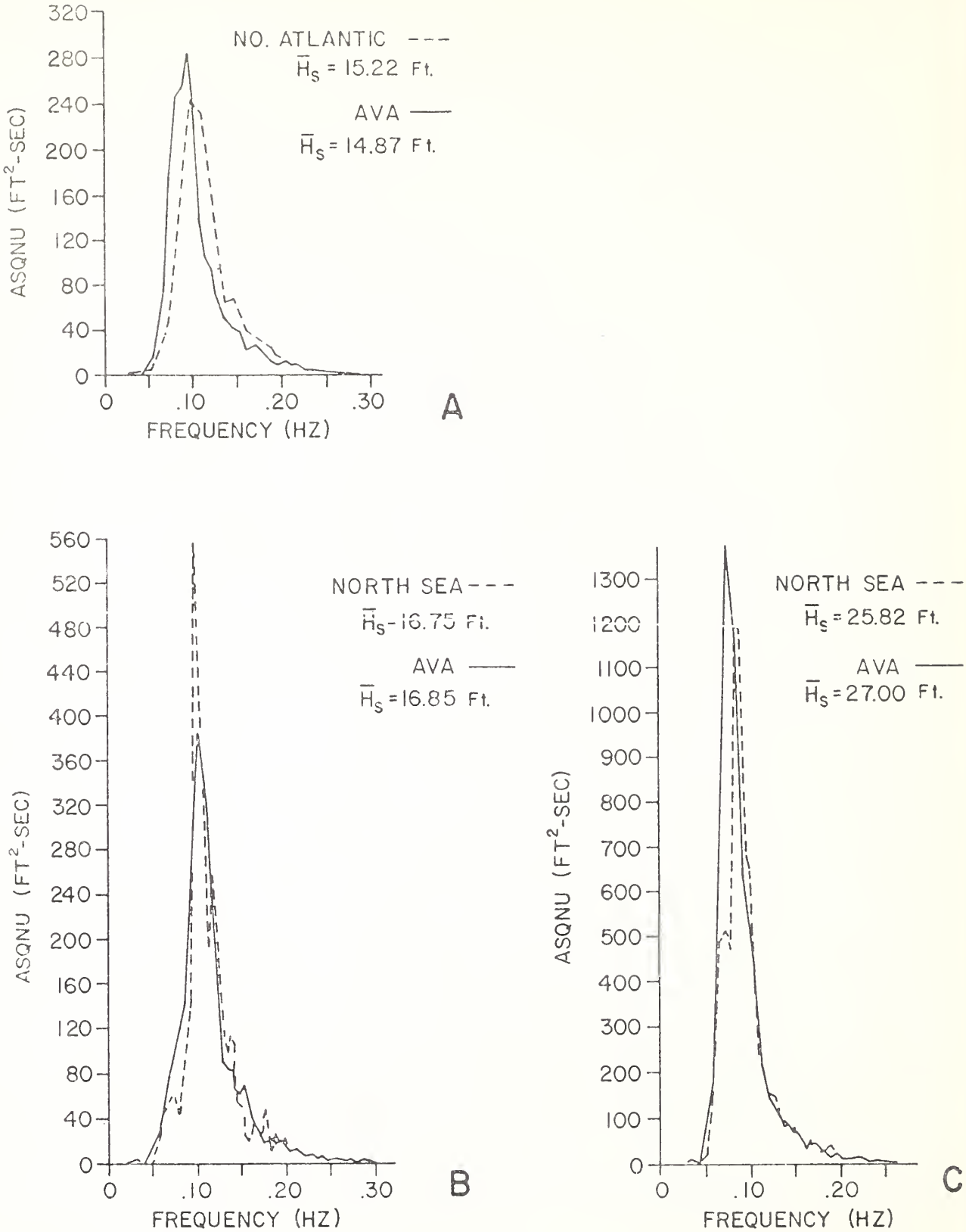

ure 13. Wave spectra measured during the aircraft penetration of Hurricane Ava along with North Sea spectra for fetch-limited 25 m/sec winds.

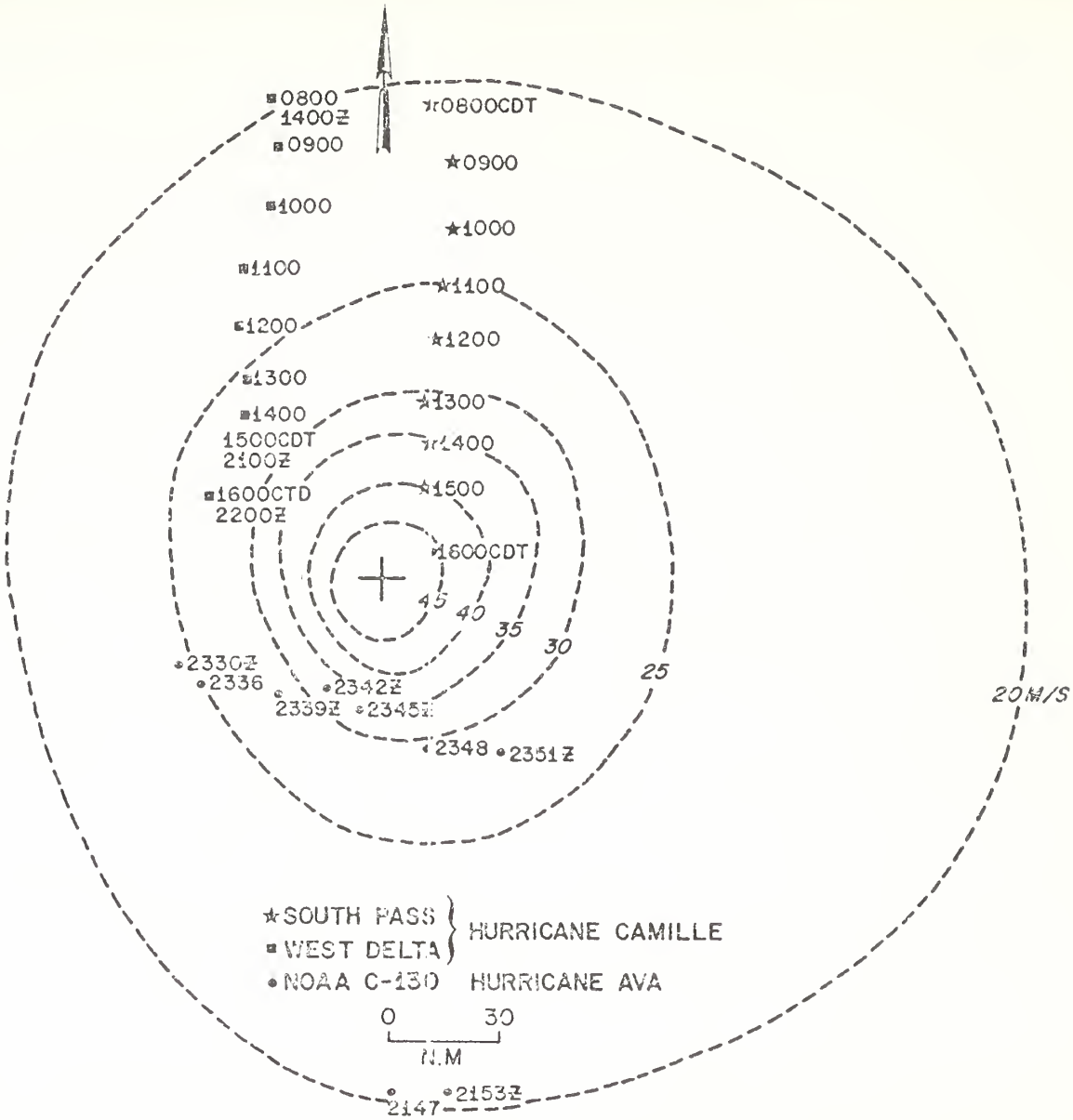

Figure 14. Surface wind analysis for hurricane Ava constructed from aircraft data along with relative positions of wave data obtained in Ava and for Hurricane Camille.

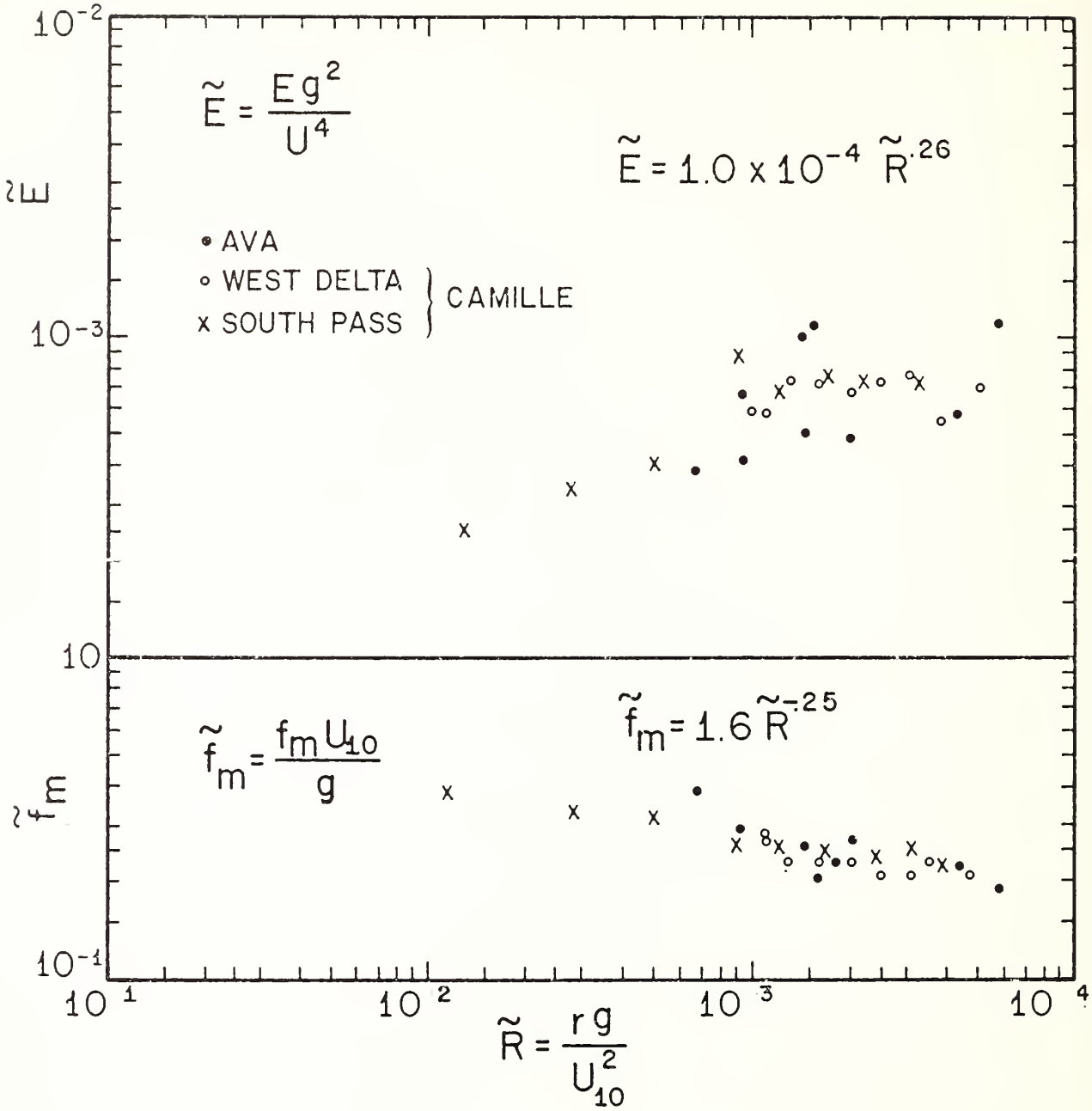

Figure 15. Behavior of nondimensional energy, E, and peak frequency, $\tilde{f}_m$, versus radial distance from eye. $\tilde{R} \approx 10^2$ constitutes the region of maximum winds.

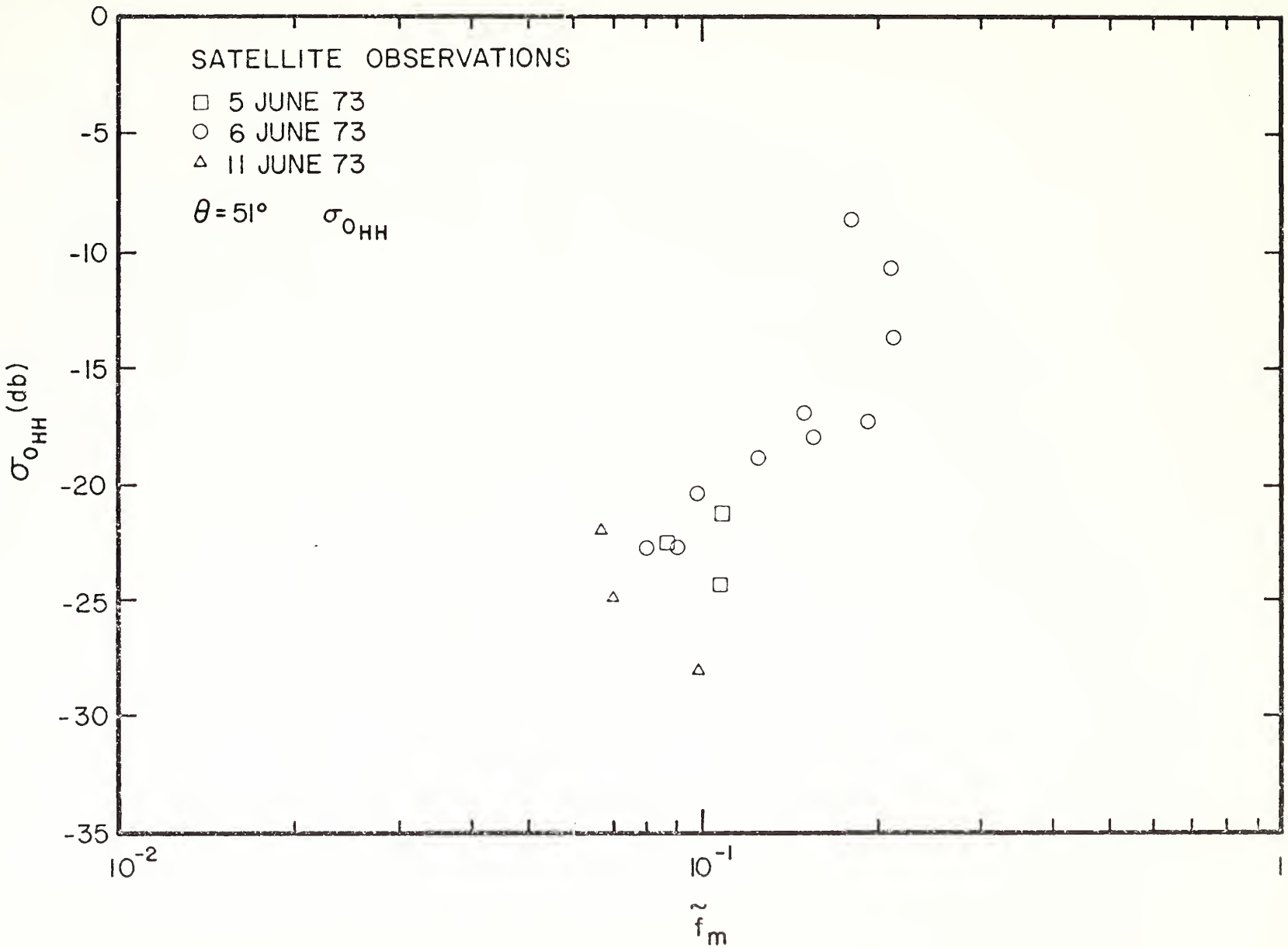

Figure 16. Radar backscatter, σ_0, versus stage of wave development as represented by non-dimensional peak frequency $\tilde{f}_m$ for the SL-2 data set.

Reprinted from: *Journal of Geophysical Research 80*, No. 27, 3841-3847.

Dropped Horizontal Coherence Based on Temperature Profiles in the Upper Thermocline

GILBERT R. STEGEN[1]

Department of Geological and Geophysical Science, Princeton University, Princeton, New Jersey 08540

KIRK BRYAN AND JOANN L. HELD

Geophysical Fluid Dynamics Laboratory, NOAA, Princeton University, Princeton, New Jersey 08540

FEODOR OSTAPOFF

Atlantic Oceanographic and Meteorological Laboratories, NOAA, Virginia Key, Florida 33149

A series of 66 temperature profiles taken in the open ocean 350 km north of Puerto Rico are analyzed to determine the displacement spectrum and the dropped horizontal coherence. The results are not inconsistent with the Garrett and Munk model. One interesting exception is a tendency for the horizontal coherence not to fall off monotonically with decreasing vertical scales

INTRODUCTION

For years, oceanographers have been aware of small-scale high-frequency variability in the ocean thermocline. This variability gives rise to a major source of sampling error in the determination of large-scale features of the thermocline from standard hydrographic data. Only recently have experimental techniques allowed direct measurements of the fine structure of temperature, salinity, and velocity in the main thermocline. Vertical profiles are now routinely obtained by detailed CTD (conductivity, temperature, and depth) measurements and free falling devices. Extensive measurements along horizontal tracks have also been obtained by towed thermistors. The most important source of data has been long time series in velocity and temperature obtained from moored instruments, sometimes located in small arrays to allow measurements of spatial coherence at different frequencies.

The time series measurements of velocity in the main thermocline carried out by the Woods Hole Oceanographic Institution [*Fofonoff*, 1969] showed that a great deal of the fluctuating energy in the thermocline is contained in the frequency range of inertial gravity waves, $N > \omega > f$, where ω is the observed frequency and N and f are the Brunt-Väisälä and inertial frequencies, respectively. Using the WKB approximation and the theory of internal inertial gravity waves, *Fofonoff* [1969] and *Webster* [1968] have been able to explain several important features of the current meter statistics. These ideas have been extended much further in an important paper by *Garrett and Munk* [1972] in which a model of the displacement and velocity spectra in the internal inertial gravity wave range is proposed. The WKB approximation is relaxed, and the model depends only on the total depth of the thermocline, the local inertial frequency, and the local range of Brunt-Väisälä frequency. The model makes use of relationships expected from small amplitude theory of internal inertial gravity waves but is calibrated against existing observations. Whether all details of this very interesting synthesis are verified by future measurements is perhaps less important than the tremendous contribution of the model in providing a guide to other investigators in analyzing and scaling diverse observations of variability in the ocean thermocline.

One prediction of the *Garrett and Munk* [1975] revised model that has not yet been tested against observations is the DHC, or dropped horizontal coherence. This quantity is a measure of the horizontal persistence of the velocity, or vertical displacement, of surfaces of constant density. The present study describes a set of measurements that provide a preliminary measure of the DHC in the tropical North Atlantic, approximately 350 km north of San Juan, Puerto Rico. In this region the temperature structure is well-defined with a mixed layer down to approximately 60 m and a strong decrease in temperature down to 500 m. At 500 m there is a layer of nearly uniform temperature. Below this, there is another layer of rapidly decreasing temperature in the main thermocline. In the present study we are only concerned with temperature profiles taken in the upper layers from the surface down to 450 m. The profiles were taken with expendable bathythermograph probes (XBT's) launched from a moving ship, the NOAA ship *Discoverer*. The XBT's were launched every 2 min as the ship maneuvered in a basic X pattern at about 6 km/hr, the minimum required for control. The track of the ship is shown in Figure 1. All the XBT launches are indicated in this plot. However, only the solid circles represent positions of profiles actually used in this study. The ship navigated in relation to a Nomad (AN/SMT-1) buoy which was drogued at 30 m. Fixes of the buoy were taken from the bridge every 5 min during the experiment. The fixes were combined with the drift pattern of the buoy to generate the absolute track of the ship shown in Figure 1.

In order to use the data from the XBT records to compute DHC it is necessary to subtract out the mean temperature profile. The next step is to divide the temperature deviation in each profile by the vertical gradient of the horizontally averaged temperature. This converts the temperature anomalies into displacement anomalies. In comparing the DHC computed from these anomalies with the *Garrett and Munk* [1975] predictions it must be recognized that the measurements are not truly synoptic, since there is a finite time interval between launches.

[1] Now at Flow Research, Inc., Kent, Washington 98031.

Copyright © 1975 by the American Geophysical Union.

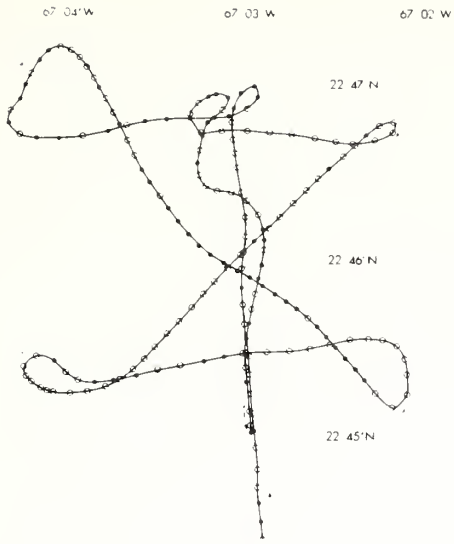

Fig. 1. Course of the NOAA ship *Discoverer* during the experiment on October 12, 1971. Each open circle marks an XBT drop. A solid circle indicates that the temperature profile was used in this study.

Some loss of coherence due to this time lag must be expected. Ultimately, completely synoptic measurements of conductivity, temperature, and depth must be carried out for different separation distances, but it will require a major effort involving a joint operation of at least two research vessels.

EXPERIMENT

Site. The measurements were made on October 12, 1971, at 22°46'N and 67°03'W. The average temperature profile from all the XBT casts used in our analysis is shown in Figure 2*a*. A persistent 'bump' in the profile is indicated at about 160 m. Its origin is not clear, but it is probably the result of an earlier water mass intrusion. Such features have been found by several investigators [e.g., *Mazeika*, 1974] in this part of the tropical Atlantic and appear to be similar to the steps found by *Tait and Howe* [1968] associated with the Mediterranean outflow. The present study is concerned with those features of the temperature structure which might be expected to be found at many sites, so that the persistent intrusions are a source of contamination which we attempt to remove from the profiles by subtracting the mean shown in Figure 2*a* from each individual profile. Estimates of the Brunt-Väisälä frequency are obtained from an STD cast made at the site a few hours before the main experiment. The data from the STD cast are first converted to N^2 and then smoothed in the vertical. The profile of N shown in Figure 2*b* is obtained from the smoothed curve of N^2. (It should be noted that the alternate procedure of first calculating a profile of N and then smoothing gives quite different results!) Mean values of N for the upper layers can also be derived by using salinity data obtained from hydrographic stations made during the IGY [*Fuglister*, 1960] in the same area and the temperature profile shown in Figure 2*a*. The results shown in Table 1 show fair agreement between the two sets of data.

XBT data. The XBT probes were the standard Sippican model T-4. The absolute temperature accuracy of the XBT system is ±0.2°C, the errors being equally divided between probe and recorder. A more important source of error is in the accuracy of the probe depth, which is specified as ±2%. The depth errors are of two kinds. Since the XBTsystem measures

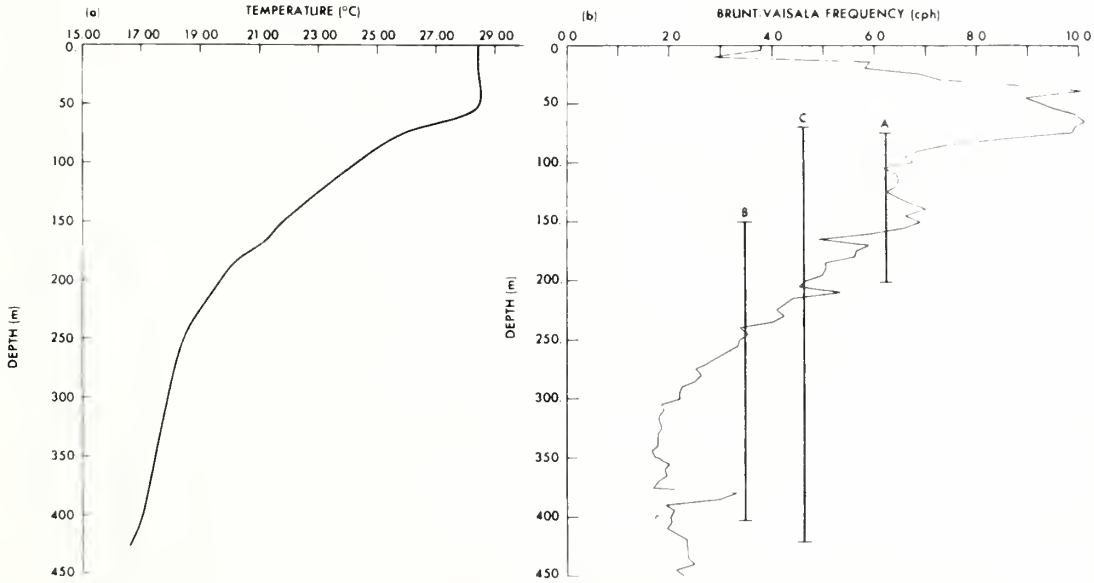

Fig. 2. (*a*) Average temperature profile. Temperature profiles from 74 XBT casts were used. (*b*) Brunt-Väisälä frequency representative of the area at the time of the experiment. It shows the frequency after nine-point smoothing was applied to STD data taken at the site. The vertical bars indicate the range of frequencies included in each of the three cases considered in this study: A, N = 6.2189 cph for depth range 75–203 m; B, N = 3.4547 cph for 150–406 m; C, N = 4.6212 cph for 69–420 m.

TABLE 1. Comparison of the Average Values of N

	75 m < -z < 203 m	150 m < -z < 406 m
N_{STD}	6.22	3.45
N_{IGY}	7.17	3.50

Values were obtained from a single STD cast and from a combination of the salinity data obtained during the IGY and the temperature data given in Figure 2a. Units are cph.

depth relative to the point at which the probe enters the water, the absolute depth below an average surface will have a random error introduced by surface waves (wave height is 1.5 m in the present study). Another source of error is due to deviations from the calibrated fall velocity of the probe. This second source gives a relative error which increases as the total depth increases. These two sources of error will be discussed further in connection with the method of data reduction.

The standard output from the XBT system is an analog trace on pressure sensitive paper. Conversion of these traces to digital data for computer analysis poses a formidable challenge. In the present study the analog traces were photographed with 'litho' film to produce a high-contrast 4 × 5 in. negative. This entire negative was then digitized with a scanning microdensitometer which had a 1000 : 1 range in sensitivity to film density and gave a matrix of 1000 × 800 values over the negative. The digitized density values were written directly onto a nine track 800 bits/in. IBM compatible magnetic tape. A computer search of the tape identified all points above a threshold intensity and delineated the trace. The data were digitized in this manner rather than by hand or by some other process in order to obtain better resolution, reduce the noise from the digitizing process, and save time. Unfortunately, not all of these objectives were realized. The XBT recording paper grid scale was almost the same intensity as the trace, so that it was often not possible to differentiate between the trace and the grid. Thus some original records which were otherwise perfectly good could not be included in the final data set.

Using fiducial marks photographed with the traces facilitated calibration of the temperature and depth scales and correction for the nonlinearities in the temperature and depth scales of the Sippican recorder. The data were interpolated to equal depth increments of 0.5 m. Finally, the computer compatible data set was plotted on an 8- × 10-in. scale and compared to the original data set. Traces whose temperatures did not agree to within ±0.05°C everywhere were discarded.

The sorted records were averaged to form the average temperature-depth curve shown in Figure 2a. In view of the uncertainties in absolute depth an additional quality control check was applied. For each individual profile the following integrals were calculated,

$$S(\Delta z) = \frac{1}{N} \sum_n [\bar{T}(z_n) - T(z_n + \Delta z)]$$

and

$$\sigma(\Delta z) = \frac{1}{N} \sum_n [\bar{T}(z_n) - T(z_n + \Delta z)]^2$$

where $\bar{T}(z)$ is the average profile in Figure 2a. Figure 3 shows a typical plot of $\sigma(\Delta z)$ as a function of the vertical displacement. In most cases the displacement Δz at which $S(\Delta z)$ and $\sigma(\Delta z)$ were a minimum closely coincided. Where the two minimums

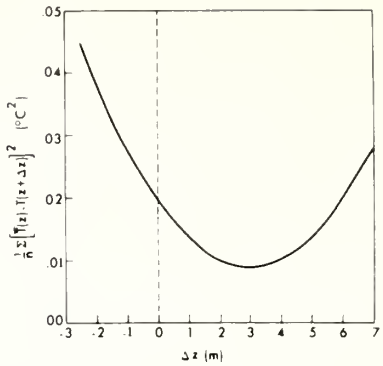

Fig. 3. Temperature variance of a typical curve for various vertical displacements. This information was calculated for each temperature profile and the displacement associated with the minimum variance was used to correct the depth.

were located more than 2.5 m apart, the profile was discarded. To correct for possible errors in the depth scale in the raw data or because of the data processing, the whole profile is shifted vertically to minimize $\sigma(\Delta z)$. In all cases the adjustment of the depth scale was within the specified uncertainty of the probes. A description of the final data set is shown in Table 2.

The adjustment described above minimizes the effect of a uniform depth error throughout the profile that might be caused by the processing procedure or by the distortion of the free surface due to wind waves. To investigate whether some of the variance of temperature may be associated with errors in fall velocity, the following test was carried out. For a single profile the depth corresponding to a given temperature was changed corresponding to a difference in fall velocity of 1, 2, and 3%. This is equivalent to displacements of $\Delta z = 1.01z$, $1.02z$, and $1.03z$. With these new displacements the variances of the mean temperature minus the temperature $\sigma(\Delta z)$ are recalculated. The variances associated with a 1% error in fall speed fell within the range calculated before a constant depth correction was made. Variances associated with a 2% or greater error in fall speed fell outside of the variance range of the corrected traces. The conclusion from this test is that random errors of 1% of the depth due to erroneous fall rates are possible but greater random errors would lead to larger values of $\sigma(\Delta z)$ than are seen in the profiles retained in the data set.

SCALING AND THE GM75 MODEL

For convenience in comparing our data set with the *Garrett and Munk* [1972] model we will adopt the same scaling

TABLE 2. Total Number of Pairs for Different Separation Distance Out of a Total of 66 Records

Space Separation, m	Time Separation, min	Number of Records
0-150	<2	12
150-300	<4	34
300-450	<6	31
450-600	<8	31
600-750	<10	22
750-900	<12	18
900-1050	<14	19
1050-1200	<16	19

TABLE 3. Dimensioned Variables and Scale Parameters

Quantity	Symbol	Value
Vertical wave number	$\hat{\beta}$	...
Horizontal wave number	$\hat{\alpha}$	...
Horizontal separation	$\hat{X}$	...
Displacement squared	$\hat{F}_\zeta$	...
Scale wave number	$\hat{M}_0$	0.122 cycle/km
Inertial frequency	$\hat{f}$	0.0312 cph
Standard B-V frequency	$\hat{N}_0$	3.0 cph

and notation. Let a circumflex denote dimensioned variables, while the absence of a circumflex denotes a dimensionless quantity. When the quantities defined in Table 3 are used, the nondimensional variables are $n = \hat{N}/\hat{N}_0$, $\omega_i = \hat{f}/\hat{N}_0$, $\beta = \hat{\beta}/\hat{M}_0$, $\alpha = \hat{\alpha}/\hat{M}_0$, and $X = \hat{X}2\pi\hat{M}_0$. Here $\hat{N}$ is the local Brunt-Väisälä frequency, and ω_i is the dimensionless inertial frequency.

With this notation the energy spectrum specified by GM75 [*Garrett and Munk*, 1975] is

$$E(\alpha, \beta) = \frac{2\pi^{-1}\omega_i E n \beta A(\beta/\beta^*)}{\beta^*(n^2\alpha^2 + \omega_i^2\beta^2)} \tag{1}$$

for the range

$$0 \le \alpha \le \beta[1 - \omega_i^2/n^2]^{1/2} \tag{2}$$

where E is a dimensionless constant and β^* is a scale vertical wave number. Both constants are chosen by *Garrett and Munk* [1975] to fit the data. Here $A(\beta/\beta^*)$ is a shape function,

$$A = 1.5(1 + \beta/\beta^*)^{-2.5} \tag{3}$$

Let Z^2 be the fraction of the total energy which is potential energy, where

$$Z^2 = \frac{\alpha^2 n^2}{\alpha^2 n^2 + \omega_i^2\beta^2} \tag{4}$$

Isotropy in the horizontal plane is assumed. The displacement spectrum is given as

$$F_\zeta(\beta) = \iint Z^2 E(\alpha, \beta)\, d\alpha \tag{5}$$

For any two points separated by some distance X the expression for the cross spectrum is [e.g., *Phillips*, 1966, pp. 74–78]

$$C(X, \beta) = \int_0^\infty (2\pi)^{-1} \int_0^{2\pi} Z^2 E(\alpha, \beta) \cdot \exp(i\alpha X \cos\phi)\, d\phi\, d\alpha \tag{6}$$

Since $\int_0^{2\pi} \exp(i\alpha X \cos\phi)\, d\phi = 2\pi J_0(\alpha X)$, the coherence of vertical scales may be expressed as

$$R(X, \beta) = \frac{\int_0^\infty Z^2 E(\alpha, \beta) J_0(\alpha X)\, d\alpha}{\int_0^\infty Z^2 E(\alpha, \beta)\, d\alpha} \tag{7}$$

It is interesting to note that shape function $A(\beta/\beta^*)$ is independent of α and cancels out in the formula for the DHC. Since the difference between GM72 and GM75 is associated with $A(\beta/\beta^*)$, both models would predict the same curve for the DHC. Making use of (1) and (4) to eliminate $E(\alpha, \beta)$ and Z^2, respectively, the expression for DHC is

$$R(X, \beta) = G(\beta\omega_i X/n) \tag{8}$$

Let $\gamma = \alpha n/\beta\omega_i$ and

$$G(\beta\omega_i X/n) = \frac{4}{\pi}\int_0^\infty \gamma^2(1 + \gamma^2)^{-2} J_0(\beta\omega_i\gamma X/n)\, d\gamma \tag{9}$$

In the next section we will compare the predictions of F_ζ given in (5) and DHC given in (8) and (9) with our data set.

ANALYSIS OF THE DATA

The displacement spectra obtained by combining all 66 profiles are shown in Figure 4. Three different depth ranges are shown. The abscissa is the log of the vertical wave number normalized by n. No band smoothing or tapering of the records is involved in the spectral estimates shown in Figure 4. Sixty-six degrees of freedom imply an 80% confidence limit of ±40% [*Blackman and Tukey*, 1958]. The spectra are shown with the predicted curve for the GM75

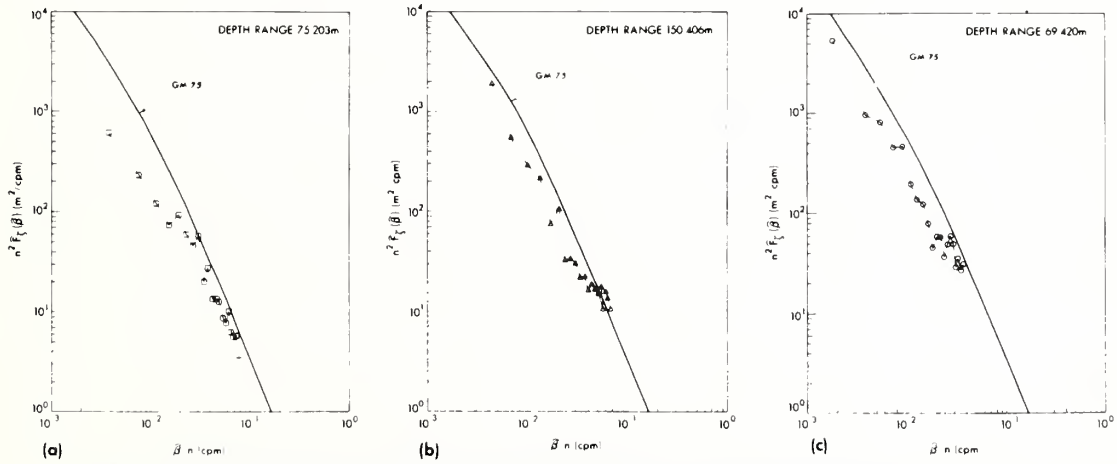

Fig. 4. Displacement spectra of the data in this study compared to GM75. $\hat{F}$ and $\hat{\beta}$ are normalized by n, the average Brunt-Väisälä frequency for the section under consideration, at (*a*) 75 m < −*z* < 203 m, (*b*) 150 m < −*z* < 406 m, and (*c*) 69 m < −*z* < 420 m. A total of 66 XBT casts were used in these calculations. The 80% confidence limits are within a range of ±40%.

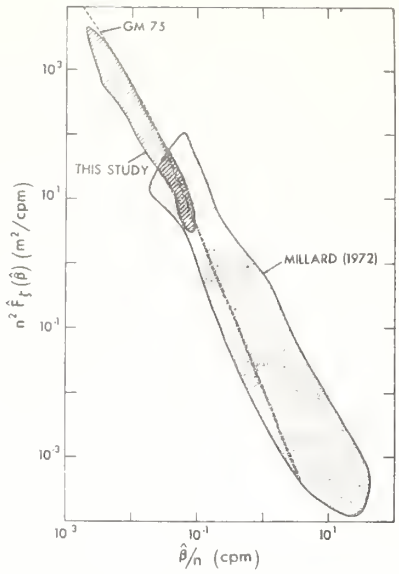

Fig. 5. Displacement spectra from *Garrett and Munk* [1975], *Millard* [1972], and this study. Comparison of the predicted curve (GM75) and experimental results.

model. In all cases the spectra lie below the predicted curve, but the trend is roughly the same. The difference is generally within the ±40% uncertainty of the spectral estimate.

Millard [1972] has made a series of measurements with a CTD in the North Atlantic which may also be used to compute a displacement spectrum. The Millard data have been used by *Garrett and Munk* [1975] as a test of GM75. A rough comparison of the *Millard* [1972] data and the present data set is provided by Figure 5. The *Millard* [1972] measurements were made at the Mode site at 28°N for various depth ranges below the seasonal thermocline. In all cases the stability is quite a bit less than that in the present study, in which we are considering the upper thermocline in a tropical area. Thus the present measurements provide information on a lower range of $\hat{\beta}n^{-1}$ with only a small overlap with the *Millard* [1972] spectra.

From the theory of internal gravity waves we expect that disturbances near the inertial frequency will have a constant aspect ratio (vertical scale/horizontal scale) much less than f/N. For disturbances of this type, horizontal coherence should decrease for both increasing vertical wave number and increasing horizontal separation. This is the behavior of the DHC predicted by the GM75 model. Results based on XBT profiles are shown in Figure 6. The ordinate is $\hat{\beta}$, and the abscissa is $\hat{X}$, the separation distance. Log-log coordinates have been used so that the predicted coherences based on (9) plot as straight diagonal lines. Since the actual separation distances at which the original observations were made have to be lumped together in broad categories resulting in an equivalent spatial smoothing, it is appropriate to smooth in wave number as well. In calculating the coherence a 10% cosine bell is used [*Bendat and Piersol*, 1971] to taper the records, a procedure omitted in calculating the displacement spectra shown in Figures 4 and 5. Band averaging is carried out by smoothing the cross spectrum and spectral components separately before dividing to find the coherence. The number of points smoothed depends on the length of the record. For the up-

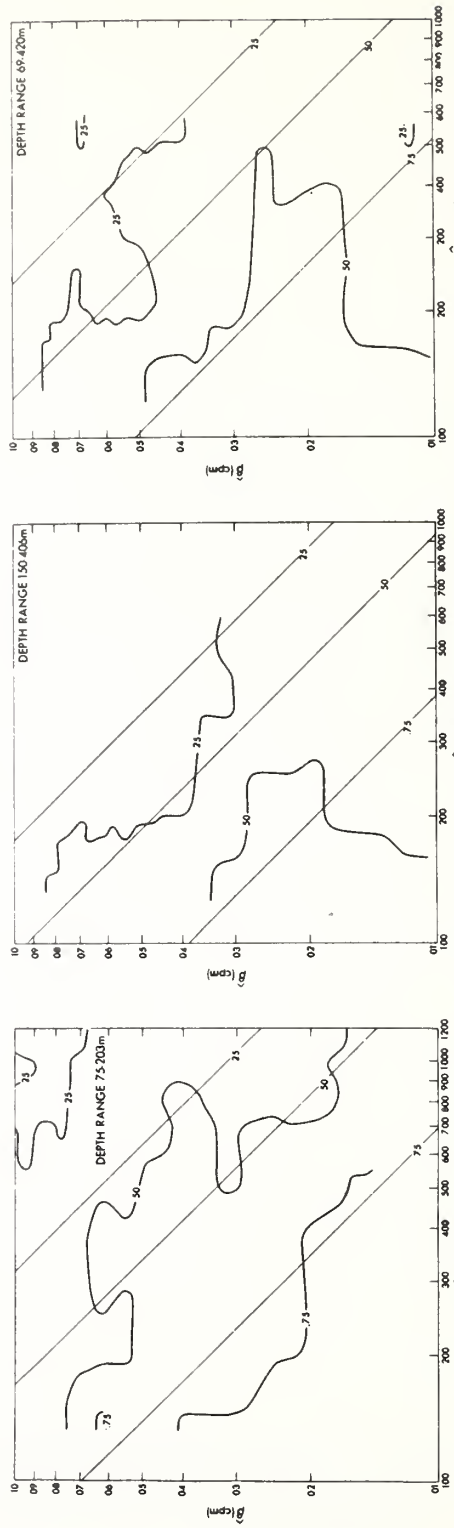

Fig. 6. Dropped horizontal coherence (DHC). The coherence as a function of vertical wave number $\hat{\beta}$, and horizontal separation $\hat{X}$. The data are compared to the curve predicted by GM75 (diagonal lines).

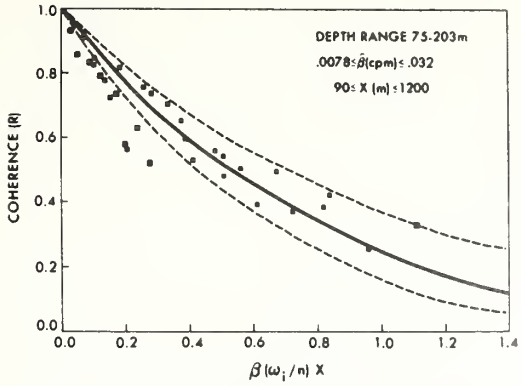

Fig. 7. DHC for the upper depth range, 75 m < $-z$ < 203 m. Solid line is the theoretical prediction of GM72. Dashed lines are 80% confidence limits based on the sample size. The open symbols represent the first wave number.

per depth range, smoothing is done for three points, for the lower depth range six points, and for the combined profile nine points.

The most consistent behavior is shown in Figure 6 for the upper depth range. The isopleths of 0.75 and 0.50 coherence have the expected trend, except for a conspicuous bulge centered at $\hat{\beta}$ = 0.04 cpm. This bulge corresponds to a vertical wavelength of 25 m. Those features of the plot above $\hat{\beta}$ = 0.07 cpm are probably not significant because of the limited vertical resolution of the original measurements. For the other depth ranges there is a strong tendency for the coherence to decrease at the lowest wave numbers, corresponding to vertical wavelengths greater than 50 m. To test the sensitivity of the coherence to the particular statistical treatment used, the coherence was computed without tapering and by using different band averaging. Although details are different and the patterns are quite broken up if no band averaging is performed, the loss of coherence at low vertical wave numbers is a persistent feature in all cases.

It was pointed out in the introduction that some loss of coherence is present due to the difference in time between XBT drops as the ship moves along its track. The measurements of lagged vertical coherence by *Hayes* [1975] are carried out in the thermocline with a background stability frequency $\hat{N}$ of about 2.5 cph. Hayes's measurements indicate a loss of coherence of unity per hour for vertical wavelengths between 25 and 37.5 m. Dividing this loss by the speed of the ship (6 km/hr), we obtain a loss of coherence due to the time lag alone of 0.14/km. From Figure 6 we can see that the expected loss of coherence is so much greater that the time interval between drops does not seriously affect the interpretation of the data.

In Figures 7 and 8 the same results are plotted in a different way. In Figure 7 the coherence results for the upper range, 75 m < $-z$ < 203 m, are plotted as a function of the nondimensional product βX. Based on an average of 30 pairs and three-point smoothing, the sampling error has been determined from tables by *Amos and Koopmans* [1963]. The envelope corresponding to an 80% confidence level is shown by dashed lines centered on the predicted curve based on the GM75 model. At low values of the coherence the confidence limits are clearly unsymmetrical indicating a large systematic bias of R at small values. In this presentation of the data the agreement with the GM72 model is surprisingly good.

The 0.5 level is a useful measure of the boundary between

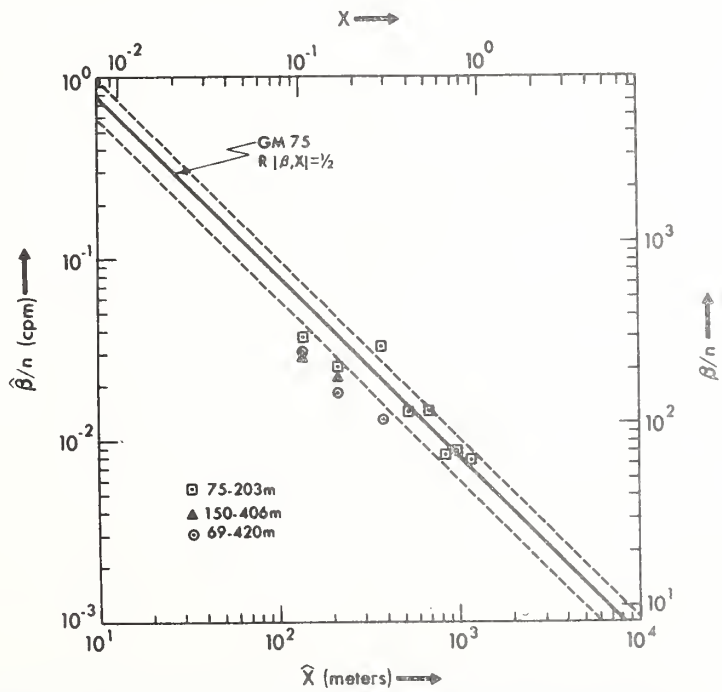

Fig. 8. The 0.5 coherence compared to the curve predicted by GM75 (solid line). The dashed lines denote the 80% confidence level. Dimensionless coordinates are shown on the upper and right-hand sides of the diagram.

meaningful coherence and lower levels that might occur by chance. In Figure 8 the ordinate is the vertical wave number scaled by n. The abscissa is the horizontal separation. The 80% confidence bands have been calculated in the same way as those in Figure 7. The confidence limits are based on a three-point band smoothing, even though a broader band smoothing is carried out for the results shown in the middle and the right-hand side of Figure 6. The behavior of the 0.5 coherence points in Figure 8 is consistent with the patterns of Figure 6. At a separation distance of 100–200 m the coherence is low in all cases. The only significant coherence for large separation distances is in the upper highly stratified depth range.

DISCUSSION

A great deal of care must be used in the physical interpretation of the statistics based on 66 XBT profiles collected in the open ocean 350 km north of San Juan, Puerto Rico. For example, we cannot be sure whether the temperature fluctuations are related to internal inertial gravity waves or some other process such as the interleaving of two water masses with different temperature-salinity curves. Possibly both processes are important. In any case the scaling procedures suggested by the *Garrett and Munk* [1975] model appear to be very useful in organizing the data. For example, the value of N differs by a factor of 2 as one goes from the upper to the lower part of the depth range over which measurements were taken, but the GM75 scaling brings the two displacement spectra taken in the upper and lower depth range into fairly close agreement. The trend and amplitude of the displacement spectra are not very different from that of the GM75 model.

Results for the dropped horizontal coherence indicate that the coherence does fall off monotonically with increasing separation but not with increasing vertical wave number. If we examine the coherence as a function of vertical wave number for a fixed separation, the maximum usually corresponds to an intermediate vertical wave number, corresponding to a vertical scale of 40–60 m.

Acknowledgments The authors gratefully acknowledge the assistance of the officers and crew of the NOAA ship *Discoverer* and that of Sylvia Worthem, Martha Jackson, and Sol Hellerman. Discussions with Christopher Garrett, Melbourne Briscoe, and Isidoro Orlanski were very helpful. GRS initially received support for this work at Princeton University under NSF grant GA-31970 and later under GFDL NOAA grant E22-2K-70(G). The field portion of this work was supported by NSF IDOE grant AG-282, which is gratefully acknowledged

REFERENCES

Amos, D. E., and L. H. Koopmans, Tables of the distribution of the coefficient of coherence for stationary bivariate Gaussian processes, *Rep. SCR-483*, Office of the Tech. Serv., Dep. of Commer., Washington, D. C., 1963.

Bendat, J. S., and A. G. Piersol, *Random Data: Analysis and Measurement Procedures*, p. 325, Interscience, New York, 1971.

Blackman, R. B., and J. W. Tukey, *The Measurement of Power Spectra*, p. 22, Dover, New York, 1958.

Fofonoff, N., Spectral characteristics of internal waves in the ocean, *Deep Sea Res.*, suppl., *16*, 58–71, 1969.

Fuglister, F. C., *Atlantic Ocean Atlas*, p. 128, Woods Hole Oceanographic Institution, Woods Hole, Mass., 1960.

Garrett, C. A., and W. Munk, Space-time scales of internal waves, *Geophys. Fluid Dyn.*, *2*, 225–264, 1972.

Garrett, C. A., and W. Munk, Space-time scales of internal waves: A progress report, *J. Geophys. Res.*, *80*, 291–298, 1975.

Hayes, S. P., Preliminary measurements of time-lagged coherence of vertical temperature profiles, *J. Geophys. Res.*, *80*, 307–311, 1975.

Mazeika, D. A., Subsurface mixed layers in the northwestern tropical Atlantic, *J. Phys. Oceanogr.*, *4*, 446–453, 1974.

Millard, R., Further comments on vertical temperature spectra in the Mode region, *MODE Hot Line News*, *18*, Nov. 1, 1972.

Phillips, O. M., *The Dynamics of the Upper Ocean*, pp. 74–78, Cambridge University Press, New York, 1966.

Tait, R. E., and M. R. Howe, Some observations of thermohaline stratification in the deep ocean, *Deep Sea Res.*, *15*, 275–280, 1968.

Webster, T. F., Vertical profiles of ocean currents, *Deep Sea Res.*, *16*, 85–98, 1968.

(Received December 6, 1974;
accepted January 17, 1975.)

Reprinted from: *Remote Sensing: Energy-Related Problems*, edited by Dr. T. Veziroglu, J. Wiley & Sons, 47-60.

SEASAT: A SPACECRAFT VIEWS THE MARINE ENVIRONMENT WITH MICROWAVE SENSORS

JOHN R. APEL

Director, Ocean Remote Sensing Laboratory
Atlantic Oceanographic and Meteorological Laboratories
Environmental Research Laboratories
National Oceanic and Atmospheric Administration
Miami, Florida 33149

ABSTRACT

Seasat-A is a new NASA satellite dedicated to oceanographic measurements of interest to a broad spectrum of the marine community. Its strong suit is an array of active and passive microwave instruments that give it the ability to view surface features on a day-night, near-all-weather basis. It will measure such features as wave heights, lengths, and directions; surface wind velocities; currents; temperatures; ice cover; and the marine geoid. Sensor capabilities and examples of their data output will be given, and the usefulness of these data for understanding the coastal marine environment will be discussed.

INTRODUCTION

Among the new programs initiated by the National Aeronautics and Space Administration for fiscal year 1975 is the ocean dynamics satellite, Seasat-A. This spacecraft has very real potential for enlarging the breadth and depth of scientific knowledge in several disciplines in earth science, and, in addition, promises to yield economic and social benefits of considerable magnitude, especially in the area of maritime affairs. This paper describes the objectives and background of the program, the spacecraft and its instruments, and delineates some of the scientific problems it can address.

The objectives of Seasat are (1) to develop and validate means for predicting the general ocean circulation, surface currents, and their transports of mass, heat, and nutrients, (2) to develop and validate means for synoptic monitoring and prediction of transient phenomena on the ocean surface such as wave heights and directions, surface winds, temperature, and storm surges, with an emphasis on identifying marine hazards, and (3) to make precision determinations of the marine geoid.

Because of the great length and breadth of the sea and the harsh environment it presents, the difficulties in obtaining detailed, timely information of sufficient observational density across most of its expanse have prevented an effective monitoring and forecasting system for the oceans. Thus, the prediction of wave heights depends on forecasts of the time and space histories of surface winds--the latter forecasts themselves being fraught with considerable uncertainty, as the loss of ships and oil drilling rigs at sea attests. Similarly, the locations of major ocean currents are known only approximately and the data required for shipping and fishing interests to efficiently exploit currents are lacking. The lack of sufficient wind and pressure data over the oceans has precluded an improved, longer-range weather

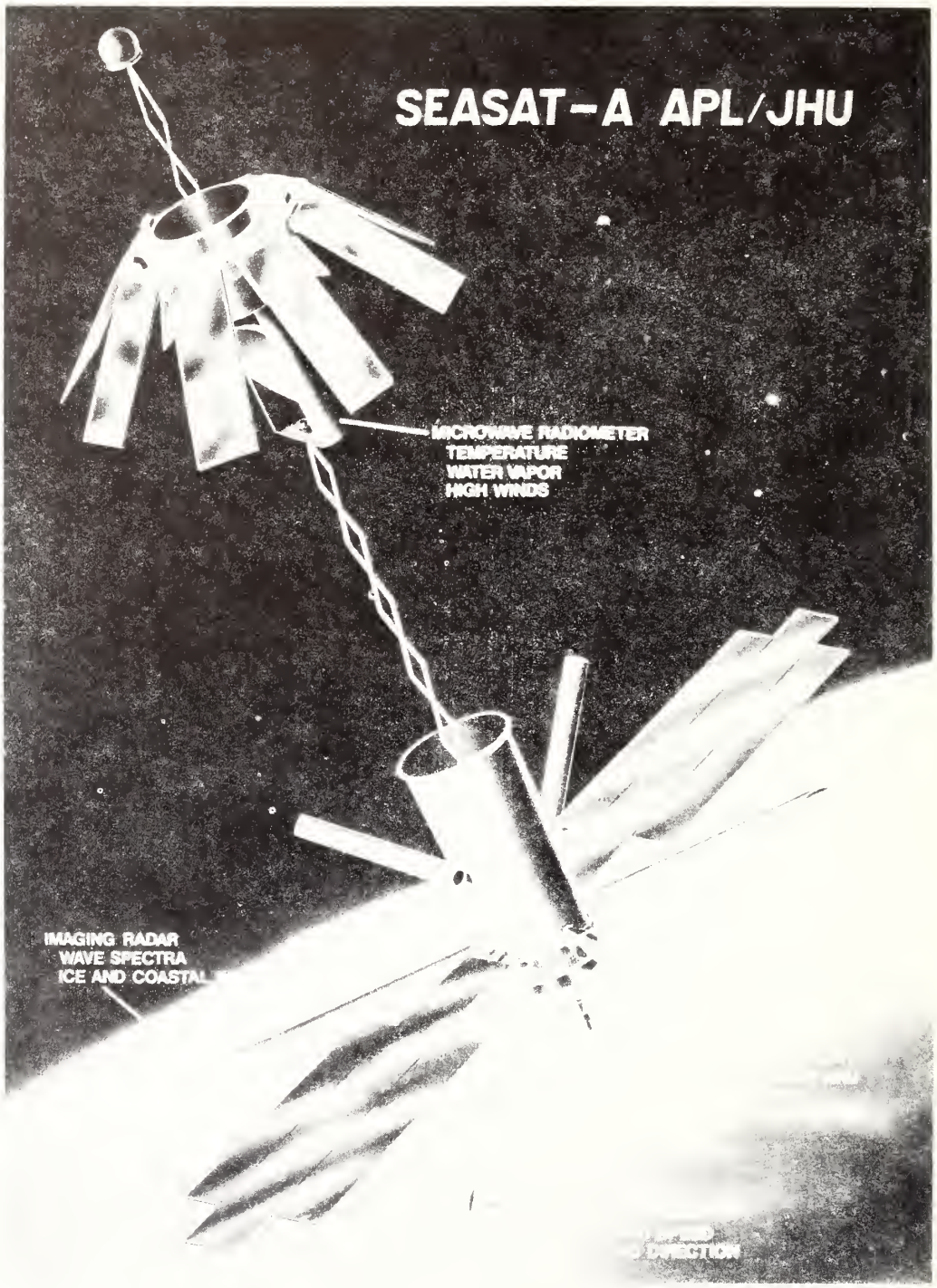

Fig. 1. - Configuration of Seasat-A, showing five sensors and their functions (JHU/APL).

forecast for continental areas. In order to achieve an effective one- to two-week forecast, observational data are needed over the oceans with about the same frequency and density as now exist in the continental United States.

SYSTEM DESCRIPTION

Basically, Seasat-A is a research-oriented program consisting of spacecraft, precision ground tracking systems, and data processing and modeling capabilities that will address both scientific and forecasting problems in ocean surface dynamics, boundary layer meteorology, and geodesy. Its strong suit is in an array of active radar and passive microwave and infrared instruments that give it the capability of observing the ocean on a day/night, near-all-weather basis. It is this group of sensors that allows Seasat-A to make quantitative measurements of oceanic, atmospheric, and geodetic parameters not only in clear weather but under wind and wave conditions perhaps approaching hurricane force, as well as over regions lying under persistent cloud cover. How this is accomplished is best appreciated after the system configuration has been laid out.

Figure 1 depicts a possible spacecraft design for Seasat-A. The prominent features on each design are the microwave antennas and, of course, the solar cell panels. The spacecraft is three-axis stabilized to point toward the vertical to within $\pm 0.5^{\circ}$

The mission profile for Seasat-A is as follows: lifetime, one year minimum; orbit, approximately 800 km altitude at an inclination of 108° (retrograde); eccentricity, less than 0.006, for a nearly circular orbit; period, 100 minutes, resulting in 14½ orbits per day. This orbit is non-sunsynchronous and will precess through a day/night cycle in approximately four and one-half months. Its ground track for one day is shown on Figure 2; as can be seen, it spans almost all of the unfrozen oceans of the world from the Antarctic to the Alaskan North Slope and the Canadian archipelago. The orbit is also optimum for fine-grained mapping of the geoid over the open ocean.

INSTRUMENTS

1. The Pulsed Radar Altimeter has two distinct functions: to measure the altitude between the spacecraft and the ocean surface to a root-mean-square precision near ±10 cm, and to determine significant wave heights along the subsatellite path. The altitude, when blended together with accurate orbit determinations, may be used to decipher the topography of sea surface including spatial variations in the geoid and time variations due to ocean dynamics.

A current NASA estimate of the geoid in the western Atlantic, as derived from satellite tracking data and surface gravity measurements, is given in Figure 3; the figure shows the geoid--that is, the theoretical elevations and depressions of the motionless ocean surface due to gravity, with contours of constant height given in meters, relative to an elliptical earth. On land, this surface is used as a reference surface in precision surveying, and at sea, for determining surface deflections of the vertical.

The prominent ocean surface depression due to the deep ocean trench north of Puerto Rico has been observed by four different methods, the Skylab radar altimeter, S-193 being the first to give a continuous direct measurement of the sea surface topography. Figure 4 shows two altimeter traces of the overlying ocean surface and island topography. The measurement was made with the Skylab altimeter, which has a one-meter precision. The spacecraft measurements bear out both other observations and detailed calculations which indicate that the ocean surface is depressed by 15-20 m over a 100- to 150-km

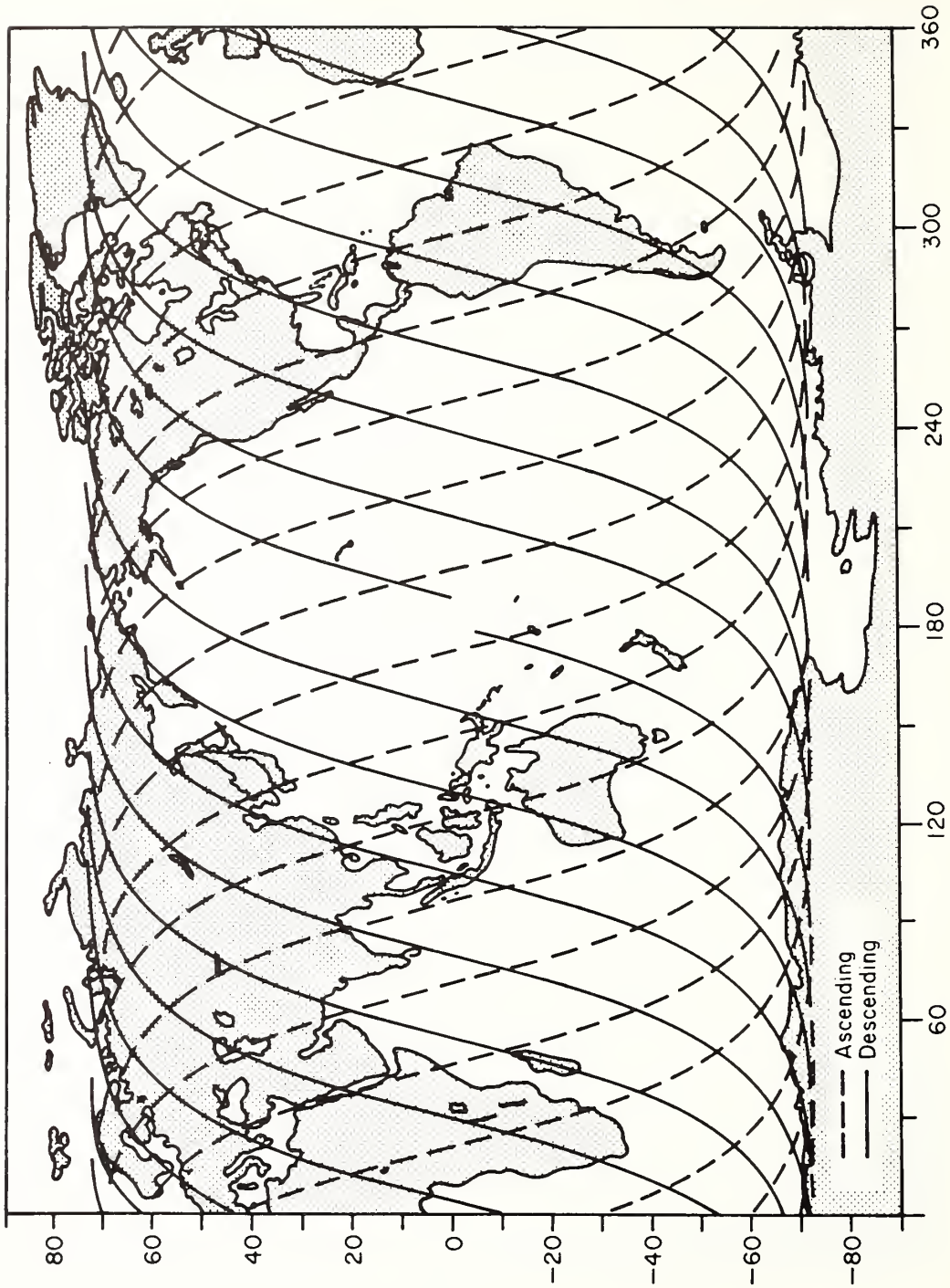

Fig. 2. - Ground track of Seasat-A for 24-hour period (JHU/APL).

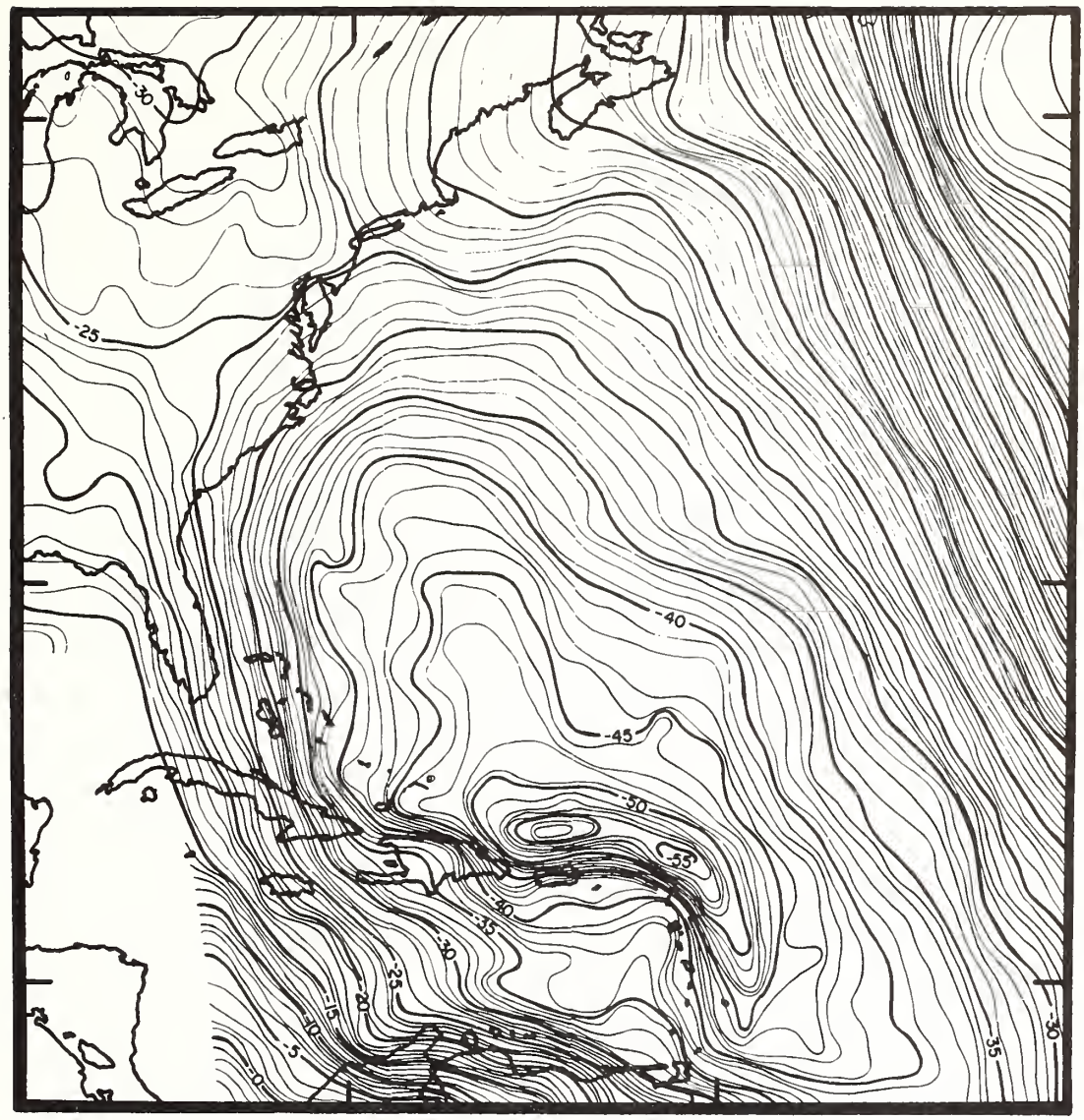

Fig. 3. - Geoid for western Atlantic as calculated from satellite orbit perturbations and marine gravity data (NASA/GSFC).

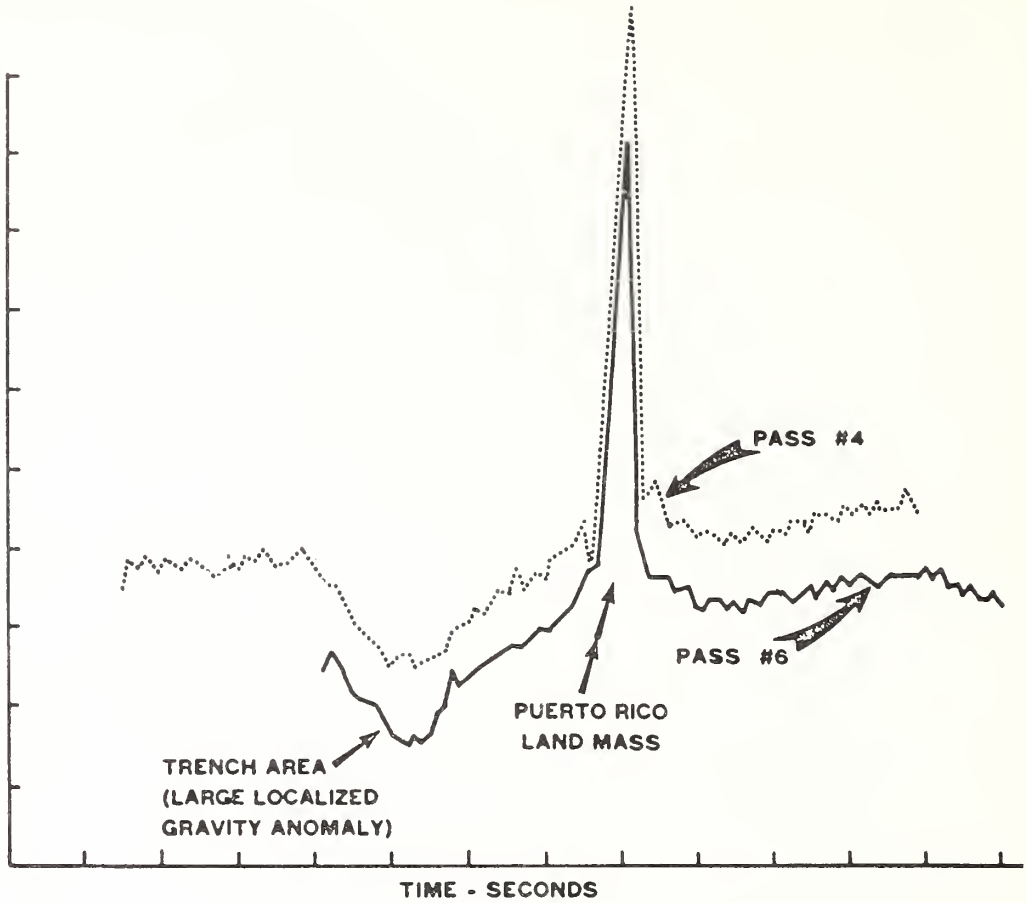

Fig. 4. - Altimeter traces from Skylab S-103 for two passes over Puerto Rico Trench. Vertical units are 10 meters (NASA/WFS).

distance north of Puerto Rico, due to the gravity anomaly associated with the trench. Anomalies which are elevations rather than depressions have also been observed from Skylab. These are due to seamounts, plateaus, and the Mid-Atlantic Ridge. Thus, the whole foundation of precision geoidal measurements via spacecraft altimetry seems to be on a reasonable theoretical and observational footing. The problems are to extend it globally and increase the precision.

There exist much smaller topographic departures from the geoid that are due to ocean dynamics effects. Such time-varying features as intense currents, tides, wind pile-up, storm surges, and tsunamis are in principle observable with an altimeter having submetric precision by way of measuring sea surface slopes relative to the geoid. For currents, the slope of the surface is proportional to the surface speed. However, the topographic variations due to even intense systems such as the Gulf Stream are quite small conpared to the gravity-caused geoidal undulations, being of order 1 to 2 m at most. Another ocean dynamical feature observable at the 10-cm level of precision are waves, which may be used along with surface wind measurements to make world-wide sea state forecasts. The principle of the measurement is that a short pulse

reflected from a rough sea will be broadened by the various reflecting heights caused by the waves. The broadened shape of the returned echo contains wave height information, with the rougher the sea, the longer the echo. Aircraft flights have shown this technique to work in low to moderate seas. On Seasat-A, wave heights from one to above 20 meters should be measurable along the subsatellite track on a near-all-weather basis. Other information derived from the sensor complement may be used to extend this measurement well out from the suborbital track.

2. Synthetic Aperture Imaging Radar. The required extension of wave information will be made by using an imaging radar to obtain images of the ocean on a sampled basis. Such a radar can function through clouds and moderate rain to yield wave patterns near shorelines and in storms and can see waves whose length is greater than about 50 m. It can also provide high-resolution pictures of ice, oil spills, current patterns, and similar features. Computations can be performed on the radar data to yield a quantity called the wave directional spectrum which gives the relative distribution of wave energy among different wavelengths traveling in various directions; this, together with the surface wind velocity, is the fundamental information needed in forecasting of wave conditions on the ocean.

Figure 5 illustrates two trains of waves off Kayak Island, Alaska, one of 150-m and the other of 60-m wavelength, taken from the NASA Convair 990 aircraft with the Jet Propulsion Laboratory imaging radar; the waves are being refracted and shortened by shoal water as they approach the island visible on the left-hand side. Also on the lower left and center of the figure is a directional spectrum computed for the relatively uniform part of the wave train to the right of the image. Distance from the center of the spectrum corresponds to increasing wave frequency, angle to direction of propagation, and intensity to wave energy.

The data rate from an imaging radar is high, and judicious use must be made of the device. Nevertheless, it should be possible to sample wave spectra over 10-km-square patches of ocean densely enough to obtain global data on sea conditions. Near the NASA receiving sites along the U. S. coasts, more generous quantities of imagery will be taken and studies of storm wave patterns near potential offshore nuclear power plant sites, deep-water oil ports, harbors, and breakwaters will be made. Over the Northwest Passage and the Great Lakes, a demonstration of real-time mapping of ice leads and open water will be made as an aid to navigation through those straits and inland seas.

3. Microwave Wind Scatterometer. The third radar system is a microwave scatterometer, intended to measure surface wind speed and direction by sensing the small capillary waves induced by the wind over the ocean. Previous aircraft experience and recent Skylab data taken over the Pacific hurricane Ava in June 1973 indicate this sensor is useful in winds approaching 20 m/s, yielding speeds with an error of ±2 m/s and directions to ±20°. Figure 6 illustrates Ava as taken from the environmental satellite NOAA-2 on the left; on the right are graphs from Skylab S-193 showing radar scattering, radiometric temperature, and, in the upper right-hand corner, wind speed. The peak wind of 45 knots (22 m/s) obtained from the scatterometer was observed some distance from the eyewall, which the sensor could not view because of look-angle constraints.

4. Scanning Multifrequency Microwave Radiometer (SMMR). The SMMR is a passive, nonradiating microwave device, in contrast to the three previous sensors. It simultaneously senses the microwave energy emitted by and reflected from the ocean, ice, and atmosphere. In order to separate out the

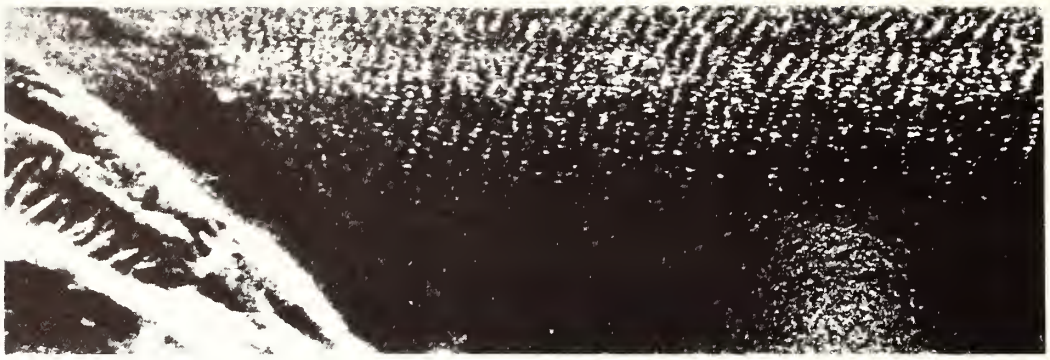

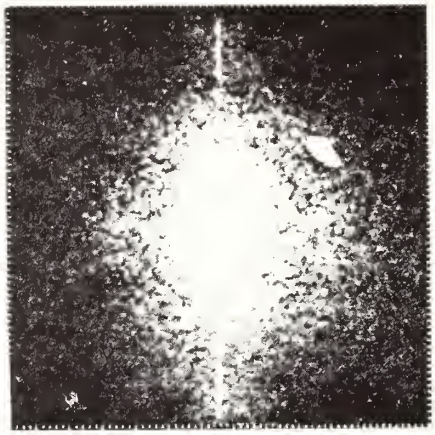

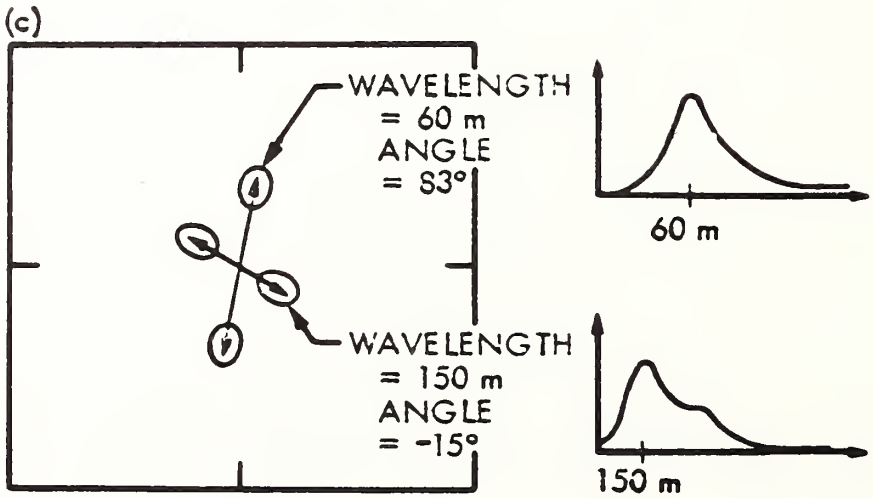

Fig. 5. - Wave data from imaging radar showing wave refraction patterns and directional spectrum (JPL/CIT).

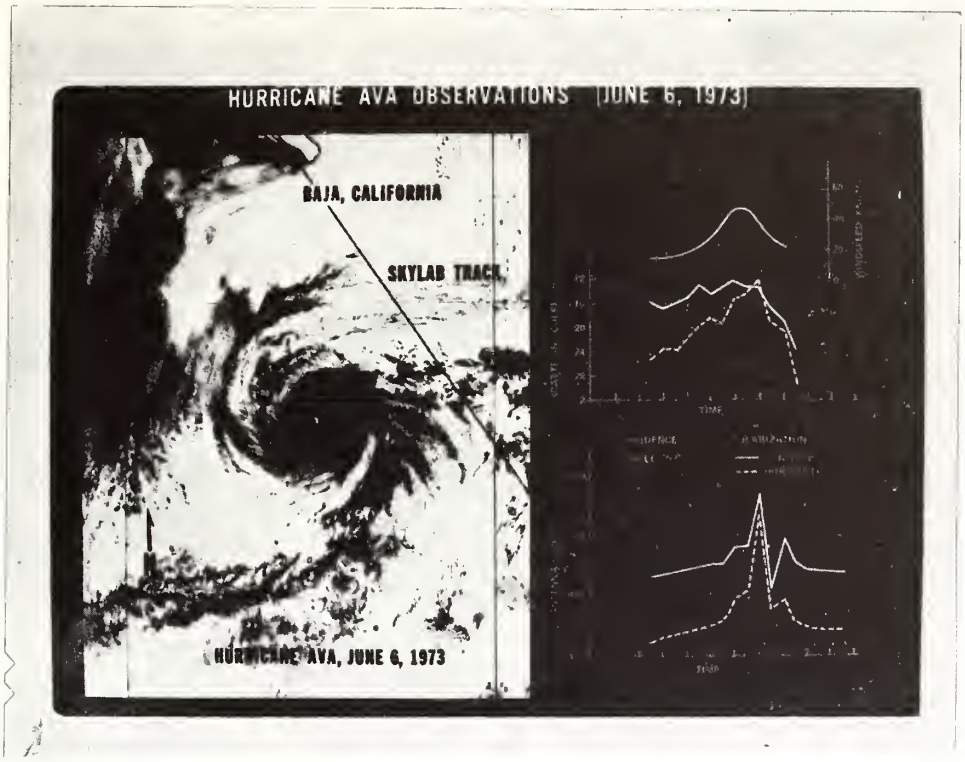

Fig. 6. - Wind scatterometer and radiometer data taken through hurricane Ava in the Pacific (NASA/HQ).

various contributions to the signal from these sources, several microwave frequencies are used with each chosen for maximum sensitivity to one of those geophysical parameters. The scanning feature will allow low-resolution images of objects along its line of sight to be constructed from the signals received.

The functions of the SMMR are severalfold. It is first a wind speed instrument that senses the increase in emitted microwave energy due to roughness, foam, and streaks on the ocean caused when higher wind speeds create wave breaking and whitecaps. The estimated observable range of speeds is from about 10 to perhaps 50 m/s, but the upper limit has yet to be firmly established. Thus, the range of speeds measurable from Seasat should be extended by SMMR from the 20-m/s limit of the scatterometer up toward hurricane-force winds. Secondly, it appears capable of measuring sea surface temperature with an accuracy of $1\frac{1}{2}$-2°C, even through light clouds, where present infrared deices are useless. Thirdly, the other frequencies are used for determining atmospheric liquid water and water vapor content, quantities that are needed in models of oceanic and atmospheric boundary layer processes as well as for important corrections to the precision altimeter measurements. Ice fields and cover will also be observed with low resolution from SMMR. When blended with the wind data from the Microwave Wind Scatterometer, the two sensors should yield a global, quantitative determination of surface wind speed wherever it is below essentially hurricane force. The measurements will be equivalent to some 20,000 ship reports a day. When combined with available ship and buoy surface information on wind and pressure, it becomes possible to compute the atmospheric surface pressure field over the entire ocean, except perhaps near severe storms; this will also be true in the data-sparse

southern hemisphere. Such results should help to improve the 24-hour weather forecasts substantially, perhaps making them extensible to two or three days. This improved predictive capability for winds implies an approximately equal improvement in forecasting waves, especially when assisted by the data on the initial state of the sea obtained from the radar altimeter and imager.

5. Infrared Radiometer. The purpose of this sensor is to provide images of thermal infrared emission from ocean, coastal, and atmospheric features, which will aid in interpreting the measurements from the other four microwave instruments. Figure 7 is an example of imagery taken from the NOAA-2 Very High Resolution Radiometer over the southeastern United States and clearly shows the Gulf Stream off the coast as a dark band of water, as well as the Gulf of Mexico Loop Current, a time-varying feature that apparently profoundly affects the fishery and the weather in that inland sea.

A word on the measurement of sea surface temperature is in order here. This seemingly inconsequential parameter is actually of considerable importance in oceanic and atmospheric processes, since it results from the absorption of that prime mover, solar energy, by the sea. For instance, the difference between active and inactive hurricane seasons may be due to just 2-3°C lower water temperature in hurricane gestation areas. Ocean temperature is a major factor determining the tone of weather and climate in many coastal regions of the world. Maps of sea surface temperature are very useful for tracing current systems such as the Gulf Stream especially in the winter months. Furthermore, open-ocean fish such as tuna tend to swim along lines of constant temperature at certain times during their excursions, and a knowledge of temperature can assist in their location. Thus, sea surface temperature offers a clue to several interesting processes in the ocean.

THE TOTAL SYSTEM

The interrelationships between data from these five sensors are suggested in Figure 8, which illustrates the complex nature of the contribution that each sensor makes to the geophysical parameters being measured. The figure indicates the importance of carrying the full sensor complement in order to achieve the measurement objectives.

Seasat-A is thus an integrated observatory addressing the objectives discussed at the beginning of this paper. Table I outlines the capabilities of the spacecraft system in meeting the requirements set forth by a community of data users who were identified by NASA at the beginning of the program.

An important element in interpreting the Seasat-A data and extending its utility will be fleshing out the information obtained from this spacecraft with the considerable data on oceans and atmosphere available from other sources. The environmental/meteorological satellites are one such obvious source for marine and weather data, as are ships, buoys, and transoceanic aircraft. In the case of ocean wave forecasts, a land-based high-frequency skywave radar that is intended for operational, detailed monitoring of wave spectra near the continental United States is expected to be in service; its fine-grained data nicely complements the necessarily coarser-space open ocean wave spectral data from Seasat-A. Similarly, research data on currents, tides, the geoid, and the other parameters of interest will be amalgamated with the Seasat-A data by individual researchers interested in specific problems.

Fig. 7. - Thermal infrared imagery of eastern U. S. showing Gulf of Mexico loop current and Gulf Stream as dark water masses.

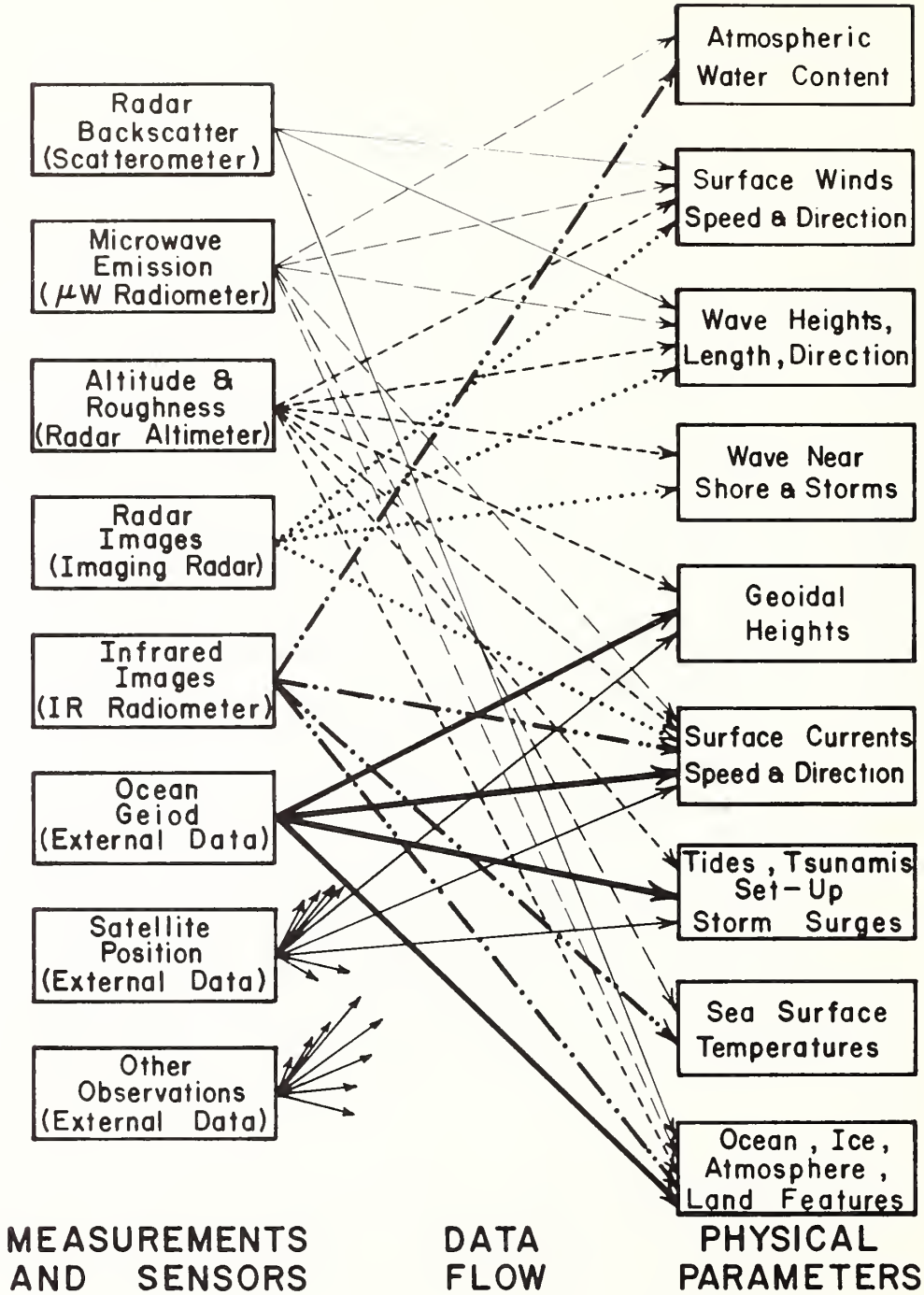

Fig. 8. - Interrelationships between Seasat-A sensors and geophysical variables to be derived.

TABLE I

20 February 1974

CAPABILITY OF SEASAT-A IN MEETING USER REQUIREMENTS

PHYSICAL PARAMETER	INSTRUMENTS	RANGE	PRECISION	RESOLUTION OR IFOV	TOTAL FOV	COMMENTS
Wave Height, $H_{1/3}$ (x,y)	Pulse Altimeter Coherent Alt.	1.0 - 20 m	±0.5 m or ±10%	2x7 km spot	2-km swath	along subsatellite track only
Directional Wave Spectrum S (λ,Θ,x,y)	Imaging Radar (2-D transform)	S: unknown λ: 50-1000 m Θ: 0-360°	S: --- λ: ±10% Θ: ±10°	50-m resolution	20x20 km squares	global samples at 250-km intervals
	2-f Wave Spectrometer	S: unknown λ: 6-500 m Θ: 90° sector	S: --- λ: ±10% Θ: ±90°	8 x 25 km spot	300-km swath about nadir	global samples at 150-km intervals
Surface Wind Field, $\vec{U}$(x,y)	Scatterometer	U: 3-25 m/s Θ: 0-360°	±2 m/s, ±10% ±20°	≤ 50 km spot	two 450-km swaths	global, 36 hrs (low speeds)
	μW Radiometer	U: 10-50 m/s Θ: unknown	±2 m/s, ±10% --	≤ 100 km spot	900-km swath about nadir	global, 36 hrs (high speeds)
Surface Temperature Field, T(x,y)	IR Radiometer	-2° to +35°C	±¼° - 1°C	1-7 km IFOV	1500-km swath about nadir	global, 36 hrs (clear air only)
	μW Radiometer	0° to 35°C	±1.5°C	100 km spot	900-km swath about nadir	global, 36 hrs (clouds & lt. rain)
Geoidal Heights, h(x,y) (above reference ellipsoid)	Pulse Altimeter Coherent Alt.	7 cm - 200 m	±7 cm	2x7 km spot	18-km spacing along equator	sampled throughout one year
Sea Surface Topography, ζ(x,y) (departures from geoid)	Pulse Altimeter Coherent Alt.	7 cm - 10 m	±7 cm	2x7 km spot	2-km swath	along subsatellite track only
Oceanic, Coastal, & Atmospheric Features (Patterns of waves, temp., currents, ice, oil, land clouds, atmospheric water content)	Imaging Radar	high resolution	all weather	25 or 100m	100 or 200 km	sampled direct or stored images
	IR Radiometer	high resolution	clear air	1-7 km	1500-km swath	broadly sampled images
	μW Radiometer	low resolution	all weather	15-100 km	900-km swath	global images

CONCLUSION

Seasat-A promises to be an exceptionally useful and productive program. It should have a large impact on earth science and on a community of users in the general populace.

The United States space program has produced satellite systems that have looked at the thin envelope of the atmosphere, at the browns and greens of rocks and plants, and at the bright thermonuclear fires of the sun and stars. The time has now arrived to mount a space-oriented investigation of the sea, that last remaining member of the ancient elemental quartet of air, earth, fire, and water.

Reprinted from: *Journal of Geophysical Research 80*, No. 6, 865-881.

Observations of Oceanic Internal and Surface Waves From the Earth Resources Technology Satellite

John R. Apel, H. Michael Byrne, John R. Proni, and Robert L. Charnell

Atlantic Oceanographic and Meteorological Laboratories, Environmental Research Laboratories, NOAA Miami, Florida 33149

Periodic features observed on the ocean surface from the Earth Resources Technology Satellite 1 have been interpreted as surface slicks due to internal wave packets. They appear to be generated at the edge of the continental shelf by semidiurnal and diurnal tidal actions and propagate shoreward. Nonlinear effects apparently distort the wave packets as they progress across the shelf. This observational technique constitutes a new tool for delineating two dimensions of the internal wave field under certain limited conditions.

Surface Observations

Visible manifestations of internal waves on the ocean surface may be due to at least two mechanisms, either of which modulates the short surface wave structure rather than causes any change in optical reflectivity or light absorption at depth. The first mechanism suggests that the high velocity of surface water arising from the large internal wave amplitude sweeps together surface oils and materials to form a slick in regions of surface water convergence, and thus the surface reflectivity is increased [*Ewing*, 1950; *Shand*, 1953]. The second mechanism predicts that capillary wave energy is focused in the convergence zones due to surface stress, and thus the small-scale roughness is enhanced and the surface reflectivity is decreased [*Gargett and Hughes*, 1972; *Thompson and West*, 1972]. In either case, quasi-periodic surface features will be produced under light wind conditions, and such effects are very often seen at sea.

Figure 1*a* is a photo taken from an aircraft in the Caribbean during Bomex in 1969 that shows a series of what almost certainly must be internal waves propagating from the left overlaid at nearly right angles by much shorter wind waves (R. B. Grossman, private communication, 1974). A ship wake crosses from left to right. The length of the internal waves is to a very rough approximation near 200 m. Figure 1*b* illustrates internal waves being generated by a tide rip and shows at least three distinct wave trains propagating at different angles [*Lafond*, 1962].

Periodic surface slicks may generally be seen from the air under conditions favorable for viewing oil on the sea, i.e., at low sun angles or in the sun glitter, when light or moderate winds prevail.

Generation Mechanisms

Internal waves can be generated by a wide variety of mechanisms. Wind stress that excites a spectrum of surface waves is one source [*Phillips*, 1966]. In this case, wave-wave scattering between two surface oscillations of wave vectors and frequencies κ_1, κ_2 and ω_1, ω_2, respectively, generates an internal wave whose parameters are set by the conservation rules $\kappa_3 = \kappa_1 - \kappa_2$ and $\omega_3 = \omega_1 - \omega_2$. The amplitude of the internal wave is partially determined by the surface wave amplitudes; the interference pattern decays exponentially with depth with a scale given by $1/|\kappa_3|$ and thus makes itself felt at levels where internal waves may propagate.

Copyright © 1975 by the American Geophysical Union.

A second mechanism for generating internal waves is the scattering of barotropic tidal energy into internal baroclinic tides by bottom roughness or by the discontinuities presented by the edges of continental shelves or island arcs [*Rattray*, 1960; *Halpern*, 1971]. The relative importance of different topographies in transforming tidal motions into internal wave motions is unknown. This phenomenon is difficult to observe in nature; extant evidence suggests that up to ⅓ of the 3×10^{12} W energy dissipation required to account for the lengthening of the day may be ascribed to such scattering [*Hendershott*, 1973]. Thus island arcs, continental shelf edges, and shallow submarine sills become important regions in which to make observations of internal waves.

A third mechanism that can cause internal waves is shear flow instability [*Rattray*, 1960; *Phillips*, 1966]. In regions of the ocean having large baroclinic currents accompanied by horizontal stratification, small fluctuations in depth of a given stratum can grow to large amplitudes in an oscillatory way by mechanisms generally akin to the Kelvin-Helmholtz instability. An indication of the onset of this growth can be obtained by evaluating the gradient Richardson number Ri, where $Ri = N^2/(\partial u_0/\partial z)^2$. Here N is the Brunt-Väisälä frequency, and $\partial u_0/\partial z$ is the vertical shear in the horizontal baroclinic current speed $u_0(z)$, which may be due to a mean motion or a tidal current. The onset of the growth generally occurs when Ri approaches ¼ (or less). The oscillation amplitude is usually a maximum at some intermediate depth, i.e., is an unstable internal wave. This mechanism may be responsible for the generation of short-period internal waves from baroclinic internal tides of semidiurnal periods or in regions of western boundary currents.

Erts 1 Observations of Internal Waves

Periodic or quasi-periodic features in or on the ocean have been detected on many Erts 1, Skylab, and U.S. Air Force Dapp meteorological satellite images taken over both continental shelf and deep ocean areas; to date we have observed these features off the North American east and west coasts, the Gulf of California, the African east and west coasts, northern South America, the central Pacific, and the Celebes Sea. These features are almost certainly surface manifestations of internal waves that are made visible to the spacecraft by one of the mechanisms described above that serve to 'tag' the waves during winds which are well below whitecapping speeds.

The observations will first be presented, and then arguments will be made to support the internal wave interpretation.

Fig. 1*a*. Aircraft observations of internal waves during Bomex (1969) (latitude 9.5°N, longitude 59.5°W). Also shown are surface waves, a ship wake, and wind rows.

Fig. 1*b*. Additional aircraft photo of internal waves [*Shand*, 1953].

Surface effects on the continental shelves. Figure 2 is a standard Erts image taken with the Erts 1 multispectral scanner southeast of New York; it is printed as a positive image and shows Long Island at the top and New Jersey at the left. The scene dimensions are 184 × 184 km^2; north lies approximately 102° counterclockwise from the horizontal edges. The scene was taken in orange-red light between 600- and 700-nm wavelength, at approximately 1007 LT on August 16, 1972. The large white objects in the center of the picture are high-altitude clouds; southeast of the mouth of the Hudson River two U-shaped acid-dumping events are visible; little else of oceanographic interest is apparent.

Fig. 2. Standard NASA Erts image. Area shown is the New York bight taken on August 16, 1972.

Figure 3 is a negative print of the same image, computer-enhanced through a process known as contrast stretching, with the land portions sacrificed in favor of ocean information. There is a wealth of data observable, including the Hudson River plume, acid and sewage sludge dumps, color discontinuities, and in the southeast corner, periodic surface slicks. (This figure is also geographically stretched by a factor of 1.4 : 1 in the east-west direction due to computer/photo recorder peculiarities.)

Figures 4, 5, and 6 are similar computer-enhanced images of the New York bight area taken on May 31, July 6, and July 24, 1973; each shows periodic striations in the southeast corner of somewhat similar characteristics. No such features were observed on scenes taken over the same area between August 1972 and May 1973.

Figure 7(*a, b, c,* and *d*) is a geographically corrected line drawing of the periodic features observed in the four scenes above superimposed over a bathymetric chart of the area. The general orientation of the lines with the local bathymetry and their concentration in the region of the Hudson Valley argues for strong interaction with the bottom topography. We shall return to this figure later.

The nature of these periodic features has recently been verified by direct measurement [*Apel et al.*, 1974], and a simple highly plausible model has been constructed whose predictions are in good quantitative agreement with the observations. It is suggested that the features are surface slicks overlying internal waves that have been generated by scattering of the barotropic tide into baroclinic modes at the edge of the continental shelf, which then propagate up on the shelf, to be absorbed and reflected when the wave breaks on the sloping bottom.

We first eliminate several other possible sources of the periodicities. (1) Atmospheric waves causing the depth of image modulation seen here do exist but would require much more atmospheric water content than is observed in the pictures; nor would atmospheric events reoccur in the same

Fig. 3. Figure 2 after computer enhancement via contrast stretching. Many oceanographic features are now visible including packets of internal waves separated by 12 to 15 km (lower right-hand corner).

geographical location over and over or be so well oriented with respect to the bottom topography. (2) Neither could the features be large surface gravity waves. The observed wavelengths are of the order of 400–1000 m; if these represented surface waves, their periods would be 16–25 s. Even if the slopes were as small as one in 30, the surface wave heights would be of the order of 7–15 m, and such a small rms slope could not account for the one-in-eight brightness change that the features represent on the image. On Figure 3, for example, the observed sea state was World Meteorological Organization code 1–2 with significant wave height, $H_{1/3} \simeq 0.5$ m. Therefore surface waves are eliminated as a possibility. (3) Finally, discussions with NASA Goddard Space Flight Center personnel (W. Hovis, private communication, 1972) have ruled out instrument artifacts as a source because of the somewhat irregular nature and orientation of the periodic variations.

The remaining possibility is that the features are the result of oceanic internal gravity waves. In light seas, such oscillations often have surface slicks associated with them whose origins may be as described above. The result of either mechanism is a periodic variation in surface roughness and hence in optical reflectivity that defines the internal wave field beneath. Such slicks are common at sea [*Shand*, 1953; *LaFond*, 1962].

To support further this hypothesis, refraction calculations have been performed by using published bottom topography and compared with the propagation patterns on Figure 3. A simple two-layer model [*Lamb*, 1932], together with topographic data and density profiles derived from bathythermographs for the area in question (obtained a day after the Erts 1 overflights), was used to compute the progression of a plane wave, originating in deep water, up on the continental shelf in the vicinity of the Hudson Canyon. The predicted phase speed (ω/κ) for conditions extant at the time of overflight is about 0.25 m/s. The wave train was assumed incident normal to the edge of the continental shelf. This is probably not a necessary assumption, since for wavelengths of the order of these, phase orientation due to refraction is so strong that by the time they have progressed to the area of the image, the wave fronts would be rendered nearly parallel to contours of local topography.

Figure 7*a* also shows the results of this calculation by way of a comparison between the observed wave packets and an arbitrarily spaced set of phase fronts (dashed lines) as computed

Fig. 4. The New York bight, May 31, 1973. Note the weak development of an internal wave field in the lower right-hand corner and the large number of ships and ship wakes visible.

from the two-layer dispersion relation. Both theory and observation show the wave fronts advancing more rapidly in the deep water over the Hudson Valley than on the adjacent continental shelf. The overall agreement is quite good.

Thus all the evidence indicates that the periodic features in these Erts 1 photos are internal waves that are being detected by their associated surface slicks. These waves have most likely been generated by tidal action at the shelf edge and are being refracted as they move up onto the shelf.

One pair of Erts 1 images has afforded a possible determina-

Fig. 5. The New York bight, July 6, 1973. Note the more pronounced internal waves compared with those in Figure 4.

tion of both the propagation speed, via time delay measurements, and the generation interval between the internal wave packets. Figure 8 was taken on July 23, 1973, exactly 24 hours before and approximately 110 km to the east of Figure 6. These two images have a good deal of overlap in coverage, allowing observation of the same geographical area. Visible are two sets of packets in the lower center left of Figure 8, separated by 29 to 34 km. Figure 9 is a line drawing showing the packets on Figures 6 and 8. These packets could be standing lee waves created by the bottom topography but more likely are propagating groups of waves. When it is assumed that the packets are propagating, it is possible to arrive at an advance of about 30–33 km for a given packet during 24 hours (solid to dashed). Note as well the aforementioned spatial interval between packets observed on a given day, also about 30 km on both days (solid to solid or dashed to dashed). This near-equality of the between-packet intervals with the distance of advance argues for daily or near-daily generation and implies a phase speed of about 0.35 m/s, which is what one would expect from a 50-m-deep mixed layer with a density contrast $\Delta\rho/\rho \simeq 10^{-3}$ in the depth of water in this region.

Figure 10 shows how the wavelengths on Figure 9 vary with front-to-back position in the packets, as is taken at two separate sectors in the easternmost group on that image. There is clearly a strong tendency observed here and in most other satellite images for a given packet to have longer wavelengths at its front than at its rear. This is probably due to a combination of a nonlinear finite amplitude effect with the dispersive character of the waves, as was recently discussed by *Lee and Beardsley* [1974]. A detailed study of these types of features should yield considerable insight into the physics controlling large amplitude internal wave propagation.

Figure 11, which was made on November 28, 1972, off southwest Africa just north of Cape Town, shows six packets of surface signatures apparently radiating from a small source at the center left. The area visible is about 180 by 250 km. On Figure 12 a line drawing of the packets superimposed on bottom topography is shown, with the depth given in meters. If the interpretation of these signatures as propagating tidally excited internal wave groups is accepted, then the image shows evidence that internal waves may have lifetimes on the shelf of several days. (Density data for this time and place have not yet been obtained, and so no refraction calculations have been made.) Also shown in Figure 11 are the intervals between packets, ranging from 41 to 20 km as shore is approached, as well as the lengths of the leading waves, which increase from 1.6 to 3.5 km as shoal water is reached. The dependence of the

Fig. 6. The New York bight, July 24, 1973. Note the well-developed internal wave fields. In this picture there is a ship wake longer than 40 km.

packet separations and length of leading wavelength as a function of distance and water depth is shown in Figure 13. This curious behavior, wherein the overall packet suffers retardation as the depth decreases while the leading edge portion is apparently accelerated, may be an anomaly, or it may be a highly significant dynamic effect. More study and additional data are obviously required.

A summary of the important characteristics of the surface slick patterns in continental shelf regions follows:

1. The waves occur in groups, or packets, separated by distances that are of the order of either 15 or 30 km, which, together with the calculated phase velocities, suggest a semidiurnal or diurnal tidal origin.

2. They are nearly always oriented parallel to the local bottom contours, as is expected of shallow water waves.

3. None have yet been found in Erts images during the winter or spring in the areas investigated to date.

4. A repeated concentration of energy occurs in the Hudson Valley in the vicinity of 60- to 80- m depth, probably owing to generation and focusing of waves by the headlands near the Hudson Canyon at the edge of the shelf.

5. The wavelengths fall between 300 and 4000 m and have

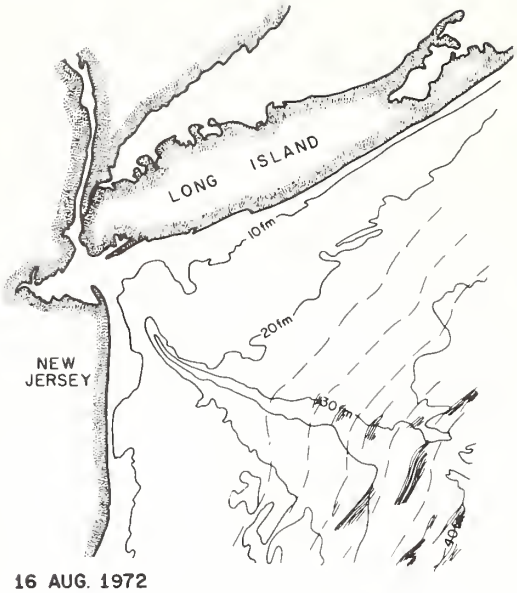

Fig. 7*a*.

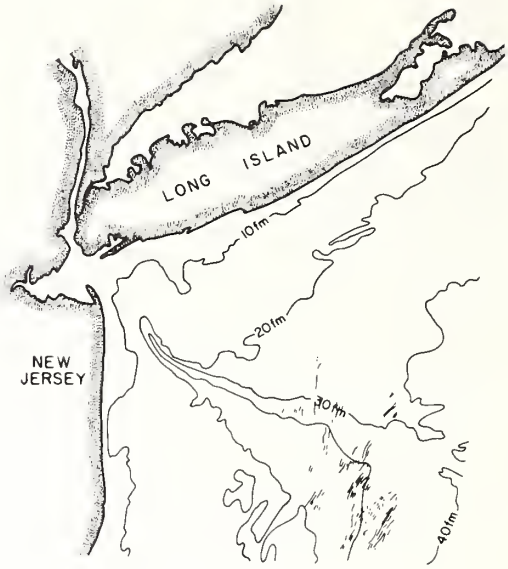

31 MAY 1973

Fig. 7*b*.

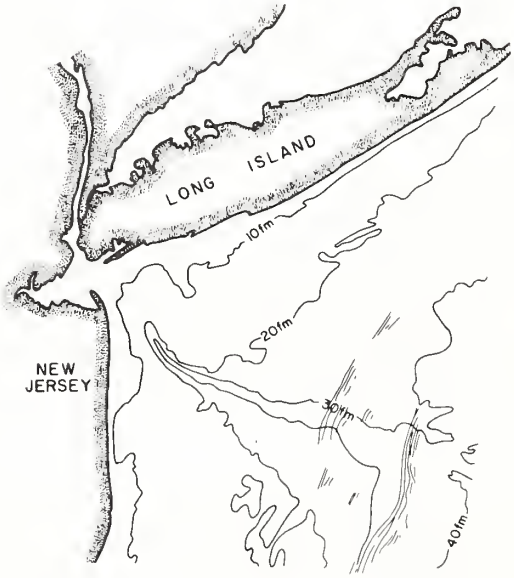

6 JULY 1973

Fig. 7*c*.

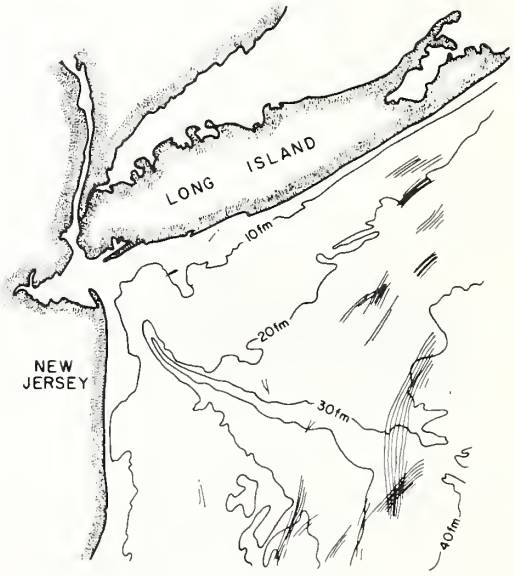

24 JULY 1973

Fig. 7*d*.

Fig. 7. Geographically corrected line drawing of the internal wave fields observed in Figures 3, 4, 5, and 6 superimposed on the bottom topography. The dashed lines on (*a*) show isophase contours as calculated from a simple internal wave model.

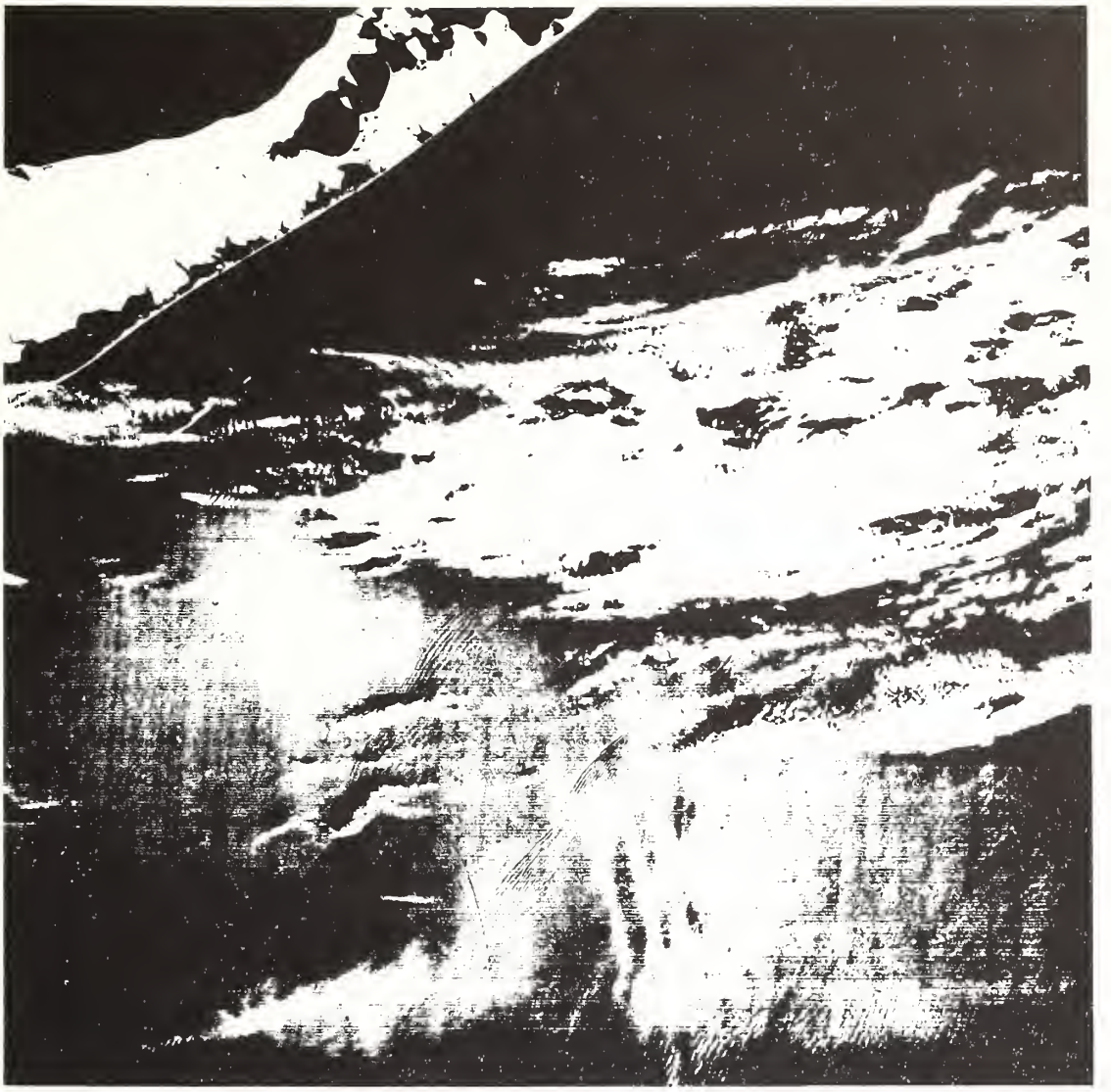

Fig. 8. Eastern Long Island area, July 23, 1973 (photographically enhanced), 24 hours prior to and 110 km to the east of the area shown in Figure 6. Note packets separated by about 30 km in lower left center.

phase speeds near 0.25 m/s, with a longer distance between crests and a greater extent of the packet occurring on the inshore side and shorter wavelengths and smaller packet extent on the offshore side; the reasons for some of these characteristics are not yet clear.

6. There is some evidence of a continued lengthening of the distance between crests, especially in the front of the packets, as the group progresses up on the shelf; an accounting for this may be had by a combination of finite amplitude and dispersive effects.

Surface effects observed in deep water. The data shown thus far have been taken on or near continental shelves, in water depths less than about 500 m. Very limited numbers of Erts 1 images have been taken over deep water in the open ocean, of which two scenes are shown in Figures 14 and 15. Figure 14 illustrates a photographically enhanced image of a portion of the deep Indian Ocean taken on December 4, 1972; equatorial east Africa is visible on the left. The continental shelf in this part of Africa extends only a few tens of kilometers off the coast. Quasi-periodic structures are apparent in the cloud-free center portion of the scene having a scale of 2–4 km and relatively little coherence. In the lower right there is a definite change in the orientation of the structure. These features lie approximately in the southward-flowing Somali current; the image was taken at a time of year when the current in the region usually undergoes sharp spatial and temporal

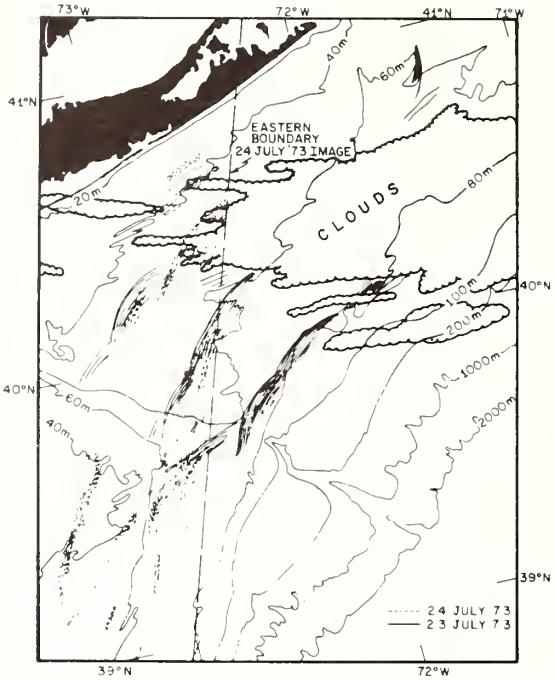

Fig. 9. Geographically corrected line drawing showing wave packets from Figures 6 and 8.

variations due to the shifting monsoon. It is thought that the structure in question may be a surface signature of deep water internal waves; however, no sea truth is available for this area, and so such an interpretation must remain speculative.

Another ocean scene is shown on Figures 15 and 16. These Erts 1 data were taken in the North Pacific at about 40°N, 160°W in September 1973. Figure 15 has dimensions of 92 × 184 km² and is a computer-enhanced negative print showing cumulus clouds in the south and a peculiar surface mottling in the north having a scale of a few kilometers. In this latter region, a microscopic examination shows an expanse of surface waves approximately 200 m in length propagating toward the southeast away from a low pressure cell several hundred kilometers away, having wind speeds of 10 to 15 m/s.

A more detailed look at a 13 × 18 km sector of this region is shown on Figure 16*a*, which clearly illustrates two trains of surface gravity waves of nearly equal wavelength intersecting at approximately 15°, as well as the mottling mentioned above; the latter is seen to be very roughly periodic with an average 'wavelength' of about 2.5 km and approximately a north-south orientation. Figure 16*b* is the logarithm of the two-dimensional Fourier transform of Figure 16*a* and shows the spatial frequency components of the mottling near the origin and those of the surface waves as two concentrations of energy separated by about 15° at nearly equal wave numbers. Under the suspicion that the origin of the mottling might be found either in (1) surface wave interference effects or (2) in the kind of internal wave generation process arising from wave-wave scattering that was discussed earlier, we have applied the wave vector conservation rule $\kappa_1 - \kappa_2 = \kappa_3$ to the scene. The magnitude of κ_3 agrees with that of κ_{mott}, the wave vector of the mottling, to within 10%; its angle, which is nearly at 90° to the mean value of κ_1 and κ_2, agrees to within 20°. Such agreement does not prove that either of the above processes suggested are at work, of course, but such interpretations are at least consistent with the data. Obviously, further controlled experiments are required.

The surface stress hypothesis might explain the visibility of internal waves on the surface of a moderately rough ocean having a wind blowing over it [*Gargett and Hughes*, 1972]. The horizontal surface currents associated with internal waves are large, being of the same order as the phase velocity of the waves themselves; they are oriented approximately either parallel or antiparallel to the direction of propagation and have opposite directions in parts of the wave separated in phase by $(2n - 1)\pi$. A wind field superimposed on the currents will excite a capillary/ultragravity wave spectrum that is steeper where the wind opposes the internal wave current than where it is parallel to it. This periodic variation in the slope spectrum would lead to periodic variations in the optical reflectivity that might serve to delineate the internal wave in the deep sea to high-altitude sensors, much as surface slicks serve to do in continental shelf waters. The difference in the two cases is that the slick cannot maintain its integrity at wind

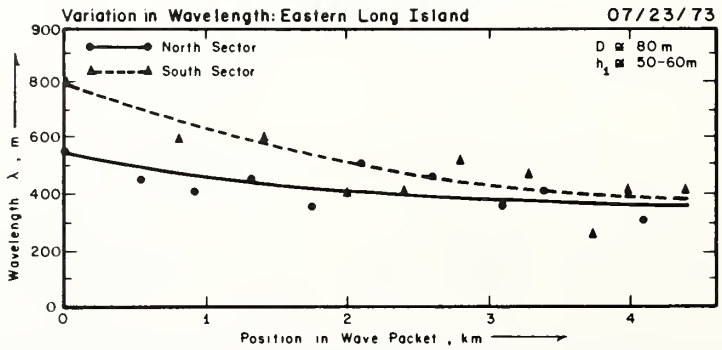

Fig. 10. Variation in internal wavelength as a function of distance from the front of the upper and lower packets seen on Figure 8.

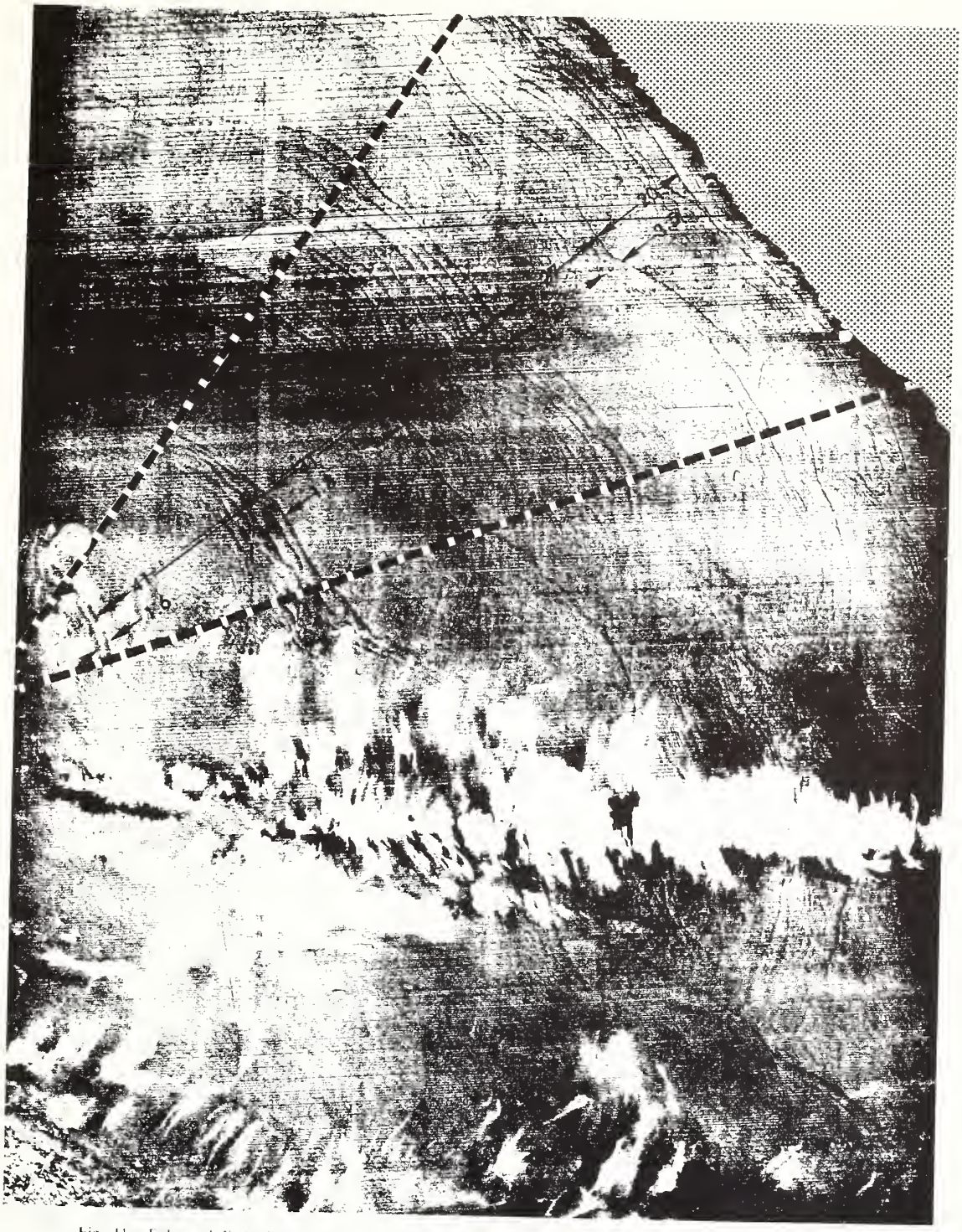

Fig. 11. Enhanced Erts photo made on November 28, 1972, off southwest Africa just north of Cape Town, showing six packets of surface slicks apparently radiating from a small source at the center left. This photo suggests internal waves may have lifetimes on the shelf of several days.

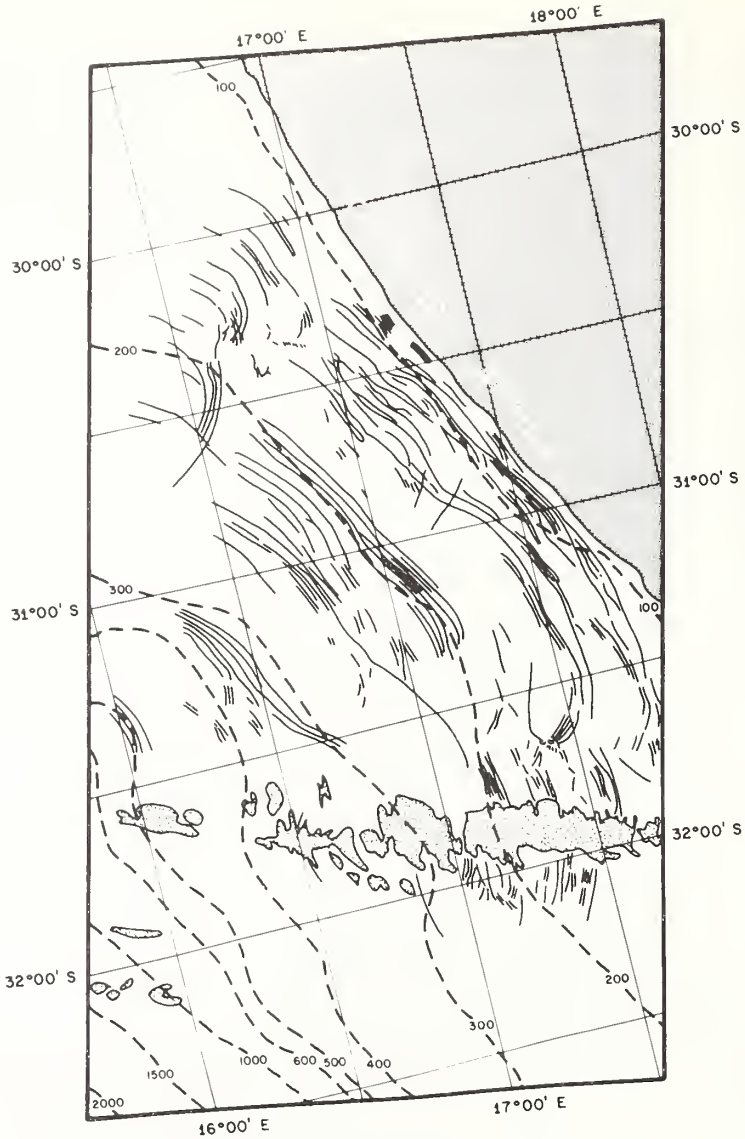

Fig. 12. Line drawing of packets of Figure 11 together with bottom topography.

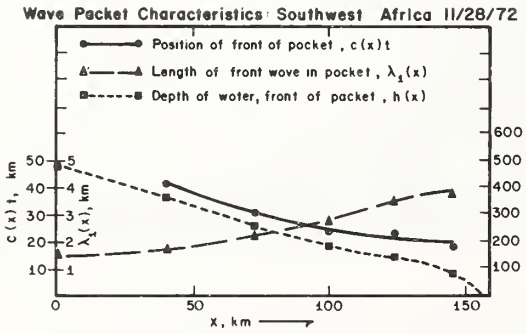

Fig. 13. Leading wavelength and interpacket separation as a function of distance; from Figures 11 and 12.

velocities above whitecapping speeds, whereas the above mechanism may.

Surface effects in the Florida current. Figure 17 is presented as a final example of possible internal waves observed from Erts 1. This is a contrast-stretched negative image of the Florida current made on August 18, 1972, with Miami located near the upper portion of the photograph. At the bottom center near the mean axis of the current is a group of periodic striations oriented roughly northwest-southeast and extending approximately 30 km along the direction of mean flow. The distance between stripes is about 800 m. It is thought that these are surface signs of internal waves excited by and propagating along the Florida current. Periodic surface slicks in this general region are common at sea, and acoustic echo-sounding from ships has indicated that internal waves often underlie

such slicks [*Proni and Apel*, 1975]. The mechanism for their generation is quite possibly a shear flow instability. On the westward side of the current in the region of cyclonic horizontal velocity shear the vertical velocity and density gradients are sometimes such that the Richardson number for the flow approaches ¼. *Düing*'s [1973] data give values for *Ri* that indicate incipient instabilities may occur. Once again, the theoretical conditions that indicate the existence of a mechanism for generating internal waves have to be verified by simultaneous field and satellite measurements.

SUMMARY AND CONCLUSIONS

Convincing proof of the assertions that (1) the periodicities observed on Erts I images are surface slicks and (2) the slicks tag internal waves under conditions of light winds has been obtained by the authors in a recent cruise between New York and Bermuda. The data are only partially analyzed and will be published in the near future [*Apel et al.*, 1974].

The limitations of the satellite technique appear to be as follows: light wind and clear sky conditions must prevail, high-frequency internal waves on the shelf are most visible, and coverage is limited by satellite dynamics and sensor characteristics. No amplitude information is currently derivable from the spacecraft images. However, as the accompanying paper shows [*Proni and Apel*, 1975], this missing dimension to the internal wave field may be partially obtained via acoustic echo sounding, so that a more nearly complete picture of the three-dimensional field may be obtained.

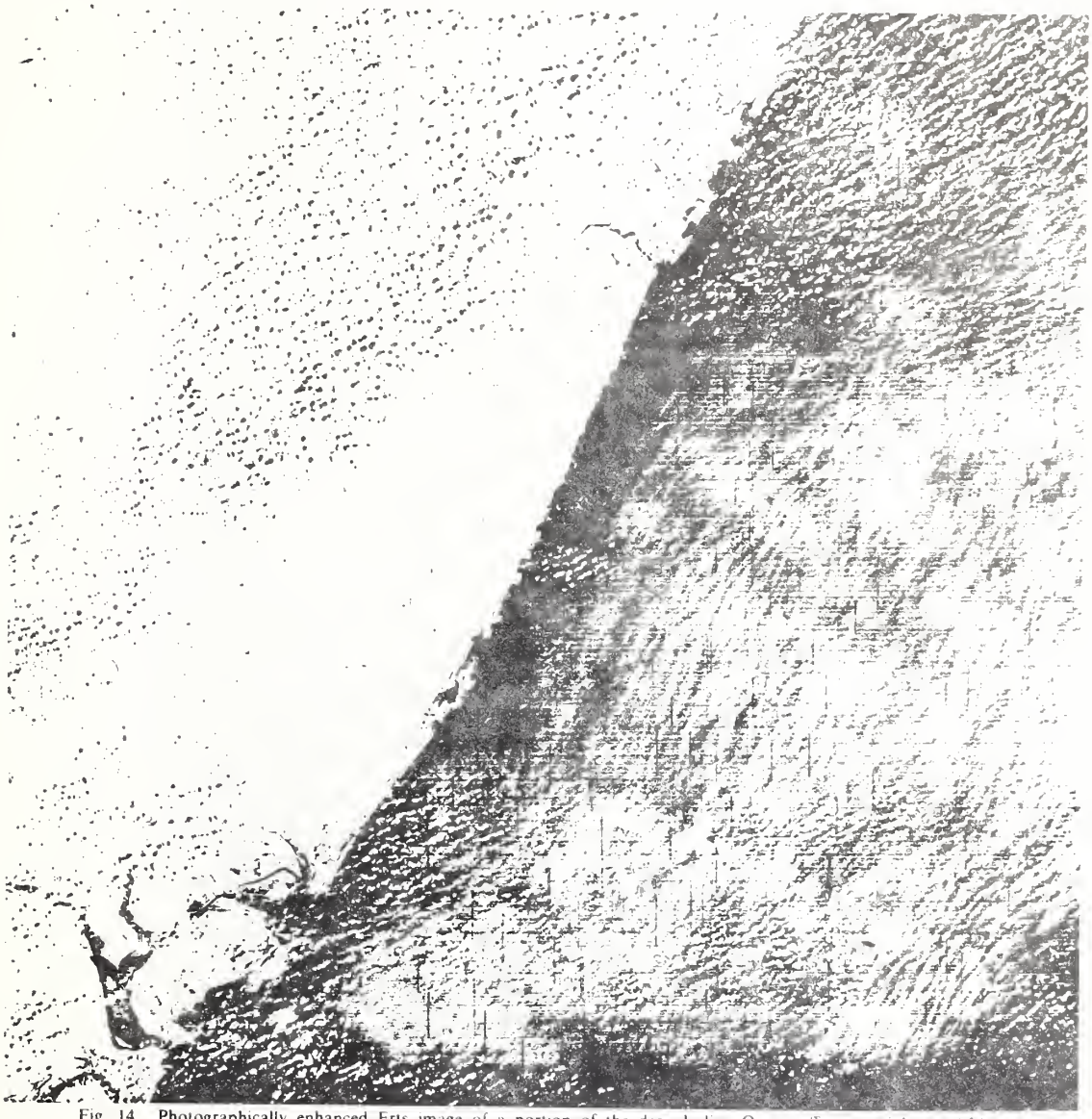

Fig. 14. Photographically enhanced Erts image of a portion of the deep Indian Ocean off equatorial east Africa taken on December 4, 1972.

Fig. 15. Enhanced Erts image (negative) taken over the North Pacific at 40°N, 160°W in September 1973. Image dimensions are 92 × 184 km². Note the peculiar surface mottling and surface wave field.

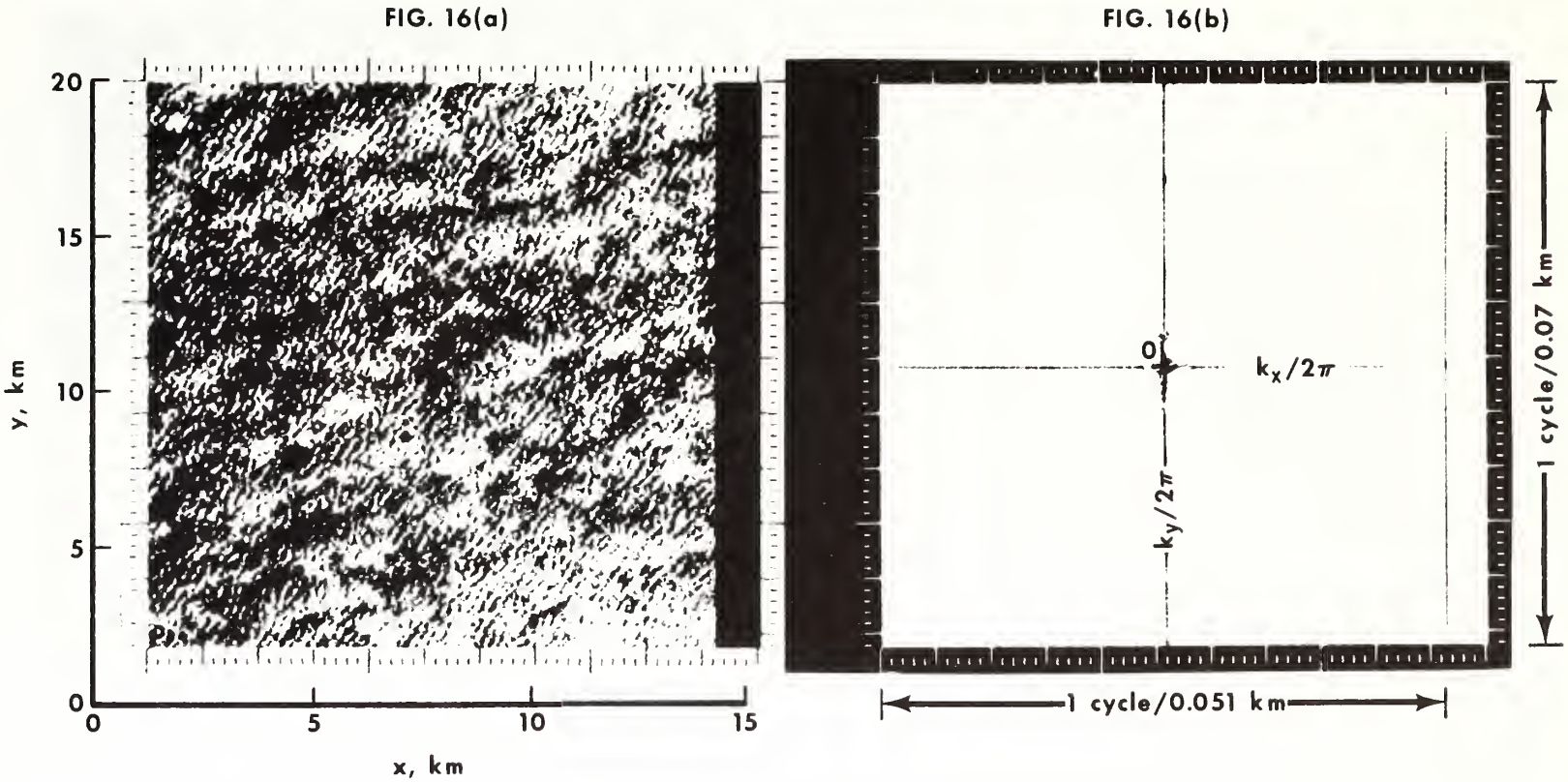

Fig. 16. (*a*) Detail of an 18 × 13 km² sector of Figure 15. Clearly visible are two surface wave trains as well as the peculiar mottling mentioned in the text. (*b*) Logarithm of the two-dimensional Fourier transform of (*a*). This figure shows the frequency components of the mottling (near the origin) and those of the surface waves (as two concentrations of energy separated by about 15° at nearly equal wave numbers).

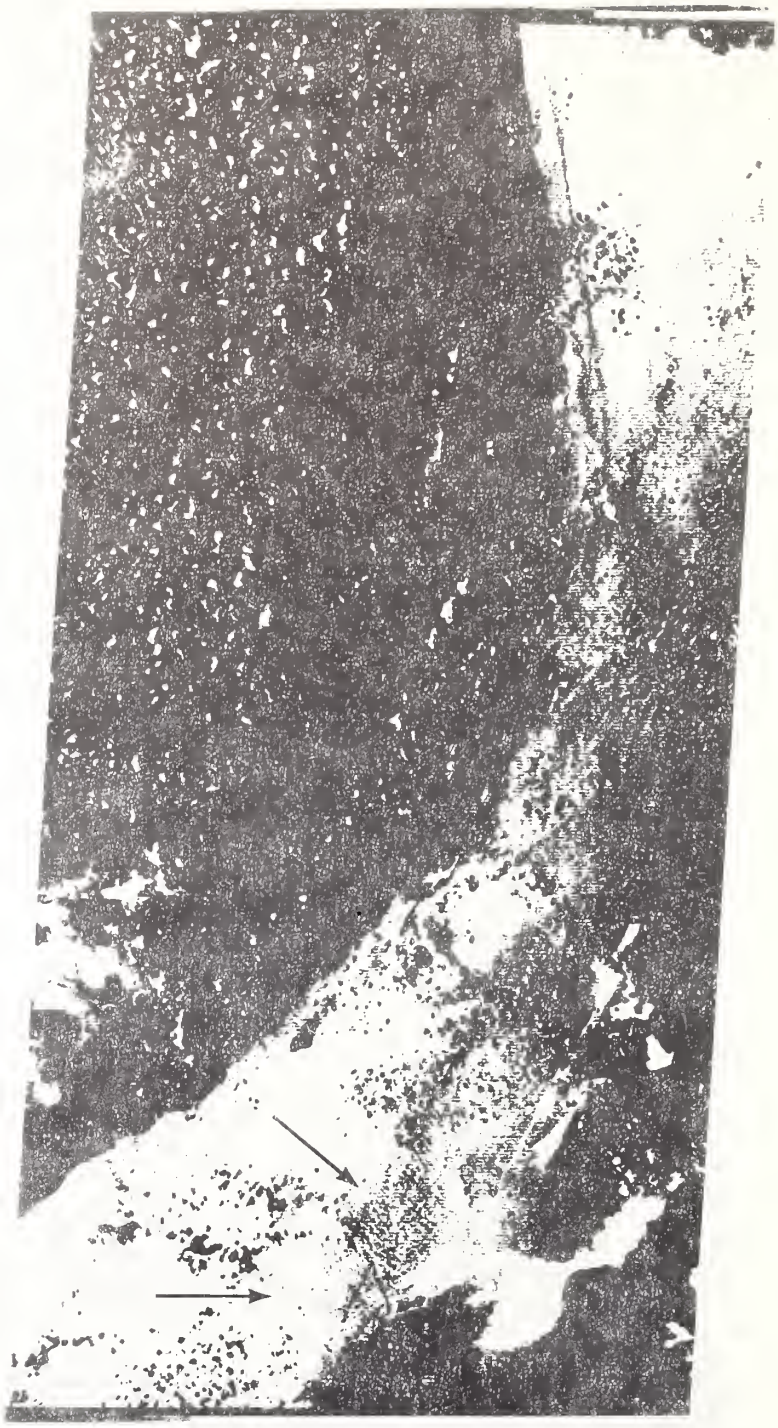

Fig. 17. Contrast stretched negative Erts image of the Florida current made on August 18, 1972. Note the periodic striations present at the bottom center of the image.

Acknowledgment. This project was partially supported by funds from the Advanced Research Projects Agency, which assumes no responsibility for the correctness of the results.

REFERENCES

Apel, J. R., J. R. Proni, H. M. Byrne, and R. L. Sellers, Near-simultaneous observations of intermittent internal waves from ship and spacecraft, submitted to *Geophys. Res. Lett.*, 1974.

Düing, W., Observations and first results from Project Synop 71, *Sci. Rep. UM-RSMAS 73010*, Univ. of Miami, Miami, Fla., 1973.

Ewing, G., Slicks, surface films and internal waves, *J. Mar. Res.*, *9*, 161, 1950.

Gargett, A. E., and B. A. Hughes, On the interaction of surface and internal waves, *J. Fluid Mech.*, *52*, 179–191, 1972.

Halpern, D., Semidiurnal internal tides in Massachusetts Bay, *J. Geophys. Res.*, *76*, 6573–6584, 1971.

Hendershott, M., Ocean tides, *Eos Trans. AGU*, *54*, 76–86, 1973.

Lafond, E. C., Internal waves, in *The Sea*, vol. 1, edited by M. N. Hill, pp. 731–763, Interscience, New York, 1962.

Lamb, H., *Hydrodynamics*, p. 370, Cambridge University Press, London, 1932.

Lee, C., and R. C. Beardsley, The generation of long nonlinear internal waves in a weakly stratified shear flow, *J. Geophys. Res.*, *79*(3), 453–462, 1974.

Phillips, O. M., *The Dynamics of the Upper Ocean*, pp. 161–197, Cambridge University Press, London, 1966.

Proni, J. R., and J. R. Apel, On the use of high-frequency acoustics for the study of internal waves and microstructure, *J. Geophys. Res.*, *80*, in press, 1975.

Rattray, M., On the coastal generation of internal tides, *Tellus*, *12*, 54–62, 1960.

Shand, J. A., Internal waves in the Georgia Strait, *Eos. Trans. AGU*, *34*, 849–856, 1953.

Thomson, A. J., and B. J. West, Interaction of non-saturated surface gravity waves with internal waves, *Tech. Rep. RADC-TR-72-280*, Phys. Dyn. Inc., Berkeley, Calif., (ARPA order 1649), October 1972.

(Received July 24, 1974;
accepted November 6, 1974.)

71 Reprinted from: *Geophysical Research Letters 2*, No. 4, 128-131.

NEAR-SIMULTANEOUS OBSERVATIONS OF INTERMITTENT INTERNAL WAVES ON THE CONTINENTAL SHELF FROM SHIP AND SPACECRAFT

John R. Apel, John R. Proni,
H. Michael Byrne, and Ronald L. Sellers

Ocean Remote Sensing Laboratory
Atlantic Oceanographic and Meteorological Laboratories
Environmental Research Laboratories
National Oceanic and Atmospheric Administration
Miami, Florida 33149

Abstract. Internal waves on the continental shelf off New York have been observed from ship and the ERTS-1 spacecraft, and positive correlations made between surface and subsurface measurements of temperature, acoustic volume reflectivity, and surface slicks. The spacecraft imagery senses the quasi-periodic variations in surface optical reflectivity induced by the internal waves. The waves appear to be tidally generated at the shelf edge and occur intermittently in packets, which propagate shoreward and disappear in water near 50-m depth.

Introduction

Surface manifestations of internal waves have frequently been identified during observations from ships, aircraft, and offshore towers, with "surface slicks" or "regions of enhanced capillary waves" being terms used to describe the state of the sea surface overlying the internal wave field. In a recent publication, we report on what appear to be surface signs of internal waves detected in visible and near-infrared imagery obtained from the multi-spectral scanner on the NASA Earth Resources Technology Satellite, ERTS-1 (Apel et al., 1975). These signs usually take the form of periodic variations in optical reflectivity of the ocean surface; they have wavelengths of order 500 to 5000 m and appear repetitively in several groups, or packets, which are separated by intervals ranging from about 15 to 40 km. The surface manifestations usually occur during conditions of light winds and relatively clear skies.

While the absolute identification of the features in the spacecraft imagery as being due to internal waves had not been attempted until now, it has nevertheless been possible to synthesize a simple, consistent internal wave model that accounts for most of their major characteristics. They appear intermittently on the continental shelf at intervals which suggest their generation by semidiurnal and diurnal tides at the edge of the shelf (Halpern, 1971); they seem to be refractively controlled in phase speed and propagation direction by the mixed layer and water depths and the Brunt-Väisälä profile; and they largely disappear where the mixed layer comes to occupy a substantial fraction of the water column. Nonlinear, dispersive behavior is indicated by certain of their characteristics, including a sharp onset and the frequent appearance of the longest wavelengths at the front of the packet (Lee and Beardsley, 1974).

Copyright 1975 by the American Geophysical Union.

New York-to-Bermuda Remote Sensing Experiment (NYBERSEX)

A cruise was scheduled during June and July 1974 aboard the R/V Westward, a 30-m auxiliary staysail schooner selected in part for her quiet acoustic characteristics. The experiment was primarily intended to observe internal waves in the New York Bight coincident with three consecutive ERTS-1 overpasses of that region (12 June, 30 June, 18 July), during the early summer, a season when previous ERTS observations of the periodic surface features had been most frequent (Apel et al., 1975).

The ship was instrumented with a salinity-temperature-depth device (STD), expendable bathythermographs (XBT), a horizontally towed underwater hull containing temperature and depth sensors, an echo sounder (20-kHz, 2-ms pulse, $12^{\circ} \times 15^{\circ}$ beam) that viewed vertically downward to delineate internal wave motion at depth (Proni and Apel, 1975), and color and infrared films for photographing surface features.

Preliminary Results of the Experiment

Measurements were made during approximately 20 days of ship operation and 16 separate spacecraft overpasses. Because of weather, it was not possible to obtain one set of simultaneous observations involving all of the available instrumentation. Nevertheless, an ample quantity of cross-correlated data was gathered to enable us to assert unequivocally that the spacecraft imagery does indeed contain surface manifestations of internal waves.

Figs. 1(a) & (b) illustrate the geographical area under investigation on 17 July 1974; a portion of the photographically enhanced ERTS-1 negative image (numbered 1724-14475-6) taken in the near-infrared between 700 and 800 nm; and a line drawing interpretation of the periodic surface features. The ship's track is located in the lower left-hand corner of Fig. 1(a), with the circle denoting its position at the time of the satellite overpass--1447.5 GMT--and the triangle the location of a well-defined internal wave field encountered later on, at approximately 2115 GMT. Four packets are visible in the image,

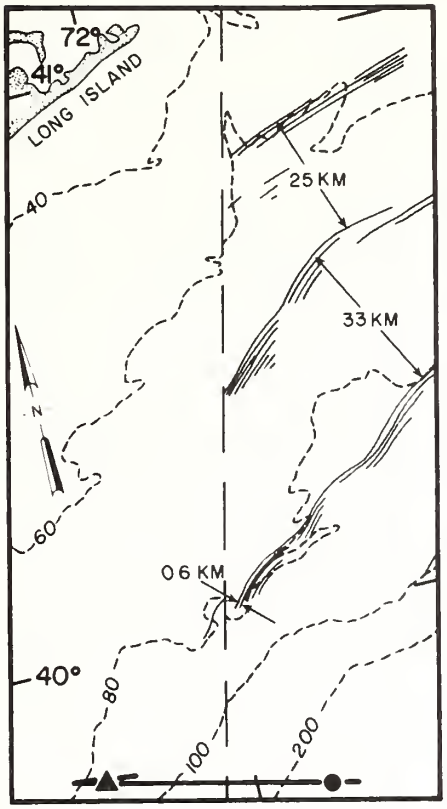

Figure 1(a) (Left). Line drawing showing internal wave packets south of Long Island (solid lines) overlain by isobaths in meters (dotted lines). Ship track at bottom shows position at time of ERTS-1 overpass (dot) and at encounter with internal wave packet (triangle). Vertical dashed line is western edge of spacecraft image. Figure 1(b) (Right). Section of negative image from ERTS showing internal wave field from which Figure 1(a) was derived. Dimensions 154 x 108 km^2. Black areas are clouds.

generally oriented along isobaths and separated by 24 to 33 km. They have wavelengths at the front of the packets ranging from approximately 400 to 1000 m and appear to be propagating shoreward, a view that is substantiated in part by the absence of packets seaward of the shelf break and in part by the observed doppler shifts discussed below.

No surface slicks were visible from the ship at the time of the overpass, nor are there any apparent at that point in the image. Nor would any waves be expected there, since the ship was beyond the edge of the shelf and hence outside of the boundary of the hypothesized generation region. However, at the position where the internal wave field was encountered (at the triangle), slicks were visible from the ship. Color photographs taken from the ship show that the slicks have the color of reflected skylight, in the low winds of 3 to 4 m/s; see Fig. 2.

Figure 3 illustrates temperature and acoustic data gathered during a maneuver involving course reversals that was executed through the region indicated by the triangle on Fig. 1. The upper trace shows the temperature at a depth of 29 m

Figure 2. Photo of internal wave slicks, taken from deck height (photo courtesy of R. L. Hughes).

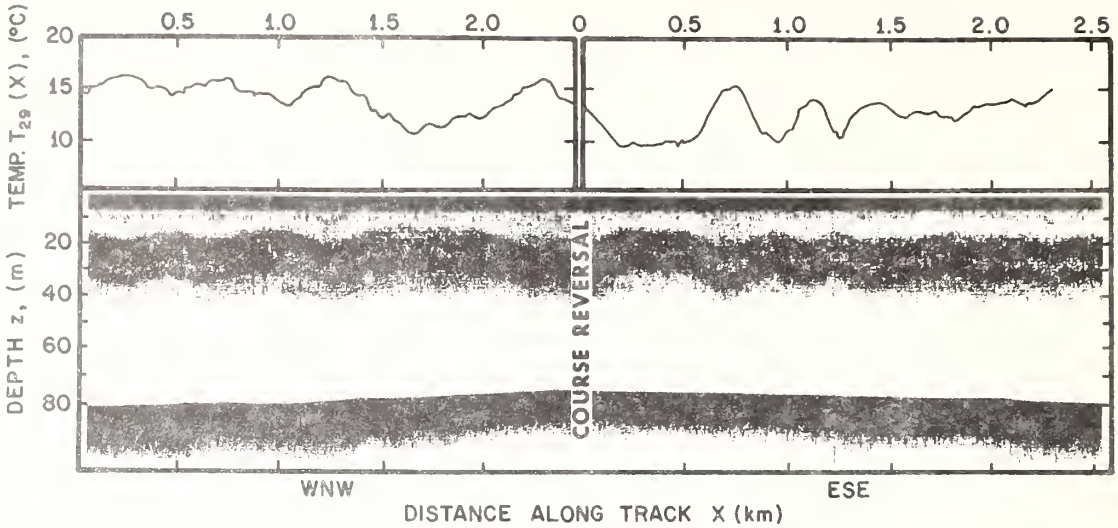

Figure 3 (upper). Temperature trace at 29 m depth taken near triangle on Figure 1; (lower). acoustic reflections from two scattering layers at 20 and 33 m depth, and from bottom at 80 m. Ship course was reversed midway through.

as obtained from the towed thermistor. The left half of the record was obtained during a 2.5-km segment of a west-northwest course, during which the internal wave packet of about 2 km total length was encountered; the right half shows the trace obtained during the reverse course. The left half shows down-shifted and the right half up-shifted oscillations. The maximum temperature excursions were of order 6°C. The lower record was obtained from the 20-kHz echo sounder and clearly shows two acoustic reflecting layers oscillating vertically with peak-to-trough amplitudes of approximately 15 m. The temperature and acoustic records are in very good correlation, with a 180° phase shift and with the troughs of the wave corresponding to downward-moving warm water from the mixed layer and the crests to upward-flowing cold water. An STD cast made approximately one-half hour before the onset of this wave packet showed a temperature profile which, if oscillated vertically by 15 m, would yield approximately the temperature excursions shown in the upper portion of Fig. 3.

This same graph can be used to derive the dominant wavelength, λ, period, T, and the projection of the internal wave phase velocity, $\vec{c}$, along the ship velocity, $\vec{u}$, by assuming negative and positive doppler shifts due to the ship motion on the reciprocal courses. From the down- and up-shifted wavelengths on that figure, one obtains approximately

$$\lambda \approx 500 \text{ m}, \quad T \approx 20 \text{ min}, \quad c \approx 0.35 \text{ m/s},$$

where a ship speed u = 1.5 m/s has been used. The phase and group speeds for a 500-m wavelength are about 0.5 m/s for λ = 500 m, as calculated from the observed density profile, for which $2\pi/N_{max} \simeq 140$ s.

Returning to Fig. 1, the wave packet that is closest to the one shown on Fig. 3 has a wavelength of approximately 600 m and a packet length of about 3 km, values quite near to those observed from the ship. In addition, the isophase lines of the packet appear to be nearly parallel to the isobaths, and it is quite reasonable to assume that the isophase fronts of the wave group marked by "0.6 km" can be extended toward the southwest parallel to the bottom topography, out of the ERTS picture and to the region of ship observation. During the seven-hour time delay between satellite overpass and shipboard measurements, the waves would have propagated only about ten km toward the northwest and could thus be expected at about the location shown. Assuming constant phase and group speeds of 0.35 m/s, the wave packet would progress about 33 km shoreward in 25 hr. This is close to the spatial intervals observed on Fig. 1, which suggests once-daily generation.

Additional spacecraft and shipboard data show weakly developed internal wave striations on 12 June 1974, a calm, moderately clear day. However, on 13 June 1974 no evidence of slicks was visible either on the ERTS image or from the ship; this was a day of fresh, 7-8 m/s northeasterly winds, and slicks apparently do not form under such conditions.

Another experiment (a) established that the echo-sounder was indeed quantitatively observing internal waves; and (b) showed the location of the reflecting layers relative to small-scale temperature gradients. Figure 4(a) (left) shows two XBT traces obtained on 1 July 1974; one was taken at the crest and the other at the trough of an internal wave packet that was propagating past the ship while it was adrift. The packet was accompanied by a well-defined series of slicks. The temperature traces show the thermocline oscillating up and down with approximately a 20-min period by an amount $\eta(z)$ that depends on depth z; by differencing the two traces, one may obtain the displacement, which is shown on the right. The lowest order mode is clearly

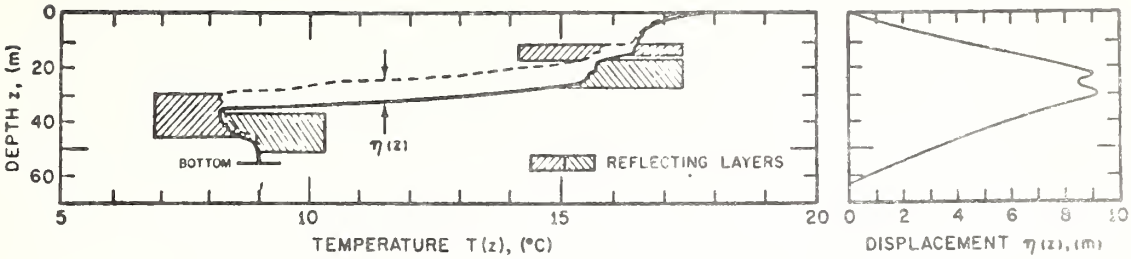

Figure 4 (Left). Temperature profile at internal wave trough (solid line) and crest (dotted line). Cross-hatching shows regions of intense acoustic reflections, as in Figure 3. (Right). Displacement of isotherms shows dominant first-order mode.

the dominant one, but higher order modes are also present. Coincident STD data demonstrate that the water column is statically stable, with the temperature inversion shown being offset by increased salinity in that region.

The coincident towed thermistor and echo-sounder records also yielded data on this internal wave field. These traces (not reproduced here) appear quite similar to those on Fig. 3. The acoustic record shows two reflecting laminae that undergo vertical excursions whose amplitudes and phases are in excellent agreement with those shown on the towed temperature and XBT records. The locations of these reflecting layers are indicated by the hatched regions of Fig. 4(a) and are clearly associated with depths where the macroscopic curvature of the temperature record, $\partial^2 T/\partial z^2$, is the largest. This is in accord with models of acoustic scattering from fluctuations in the index of refraction. Thus the experiment yields some evidence that, in addition to scattering from biological material--the mechanism that is usually invoked to explain such reflections--these signals may be partially returned from microstructure and turbulence in the water column.

Conclusions

The combined measurements of horizontal and vertical temperature variations, density structure, acoustic reflections, and spacecraft imagery have shown that the periodic features seen in ERTS images taken over the New York Bight are indeed surface slicks associated with oceanic internal waves; that such waves appear to be generated at the edge of this part of the continental shelf approximately once a day; that they propagate as intermittent high-frequency packets whose wavelengths, phase speeds, and periods are consistent with the vertical density profiles and depths for the area; and that they are detectable by high-frequency acoustic echo sounders. Thus the combination of spacecraft imagery, which yields synoptic scale data, and echo sounding, which provides amplitude information on a more restricted scale, appears to offer useful tools for investigations of higher-frequency internal waves on the continental shelves.

Acknowledgements. The authors are grateful to NASA for gathering open-ocean ERTS-1 data and to the officers, crew, and apprentices of the Westward for their help. This research was partially supported by funding from the Advanced Research Projects Agency, which assumes no responsibility for the content of this report.

References

Apel, J. R., H. M. Byrne, J. R. Proni, and R. L. Charnell, Observations of oceanic internal and surface waves from the Earth Resources Technology Satellite, J. Geophys. Res., 80, 865, 1975.

Halpern, D., Semidiurnal internal tides in Massachusetts Bay, J. Geophys. Res., 76, 6573, 1971.

Lee, C., and R. C. Beardsley, The generation of long nonlinear internal waves in a weakly stratified shear flow, J. Geophys. Res., 79, 453, 1974.

Proni, J. R., and J. R. Apel, On the use of high-frequency acoustics for the study of internal waves and microstructure, J. Geophys. Res. (to be published), 1975.

(Received November 11, 1974;
accepted March 14, 1975.)

Reprinted from: *Journal of Geophysical Research 80*, No. 9, 1147-1151.

On the Use of High-Frequency Acoustics for the Study of Internal Waves and Microstructure

JOHN R. PRONI AND JOHN R. APEL

NOAA Atlantic Oceanographic and Meteorological Laboratories, Miami, Florida 33149

Experimental data and theoretical calculations on the scattering of high-frequency acoustic signals from oceanic internal waves are presented. Acoustic data on internal waves are compared with simultaneous temperature (towed thermistor) data. The comparisons have shown a high degree of correspondence between the temperature and the acoustic data. Theoretical calculations for the acoustic scattering cross section σ are made by assuming that temperature fluctuations give rise to the acoustic scattering. An enhanced cross section for scattering from layered temperature fluctuations is to be expected, in agreement with the 1973 calculations of W. H. Munk and C. Garrett.

For some time it has been known that internal waves can be observed by using high-frequency (5- to 25-kHz) acoustic echo sounders [*Hersey*, 1962]. Chance observations of internal waves using high-frequency echo sounders have generally been attributed to scattering occurring from biological organisms riding upon isopycnal layers oscillating in the vertical due to the passage of internal waves. Recently, however, another mechanism has been proposed that may also contribute to making detectable scattering occur from internal waves. This mechanism is the scattering of high-frequency acoustic signals from temperature and density microstructure and microstructural fluctuations.

If it can be demonstrated that the vertical amplitudes and phase variations of upper-ocean internal waves can be measured by using echo sounders from ships and that these measurements do not necessarily rely on the presence of plankton and fish for their general utility, a new tool will be recognized that will enable rapid surveys of internal wave directional spectra to be made. These data, coupled with the synoptic view of wave patterns obtained from spacecraft [*Apel et al.*, 1975], would come close to specifying the three-dimensional vector wave field that is of ultimate interest.

The possibility of detection of oceanic internal waves via acoustic scattering from temperature microstructure fluctuations has received support from several different areas, some of which are as follows:

1. Theoretical calculations carried out by the coauthors and others [*Munk and Garrett*, 1973] indicate that an enhanced acoustic scattering cross section is possible for the type of layered microstructural fluctuations thought to be associated with internal waves.

2. Analogous experiments on acoustic echo sounding in the atmosphere [*Hall*, 1972] have clearly revealed atmospheric internal waves where there is an obvious absence of biological scatterers. Some additional experiments [*Little*, 1969] have been carried out by comparing in situ measurements of atmospheric microstructural fluctuations with those obtained acoustically, the result being that the microstructure seems theoretically and observationally capable of producing the backscatter.

3. Recent measurements on oceanic microstructure suggest a generally horizontally layered model of fluctuations with considerable fine structure present [*Woods*, 1968; *Osborn and Cox*, 1972]. This model is consistent with acoustic observations and supportive of layered acoustic scattering theory. Again measurements of microstructure and acoustic backscatter in the ocean imply that the temperature fluctuations are capable of backscattering at detectable levels.

The virtue of obtaining data on internal waves by using high-frequency acoustic echo sounding is that large volumes of data on both vertical and horizontal distributions of the waves can be gathered rapidly while the vessel is underway at speeds large in comparison with the phase speed of the waves. In other words, by this method, compared with thermistor chain towing, for example, a large-area synoptic body of data can be gathered relatively quickly. Directional spectra may be constructed by sampling along five-point star patterns, for instance, and the phase relationships between surface slicks and the underlying internal waves may be studied conveniently. (Mel Briscoe has correctly pointed out that perhaps a factor of 2 is involved in increased data over traditional thermistor methods. He has also mentioned the article by *Voorhis and Perkins* [1966] as indicating some limitations on obtaining internal wave spectra from moving platforms.) This kind of data is extremely valuable in its own right as well as essential for comparison with satellite data on internal waves.

Woods advances the model of a vertical stratification that consists of alternate homogeneous layers of meter thickness separated by narrow (e.g., 10-cm) sheets in which there exist sharp temperature gradients. We assume that these layers contain microstructural temperature fluctuations that are capable of scattering high-frequency acoustic signals. The regions of sharp relatively stable temperature gradients are apparently also capable of scattering high-frequency sound, as is mentioned earlier; the fact that a layering is present gives rise to an enhanced acoustic return. This model is considered in greater detail in the section on theoretical calculations. Finally, these layers and sheets are assumed to oscillate vertically with the passage of internal waves, their oscillation thus permitting high-frequency sound to be used to observe the internal waves.

EXAMPLE OF ACOUSTIC DATA

A typical example of the type of data obtained by the coauthors is shown in Figure 1. A 20-kHz hull-mounted echo sounder was used in obtaining the record shown in Figure 1. In this picture, time runs from left to right, time marks being placed every 5 min. The record was made in May 1970 approximately 320–480 km off the Ecuadorian coast. The deep

Copyright © 1975 by the American Geophysical Union.

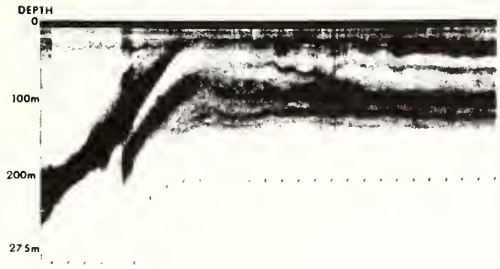

Fig. 1. Internal wave observations made during a rise of the scattering layer. Time marks are given every 5 min.

scattering layer (DSL) is plainly visible, rising from about 225 m at the left of the figure to a depth of less than 100 m at the center of the figure.

Notice a thin layer of high acoustic reflectivity at a depth of about 30 m at the left of Figure 1. This layer undergoes erratic oscillations with a gradual increase of the acoustic return. As time goes on, returns from this reflecting layer become merged with returns from the DSL as it rises; 20–25 min later a reflecting layer becomes visible again at about a depth of 30 m. In addition, other reflecting layers have also become visible at depths of 70, 100, and 130 m.

It appears from the data shown in Figure 1 and from a great deal of other similar data that the model of acoustic reflectors distributed in discrete vertical layers is tenable. Indeed these layers do appear to outline the vertical distribution of internal wave oscillations present. The fundamental questions are, of course, What are the sources of the acoustic return and how accurately does the acoustic record portray the vertical internal wave field distribution?

THEORETICAL CALCULATIONS

First a calculation is carried out for acoustic scattering from a completely homogeneous volume of temperature fluctuations (no layering is assumed). A calculation is then carried out for acoustic scattering from a layered region, and the results are compared with results from the homogeneous calculation. It is assumed in the homogeneous calculation that the temperature fluctuations can be characterized as having a Kolmogorov spectrum.

Acoustic scattering from homogeneous isotropic temperature fluctuations. The acoustic scattering cross section σ for this case can be written as [*Tatarski*, 1961]

$$\sigma(\theta) = 0.03\lambda^{-1/3} \cos^2\theta \left(\sin\frac{\theta}{2}\right)^{-11/3} \cdot \left[0.55\left(\frac{1}{C_0}\frac{\partial C}{\partial T}\right)^2 C_T^2 + \frac{C_V^2}{C_0}\cos^2\frac{\theta}{2}\right] \quad (1)$$

with the speed of sound in seawater written as

$$C(T) \cong 1449 + 4.62T - 0.05T^2 \quad \text{m/s} \quad (2)$$

and where

- $\sigma(\theta)$ acoustic scattering cross section per unit volume;
- θ scattering angle (for direct backscatter, $\theta = 180°$);
- λ acoustic wavelength;
- C sound speed;
- C_V structure constant for velocity fluctuations;
- T temperature, °K;
- C_T structure constant for temperature fluctuations.

Reliable measures of C_V and C_T are difficult to obtain. However, a survey of measured values for C_T in the ocean has been given by two Russian authors, *Gostev and Shvachko* [1969]. A representative value for C_T in the ocean is 10^{-1} deg $m^{-1/3}$. By way of comparison, C_T for the atmosphere is typically 5×10^{-2} deg $m^{-1/3}$. An estimate for $\sigma(180°)$, the direct backscatter case, can now be made.

For $\theta = 180°$ the expression for σ becomes

$$\sigma(180°) = (0.03)\cdot\lambda^{-1/3}\cdot(5 \times 10^{-1})\cdot\left(\frac{1}{C_0}\frac{\partial C}{\partial T}\right)^2 \cdot C_T^2 \quad (3)$$

At $T = 10°C$ and with $\lambda \cong 1.0 \times 10^{-1}$ m,

$$\sigma \cong 4 \times 10^{-10} \text{ m}^2/\text{m}^3 \quad (4)$$

An acoustic cross section of the magnitude given above is possibly detectable with present acoustic transmitting, receiving, and processing equipment. Estimates for C_V are available, but we shall not discuss velocity fluctuations except to note that, as can be seen from (1) and (2), everything contained within the brackets defined by (1) is positive definite. Therefore an additional contribution made to σ by C_V can only serve to increase the magnitude of σ as given by (1).

Acoustic scattering from nonisotropic temperature fluctuations. The preceding calculation for σ was carried out for isotropic homogeneous fluctuations with a Kolmogorov spectrum. Now, however, we must examine the case of high-frequency acoustic scattering from horizontally layered temperature and velocity fluctuations. To the authors' knowledge the first calculation of acoustic scattering from oceanic horizontally layered refractive index fluctuations appears to have been done by *Munk and Garrett* [1973]. Under certain layering conditions, Munk and Garrett show that scattering cross section increases of 10^3 m^2/m^3 are possible in certain scattering directions.

The general expression for the acoustic scattering cross section $d\sigma/d\Omega$ from a region of refractive index fluctuations is

$$\frac{d\sigma}{d\Omega} = \frac{\pi}{2}k^4 \iiint_{\text{all } \kappa} \phi_3(\kappa)\cdot I \cdot d\kappa \quad (5)$$

where

- k acoustic wave number;
- $\mathbf{K}$ difference wave vector between the incident and the scattered wave vector;
- κ refractive index fluctuation wave number vector;
- $\rho = \mathbf{r}_1 - \mathbf{r}_2$, difference vector between points $\mathbf{r}_1$ and $\mathbf{r}_2$ in the scattering region;
- $\phi_3(\kappa)$ three-dimensional spectral density of index of refraction fluctuations:

and for the layered geometry under consideration I can be approximated by

$$I \cong \frac{\Delta R_i^2}{4}\cdot\frac{\Delta R_i^2}{4}\cdot\frac{\Delta Z^2}{4} \quad (6)$$

where ΔR_i is the diameter of illumination and Δz is the vertical thickness of fluctuational layer for

$$K_x - \mathrm{K}_x \leq 2\pi/\Delta R_i$$

$$K_y - \mathrm{K}_y \leq 2\pi/\Delta R_i$$

$$K_z - \mathrm{K}_z \leq 2\pi/\Delta z$$

and zero elsewhere.

Then

$$\frac{d\sigma}{d\Omega} = \frac{4k^4}{\pi} \int_{K_x-(2\pi/\Delta R_i)}^{K_x+(2\pi/\Delta R_i)} \int_{K_y-(2\pi/\Delta R_i)}^{K_y+(2\pi/\Delta R_i)} \int_{K_z-(2\pi/\Delta Z)}^{K_z+(2\pi/\Delta Z)} \frac{\Delta R_i^4}{16} \cdot \frac{\Delta Z^2}{4} \phi_3(\kappa)\, d\kappa_z\, d\kappa_x\, d\kappa_y \qquad (7)$$

The layered geometry also puts restrictions directly on $\phi_3(\kappa)$ and indirectly on **K**.

Our layered model assumes that all vertical (i.e., z) fluctuation wavelengths are less than a layer thickness; hence $\phi_3(\kappa) \neq 0$ for

$$\kappa_z \geq 2\pi/\Delta Z \qquad (8)$$

The restriction on the horizontal wave number $\kappa_r(=(\kappa_x^2 + \kappa_y^2)^{1/2})$ is not modeled so easily as that for κ_z (given by (8)). Munk and Garrett assume a relationship between κ_z and κ_r, namely

$$\kappa_r \leq \alpha\kappa_z \qquad (9)$$

where α is a constant, and also assume that when the above condition is satisfied, one may write

$$\phi_3(\kappa_z, \kappa_x, \kappa_y) \cong \phi_3(\kappa_z) \qquad (10)$$

In the present development a different point of view is taken with regard to the above assumptions. By using an assumption different from that in (9) but in agreement with that in (9) a different scattering dependence on acoustic wavelength appears. A restriction that may be imposed on κ_r for a wide variety of possible fluctuation spectra is that

$$\kappa_r \leq 2\pi/\Delta R_c \qquad (11)$$

where ΔR_c is the horizontal fluctuation correlation distance. This is a measure of the width of the spectrum in horizontal wave number space. As of yet no relation has been made between the allowable range for κ_z and that for κ_r. To recover the two assumptions of Munk and Garrett (but in an amended form), we ourselves make the following assumptions: (1) $\Delta R_c > \Delta Z$ and (2) $\Delta R_i < \Delta R_c$. From assumption 1 it follows immediately that the allowable range of values for κ_z is greater than that for κ_r; i.e., allowable κ_z is greater than allowable κ_r. From assumption 2, assumption (10) of Munk and Garrett follows, since assumption 2 implies that over any given area illuminated by an acoustic beam, no appreciable fraction of a fluctuation wavelength is incorporated (i.e., near-specular conditions are present). To reiterate, by not making assumption (9) in the form of Munk and Garrett, a different dependence on acoustic wavelength of the acoustic scattering cross section will emerge. Also beam width information is contained in the factor I and does not come directly from the relation between κ_z and κ_r.

Thus according to our model, only a certain volume in κ space (a cylinder) contains fluctuation wavelengths. Only in this volume will impinging **K** (acoustic difference vectors) encounter fluctuation wavelengths from which to scatter. This volume may be symmetric about the κ_z axis, or it may not be.

Now

$$\phi_1(\kappa_z) \equiv \int_{\text{all } \kappa_x, \kappa_y} \int \phi_3(\kappa_z, \kappa_x, \kappa_y)\, d\kappa_x\, d\kappa_y \qquad (12)$$

or

$$\phi_1(\kappa_z) = 2 \int_{-2\pi/\Delta R_{cy}}^{2\pi/\Delta R_{cy}} \int_{-2\pi/\Delta R_{cx}}^{2\pi/\Delta R_{cx}} \phi_3(\kappa_z, \kappa_x, \kappa_y)\, d\kappa_x\, d\kappa_y \qquad (13)$$

(Henceforth we take $\Delta R_{cx} = \Delta R_{cy} = \Delta R_c$, where ΔR_c is the horizontal correlation distance of the temperature fluctuations.) We assume, following Munk and Garrett and assumption 2, that $\phi_3(\kappa_z, \kappa_x, \kappa_y) \cong \phi_3(\kappa_z)$. Then

$$\phi_3(\kappa_z) = (\Delta R_c^2/32\pi^2)\phi_1(\kappa_z) \qquad (14)$$

with $\phi_3(\kappa_z) = 0$ when either

$$|K_x| \geq 2\pi/\Delta R_c \qquad (15a)$$

$$|K_y| \geq 2\pi/\Delta R_c \qquad (15b)$$

$$|K_z| < 2\pi/\Delta Z \qquad (15c)$$

We may now write (7) as

$$\frac{d\sigma}{d\Omega} = \frac{4k^4}{\pi} \int_{K_x-(2\pi/\Delta R_i)}^{K_x+(2\pi/\Delta R_i)} \int_{K_y-(2\pi/\Delta R_i)}^{K_y+(2\pi/\Delta R_i)} \int_{K_z-(2\pi/\Delta Z)}^{K_z+(2\pi/\Delta Z)} \frac{\Delta R_i^4}{16} \cdot \frac{\Delta Z^2}{4} \frac{\Delta R_c^2}{32\pi^2} \phi_1(\kappa_z)\, d\kappa_z\, d\kappa_x\, d\kappa_y \qquad (16)$$

(Christopher Mooers has kindly pointed out that the integral over κ_z in (16) should be broken into two integrals with limits of integration from $-\infty$ to $K_z - (2\pi/\Delta Z)$ and from $K_z + (2\pi/\Delta Z)$ to $+\infty$, respectively; this is, of course, correct, so that one must add that the contributions at $+\infty$ and $-\infty$ are zero (for the spectrum given in (17)) and do not affect the resulting value of the integral.)

A possible form for $\phi_1(\kappa_z)$ according to *Gregg and Cox* [1972] is

$$\phi_1(\kappa_z) = B\kappa_z^{-2} \qquad (17)$$

where $B = 5 \times 10^{-10}$.

Substituting (17) into (16) and integrating, one has

$$\frac{d\sigma}{d\Omega} = \frac{k^4}{32} B \cdot \Delta R_c^2 \cdot \Delta R_i^2 \cdot \Delta Z \left[\frac{16\pi^2}{\lambda^2} \sin^2 \frac{\theta}{2} - \frac{4\pi^2}{\Delta Z^2}\right]^{-1} \qquad \left|\sin \frac{\theta}{2}\right| > \frac{1}{2}\frac{\lambda}{\Delta Z} \qquad (18)$$

where θ is the angle between incoming and scattered (received) acoustic transmissions.

We can now make a numerical estimate for $d\sigma/d\Omega$. We take for vertical incidence

$$K_z = 2 \cdot k = 1.67 \times 10^{+2}\ \text{m}^{-1} \qquad (19)$$

(at 20 kHz, $\lambda = 7.5$ cm). We take $\Delta z = 5$ m, and then

$$\frac{1}{\Delta R_i^2 \Delta Z} \cdot \frac{d\sigma}{d\Omega} \cong \frac{k^4}{32} \cdot \frac{5 \times 10^{-10}}{(1.7 \times 10^2)^2} \cdot \Delta R_c \qquad (20)$$

or

$$d\sigma'/d\Omega = 2.8 \times 10^{-8} \cdot \Delta R_c \qquad \sigma' \equiv \sigma/\Delta R_i^2 \Delta Z \qquad (21)$$

We take for ΔR_c, $\Delta R_c = 20$ m. (Different researches report values of ΔR_c ranging in size from the order of meters [*Leibermann*, 1951] to the order of tens of meters [*Black*, 1965]. A value 10 m is chosen as a reasonable numerical estimate for ΔR_c.) Then

$$d\sigma'/d\Omega \cong 2.8 \times 10^{-7}\ \text{m}^2/\text{m}^3 \qquad (22)$$

per unit solid angle, which is a significant increase over the value given for nonlayered scattering in (4).

Note that for $\lambda \ll \Delta z \cdot \sin(\theta/2)$,

$$\frac{d\sigma}{d\Omega} \cong \frac{\pi^2 B \Delta R_c^2 \Delta R_i^2 \Delta Z}{8 \sin^2 \theta/2} \lambda^{-2} \qquad (23)$$

Thus $d\sigma/d\Omega$ varies with λ^{-2}.

In summary then, under conditions of layered acoustic temperature and density fluctuations, compared with three-dimensional isotropic fluctuations, two major differences appear: (1) An enhanced acoustic return of perhaps 20 dB or so over three-dimensional fluctuations is observed. (2) A λ^{-2} acoustic wavelength dependence is observed, as compared with $\lambda^{-1/3}$ for three-dimensional fluctuations and λ^{-4} for particulate matter [*Tatarski*, 1961].

The latter result suggests that a multifrequency system would be useful in providing information on the nature of the acoustic scatterers. This conclusion is well known and arises from other acoustic studies such as scattering from bubbles.

Additional Example of Acoustic Data

(The data in this section may be compared with those obtained by *Curtin and Mooers* [1975] along the west coast of the United States.)

The following data were gathered on the U.S. continental shelf off New York (40°7.25′N, 71°34′W) on June 30, 1974. The data shown here were gathered during the New York to Bermuda remote sensing experiment. This is the area referred to in the paper by *Apel et al.* [1975].

Acoustic reflections from a packet of internal waves are shown in Figure 2. The packet is propagating shoreward (to the right in the figure) in water of 85-m depth. Immediately below the acoustic record of the packet is a temperature record made by using a towed thermistor. The thermistor was towed in a vee fin device with minimal vertical movement. (The total vertical excursion for the duration of the record shown in Figure 2 was less than 1.2 m, the vee fin being centered at a depth of 31 m.) The records represent Doppler-shifted internal waves, the ship proceeding at about 2.5 m/s in the general direction of propagation of the wave packet, as is evidenced by surface slicks and bottom topography. It can be seen that correlated oscillations occur in both records (to quantify the correspondence between the two records, the cross correlation is presently being calculated for a many-kilometer-long stretch, of which the data in Figure 2 form a part). Note that troughs in the acoustic signal correspond to troughs in the temperature trace; i.e., warm water is sweeping by the towed thermistor.

A periodogram for acoustic records is shown in Figure 3; also shown in Figure 3 is an expendable bathythermograph record taken during the encounter with the internal wave packet. Note that the dominant peak in both records occurs at $K = 2.2$ cycles/km, or $\lambda = 450$ m. This is roughly the dominant wavelength that one would eyeball-estimate from the data records of Figure 2. This periodogram was made from data that were demeaned, detrended (i.e., a linear trend), and cosine-tapered. The wave packet is a transient phenomenon of limited duration. The periodogram has 2 d.f.

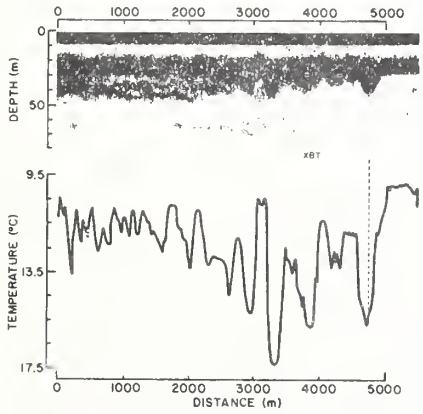

Fig. 2. Acoustic and temperature traces for an internal wave packet. (Note the location of the XBT mark.)

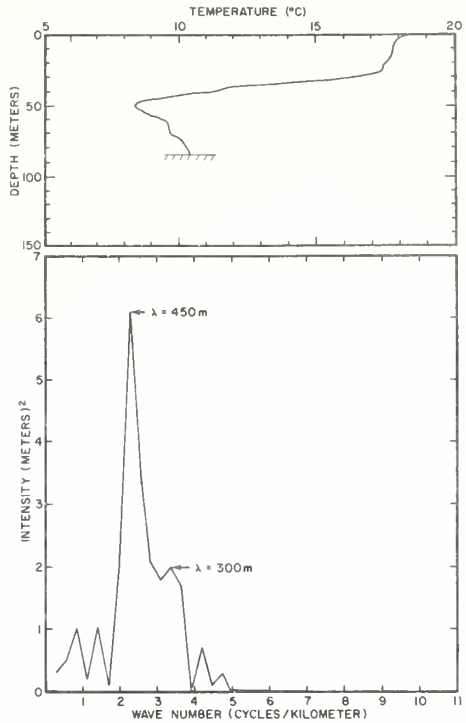

Fig. 3. (Top) XBT trace made during the passage of the packet shown in Figure 2. (Bottom) Periodogram for the acoustic trace shown in Figure 2. (This is not a variance-preserving plot.)

(There is an interesting problem here in spectral analysis. The high-frequency/short-wavelength internal waves present in New York to Bermuda remote sensing experiment NYBERSEX) data occur in the form of discreet packets. These packets appear to contain only a few cycles (e.g., 5–10) of the dominant internal wave wavelengths. Thus the number of degrees of freedom attainable is limited. The process of packet generation is intermittent (e.g., semidiurnal tidal excitation) and is nonstationary and nonhomogeneous. Furthermore, the internal wave amplitude η regarded as a random variable is non-Gaussianly distributed (η is distributed in fact somewhat as a sine distribution).

The approach taken in this paper may be compared with that of *Halpern* [1971], in which a sequence of internal wave packets was analyzed as a unified time series. By using Halpern's approach a high number of degrees of freedom are available. In this paper, one realization of a wave packet is analyzed.)

An amplitude estimate based on the temperature record can be constructed by using the XBT data and the towed thermistor data. Assuming the amplitude η can be written as [*Defant*, 1961]

$$\eta \cong -\Delta T \Big/ \left(\frac{dT}{dZ}\right)_{31\,\mathrm{m}}$$

(T is temperature) one has, using a value of ΔT taken from the

peak-to-peak oscillation present in the 3000- to 3500-m range,

$$\eta \cong (17.4° - 10.5°)/0.38°C/m = 18.1 \text{ m}$$

Reading directly from the acoustic record, one has a double amplitude of approximately 18–20 m. This comparison has been made for only a small portion of the internal wave packet, but if one assumes that dT/dZ does not vary much over the length of the packet, several points for amplitude estimate comparisons can be had. In general, the acoustic and temperature internal wave amplitude estimates have been found to lie within 10% of one another. The greatest source of uncertainty in reading the internal wave amplitudes from the acoustic records lies in the width of the acoustic trace. (Flow noise, ship motion, and cavitation noise all contribute to the widening of the acoustic trace.) The records can he enhanced by signal processing (the data are recorded on magnetic tapes), so that less ambiguous amplitude estimates can be made.

SUMMARY AND CONCLUSIONS

It appears that high frequency acoustics may be a more potent tool for the study of internal waves than has been suspected in the past. This will be particularly true if, as is indicated in this paper, the acoustic technique does not have to rely upon the presence of biological or other material to outline the presence of internal waves. The calculations presented in this paper indicate a higher expected acoustic scattering cross section from layered fluctuations than from nonlayered fluctuations provided the many assumptions made in the calculations prove to be correct. The fundamental question remaining, of course, concerns which type of scatterer is contributing which part of the acoustic return. It appears that extensive research remains to be carried out in order to determine the relative contribution of such ocean features as temperature microgradients, temperature fluctuations, turbulence, biological material, gas microbubbles, and suspended sediments to acoustic return in various oceanic conditions.

ADDITIONAL COMMENTS

The NYBERSEX cruise, recently (July–August 1974) carried out by the Ocean Remote Sensing Laboratory of NOAA, had the goal of obtaining concurrent satellite and acoustic data on internal waves. Goals of the cruise included obtaining acoustic records concurrently with the passage of surface slicks or signatures of internal waves (see the accompanying paper by Apel et al. in this issue). Goals also included studying the correlation of isotherm oscillations, temperature step oscillations, and acoustic records of internal wave oscillations. Preliminary reduction of some of the data (some of which were presented) from this cruise indicates a significant degree of correlation among temperature, surface slick, and acoustic records.

This paper has dealt with high-frequency (5- to 25-kHz) acoustic interactions with internal waves. Not discussed has been the field of low-frequency (e.g., 5-Hz to 5-kHz) acoustic interactions with internal waves. The prime effect of internal waves on low-frequency sound propagation is on the propagation times of acoustic signals from source to receiver. Several researchers over the last 20 or so years have studied the effects of internal waves on low-frequency multipath acoustic propagation [*Clark and Kronengold*, 1974]. There have also been experiments in which concurrent high- and low-frequency acoustic measurements on internal waves have been made [*Weston et al.*, 1970]. One of the most interesting current research problems in the propagation of long-range low-frequency acoustic signals is determining how to use a best model of an internal wave spectrum to predict the spectrum of acoustic phase fluctuations. An exciting possibility is that if satellite observations prove to be a means of obtaining reasonable estimates of internal wave fields in a given area, then it may prove to be possible to make predictions on what range of fluctuations may be imposed on acoustic signals by the internal wave field in that area. From illustrations contained in the paper by Apel et al. it is clear, for example, that there is a significant difference between the type of internal wave field modulation to be expected in shelf areas and that to be expected in the deep ocean.

Acknowledgments. Melvin Briscoe and Christopher Mooers provided many useful comments and criticisms. Manuel Huerta, Henry Diaz, and Fred Newman assisted in clarifying the ideas in this paper. Thanks are extended to them all.

REFERENCES

Apel, J. R., H. M. Byrne, R. L. Charnell, and J. R. Proni, Observations of oceanic internal and surface waves from the Earth Resources Technology satellite, *J. Geophys. Res.*, *80*, 865–871, 1975.

Black, C. F., *The Turbulent Distribution of Temperature in the Ocean*, Bissett-Berman Corporation, Santa Monica, Calif., 1965.

Clark, J. G., and M. Kronengold, Long period fluctuations of CW signals in deep and shallow water, *J. Acoust. Soc. Amer.*, *56*(4), 1071–1083, 1974.

Curtin, T. B., and C. N. K. Mooers, Observation and interpretation of a high-frequency internal wave packet and surface slick pattern, *J. Geophys. Res.*, *80*, 872–894, 1975.

Defant, A., *Physical Oceanography*, vol. 2, p. 537, Pergamon, New York, 1961.

Gregg, M., and C. Cox, The vertical microstructure of temperature and salinity, *Deep Sea Res.*, *19*, 355–376, 1972.

Gostev, V. S., and R. F. Shvachko, The microstructure of the temperature field in the ocean, *Atmos. Ocean Phys.*, *5*(10), 1066–1074, 1969.

Hall, F. F., Acoustic remote sensing of temperature and velocity structure in the atmosphere, Collected Reprints: 1970–1971, pp. 168–181, Wave Propagation Lab., Boulder, Colo., 1972.

Hersey, J. B., Sound scattering by marine organisms, in *The Sea*, vol. 1, pp. 498–566, U.S. Government Printing Office, Washington, D.C., 1962.

Halpern, D., Semidiurnal internal tides in Massachusetts Bay, *J. Geophys. Res.*, *76*, 6573–6584, 1971.

Liebermann, L., The effect of temperature inhomogeneities in the ocean on the propagation of sound, *J. Acoust. Soc. Amer.*, *23*, 563–570, 1951.

Little, C. G., Acoustic methods for the remote probing of the lower atmosphere, *Proc. IEEE*, *57*(4), 571–578, 1969.

Munk, W. H., and C. Garrett, Internal wave breaking and microstructure (the chicken and the egg), *Boundary Layer Meteorol.*, *4*, 37–45, 1973.

Tatarski, V. I., *Wave Propagation in a Turbulent Medium*, chap. 4, McGraw-Hill, New York, 1961.

Voorhis, A. D., and H. T. Perkins, The spatial spectrum of short-wave temperature fluctuations in the near surface thermocline, *Deep Sea Res.*, *13*, 641–654, 1966.

Weston, D. E., J. Review, F. R. Jones, and J. W. Ranster, An echo-sounding record and a sound transmission record showing internal waves, *Rep. ARL/L/R88*, Admiralty Res. Lab., Teddington, Middlesex, England, 1970.

Woods, J. W., Wave-induced shear instability in the summer thermocline, *J. Fluid Mech.*, *32*, 791–800, 1968.

(Received April 25, 1974;
accepted November 4, 1974.)

Reprinted from: Nature 254, No. 5499, 413-415.

Acoustic observations of suspended particulate matter in the ocean

CLOUDS of suspended particulate matter in the ocean have been observed by satellite[1], sensed by nephelometers[2], and sampled by water bottles. We present here evidence that it may be possible to observe oceanic suspended particulate matter acoustically. The particulate matter discussed is thought to have arisen from a dredging operation. It is also thought that the suspended matter is present at lower concentrations than any in any other case recorded acoustically[3]. Certain questions, as yet unresolved, regarding acoustic scattering strengths are also discussed.

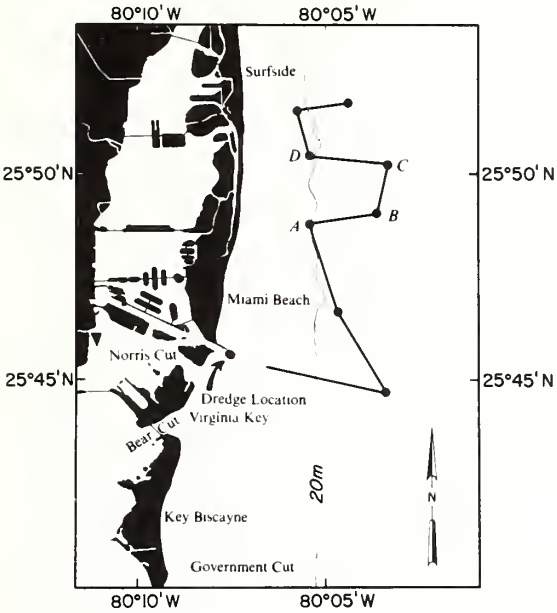

Fig. 1 Typical trackline in area of investigation (May 22, 1974, RV Virginia Key). A–D indicates locations shown on Fig. 2.

An experiment to determine the feasibility of acoustic surveys of suspended sediments was conceived during field testing of a 20-kHz LODAR echo-sounding system. The LODAR system has a downward-looking acoustic beam of 12° by 18° and a pulse duration of 2.2 ms. Initial acoustic records of a cloud-like feature were coincident with visual sightings of suspended sediment down-current of a working dredge. During this initial experiment, the dredge was operating for five days out of eight and data were taken on both incoming and outgoing tides. In conjunction with the LODAR records, measurements were made with expendable bathythermographs (XBTs) and a continuous recording light beam transmissometer (LBT).

On the five days when the hydraulic suction dredge was working, a visible cloud of suspended sediment and the acoustic 'cloud' were observed down-current of the dredge. On incoming tides the sediment flowed into the bay where the water is too shallow to operate the LODAR system. On outgoing tides the suspended sediment flowed out of the channel; the surface manifestation disappeared between 200 and 600 m seaward of the channel, depending on the state of the sea. Figure 1 is a typical trackline and Fig. 2 is the acoustic record from part of that track. The same general trackline was traversed each day. The minimum volume of the cloud estimated from acoustic records was about 60,000 m^3. During the three days when the dredge was not in operation, clouds were not observed either by the acoustic equipment or by visual observation of any surface manifestation.

The continuous recording LBT records the percentage transmission of a beam of white light 2 cm in diameter over a 1-m path; filters maximise the sensitivity at 475 nm. Although the light transmission characteristics involve more than one parameter[3,4], the instrument is useful for obtaining approximate particulate concentrations and distributions. LBT station depths were limited by the length of telemetering cable aboard, but shallow casts (less than 100 m) indicated a reduction in transmittance of between 10% and 15% in the upper regions of the cloud. The developed cloud occupied a region between inflection points on the XBT temperature traces (Fig. 3). A volumetric concentration on the order of 0.01–1%, obtained from the acoustic data, enabled us to carry out a first-cut check of acoustic and transmissometer readings. For the LBT used[5], a reduction in transmittance from 85% to 60% implies a particulate concentration of roughly 0.03%, so that the acoustic and transmissometer devices are consistent.

The observed acoustic 'cloud' cannot be accounted for either by temperature anomalies or by a package of contaminated bay water which would occur independently of dredging operations (see ref. 6). Temperature anomalies, however, seem to influence the location in depth of the acoustic cloud which occupies a region between inflection points on the XBT records (Fig. 3). This observation is consistent with the finding that temperature-induced density gradients are an important controlling factor in the transport of fine-grained sediment[7]. Large biological reflectors cannot account for the cloud as there is no evidence of point source reflectors on the records. The possible role of small biota in producing such a cloud requires further investigation. Although unlikely, the stirring up of bottom nutrients by the dredging operation may have produced a short-lived bloom of microscopic biota.

It is unlikely that the cloud results from microbubbles produced by organic processes in the sediment and released by

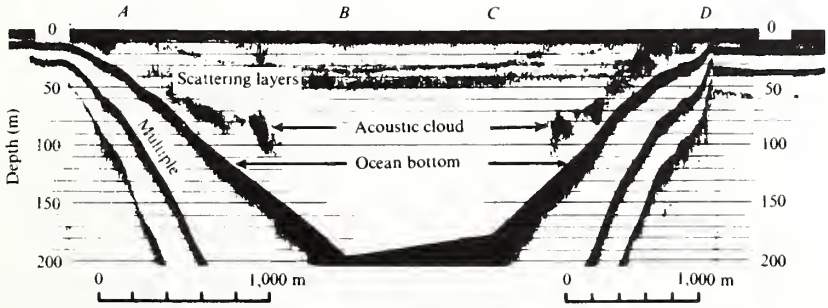

Fig. 2 Acoustic LODAR record along typical trackline, locations as indicated on Fig. 1. The shallow scattering layer is indicated. May 22, 1974.

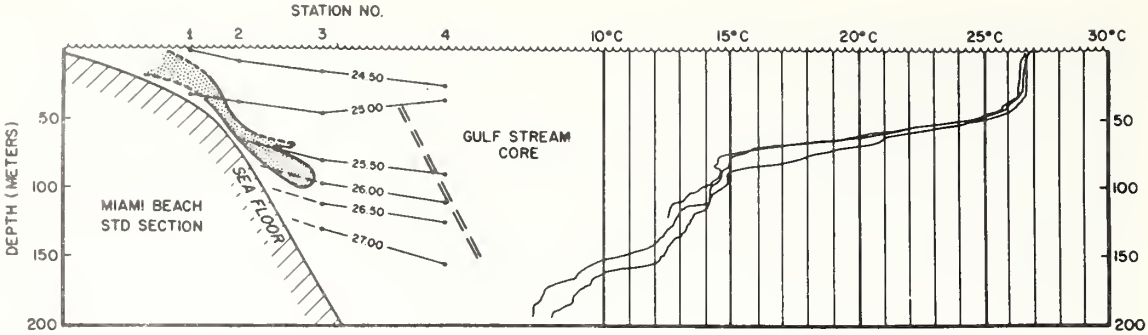

Fig. 3 Sketch of the acoustic cloud with overlay of Sigma-T (σ_T) curves (T. Lee and D. Mayer of National Oceanic and Atmospheric Administration) with XBTs on same scale, May 22, 1974. $\sigma_T \equiv (\rho - 1) \times 1{,}000$ where ρ = water density). σ_T is obtainable from STD (salinity-temperature-depth) measurements. Gulf Stream core based on salinity of March 27, 1974.

the dredging operation. An extraordinary amount of decay of organic matter would have to occur to produce clouds of the magnitude observed on every outgoing tide when the dredge was in operation. Such extraordinary quantities would have been observed as seeps emanating from the bottom when the dredge was inoperative.

The observed behaviour and properties of the acoustic cloud support our interpretation that it is the product of acoustic scattering from suspended sediment particles in the water column. The nature of a suspended sediment cloud and its movements would be affected by the tides, temperature-induced density gradients, and the northward flow of the Gulf Stream current. The observed cloud varied in size, shape, and location corresponding to the changes in dredging operations and tides. The tides affect both the direction of flow in Government Cut and the flow of warmer bay waters out to sea on outgoing tides, thus inducing the density gradients at the outflow of the cut. Also, the observed acoustic clouds moved to the north on leaving the cut, with the easternmost extent of the cloud approaching the Gulf Stream.

How is it, though, that particles with diameters that may be of the order of 1–100 μm can reflect detectable sound signals at 20 kHz? The present hypothesis is that the sediment cloud may have regions of relatively high particulate concentration which are detectable but not resolvable using the acoustic system described here. Studies are under way to determine the validity of that hypothesis.

Theoretical work and further field work are under way to develop what may prove to be a valuable survey tool, with immediate applications for the sedimentologist, geologist, ecologist and pollution monitoring agencies.

Dr David Drake assisted with the transmissometer measurements; his comments and advice are appreciated. We thank the referee who pointed out the consistency check between the acoustic level received and the transmissivity decrease.

J. R. Proni
D. C. Rona
C. A. Lauter Jr
R. L. Sellers

Atlantic Oceanographic and Meteorological Laboratories,
Environmental Research Laboratories,
National Oceanic and Atmospheric Administration,
Miami, Florida 33149

Received December 11, 1974; revised February 25, 1975.

[1] Klemas, V., Borchardt, J. F., and Treasure, W. M., *Remote Sensing of Environment*, 2 (4) (1973).
[2] Ewing, M., and Thorndike, E. M., *Science*, **147**, 1291–1294 (1965).
[3] Gallenne, B., *Estuar. coast. mar. Sci.*, 2, 261–272 (1974).
[4] Jerlov, N. G., *Optical Oceanography* (Elsevier, Amsterdam, 1968).
[5] Beardsley, G. F., Pak, H., Carder, K., and Lundgren, B., *J. geophys. Res.*, 75, 2837–2845 (1970).
[6] Proni, J. R., and Apel, J. R., *J. geophys. Res.* (in the press).
[7] Drake, D. E., *Shelf Sediment Transport* (edit. by Swift, D. J. P., Duane, D. B., and Pilkey, O. H.), 307–331 (Dowden, Hutchinson, and Ross, Stroudsburg, 1972).

Printed in Great Britain by Henry Ling Ltd., at the Dorset Press, Dorchester, Dorset

☆ U.S. Government Printing Office: 1977-778-938/160 Region 8

PENN STATE UNIVERSITY LIBRARIES
A000072832714